

**HIGH PERFORMANCE  
CONTROL OF AC  
DRIVES WITH  
MATLAB/SIMULINK  
MODELS**

# **HIGH PERFORMANCE CONTROL OF AC DRIVES WITH MATLAB/SIMULINK MODELS**

**Haitham Abu-Rub**

Texas A&M University at Qatar, Qatar

**Atif Iqbal**

Qatar University, Qatar and Aligarh Muslim University, India

**Jaroslav Guzinski**

Gdansk University of Technology, Poland



A John Wiley & Sons, Ltd., Publication

This edition first published 2012  
© 2012 John Wiley & Sons Ltd

*Registered office*

John Wiley & Sons Ltd, The Atrium, Southern Gate, Chichester, West Sussex, PO19 8SQ, United Kingdom

For details of our global editorial offices, for customer services and for information about how to apply for permission to reuse the copyright material in this book please see our website at [www.wiley.com](http://www.wiley.com).

The right of the author to be identified as the author of this work has been asserted in accordance with the Copyright, Designs and Patents Act 1988.

All rights reserved. No part of this publication may be reproduced, stored in a retrieval system, or transmitted, in any form or by any means, electronic, mechanical, photocopying, recording or otherwise, except as permitted by the UK Copyright, Designs and Patents Act 1988, without the prior permission of the publisher.

Wiley also publishes its books in a variety of electronic formats. Some content that appears in print may not be available in electronic books.

Designations used by companies to distinguish their products are often claimed as trademarks. All brand names and product names used in this book are trade names, service marks, trademarks or registered trademarks of their respective owners. The publisher is not associated with any product or vendor mentioned in this book. This publication is designed to provide accurate and authoritative information in regard to the subject matter covered. It is sold on the understanding that the publisher is not engaged in rendering professional services. If professional advice or other expert assistance is required, the services of a competent professional should be sought.

MATLAB® is a trademark of The MathWorks, Inc. and is used with permission. The MathWorks does not warrant the accuracy of the text or exercises in this book. This book's use or discussion of MATLAB® software or related products does not constitute endorsement or sponsorship by The MathWorks of a particular pedagogical approach or particular use of the MATLAB® software.

*Library of Congress Cataloging-in-Publication Data*

Abu-Rub, Haithem.

High performance control of AC drives with MATLAB/Simulink models / Haitham

Abu Rub, Atif Iqbal, Jaroslaw Guzinski.

p. cm.

Includes bibliographical references and index.

ISBN 978-0-470-97829-0 (hardback)

1. Electric motors, Alternating current—Computer simulation. 2. Electric motors, Alternating current—Automatic control. 3. MATLAB. 4. SIMULINK. I. Iqbal, Atif. II. Guzinski, Jaroslaw. III. Title.

TK2781.A28 2012

621.46—dc23

2011052004

A catalogue record for this book is available from the British Library.

Print ISBN: 9780470978290

Typeset in 10/12pt Times by Thomson Digital, Noida, India

*Dedicated to my parents, my wife Beata, and my children Fatima,  
Iman, Omar, and Muhammad.*

*—Haitham Abu-Rub*

*Dedicated to my parents, parents in-law, my wife Shadma, and my kids  
Abuzar, Noorin, and Abu Baker who have inspired me to write this book.*

*—Atif Iqbal*

*Dedicated to my parents, my wife Anna, and my son Jurek.*

*—Jaroslaw Guzinski*

# Contents

<b>Acknowledgment</b>	<b>xiii</b>
<b>Biographies</b>	<b>xv</b>
<b>Preface</b>	<b>xvii</b>
<b>1 Introduction to High Performance Drives</b>	<b>1</b>
1.1 Preliminary Remarks	1
1.2 General Overview of High Performance Drives	6
1.3 Challenges and Requirements for Electric Drives for Industrial Applications	10
1.3.1 <i>Power Quality and LC Resonance Suppression</i>	11
1.3.2 <i>Inverter Switching Frequency</i>	12
1.3.3 <i>Motor Side Challenges</i>	12
1.3.4 <i>High dv/dt and Wave Reflection</i>	12
1.3.5 <i>Use of Inverter Output Filters</i>	13
1.4 Organization of the Book	13
References	16
<b>2 Mathematical and Simulation Models of AC Machines</b>	<b>19</b>
2.1 Preliminary Remarks	19
2.2 DC Motors	19
2.2.1 <i>Separately Excited DC Motor Control</i>	20
2.2.2 <i>Series DC Motor Control</i>	22
2.3 Squirrel Cage Induction Motor	25
2.3.1 <i>Space Vector Representation</i>	25
2.3.2 <i>Clarke Transformation (ABC to <math>\alpha\beta</math>)</i>	26
2.3.3 <i>Park Transformation (<math>\alpha\beta</math> to dq)</i>	29
2.3.4 <i>Per Unit Model of Induction Motor</i>	30
2.3.5 <i>Double Fed Induction Generator (DFIG)</i>	32
2.4 Mathematical Model of Permanent Magnet Synchronous Motor	35
2.4.1 <i>Motor Model in dq Rotating Frame</i>	36
2.4.2 <i>Example of Motor Parameters for Simulation</i>	38
2.4.3 <i>PMSM Model in Per Unit System</i>	38
2.4.4 <i>PMSM Model in <math>\alpha</math>-<math>\beta</math> (x-y)-Axis</i>	40
2.5 Problems	42
References	42

<b>3</b>	<b>Pulse Width Modulation of Power Electronic DC-AC Converter</b>	<b>45</b>
3.1	Preliminary Remarks	45
3.2	Classification of PWM Schemes for Voltage Source Inverters	46
3.3	Pulse Width Modulated Inverters	46
3.3.1	<i>Single-Phase Half-bridge Inverters</i>	46
3.3.2	<i>Single-Phase Full-bridge Inverters</i>	54
3.4	Three-phase PWM Voltage Source Inverter	56
3.4.1	<i>Carrier-based Sinusoidal PWM</i>	64
3.4.2	<i>Third-harmonic Injection Carrier-based PWM</i>	67
3.4.3	<i>Matlab/Simulink Model for Third Harmonic Injection PWM</i>	68
3.4.4	<i>Carrier-based PWM with Offset Addition</i>	69
3.4.5	<i>Space Vector PWM</i>	72
3.4.6	<i>Discontinuous Space Vector PWM</i>	77
3.4.7	<i>Matlab/Simulink Model for Space Vector PWM</i>	78
3.4.8	<i>Space Vector PWM in Over-modulation Region</i>	90
3.4.9	<i>Matlab/Simulink Model to Implement Space Vector PWM in Over-modulation Regions</i>	96
3.4.10	<i>Harmonic Analysis</i>	96
3.4.11	<i>Artificial Neural Network-based PWM</i>	96
3.4.12	<i>Matlab/Simulink Model of Implementing ANN-based SVPWM</i>	100
3.5	Relationship between Carrier-based PWM and SVPWM	100
3.5.1	<i>Modulating Signals and Space Vectors</i>	102
3.5.2	<i>Relationship between Line-to-line Voltages and Space Vectors</i>	104
3.5.3	<i>Modulating Signals and Space Vector Sectors</i>	104
3.6	Multi-level Inverters	104
3.6.1	<i>Diode Clamped Multi-level Inverters</i>	106
3.6.2	<i>Flying Capacitor Type Multi-level Inverter</i>	109
3.6.3	<i>Cascaded H-Bridge Multi-level Inverter</i>	112
3.7	Impedance Source or Z-source Inverter	117
3.7.1	<i>Circuit Analysis</i>	120
3.7.2	<i>Carrier-based Simple Boost PWM Control of a Z-source Inverter</i>	122
3.7.3	<i>Carrier-based Maximum Boost PWM Control of a Z-source Inverter</i>	123
3.7.4	<i>Matlab/Simulink Model of Z-source Inverter</i>	124
3.8	Quasi Impedance Source or qZSI Inverter	127
3.8.1	<i>Matlab/Simulink Model of qZ-source Inverter</i>	129
3.9	Dead Time Effect in a Multi-phase Inverter	129
3.10	Summary	133
3.11	Problems	134
	References	135
<b>4</b>	<b>Field Oriented Control of AC Machines</b>	<b>139</b>
4.1	Introduction	139
4.2	Induction Machines Control	140

4.2.1	<i>Control of Induction Motor using V/f Method</i>	140
4.2.2	<i>Vector Control of Induction Motor</i>	143
4.2.3	<i>Direct and Indirect Field Oriented Control</i>	148
4.2.4	<i>Rotor and Stator Flux Computation</i>	149
4.2.5	<i>Adaptive Flux Observers</i>	150
4.2.6	<i>Stator Flux Orientation</i>	152
4.2.7	<i>Field Weakening Control</i>	152
4.3	<b>Vector Control of Double Fed Induction Generator (DFIG)</b>	153
4.3.1	<i>Introduction</i>	153
4.3.2	<i>Vector Control of DFIG Connected with the Grid (<math>\alpha\beta</math> Model)</i>	155
4.3.3	<i>Variables Transformation</i>	156
4.3.4	<i>Simulation Results</i>	159
4.4	<b>Control of Permanent Magnet Synchronous Machine</b>	160
4.4.1	<i>Introduction</i>	160
4.4.2	<i>Vector Control of PMSM in dq Axis</i>	160
4.4.3	<i>Vector Control of PMSM in <math>\alpha</math>-<math>\beta</math> Axis using PI Controller</i>	164
4.4.4	<i>Scalar Control of PMSM</i>	166
	Exercises	168
	Additional Tasks	168
	Possible Tasks for DFIG	168
	Questions	169
	References	169
<b>5</b>	<b>Direct Torque Control of AC Machines</b>	<b>171</b>
5.1	Preliminary Remarks	171
5.2	Basic Concept and Principles of DTC	172
5.2.1	<i>Basic Concept</i>	172
5.2.2	<i>Principle of DTC</i>	173
5.3	DTC of Induction Motor with Ideal Constant Machine Model	179
5.3.1	<i>Ideal Constant Parameter Model of Induction Motors</i>	179
5.3.2	<i>Direct Torque Control Scheme</i>	182
5.3.3	<i>Speed Control with DTC</i>	184
5.3.4	<i>Matlab/Simulink Simulation of Torque Control and Speed Control with DTC</i>	185
5.4	DTC of Induction Motor with Consideration of Iron Loss	199
5.4.1	<i>Induction Machine Model with Iron Loss Consideration</i>	199
5.4.2	<i>Matlab/Simulink Simulation of the Effects of Iron Losses in Torque Control and Speed Control</i>	202
5.4.3	<i>Modified Direct Torque Control Scheme for Iron Loss Compensation</i>	213
5.5	DTC of Induction Motor with Consideration of both Iron Losses and Magnetic Saturation	217
5.5.1	<i>Induction Machine Model with Consideration of Iron Losses and Magnetic Saturation</i>	217
5.5.2	<i>Matlab/Simulink Simulation of Effects of both Iron Losses and Magnetic Saturation in Torque Control and Speed Control</i>	218

5.6	Modified Direct Torque Control of Induction Machine with Constant Switching Frequency	233
5.7	Direct Torque Control of Sinusoidal Permanent Magnet Synchronous Motors (SPMSM)	233
5.7.1	<i>Introduction</i>	233
5.7.2	<i>Mathematical Model of Sinusoidal PMSM</i>	234
5.7.3	<i>Direct Torque Control Scheme of PMSM</i>	236
5.7.4	<i>Matlab/Simulink Simulation of SPMSM with DTC</i>	236
	References	253
<b>6</b>	<b>Non-Linear Control of Electrical Machines Using Non-Linear Feedback</b>	<b>255</b>
6.1	Introduction	255
6.2	Dynamic System Linearization using Non-Linear Feedback	256
6.3	Non-Linear Control of Separately Excited DC Motors	258
6.3.1	<i>Matlab/Simulink Non-Linear Control Model</i>	258
6.3.2	<i>Non-Linear Control Systems</i>	259
6.3.3	<i>Speed Controller</i>	260
6.3.4	<i>Controller for Variable <math>m</math></i>	261
6.3.5	<i>Field Current Controller</i>	262
6.3.6	<i>Simulation Results</i>	262
6.4	Multiscalar model (MM) of Induction Motor	262
6.4.1	<i>Multiscalar Variables</i>	262
6.4.2	<i>Non-Linear Linearization of Induction Motor Fed by Voltage Controlled VSI</i>	264
6.4.3	<i>Design of System Control</i>	266
6.4.4	<i>Non-Linear Linearization of Induction Motor Fed by Current Controlled VSI</i>	267
6.4.5	<i>Stator Oriented Non-Linear Control System (based on <math>\Psi_s, i_s</math>)</i>	270
6.4.6	<i>Rotor-Stator Fluxes-based Model</i>	271
6.4.7	<i>Stator Oriented Multiscalar Model</i>	272
6.4.8	<i>Multiscalar Control of Induction Motor</i>	274
6.4.9	<i>Induction Motor Model</i>	275
6.4.10	<i>State Transformations</i>	275
6.4.11	<i>Decoupled IM Model</i>	277
6.5	MM of Double Fed Induction Machine (DFIM)	278
6.6	Non-Linear Control of Permanent Magnet Synchronous Machine	281
6.6.1	<i>Non-Linear Control of PMSM for a <math>dq</math> Motor Model</i>	283
6.6.2	<i>Non-Linear Vector Control of PMSM in <math>\alpha</math>-<math>\beta</math> Axis</i>	285
6.6.3	<i>PMSM Model in <math>\alpha</math>-<math>\beta</math> (<math>x</math>-<math>y</math>) Axis</i>	285
6.6.4	<i>Transformations</i>	285
6.6.5	<i>Control System</i>	288
6.6.6	<i>Simulation Results</i>	288
6.7	Problems	289
	References	290



<b>7</b>	<b>Five-Phase Induction Motor Drive System</b>	<b>293</b>
7.1	Preliminary Remarks	293
7.2	Advantages and Applications of Multi-Phase Drives	294
7.3	Modeling and Simulation of a Five-Phase Induction Motor Drive	295
7.3.1	<i>Five-Phase Induction Motor Model</i>	295
7.3.2	<i>Five-Phase Two-Level Voltage Source Inverter Model</i>	304
7.3.3	<i>PWM Schemes of a Five-Phase VSI</i>	328
7.4	Indirect Rotor Field Oriented Control of Five-Phase Induction Motor	344
7.4.1	<i>Matlab/Simulink Model of Field-Oriented Control of Five-Phase Induction Machine</i>	347
7.5	Field Oriented Control of Five-Phase Induction Motor with Current Control in the Synchronous Reference Frame	348
7.6	Model Predictive Control (MPC)	352
7.6.1	<i>MPC Applied to a Five-Phase Two-Level VSI</i>	354
7.6.2	<i>Matlab/Simulink of MPC for Five-Phase VSI</i>	356
7.6.3	<i>Using Eleven Vectors with <math>\gamma = 0</math></i>	356
7.6.4	<i>Using Eleven Vectors with <math>\gamma = 1</math></i>	359
7.7	Summary	359
7.8	Problems	359
	References	361
<b>8</b>	<b>Sensorless Speed Control of AC Machines</b>	<b>365</b>
8.1	Preliminary Remarks	365
8.2	Sensorless Control of Induction Motor	365
8.2.1	<i>Speed Estimation using Open Loop Model and Slip Computation</i>	366
8.2.2	<i>Closed Loop Observers</i>	366
8.2.3	<i>MRAS (Closed-loop) Speed Estimator</i>	375
8.2.4	<i>The Use of Power Measurements</i>	378
8.3	Sensorless Control of PMSM	380
8.3.1	<i>Control system of PMSM</i>	382
8.3.2	<i>Adaptive Backstepping Observer</i>	383
8.3.3	<i>Model Reference Adaptive System for PMSM</i>	385
8.3.4	<i>Simulation Results</i>	388
8.4	MRAS-based Sensorless Control of Five-Phase Induction Motor Drive	388
8.4.1	<i>MRAS-based Speed Estimator</i>	389
8.4.2	<i>Simulation Results</i>	396
	References	396
<b>9</b>	<b>Selected Problems of Induction Motor Drives with Voltage Inverter and Inverter Output Filters</b>	<b>401</b>
9.1	Drives and Filters – Overview	401
9.2	Three-Phase to Two-Phase Transformations	403
9.3	Voltage and Current Common Mode Component	404
9.3.1	<i>Matlab/Simulink Model of Induction Motor Drive with PWM Inverter and Common Mode Voltage</i>	405

9.4	Induction Motor Common Mode Circuit	408
9.5	Bearing Current Types and Reduction Methods	410
	9.5.1 <i>Common Mode Choke</i>	412
	9.5.2 <i>Common Mode Transformers</i>	414
	9.5.3 <i>Common Mode Voltage Reduction by PWM Modifications</i>	415
9.6	Inverter Output Filters	420
	9.6.1 <i>Selected Structures of Inverter Output Filters</i>	420
	9.6.2 <i>Inverter Output Filters Design</i>	425
	9.6.3 <i>Motor Choke</i>	435
	9.6.4 <i>Matlab/Simulink Model of Induction Motor Drive with PWM Inverter and Differential Mode (Normal Mode) LC Filter</i>	437
9.7	Estimation Problems in the Drive with Filters	440
	9.7.1 <i>Introduction</i>	440
	9.7.2 <i>Speed Observer with Disturbances Model</i>	442
	9.7.3 <i>Simple Observer based on Motor Stator Models</i>	445
9.8	Motor Control Problems in the Drive with Filters	447
	9.8.1 <i>Introduction</i>	447
	9.8.2 <i>Field Oriented Control</i>	449
	9.8.3 <i>Non-Linear Field Oriented Control</i>	453
	9.8.4 <i>Non-Linear Multiscalar Control</i>	457
9.9	Predictive Current Control in the Drive System with Output Filter	461
	9.9.1 <i>Control System</i>	461
	9.9.2 <i>Predictive Current Controller</i>	464
	9.9.3 <i>EMF Estimation Technique</i>	467
9.10	Problems	471
9.11	Questions	475
	References	475
	<b>Index</b>	<b>479</b>

# Acknowledgment

We would like to take this opportunity to express our sincere appreciation to all the people who directly or indirectly helped us in making this book a reality. Our thanks go to our colleagues and students at Texas A&M University at Qatar, Qatar University, Aligarh Muslim University, Gdansk University of Technology, and Ho Chi Minh City University of Technology. Our special thanks go to Mr Wesam Mansour, Mr S.K. Moin Ahmed, Dr M. Rizwan Khan, and Mr M. Arif Khan for assisting us in this work. We are also very grateful to Dr Khalid Khan for his very valuable assistance in preparing the Matlab/Simulink models and converting the C/C++ files into Matlab. The authors would like to put on record the help extended by Mr. Puneet Sharma in developing the simulation model of over-modulation PWM. Furthermore, we would like to also thank Dr Shaikh Moinoddin for his help in Chapters 3 and 7 of the book, as well as Miss Marwa Qaraqe and Mrs Amy Hamar for their help in revising the language of the text.

We are indebted to our family members for their continuous support, patience, and encouragement without which this project would not have been completed. We would also like to express our appreciation and sincere gratitude to the staff of Wiley, especially Laura Bell, Liz Wingett, and the late Nicky Skinner for their help and cooperation.

Above all we are grateful to the almighty, the most beneficent and merciful, who provided us the continuous confidence and determination in accomplishing this work.

*Haitham Abu-Rub, Atif Iqbal and Jaroslaw Guzinski*

# Biographies

**Haitham Abu-Rub** is an Associate Professor at Texas A&M University at Qatar. He holds two PhDs, from Gdansk University of Technology and from Gdansk University in Poland, received in 1995 and 2004, respectively. He was an Assistant Professor at the Gdansk University, and then at Birzeit University in Palestine, where he held the positions of Assistant Professor and Associate Professor for eight years. For four of those years, he was chair of the Electrical Engineering Department. His main research interests are electrical machine drives and power electronics. Dr Abu-Rub has earned many international, prestigious fellowships, such as the American Fulbright Scholarship (at Texas A&M University), the German Alexander von Humboldt Fellowship (at Wuppertal University), the German DAAD Scholarship (at Bochum University), and the British Royal Society Scholarship (at Southampton University).

Dr Abu-Rub is a senior IEEE member, with more than one hundred and thirty published journal and conference papers to his credit. He has also served as an Associate Editor with two journals, and has been on their editorial boards.

**Atif Iqbal** received his BS and MS of Electrical Engineering degrees in 1991 and 1996, respectively, from the Aligarh Muslim University (AMU), Aligarh, India, and PhD in 2006 from Liverpool John Moores University in the United Kingdom. He has been employed as a lecturer at AMU in India since 1991, where he is an Associate Professor. He has been on academic leave to work in a research position at Texas A&M University at Qatar from April 2009 and serve as a faculty member in the Department of Electrical Engineering at Qatar University, where he is working at present. He has published more than 150 research papers in the field of power electronics and drives, including 50 international journal papers. He has completed large R&D projects, and is the recipient of Maulana Tufail Ahmad Gold Medal for his BS Engineering exams in 1991 from AMU and EPSRC, a UK fellowship for his PhD.

Atif Iqbal is a senior IEEE member. He is an Associate Editor of the *Journal of Computer Science, Informatics and Electrical Engineering*. He also serves on the editorial board of the *International Journal of Science Engineering and Technology*, and is a manager for the *Journal of Electrical Engineering*, the *International Journal of Power Electronics Converter (IJPEC)*, the *International Journal of Power Electronics and Drive System (IJPEDS)* and the *International Journal of Power Electronics and Energy (IJPEE)*.

**Jaroslaw Guzinski** received his MS and PhD degrees from the Electrical Engineering Department at the Technical University of Gdansk, Poland, in 1994 and 2000, 2006 to 2009, he was involved in European Commission Project PREMAID Marie Curie, 'Predictive Maintenance and Diagnostics of Railway Power Trains', coordinated by Alstom Transport. He obtained scholarships in the Socrates/Erasmus programme, and headed two grants supported by the Polish government in the area of speed sensorless control and diagnostics for drives with LC filters. He has authored and coauthored more than 100 papers in journals and conferences.

He has patented solutions for speed sensorless drives with LC filters. His current interests include sensorless control of electrical motors, digital signal processors, and electric vehicles.

**Truc Phamdinh** received his BE degree in electrical engineering from the University of New South Wales (Australia) with first class honours. He then successfully completed his PhD studies, producing a dissertation entitled 'Direct Torque Control of Induction Machine Considering Iron Losses' at Liverpool John Moores University (UK). He is at present a lecturer with the Faculty of Electrical and Electronic Engineering, Ho Chi Minh City University of Technology, Vietnam National University, Ho Chi Minh. He is responsible for courses in advanced controls of electrical machines at both undergraduate and postgraduate levels. His research interests include high-performance drives of AC machines, such as field-oriented control and direct torque control, sensorless speed controls, and controls of doubly fed induction generator for wind power.

**Zbigniew Krzeminski** received his PhD degree from the Technical University of Lodz, Lodz, Poland, in 1983 and the DSc degree from Silesian Technical University, Gliwice, Poland, in 1991. He is a Professor with Gdansk University of Technology, Gdansk, Poland. His main areas of research are modeling and simulation of electric machines, control of electric drives, and DSP systems.

# Preface

The book describes the concept of advanced control strategies of AC machine drives along with their complete simulation models using MATLAB/Simulink. Electrical Motors consume the most energy of the electricity generated worldwide. Thus, there exists a huge scope of saving energy by devising efficient operation schemes of these electrical machines. One approach could be the special design of motors with high-energy efficiency. Other approach lies in the proper control of the machines. The electrical motors employed in various applications run at fixed speed. However, it is found that by varying the speed of motors depending upon the load requirements, the efficiency can be improved significantly; thus, the variable speed operation is extremely important in obtaining highly efficient operations of the machines. As a result, the speed control of a machine for industrial and household applications is most vital for limiting greenhouse gas emission and offering an environment-friendly solution. Controlling the operation of an electrical machine by varying its speed, in literature, is called 'variable speed drives' or 'adjustable speed drives'.

This book discusses the advanced technology used to obtain variable speed AC drives. This book also describes the basic modeling procedures of power electronic converters and AC machines. The mathematical model thus obtained will be used to develop a simulation model using MATLAB/Simulink. The Pulse Width Modulation (PWM) techniques for voltage source inverters and their simulation models are described in one chapter. The AC machines that are taken up for discussion are the most popular squirrel cage induction machine, permanent magnet synchronous machine, and the double-fed induction machine. The book illustrates the advance control techniques of electric drives such as 'field-oriented control', 'direct torque control', 'feedback linearization control', 'sensorless operation', and advances in 'multi-phase (more than three-phase) drives'. A separate chapter is dedicated to a five-phase motor drive system. The effect of using an output LC filter at the inverter side on the motor drive control is elaborated on in another chapter.

These control techniques are in general called 'high-performance drives' as they offer extremely fast and precise dynamic and steady-state response of electric machines. Thus, this book describes the most important and industrially accepted advanced control technology of AC machines. The book encompasses these diverse topics in a single volume.

This book features exhaustive simulation models based on MATLAB/Simulink. MATLAB/Simulink is an integral part of taught courses at undergraduate and postgraduate programs and is also extensively used in industries. Thus, the simulation models will provide a handy tool to students, practicing engineers, and researchers to verify the algorithms, techniques, and models. Once familiar with the models presented in the book, students and practicing engineers can develop and verify their own algorithms and techniques.

The book is useful for students studying electric drives/motor control at UG/PG levels. The prerequisite will be the basic courses of electric machines, power electronics, and

controls. Lecturers can find tutorial materials and Solutions to the problems set out in the book on the companion website: [www.wiley.com/go/aburub\\_control](http://www.wiley.com/go/aburub_control). The contents of the book will also be useful to researchers and practicing engineers, as well as specialists.

# 1

## Introduction to High Performance Drives

### 1.1 Preliminary Remarks

The function of an electric drives system is the controlled conversion of electrical energy to a mechanical form, and vice versa, via a magnetic field. Electric drives is a multi-disciplinary field of study, requiring proper integration of knowledge of electrical machines, actuators, power electronic converters, sensors and instrumentation, control hardware and software, and communication links (Figure 1.1). There have been continued developments in the field of electric drives since the inception of the first principle of electrical motors by Michael Faraday in 1821 [1]. The world dramatically changed after the first induction machine was patented (US Patent 381968) by Nikola Tesla in 1888 [2]. Initial research focused on machine design with the aim of reducing the weight per unit power and increasing the efficiency of the motor. Constant efforts by researchers have led to the development of energy efficient industrial motors with reduced volume machines. The market is saturated with motors reaching a high efficiency of almost 95–96%, resulting in no more significant complaints from users [3]. AC motors are broadly classified into three groups: synchronous, asynchronous (induction), and electronically commutated motors. Asynchronous motors are induction motors with a field wound circuit or with squirrel cage rotors. Synchronous motors run at synchronous speeds decided by the supply frequency ( $N_s = 120f/P$ ) and are classified into three major types: rotor excited, permanent magnets, and synchronous reluctance types. Electronic commutated machines use the principle of DC machines but replace the mechanical commutator with inverter-based commutations. There are two main types of motors that are classified under this category: brushless DC motors and switched reluctance motors. There are several other variations of these basic configurations of electric machines used for specific applications, such as stepper motors, hysteresis motors, permanent magnet assisted synchronous reluctance motors, hysteresis-reluctance motors, universal motors,



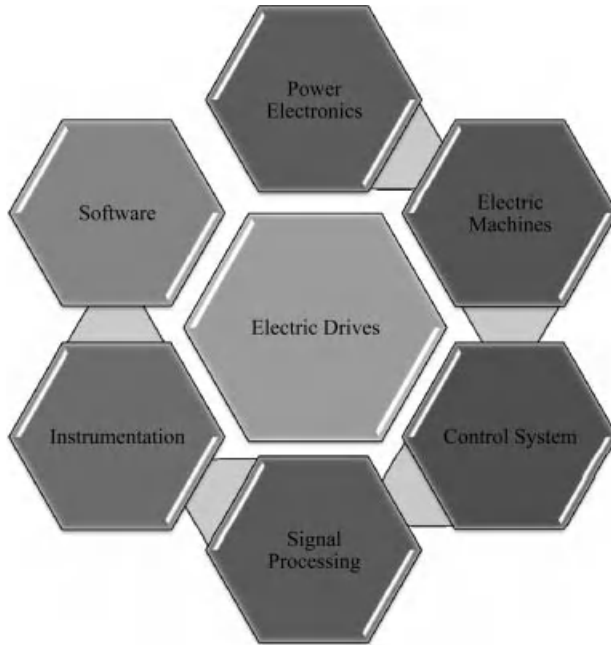


**Figure 1.1** Electric drive system

claw pole motors, frictionless active bearing-based motors, linear induction motors, etc. Active magnetic bearing systems work on the principle of magnetic levitation and, therefore, do not require working fluid, such as grease or lubricating oils. This feature is highly desirable in special applications, such as artificial heart or blood pumps, as well as in the oil and gas industry.

Induction motors are called the workhorse of industry due to their widespread use in industrial drives. They are the most rugged and cheap motors available off the shelf. However, their dominance is challenged by permanent magnet synchronous motors (PMSM), because of their high power density and high efficiency due to reduced rotor losses. Nevertheless, the use of PMSMs is still restricted to the high performance application area, due to their moderate ratings and high cost. PMSMs were developed after the invention of Alnico, a permanent magnet material, in 1930. The desirable characteristics of permanent magnets are their large coercive force and high reminiscence. The former characteristics prevent demagnetization during start and short-conditions of motors and the latter maximizes the air gap flux density. The most used permanent magnet material is Neodymium-Boron-Iron (NdBF<sub>e</sub>), which has almost 50 times higher B-H energy compared to Alnico. The major shortcomings of permanent magnet machines are the non-adjustable flux, irreversible demagnetization, and expensive rare-earth magnet resources. Variable flux permanent magnet (VFPM) machines have been developed to incorporate the adjustable flux feature. This variable flux feature offers flexibility by optimizing efficiency over the whole machine operation range, enhancing torque at low speed, extending the high speed operating range, and reducing the likelihood of an excessively high back-EMF being induced at high speed

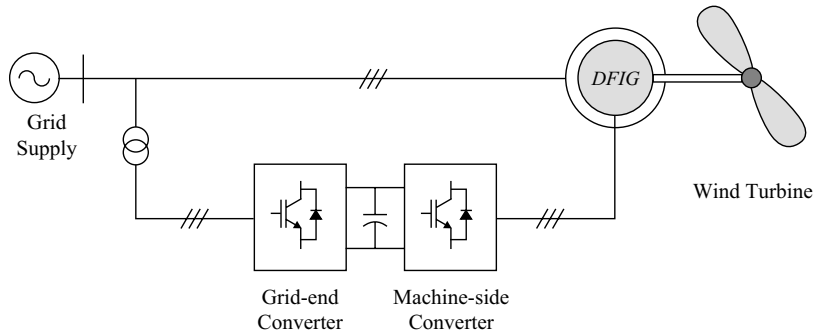


**Figure 1.2** General view of a DFIG connected to wind system and utility grid

during inverter fault conditions. The VFPM are broadly classified into hybrid-excited machines (they have the field coils and the permanent magnets) and mechanically adjusted permanent magnet machines. Detailed reviews on the variable flux machines are given in [4]. The detailed reviews on the advances on electric motors are presented in [5–16].

Another popular class of electrical machine is the double-fed induction machine (DFIM) with a wound rotor. The DFIM is frequently used as an induction generator in wind energy systems. The double-fed induction generator (DFIG) is a rotor-wound, three-phase induction machine that is connected to the AC supply from both stator and rotor terminals (Figure 1.2). The stator windings of the machine are connected to the utility grid without using power converters, and the rotor windings are fed by an active front-end converter. Alternatively, the machine can be fed by current or voltage source inverters with controlled voltage magnitude and frequency [17–22].

In the control schemes of DFIM, two output variables on the stator side are generally defined. These variables could be electromagnetic torque and reactive power, active and reactive power, or voltage and frequency, with each pair of variables being controlled by different structures.

The machine is popular and widely adopted for high power wind generation systems and other types of generators with similar variable speed high power sources (e.g. hydro systems). The advantage of using this type of machine is that the required converter capacity is up to three times lower than those that connect the converter to the stator side. Hence, the costs and losses in the conversion system are drastically reduced [17].

A DFIG can be used either in an autonomous generation system (stand-alone) or, more commonly, in parallel with the grid. If the machine is working autonomously, the stator voltage and frequency are selected as the controlled signals. However, when the machine is connected to the infinite bus, the stator voltage and frequency are dictated by the grid system. In the grid-interactive system, the controlled variables are the active and reactive powers [23–25]. Indeed, there are different types of control strategies for this type of machine; however, the most widely used is vector control, which has different orientation frames similar to the squirrel cage induction motor, but the most popular of these is the stator orientation scheme.

Power electronics converters are used as an interface between the stiff voltage and frequency grid system and the electric motors to provide adjustable voltage and frequency.

This is the most vital part of a drive system that provides operational flexibility. The development in power electronic switches is steady and nowadays high frequency low loss power semiconductor devices are available for manufacturing efficient power electronic converters. The power electronic converter can be used as DC-DC (buck, buck-boost, boost converters), AC-DC (rectifiers), DC-AC (inverters), and AC-AC (cyclo-converters and matrix converters) modes. In AC drive systems, inverters are used with two-level output or multi-level output (particularly for higher power applications). The input side of the inverter system can consist of a diode-based, uncontrolled rectifier or controlled rectifier for regeneration capability called back-to-back or active front-end converter. The conventional two-level inverter has the disadvantages of the poor source side (grid side) power factor and distorted source current. The situation is improved by using back-to-back converters or matrix converters in drive systems.

The output side (AC) voltage/current waveforms are improved by employing the appropriate Pulse Width Modulation (PWM) technique, in addition to using a multi-level inverter system. In modern motor drives, the transistor-based (IGBT, IGCT, MOSFET) converters are most commonly used. The increase in transistors switching frequency and decrease in transistor switching times are a source of some serious problems. The high  $dv/dt$  and the common mode voltage generated by the inverter PWM control results in undesirable bearing currents, shaft voltages, motor terminal over-voltages, reduced motor efficiency, acoustic noise, and electromagnetic interference (EMI) problems, which are aggravated by the long length of the cable between the converter and the motor. To alleviate such problems, generally the passive LC filters are installed on the converter output. However, the use of an LC filter introduces unwanted voltage drops and causes a phase shift between the filter input and output voltages and currents. These can negatively influence the operation of the whole drive system, especially when sophisticated speed, sensorless control methods are employed, requiring some estimation and control modifications for an electric drive system with an LC filter at its output. With the LC filter, the principal problem is that the motor input voltages and currents are not precisely known; hence, additional voltage and current sensors are employed. Since the filter is an external element of the converter, the requirement of additional voltage and current sensors poses technical and economical problems in converter design. The more affordable solution is to develop proper motor control and use estimation techniques in conjunction with LC filter-based drive [26–30].

The simulation tool is a significant step for performing advanced control for industry. However, for practical implementation, the control platform for the electric drive system is provided with microcontrollers ( $\mu$ Cs), digital signal processors (DSPs), and/or field programmable gate arrays (FPGAs). These control platforms offer flexibility of control and make possible the implementation of complex control algorithms, such as field oriented control (FOC), direct torque control (DTC), non-linear control, and artificial intelligence-based control. The first microprocessor, the Intel 4004 (US Patent # 3821715), was invented by Intel engineers Federico Faggin, Ted Hoff, and Stan Mazor in November 1971 [31]. Since then, the development of faster and more capable microprocessors and  $\mu$ Cs has grown tremendously. Microcontroller is a single IC containing the processor core, the memory, and the peripherals. Microprocessors are used for general-purpose applications, such as in PCs, laptops, and other electronic items, and are used in embedded applications for actions such as motor control. The first DSP was produced by Texas Instruments, TMS32010, in 1983 [32], followed by several DSPs being produced and used for several applications, ranging from motor control

to multi-media applications to image processing. Texas Instruments has developed some specific DSPs for electric drive applications, such as the TMS320F2407, TMS320F2812, and TMS320F28335. These DSPs have dedicated pins for PWM signal generation that serve by controlling power converters. Nowadays, control algorithms implement more powerful programmable logic components called FPGAs, the first of which, XC2064, was invented by Xilinx co-founders Ross Freeman and Bernard Vonderschmitt in 1985. FPGAs have logic blocks with memory elements that can be reconfigured to obtain different logic gates. These reconfigurable logic gates can be configured to perform complex combinational functions. The first FPGA XC2064 had 64 configurable logic blocks, with two three-input lookup tables. In 2010, an extended processing platform was developed for FPGAs that combines the features of an Advanced Reduced Instruction Set Machine (ARM) high-end micro-controller (32-bit processor, memory, and I/O) with an FPGA fabric for easier use in embedded applications. Such configurations make it possible to implement a combination of serial and parallel processing to address the challenges in designing today's embedded systems [33].

The primitive electric drive system uses a fixed-speed drive supplied from the grid, while mostly employing the DC motor. Adjustable speed drive systems offer more flexible control and increased drive efficiency when compared to the fixed speed drive. DC motors inherently offer decoupled flux and torque control, with fast dynamic response and simple control mechanism. However, the operating voltage of the DC machines is limited by the mechanical commutator's withstand voltage; in addition, the maintenance requirement is high due to its brush and commutator arrangement. DC drives are now increasingly replaced by AC drives due to the advent of the high performance control of AC motors, such as vector control, Direct Torque Control (DTC), and predictive control, offering precise position control and an extremely fast dynamic response [34]. The major advantages of AC drives over DC drives include their robustness, compactness, economy, and low maintenance requirements.

Biologically inspired artificial intelligence techniques are now being increasingly used for electric drive control, and are based on artificial neural networks (ANN), fuzzy logic control (FLC), adaptive neuro-fuzzy inference system (ANFIS), and genetic algorithm (GA) [35,36]. A new class of electric drive controls, called brain emotional learning-based intelligent controller (BELBIC), is reported in the literature [37]. The control relies on the emotion processing mechanisms in the brain, with the decisions made on the basis of an emotional search. This emotional intelligence controller offers a simple structure with a high auto-learning feature that does not require any motor parameters for self performance. The high performance drive control requires some sort of parameter estimation of motors, in addition to the current, speed, and flux information for a feedback closed-loop control. Sensors are used to acquire the information and are subsequently used in the controller. The speed sensors are the most delicate part in the whole drive system, thus extensive research efforts are being made to eliminate the speed sensors from the drive system, with the resulting drive system becoming a 'sensorless' drive. In sensorless drive schemes, existing current and voltage sensors are used to compute the speed of the machine, and the computed speed is used for closed-loop control. The literature on sensorless drives is too vast to list, but a comprehensive review is available in [38–40]. A sensorless drive offers the advantages of a compact drive with reduced maintenance, reduced cost, and its ability to withstand harsh environmental conditions. Despite impressive progress in drive automation, there are still a number of

persistent challenges, including a very low speed near to zero, operation at zero speed with full load condition, and an overly high-speed operation.

Network-based control and remote control of the drive systems are still in progress. Plug-and-play types of electric drives are an important area that can serve the applications that have a direct impact on the quality of life, such as renewable energy, automotive applications, and biomedical applications. Integrated converter-motor drive systems for compact design, as well as reduced EMI due to cabling wave reflection, are also in progress. More diversity in machine design with rare earth free motors is the subject of research, and high air gap flux density machines using superconductors are the direction of research in electric drive systems.

## 1.2 General Overview of High Performance Drives

High performance drive refers to the drive system's ability to offer precise control, in addition to a rapid dynamic response and a good, steady state response. High performance drives are considered for safety critical applications due to their precision of control [41]. Since the inception of AC machines, several techniques have evolved to control their speed, torque, and flux. The basic controlling parameters are the voltage and frequency of the applied voltage/current to the motor. The grid supplies fixed magnitude and frequency voltages/currents, and are thus not suitable for obtaining controlled operation of machines. Hence, power electronic converters are used as an interface between the grid supply and the electric motors. These power electronic converters, in most cases, are AC-DC-AC converters for AC machine drives. Other alternatives are direct AC-AC converters, such as cyclo-converters and matrix converters. However, these direct AC-AC converters suffer from some serious drawbacks, including the limited output frequency, as low as one-third in cyclo-converters, and the limited output voltage magnitude, which is limited to 86% of the input voltage magnitude in matrix converters. Moreover, the control is extremely complex for direct AC-AC converters. Thus, invariably AC-DC-AC converters are more commonly called 'inverters,' and are used to feed the motors for adjustable speed applications. This book will describe the modeling procedures of the inverters, followed by the illustration of their existing control techniques. The basic energy processing technique in an inverter is called 'Pulse Width Modulation' (PWM); hence, PWM will be discussed at length.

The control of AC machines can be broadly classified into 'scalar' and 'vector' controls (Figure 1.3). Scalar controls are easy to implement and offer a relatively steady-state response, even though the dynamics are sluggish. To obtain high precision and good dynamics, as well as a steady-state response, 'vector' control approaches are to be employed with closed-loop feedback control. Thus, this book focuses on the 'vector' based approaches, namely 'Field Oriented Control,' 'Direct Torque Control,' 'Non-linear Control,' and 'Predictive Control.'

It is well-known that the variable speed drive offers significant energy savings in an industrial set-up. Thus, by employing variable speed drives in industry, there exists huge scope for energy saving. The older installations relied on DC machines for variable speed applications, because of their inherent decoupled torque and flux control with minimum electronics involved; however, in the early 1970s, the principle of decoupled torque and flux control, more commonly called 'field oriented control' or 'vector control,' were achieved in more robust induction machines. Later, it was realized that such control was also possible in synchronous

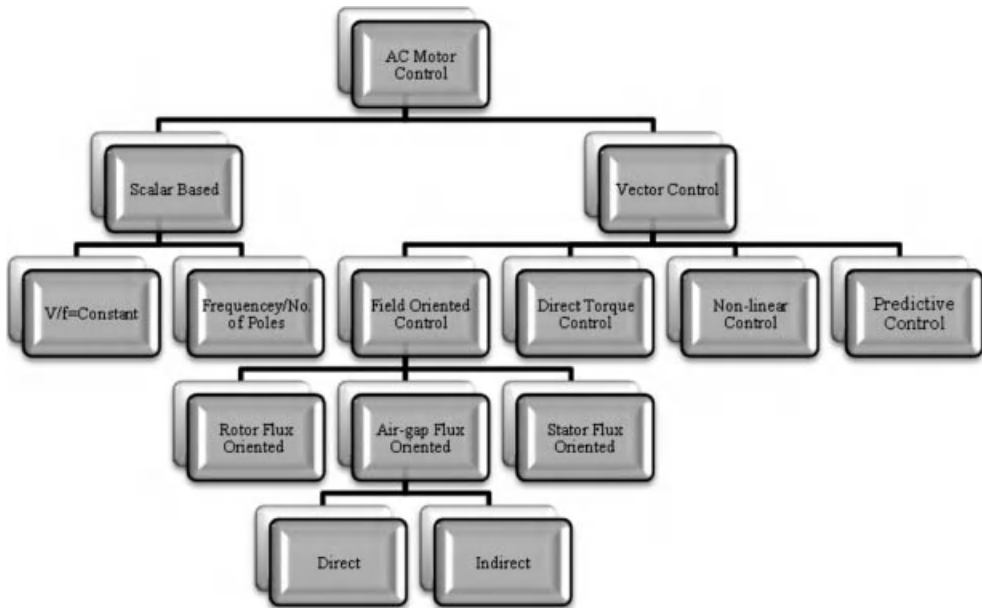


**Figure 1.3** Motor control schemes

machines. However, the pace of development in variable speed AC machine drives was slow and steady until the early 1980s, when the microprocessor era began and the realization of complex control algorithms became feasible [34,35].

The FOC principle relies on the instantaneous control of stator current space vectors. The research on FOC is still active, with the idea of incorporating more advanced features for highly precise and accurate control, such as sensorless operation, and utilization of on-line parameter adaptations. The effect of parameter variations, magnetic saturation, and stray-load losses on the behavior of field oriented controlled drives are the subject of research in obtaining robust sensorless drives.

Theoretical principles of ‘direct torque control’ for high performance drives were introduced in the mid- and second half of the 1980s. Compared with FOC which had its origin at the beginning of the 1970s, DTC is a significantly newer concept. It took almost 20 years for the vector control to gain acceptance by the industry. In contrast, the concept of DTC has been received by industry relatively quickly, in only ten years. While FOC predominantly relies on the mathematical modeling of an induction machine, DTC makes direct use of physical interactions that take place within the integrated system of the machine and its supply. The DTC scheme requires simple signal processing methods, relying entirely on the non-ideal nature of the power source that is used to supply an induction machine, within the variable speed drive system (two-level or three-level voltage source inverters, matrix converters, etc.). It can, therefore, be applied to power electronic converter-fed machines only. The on-off control of converter switches is used for the decoupling of the non-linear structure of the AC machines. The most frequently discussed and used power electronic converter in DTC drives is a voltage source inverter.

DTC takes a different look at the machine and the associated power electronic converter. First, it is recognized that, regardless of how the inverter is controlled, it is by default a voltage source rather than a current source. Next, it dispenses with one of the main characteristics of the vector control, indirect flux, and torque control by means of two stator current components. In essence, DTC recognizes that if flux and torque can be controlled indirectly by these two current components, then there is no reason why it should not be possible to control flux and torque directly, without intermediate current control loops.

DTC is inherently sensorless. Information about actual rotor speed is not necessary in the torque mode of operation, because of the absence of co-ordinate transformation. However, correct estimations of stator flux and torque is important for the accurate operation of hysteresis controllers. An accurate mathematical model of an induction machine is, therefore, essential in DTC. The accuracy of DTC is also independent of the rotor's parameters variations. Only the variation of stator resistance, due to a change in thermal operating conditions, causes problems for high performance DTC at low speeds [38].

In summary, the main features of DTC and its differences from the vector control are:

- direct control of flux and torque;
- indirect control of stator currents and voltages;
- absence of co-ordinate transformation;
- absence of separate voltage modulation block, usually required in vector drives;
- ability to know only the sector in which the stator flux linkage space vector is positioned, rather than the exact position of it (necessary in vector drives for co-ordinate transformation);
- absence of current controllers;
- inherently sensorless control since speed information is not required in the torque mode of operation;
- in its basic form, the DTC scheme is sensitive to only variation in stator resistance.

The research on the direct torque is still active and the effects of non-linearity in the machine models are being explored; the flexibility and simple implementation of the algorithms will be the focus of research in the near future. The use of artificial intelligence is another direction of research in this area. It is important to emphasize that many manufacturers offer variable speed drives based on the 'field oriented control' and 'DTC' principles and are readily available in the market.

The main disadvantage of vector control methods is the presence of non-linearity in the mechanical part of the equation during the changing of rotor flux linkage. Direct use of vector methods to control an induction machine fed by a current source inverter provides a machine model with high complexity, which is necessary to obtain precise control systems. Although positive results from field oriented/vector control have been observed, attempts to obtain new, beneficial, and more precise control methods are continuously made. One such development is the 'non-linear control' of an induction machine. There are a few methods that are encompassed in this general term of 'non-linear control,' such as 'feedback linearization control' or 'input-output decoupling control,' and 'multi-scalar model based non-linear control'. Multi-scalar-based non-linear control or MM control was presented for the first time in 1987 [38,39], and is discussed in the book. The multi-scalar model-based control relies on the choice of specific state variables and, thus, the model obtained completely decoupled mechanical and electromagnetic subsystems. It has been shown that it is possible to have non-linear control and

decoupling between electromagnetic torque and the square of linear combination of a stator current vector and the vector of rotor linkage flux.

When a motor is fed by voltage source inverters, and when the rotor flux linkage magnitude is kept constant, the non-linear control system control is equivalent to the vector control method. In many other situations, the non-linear control gives more system structure simplicity and good overall drive response [35,38,39].

The use of variables transformation to obtain non-linear model variables makes the control strategy easy to perform, because only four state variables have been obtained with a relatively simple non-linearity form [38]. This makes it possible to use this method in the case of change flux vector, as well as to obtain simple system structures. In such systems, it is possible to change the rotor flux linkage with the operating point without affecting the dynamic of the system. The relations occurring between the new variables make it possible to obtain novel control structures that guarantee a good response of the drive system, which is convenient for the economical operation of drive systems in which this flux is reduced if the load is decreased.

The use of variables transformation to obtain MM makes the control strategy easier than the vector control method, because four variables are obtained within simple non-linearity form. This makes it possible to use this method in the field-weakening region (high speed applications) more easily when compared to the vector control methods. Extensive research has been done on the non-linear control theory of induction machines, leading to a number of suggested improvements. It is expected that more such control topology will evolve in time.

High performance control of AC machines requires the information of several electromagnetic and mechanical variables, including currents, voltages, fluxes, speed, and position. Currents and voltage sensors are robust and give sufficiently accurate measurements, and so are adopted for the closed-loop control. The speed sensors are more delicate and often pose serious threats to control issues, so speed sensorless operation is sought in many applications that require closed-loop control. Several schemes have been developed recently to extract speed and position information without using speed sensors. Similarly, rotor flux information is typically obtained using 'observer' systems. Much research efforts occurred throughout the 1990s to develop robust and precise observer systems. Improvements have been offered by the development of the methods, including the 'model reference adaptive system,' the 'Kalman filters,' and the 'Luenberger observers,' [40–42].

Initially, observers were designed based on the assumption of a linear magnetic circuit and were later improved by taking into account different non-linearities. The methods developed so far still suffer from stability problems around zero frequency. They fail to prove global stability for sensorless AC drives. This has led many researchers to conclude that globally asymptotically stable model-based systems for sensorless induction motor drives may not exist. Indeed, most investigations on sensorless induction motor drives today focus on providing sustained operation at high dynamic performance at very low speed, particularly at zero speed or at zero stator frequency. Two advanced methodologies are competing to reach this goal. The first category comprises the methods that model the induction motor by its state equations. A sinusoidal flux density distribution in the air gap is then assumed, neglecting space harmonics and other secondary effects. The approach defines the class of fundamental models. They are either implemented as open-loop structures, such as the stator model, or as closed-loop observers. The adaptive flux observer is a combination of the non-linear observer with a speed adaptation process. This structure is now receiving considerable attention and many new solutions follow a similar generic approach [41].



Three-phase electric power generation, transmission, distribution, and utilization have been well-known for over a century. It was realized that generation and transmission of power with more than three phases do not offer significant advantages in terms of power density (generation) and right-of-way and initial cost (transmission). A five-phase induction motor drive system was first tested for in 1969 [43]. The supply to a five-phase drive system was made possible by using a five-phase voltage source inverter, since simply adding an extra leg increases the output phases in an inverter. It was realized that the five-phase induction motor drive systems offered some distinct advantages over three-phase drive system counterparts, such as reduced torque pulsation and enhanced frequency of pulsation, reduced harmonic losses, reduced volume for the same power output, reduced DC link current harmonics, greater fault tolerance, and better noise characteristics.

In addition, there is a significant advantage on the power converter end, due to the reduced power per leg, the power semiconductor switch rating reduces, thus avoiding their series/parallel combination and eliminating the problem of static and dynamic voltage sharing. Furthermore, the stress on the power semiconductor switches reduces due to the reduced  $dv/dt$ . The attractive features of multi-phase drive systems means enormous research efforts have been made globally in the last decade to develop commercially feasible and economically viable solutions. Niche application areas are then identified for multi-phase drive systems, such as ship propulsion, traction, 'more electric aircraft' fuel pumps, and other safety critical applications. Due to their complex control structure, their widespread use in general purpose application is still not accepted. One of the commercial applications of a 15-phase induction motor drive system is in the British naval ship 'Destroyer II.' Similar drive systems are under preparation for US naval ships and will be commissioned soon. Nevertheless, there are many challenges still to be met before the widespread use of multi-phase drive systems, especially in general purpose electric drive systems [44].

### 1.3 Challenges and Requirements for Electric Drives for Industrial Applications

Industrial automation requires precisely controlled electric drive systems. The challenges and requirements for electric drive systems depend upon the specific applications being used. Among different classes of electric drives, medium voltage drives (0.2–40 MW at the voltage level of 2.3–13.8 kV) are more popular for use in industry, such as in the oil and gas sector, rolling and milling operations, production and process plants, petrochemical industry, cement industry, metal industry, marine drive, and traction drive. However, only 3% of the existing medium voltage (MV) motors are variable-speed drives, with the rest of these running at a fixed speed [45]. The installation of properly speed controlled MV drives will significantly reduce losses and total drive costs, as well as improve power quality in any industrial set-up. There are several challenges associated with the controlled MV drives that are related to the line/source side (e.g. power quality, resonance, and power factor), motor side (e.g.  $dv/dt$ , torsional vibration, and traveling wave reflections), and power semiconductor switching devices (e.g. switching losses and voltage and current handling capability). The power rectifier at the source side produces distorted currents at the source, in addition to poor power factors, thus posing a challenge to the designer of the controlled electric drive system. The Pulse Width

Modulation of inverter generates a common mode voltage on the motor side, which poses another challenge. The rating of the power semiconductor devices is also an important factor to be considered while designing an electric drive. High-quality voltage and current waveforms at the converter input and output is essential in all types of electric drive systems.

The power quality is a factor of the converter topology used, and refers to the characteristic of the load, the size and type of the filter, the switching frequency, and the adopted control strategy. The switching losses of power converter devices contribute to the major portion of the drive losses; therefore, operation at a low switching frequency makes it possible to increase the maximum power of the inverter. However, an increase in the switching frequency of an inverter increases the harmonic distortion of the input and output waveforms. Another solution is to use multi-level inverters that deliver waveforms with better harmonic spectrum and lower  $dv/dt$ , which limits the insulation stress of the motor windings. However, increasing the number of switching devices in multi-level inverters tends to reduce the overall reliability and efficiency of the power converter. On the other hand, an inverter with a lower level of output voltage requires a large LC output filter to reduce the motor winding insulation stress. The challenge then is to reduce output voltage and current waveform distortions when low switching frequency is used to ensure high power quality and high efficiency.

The maximum voltage blocking capability of modern power semiconductor switching devices is nearly 6.5 kV. This sets the maximum voltage limit of the inverter and the motor in an electric drive system. Referring to the two-level voltage source inverter and the maximum conducting current (600 A) of available voltage IGBT switches, the obtained maximum apparent power is less than 1 MVA [45]. To overcome the limits of inverter ratings, series and/or parallel combinations of power devices are suggested. In such instances, extra measurements are required to balance the current between devices during turning on and turning off. Due to inherent differing device characteristics, more losses are generated, requiring a reduction in the de-rating of the inverter. There is a need to find a solution to increase the power range of inverter, while avoiding the problems associated with series/parallel connections of switches. One possible solution is using machines and converters with a high phase number (more than three). Drive systems using motors and converters of high phase orders have gained popularity in recent times, and extensive research efforts are being put into developing such commercially feasible drives.

Essential requirements for general purpose electric drives for industrial application include high efficiency, low cost, compact size, high reliability, fault protection features, easy installation, maintenance, and, in some applications, high dynamic performance, better power quality at the input side, precise position control, and regeneration capability.

### *1.3.1 Power Quality and LC Resonance Suppression*

Unwanted harmonics are introduced in power grids due to the power electronic switching converters on the load side, which poses a serious problem that needs to be effectively solved. Uncontrolled diode based rectifiers at the source side of the inverter draw distorted currents from the grid and cause notches in voltage waveforms. This results in several problems, such as computer data loss, malfunction of communication equipment and protective equipment, and noise. Therefore, many standards define the limit of harmonics injected into the power grid, including IEEE 519-1999, IEC 1000-3-2 International Standard, 1995, and IEC 61000-3-2

International Standard, 2000. Current research and industrial applications tend to comply with these international standards.

The LC line side filter is used for current harmonic reduction or power factor compensation. Such LC filters may exhibit resonance phenomena. The supply system at the MV level has very low impedance, therefore lightly damped LC resonances may cause undesired oscillations or over-voltages. This may shorten the life of the switching devices or other components of the rectifier circuits. Effective solutions should guarantee low harmonics and low  $dv/dt$  using just a reactor instead of an LC filter, or using a small filter to solve the problem of LC resonance.

### *1.3.2 Inverter Switching Frequency*

The use of high switching frequency devices in power converters causes rapid voltages and current transitions. This leads to serious problems in the drive system, such as the generation of unwanted common-mode (CM) currents, EMI, shaft voltage, with consequent generation of bearing currents, and deterioration of the winding insulation of motors and transformers.

Switching losses is a crucial issue that should be taken into account in designing electric drives, because they pose a limit on the switching frequency value and the output power level of the power converters. The switching losses of semiconductor devices contribute to a major portion of total device losses. A reduction of switching frequencies increases the maximum output power of the power converter. However, the reduction of switching frequency may cause an increase in harmonic distortion of the line and motor side. Hence, a trade-off exists between these two conflicting requirements.

### *1.3.3 Motor Side Challenges*

Fast switching transients of the power semiconductor devices at high commutation voltages causes high switching losses and poor harmonic spectrum of the output voltages, generating additional losses in the machine. The problems are aggravated due to the long length of the cables between the converters and motors, as well as generating bearing currents due to switching transients.

### *1.3.4 High $dv/dt$ and Wave Reflection*

The high switching frequency of power devices causes high  $dv/dt$  at the rising and falling edges of the inverter output voltage waveform. This may cause failure of the motor winding insulation due to partial discharges and high stress. High  $dv/dt$  also produces rotor shaft voltages, which creates current flow into the shaft bearing through the stray coupling capacitors, ultimately leading to motor bearings failure. This is a common problem in adjustable speed drive systems in industry.

The wave reflections are caused by the mismatch between the cable, the inverter, and the motor wave impedance. Wave reflections can double the voltage on the motor terminals at each switching transient, if the cable length exceeds a certain limit. The critical cable length for 500 V/ $\mu$ s is in the 100-m range, while for 10,000 V/ $\mu$ s it is in the 5-m range [45]. The  $dv/dt$  also

causes electromagnetic emission in the cables between the inverter and the motor. Expensive shielded cables are used to avoid these effects; nevertheless, the electromagnetic emission may affect the operation of nearby sensitive electronic equipment, which is called electromagnetic interference.

The design of the filters should achieve international standards (e.g. IEEE 519-1999). Filters also reduce the switching frequency. The widely used passive filters are designed to ensure very low total harmonic distortion (THD) in both motor and line sides. A large inductor in the LC filter must be used in most high power drive systems, resulting in undesirable voltage drops across the inductor. The increase in capacitor size reduces LC resonant frequency, which is then affected by the parallel connection of the filter capacitor and motor magnetizing inductance.

In an electric drive with an LC filter, instability could appear due to electric resonance between L and C parameters. Such phenomena are mostly observed in over-modulation regions when some inverter output voltage harmonics are close to LC filter resonant frequency. Active damping techniques could be then employed to resolve the problem of instability, while at the same time suppressing the LC resonance.

### *1.3.5 Use of Inverter Output Filters*

The output voltage quality at the inverter side can be improved by using active and passive filters. Today, passive filtering is widely used at the output of the inverter to improve the voltage waveform. Such filters are hardware circuits that are installed on the output of the converter structure. The most common approach is the use of filters based on resistors, inductors, and capacitors (LC filters). In order to reduce the over-voltages that can occur, because of wave reflection at the motor terminals when long cables are used, differential mode LC filters are used. The cable length is important in determining the output performance of the drive system; however, the cable layout on the user end is generally unknown to the inverter manufacturer. Moreover, such filters components are decided according to the switching frequency of the inverter. When an inverter output filter is installed in the electric drive, the voltage drops and the phase shifts between the filter's input while output voltages and currents appear. This complicates the control system design, particularly for low speed conditions. The control systems are generally designed assuming the inverter's output voltages and currents are equal to the motor input values. In the case of a discrepancy between voltages and currents, the region of proper motor operation is limited. Therefore, in a control system of electric drives with an inverter output filter, it is essential to provide modification in the measurement circuits or in the control algorithms. A simple way to improve the performance of the electric drive with inverter output filter is to introduce additional sensors for motor voltages and current measurements. Such a solution is not practical because it requires changes in the inverter structure so, in this case, an accepted solution is to keep the inverter structure unchanged but to modify a control algorithm.

## **1.4 Organization of the Book**

This book is comprised of nine different chapters dealing with different issues of High Performance AC Drives along with the MATLAB/Simulink models. Chapter 1 discusses the components of AC drive system and presents an overview on High Performance Drives.

The classification of electrical machines and their state-of-the-art control strategies, including field oriented control and direct torque control, are elaborated on. The persisting challenges for the industrial application of AC drives are further illustrated in Section 1.3. This chapter give an overall view of High Performance Drives.

Chapter 2 discusses the basic modeling procedures of different types of electrical machines. For the sake of completeness, DC machine modeling is presented in Section 2.2, followed by the modeling of the squirrel cage induction machine, which is presented based on the space vector approach. The obtained dynamic model is then converted into a per unit system for further simulation and generalization of this approach. This is followed by the modeling of double-fed induction machine and permanent magnet synchronous machine. The simulation using MATLAB/Simulink is also presented.

Chapter 3 describes the Pulse Width Modulation control of DC-AC converter system. The basic modeling of a two-level inverter based on the space vector approach is discussed, followed by different PWM approaches such as carrier-based sinusoidal PWM, harmonic injection schemes, offset addition methods, and space vector PWM techniques. This is followed by discussion on multi-level inverter operation and control. Three most popular topologies (Diode clamped, Flying capacitor, and Cascaded H-bridge) are illustrated. A new class of inverter, most popular in renewable energy application, called the Z-source inverter and its modified form called the quasi Z-source, are discussed in this chapter. The discussed techniques are further simulated using MATLAB/Simulink and the simulation models are presented.

Chapter 4 is dedicated to the field oriented control or vector control of AC machines, including the squirrel cage induction machine, the double-fed induction machine, and the permanent magnet synchronous machine. For consistency, scalar control ( $v/f = \text{constant}$ ) is also presented. Different types of vector control are presented along with their simulation models. Wide speed control range from low to high (field weakening) is elaborated on. The field weakening region is discussed in detail, with the aim of producing high torque at high speed. Vector control of DFIG with grid interface is also described, as is the basic rotor flux estimation scheme using the Luenberger observer system.

Principles of DTC for High Performance Drives are introduced in Chapter 5. DTC takes a different look at the induction machine and the associated power electronic converter. First, it recognizes that, regardless of how the inverter is controlled, it is by default a voltage source rather than a current source. Next, it dispenses with one of the main characteristics of vector control, indirect flux, and torque control, by means of two stator current components. In essence, DTC recognizes that if flux and torque can be controlled indirectly by these two current components, then it should not be possible to control flux and torque directly, without intermediate current control loops. This concept is discussed in Chapter 5. The main features, advantages, shortcomings, and implementation of d DTC are elaborated on. A simulation model for implementing d DTC is presented.

High Performance Drives are a solution intended to embed separately excited DC motor characteristics into AC machines. This goal has been almost achieved with the inception of vector control principle. The main disadvantage of vector control methods is the presence of non-linearity in the mechanical part of the equation during the changing of rotor flux linkage. Although good results from vector control have been observed, attempts to obtain new control methods are still being made. Non-linear control of induction motors is another alternative to obtain decoupled dynamic control of torque and flux. This method of control to obtain High Performance Drive is presented in Chapter 6. Such a control technique introduces a novel

mathematical model for induction motors, which makes it possible to avoid using sin/cos transformation of state variables. The model consists of two completely decoupled subsystems, mechanical and electromagnetic. It has been shown that in such a situation it is possible to have non-linear control and decoupling between electromagnetic torque and the rotor linkage flux. Non-linear control of induction machine based on multi-scalar model is discussed. Non-linear control of a separately excited DC motor is also presented. Non-linear control of non-linear induction machine and permanent magnet synchronous machine is illustrated. The discussed techniques are supported by their simulation model using MATLAB/Simulink.

Chapter 7 is devoted to a five-phase induction motor drive system. The advantages and applications of a multi-phase (more than three phases) system are described. The chapter discusses the dynamic modeling of a five-phase induction machine, followed by space vector model of a five-phase voltage source inverter. The pulse width modulation control of a five-phase voltage source inverter is elaborated on. The vector control principle of a five-phase induction motor in conjunction with the current control in the stationary reference frame and the synchronously rotating reference frame is presented. Finite state model predictive control applied to a five-phase voltage source inverter for current control is also presented. The simulation models of a five-phase induction motor and five-phase voltage source inverter are illustrated using MATLAB/Simulink.

Chapter 8 describes the speed sensorless operation of high performance drive systems. Speed sensors are the most delicate component of a drive system, which are susceptible to faults and malfunctioning. A more robust drive system is obtained by replacing the physical speed sensors with the observer system that compute the speed and use the information for the closed-loop control. Several observer systems and their tuning are elaborated on in this chapter. A model reference adaptive speed estimator system for a three-phase and a five-phase induction machine is described along with their simulation model. Sensorless control scheme of permanent magnet synchronous machine is also discussed. Model reference adaptive speed estimator system for a three-phase permanent magnet synchronous motor is also illustrated.

Nowadays, electric drives with induction motors and voltage source type inverters are commonly used as adjustable speed drives in industrial systems. The inverters are built with the insulated gate bipolar transistors, IGBT, whose dynamic parameters are high, i.e. the on- and off-switch times are extremely short. Fast switching of power devices causes high  $dv/dt$  at the rising and falling edges of the inverter output waveform. High  $dv/dt$  in modern inverters is the source of numerous disadvantageous effects in the drives systems. The main negative effects are faster motor bearings degradation, over-voltages on motor terminals, failure or degradation of the motor winding insulation due to partial discharges, increase of motor losses, and a higher EMI level. The prevention or limiting of the negative effects of  $dv/dt$  is possible if proper passive or active filters are installed in the drive. Particularly passive filters are preferable for industrial applications. This issue is described in detail in the Chapter 9. The problems due to use of passive LC filters at the output of the inverter and their solutions are discussed.

Chapter 1 was prepared by Atif Iqbal with help from Haitham Abu-Rub. Chapters 2, 4 and 8 were mainly prepared by Haitham Abu-Rub with help from Jaroslaw Guzinski. Chapter 6 was prepared by Zbigniew Krzeminski and Haitham Abu-Rub. Chapters 3 and 7 are the responsibility of Atif Iqbal. Chapter 5 was written by Truc Pham-dinh and Chapter 9 was written by Jaroslaw Guzinski with help from Haitham Abu-Rub. All chapters were revised by an English expert from the research team of Haitham Abu-Rub.

## References

1. <http://www.sparkmuseum.com/MOTORS.HTM>
2. <http://www.google.com/patents?vid=381968>
3. Mecrow, B. C. and Jack, A. G. (2008) Efficiency trends in electric machines and drives. *Energy Policy*, **36**, 4336–4341.
4. Zhu, Z. Q. (2011) Recent advances on Permanent Magnet machines including IPM technology. *Keynote Lect. IEEE IEMDC*, 15–18 May, Niagara Falls.
5. Jahns, T. M. and Owen, E. L. (2001) AC adjustable-speed drives at the millennium: How did we get here? *IEEE Trans. Power Elect.*, **6**(1), 17–25.
6. Rahman, M. A. (1993) *Modern Electric Motors in Electronic World*. 0-7803-0891-3/93, pp. 644–648.
7. Lorenz, R. D. (1999) Advances in electric drive control. *Proc. Int. Conf. on Elec. Mach. Drives IEMD*, pp. 9–16.
8. Rahman, M. A. (2005) Recent advances of IPM motor drives in power electronics world. *Proc. IEEE Int. Conf. Power Elect. Drives Syst., PEDES*, pp. 24–31.
9. De Doncker, R. W. (2006) Modern electrical drives: Design and future trends. *Proc. IPEMC-2006* 14–16 August, Shanghai, pp. 1–8.
10. Finch, J. W. and Giaouris, D. (2008) Controlled AC electrical drives. *IEEE Trans. Ind. Elect.*, **55**(2), 481–491.
11. Toliyat, H. A. (2008) Recent advances and applications of power electronics and motor drives: Electric machines and motor drives. *Proc. 34th IEEE Ind. Elect. Conf., IECON*, Orlando, FL, pp. 34–36.
12. Bose, B. K. (1998) Advances in power electronics and drives: Their impact on energy and environment. *Proc. Int. Conf. on Power Elect. Drives Ener. Syst. Ind. Growth, PEDES*, vol. 1.
13. Jahns, T. M. and Blasko, V. (2001) Recent advances in power electronics technology for industrial and traction machine drives. *Proc. of IEEE*, **89**(6), 963–975.
14. Bose, B. K. (2005) Power electronics and motor drives: Technology advances, trends and applications. *Proc. IEEE Int. Conf. on Ind. Tech., ICIT*, pp. 20–26.
15. Bose, B. K. (2008) Recent advances and applications of power electronics and motor drives: Introduction and perspective. *Proc. IEEE Ind. Elect. Conf.*, pp. 25–27.
16. Capilino, G. A. (2008) Recent advances and applications of power electronics and motor drives: Advanced and intelligent control techniques. *Proc. IEEE Ind. Elect. Conf., IECON*, pp. 37–39.
17. Lin, F.-J., Hwang, J.-C., Tan, K.-H., Lu, Z.-H., and Chang, Y.-R. (2010) Control of double-fed induction generator system using PIDNNs. *9th Int. Conf. Mach. Learn. Appl.*, pp. 675–680.
18. Muller, S., Deicke, M., and De Doncker, R. W. (2002) Doubly-fed induction generator systems for wind turbines. *IEEE IAS Mag.*, **8**(3), 26–33.
19. Bogalecka, E. (1993) Power control of a non-linear induction generator without speed or position sensor. *Conf. Rec. EPE*, **377**(8), 224–228.
20. Jain, A. K. and Ranganathan, V. T. (2008) Wound rotor induction generator with sensorless control and integrated active filter for feeding non-linear loads in a stand-alone grid. *IEEE Trans. Ind. Elect.*, **55**(1), 218–228.
21. Iwanski, G. and Koczara, W. (2008) DFIG-based power generation system with UPS function for variable-speed applications. *IEEE Trans. Ind. Elect.*, **55**(8), 3047–3054.
22. Pena, R., J. Clare, J. C., and Asher, G. M. (1996) Doubly fed induction generator using back-to-back PWM converters and its application to variable-speed wind-energy generation. *IEEE Proc. Elect. Power Appl.*, **143**(3), 231–241.
23. Forchetti, D., Garcia, G., and Valla, M. I. (2002) Vector control strategy for a doubly-fed stand-alone induction generator. *Proc. 28th IEEE Int. Conf., IECON.*, **2**, 991–995.

24. Pena, R., Clare, J. C., and Asher, G. M (1996) A doubly fed induction generator using back-to-back PWM converters supplying an isolated load from a variable speed wind turbine. *IEEE Proc. Elect. Power Appl.*, **143**(5), 380–387.
25. *The Industrial Electronics Handbook* (2011) CRC Press, Taylor & Francis Group, New York.
26. Forest, F., Labouri, E., Meynard, T. A., and Smet, V. A. (2009) Design and comparison of inductors and inter cell transformers for filtering of PWM inverter output. *IEEE Trans. on Power Elect.*, **24**(3), 812–821.
27. Shen, G., Xu, D., Cao, L., and Zhu, X. (2008) An improved control strategy for grid-connected voltage source inverters with an LCL filter. *IEEE Trans. on Power Elect.*, **23**(4), 1899–1906.
28. Gabe, I. J., Montagner, V. F., and Pinheiro, H. (2009) Design and implementation of a robust current controller for VSI connected to the grid through an LCL filter. *IEEE Trans. on Power Elect.*, **24**(6), 1444–1452.
29. Kojima, M., Hirabayashi, K., Kawabata, Y., Ejiogu, E. C., and Kawabata, T. (2004) Novel vector control system using deadbeat-controlled PWM inverter with output LC filter. *IEEE Trans. on Ind. Appl.*, **40**(1), 162–169.
30. Pasterczyk, R. J., Guichon, J.-M., Schanen, J.-L., and Atienza, E. (2009) PWM inverter output filter cost-to-losses trade off and optimal design. *IEEE Trans. on Ind. Appl.*, **45**(2), 887–897.
31. Bhattacharya, S. S., Deprettere, F., Leupers, R., and Takala, J. (2010) *Handbook of Signal Processing Systems*. Springer.
32. www.ti.com
33. Rich, N. (2010) ‘Xilinx puts ARM core into its FPGAs.’ EE times. Available from, <http://www.eetimes.com/electronics-products/processors/4115523/Xilinx-puts-ARM-core-into-its-FPGAs> (accessed April 27 2010).
34. Leonhard, W. (1996) *Control of Electrical Drives*, 2nd edn. Springer-Verlag.
35. Vas, P. (1998) *Sensorless Vector and Direct Torque Control*. London, Oxford University Press.
36. Vas, P. (1999) *Artificial Intelligence Based Electric Machine and Drives: Application of Fuzzy, Neural, Fuzzy-Neural and Genetic Algorithm Based Techniques*. Oxford, Oxford University Press.
37. Daryabeigi, E., Markadeh, G. R. A., and Lucas, C. (2010) Emotional controller (BELBIC) for electric drives: A review. *Proc. IEEE IECON-2010* pp. 2901–2907.
38. Krzeminski, Z. (1987). Non-linear control of induction motor. *IFAC 10th World Congr. Auto. Cont.*, Munich, pp. 349–354.
39. Abu-Rub, H., Krzeminski, Z., and Guzinski, J. (2000) Non-linear control of induction motor: Idea and application. *EPE–PEMC (9th Int. Power Elect. Mot. Cont. Conf.)* Kosice/Slovak Republic, **6**, 213–218.
40. Holtz, J. (2006) Sensorless control of induction machines: With or without signal injection? *IEEE Trans. Ind. Elect.*, **53**(1), 7–30.
41. Holtz, J. (2002) Sensorless control of induction motor drives. *Proc. IEEE*, **90**(8), 1359–1394.
42. Acarnley, P. P. and Watson, J. F. (2006) Review of position-sensorless operation of brushless permanent-magnet machines. *IEEE Trans. Ind. Elect.*, **53**(2), 352–362.
43. Ward, E. E. and Harer, H. (1969) Preliminary investigation of an inverter-fed 5-phase induction motor. *Proc. IEEE*, **116**(6), 980–984.
44. Levi, E. (2008) Multiphase electric machines for variable-speed applications. *IEEE Trans on Ind. Elect.*, **55**(5), 1893–1909.
45. Abu-Rub, H., Iqbal, A., and Guzinski, J. (2010) Medium voltage drives: Challenges and requirements. *IEEE Int. Symp. on Ind. Elect., ISIE 2010* 4–7 July, Bari, Italy, pp. 1372–1376.



# 2

## Mathematical and Simulation Models of AC Machines

### 2.1 Preliminary Remarks

This chapter describes the basic modeling procedures of power electronic converters and AC machines. The mathematical model thus obtained will be used to develop simulation models using MATLAB/Simulink. The standard approach of mathematical modeling will be described in addition to advanced modeling procedures such as the signal flow graph.

The modeling and simulation of AC machines will be presented. DC motors will be briefly modeled and discussed for educational benefit; those machines are currently rarely used and analyzed, therefore will not be discussed in depth. The AC machines that will be discussed are the most popular three-phase induction machine (squirrel cage and rotor-wound) and three-phase permanent magnet synchronous machine. Machine modeling is a first important step in a better understanding of the topic. The modeling of these machines will introduce the reader to the basics for understanding and analyzing the advanced control techniques of electric drives, such as ‘field oriented control,’ ‘direct torque control,’ ‘feedback linearization control,’ ‘predictive control,’ and ‘sensorless operation.’

The modeling of multiphase machines and IM with inverter output filters will be discussed in later chapters. This also applies to non-linear models of AC machines.

### 2.2 DC Motors

This section presents the modeling of separately excited and series DC motors, to provide educational benefits rather than for practical use. The mathematical models AC and DC machines can be found in [1–5].

### 2.2.1 Separately Excited DC Motor Control

An equivalent circuit of a separately excited DC motor is shown on Figure 2.1. The armature side of the motor is modeled using an ideal voltage source (back EMF) and an armature resistance. The excitation circuit is represented by a field resistor and an inductor. The two circuits are fed by separate voltage sources.

The mathematical model of the separately excited DC motor can be represented as [1–5]

$$u_a = R_a \cdot i_a + L_a \cdot \frac{di_a}{dt} + e \quad (2.1)$$

$$u_f = R_f \cdot i_f + \frac{d\Psi_f}{dt} \quad (2.2)$$

$$J \cdot \frac{d\omega_r}{dt} = t_e - t_l \quad (2.3)$$

where  $u_a$ ,  $u_f$ ,  $i_a$ , and  $i_f$  are armature voltage, field voltage, armature current, and field current, respectively;  $R_a$ ,  $R_f$  are armature and field resistances;  $L_a$  is armature inductance;  $J$  is machine inertia;  $\omega_r$  is rotor angular speed;  $\psi_f$  is field flux;  $e$  is electromagnetic force induced in the armature; and  $t_l$  is the load torque.

The induced voltage  $e$  and motor torque ( $t_e$ ) in the motor are given by

$$e = c_E \cdot i_f \cdot \omega_r \quad (2.4)$$

$$t_e = c_M \cdot \Psi_f \cdot i_a \quad (2.5)$$

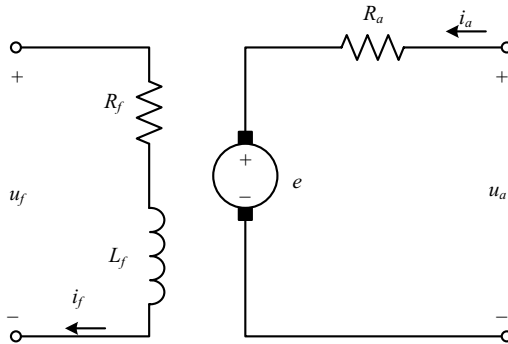


**Figure 2.1** An equivalent circuit of a separately excited DC motor

Assuming a linear magnetic path, the flux is

$$\Psi_f = L_f \cdot i_f \quad (2.6)$$

Using the above equations, the mathematical model presented as differential equations of state is described as

$$\frac{di_a}{dt} = \frac{1}{L_a} \cdot u_a - \frac{R_a}{L_a} \cdot i_a - \frac{c_e \cdot i_f \cdot \omega_r}{L_a} \quad (2.7)$$

$$\frac{di_f}{dt} = \frac{u_f - R_f \cdot i_f}{L_f} \quad (2.8)$$

$$\frac{d\omega_r}{dt} = \frac{1}{J} (c_M \cdot L_f \cdot i_f \cdot i_a - t_l) \quad (2.9)$$

Let us now assume the next nominal values:

$$T_m = \frac{J \cdot \omega_{rn}}{t_n} \quad (2.10)$$

$$T_a = \frac{L_a}{R_a} \quad (2.11)$$

$$T_f = \frac{L_f}{R_f} \quad (2.12)$$

$$K_1 = \frac{u_{na}}{i_{na}} \cdot \frac{1}{R_a} \quad (2.13)$$

$$K_2 = \frac{u_{nf}}{i_{nf}} \cdot \frac{1}{R_f} \quad (2.14)$$

$$K_3 = \frac{E_n}{i_n \cdot R_a} \quad (2.15)$$

where  $u_{na}$ ,  $u_{nf}$ ,  $i_{na}$ , and  $i_{nf}$  are rated values of armature voltage, field voltage, armature current, and field current, respectively;  $t_n$  is the rated torque;  $\omega_{rn}$  is the rated speed; and the rated induced voltage is

$$E_n = c_E \cdot i_{nf} \cdot \omega_{rn} \quad (2.16)$$

This voltage can be also presented as

$$E_n = u_{na} - R_a \cdot i_{na} \quad (2.17)$$

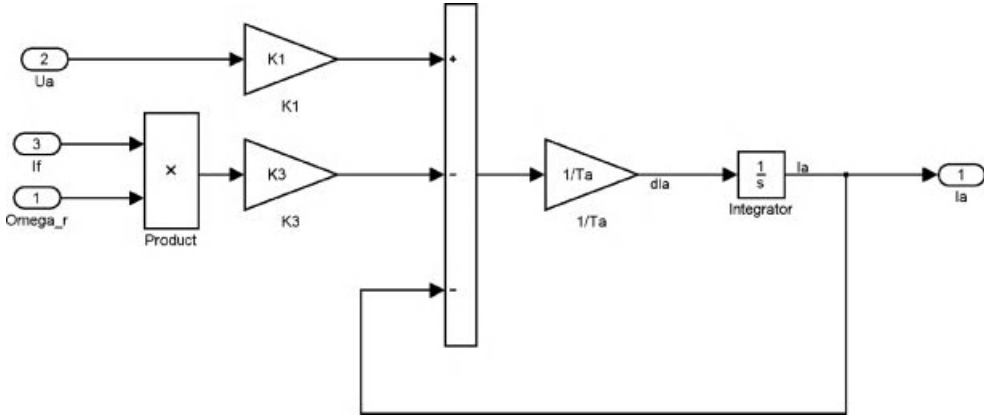


**Figure 2.2** Model of an armature current loop

The per unit model of the motor is

$$\frac{di_a}{dt} = K_1 \cdot \frac{1}{T_a} \cdot u_a - \frac{1}{T_a} \cdot i_a - \frac{K_a \cdot i_f \cdot \omega_r}{T_a} \tag{2.18}$$

$$\frac{di_f}{dt} = K_2 \cdot \frac{u_f}{T_f} - \frac{i_f}{T_f} \tag{2.19}$$

$$\frac{d\omega_r}{dt} = \frac{1}{T_m} (i_f \cdot i_a - t_l) \tag{2.20}$$

The Simulink sub-blocks of the motor model are shown in Figures 2.2–2.4.

### 2.2.2 Series DC Motor Control

An equivalent circuit of a series DC motor is shown in Figure 2.5. The armature side of the motor is connected in series with the field side.

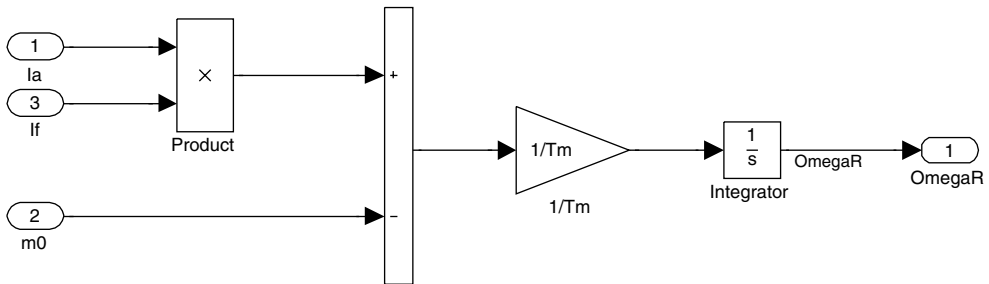


**Figure 2.3** Model of a rotor speed loop

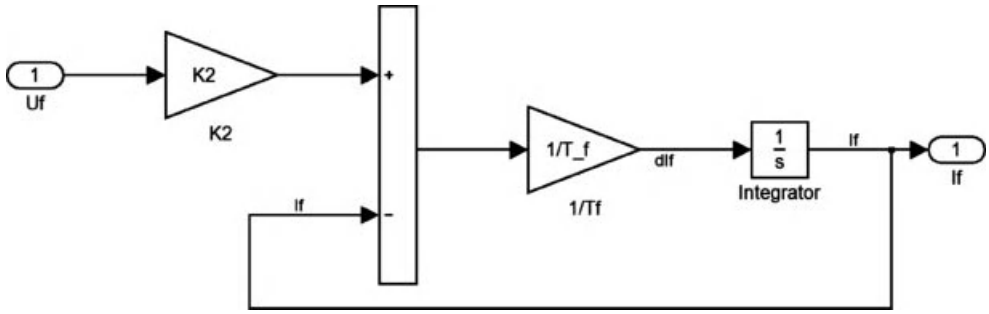


**Figure 2.4** Model of a field current loop

The mathematical model of a series DC motor is

$$\frac{di}{dt} = \frac{1}{L}(u_s - i_a \cdot R - e) \tag{2.21}$$

$$\frac{d\omega_r}{dt} = \frac{1}{J}(t_e - t_l - t_f) \tag{2.22}$$

where  $u_s$  is the voltage source;  $i_a$  is the armature current;  $t_l$  is load torque; and  $J$  is the moment of inertia. The electromagnetic torque  $t_e$  is

$$t_e = c \cdot i^2 \tag{2.23}$$

where  $c$  is the motor constant and the  $t_f$  friction torque is

$$t_f = B \cdot \omega_r \tag{2.24}$$

The back EMF is

$$e = c \cdot i \cdot \omega_r \tag{2.25}$$

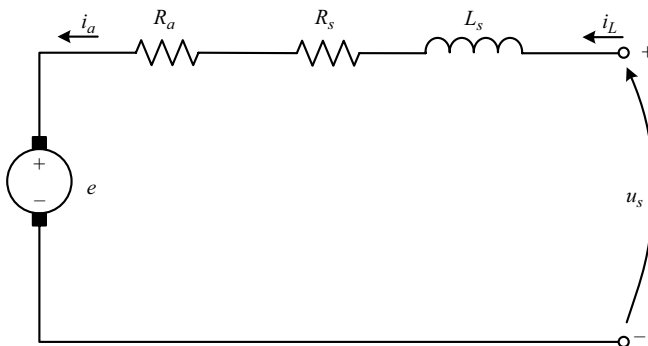


**Figure 2.5** An equivalent circuit of a series DC motor

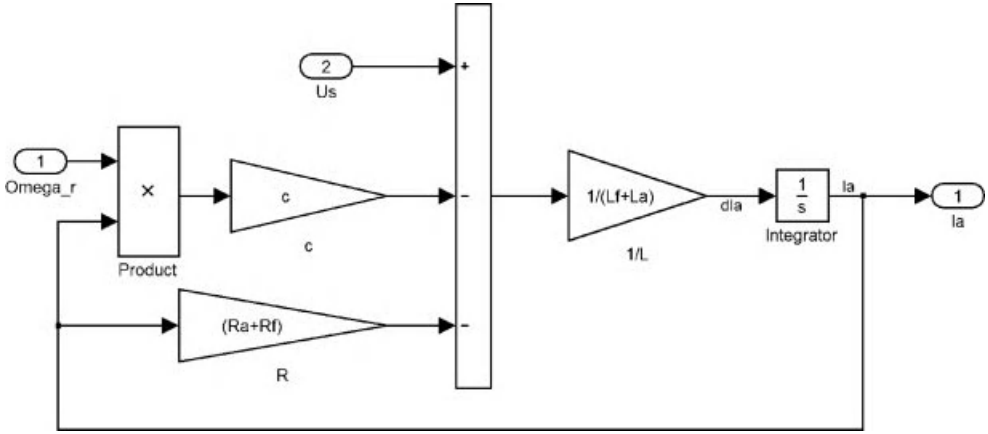


**Figure 2.6** Armature current loop model

The resistance  $R$  is

$$R = R_f + R_a \tag{2.26}$$

The inductance  $L$  is

$$L = L_f + L_a \tag{2.27}$$

The DC series motor model, consisting of an armature current subsystem and a rotor speed subsystem, is shown in Figures 2.6 and 2.7.

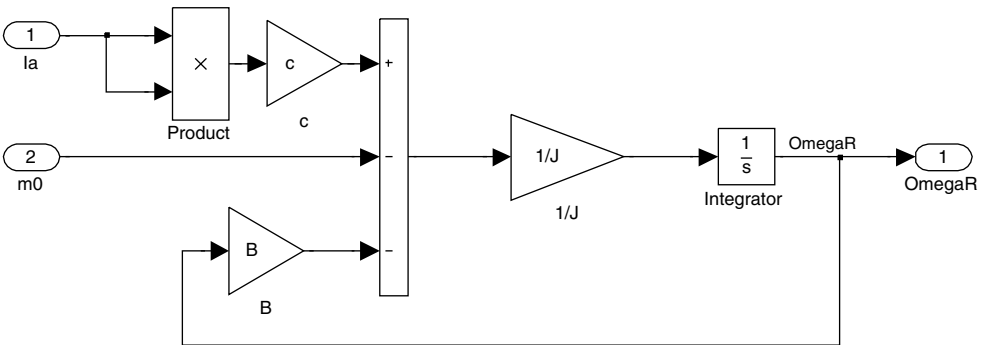


**Figure 2.7** Rotor speed loop model

## 2.3 Squirrel Cage Induction Motor

### 2.3.1 Space Vector Representation

A three-phase AC machine may be described using the space vector method [1–9], as was shown by Kovacs and Racz [6]. For this reason, the AC motor variables  $K_A(t)$ ,  $K_B(t)$ ,  $K_C(t)$  for a symmetrical machine fulfill the condition:

$$K_A(t) + K_B(t) + K_C(t) = 0 \quad (2.28)$$

The summation of these variables gives the space vector:

$$K = \frac{2}{3} [K_A(t) + aK_B(t) + a^2K_C(t)] \quad (2.29)$$

where  $a = e^{j\frac{2}{3}\pi}$  and  $a^2 = e^{j\frac{4}{3}\pi}$

Figure 2.8 shows the stator current complex space vector.

The space vector  $\mathbf{K}$  may represent the motor variables (e.g. current, voltage, and flux). The vector control principle on AC machines takes advantages of transforming the variables from the physical three-phase  $ABC$  system to a stationary frame  $\alpha\beta$ , or rotating frame  $dq$  [3,6].

Let us analyze, as an example, the stator sinusoidal currents  $[i_{SA}, i_{SB}, i_{SC}]$  transformation. The first transformation can be done to a stationary frame  $\alpha\beta$  (Clark transformation), and then to a rotating frame  $dq$  (Park transformation) [1–9].

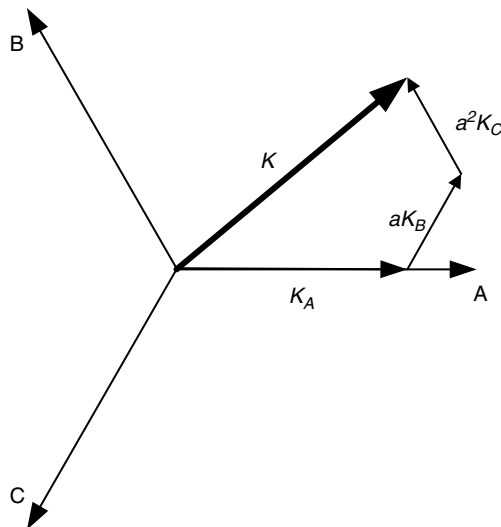


**Figure 2.8** Space vector representation for three-phase variables

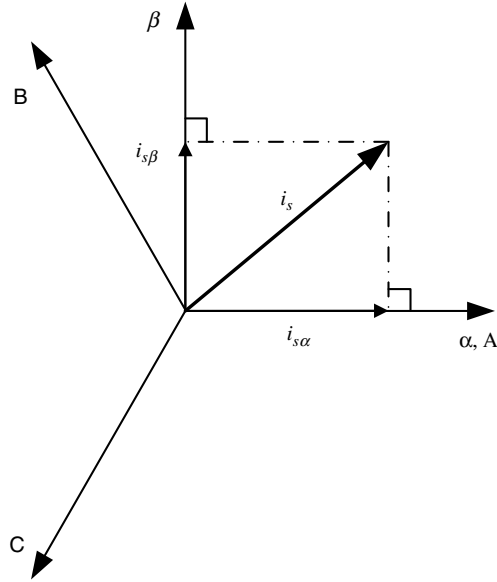


**Figure 2.9** Stator current vector  $\alpha\beta$  components

### 2.3.2 Clarke Transformation ( $ABC$ to $\alpha\beta$ )

The sinusoidal three-phase variables can be represented as a space vector expressed on a two orthogonal axis ( $\alpha\beta$ ), as shown in Figure 2.9.

The stator current as a vector is described by the complex form:

$$\bar{i}_s = i_{s\alpha} + j i_{s\beta} \quad (2.30)$$

where

$$i_{s\alpha} = R_e \left\{ \frac{2}{3} [i_{sA} + a i_{sB} + a^2 i_{sC}] \right\} \quad (2.31)$$

$$i_{s\beta} = \text{Im} \left\{ \frac{2}{3} [i_{sA} + a i_{sB} + a^2 i_{sC}] \right\} \quad (2.32)$$

then

$$i_{s\alpha} = i_{sA} \quad (2.33)$$

$$i_{s\beta} = \frac{1}{\sqrt{3}} (i_{sA} + 2i_{sB}) \quad (2.34)$$



This is equivalent to

$$\begin{bmatrix} i_{s\alpha} \\ i_{s\beta} \end{bmatrix} = \begin{bmatrix} 1 & 0 & 0 \\ \frac{1}{\sqrt{3}} & \frac{2}{\sqrt{3}} & 0 \end{bmatrix} \begin{bmatrix} i_{sA} \\ i_{sB} \\ i_{sC} \end{bmatrix} \quad (2.35)$$

The inverse Clarke transformation from  $\alpha\beta$  to  $ABC$  is

$$\begin{bmatrix} i_{sA} \\ i_{sB} \\ i_{sC} \end{bmatrix} = \begin{bmatrix} 1 & 0 \\ -\frac{1}{2} & -\frac{\sqrt{3}}{2} \\ -\frac{1}{2} & \frac{\sqrt{3}}{2} \end{bmatrix} \begin{bmatrix} i_{s\alpha} \\ i_{s\beta} \end{bmatrix} \quad (2.36)$$

The above transformation does not take into account zero components and it concedes maintaining variable vector length. It is also possible to have a transformation that maintains system power.

The matrix of variables transformation from the three-phase system  $ABC$  to the stationary  $\alpha\beta 0$  system with retaining vector length is

$$\mathbf{A}_W = \begin{bmatrix} \frac{1}{3} & \frac{1}{3} & \frac{1}{3} \\ \frac{2}{3} & -\frac{1}{3} & -\frac{1}{3} \\ 0 & \frac{1}{\sqrt{3}} & -\frac{1}{\sqrt{3}} \end{bmatrix} \quad (2.37)$$

where subscript  $W$  denotes transformation with retaining vector length.

The matrix of variables transformation from  $\alpha\beta 0$  to  $ABC$  with retaining vector length is

$$\mathbf{A}_W^{-1} = \begin{bmatrix} 1 & 1 & 0 \\ 1 & -\frac{1}{2} & \frac{\sqrt{3}}{2} \\ 1 & -\frac{1}{2} & -\frac{\sqrt{3}}{2} \end{bmatrix} \quad (2.38)$$

The matrix of variables transformation from the three-phase system  $ABC$  to the stationary  $\alpha\beta 0$  system with retaining system power is

$$\mathbf{A}_P = \begin{bmatrix} \frac{1}{\sqrt{3}} & \frac{1}{\sqrt{3}} & \frac{1}{\sqrt{3}} \\ \frac{\sqrt{2}}{\sqrt{3}} & -\frac{1}{\sqrt{6}} & -\frac{1}{\sqrt{6}} \\ 0 & \frac{1}{\sqrt{2}} & -\frac{1}{\sqrt{2}} \end{bmatrix} \quad (2.39)$$

where  $\mathbf{A}_P$  denotes transformation with retaining system power.

The matrix of variables transformation from  $\alpha\beta 0$  to  $\mathbf{ABC}$  with retaining system power is

$$\mathbf{A}_P^{-1} = \begin{bmatrix} \frac{1}{\sqrt{3}} & \frac{\sqrt{2}}{\sqrt{3}} & 0 \\ \frac{1}{\sqrt{3}} & -\frac{1}{\sqrt{6}} & \frac{\sqrt{2}}{2} \\ \frac{1}{\sqrt{3}} & -\frac{1}{\sqrt{6}} & -\frac{\sqrt{2}}{2} \end{bmatrix} \quad (2.40)$$

Variables transformation from one reference frame to another is done according to the procedures:

- For transformation with retaining vector length:

$$\begin{bmatrix} x_0 \\ x_\alpha \\ x_\beta \end{bmatrix} = \mathbf{A}_W \begin{bmatrix} x_A \\ x_B \\ x_C \end{bmatrix} \quad (2.41)$$

$$\begin{bmatrix} x_A \\ x_B \\ x_C \end{bmatrix} = \mathbf{A}_W^{-1} \begin{bmatrix} x_0 \\ x_\alpha \\ x_\beta \end{bmatrix} \quad (2.42)$$

- For transformation with retaining system power:

$$\begin{bmatrix} x_0 \\ x_\alpha \\ x_\beta \end{bmatrix} = \mathbf{A}_P \begin{bmatrix} x_A \\ x_B \\ x_C \end{bmatrix} \quad (2.43)$$

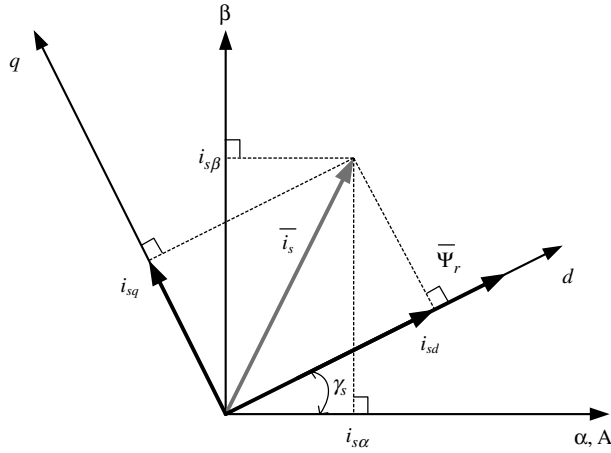


**Figure 2.10** Stator current space vector and its component in  $(\alpha, \beta)$  and in the  $(d, q)$  rotating reference frame

$$\begin{bmatrix} x_A \\ x_B \\ x_C \end{bmatrix} = \mathbf{A}_P^{-1} \begin{bmatrix} x_0 \\ x_\alpha \\ x_\beta \end{bmatrix} \quad (2.44)$$

where  $x$  denotes arbitrary variable in specific reference system.

### 2.3.3 Park Transformation ( $\alpha\beta$ to $dq$ )

This transformation aims to project the two phase components  $\alpha\beta$  in stationary frame to the  $dq$  rotating reference frame rotating with angular speed  $\omega_k$ . If we consider the  $d$ -axis aligned with the rotor flux in axis  $d$ , then we speak about rotor flux oriented system. As an example, stator current space vector and its component in  $(\alpha, \beta)$  and in the  $(d, q)$  are shown in Figure 2.10.

The current vector in  $dq$  frame is

$$\bar{i}_s = i_{sd} + j i_{sq} \quad (2.45)$$

which is equivalent to

$$\bar{i}_s = (i_{s\alpha} \cos(\gamma_s) + i_{s\beta} \sin(\gamma_s)) + j(i_{s\beta} \cos(\gamma_s) - i_{s\alpha} \sin(\gamma_s)) \quad (2.46)$$

Following this:

$$\bar{i}_s = \begin{bmatrix} i_{sd} \\ i_{sq} \end{bmatrix} = \begin{bmatrix} \cos(\gamma_s) & \sin(\gamma_s) \\ -\sin(\gamma_s) & \cos(\gamma_s) \end{bmatrix} \begin{bmatrix} i_{s\alpha} \\ i_{s\beta} \end{bmatrix} \quad (2.47)$$

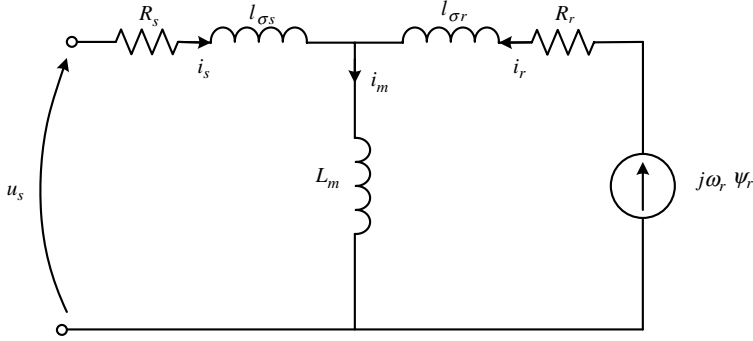


**Figure 2.11** Per-phase equivalent circuit of induction motor

The inverse Park transformation is

$$\bar{i}_s = \begin{bmatrix} i_{s\alpha^*} \\ i_{s\beta^*} \end{bmatrix} = \begin{bmatrix} \cos(\gamma_s) & -\sin(\gamma_s) \\ \sin(\gamma_s) & \cos(\gamma_s) \end{bmatrix} \begin{bmatrix} i_{sd^*} \\ i_{sq^*} \end{bmatrix} \quad (2.48)$$

The transformation may be applied to all space vectors (e.g. stator voltage, rotor flux, etc.).

### 2.3.4 Per Unit Model of Induction Motor

A per-phase equivalent circuit of an induction motor is shown in Figure 2.11. It consists of stator side resistance and leakage inductance, mutual inductance, rotor side resistance, inductance, and induced voltage.

The induction motor in arbitrary reference frame  $\mathbf{K}$  can be presented per unit rotating angular speed  $\omega_k$  as

$$u_{sk} = R_{sk}i_{sk} + \frac{d\psi_{sk}}{dt} + j\omega_k\psi_{sk} \quad (2.49)$$

$$u_{rk} = R_{rk}i_{rk} + \frac{d\psi_{rk}}{dt} + j(\omega_k - \omega_r)\psi_{sk} \quad (2.50)$$

$$\psi_{sk} = L_s i_{sk} + L_m i_{rk} \quad (2.51)$$

$$\psi_{rk} = L_r i_{rk} + L_m i_{sk} \quad (2.52)$$

$$\frac{d\omega_r}{dt} = \frac{1}{T_M} [I_m(\psi_{sk}^* i_{sk}) - t_l] \quad (2.53)$$

where  $T_M$  is the mechanical time constant; where  $u_s, i_s, i_r, \psi_s, \psi_r$  are voltage, current, and flux (stator and rotor) vectors;  $R_s, R_r$  are stator and rotor resistances;  $\omega_r$  is rotor angular speed;  $\omega_a$  an angular speed of reference frame;  $J$  a moment of inertia; and  $t_l$  is load torque.

The currents relations are:

$$i_s = \frac{1}{L_s} \Psi_s - \frac{L_m}{L_s} i_r, \quad (2.54)$$

$$i_r = \frac{1}{L_r} \Psi_r - \frac{L_m}{L_r} i_s, \quad (2.55)$$

The induction motor (IM) model presented per unit in the rotating frame with arbitrary speed is given by [10,21]

$$\frac{di_{sx}}{d\tau} = \frac{R_s L_r^2 + R_r L_m^2}{L_r w_\sigma} i_{sx} + \frac{R_r L_m}{L_r w_\sigma} \psi_{rx} + \omega_k \cdot i_{sy} + \omega_r \frac{L_m}{w_\sigma} \psi_{ry} + \frac{L_r}{w_\sigma} u_{sx} \quad (2.56)$$

$$\frac{di_{sy}}{d\tau} = \frac{R_s L_r^2 + R_r L_m^2}{L_r w_\sigma} i_{sy} + \frac{R_r L_m}{L_r w_\sigma} \psi_{ry} - \omega_k \cdot i_{sx} - \omega_r \frac{L_m}{w_\sigma} \psi_{rx} + \frac{L_r}{w_\sigma} u_{sy} \quad (2.57)$$

$$\frac{d\psi_{rx}}{d\tau} = -\frac{R_r}{L_r} \psi_{rx} + \omega_r \psi_{ry} + \frac{R_r L_m}{L_r} i_{sx} \quad (2.58)$$

$$\frac{d\psi_{ry}}{d\tau} = -\frac{R_r}{L_r} \psi_{ry} + \omega_r \psi_{rx} + \frac{R_r L_m}{L_r} i_{sy} \quad (2.59)$$

$$\frac{d\omega_r}{d\tau} = \frac{L_m}{J L_r} (\psi_{rx} i_{sy} - \psi_{ry} i_{sx}) - \frac{1}{J} t_o \quad (2.60)$$

Here,  $u_s, i_s, i_r, \psi_s, \psi_r$  are voltage, current, and flux (stator and rotor) vectors;  $R_s, R_r$  are stator and rotor resistances;  $\omega_r$  is rotor angular speed;  $\omega_k$  is angular speed of reference frame;  $J$  is moment of inertia; and  $t_o$  is load torque.

The mathematical model of IM as differential equations of state variables presented in  $(\alpha\beta)$  stationary reference frame and  $(\omega_k = 0)$  is [10]

$$\frac{di_{s\alpha}}{dt} = a_1 \cdot i_{s\alpha} + a_2 \cdot \Psi_{r\alpha} + \omega_r \cdot a_3 \cdot \Psi_{r\beta} + a_4 \cdot u_{s\alpha} \quad (2.61)$$

$$\frac{di_{s\beta}}{dt} = a_1 \cdot i_{s\beta} + a_2 \cdot \Psi_{r\beta} - \omega_r \cdot a_3 \cdot \Psi_{r\alpha} + a_4 \cdot u_{s\beta} \quad (2.62)$$

$$\frac{d\Psi_{r\alpha}}{dt} = a_5 \cdot \Psi_{r\alpha} + (-\omega_r) \cdot \Psi_{r\beta} + a_6 \cdot i_{s\alpha} \quad (2.63)$$

$$\frac{d\Psi_{r\beta}}{dt} = a_5 \cdot \Psi_{r\beta} + (-\omega_r) \cdot \Psi_{r\alpha} + a_6 \cdot i_{s\beta} \quad (2.64)$$

$$\frac{d\omega_r}{d\tau} = \frac{L_m}{L_r J} (\psi_{r\alpha} i_{s\beta} - \psi_{r\beta} i_{s\alpha}) - \frac{1}{J} t_o \quad (2.65)$$

where:

$$a_1 = -\frac{R_s L_r^2 + R_r L_m^2}{L_r w} \quad (2.66)$$

$$a_2 = \frac{R_r L_m}{L_r w} \quad (2.67)$$

$$a_3 = \frac{L_m}{w} \quad (2.68)$$

$$a_4 = \frac{L_r}{w} \quad (2.69)$$

$$a_5 = -\frac{R_r}{L_r} \quad (2.70)$$

$$a_6 = R_r \frac{L_m}{L_r} \quad (2.71)$$

$$w = \sigma L_r L_s = L_r L_s - L_m^2 \quad (2.72)$$

$$\sigma = 1 - \frac{L_m^2}{L_r L_s} \quad (2.73)$$

The above equations are modeled in Figure 2.12.

### 2.3.5 Double Fed Induction Generator (DFIG)

The mathematical model of DFIG is similar to the squirrel cage induction machine, the only difference being that the rotor voltage is not zero [10–15]. The equations representing the DFIG [10–15] are

$$\vec{v}_s = R_s \vec{i}_s + \frac{d\vec{\psi}_s}{dt} + j\omega_s \vec{\psi}_s \quad (2.74)$$

$$\vec{v}_r = R_r \vec{i}_r + \frac{d\vec{\psi}_r}{dt} + j(\omega_s - \omega_r) \vec{\psi}_r \quad (2.75)$$

$$\vec{\psi}_s = L_s \vec{i}_s + L_m \vec{i}_r \quad (2.76)$$

$$\vec{\psi}_r = L_r \vec{i}_r + L_m \vec{i}_s \quad (2.77)$$

where  $v_r$  and  $v_s$  are rotor and stator voltages;  $\psi_r$  and  $\psi_s$  are rotor and stator fluxes;  $R_r$ ,  $R_s$ ,  $L_r$ , and  $L_s$  are rotor and stator resistances and inductances;  $L_m$  represents mutual inductance; and  $\omega_r$  and  $\omega_s$  are rotor and synchronous angular speeds.

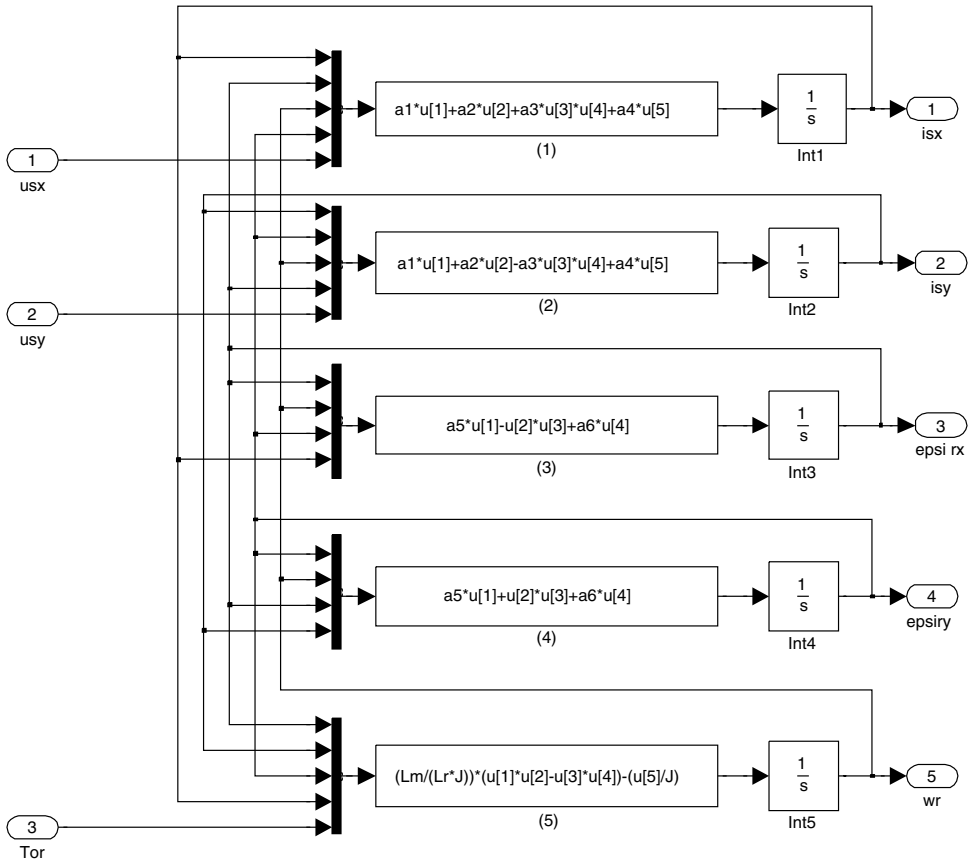


Figure 2.12 Induction motor model

In the rotating  $dq$  reference frame, the machine model is

$$v_{ds} = R_s i_{ds} - \omega_s \psi_{qs} + \frac{d\psi_{ds}}{dt} \tag{2.78}$$

$$v_{qs} = R_s i_{qs} - \omega_s \psi_{ds} + \frac{d\psi_{qs}}{dt} \tag{2.79}$$

$$v_{dr} = R_r i_{dr} - (\omega_s - \omega_r) \psi_{qr} + \frac{d\psi_{dr}}{dt} \tag{2.80}$$

$$v_{qr} = R_r i_{qr} + (\omega_s - \omega_r) \psi_{dr} + \frac{d\psi_{qr}}{dt} \tag{2.81}$$

$$\psi_{ds} = L_s i_{ds} + L_m i_{dr} \tag{2.82}$$

**Table 2.1** Base values of DFIG

<i>Base Values</i>	
Voltage	$V_b = V_n$
Power	$S_b = S_n$
Current	$I_b = \frac{S_b}{\sqrt{3}V_b}$
Impedance	$Z_b = \frac{V_b^2}{S_n}$
Speed	$\omega_b = 2\pi f_n$
Torque	$T_b = \frac{S_b}{\omega_b / p}$
Flux	$\psi_b = \frac{V_b}{\omega_b}$
Torque	$T_b = \frac{S_b}{\omega_b^3 / p}$

$$\psi_{qs} = L_s i_{qs} + L_m i_{qr} \quad (2.83)$$

$$\psi_{dr} = L_r i_{dr} + L_m i_{ds} \quad (2.84)$$

$$\psi_{qr} = L_r i_{qr} + L_m i_{qs} \quad (2.85)$$

The produced torque is

$$T_e = \frac{3}{2}p(\psi_{dr}i_{qs} - \psi_{qr}i_{ds}) = \frac{3}{2}pL_m(i_{dr}i_{qs} - i_{qr}i_{ds}) \quad (2.86)$$

and the mechanical part of the model is

$$\frac{d\omega_m}{dt} = \frac{p}{J}(T_e - T_L) \quad (2.87)$$

The base values of the machine used to derive the above per unit model are shown in Table 2.1.

The  $\alpha\beta$  ( $xy$ ) per unit model of DFIG, connected with the grid, is described by following deferential equations of state variables (stator flux components and rotor current referred to the rotor side) as

$$\frac{d\phi_{sx}}{dt} = a_{11}\phi_{sx} + a_{12}u_{sx}i_{rx} \quad (2.88)$$

$$\frac{d\phi_{sy}}{dt} = a_{11}\phi_{sy} + a_{12}u_{sy}i_{ry} \quad (2.89)$$



$$\frac{di_{rxR}}{dt} = a_{21}i_{rxR} + a_{22}\phi_{sxR} - a_{23}\omega_r\phi_{syR} + b_{21}u_{rx} - b_{22}u_{sxR} \quad (2.90)$$

$$\frac{di_{ryR}}{dt} = a_{21}i_{ryR} + a_{22}\phi_{syR} - a_{23}\omega_r\phi_{sxR} + b_{21}u_{ry} - b_{22}u_{syR} \quad (2.91)$$

$$\frac{d\gamma_{fir}}{dt} = \omega_r \quad (2.92)$$

$$\frac{d\gamma_{ksi}}{dt} = \omega_s - \omega_r \quad (2.93)$$

The system constants  $a, b$  are defined as

$$a_{11} = -\frac{R_s}{L_s}, \quad a_{12} = \frac{R_s L_m}{L_s} \quad (2.94)$$

$$a_{21} = -\frac{(L_s^2 R_r + L_m^2 R_s)}{L_s(L_s L_r - L_m^2)}, \quad a_{22} = -\frac{L_m R_s}{L_s(L_s L_r - L_m^2)}, \quad a_{23} = -\frac{L_m}{L_s L_r - L_m^2} \quad (2.95)$$

$$b_{21} = -\frac{L_s}{L_s L_r - L_m^2}, \quad b_{22} = -\frac{L_m}{L_s L_r - L_m^2} \quad (2.96)$$

In these formulas,  $u_s, i_s$  are stator voltage and current vectors;  $R_s, L_s$  are stator resistances and inductances; and  $\omega_r, \omega_s$  are rotor and stator angular speed. The angle  $\gamma_{fir}$  is in the rotor angular position (fir in MATLAB/Simulink) and  $\gamma_{ksi}$  is the angle between stator flux and rotor speed (ksi in MATLAB/Simulink). The above equations are modeled using MATLAB/Simulink, as shown in Figure 2.13.

## 2.4 Mathematical Model of Permanent Magnet Synchronous Motor

The mathematical model of PMSM per unit in an arbitrary reference frame rotating with  $\omega_k$  is [16–20,22,23]

$$\vec{u}_s = R_s \vec{i}_s + \frac{d\vec{\psi}_s}{dt} + j\omega_k \vec{\psi}_s, \quad (2.97)$$

$$\vec{\psi}_s = L_s \vec{i}_s + \vec{\psi}_f, \quad (2.98)$$

$$\frac{d\omega_r}{dt} = \frac{1}{J}(t_e - t_l), \quad (2.99)$$

$$\frac{d\theta}{dt} = \omega_r, \quad (2.100)$$

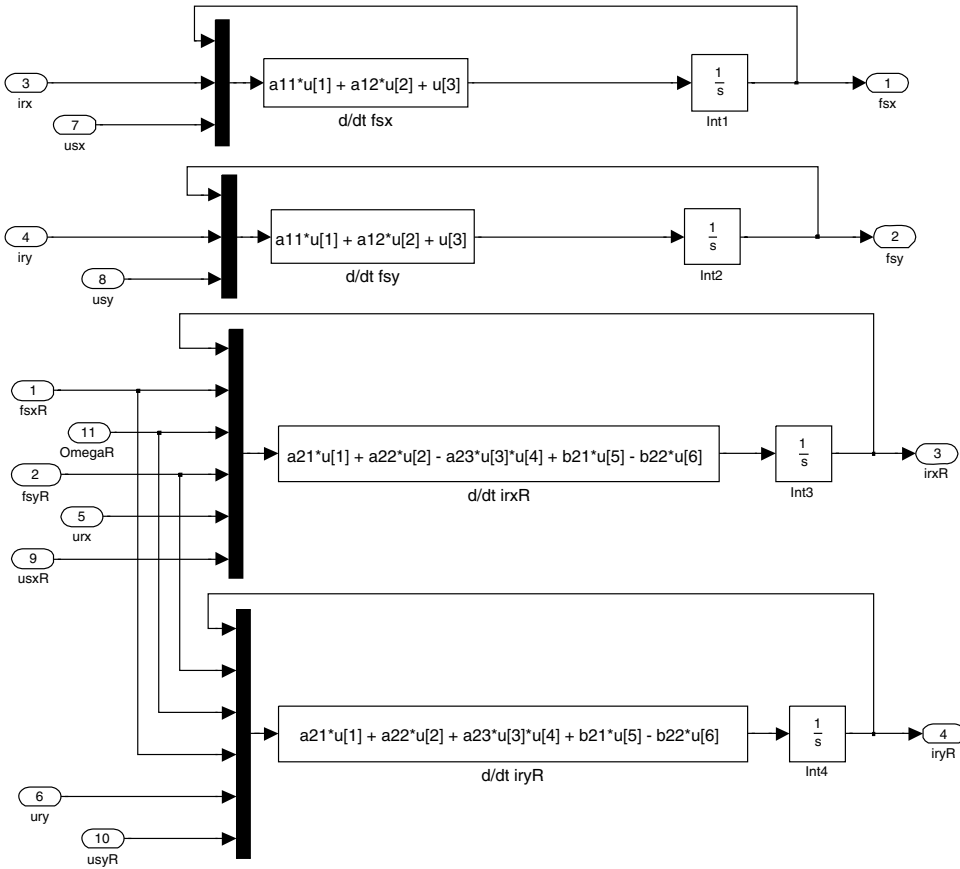


Figure 2.13 DFIG model in  $\alpha$ - $\beta$ -axis

where  $\omega_r$  is the rotor angular speed;  $\theta$  is the position of the rotor angle; and  $\psi_f$  is the permanent magnet flux.

### 2.4.1 Motor Model in $dq$ Rotating Frame

It is convenient to design the control scheme and represent the motor model in a  $dq$  frame rotating with rotor speed. The variables transformation from/to the stationary frame ( $\alpha\beta$ ) to/from the rotating one ( $dq$ ) is realized according to space vector theory, using the equations presented earlier in this chapter.

The schematic of the PMSM for the  $dq$ -axis is represented in Figure 2.14.

In the PMSM, the main magnetic field is produced by permanent magnets. Those magnets are placed on the rotor. The result flux is constant in time, assuming that stator current has no effect (no armature reaction). In reality the stator current produces its own magnetic field affecting the original, which is called the armature reaction. The net stator flux is the summation of the two fluxes (Figure 2.15) as [20]

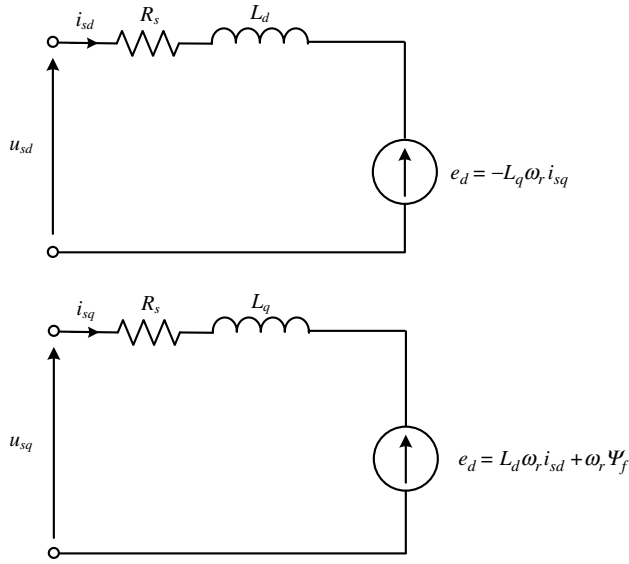


**Figure 2.14** Schematics of the PMSM in  $dq$  frame

$$\Psi_d = \Psi_{ad} + \Psi_f = L_d i_d + \Psi_f, \tag{2.101}$$

$$\Psi_q = \Psi_{aq} = L_q i_q. \tag{2.102}$$

where stator leakage fluxes are

$$\Psi_{ad} = L_d i_d \tag{2.103}$$

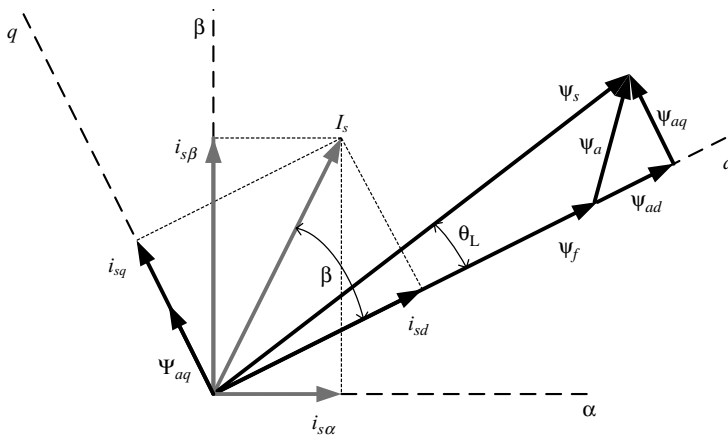


**Figure 2.15** Phasor diagram of stator flux and stator current

$$\Psi_{aq} = L_q i_q \quad (2.104)$$

From Figure 2.15 it is evident that the distortion of the magnetic field depends on the stator current position and magnitude. At no load condition, the armature reaction is assumed to be zero because of negligible amounts of stator current.

Back EMF ( $e$ ) induced in the motor coils can be presented on the  $dq$ -axis as

$$e_d = -L_q \omega_r i_q \quad (2.105)$$

$$e_q = L_d \omega_r i_d + \omega_r \psi_f \quad (2.106)$$

The produced torque of the machine can be presented as a function of the back EMF in the  $\alpha\beta$  reference frame as

$$t_e = \frac{(e_\alpha i_\alpha + e_\beta i_\beta)}{\omega_r} \quad (2.107)$$

The maximum rotor speed can be identified from the relationship:

$$\omega_{max} = \frac{E_{s\ max}}{\Psi_s} \quad (2.108)$$

where  $E_{s\ max}$  is the maximum induced phase voltage in the machine and  $\omega_{max}$  is the maximum motor speed for the rated flux. Higher speed can be obtained by weakening the flux.

Therefore, for a motor with  $E_{s\ max} = 248$  V and  $\omega_{max} = 209.4$  rad/sec, the flux is

$$\Psi_s = \frac{E_{s\ max}}{\omega_{max}} = \frac{248}{209.4} = 1.18[\text{Wb}]$$

#### 2.4.2 Example of Motor Parameters for Simulation

Motor parameters are presented in Tables 2.2 and 2.3 for rated values and in per unit [17,18].

#### 2.4.3 PMSM Model in Per Unit System

Mathematical models of the PMSM can be presented as differential equations of state variables. This can be presented either on the  $dq$ -axis, which is the preferred solution, or in a stationary frame. The motor model in the  $dq$ -axis rotating with rotor speed is [18,22]

$$\frac{di_d}{dt} = -\frac{R_s}{L_d} i_d + \frac{L_q}{L_d} \omega_r i_q + \frac{1}{L_d} u_d \quad (2.109)$$

**Table 2.2** Base values for PMSM motor model

Variable	Value	Unit	Description
$U_b$	429.5	[V]	voltage
$I_b$	467.7	[A]	current
$Z_b$	0.918518519	[Ohm]	impedance
$\Omega_{mb}$	868.7	[rad/s]	mechanical speed
$\Psi_b$	0.514020925	[Wb]	flux
$L_b$	0.001099149	[H]	inductance
$T_b$	961.5	[Nm]	torque
$\Omega_0$	835.7	[rad/s]	electrical pulsation
$J_b$	0.001324577	[kg*m <sup>2</sup> ]	inertia

$$\frac{di_q}{dt} = -\frac{R_s}{L_q} i_q - \frac{L_d}{L_q} \omega_r i_d - \frac{1}{L_q} \omega_r \psi_f + \frac{1}{L_q} u_q \quad (2.110)$$

$$\frac{d\omega_r}{dt} = \frac{1}{T_M} [\psi_f i_q + (L_d - L_q) i_d i_q - t_l] \quad (2.111)$$

$$\frac{d\theta_r}{dt} = \omega_r \quad (2.112)$$

where  $u_s, i_s$  are stator voltage and current vectors;  $R_s$  is stator resistances;  $R_s, R_q, L_d, L_q$  are rotor resistances and inductances when referring to  $d$  and  $q$  axes;  $\omega_r$  is rotor angular speed;  $J$  is moment of inertia;  $t_l$  is the load torque and  $T_M$  is the mechanical time constant.

The above equations are modeled in MATLAB/Simulink, as shown in Figure 2.16.

**Table 2.3** Motor parameters in per unit system [21]:

Parameter	Value	Unit	Description
$R_s$	0.021774	[p.u.]	for 20[C]
$R_s$	0.032988	[p.u.]	for 150[C]
$l_f$	0.24564	[p.u.]	
$L_{ad} = L_m$	0.61866	[p.u.]	
$L_d$	0.86431	[p.u.]	
$L_q$	0.864305343	[p.u.]	
$\psi_e$	2.304	[p.u.]	
$J$	189	[p.u.]	For the motor only
$T_n$	0.65	[p.u.]	Rated torque

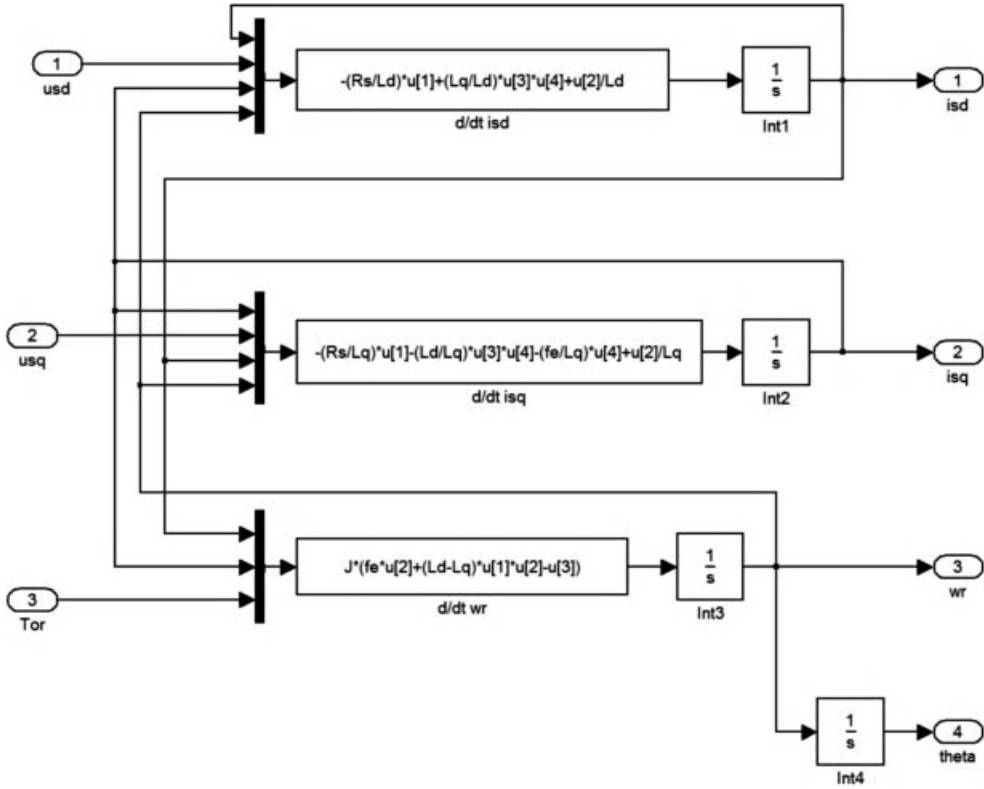


Figure 2.16 Simulink model of interior PMSM

The parameters of the interior type PMSM to be simulated are

$$R_s = 0.032988;$$

$$L_d = 0.86431;$$

$$L_q = 0.86431;$$

$$\psi_f = \psi_f = 2.3036;$$

$$J = 0.00529. \text{ Rated speed is } 2000 \text{ rpm.}$$

#### 2.4.4 PMSM Model in $\alpha$ - $\beta$ ( $x$ - $y$ )-Axis

The Permanent Magnet Synchronous Machine (PMSM) model presented in per unit  $\alpha$ - $\beta$  reference frame is given by [23]

$$\frac{di_{sx}}{dt} = \frac{1}{L_d} \omega_r \phi_{sy} + (u_{sx} - R_s i_{sx}) \left( \frac{1}{L_d} \cos^2 \theta + \frac{1}{L_q} \sin^2 \theta \right) + 0.5 (u_{sy} - R_s i_{sy}) \sin 2\theta \left( \frac{1}{L_d} - \frac{1}{L_q} \right) \quad (2.113)$$

$$\frac{di_{sy}}{dt} = \frac{1}{L_d} \omega_r \phi_{sx} + (u_{sy} - R_s i_{sy}) \left( \frac{1}{L_d} \sin^2 \theta + \frac{1}{L_q} \cos^2 \theta \right) + 0.5(u_{sx} - R_s i_{sx}) \sin 2\theta \left( \frac{1}{L_d} - \frac{1}{L_q} \right) \tag{2.114}$$

$$\frac{d\omega_r}{dt} = J [\phi_{sx} i_{sy} - \phi_{sy} i_{sx} - t_l] \tag{2.115}$$

$$\frac{d\theta}{dt} = \omega_r \tag{2.116}$$

where

$$\phi_{sx} = \frac{L_d}{L_q} F_f \cos \theta - \left( 1 - \frac{L_d}{L_q} \right) L_0 (i_{sx} \cos 2\theta + i_{sy} \sin 2\theta) + L_2 i_{sx} \tag{2.117}$$

$$\phi_{sy} = \frac{L_d}{L_q} F_f \sin \theta - \left( 1 - \frac{L_d}{L_q} \right) L_0 (i_{sy} \cos 2\theta + i_{sx} \sin 2\theta) + L_2 i_{sy} \tag{2.118}$$

$$L_0 = \frac{L_d + L_q}{2} \quad \text{and} \quad L_2 = \frac{L_d - L_q}{2} \tag{2.119}$$

where,  $u_s, i_s$  are stator voltage and current vectors;  $R_s$  is stator resistances, which are rotor inductances when referred to on the  $d$  and  $q$  axes;  $\omega_r$  is rotor angular speed;  $J$  is the moment of inertia; and  $t_l$  is the load torque. The above equations are modeled in Figure 2.17.

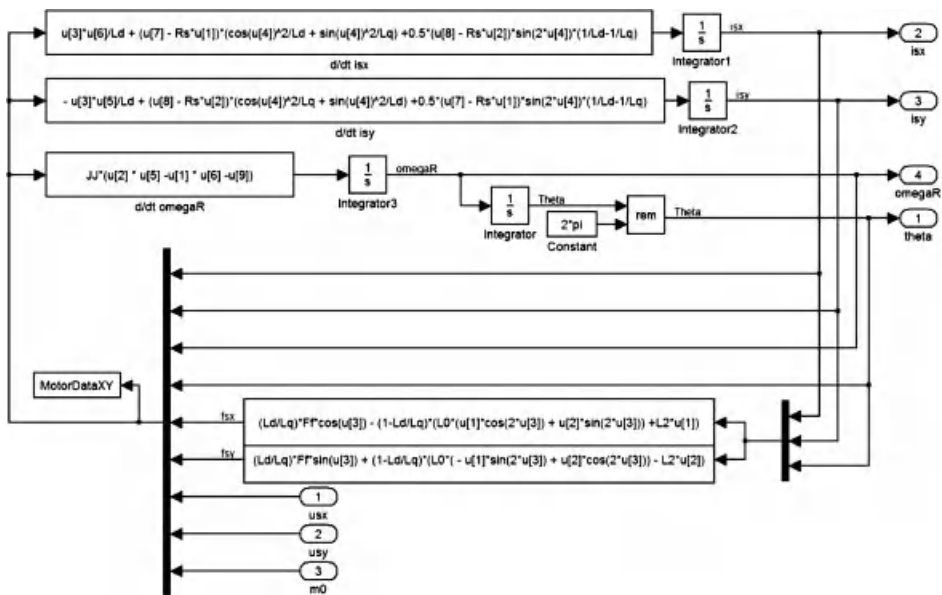


Figure 2.17 PMSM model in  $\alpha$ - $\beta$  axis

## 2.5 Problems

Design the models for IM, DFIG, and PMSM, by working with sinusoidal input signals.

## References

1. Mohan, N. (2001) *Electric Drives an Integrative Approach*, 2nd edn, MNPERE, Minneapolis.
2. Bose, B. K. (2006) *Power Electronics and Motor Drives: Advances and Trends*. Amsterdam, Academic Press, Elsevier.
3. Leonhard, W. (2001) *Control of Electrical Drives*. Berlin, Springer.
4. Krishnan, R. (2001) *Electric Motor Drives: Modeling, Analysis and Control*. Prentice Hall.
5. Chiasson, J. (2005) *Modeling and High Performance Control of Electric Machines*. Chichester, John Wiley & Sons.
6. Kovacs, K.P. and Racz, I. (1959) *Transiente Vorgange in Wechselstrommaschinen*. Budapest, Akad. Kiado.
7. Blaschke F. (1971) Das Prinzip der Feldorientierung, die Grundlage für Transvector-regelung von Drehfeld-maschine, *Siemens Z*, **45**, 757–760.
8. Texas Instruments Europe (1998) *Field Orientated Control of 3-Phase AC-Motors*. Texas Instruments, Inc.
9. Mohan, N. (2001) *Advanced Electric Drives Analysis, Control, and Modeling using Simulink*. MNPERE, Minneapolis.
10. Bogdan, M. Wilamowski, J., and Irwin, D. (2011) *The Industrial Electronics Handbook: Power Electronics and Motor Drives*. Taylor and Francis Group, LLC.
11. Bogalecka, E. (1993) Power control of a double fed induction generator without speed or position sensor. *Conf. Rec. EPE*, pt. 8, vol **377**, ch. **50**, pp. 224–228.
12. Iwanski, G. and Koczara, W. (2008) DFIG-based power generation system with UPS function for variable-speed applications. *IEEE Trans. Ind. Electn.*, **55**(8), 3047–3054.
13. Lin, F-J., Hwang, J-C., Tan, K-H., Lu, Z-H., and Chang, Y-R. (2010) Control of doubly-fed induction generator system using PIDNNs. *2010 9th Int. Conf. Mach. Learn. Appl.* pp. 675–680.
14. Pena, R., Clare, J. C., and Asher, G. M. (1996) Doubly fed induction generator using back-to-back PWM converters and its application to variable-speed wind-energy generation. *IEEE Proc. -Electr. Power Appl.*, **143**(3), 231–241.
15. Muller, M. and De Doncker, R. W. (2002) Doubly-fed induction generator systems for wind turbines. *IEEE IAS Mag.*, **8**(3), 26–33.
16. Pillay, P. and Knshnan, R. (1988) Modeling of permanent magnet motor drives. *IEEE Trans. Ind. Elect.*, **35**(4)
17. Burgos, R. P., Kshirsagar, P., Lidozzi, A., Wang, F., and Boroyevich, D. (2006) Mathematical model and control design for sensorless vector control of permanent magnet synchronous machines. *IEEE COMPEL Workshop, Rensselaer Polytech. Inst.*, Troy, NY, July 16–19.
18. Pajchrowski, T. and Zawirski, K. (2005) Robust speed control of servodrive based on ANN. *IEEE ISIE 2005* June 20–23, Dubrovnik.
19. Pillay, P. and Krishnan, R. (1988) Modeling of permanent magnet motor drives. *IEEE Trans. Ind. Elect.*, **35**(4).
20. Stulrajter, M., Hrabovcova, V., and Franko, M. (2007) Permanent magnets synchronous motor control theory. *J. Elect. Eng.*, **58**(2), 79–84.
21. Krzemiński, Z. (1987) Nonlinear control of induction motor. *10th World Cong. Auto. Cont., IFAC '87*, Monachium, Niemcy. pp. 27–31.



22. Zawirski, K. (2005) *Control of Permanent Magnet Synchronous Motors (in Polish)* Poznan, Poland.
23. Morawiec, M., Krzemiński, Z., and Lewicki, A. (2009) Control of PMSM with rotor speed observer: Sterowanie silnikiem o magnesach trwałych PMSM z obserwatorem prędkości kątovej wirnika. *Przegląd Elektrotechniczny (Electrical Review) (in Polish)*, 0033-2097 R. 85 NR 8/2009.

# 3

## Pulse Width Modulation of Power Electronic DC-AC Converter

### 3.1 Preliminary Remarks

The Pulse Width Modulation (PWM) technique is applied in the inverter (DC/AC converter) to output an AC waveform with variable voltage and variable frequency for use in mostly variable speed motor drives. The input to the inverter is DC, obtained from either a controlled or uncontrolled rectifier. Hence, an inverter is a two-stage power converter that transforms first the grid AC to DC and then DC to AC. PWM and the control of the Power Electronic DC-AC converter has attracted much attention in the last three decades. Research is still active in this area and several schemes have been suggested in the literature [1–6]. The basic idea is to modulate the duration of the pulses or duty ratio in order to achieve controlled voltage/current/power and frequency, satisfying the criteria of equal area. The implementation of the complex PWM algorithms have been made easier due to the advent of fast digital signal processors, microcontrollers, and Field Programmable Gate Arrays (FPGA). The PWM is the basic energy processing technique used in Power Electronic converters initially implemented with the analog technology using discrete electronic components. Nowadays, they are digitally implemented through modern signal processing devices. This chapter gives an overview of the PWM techniques based on the most basic and classical sinusoidal carrier-based scheme to modern space vector PWM (SVPWM). The literature shows an implicit relationship between the sinusoidal carrier-based PWM (SPWM) and SVPWM technique. A section is devoted to understanding the underlying relationship between these two techniques. The linear modulation range is mostly covered by PWM techniques and a special section is devoted to over-modulation methods (Section 3.4.8). The analytical approach is validated using a MATLAB/Simulink based simulation. An artificial neural network offers a good non-linear mapping tool used to produce PWM for a three-phase voltage source inverter and elaborated on in Section 3.4.11. A comprehensive relationship between the SVPWM and SPWM is discussed in Section 3.5. For medium voltage high power

applications, multi-level inverters are employed. Basic topologies and PWM for multi-level inverters are discussed in Section 3.6. Special inverters based on an impedance source to incorporate the boost function, called Z-source and quasi Z-source inverters, are described in Section 3.7. The effect of using dead time between the switching on and off of one inverter leg is presented in Section 3.9, and the summary is given in Section 3.10.

## 3.2 Classification of PWM Schemes for Voltage Source Inverters

Different types of PWM techniques are available in the literature, but the most basic PWM is the SPWM. The high frequency carrier-wave is compared with the sinusoidal modulating signals to generate the appropriate gating signals for the inverters. The other PWM techniques are evolved from this basic PWM technique. SVPWM, although appearing different to the SPWM, has a strong implicit relationship with SPWM [1–5]. The gating time of each power switch is directly calculated from the analytical time equations in SVPWM [6]. The power switches are then switched according to the predefined switching patterns. The achievable output in the case of SVPWM is higher when compared to the SPWM. The main aim of the modulation techniques is to attain the maximum voltage with the lowest Total Harmonic Distortion (THD) in the output voltages. The PWM techniques can be broadly classified as:

- Continuous PWM;
- Discontinuous PWM.

In discontinuous PWM techniques, the power switches are not switched at regular intervals. Some of the switches do not change states in a sampling period. This technique is employed to reduce the switching losses. The SVPWM method is modified to achieve discontinuous switching. A detailed discussion is provided in Section 3.4.6.

## 3.3 Pulse Width Modulated Inverters

This section elaborates on some basic inverter circuit topologies. The square wave and PWM operation are described along with the harmonic spectrum of the output voltages.

### 3.3.1 Single-Phase Half-bridge Inverters

The power circuit topology of a single-phase half-bridge voltage source inverter is shown in Figure 3.1. As shown in Figure 3.1a, the inverter consists of two power semiconductor switching devices. Each switch is composed of a transistor (BJT, MOSFET, IGBTs, etc.) and a freewheeling diode that provides an alternating path for the current. In this circuit topology, either  $S_1$  is on or  $S_1'$  is on. The freewheeling diodes conduct when the load is inductive and a sudden change in the output voltage polarity does not change the direction of the current simultaneously. Indeed, for resistive loads, the diodes do not operate. When switching device  $S_1$  is conducting, the input voltage  $0.5 V_{dc}$  appears across the

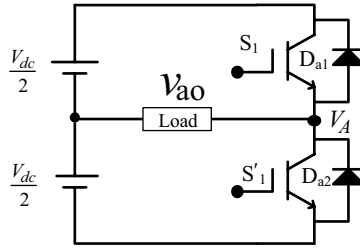


**Figure 3.1** Power Circuit of a half-wave bridge inverter

load. On the other hand, when transistors  $S_1$  is turned on, the voltage across the load is reversed and is  $(-0.5V_{dc})$ . The switching states, the path of current flow, and the output voltage polarity are illustrated in Figure 3.2 and switching signals along with the output voltage waveform are depicted in Figure 3.3. The operation of the inverter can be well understood from Figures 3.2 and 3.3. The output fundamental frequency of the inverter can be varied by altering the switching period and the voltage can be changed by changing the value of the DC link voltage.

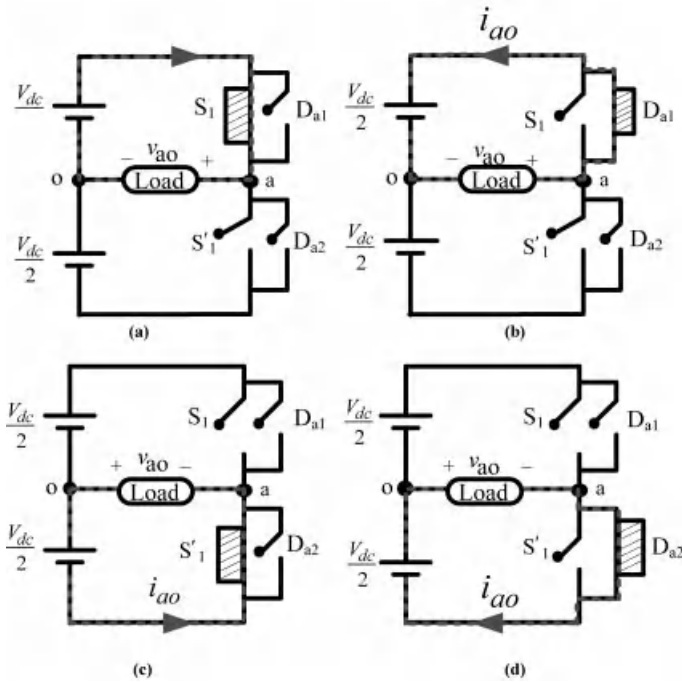


**Figure 3.2** Switching states in half-bridge inverter: (a) and (c)  $i_{ao} > 0$ ; (b) and (d)  $i_{ao} < 0$

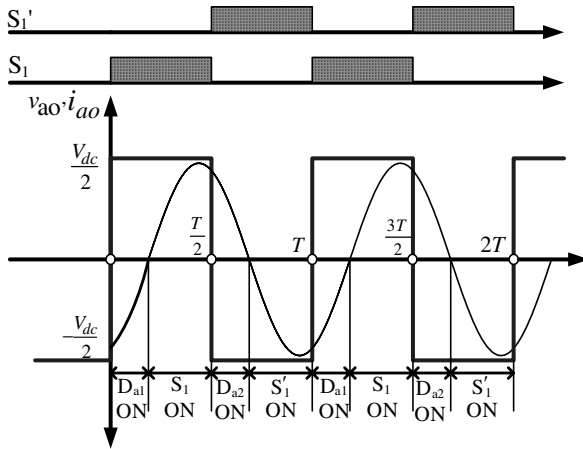


**Figure 3.3** Switching signal and the output voltage and current in a half-bridge inverter

The output voltage is a square wave, as shown in Figure 3.3, and the Fourier analysis gives

$$v_{ao}(t) = \sum_{n=1}^{\infty} \frac{4}{n\pi} (0.5V_{dc}) \sin(n \omega t) \tag{3.1}$$

where  $\omega = 2\pi f = 2\pi/T$ ;  $T$  is the output period and  $f$  is the output fundamental frequency.

The fundamental component of  $v_{ao}$  is obtained as  $v_{ao1} = \frac{4}{\pi} (0.5V_{dc}) \sin(\omega t)$ ; the peak value of the fundamental is  $V_{ao} = \frac{4}{\pi} (0.5V_{dc})$ ; and the rms value is  $V_{ao,rms} = \frac{4}{\pi\sqrt{2}} (0.5V_{dc})$ . A graphical view of the harmonic content in the output phase voltage is shown in Figure 3.4. The figure shows that the output contains a considerable amount of low-order harmonics such as 3rd, 5th, 7th, etc. and the magnitude of the harmonics varies as the inverse of its order.

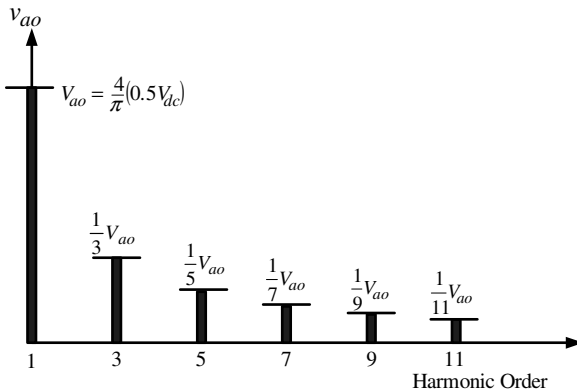


**Figure 3.4** A typical harmonic spectrum of output voltage in a half-bridge inverter

An SPWM scheme is implemented in this inverter topology by comparing a sinusoidally/cosinusoidally varying control/modulating voltage  $v_m(t)$  with amplitude  $V_m$  and frequency  $f_m$  (the frequency of the modulating signal is low corresponding to the motor speed, if motor load is assumed) with a high frequency carrier signal. The carrier frequency is  $f_c$  and the shape of the carrier wave is triangular in most applications. If a triangular shape of the carrier wave is chosen, it is called a double-edge modulation. A simpler shape is a saw tooth carrier and the modulation using this type of carrier is called a single-edge modulation. Other shapes of the carrier wave, such as the inverted rectified sine wave, are also reported in the literature [6,7]. Nevertheless, the triangular carrier is the most popular, as it offers good harmonic performance.

The ratio of the amplitude of the carrier signal and the control signal is called ‘amplitude modulation ratio’ or ‘modulation index’:

$$m = \frac{|v_m|}{|v_c|} = \frac{V_m}{V_c} \quad (3.2)$$

When the modulating signal is less than equal to the carrier signal, it is called the ‘linear modulation region.’ When the amplitude of the modulating signal becomes more than the carrier signal, it is called the ‘pulse dropping mode’ or the ‘over modulation region’. The name is given because some of the edges of the modulating signal will not intersect with the carrier. The modulating signal is then modified accordingly. The output voltage increases or the modulation range increases, but low-order harmonics are introduced. Details on over-modulation are discussed separately in Section 3.4.8. The discussion here is limited to linear modulation region. Another parameter defined by the SPWM is called the ‘frequency modulation ratio,’ and is given as

$$m_f = \frac{f_c}{f_m} \quad (3.3)$$

This is also an important parameter that decides the harmonic performance of the output voltage. The choice of this ratio is discussed later in this chapter.

The inverter leg switching frequency is equal to the frequency of the triangular carrier signal and the switching period is  $T_c = \frac{1}{f_c}$ .

The gating signals/switching signals are generated at the instant of intersection of the carrier signal and control or modulating signal. If the control or modulating signal amplitude  $V_m$  is more than the carrier signal amplitude ( $V_c$ ), the upper switch  $S_1$  is On and  $v_{ao} = \frac{V_{dc}}{2}$ .

If the control or modulating signal amplitude ( $V_m$ ) is less than the carrier signal amplitude ( $V_c$ ), the lower switch  $S_1'$  is On and  $v_{ao} = -\frac{V_{dc}}{2}$ .

With this type of switching of the inverter leg, the output voltage varies between  $V_{dc}/2$  and  $-V_{dc}/2$ , as shown in Figure 3.5 and is called the bipolar PWM. The name ‘bipolar’ is given since the output leg voltage has both positive and negative values. The value of the average leg voltage  $V_{AO}$  during a switching period  $T_c$  can be determined from Figure 3.6, which shows one period of the triangular waveform. During an inverter switching period  $T_c$ , the amplitude of the modulating signal can be assumed to be nearly constant, as the switching frequency of the triangular carrier wave is high compared to modulating signal. The duration of  $S_1$  being On is

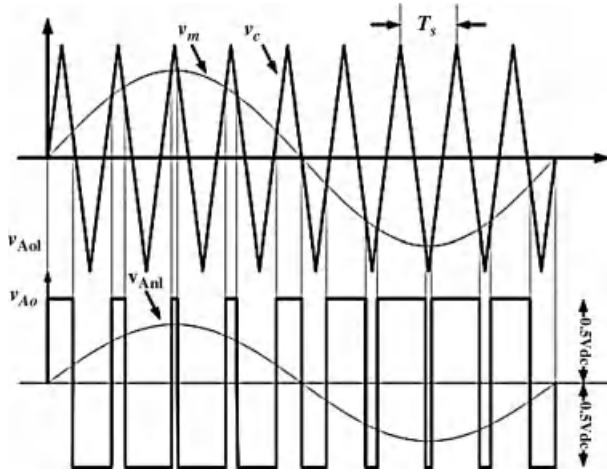


**Figure 3.5** Bipolar PWM of single inverter leg

denoted by  $\delta_1$  and the On period of  $S_1'$  is denoted by  $\delta_1'$ . By using equivalence of triangles, the following relation can be written:

$$\frac{\delta_1'/2}{T_c/2} = \frac{V_c + V_m}{V_c + V_c} \tag{3.4}$$

$$\delta_1' = T_c \left( \frac{V_c + V_m}{2V_c} \right)$$

and,  $\delta_1 = T_c - \delta_1' = T_c \left( 1 - \left( \frac{V_c + V_m}{2V_c} \right) \right)$  (3.5)

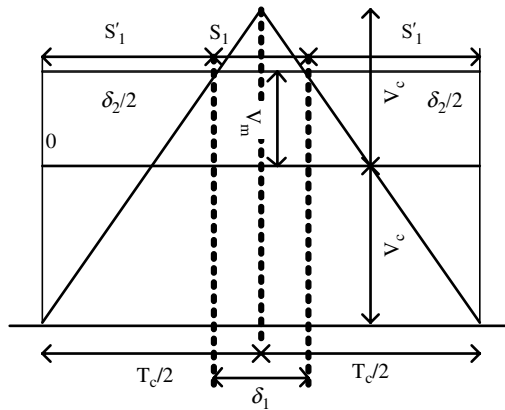


**Figure 3.6** One switching cycle in SPWM

To determine the average output voltage during one switching period, the equal volt-second principle (the product of voltage and time should be equal for the two switches and the average output) is applied:

$$\delta_1 \frac{V_{dc}}{2} - \delta'_1 \frac{V_{dc}}{2} = T_c V_{Ao} \quad (3.6)$$

$$V_{Ao} = \frac{1}{T_c} \frac{V_{dc}}{2} (\delta_1 - \delta'_1) = \frac{V_m V_{dc}}{V_c} \frac{1}{2} \quad (3.7)$$

$$V_{Ao} = m \frac{V_{dc}}{2} \quad (3.8)$$

The average leg voltage of the inverter is proportional to the modulation index ( $m$ ) and the maximum value is  $V_{dc}/2$  when the modulation index is 1. When the modulation signal is sinusoidal in nature, the output voltage varies sinusoidally with peak value of  $V_{dc}/2$  for  $m = 1$ .

In the SPWM method, the harmonics in the inverter output voltage waveform appear as side bands centered on the switching frequency and its multiples, i.e. around  $f_c$ ,  $2f_c$ ,  $3f_c$ , etc. A general form for the frequency at which harmonics appear is [3]

$$f_h = \left( j \frac{f_c}{f_m} \pm k \right) f_m \quad (3.9)$$

and the harmonic order  $h$  is

$$h = \frac{f_h}{f_m} = \left( j \frac{f_c}{f_m} \pm k \right) \quad (3.10)$$

It is important to note that for all odd  $j$ , the harmonics will appear for even values of  $k$  and vice-versa. Normally the frequency modulation ratio is chosen to be an odd integer, to avoid even harmonics appearing in the output voltage. The choice of switching frequency of an inverter depends upon the application. Ideally, the switching frequency should be as low as possible to avoid losses due to the switching of the power switches. However, when the switching frequency is low, the output voltage quality is poor. Hence, the switching frequency for the medium power motor drive system is kept between 4 kHz and 10 kHz.

For low values of the frequency modulation ratio, usually for  $m_f \leq 21$ , the modulating or control signal and carrier signal are synchronized with each other, called synchronous PWM. The frequency modulation ratio is chosen as an integer number to facilitate the proper synchronization. If the frequency modulation ratio is a non-integer, sub-harmonics (lower than the fundamental frequency) appear in the output voltage waveform. Hence, in synchronous PWM, the switching frequency should be changed with the change in the fundamental output frequency, to keep the ratio an integer and subsequently to avoid the production of sub-harmonics.

For higher values of the frequency modulation ratio,  $m_f > 21$ , the synchronization of the carrier wave and modulating signals are not necessary and the result is asynchronous PWM. Since the amplitude of the sub-harmonics will be small, asynchronous PWM can be used.



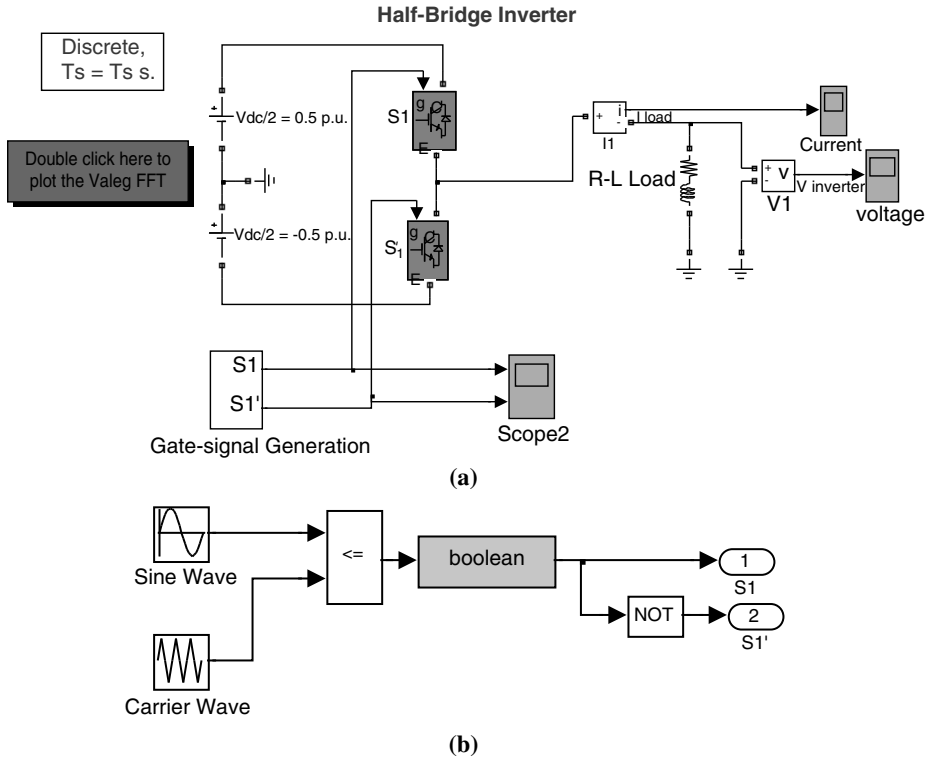


**Figure 3.7** Simulink model to implement SPWM: (a) main model; (b) gate signal generation (file name: *Half\_bridge\_PWM.mdl*)

Nevertheless, in high power applications, even small sub-harmonics may lead to appreciable losses. Thus it is recommended to use synchronous PWM for high power applications.

### 3.3.1.1 MATLAB/Simulink Model of Half-bridge Inverter

The Simulink model shown in this section uses 'simpowersystem' block-sets of the Simulink library. The IGBT switches are chosen from the built-in library. The gating signals are generated using the SPWM principle. The modulating signal is assumed to be a sinusoidal wave of unit amplitude and 50 Hz fundamental frequency. The switching frequency of the inverter is chosen as 1250 Hz ( $m_f = 25$ ) (this can be changed by varying the frequency of the carrier wave) and hence the frequency of the triangular carrier wave is 1250 Hz. The gating signal generated is split into two complimentary switching signals using a NOT gate (Note: dead band is not used in the model). The amplitude of the modulating signal is kept at 0.475 p.u. ( $m = 0.95$ ) (Note: the maximum output voltage is  $0.5 V_{dc}$ , hence the maximum amplitude of the modulating signal is limited to  $0.5 V_{dc}$ ). The DC link voltage is assumed at 1 p.u. The load used in the simulation model is R-L, with values  $R = 10 \Omega$  and  $L = 100$  mH. The simulation model is shown in Figure 3.7 and the resulting spectrum of the output voltage waveforms is shown in Figure 3.8. The harmonic components are marked in the output voltage spectrum.

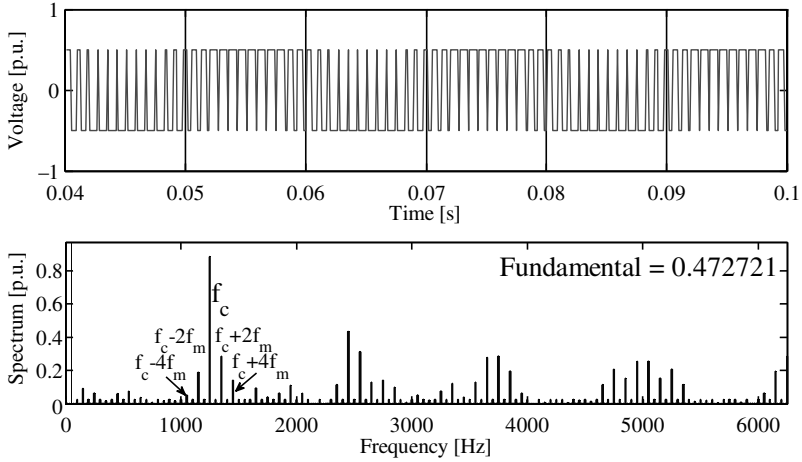


**Figure 3.8** Output voltage and its spectrum for half-bridge inverter

Practically, the switching signals or gate drive signals are complimentary but have some dead band that is introduced intentionally to prevent the two power switches of the same leg conducting simultaneously. An example of the dead band is shown in Figure 3.9a. To observe the effect of introducing dead band (the two switches are not On at the same time for safety purpose) in the switching signal, the dead band circuit shown in Figure 3.9b can be added to the gate signals of each switch. The dead band period can be defined and adjusted in the dialog box of the edge detector ‘sample time.’ Adding the dead band is left to the reader.

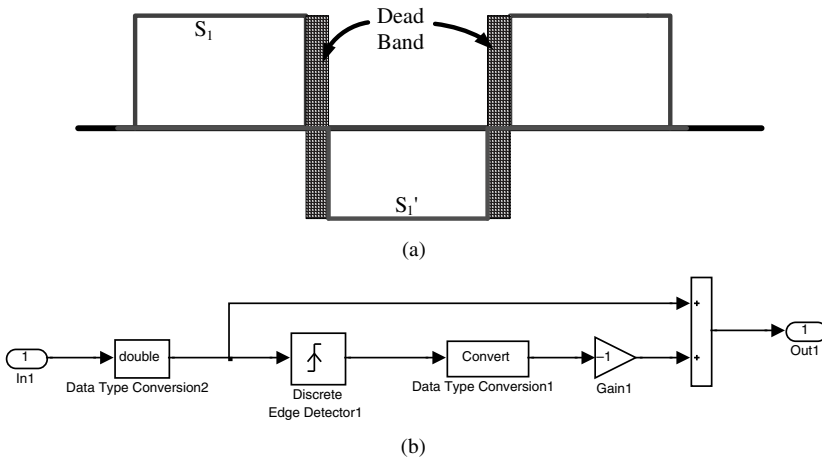


**Figure 3.9** (a) Dead band between upper and lower gating signals; and (b) Dead band circuit

### 3.3.2 Single-Phase Full-bridge Inverters

The power circuit topology of a single-phase full-bridge inverter is depicted in Figure 3.10a. There are four power semiconductor switches and two legs in this topology. This is also called the ‘H-bridge’ inverter due to its shape. Each switch is composed of a transistor (IGBTs, MOSFETs, BJT, etc.) and a freewheeling diode, which provides an alternating path for the current. When transistors  $S_1$  and  $S_2'$  are conducting simultaneously, the input voltage  $V_{dc}$  appears across the load. On the other hand, when transistors  $S_2$  and  $S_2'$  are turned on at the same time, the voltage across the load is reversed and is  $(-V_{dc})$  and therefore an alternating current is obtained at the output side while the input side is DC. The output voltage frequency can be varied by varying the switching time of the power switches and the voltage magnitude can be changed by changing the DC link voltage. The switching states and the path of the current flow and the output voltage polarity are shown in Figure 3.10a. The alteration in the direction of the voltage and current is evident from Figure 3.10b.

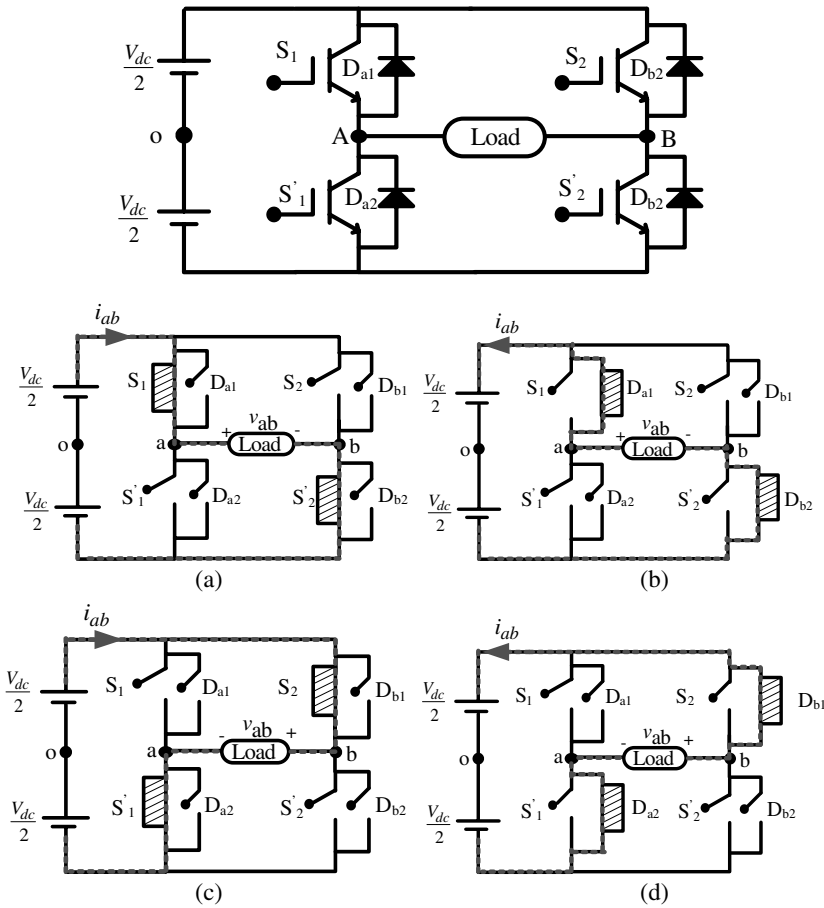


**Figure 3.10** Power circuit topology of a single-phase full-bridge inverter: (b) Switching states in full-bridge inverter; (a) and (c)  $i_{ab} > 0$ ; (b) and (d)  $i_{ab} < 0$

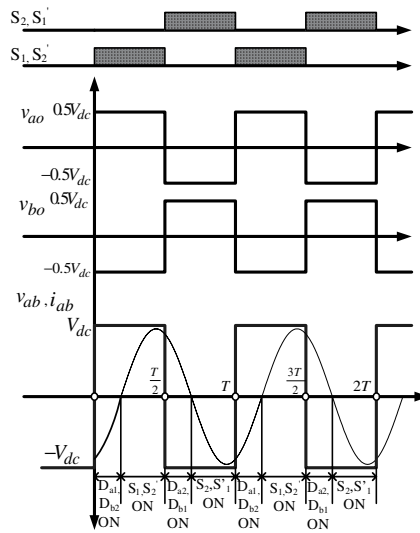


**Figure 3.11** Switching signal and the output voltage and current in a half-bridge inverter

The output voltage and current waveforms for a fictitious R-L load is shown in Figure 3.11. The currents do not change direction instantaneously due to the inductive load. The pole voltages vary between  $0.5 V_{dc}$  and  $-0.5 V_{dc}$ , while the voltages across the load vary between  $V_{dc}$  and  $-V_{dc}$ . The switching signals are shown to be applied for 180 degrees but in practice some dead band is given between the application of gating pulses for the upper and lower power switch. The output the voltage is the same as that of the half-wave bridge inverter, except that the magnitude of the phase voltage, which is doubled in this case. Hence the harmonic spectrum remains the same as that of a half-bridge inverter output, except with double fundamental voltage.

The SPWM technique is implemented in a full-bridge inverter by comparing either one or two modulating or control signals (180-degree phase shifted) with the high frequency triangular carrier wave. The former is called the bipolar PWM and the latter is called the unipolar PWM. The fundamental frequency of the output is decided by the frequency of the modulating or control signal. The switching frequency of the inverter is dictated by the frequency of the carrier wave. The frequency of the carrier wave is usually much higher than the frequency of the modulating signal. In the bipolar PWM scheme, the switching of the power switches is decided by the intersection of the modulating and carrier wave. The switch pair  $S_1$  and  $S_2'$  operate when the modulating signal is greater than the triangular carrier wave ( $v_m > v_c$ ) and the switch pair  $S_2$  and  $S_1'$  operate when the modulating signal is smaller than the triangular carrier wave ( $v_m < v_c$ ). It is also noted that the operation of the upper and lower switch is still complimentary. A small dead band is introduced between the switching of the upper and lower switches in real time implementation. The switching scheme for the bipolar PWM is not shown, as it is similar to that shown for the half-bridge inverter.

In the case of a unipolar PWM scheme, the two pairs of switches ( $S_1$  and  $S_2'$ ) and ( $S_2$  and  $S_1'$ ) operate simultaneously, as in the previous case. The switching signal for the upper switch  $S_1$  is produced by comparing the positive modulating signal with the carrier signal. The switching

signal for the upper switch  $S_2$  is produced by comparing the phase shifted or negative modulating signal with the carrier signal. The switching is done at the instant where  $v_m > v_c$  for both  $S_1$  and  $S_2$  switches. The switching of the switches  $S_1$  and  $S_1'$  and switches  $S_2$  and  $S_2'$  are complimentary. To obtain a better harmonic spectrum with reduced ripples in the current, a unipolar switching scheme is suggested. The switching scheme and the voltages are depicted in Figure 3.12. The leg voltages vary between  $+V_{dc}/2$  and  $-V_{dc}/2$  for both legs A and B. The output voltages across the load vary between  $+V_{dc}$  and 0 in the positive half cycle and  $-V_{dc}$  and 0 for the negative half cycle, thus it is called the 'unipolar PWM.'

The maximum fundamental output voltage is  $V_{dc}$  for both unipolar and bipolar PWM. In the case of bipolar PWM, the harmonic components in the output voltage is centered on  $m_f$  and multiples of  $m_f$ , i.e.  $2m_f$ ,  $3m_f$  and so on, similar to the half-bridge inverter.

In the case of a unipolar PWM scheme, the ratio between the modulating signal and the triangular carrier signal is chosen as even. The harmonic components at the output voltage is once again given by equation (3.9), but the harmonic at the switching frequency, three times the switching frequency, five times the switching frequency etc. do not appear, i.e. to say that  $j$  is only even and  $k$  is odd. The harmonic at the carrier signal frequency is eliminated due to the fact that the output voltage is the difference between the leg voltages ( $V_{AB} = V_{AO} - V_{BO}$ ). The harmonic in the leg voltages appears at the multiple of the switching frequency or the carrier signal frequency. Since the modulation signals are out of phase by 180 degrees, the harmonics at the switching will cancel out during subtraction at the load side.

### 3.3.2.1 MATLAB/Simulink Model of Single-phase Full-bridge Inverter

The Simulink model shown uses 'simpowersystem' block-sets of the Simulink library. The IGBT switches are chosen from the built-in library. The gating signals are generated using the unipolar SPWM principle. The implementation of bipolar PWM is left as an exercise. The modulating signals are assumed as two sinusoidal waves of unit amplitude and have a 180-degree phase shift and 50-Hz fundamental frequency. The switching frequency of the inverter is chosen as 1250 Hz (this can be changed by varying the frequency of the carrier wave) and hence the frequency of the triangular carrier wave is 1250 Hz. The gating signal generated is split into two complimentary switching signals using a NOT gate (Note: dead band is not used in the model). The load used in the simulation model is R-L, with values  $R = 10 \Omega$  and  $L = 100 \text{ mH}$ . The modulating signal is given as sinusoidal waves with a 180-degree phase shift and a peak value of 0.95 p.u. The simulation model is shown in Figure 3.13 and the resulting voltage spectrum is shown in Figure 3.14. The spectrum shows the peak magnitude of the fundamental frequency. The effect of introducing a dead band can be observed by adding the dead band circuit of Figure 3.9. This PWM can also be implemented by using two 180-degree phase shifted triangular carrier signals and one sinusoidal modulating signal. The resulting waveform will have the same quality as that of the method elaborated in this section.

## 3.4 Three-phase PWM Voltage Source Inverter

The power circuit topology of a three-phase voltage source inverter is shown in Figure 3.15. Each power switch is a transistor or IGBT with anti-parallel diodes. The pole or the leg

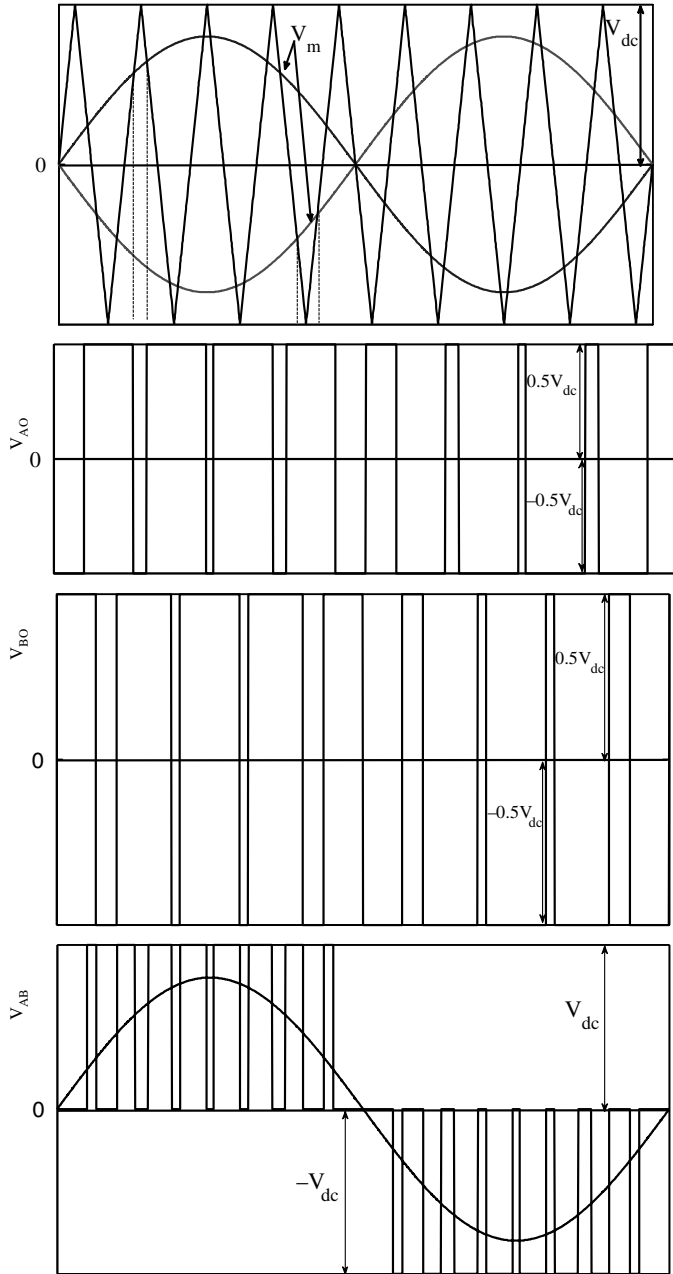
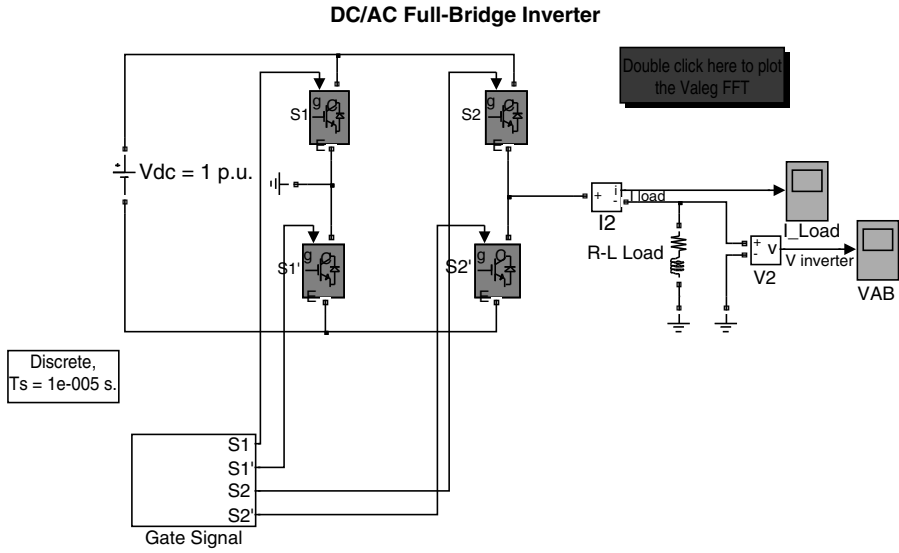
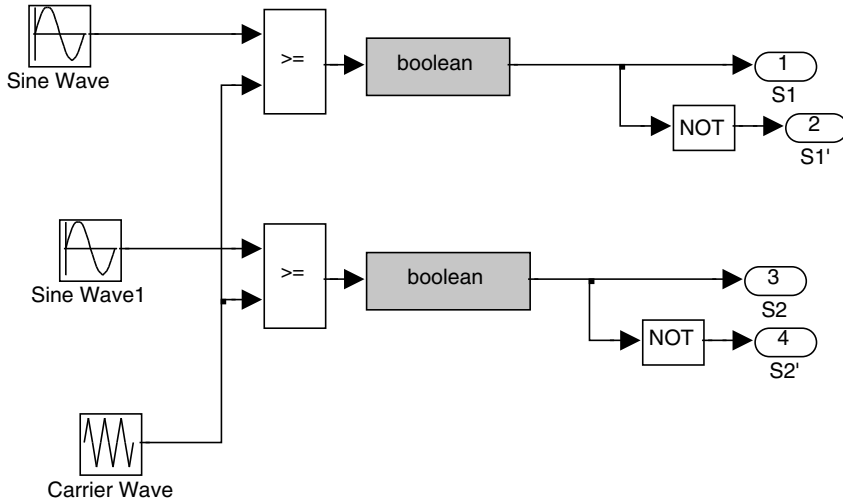


**Figure 3.12** Unipolar PWM scheme for single-phase full-bridge inverter



(a)



(b)

**Figure 3.13** Simulink model to implement unipolar PWM scheme in a full-bridge single-phase inverter (file name: *Full\_bridge\_PWM.mdl*)

voltages are denoted by a capital suffix letter  $V_A$ ,  $V_B$ ,  $V_C$  and can attain the value  $+0.5 V_{dc}$  when the upper switch is operating and  $-0.5 V_{dc}$  when the lower switch is operating. The phase voltage applied to the load is denoted by the letters  $v_{an}$ ,  $v_{bn}$ ,  $v_{cn}$ . The operation of the upper and the lower switches are complimentary (a small dead band is provided in real time implementation).

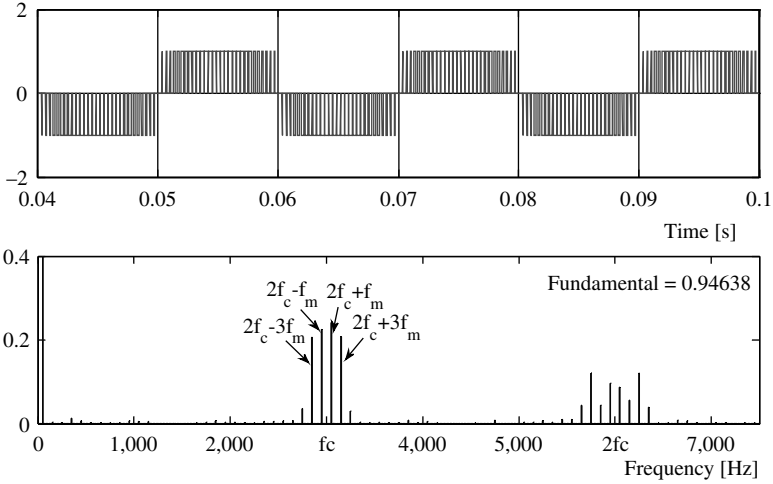


**Figure 3.14** Voltage ( $V_{AB}$ ) and its spectrum for unipolar PWM scheme in a single-phase inverter

The relationship between the leg voltage and switching signals are

$$V_k = S_k V_{dc}; \quad k \in A, B, C \tag{3.11}$$

where  $S_k = 1$  when the upper power switch is ‘ON’ and  $S_k = 0$  when the lower switch is ‘ON.’ If the load is assumed to be a star connected three-phase, then the relation between the phase-to-neutral load voltage and the leg voltages can be written as

$$\begin{aligned} V_A(t) &= v_a(t) + v_{nN}(t) \\ V_B(t) &= v_b(t) + v_{nN}(t) \\ V_C(t) &= v_c(t) + v_{nN}(t) \end{aligned} \tag{3.12}$$

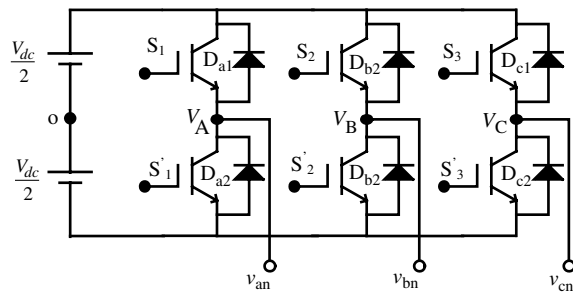


**Figure 3.15** Power circuit topology of a three-phase voltage source inverter



where  $v_{nN}$  is the voltage difference between the star point  $n$  of the load and the negative rail of the DC bus  $N$ , called the ‘Common Mode Voltage’. This common mode voltage or neutral voltage is responsible for leakage bearing currents and their subsequent failure. This issue is taken up in more detail in Chapter 9.

By adding each term of the equation (3.12), and setting the sum of phase-to-neutral voltage to zero (assuming a balanced three-phase voltage whose instantaneous sum is always zero), the following is obtained:

$$v_{nN}(t) = \frac{1}{3}[V_A(t) + V_B(t) + V_C(t)] \quad (3.13)$$

Substituting equation (3.13) back into equation (3.12), the following expressions for the phase-to-neutral voltage are obtained:

$$\begin{aligned} v_a(t) &= \frac{2}{3}V_A(t) - \frac{1}{3}[V_B(t) + V_C(t)] \\ v_b(t) &= \frac{2}{3}V_B(t) - \frac{1}{3}[V_A(t) + V_C(t)] \\ v_c(t) &= \frac{2}{3}V_C(t) - \frac{1}{3}[V_B(t) + V_A(t)] \end{aligned} \quad (3.14)$$

Equation (3.14) can also be written using the switching function definition of equation (3.11):

$$\begin{aligned} v_a(t) &= \left(\frac{V_{dc}}{3}\right)[2S_A - S_B - S_C] \\ v_b(t) &= \left(\frac{V_{dc}}{3}\right)[2S_B - S_A - S_C] \\ v_c(t) &= \left(\frac{V_{dc}}{3}\right)[4S_C - S_B - S_A] \end{aligned} \quad (3.15)$$

Equation (3.15) can be used to model a three-phase inverter in MATLAB/Simulink. The switching signals can be generated by analog circuits or by a digital signal processors/microprocessor for operation in six-step or PWM modes. The following section describes the operation of the inverter in both square wave/six-step mode and PWM mode.

For inverter operation in square wave or six-step mode, switching/gate signals are provided in such a way that the power switches change the state only twice in one fundamental cycle (OFF to ON and then ON to OFF). Each leg receives the gating signal with a phase shift of 120 degrees, so as to maintain the same phase shift among three output voltages. The output in this case is highest and the switching losses are minimal; however, the output voltages contain strong low-order harmonics, especially 5th and 7th. With the advent of fast signal processing devices, it is easier to implement a PWM operation and hence a normal step operation is avoided. The associated waveforms for six-step modes are shown in Figure 3.16. The leg

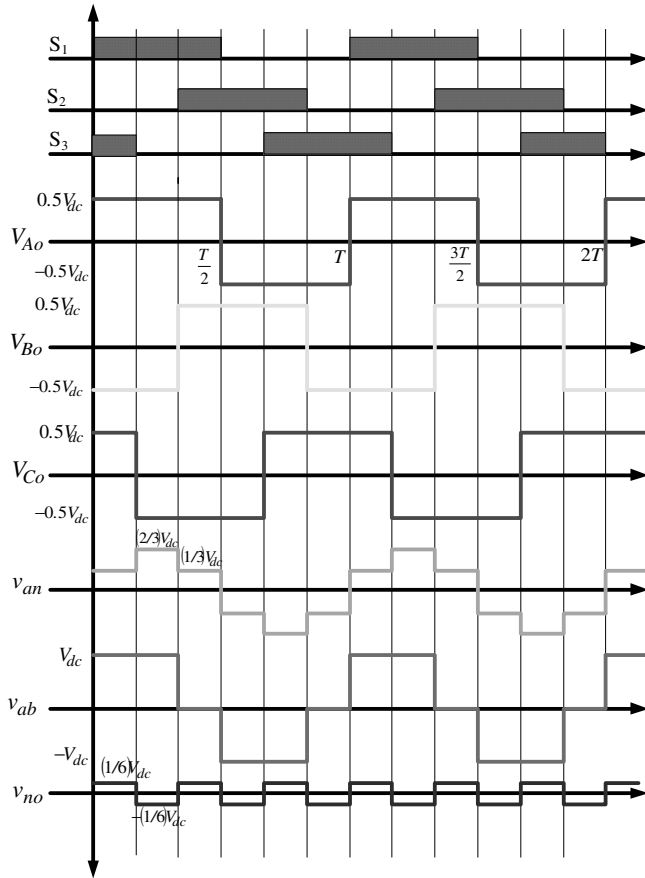


**Figure 3.16** Waveforms for square wave/six-step mode of operation of a three-phase inverter

voltage takes on the values  $+0.5 V_{dc}$  and  $-0.5 V_{dc}$  and the phase voltage has six steps in one fundamental cycle. The steps in the phase voltages have amplitudes of  $\pm 1/3 V_{dc}$  and  $\pm 2/3 V_{dc}$  and the line voltage varies between  $+V_{dc}$  and  $-V_{dc}$ , while the common mode voltage varies between  $+1/6 V_{dc}$  and  $-1/6 V_{dc}$ . During the six-step operation of the inverter, the values of the leg voltages are shown in Table 3.1.

To determine the phase-to-neutral voltages for the six-step mode, the leg voltages from Table 3.1 is substituted into equation (3.14), and the corresponding values are listed in Table 3.2 for a star-connected load. The line voltages are obtained by using equation (3.16) and are listed in Table 3.3:

$$\begin{aligned}
 v_{ab} &= v_{an} - v_{bn} \\
 v_{bc} &= v_{bn} - v_{cn} \\
 v_{ca} &= v_{cn} - v_{an}
 \end{aligned}
 \tag{3.16}$$

**Table 3.1** Leg/Pole voltages of a three-phase VSI during six-step mode of operation

Switching Mode	Switches ON	Leg voltage $V_A$	Leg voltage $V_B$	Leg voltage $V_C$
1	$S_1, S'_2, S_3$	$0.5V_{dc}$	$-0.5V_{dc}$	$0.5V_{dc}$
2	$S_1, S'_2, S'_3$	$0.5V_{dc}$	$-0.5V_{dc}$	$-0.5V_{dc}$
3	$S_1, S_2, S'_3$	$0.5V_{dc}$	$0.5V_{dc}$	$-0.5V_{dc}$
4	$S'_1, S_2, S'_3$	$-0.5V_{dc}$	$0.5V_{dc}$	$-0.5V_{dc}$
5	$S'_1, S_2, S_3$	$-0.5V_{dc}$	$0.5V_{dc}$	$0.5V_{dc}$
6	$S'_1, S'_2, S_3$	$-0.5V_{dc}$	$-0.5V_{dc}$	$0.5V_{dc}$

**Table 3.2** Phase-to-neutral voltages for six-step mode of operation

Switching mode	Switches ON	Phase Voltage $v_{an}$	Phase voltage $v_{bn}$	Phase voltage $v_{cn}$
1	$S_1, S'_2, S_3$	$1/3 V_{dc}$	$-2/3 V_{dc}$	$1/3 V_{dc}$
2	$S_1, S'_2, S'_3$	$2/3 V_{dc}$	$-1/3 V_{dc}$	$-1/3 V_{dc}$
3	$S_1, S_2, S'_3$	$1/3 V_{dc}$	$1/3 V_{dc}$	$-2/3 V_{dc}$
4	$S'_1, S_2, S'_3$	$-1/3 V_{dc}$	$2/3 V_{dc}$	$-1/3 V_{dc}$
5	$S'_1, S_2, S_3$	$-2/3 V_{dc}$	$1/3 V_{dc}$	$1/3 V_{dc}$
6	$S'_1, S'_2, S_3$	$-1/3 V_{dc}$	$-1/3 V_{dc}$	$2/3 V_{dc}$

The maximum output peak phase-to-neutral voltage in the six-step mode is  $0.6367 V_{dc}$  or  $(2/\pi) V_{dc}$  and that of the line-to-line voltage is  $1.1 V_{dc}$ . The Fourier series of phase-to-neutral voltage and line-to-line voltage can be obtained as

$$v_{an}(t) = \frac{2}{\pi} V_{DC} \left[ \sin \omega t + \frac{1}{5} \sin 5\omega t + \frac{1}{7} \sin 7\omega t + \frac{1}{11} \sin 11\omega t + \frac{1}{13} \sin 13\omega t + \dots \right] \quad (3.17)$$

$$v_{ab}(t) = \frac{2\sqrt{3}}{\pi} V_{DC} \left[ \sin \left( \omega t - \frac{\pi}{6} \right) + \frac{1}{5} \sin 5 \left( \omega t - \frac{\pi}{6} \right) + \frac{1}{7} \sin 7 \left( \omega t - \frac{\pi}{6} \right) + \dots \right] \quad (3.18)$$

**Table 3.3** Line voltages for six-step mode of operation

Switching mode	Switches ON	Line Voltage $v_{ab}$	Phase voltage $v_{bc}$	Phase voltage $v_{ca}$
1	$S_1, S'_2, S_3$	$V_{dc}$	$-V_{dc}$	0
2	$S_1, S'_2, S'_3$	$V_{dc}$	0	$-V_{dc}$
3	$S_1, S_2, S'_3$	0	$V_{dc}$	$-V_{dc}$
4	$S'_1, S_2, S'_3$	$-V_{dc}$	$V_{dc}$	0
5	$S'_1, S_2, S_3$	$-V_{dc}$	0	$V_{dc}$
6	$S'_1, S'_2, S_3$	0	$-V_{dc}$	$V_{dc}$

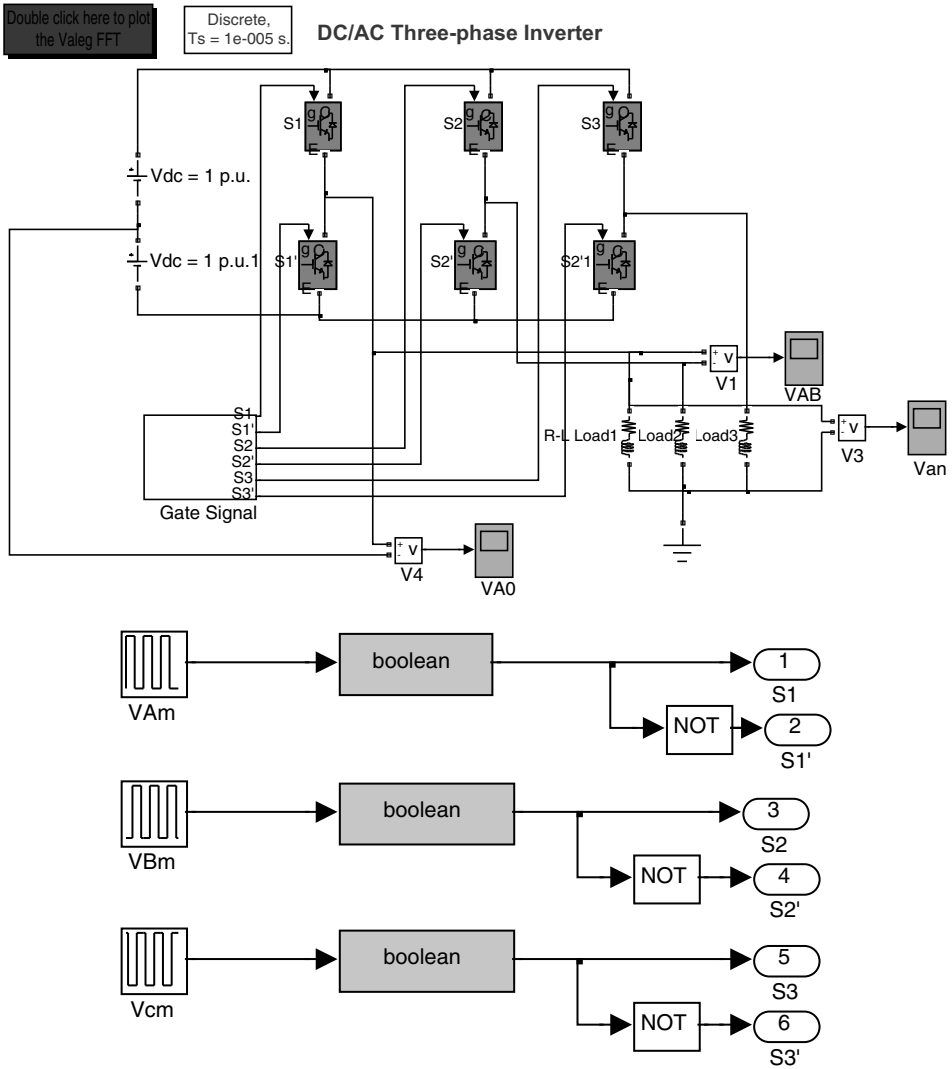


**Figure 3.17** Simulink for six-step operation of inverter (File name: *Six-stepmode.mdl*)

The Fourier series of a phase-to-neutral voltage and the line-to-line voltage shows that the triplen harmonic (multiple of three) does not appear (since the load is assumed with isolated neutral). The other harmonics have the inverse amplitude of their order. The output voltage magnitude can be controlled by controlling the DC link voltage  $V_{dc}$ .

The MATLAB/Simulink model for generating the six-step waveform is given in Figure 3.17. The gating signal is generated using the repetitive block of the Simulink where the switching signal values are stored. In the six-step mode, the switching is done at fundamental frequency, and hence the period of the gate drive signal depends upon the fundamental frequency of the output.

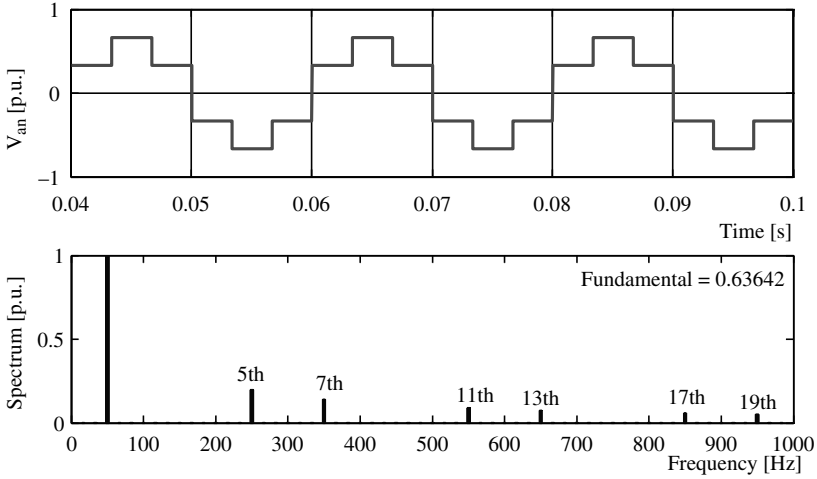


**Figure 3.18** Harmonic spectrum for six-step phase voltage

### 3.4.1 Carrier-based Sinusoidal PWM

In the carrier-based sinusoidal PWM method (SWPM), three-phase sinusoidal wave:

$$\begin{aligned}
 v_{Am} &= V_m \sin(\omega t) \\
 v_{Bm} &= V_m \sin\left(\omega t - 2\frac{\pi}{3}\right) \\
 v_{Cm} &= V_m \sin\left(\omega t + 2\frac{\pi}{3}\right)
 \end{aligned} \tag{3.19}$$

are used for the modulating or control signal and compared with a high frequency triangular wave. One common triangular wave is used for the comparison for all three phases. The upper switch of leg A is ON when the modulating signal of phase A is greater than the amplitude of the triangular carrier wave, i.e.  $v_{Am} \geq V_c$ . The lower switch has a complimentary operation. A small dead band is provided between the switching OFF of upper switch and switching ON of the lower switch and vice versa. The waveforms associated with the SPWM are given in Figure 3.19. The leg voltage, phase voltage, and line voltage are illustrated. The waveform is shown for  $m_f = 9$ .

The MATLAB/Simulink model for implementing a SPWM is shown in Figure 3.20a (power circuit is the same as that in Figure 3.17). The modulating index chosen is 0.95 (the reference modulating signal is given as  $0.95 \times 0.5 V_{dc}$ , where  $V_{dc} = 1$  p.u.). The switching frequency or the carrier frequency is chosen as 1500 Hz (hence  $m_f = 1500/50 = 30$ ). No dead band is shown in the simulation. The resulting phase-to-neutral voltage waveform and its spectrum are given in Figure 3.20b. The harmonics appear as the side band of the switching frequency.

The choice of  $m_f$  is important from the harmonic spectrum point of view. Harmonic spectrum for six-step phase voltage is shown on Figure 3.18. Normally, this frequency ratio  $m_f$  is chosen to be an odd multiple of three. This will ensure that the triple harmonic (multiple of three) will

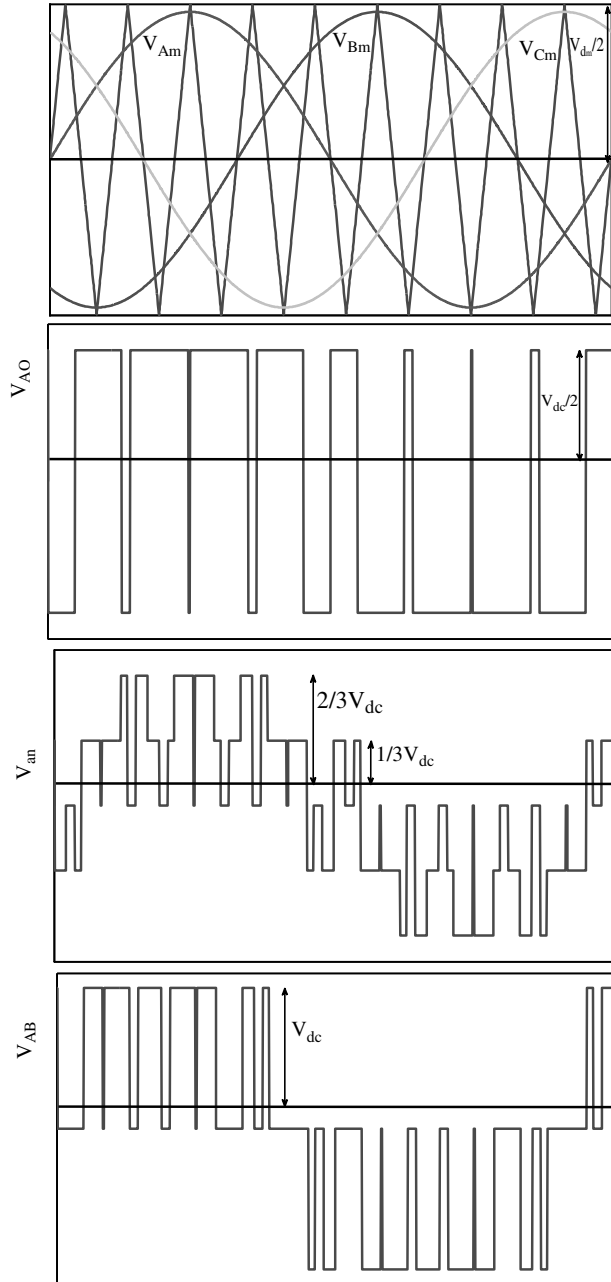


**Figure 3.19** SPWM of a three-phase inverter

be eliminated from the motor phase currents, since for the three-phase inverter, these harmonics are in phase and cancel out.

In an adjustable speed drive system with constant  $v/f$  control, variable frequency output is required. If the frequency modulation ratio  $m_f$  is kept constant, the switching frequency will

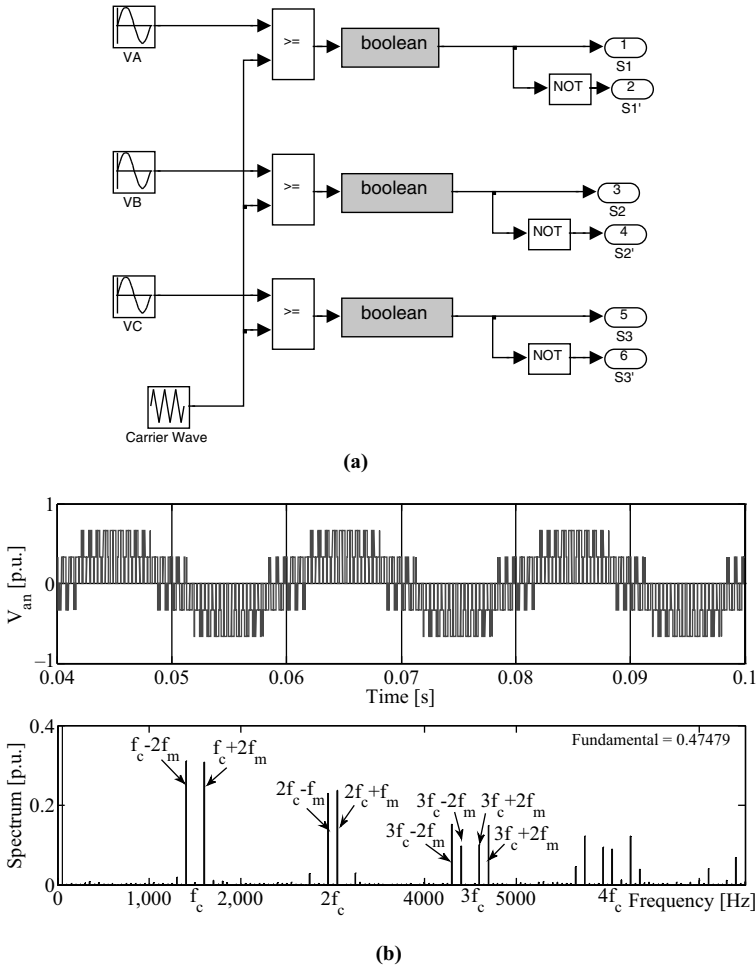


**Figure 3.20** (a) Gate signal generation in MATLAB for three-phase inverter (File name: *PWM\_Three\_phase\_CB.mdl*); (b) Phase-to-neutral voltage and spectrum for SPWM

be constant and high at a high fundamental output frequency ( $f_c = m_f f_m$ ). Therefore, the frequency modulation ratio  $m_f$  is varied for different frequency operations of the drive system. Changing the frequency modulation ratio in essence changes the slope of the line between  $f_c$  and  $f_m$ . There is sudden jump in the slope of the line and this may cause jittering at the transition points. A typical relationship is shown in Figure 3.21. To avoid this, usually a hysteresis block is used. For a low range of fundamental output frequencies up to say  $f_L$ , asynchronous PWM is employed. The synchronous PWM method is used until it reaches a frequency value  $f_M$  and then a six-step operation is initiated. The typical value of  $f_L$  and  $f_M$  are 10 Hz and 50 Hz, respectively.

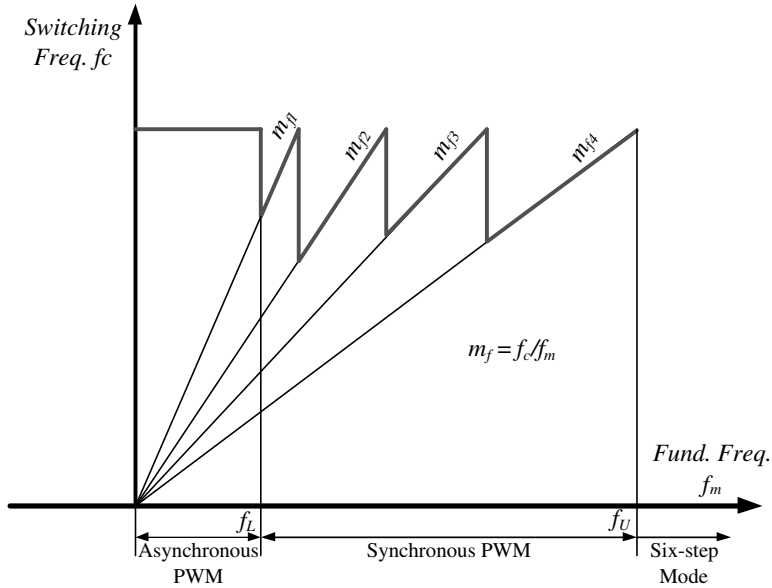


**Figure 3.21** Varying frequency modulation ratios for different output frequency

### 3.4.2 Third-harmonic Injection Carrier-based PWM

The output voltage using the SPWM technique is limited to  $0.5 V_{dc}$ . If the SPWM technique is used in motor drive applications, the available voltage may not be sufficient to run the motor at rated condition. In this situation, the machine needs to be derated and a reduced torque is produced. To enhance the output voltage from the PWM inverter using carrier-based scheme, third-harmonic injection in the modulating signal is done. It is shown that by adding an appropriate third-harmonic component of the modulating signal in the fundamental modulating signal leads to a reduction in the peak of the resultant modulating signal. Hence, the reference value of the resulting modulated signals can be increased beyond  $0.5 V_{dc}$  and that leads to the higher output voltage at the inverter. The injected third-harmonic component in the modulated signal or reference leg voltages cancels out in the legs and does not appear in the output phase voltages. Thus the output voltage does not contain the undesired low-order harmonics. The optimal level of the third-harmonic injection can be determined by considering the modulating signals:

$$\begin{aligned}
 v_{Am} &= V_{m1} \sin(\omega t) + V_{m3} \sin(3\omega t) \\
 v_{Bm} &= V_m \sin\left(\omega t - 2\frac{\pi}{3}\right) + V_{m3} \sin(3\omega t) \\
 v_{Cm} &= V_m \sin\left(\omega t + 2\frac{\pi}{3}\right) + V_{m3} \sin(3\omega t)
 \end{aligned} \tag{3.20}$$

For the SPWM without harmonic injection, the fundamental peak magnitude of the output voltage is  $0.5 V_{dc}$ . It is noted that the third harmonic has no effect on the value of the reference



waveform when  $\omega t = (2k + 1)\frac{\pi}{3}$ , since  $\sin(3(2k + 1)\frac{\pi}{3}) = 0$  for all odd  $k$ . Thus the third harmonic is chosen to make the peak magnitude of the reference of equation (3.20) occur where the third harmonic is zero. This ensures the maximum possible value of the fundamental component. The reference voltage reaches a maximum when

$$\frac{dv_{am}}{d\omega t} = V_{m1}\cos(\omega t) + 3V_{m3}\cos(3\omega t) = 0 \quad (3.21)$$

This yields

$$V_{m3} = -\frac{1}{3}V_{m1}\cos\left(\frac{\pi}{3}\right) \text{ for } \omega t = \frac{\pi}{3} \quad (3.22)$$

So the maximum modulation index can be

$$|v_{am}| = \left| V_{m1}\sin(\omega t) - \frac{1}{3}V_{m1}\cos\left(\frac{\pi}{3}\right)\sin(3\omega t) \right| = 0.5V_{dc}, \text{ The above equation gives;} \\ V_{m1} = \frac{0.5V_{dc}}{\sin\left(\frac{\pi}{3}\right)} \text{ for } \omega t = \frac{\pi}{3} \quad (3.23)$$

Thus the output fundamental voltage is increased by 15.47% of the value obtainable using simple SPWM by injecting 1/6th third-harmonic originally.

The implementation block diagram of the proposed method of PWM is shown in Figure 3.22. The reference modulating signal, the third-harmonic signal, and the resultant modulating signal after injecting third harmonic are shown in Figure 3.23.

### 3.4.3 MATLAB/Simulink Model for Third Harmonic Injection PWM

The MATLAB/Simulink model of third-harmonic injection based PWM is shown in Figure 3.24. The power circuit remains the same as that of Figure 3.17 and the gate signal generation is shown in Figure 3.24. The output voltage spectrum is shown in Figure 3.25, where

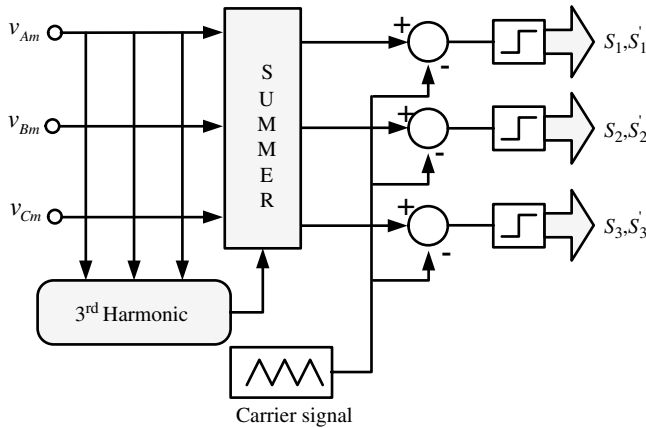


**Figure 3.22** Block diagram of SPWM with third-harmonic injection

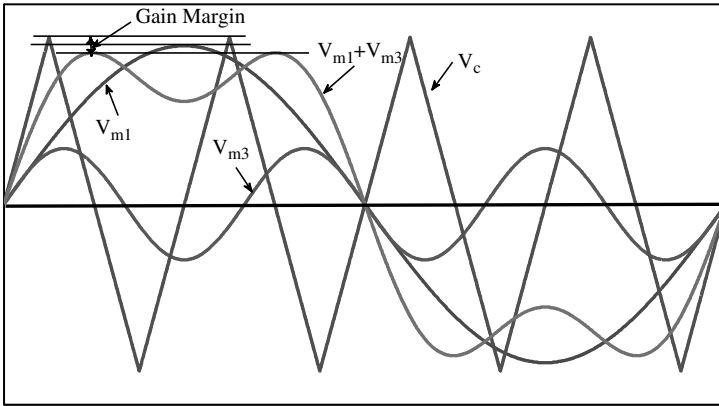


**Figure 3.23** Modulating signals and carrier-wave for third-harmonic injection PWM

the output is increased by 15.47% when compared to the simple SPWM scheme. The reference of the modulating signal is increased to  $0.575 V_{dc}$ .

### 3.4.4 Carrier-based PWM with Offset Addition

The output voltage magnitude from a three-phase voltage source inverter can be enhanced by adding an offset to the sinusoidal modulating signal. The offset addition PWM scheme follows the same principle as that of the third-harmonic injection; reducing the peak of the modulating signal and hence increasing the modulation index. In essence, the offset addition injects the triplen-harmonics (multiple of three) into the modulating signal,

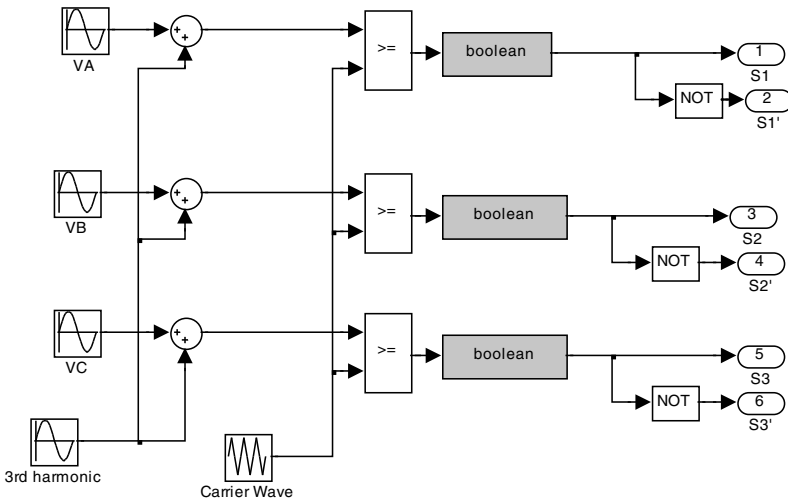


**Figure 3.24** Gate signal generation for third-harmonic injection PWM (File name: *PWM\_three-phase\_CB\_3rd\_harmonic.mdl*)

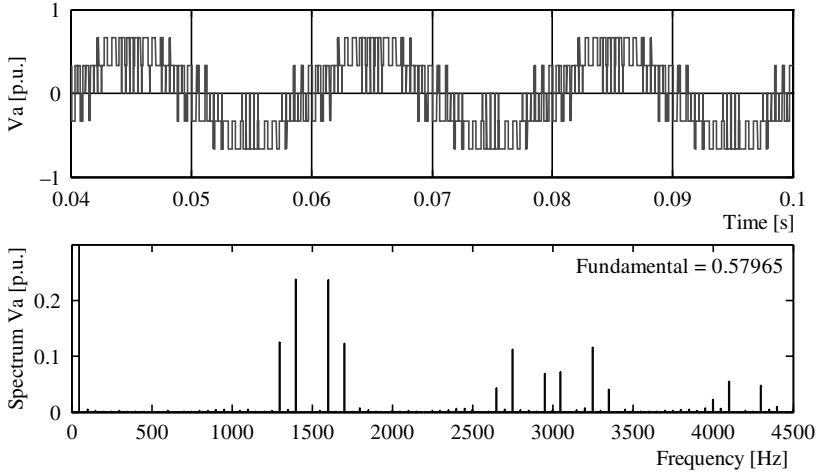


**Figure 3.25** Spectrum of phase ‘a’ voltage for third-harmonic injection

reducing the peak of the resultant, as shown in Figure 3.26. The resultant modulating signals are given as

$$\begin{aligned}
 v_{Am} &= V_{m1} \sin(\omega t) + offset \\
 v_{Bm} &= V_m \sin\left(\omega t - 2\frac{\pi}{3}\right) + offset \\
 v_{Cm} &= V_m \sin\left(\omega t + 2\frac{\pi}{3}\right) + offset
 \end{aligned}
 \tag{3.24}$$

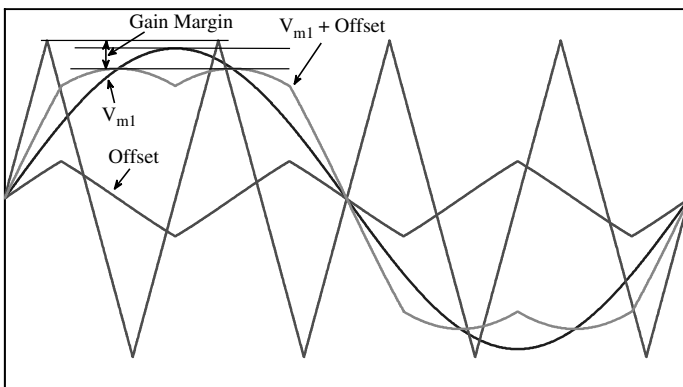


**Figure 3.26** Modulating signals and carrier wave for offset addition PWM

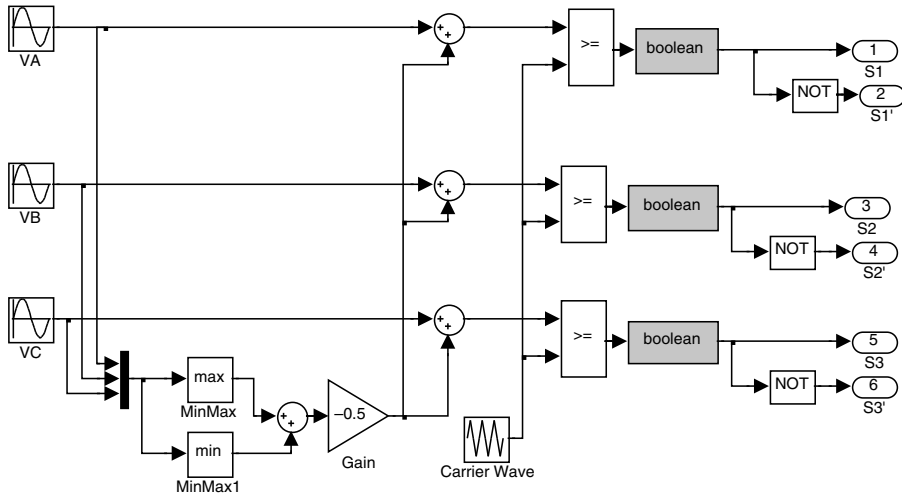


**Figure 3.27** MATLAB/Simulink for offset addition PWM (File name: *PWM\_3\_phase\_CB\_offset.mdl*)

where offset is given as

$$Offset = -\frac{V_{max} + V_{min}}{2}; V_{max} = Max\{v_{Am}, v_{Bm}, v_{Cm}\}, V_{min} = Min\{v_{Am}, v_{Bm}, v_{Cm}\} \quad (3.25)$$

The output voltage magnitude reaches the same value as that of the third-harmonic injection PWM. The MATLAB/Simulink model is shown in Figure 3.27. The resulting voltage and spectrum is shown in Figure 3.28.

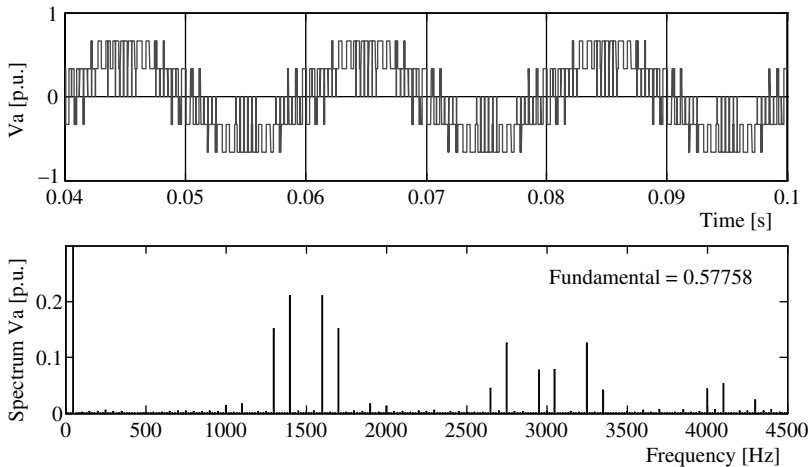


**Figure 3.28** Output voltage and voltage spectrum for offset addition PWM

### 3.4.5 Space Vector PWM

The SVPWM technique is one of the most popular PWM techniques due to a higher DC bus voltage use (higher output voltage when compared with the SPWM) and easy digital realization [8]. The concept of the SVPWM relies on the representation of the inverter output as space vectors or space phasors. Space vector representation of the output voltages of the inverter is realized for the implementation of SVPWM. Space vector simultaneously represents three-phase quantities as one rotating vector, hence each phase is not considered separately. The three phases are assumed as only one quantity. The space vector representation is valid for both transient and steady state conditions in contrast to phasor representation, which is valid only for steady state conditions. The concept of the space vector arises from the rotating air-gap MMF in a three-phase induction machine. By supplying balanced three-phase voltages to the three-phase balanced winding of a three-phase induction machine, rotating MMF is produced, which rotates at the same speed as that of individual voltages, with an amplitude of 1.5 times the individual voltage amplitude.

The space vector is defined as

$$\underline{f}_s = \frac{2}{3} \left[ f_a + e^{j2\frac{\pi}{3}} f_b + e^{j4\frac{\pi}{3}} f_c \right] \quad (3.26)$$

where  $f_a$ ,  $f_b$ , and  $f_c$  are the three-phase quantities of voltages, currents, and fluxes. In the inverter PWM, the voltage space vectors are considered.

Since the inverter can attain either  $+0.5 V_{dc}$  or  $-0.5 V_{dc}$  (if the DC bus has mid-point) or  $V_{dc}$ , 0, i.e. only two states, the total possible outputs are  $2^3 = 8$  (000, 001, 010, 011, 100, 101, 110, 111). Here 0 indicates the upper switch is 'OFF' and 1 represents the upper switch is 'ON.' Thus there are six active switching states (power flows from the input/DC link side of the inverter to the output/load side of the inverter) and two zero switching states (no power transfer from input/DC link to the load/load side). The operation of the lower switches are complementary. By using equation (3.26) and Table 3.2, the possible space vectors are computed and listed in Table 3.4.

The space vectors are shown graphically in Figure 3.29. The tips of the space vectors, when joined together, form a hexagon. The hexagon consists of six distinct sectors spanning over 360 degrees (one sinusoidal wave cycle corresponds to one rotation of the hexagon) with each sector of 60 degrees. Space vectors 1, 2, ...6 are called active state vectors and 7, 8 are called zero state vectors. The zero state vectors are redundant vectors but they are used to minimize the switching frequency. The space vectors are stationary while the reference vector  $v_s^*$  is rotating at the speed of the fundamental frequency of the inverter output voltage. It circles once for one cycle of the fundamental frequency.

The reference voltage follows a circular trajectory in a linear modulation range and the output is sinusoidal. The reference trajectory will change in over-modulation and the trajectory will be a hexagon boundary when the inverter is operating in the six-step mode. In implementing the SVPWM, the reference voltage is synthesized by using the nearest two neighboring active vectors and zero vectors. The choice of the active vectors depends upon the sector number in which the reference is located. Hence, it is important to locate the position of the reference voltage. Once the reference vector is located, the vectors to be used for the SVPWM implementation to be identified. After identifying the vectors to

**Table 3.4** Phase-to-neutral Space vector for a three-phase voltage source inverter

Switching States	Space Vector Number	Phase-to-neutral Voltage Space Vectors
000	7	0
001	5	$\frac{2}{3}V_{dc}e^{j\frac{4\pi}{3}}$
010	3	$\frac{2}{3}V_{dc}e^{j\frac{2\pi}{3}}$
011	4	$\frac{2}{3}V_{dc}e^{j\pi}$
100	1	$\frac{2}{3}V_{dc}e^{j0}$
101	6	$\frac{2}{3}V_{dc}e^{j\frac{5\pi}{3}}$
110	2	$\frac{2}{3}V_{dc}e^{j\frac{\pi}{3}}$
111	8	0

be used, the next task is to find the time of application of each vector, called the ‘dwell time’. The output voltage frequency of the inverter is the same as the speed of the reference voltage and the output voltage magnitude is the same as the magnitude of the reference voltage.

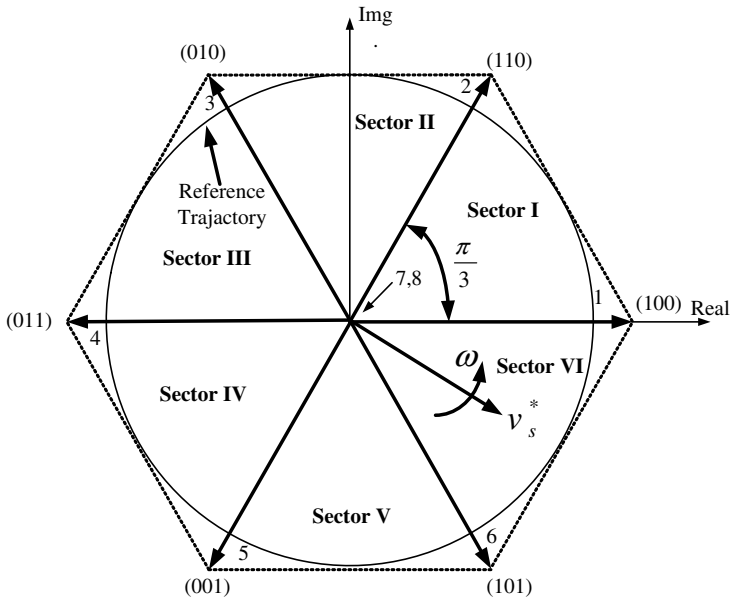


**Figure 3.29** Voltage space vector locations corresponding to different switching states

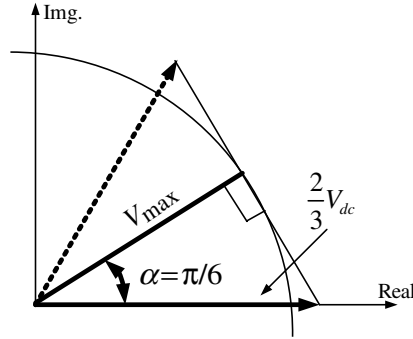


**Figure 3.30** Determining the maximum possible output using SVPWM

The maximum modulation index or the maximum output voltage that is achievable using the SVPWM technique is the radius of the largest circle that can be inscribed within the hexagon. This circle is tangential to the mid-points of the lines joining the ends of the active space vector. Thus the maximum obtainable fundamental output voltage is calculated from the right-angled triangle (Figure 3.30) as

$$V_{\max} = \left(\frac{2}{3}\right) V_{dc} \cos\left(\frac{\pi}{6}\right) = \frac{1}{\sqrt{3}} V_{dc} \quad (3.27)$$

The maximum possible output voltage using SPWM is  $0.5 V_{dc}$  and hence the increase in the output, when using SVPWM, is  $(2/3 V_{dc}) / (0.5 V_{dc}) = 1.154$ .

The time of application of the different space vectors are calculated using the 'equal volt-second principle'. According to this principle, the product of the reference voltage and the sampling/switching time ( $T_s$ ) must be equal to the product of the applied voltage vectors and their time of applications, assuming that the reference voltage remains fixed during the switching interval. When the reference voltage is in sector I, the reference voltage can be synthesized by using the vectors  $V_1$ ,  $V_2$ , and  $V_o$  (zero vector), applied for time  $t_a$ ,  $t_b$ , and  $t_o$ , respectively. Hence, using the equal volt-second principle, for sector I:

$$v_s^* T_s = V_1 t_a + V_2 t_b + V_o t_o \quad (3.28a)$$

$$\text{where } T_s = t_a + t_b + t_o \quad (3.28b)$$

The space vectors are given as

$$v_s^* = |v_s^*| e^{j\alpha} \quad V_1 = \frac{2}{3} V_{dc} e^{j0} \quad V_2 = \frac{2}{3} V_{dc} e^{j\frac{\pi}{3}} \quad V_o = 0 \quad (3.29)$$

Substituting equation (3.29) into equation (3.28a) and separating the real ( $\alpha$ -axis) and imaginary ( $\beta$ -axis) components:

$$|v_s^*| \cos(\alpha) T_s = \frac{2}{3} V_{dc} t_a + \frac{2}{3} V_{dc} \cos\left(\frac{\pi}{3}\right) t_b \quad (3.30a)$$

$$|v_s^*| \sin(\alpha) T_s = \frac{2}{3} V_{dc} \sin\left(\frac{\pi}{3}\right) t_b \quad (3.30b)$$

Where  $\alpha = \pi/3$ .

Solving equations (3.30a) and (3.30b) for the time of applications  $t_a$  and  $t_b$ :

$$\begin{aligned} t_a &= \frac{\sqrt{3}|v_s^*|}{V_{dc}} \sin\left(\frac{\pi}{3} - \alpha\right) T_s \\ t_b &= \frac{\sqrt{3}|v_s^*|}{V_{dc}} \sin(\alpha) T_s \\ t_o &= T_s - t_a - t_b \end{aligned} \quad (3.31)$$

Generalizing the above equation for six sectors gives the following, where  $k = 1, 2, \dots, 6$  is the sector number:

$$\begin{aligned} t_a &= \frac{\sqrt{3}|v_s^*|}{V_{dc}} \sin\left(k\frac{\pi}{3} - \alpha\right) T_s \\ t_b &= \frac{\sqrt{3}|v_s^*|}{V_{dc}} \sin\left(\alpha - (k-1)\frac{\pi}{3}\right) T_s \\ t_o &= T_s - t_a - t_b \end{aligned} \quad (3.32)$$

After locating the reference location and calculating the dwell time, the next step in SVPWM implementation is the determination of the switching sequence. The requirement is the minimum number of switchings to reduce switching loss, ideally one power switch should turn 'ON' and turn 'OFF' in one switching period.

In order to obtain a fixed switching frequency and optimum harmonic performance from SVPWM, each leg should change its state only once in each switching period. This is achieved by applying the zero state vector followed by two adjacent active state vectors in a half switching period. The next half of the switching period is the mirror image of the first half. The total switching period is divided into seven parts, the zero vector (000) is applied for 1/4th of the total zero vector time, followed by the application of active vectors for half of their application time and then again zero vector (111) is applied for 1/4th of the zero vector time. This is then repeated in the next half of the switching period. This is how symmetrical SVPWM is obtained. The switching patterns showing the leg voltages in one switching period is depicted in Figure 3.31 for sectors I to VI.



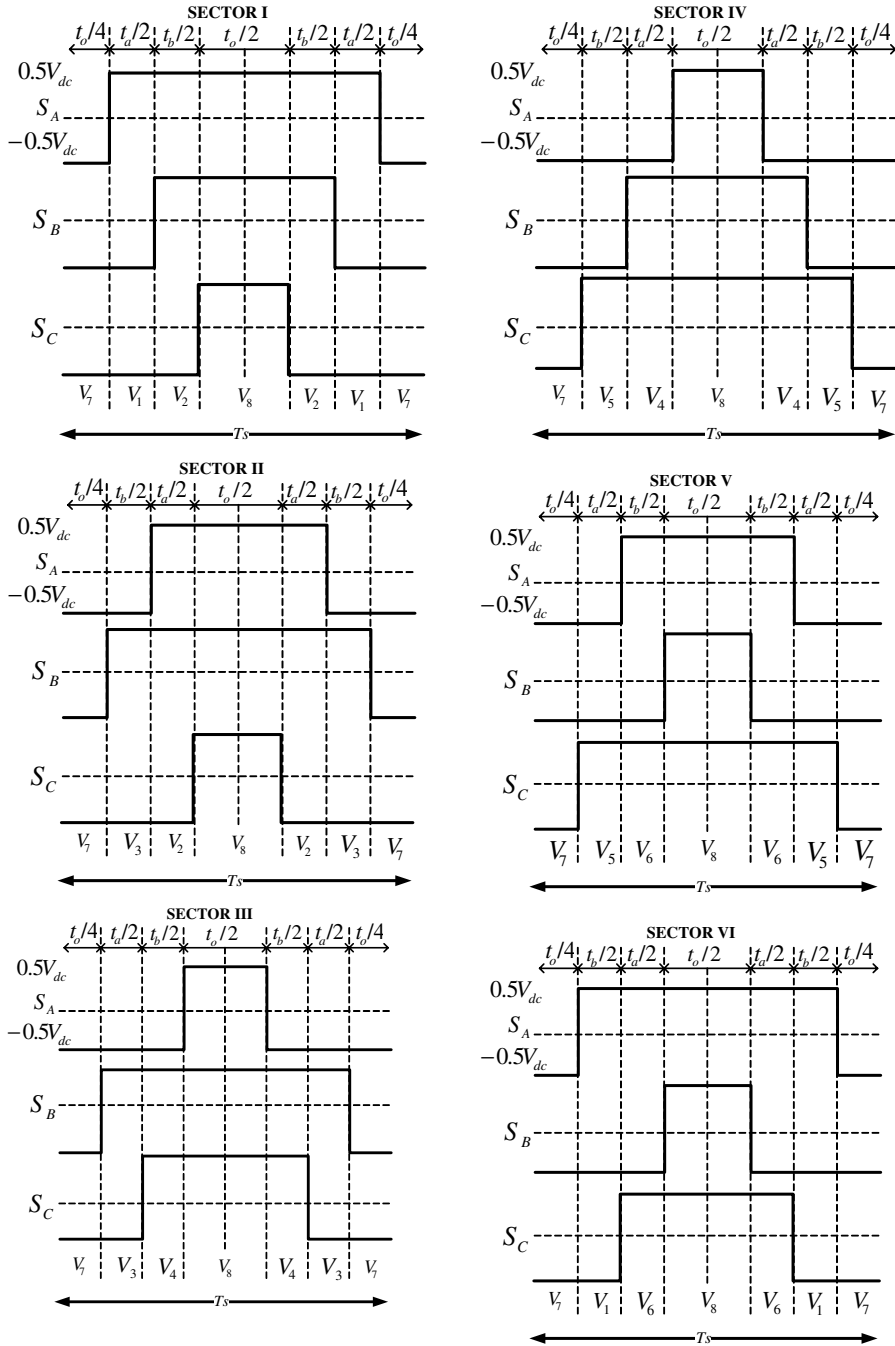


Figure 3.31 Switching pattern for SVPWM for sector I to VI

Average leg voltages can be determined from the switching patterns of Figure 3.31, for example, for sector I:

$$\begin{aligned} V_{A,avg} &= \frac{(V_{dc}/2)}{T_s} [t_0 + t_a + t_b - t_0] \\ V_{B,avg} &= \frac{(V_{dc}/2)}{T_s} [t_0 - t_a + t_b - t_0] \\ V_{C,avg} &= \frac{(V_{dc}/2)}{T_s} [t_0 - t_a - t_b - t_0] \end{aligned} \quad (3.33)$$

Substituting the equation of time of applications from equation (3.31) into equation (3.33), the following is obtained for sector I and similarly can be derived for other sectors:

$$\begin{aligned} V_{A,avg} &= \frac{\sqrt{3}}{2} |v_s^*| \sin\left(\alpha + \frac{\pi}{3}\right), & V_{B,avg} &= \frac{3}{2} |v_s^*| \sin\left(\alpha - \frac{\pi}{6}\right), \\ V_{C,avg} &= -\frac{\sqrt{3}}{2} |v_s^*| \sin\left(\alpha + \frac{\pi}{3}\right) \end{aligned} \quad (3.34)$$

### 3.4.6 Discontinuous Space Vector PWM

Discontinuous SVPWM results when one of the two zero vectors is not used in the implementation of the SVPWM. One leg of the inverter does not switch during the whole switching period and remains tied to either the positive or negative DC bus [9,10]. This is known as discontinuous SVPWM, since the switching is not continuous. Due to the manipulation of the zero space vector application in a switching period, one branch of the inverter remains unmodulated during one switching interval. Switching takes place in two branches: one branch is either tied to the positive DC bus or the negative DC bus, as shown in Figure 3.32 (when zero voltage (000) is eliminated, the leg voltage is tied to positive DC bus  $0.5 V_{dc}$  and when zero voltage (111) is eliminated, the leg voltage is tied to the negative bus voltage  $-0.5 V_{dc}$ ). The number of switchings is thus reduced to two-thirds compared to the continuous SVPWM and hence switching losses are reduced significantly. This type of PWM is especially useful when switching losses are to be reduced. There are several schemes of discontinuous SVPWM; however, all essentially merely rearrange the placement of the zero output voltage pulse within each half carrier or carrier interval. Discontinuous SVPWM are classified according to the location of the zero space vector and for how long it is not applied. The nine different discontinuous SVPWM techniques are:

1.  $t_7 = 0$  for all sectors, known as DPWMMAX;
2.  $t_8 = 0$  for all sectors, known as DPWMMIN;  
Zero vectors are made inoperative alternatively in a different sector;
3. Discontinuous modulation DPWM 0 (zero vector (000), i.e.  $t_7$  eliminated in odd sectors and zero vector (111), i.e.  $t_8$  is eliminated in even sectors);

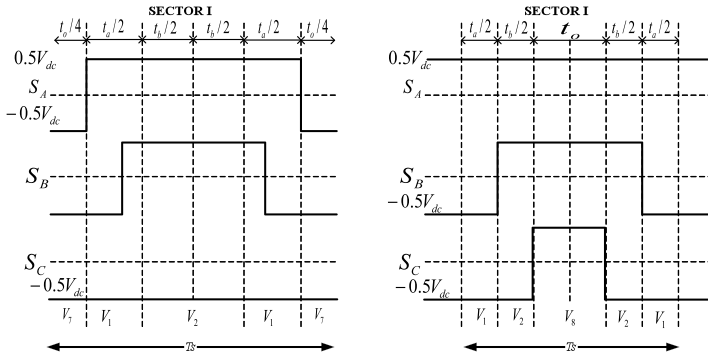


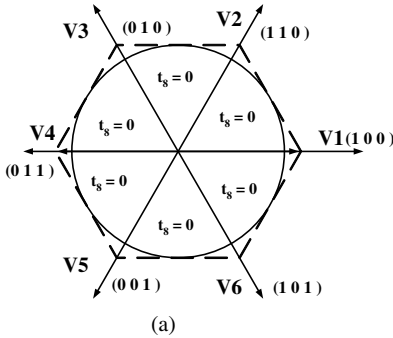
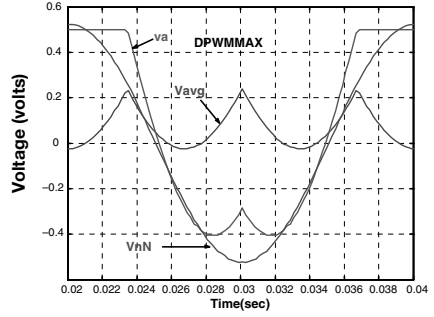
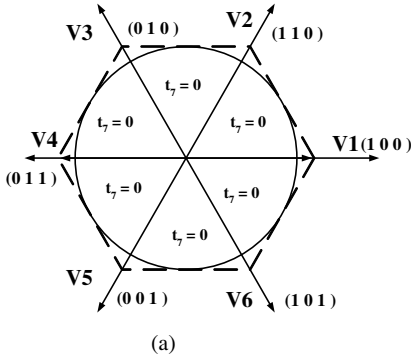
**Figure 3.32** Leg voltage (switching pattern) for discontinuous SVPWM.

4. Discontinuous modulation DPWM 1 (zero vector (000), i.e.  $t_7$  eliminated in even sectors and zero vector (111), i.e.  $t_8$  is eliminated in odd sectors);
5. Discontinuous modulation DPWM 2 (each sector is subdivided into parts and zero vector (000), i.e.  $t_7$  eliminated in odd sectors and zero vector (111), i.e.  $t_8$  is eliminated in even sectors);
6. Discontinuous modulation DPWM 3 (each sector is subdivided into parts and zero vector (000), i.e.  $t_7$  eliminated in even sectors and zero vector (111), i.e.  $t_8$  is eliminated in odd sectors);
7. Discontinuous modulation DPWM 4 (region is divided into 4 sectors each spanning 90 degrees and zero vector (000), i.e.  $t_7$  eliminated in odd sectors and zero vector (111), i.e.  $t_8$  is eliminated in even sectors);
8. Discontinuous modulation DPWM 5 (zero vector (000), i.e.  $t_7$  eliminated in sectors 1, 2, 3 and zero vector (111), i.e.  $t_8$  is eliminated in sectors, 4, 5, 6);
9. Discontinuous modulation DPWM 6 (the whole region is divided into 8 sectors of 45 degrees each, zero vector (000), i.e.  $t_7$  eliminated in odd sectors and zero vector (111), i.e.  $t_8$  is eliminated in even sectors).

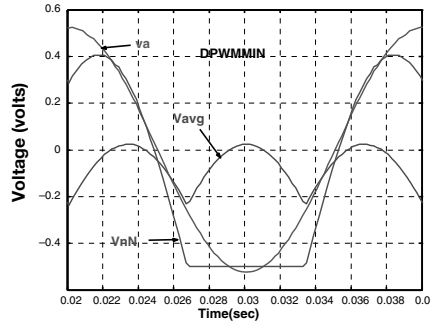
The placement of the zero vectors and corresponding voltages ( $V_{avg}$  (leg voltage),  $V_a$  (phase voltage),  $V_{nN}$  (voltage between neutral point)) for the discontinuous SVPWM are shown in Figure 3.33.

### 3.4.7 MATLAB/Simulink Model for Space Vector PWM

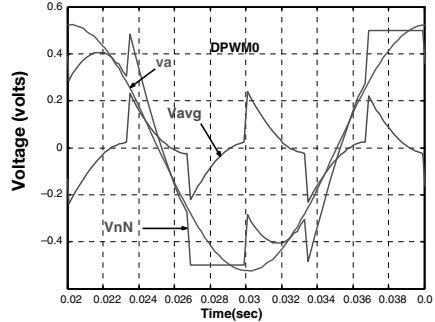
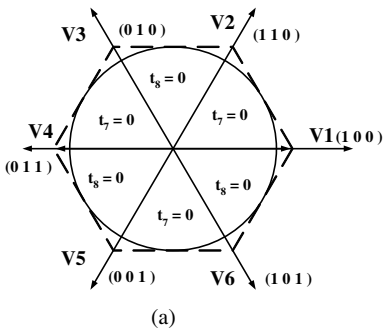
The MATLAB/Simulink model can be developed using different approaches, using all Simulink blocks or all MATLAB coding [11,12]. This section shows a model developed using the MATLAB function block and Simulink blocks. The model shown is flexible in nature and can be used to model continuous as well as discontinuous SVPWM by changing in the MATLAB function command. The simulation model is shown in Figure 3.34. Each block is further elaborated on in Figure 3.35.



(b) DPWMMAX



(b) DPWMMIN

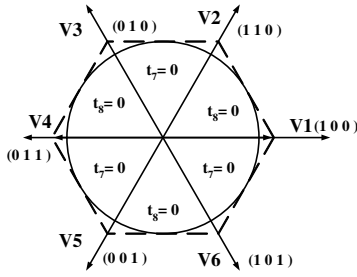


(b) DPWMM0

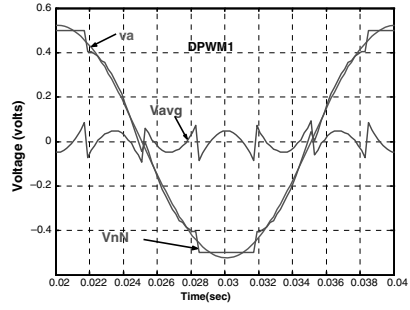
**Figure 3.33** (a) Zero voltage distributions and (b) associated voltage waveforms for discontinuous SVPWM

**3.4.7.1 Reference Voltage Generation Block**

This block is used to simulate the balanced three-phase input reference. The three-phase input sinusoidal voltage is generated using the ‘function’ block from the ‘Functions & Tables’ sub-library of Simulink. This is then converted into a two-phase equivalent using Clark’s

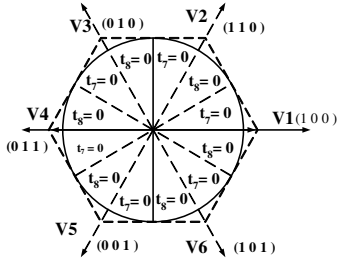


(a)

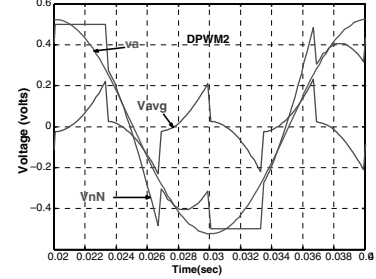


(b)

**DPWM1**

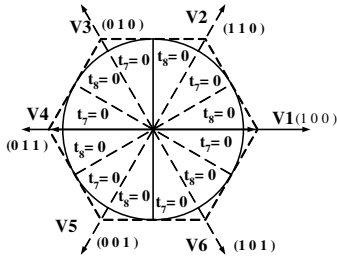


(a)

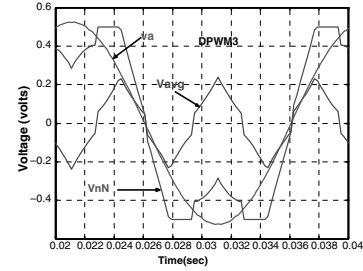


(b)

**DPWM2**

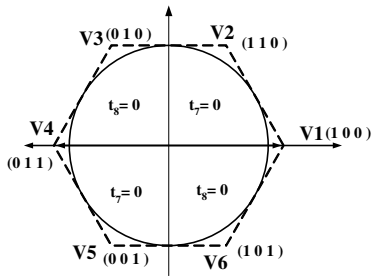


(a)

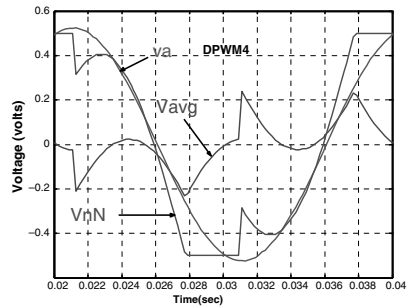


(b)

**DPWM3**



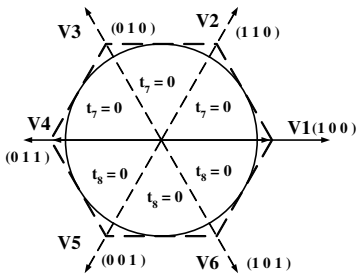
(a)



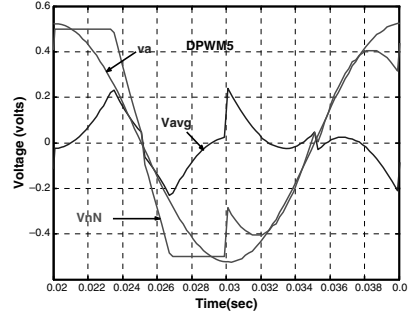
(b)

**DPWM4**

Figure 3.33 (Continued)

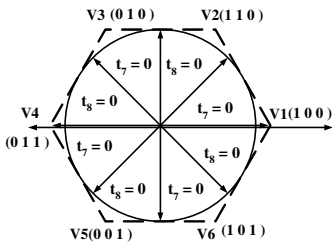


(a)

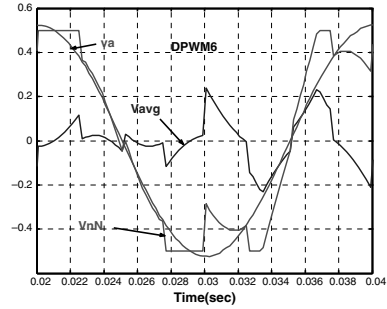


(b)

**DPWM5**



(a)



(b)

**DPWM6**

**Figure 3.33 (Continued)**

transformation equations. This is once again implemented using the ‘function’ blocks. Furthermore, the two-phase equivalent is transformed into polar form using the ‘Cartesian to polar’ block from the ‘Simulink extras’ sub-library. The output of this block is the magnitude of the reference as the first output and the corresponding angle of the reference as the second output. The waveform of the magnitude is simply a constant line, as its value remains fixed in an open-loop mode. In the closed-loop mode, the reference voltage can be dictated by the closed-loop controller. The waveform of the angle is shown in Figure 3.36. It is a saw tooth signal with peak value of  $\pm\pi$ . Sector identification is done using the comparison of the angle waveform with the predefined values, as shown in Figure 3.36. The number inside the waveform represents the sector number.

**3.4.7.2 Switching Time Calculation**

The switching time and the corresponding switch state for each power switch is calculated in MATLAB function block ‘sf.’ The MATLAB code requires magnitude of the reference, the angle of the reference, and the timer signal for comparison. The angle of the reference voltage is kept constant for one sampling period using the ‘zero order hold’ block so that its value does not change during time calculation. The angle information is used for sector identification in the

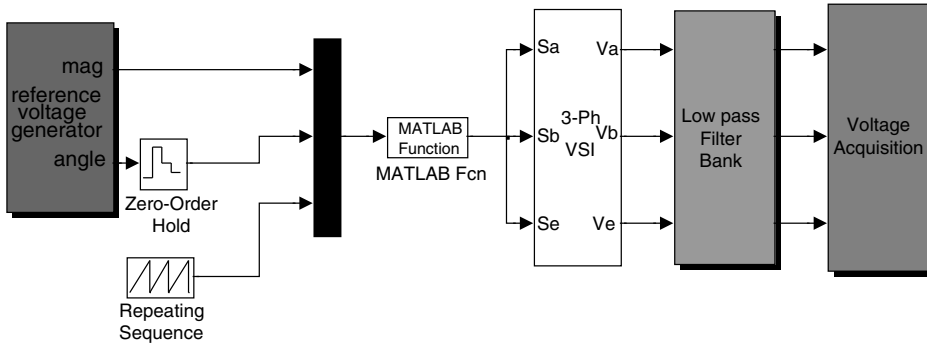


Figure 3.34 MATLAB/Simulink Model of space vector PWM

MATLAB code ‘aaa’ for continuous SVPWM and code ‘a1’ for the discontinuous SVPWM (DPWMMAX). Furthermore, a ramp time signal is generated to be used in the MATLAB code. The height and width of the ramp signal is equal to the switching time of the inverter branch. This ramp is generated using a ‘repeating sequence’ from the source sub-library.

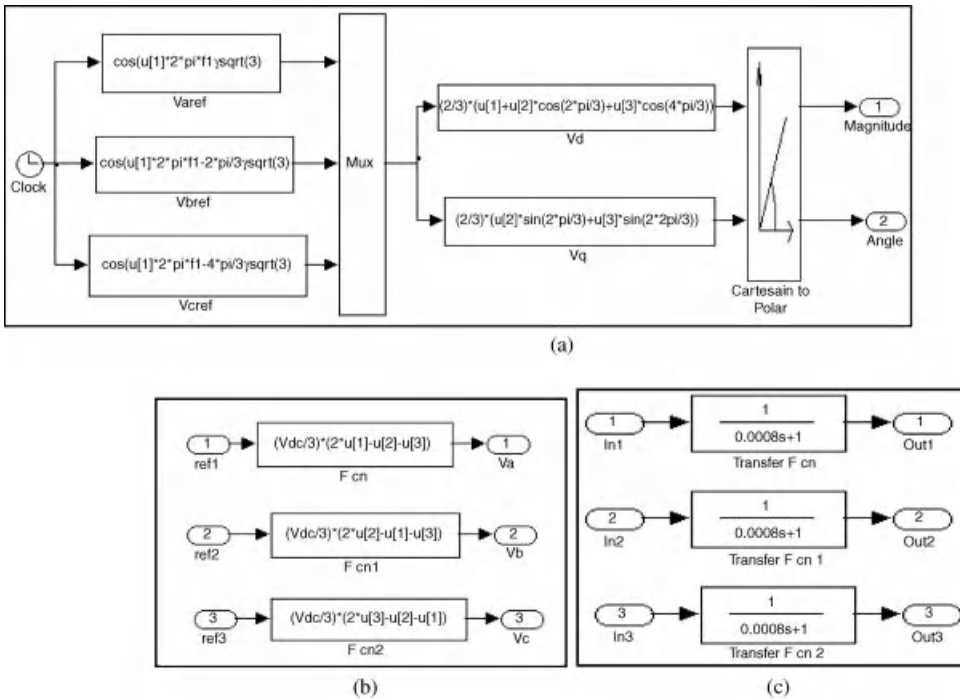
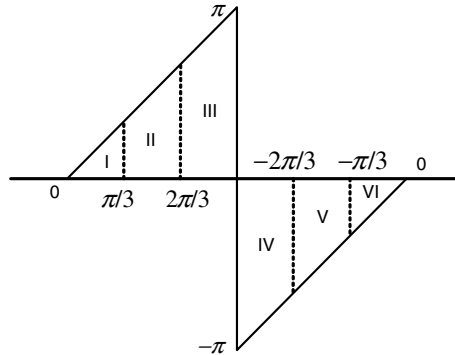


Figure 3.35 Sub-blocks of MATLAB/Simulink model: (a) Reference voltage generation; (b) VSI; (c) Filters (File name: *Space3.mdl* and *aaa.m*)



**Figure 3.36** Sector Identification logic

The MATLAB code first identifies the sector of the reference voltage. The time of application of the active and zero vectors are then calculated. The times are then arranged according to the predefined switching pattern (Figure 3.31). This time is then compared with the ramp timer signal. The height and width of the ramp is equal to the switching period of the inverter branch. Depending upon the location of the time signal within the switching period, the switch state is defined. This switch state is then passed on to the inverter block for further calculation.

### 3.4.7.3 Three-phase Inverter Block

This block is built to simulate a voltage source inverter assuming a constant DC link voltage. The inputs to the inverter block are the switching signals and the outputs are the PWM phase-to-neutral voltages. The inverter model is built using ‘function’ blocks.

### 3.4.7.4 Filter Blocks

To visualize the actual output of the inverter block, the filtering of the PWM ripple is required. The PWM voltage signal is filtered here using the first-order filter. This is implemented using the ‘Transfer function’ block from ‘Continuous’ sub-library. The time constant of the first-order filter is chosen as 0.8 ms.

### 3.4.7.5 Voltage Acquisition

This block stores the output results. The results are stored in a ‘workspace’ taken from the ‘sink’ library of the Simulink. The simulation waveform is shown in Figure 3.37. The input reference fundamental frequency is kept at 50 Hz and the switching frequency of the inverter is chosen as 5 kHz. The output is seen to be sinusoidal without any ripple except the switching harmonics. By simply changing the input reference’s magnitude and the frequency, the output voltage magnitude and frequency can be varied.



### 3.4.7.6 Continuous SVPWM – % MATLAB Code to Generate Switching Functions

```

% Inputs are magnitude u1(:), angle u2(:), and
% ramp time signal for comparison u3(:)

function [sf]=aaa(u)
ts=0.0002;vdc=1;peak_phase_max= vdc/sqrt(3);
x=u(2); y=u(3);
mag=(u(1)/peak_phase_max) * ts;
%sector I
if (x>=0) & (x<pi/3)
ta = mag * sin(pi/3-x);
tb = mag * sin(x);
t0 = (ts-ta-tb);
t1=[t0/4 ta/2 tb/2 t0/2 tb/2 ta/2 t0/4];
t1=cumsum(t1);
    v1=[0 1 1 1 1 0];
    v2=[0 0 1 1 1 0];
v3=[0 0 0 1 0 0];
    for j=1:7
        if(y<t1(j))
            break
        end
    end
    sa=v1(j);
    sb=v2(j);
    sc=v3(j);
end

% sector II
if (x>=pi/3) & (x<2*pi/3)
adv= x-pi/3;
tb = mag * sin(pi/3-adv);
ta = mag * sin(adv);
t0 = (ts-ta-tb);
t1=[t0/4 ta/2 tb/2 t0/2 tb/2 ta/2 t0/4];
t1=cumsum(t1);
v1=[0 0 1 1 1 0];
v2=[0 1 1 1 1 0];
v3=[0 0 0 1 0 0];
    for j=1:7
        if(y<t1(j))
            break
        end
    end
end
end

```

```

sa=v1(j);
sb=v2(j);
sc=v3(j);
end

%sector III
if (x>=2*pi/3) & (x<pi)
adv=x-2*pi/3;
ta = mag * sin(pi/3-adv);
tb = mag * sin(adv);
t0 = (ts-ta-tb);
t1=[t0/4 ta/2 tb/2 t0/2 tb/2 ta/2 t0/4];
t1=cumsum(t1);
v1=[0 0 0 1 0 0 0];
v2=[0 1 1 1 1 1 0];
v3=[0 0 1 1 1 0 0];
    for j=1:7
        if (y<t1(j))
            break
        end
    end
sa=v1(j);
sb=v2(j);
sc=v3(j);
end

%sector IV
if (x>=-pi) & (x<-2*pi/3)
adv = x + pi;
tb= mag * sin(pi/3 - adv);
ta = mag * sin(adv);
t0 = (ts-ta-tb);
t1=[t0/4 ta/2 tb/2 t0/2 tb/2 ta/2 t0/4];
t1=cumsum(t1);
v1=[0 0 0 1 0 0 0];
v2=[0 0 1 1 1 0 0];
v3=[0 1 1 1 1 1 0];
    for j=1:7
        if (y>t1(j))
            break
        end
    end
sa=v1(j);
sb=v2(j);
sc=v3(j);
end

```

```

% sector V
if (x>=-2*pi/3) & (x<=-pi/3)
adv = x+2*pi/3;
ta = mag * sin(pi/3-adv);
tb = mag * sin(adv);
t0 = (ts-ta-tb);
t1=[t0/4 ta/2 tb/2 t0/2 tb/2 ta/2 t0/4];
t1=cumsum(t1);
v1=[0 0 1 1 1 0 0];
v2=[0 0 0 1 0 0 0];
v3=[0 1 1 1 1 1 0];
    for j=1:7
        if(y<t1(j))
            break
        end
    end
end
sa=v1(j);
sb=v2(j);
sc=v3(j);
end

%Sector VI
if (x>=-pi/3) & (x<0)
adv = x+pi/3;
tb = mag * sin(pi/3-adv);
ta = mag * sin(adv);
t0 = (ts-ta-tb);
t1=[t0/4 ta/2 tb/2 t0/2 tb/2 ta/2 t0/4];
t1=cumsum(t1);
v1=[0 1 1 1 1 1 0];
v2=[0 0 0 1 0 0 0];
v3=[0 0 1 1 1 0 0];
for j=1:7
    if(y<t1(j))
        break
    end
end
end
sa=v1(j);
sb=v2(j);
sc=v3(j);
end
sf=[sa, sb, sc];

```

### 3.4.7.7 Discontinuous SVPWM – % MATLAB Code

```

function [sf]=a1(u)
f=50;
ts=0.0002;
vdc=1;
peak_phase_max = vdc/sqrt(3);
x=u(2); y=u(3);
mag=(u(1)/peak_phase_max) * ts;

%sector I
if (x>=0) & (x<pi/3)
    ta = mag * sin(pi/3-x);
tb = mag * sin(x);
t0 = (ts-ta-tb);
t1 = [ta/2 tb/2 t0 tb/2 ta/2];
t1 = cumsum(t1);
v1 = [ 1 1 1 1 1];
v2 = [ 0 1 1 1 0];
v3 = [0 0 1 0 0];
for j = 1:5
    if(y<t1(j))
        break
    end
end
sa=v1(j);
sb=v2(j);
sc=v3(j);
end

% sector II
if (x>=pi/3) & (x<2*pi/3)
    adv= x-pi/3;
tb = mag * sin(pi/3-adv);
ta = mag * sin(adv);
t0 = (ts-ta-tb);
t1=[ta/2 tb/2 t0 tb/2 ta/2 ];
t1=cumsum(t1);
v1=[0 1 1 1 0];
v2=[1 1 1 1 1];
v3=[ 0 0 1 0 0];
for j=1:5
    if(y<t1(j))

```

```

        break
    end
end
sa=v1(j);
sb=v2(j);
sc=v3(j);
end

%sector III
if (x>=2*pi/3) & (x<pi)
    adv=x-2*pi/3;
    ta = mag * sin(pi/3-adv);
    tb = mag * sin(adv);
    t0 = (ts-ta-tb);
    t1=[ta/2 tb/2 t0 tb/2 ta/2];
    t1=cumsum(t1);
    v1=[ 0 0 1 0 0];
    v2=[ 1 1 1 1 1];
    v3=[ 0 1 1 1 0];
    for j=1:5
        if(y<t1(j))
            break
        end
    end
    sa=v1(j);
    sb=v2(j);
    sc=v3(j);
end

%sector IV
if (x>=-pi) & (x<-2*pi/3)
    adv = x + pi;
    tb= mag * sin(pi/3 - adv);
    ta = mag * sin(adv);
    t0 = (ts-ta-tb);
    t1=[ta/2 tb/2 t0 tb/2 ta/2];
    t1=cumsum(t1);
    v1=[ 0 0 1 0 0];
    v2=[ 0 1 1 1 0];
    v3=[ 1 1 1 1 1];
    for j=1:5
        if(y<t1(j))
            break
        end
    end
end
end

```

```

    sa=v1(j);
    sb=v2(j);
    sc=v3(j);
end

% sector V
if (x>=-2*pi/3) & (x<-pi/3)
    adv = x+2*pi/3;
    ta = mag * sin(pi/3-adv);
    tb = mag * sin(adv);
    t0 = (ts-ta-tb);
    t1=[ta/2 tb/2 t0 tb/2 ta/2];
t1=cumsum(t1);
v1=[0 1 1 1 0];
v2=[0 0 1 0 0];
v3=[1 1 1 1 1];
for j=1:5
    if(y<t1(j))
        break
    end
end
sa=v1(j);
sb=v2(j);
sc=v3(j);
end

%Sector VI
if (x>=-pi/3) & (x<0)
    adv = x+pi/3;
    tb = mag * sin(pi/3-adv);
    ta = mag * sin(adv);
    t0 = (ts-ta-tb);
    t1=[ta/2 tb/2 t0 tb/2 ta/2];
    t1=cumsum(t1);
    v1=[1 1 1 1 1];
    v2=[0 0 1 0 0];
v3=[0 1 1 1 0];
for j=1:5
    if(y<t1(j))
        break
    end
end
sa=v1(j);
sb=v2(j); sc=v3(j); end sf=[sa, sb, sc]

```

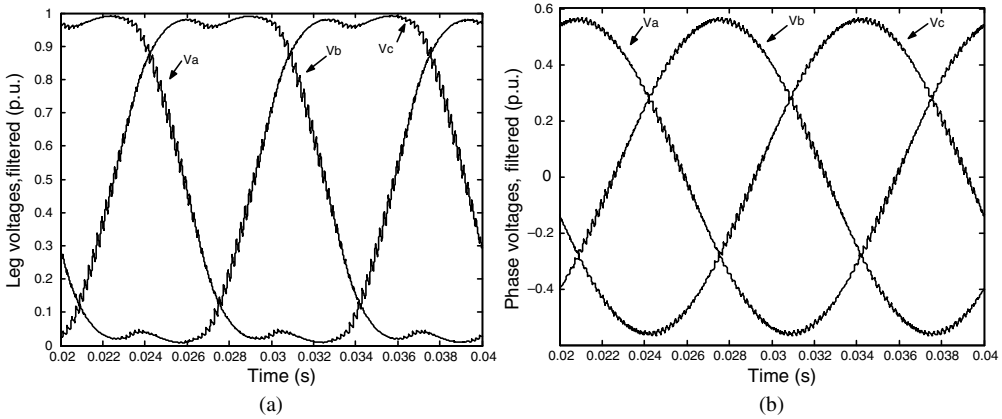


**Figure 3.37** (a) Filtered leg voltages for continuous SVPWM; (b) Filtered phase voltages for DSVPWM

### 3.4.8 Space Vector PWM in Over-modulation Region

In the SVPWM method, the maximum sinusoidal output is obtained when the reference is  $|v_s^*| = 1/\sqrt{3}V_{dc}$  and the trajectory is a circle inscribed inside the hexagon, called the linear modulation range. If the references increase more than this value, then the output cannot be realized by using the linear modulation technique and this is called the over-modulation region [13–16]. Since the time of application of the zero space vector becomes negative, it does not make any physical sense. Considering equation (3.31) and assuming  $|v_s^*| = 1/\sqrt{3}V_{dc}$ ,  $V_{dc} = 1\text{p.u.}$  and  $T_s = 1\text{sec.}$ , the time of application of the zero space vector in sector I is calculated (Figure 3.38). It is seen that the zero vector time of application just touches zero in the middle of the sector at 30 degrees. Increasing further the length of the reference voltage space vector will lead to a negative value of time of application. This is true for the other sectors too. Hence, for reference voltage vectors exceeding this limit, the zero voltage vectors cannot be used as such.

When the reference voltage vector is more than this limiting value of  $|v_s^*| = 1/\sqrt{3}V_{dc}$ , the inverter moves into the over-modulation region for  $\frac{1}{\sqrt{3}}V_{dc} < |v_s^*| < \frac{2}{\pi}V_{dc}$ . When the reference voltage vector is  $|v_s^*| = \frac{2}{\pi}V_{dc}$ , the inverter operates in the square wave mode or six-step mode, as shown in Figure 3.39.

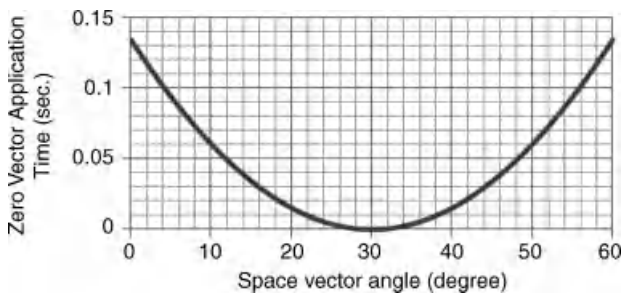


**Figure 3.38** Zero vector time of application in linear modulation range in sector I

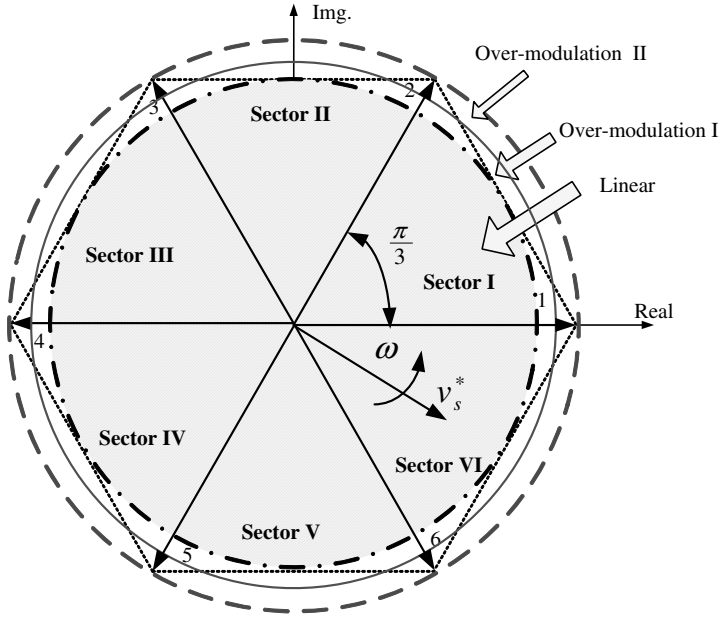


Figure 3.39 Linear and over-modulation range

The over-modulation region is further divided into two sub-modes, the over-modulation region I ( $0.5773 < |v_s^*| < 0.6061$ ) and the over-modulation region II ( $0.6061 < |v_s^*| < 0.6366$ ). In over-modulation region I, the reference voltage space vector is modified in such a way that it becomes a ‘distorted continuous reference voltage space vector.’ The magnitude of the reference voltage vector is altered but the angle is not modified. However, in the over-modulation region II, both the reference voltage space vector magnitude and the angles are modified in such a way that it becomes a ‘distorted discontinuous reference voltage space vector.’

**3.4.8.1 Over-modulation Region I**

Consider Figure 3.40 (called Case-1): the outer circle shows the trajectory of the desired reference voltage vector, while the inner circle shows the end of linear modulation region. The reference voltage vector follows the desired circular trajectory from point  $x$  to point  $y$ . When the reference voltage space vector goes beyond the hexagon from point  $y$  to point  $p$ , the reference voltage space vector trajectory slides along the hexagonal straight line. After the end of the straight line (at point  $p$ ), the trajectory once again follows the circular path from point  $p$  to  $q$ ; this repeats in other sectors too. In this way the reference voltage vector is modified for over-modulation region I.

The reference voltage space vector follows a circular trajectory for some time and then a straight line trajectory. The time of the application of the active space vectors for the circular trajectory is given by equation (3.31). The time of application of the active space vectors for the region  $y$  to  $p$  (straight line) can be obtained as follows:



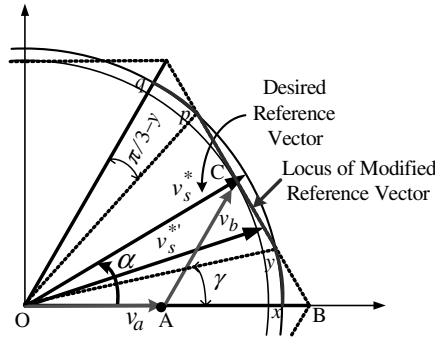


**Figure 3.40** Over-modulation I in SVPWM-Case 1

Let the modified space vector be  $|v_s^{*'}|$  and be decomposed into a real and an imaginary part:

$$|v_s^{*'}| \cos(\alpha) = |v_a| + |v_b| \cos\left(\frac{\pi}{3}\right) \quad \text{for } \gamma < \alpha < \frac{\pi}{3} - \gamma \quad (3.35)$$

$$|v_s^{*'}| \sin(\alpha) = |v_b| \sin\left(\frac{\pi}{3}\right)$$

Solving equation (3.35) for  $v_a$ :

$$|v_a| = |v_s^{*'}| \left( \cos(\alpha) - \frac{1}{\sqrt{3}} \sin(\alpha) \right) \quad (3.36)$$

From Figure 3.40, ABC forms an equilateral triangle, hence:

$$OB = OA + AB = |v_a| + |v_b| = \frac{2}{3} V_{dc} \quad (3.37)$$

Using equations (3.35), (3.36), and (3.37) to determine the length of the modified space vector:

$$|v_s^{*'}| = \frac{\frac{2}{3} V_{dc}}{\left( \cos(\alpha) + \frac{1}{\sqrt{3}} \sin(\alpha) \right)} \quad (3.38)$$

The length of the component vectors are obtained for  $\gamma < \alpha < \frac{\pi}{3} - \gamma$ :

$$|v_a| = \frac{2}{3} V_{dc} \left[ \frac{\sqrt{3} \cos(\alpha) - \sin(\alpha)}{\sqrt{3} \cos(\alpha) + \sin(\alpha)} \right] \tag{3.39a}$$

$$|v_b| = \frac{2}{3} V_{dc} \left[ \frac{2 \sin(\alpha)}{\sqrt{3} \cos(\alpha) + \sin(\alpha)} \right] \tag{3.39b}$$

To obtain the expression for the time of application of the active space voltage vectors, the equal volt-second principle is applied:

$$v_a t_a + v_b t_b = v_s^* T_s \tag{3.40}$$

$$t_a = \left( \frac{\sqrt{3} \cos(\alpha) - \sin(\alpha)}{\sqrt{3} \cos(\alpha) + \sin(\alpha)} \right) T_s \tag{3.41}$$

$$t_b = T_s - t_a$$

$$t_o = 0$$

These equations are valid for the first sector; nevertheless, a similar relationship can be derived for other sectors. Implementation of the SVPWM follows the same procedure as that of the linear mode, except the time of application is now governed by equation (3.41).

From Figure 3.41 (called Case-2), it is seen that by modifying the trajectory of the reference space vector, the actual output becomes smaller than the desired reference. This is due to the fact that the volt-second balance is not met and the loss in the output corresponds to the volt-second area  $A_2$ . To compensate for this loss and to maintain the volt-second balance, the reference voltage vector is further modified. The trajectory of the reference voltage vector follows the outer circle for a small distance when the hexagon boundary is met at point  $r$ . It then slides along the hexagon straight line up to point  $s$ , where it meets the circular trajectory

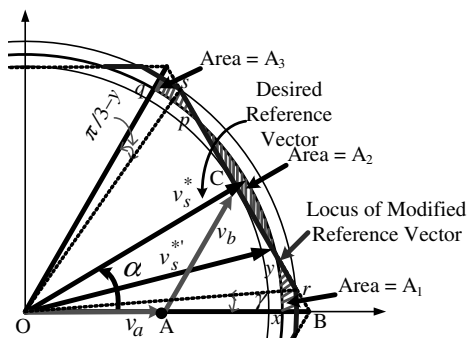


Figure 3.41 Over-modulation I in SVPWM-Case 2

and then moves along this circle. In this way the volt-second lost in  $A_2$  is gained in area  $A_1$  and  $A_3$ . A more precise calculation of the modified trajectory is needed in this case. The modified reference voltage expression is derived for different parts of the sectors. Once the voltage modified voltage reference is known, the time of application of the vector is calculated using equation (3.31) and accordingly the switching pattern is obtained and further used for the SVPWM implementation. The modified space voltage vector expression is obtained as [14].

$$|v_s^*| = \frac{1}{\sqrt{3}} V_{dc} \tan(\alpha) \quad \text{for } 0 < \alpha < \left(\frac{\pi}{6} - \gamma\right) \quad (3.42a)$$

$$|v_s^*| = \frac{1}{\sqrt{3}} V_{dc} \frac{1}{\cos\left(\frac{\pi}{6} - \gamma\right)} \quad \text{for } \left(\frac{\pi}{6} - \gamma\right) < \alpha < \left(\frac{\pi}{6} + \gamma\right) \quad (3.42b)$$

$$|v_s^*| = \frac{1}{\sqrt{3}} V_{dc} \frac{1}{\cos\left(\frac{\pi}{3} - \alpha\right)} \quad \text{for } \left(\frac{\pi}{6} + \gamma\right) < \alpha < \left(\frac{\pi}{2} - \gamma\right) \quad (3.42c)$$

$$|v_s^*| = \frac{1}{\sqrt{3}} V_{dc} \frac{1}{\cos\left(\frac{\pi}{6} - \gamma\right)} \quad \text{for } \left(\frac{\pi}{2} - \gamma\right) < \alpha < \frac{\pi}{2} \quad (3.43)$$

A linearized relationship between the angle  $\gamma$  and the modulation index is obtained as [14]

$$\gamma = \begin{cases} -30.23 MI + 27.94 & \text{for } 0.9068 \leq MI < 0.9095 \\ -8.58 MI + 8.23 & \text{for } 0.9095 \leq MI < 0.9485 \\ -26.43 MI + 25.15 & \text{for } 0.9485 \leq MI < 0.9517 \end{cases} \quad (3.44)$$

where  $MI = \frac{|v_s^*|}{\frac{2}{3} V_{dc}}$ . After determining the angle  $\gamma$ , the modified reference voltage vectors length is calculated from equation (3.43), which is then used to calculate the time of application of the space vector using equation (3.31).

### 3.4.8.2 Over-modulation Region-II

In the over-modulation region I, the angular velocity of the modified reference voltage space vector and desired reference voltage space vector is the same and constant for each fundamental cycle. The reference voltage and actual output voltage is equal during the over-modulation region I, due to the fact that the loss in the Area  $A_2$  (due to reduced length of the reference vector, since it cannot go beyond the hexagon boundary) is compensated for by increasing the length of the reference in area  $A_1$  and area  $A_3$ . A situation arises when the desired reference voltage vector reaches  $0.6061 V_{dc}$ , where no more room exists in area  $A_1$  and area  $A_3$  to compensate for the loss in area  $A_2$ . At this point, over-modulation region II starts. During this mode of over-modulation, both the reference voltage space vector length and angle is modified. For the region  $x$  to  $y$  and  $p$  to  $q$  (Figure 3.42), the modified space vector is held constant at the vertex of the hexagon. Hence, the desired reference voltage moves while the modified voltage vector does not. Once the desired reference reaches point  $y$ , the modified vector starts to

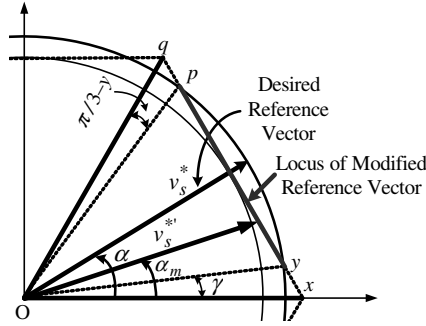


**Figure 3.42** Over-modulation II in SVPWM

slide along the side of the hexagon. In this way the reference becomes discontinuous. The angle of the modified reference voltage is

$$\alpha_m = \begin{cases} 0 & 0 \leq \alpha \leq \gamma \\ \frac{\pi}{6} \frac{\alpha - \gamma}{\pi/6 - \gamma} & \gamma \leq \alpha \leq \pi/3 - \gamma \\ \pi/6 & \pi/3 - \gamma \leq \alpha \leq \pi/3 \end{cases} \quad (3.45)$$

The expression for the modified reference voltage vector is [14]

$$|v_s^{*'}| = \frac{1}{\sqrt{3}} V_{dc} \tan(\alpha) \quad \text{for } 0 < \alpha < \left(\frac{\pi}{6} - \gamma\right) \quad (3.46a)$$

$$|v_s^{*'}| = \frac{1}{3} V_{dc} \quad \text{for } \left(\frac{\pi}{6} - \gamma\right) < \alpha < \left(\frac{\pi}{6} + \gamma\right) \quad (3.46b)$$

$$|v_s^{*'}| = \frac{1}{\sqrt{3}} V_{dc} \frac{1}{\cos\left(\frac{\pi}{3} - \alpha_m\right)} \quad \text{for } \left(\frac{\pi}{6} + \gamma\right) < \alpha < \left(\frac{\pi}{2} - \gamma\right) \quad (3.46c)$$

$$|v_s^{*'}| = \frac{2}{3} V_{dc} \quad \text{for } \left(\frac{\pi}{2} - \gamma\right) < \alpha < \frac{\pi}{2} \quad (3.46d)$$

The linearized equation is found for the modified angle is

$$\gamma = \begin{cases} 6.4MI - 6.09 & \text{for } 0.95 \leq MI < 0.98 \\ 11.75MI - 11.34 & \text{for } 0.98 \leq MI < 0.9975 \\ 48.96MI - 48.43 & \text{for } 0.9975 \leq MI < 1.0 \end{cases} \quad (3.47)$$

The SVPWM in the over-modulation region II is implemented using equations (3.31), (3.46), and (3.47).

### 3.4.9 MATLAB/Simulink Model to Implement Space Vector PWM in Over-modulation Regions

The MATLAB/Simulink model for implementing over-modulation using SVPWM is the same as that in Figure 3.34. The MATLAB function block is modified in order to account for the over-modulation. The time of application of the space vector is calculated using equation (3.31) for the period when the reference space vector lies between the region ( $0 < \alpha \leq \gamma$  and  $\pi/3 - \gamma < \alpha \leq \pi/3$ ) and for the remaining period, time of application is computed using equation (3.41). The angle  $\gamma$  is calculated using equation (3.44). The MATLAB code requires the magnitude of the reference, the angle of the reference, and the timer signal for comparison. The angle of the reference voltage is on hold for each switching period, so that its value does not change during time calculation. The angle information is used for sector identification in the MATLAB code 'aaa\_OM1' for over-modulation I and 'aaa\_OM2' for over-modulation II and subsequent generation of gating signals for the inverter. For the 50-Hz fundamental, filtered output voltages for different modulation indices are shown in Figure 3.43.

### 3.4.10 Harmonic Analysis

Harmonic components of the output voltage are given, using the Fourier series expression, as

$$F_n(\theta) = \frac{4}{\pi} \left[ \int_0^{\pi/2} f(\theta) \sin(n\theta) d\theta \right] \quad (3.48)$$

where  $f(\theta)$  is given by equations (3.42a)–(3.42d) in the over-modulation mode I and equations (3.46a)–(3.46d) in the over-modulation mode II. A numerical integration of equation (3.48) shows that even-ordered harmonics and triplen harmonics are eliminated in the output voltages. The six lowest harmonic components (3rd, 5th, 7th, 9th, 11th, and 13th) versus the modulation index (MI) are shown in Figure 3.44. The low-order harmonic components increase with the increase of the modulation index.

The THD factor is defined as

$$THD = \frac{\sqrt{(V_r^2 - V_1^2)}}{V_1} \quad (3.49)$$

where  $V_r$  and  $V_1$  are the rms values of the  $r$ th harmonic components and fundamental component of the phase voltage, respectively. Figure 3.45 shows the THD factor of the output voltage up to the 25th harmonic. As the modulation index increases, especially in over-modulation mode II, the THD increases steeply and culminates to 31.1% at  $MI = 1$ .

### 3.4.11 Artificial Neural Network-based PWM

The SVPWM can be implemented by a feed-forward neural network, because the SVPWM algorithm is a non-linear input/output mapping and the Artificial Neural Network (ANN) is a

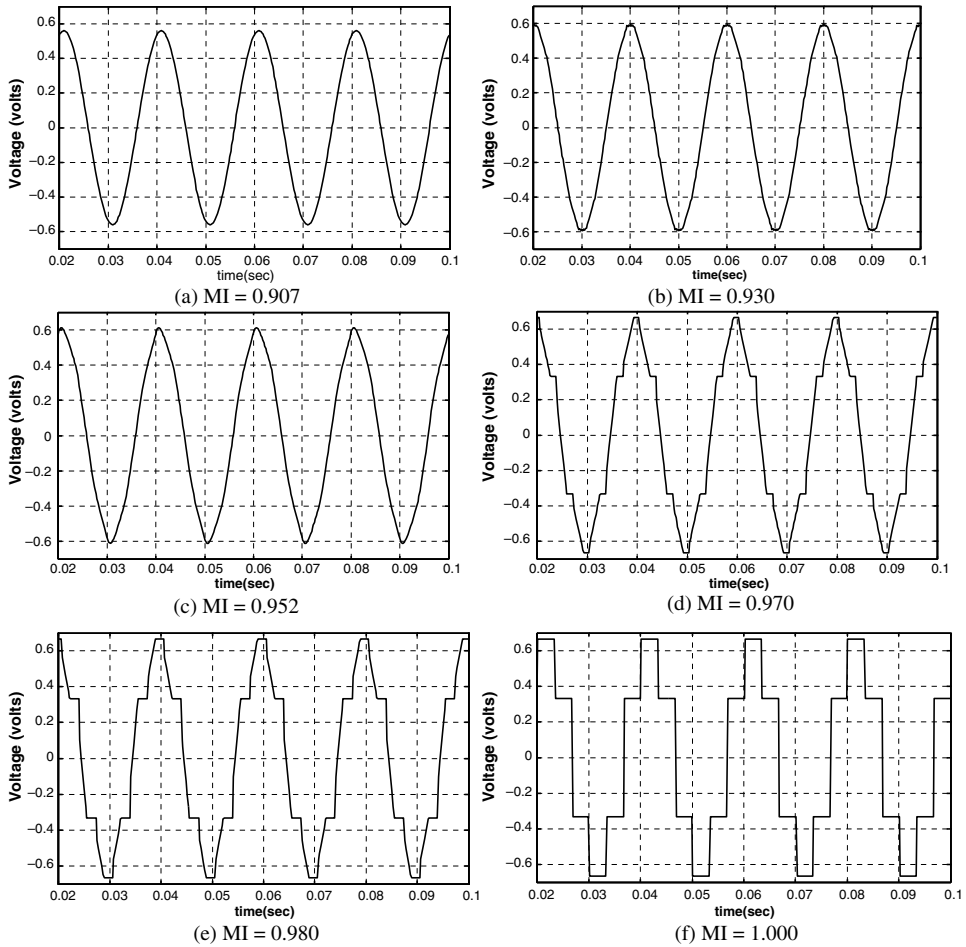


**Figure 3.43** Inverter Phase ‘a’ voltage waveform at different modulation indices

powerful non-linear mapping technique. This means that the reference voltage vector  $V^*$  magnitude, and the angle,  $\alpha^*$ , can be impressed at the input of the network and the corresponding pulse width pattern of the three phases can be generated at the output. There are two approaches in implementing the SVPWM; using the ANN called ‘Direct method’ and the second is the ‘Indirect method’ [1]. In the so-called ‘Direct method,’ the feed-forward back-propagation ANN directly replaces the conventional SVPWM algorithm. Since the feed-forward ANN network can map only one input pattern onto only one output pattern, the switching period  $T_s$  is divided into  $n$  subintervals. Thus each sub-interval includes only one output switching pattern for every input pattern, so requires a huge data set for proper training of the network. Therefore this approach is limited in use [17–21]. The ‘indirect method’ uses two separate feed-forward back-propagation ANN; one for the magnitude of the reference voltage and other for the reference voltage position. The magnitude network yields a voltage magnitude scaling function, which is linear in the linear modulation region and is a non-linear

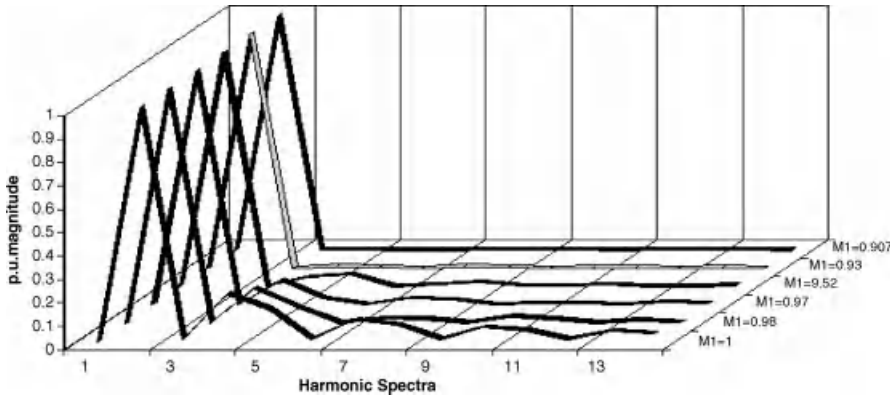


**Figure 3.44** Harmonic spectra by FFT, normalized to fundamental component

function of  $V_{DC}$  in the over-modulation region. The reference position network yield turn on pulse width function at unit voltage magnitude. This pulse-width functions are then multiplied by a suitable bias signal and the product is compared with the up/down counter to generate the appropriate switching signals for the inverter. The complete implementation block is shown in Figure 3.46.

The phase ‘A’ turn on time can be given as

$$T_{A=ON} = \begin{cases} \left( \frac{t_0}{4} = \frac{T_s}{4} + K.V^* \left[ -\sin \left( \frac{\pi}{3} - \alpha^* \right) - \sin (\alpha^*) \right], S = 1, 6 \right. \\ \left. \frac{t_0}{2} + t_b = \frac{T_s}{4} + K.V^* \left[ -\sin \left( \frac{\pi}{3} - \alpha^* \right) + \sin (\alpha^*) \right], S = 2 \right. \\ \left. \frac{t_0}{2} + t_0 + t_b = \frac{T_s}{4} + K.V^* \left[ \sin \left( \frac{\pi}{3} - \alpha^* \right) + \sin (\alpha^*) \right], S = 3, 4 \right. \\ \left. \frac{t_0}{2} + t_a = \frac{T_s}{4} + K.V^* \left[ \sin \left( \frac{\pi}{3} - \alpha^* \right) - \sin (\alpha^*) \right], S = 5 \right. \end{cases} \quad (3.50)$$

where S is the sector number and  $K = \sqrt{3}T_s/4V_{dc}$ . Equation (3.50) can be written in the general form:

$$T_{A=ON} = T_s/4 + f(V^*)g_A(\alpha^*) \quad (3.51)$$

where  $f(V^*)$  is the voltage amplitude scale factor;  $T_s/4$  is the bias time; and  $g(\alpha^*)$  is called the turn-on signal at unit voltage and is given as (Figure 3.47).

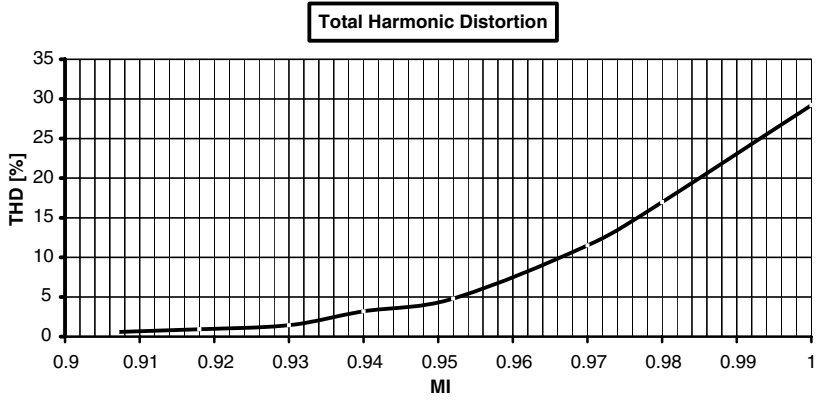


Figure 3.45 THD in over-modulation region

$$g_A(\alpha^*) = \begin{pmatrix} K \left[ -\sin\left(\frac{\pi}{3} - \alpha^*\right) - \sin(\alpha^*) \right], S = 1, 6 \\ K \left[ -\sin\left(\frac{\pi}{3} - \alpha^*\right) + \sin(\alpha^*) \right], S = 2 \\ K \left[ \sin\left(\frac{\pi}{3} - \alpha^*\right) + \sin(\alpha^*) \right], S = 3, 4 \\ K \left[ \sin\left(\frac{\pi}{3} - \alpha^*\right) - \sin(\alpha^*) \right], S = 5 \end{pmatrix} \quad (3.52)$$

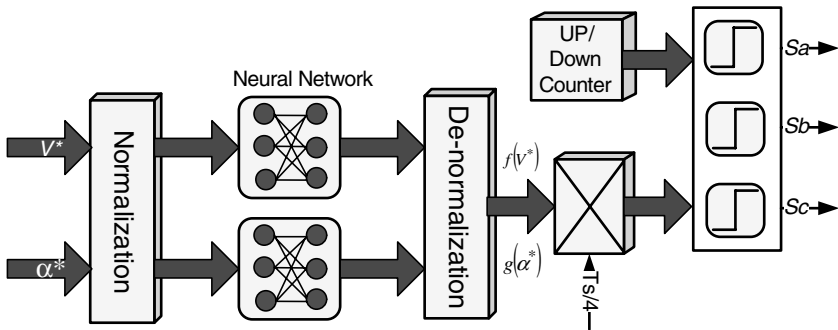
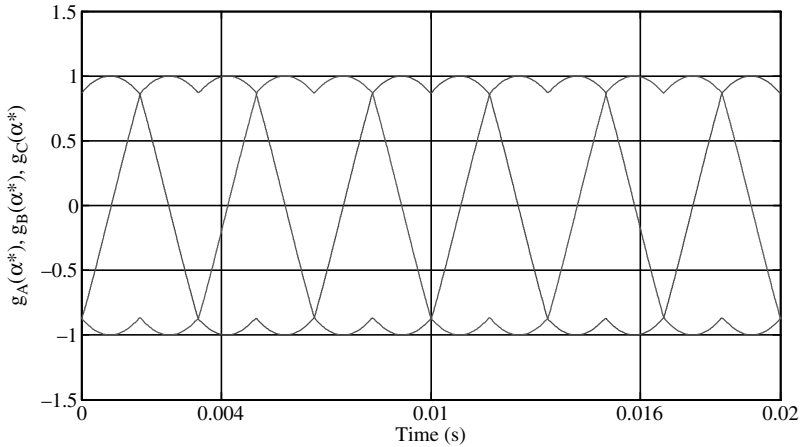


Figure 3.46 Functional block diagram of ANN based SVPWM for a three-phase VSI





**Figure 3.47** Turn-on pulse width function of phase A, B, C as a function of angle  $\alpha$  in different sectors

### 3.4.12 MATLAB/Simulink Model of Implementing ANN-based SVPWM

The MATLAB/Simulink model for implementing the ANN-based SVPWM is shown in Figure 3.48. Initially a neural network is trained with the reference voltage input and the turn-on time as output using equations (3.50–3.52). The ANN model is then generated using the neural network toolbox and the generated model is placed in the Simulink, as shown in Figure 3.48. The input signal to the neural network is the reference voltage position  $\alpha^*$ . The model uses a multilayer function in the first and second layers. The number of nodes can be set at the training stage. The number of hidden nodes can be chosen between 10 and 20. The weights are generated during the training mode. The digital words corresponding to turn-on time are generated by multiplying the output of the neural network with  $V^* T_s$  and then adding  $T_s/4$ , as shown in the figure. The PWM signals are then generated by comparing the turn-on time with a triangular reference having a time period of  $T_s$  and amplitude  $T_s/2$ , and the PWM signals thus obtained are then applied to the inverter.

The resulting simulation waveform is presented in Figure 3.49.

## 3.5 Relationship between Carrier-based PWM and SVPWM [22]

Although the two PWM schemes, carrier-based and SVPWM, appear different, there exists a similarity between the two approaches. In the SPWM approach, the three-phase modulating waves are compared with a triangular high frequency carrier to determine the switching instants of the three phases. The modulating wave of a given phase is the average leg voltage corresponding to that phase. The most commonly used modulating signals are sinusoidal waves. The triplen (multiple of three) frequency component can be added as a zero sequence component to the three-phase sinusoidal waves or modulating signals. Hence, the choice of the triplen frequency components to be added to the fundamental signals lead to different modulating waveforms with different harmonic spectrum. The choice of these triplen frequency components is thus a degree of freedom in the SPWM technique.

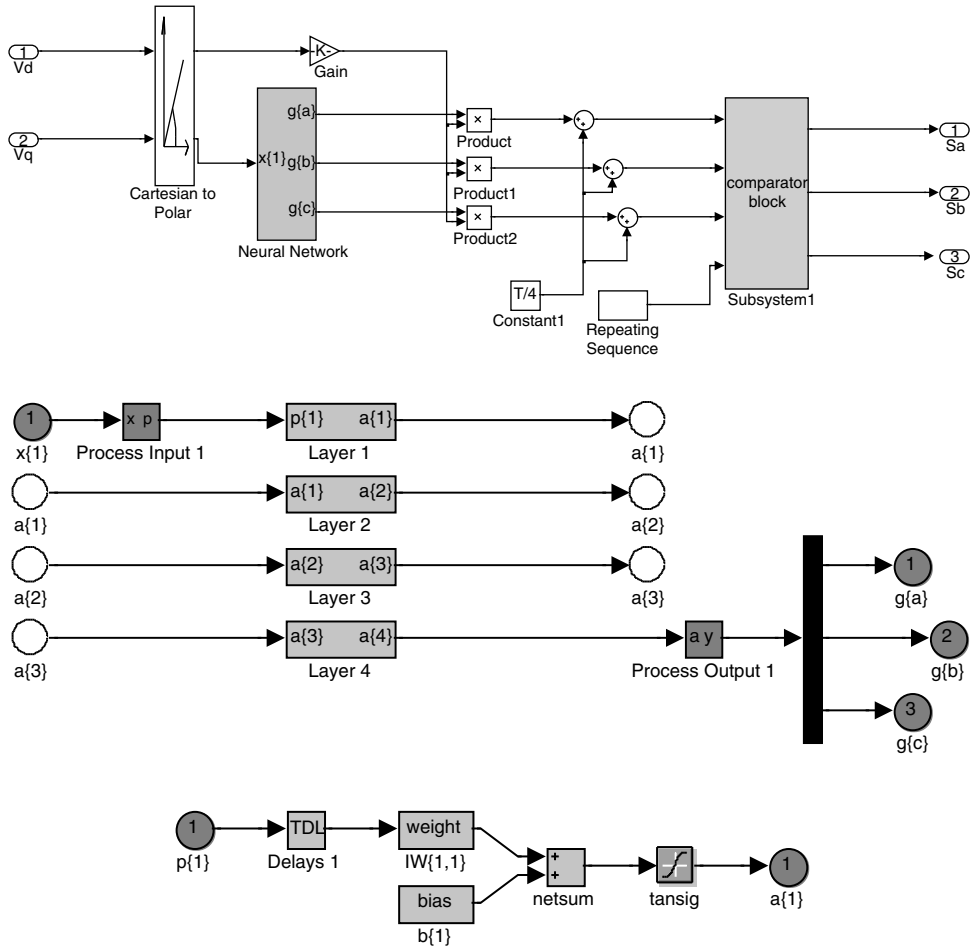


**Figure 3.48** MATLAB/Simulink model of ANN-based SVPWM (File name: *ANN\_SVPWM\_3\_phase.mdl*)

In the SVPWM technique, the voltage reference is provided in terms of a rotating space vector. The magnitude and the frequency of the fundamental component of the output are specified by the magnitude and frequency of the reference vector. The reference vector is sampled once in every switching period. The inverter is switched such that the average voltage vector is equal to the sampled reference vector in every switching period. The inverter switching is done according to the reference voltage vector location. Two active and two zero vectors are used in every switching period. The time of application of each vector is obtained from the relationship obtained on the basis of the ‘equal volt-second’ principle. The degree of freedom used in the SVPWM is the division of the time between the two zero states (000 and 111). The distribution of the time duration between the two zero states 7(000) and 8(111) is equivalent to adding the zero sequence component to the three-phase average leg voltages. Hence, the two PWM approaches are equivalent in this sense.

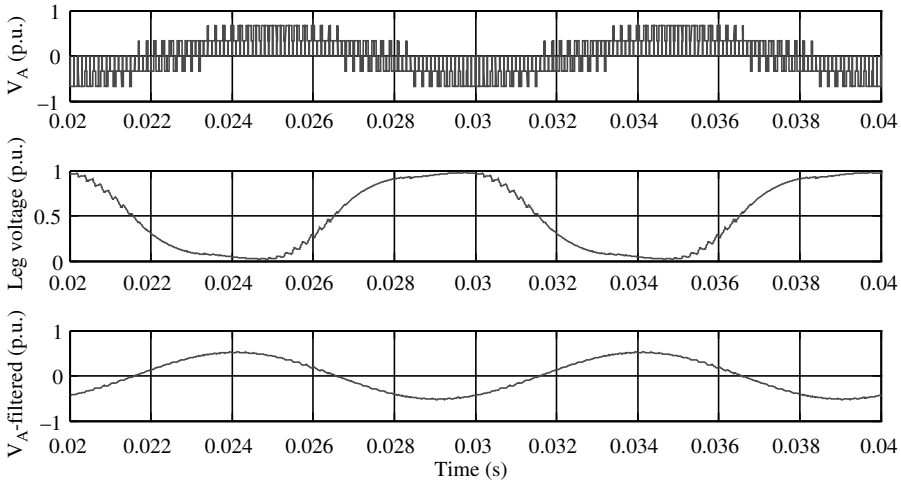


**Figure 3.49** ANN-based SVPWM waveforms

### 3.5.1 Modulating Signals and Space Vectors

The switching pattern generated due to the interaction between a triangular carrier signal and the modulating signal is shown in Figure 3.50; the magnitude of the modulating signal is assumed constant during the sampling period. The switching pattern shown is the leg voltage with magnitude  $\pm 0.5V_{dc}$ . By comparing Figures 3.50 and 3.31, it is seen that the same switching pattern and space vector disposition is available in the SVPWM in sector I.

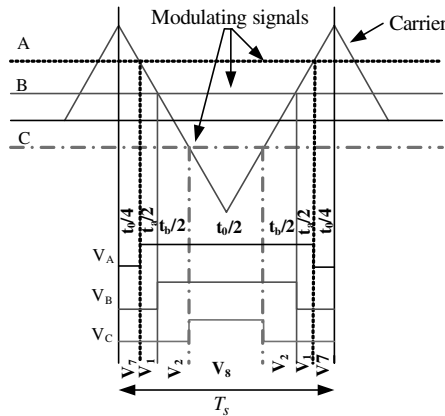


**Figure 3.50** Relationship between carrier-based and SVPWM in sector I

The same similarity also exists in other sectors. The relationship between the modulating signals and space vector in different sectors can be found from Figure 3.31 as

$$\begin{aligned} V_A T_s &= 0.5V_{dc}(V_A^* + v_{nN})T_s = 0.5V_{dc}(t_a + t_b + t_8 - t_7) \\ V_B T_s &= 0.5V_{dc}(V_B^* + v_{nN})T_s = 0.5V_{dc}(-t_a + t_b + t_8 - t_7) \\ V_C T_s &= 0.5V_{dc}(V_C^* + v_{nN})T_s = 0.5V_{dc}(t_a + t_b + t_8 - t_7) \end{aligned} \quad (3.53)$$

The relationship between the modulating signal and the space vector in sector I is

$$\begin{aligned} U_A &= (t_a + t_b + t_8 - t_7)/T_s \\ U_B &= (-t_a + t_b + t_8 - t_7)/T_s \\ U_C &= (-t_a - t_b + t_8 - t_7)/T_s \end{aligned} \quad (3.54)$$

where  $t_8$  is the time of application of the zero vector 111;  $t_7$  is the time of application of the zero vector 000; and  $U_A$ ,  $U_B$ ,  $U_C$  represents the three-phase modulating signals for the SPWM. The modulating signals for SPWM are

$$\begin{aligned} U_A &= V_A^* + v_{nN} \\ U_B &= V_B^* + v_{nN} \\ U_C &= V_C^* + v_{nN} \end{aligned} \quad (3.55)$$

$$\text{where } v_{nN} = \frac{1}{3}(U_A + U_B + U_C) \quad (3.56)$$

is the zero sequence signal.

The relationship between the modulating signals and the space vectors in the other five sectors can be obtained in a similar fashion by using Figure 3.31, and are listed in Table 3.5.

The relation between the zero sequence signal and the space vector time of applications can be determined by substituting equation (3.54) into equation (3.56). The resulting relationships

**Table 3.5** Relationship between the space vector and modulating signal

Sector No.	$U_A$	$U_B$	$U_C$
I	$(t_a + t_b + t_8 - t_7)/T_s$	$(-t_a + t_b + t_8 - t_7)/T_s$	$(-t_a - t_b + t_8 - t_7)/T_s$
II	$(t_a - t_b + t_8 - t_7)/T_s$	$(t_a + t_b + t_8 - t_7)/T_s$	$(-t_a - t_b + t_8 - t_7)/T_s$
III	$(-t_a - t_b + t_8 - t_7)/T_s$	$(t_a + t_b + t_8 - t_7)/T_s$	$(-t_a + t_b + t_8 - t_7)/T_s$
IV	$(-t_a - t_b + t_8 - t_7)/T_s$	$(t_a - t_b + t_8 - t_7)/T_s$	$(t_a + t_b + t_8 - t_7)/T_s$
V	$(-t_a + t_b + t_8 - t_7)/T_s$	$(-t_a - t_b + t_8 - t_7)/T_s$	$(t_a + t_b + t_8 - t_7)/T_s$
VI	$(t_a + t_b + t_8 - t_7)/T_s$	$(-t_a - t_b + t_8 - t_7)/T_s$	$(t_a - t_b + t_8 - t_7)/T_s$

**Table 3.6** Line-to-line voltages and space vectors

Sector No.	$U_{AB}$	$U_{BC}$	$U_{CA}$
I	$2t_a/T_s$	$2t_b/T_s$	$-2(t_a + t_b)/T_s$
II	$-2t_b/T_s$	$2(t_a + t_b)/T_s$	$-2t_a/T_s$
III	$-2(t_a + t_b)/T_s$	$2t_a/T_s$	$2t_b/T_s$
IV	$-2t_a/T_s$	$-2t_b/T_s$	$2(t_a + t_b)/T_s$
V	$2t_b/T_s$	$-2(t_a + t_b)/T_s$	$2t_a/T_s$
VI	$2(t_a + t_b)/T_s$	$-2t_a/T_s$	$-2t_b/T_s$

are given for odd sectors (sectors I, III, and V) and for even sectors (sectors II, IV, and VI) in equations (3.57) and (3.58), respectively:

$$v_{nN} = \frac{1}{3T_s} [-t_a + t_b - 3t_7 + 3t_8] \quad (3.57)$$

$$v_{nN} = \frac{1}{3T_s} [t_a - t_b - 3t_7 + 3t_8] \quad (3.58)$$

### 3.5.2 Relationship between Line-to-line Voltages and Space Vectors

A relationship between the line-to-line voltage and space vectors can be obtained using the equations of Table 3.5 and equation (3.54), now listed in Table 3.6:

$$U_{ij}T_s = (U_i - U_j)T_s = \frac{V_{dc}}{2} (U_i^* - U_j^*)T_s, \text{ Where } i, j = a, b, c \text{ and } i \neq j \quad (3.59)$$

A direct relationship between the line-to-line voltages and space vectors exist. It can be noted that the line-to-line voltages are determined by only active vectors, there being no role of zero vectors.

### 3.5.3 Modulating Signals and Space Vector Sectors

The relationship between the modulating signals and the sectors of the space vector can be obtained by plotting the three-phase sinusoidal waveform and identifying the region of 0 to 60 degrees (sector I), 60 to 120 degrees (sector II), 120 to 180 degrees (sector III), 180 to 240 degrees (sector IV), 240 to 300 degrees (sector V), and 300 to 360 degrees (sector VI). The relationship is shown in Figure 3.51.

## 3.6 Multi-level Inverters

The voltage source inverters discussed so far produces only two levels of output, either  $\pm 0.5V_{dc}$  or 0 and  $V_{dc}$ , hence called the two-level inverter. Two-level inverters pose several problems in high power medium voltage applications, due to limited voltage blocking capability of the

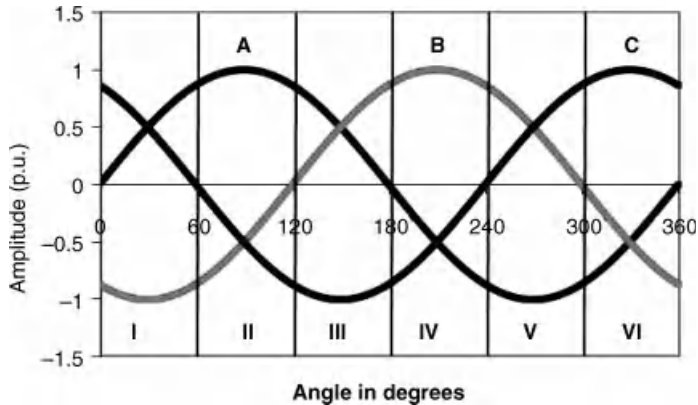


**Figure 3.51** Relationship between modulating signal and space vector sectors

power semiconductor switches. Moreover,  $dv/dt$  is considerably higher, causing high stress on the switching devices. The solution to this problem lies in using a series connection of several power switching devices or alternatively using multi-level inverters [23–30]. The former solution may lead to unequal voltage sharing among the devices. Hence, the later solution is preferred. The output voltage waveform of the multi-level inverter is significantly improved when compared to a two-level output. The THD is low and the output quality is acceptable, even at low switching frequency. In high power drives, switching losses constitute a considerable portion of the total losses and hence the reduction of this is a major goal. Nevertheless, the number of power switching devices used in a multi-level inverter is high and additional diodes and capacitors are needed. Another important shortcoming of the multi-level inverter is imbalance in the capacitor voltages at the DC link. This issue is addressed in [31–34].

Multi-level inverters have many attractive features, such as high voltage capability, reduced common mode voltages near sinusoidal outputs, low  $dv/dt$ , and smaller or even no output filter; sometimes no transformer is required at the input side, called the transformer-less solution, making them suitable for high power applications [35–38].

There are several topologies of multi-level inverters proposed in the literature. However, the most popular configurations are:

- Diode Clamped or Neutral point clamped multi-level inverters;
- Capacitor clamped or flying capacitor multi-level inverters;
- Cascaded H-bridge multi-level inverters.

The neutral point topology uses diodes to clamp the voltage levels, while the flying-capacitor topology uses floating capacitors to clamp the voltage levels. The major problems associated with these two topologies are the balancing of capacitors voltages. Additional problems associated with the flying capacitor type is the starting procedure, as the clamping capacitors are required to be charged to the appropriate voltage level. The balancing problem becomes more pronounced with increasing number of levels. However, the cascaded H-bridge inverter is modular in nature, with each unit connected in series and there is no problem of balancing. The major problem with this type of topology is the requirement of complex transformers [5].

### 3.6.1 Diode Clamped Multi-level Inverters

The three-level neutral point/diode clamped inverter was first proposed by [39]. The power circuit topology of a three-level neutral point clamped or diode clamped inverter is shown in Figure 3.52. One leg consists of four power semiconductor switches (IGBTs) and two power diodes for clamping. At the DC link side, one capacitor is needed at the source end and two capacitors are halved and connected in series to form a neutral point N. In this configuration, two power switches conduct simultaneously. When the upper two switches, middle two switches, and lower two switches are on the inverter leg, voltage attains  $0.5 V_{dc}$ , 0, and  $-0.5 V_{dc}$  voltages, respectively. The switches  $S_a$  and  $S'_a$ ,  $S_b$  and  $S'_b$ , and  $S_c$  and  $S'_c$  are complimentary in operation. Defining the switching function  $S_{k1}$ ,  $S_{k0}$ , and  $S_{k2}$  ( $k=A, B, C$ ) (zero when switch is off and one when switch is 1, with the constraint:  $S_{k1} + S_{k0} + S_{k2} = 0$ ) when the upper two switches are on, the middle two switches are on, and the lower two switches are on, respectively. The leg voltages can then be written as

$$\begin{aligned} V_{AN} &= (S_{A1} - S_{A2})V_{dc} \\ V_{BN} &= (S_{B1} - S_{B2})V_{dc} \\ V_{CN} &= (S_{C1} - S_{C2})V_{dc} \end{aligned} \tag{3.60}$$

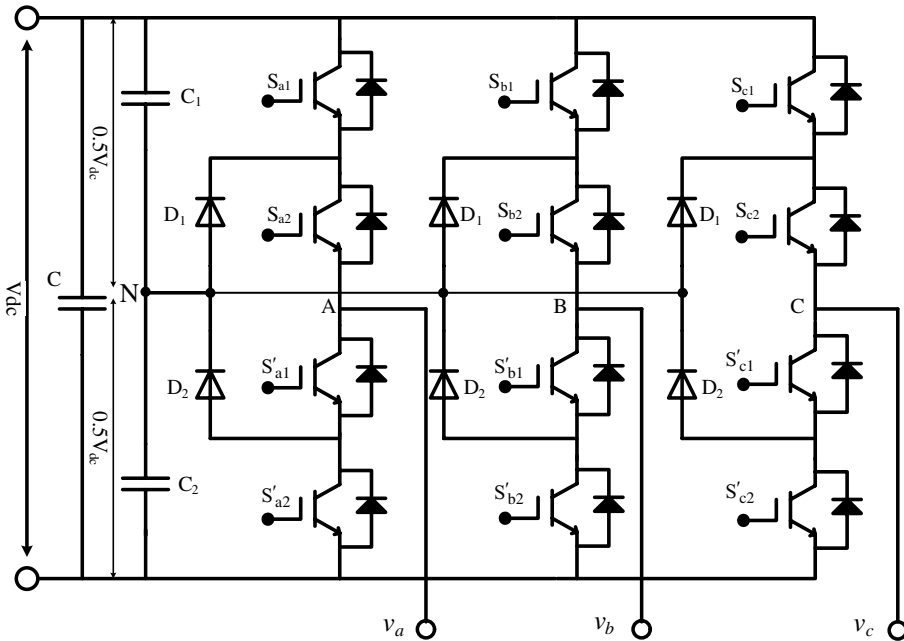


Figure 3.52 Neutral Point Clamped three-level inverter topology

The line voltage relation can be obtained as

$$\begin{aligned} v_{ab} &= V_{AN} - V_{BN} = (S_{A1} - S_{A2} - S_{B1} + S_{B3})V_{dc} \\ v_{bc} &= V_{BN} - V_{CN} = (S_{B1} - S_{B2} - S_{C1} + S_{C3})V_{dc} \\ v_{ca} &= V_{CN} - V_{AN} = (S_{C1} - S_{C2} - S_{A1} + S_{A3})V_{dc} \end{aligned} \quad (3.61)$$

The phase to load neutral voltage can be obtained as

$$\begin{aligned} v_{an} &= \frac{2}{3}V_{dc}(S_{A1} - S_{A3} - 0.5(S_{B1} - S_{B3} + S_{C1} - S_{C3})) \\ v_{bn} &= \frac{2}{3}V_{dc}(S_{B1} - S_{B3} - 0.5(S_{A1} - S_{A3} + S_{C1} - S_{C3})) \\ v_{cn} &= \frac{2}{3}V_{dc}(S_{C1} - S_{C3} - 0.5(S_{A1} - S_{A3} + S_{B1} - S_{B3})) \end{aligned} \quad (3.62)$$

The common mode voltage (voltage between the load neutral and inverter neutral) is

$$v_{nN} = \frac{1}{3}V_{dc}(S_{A1} + S_{B1} + S_{C1} - S_{A3} - S_{B3} - S_{C3}) \quad (3.63)$$

### 3.6.1.1 Carrier-based PWM Technique for NPC Three-level Inverter

A SPWM scheme of a two-level inverter can be readily extended to a multi-level inverter. However, the number of triangular carrier waves is equal to  $L - 1$ , where  $L$  is the level number. Multi-carrier signals are generated and compared with the sinusoidal modulating signal of SPWM fundamental frequency. The switching/gating signals are thus generated. Broadly classified, a SPWM scheme is of two types, phase shifted and level shifted. In phase shifted SPWM schemes, the required phase shifts among different carriers and is given as

$$\phi = \frac{2\pi}{(L - 1)} \quad (3.64)$$

Thus, in a three-level phase shifted SPWM, two carrier waves are needed, with a 180-degree phase shift. In a five-level inverter, four carrier waves are required, with a 90-degree phase shift. As the number of level increases, the number of carrier waves increases and the phase shift angle decreases.

Level shifted SPWM schemes are further classified as:

- in-phase disposition (IPD), in which all triangular signals are in phase;
- phase opposition disposition (POD), in which all the carrier above reference zero are in opposite phase to those below zero reference;
- alternate phase opposition disposition (APOD), in which in each carrier pair is in opposite phase.



The principle of different types of SPWM schemes, as applied to a five-level diode clamped inverter, is shown in Figure 3.53. In a five-level inverter, four carrier signals are required, as shown in Figure 3.53 and are compared with the three-phase sinusoidal modulating wave (in the figure, only the phase ‘a’ modulating signal is shown). The gating signals are generated at the point of intersection of the modulating wave and the carrier wave. The operation of the

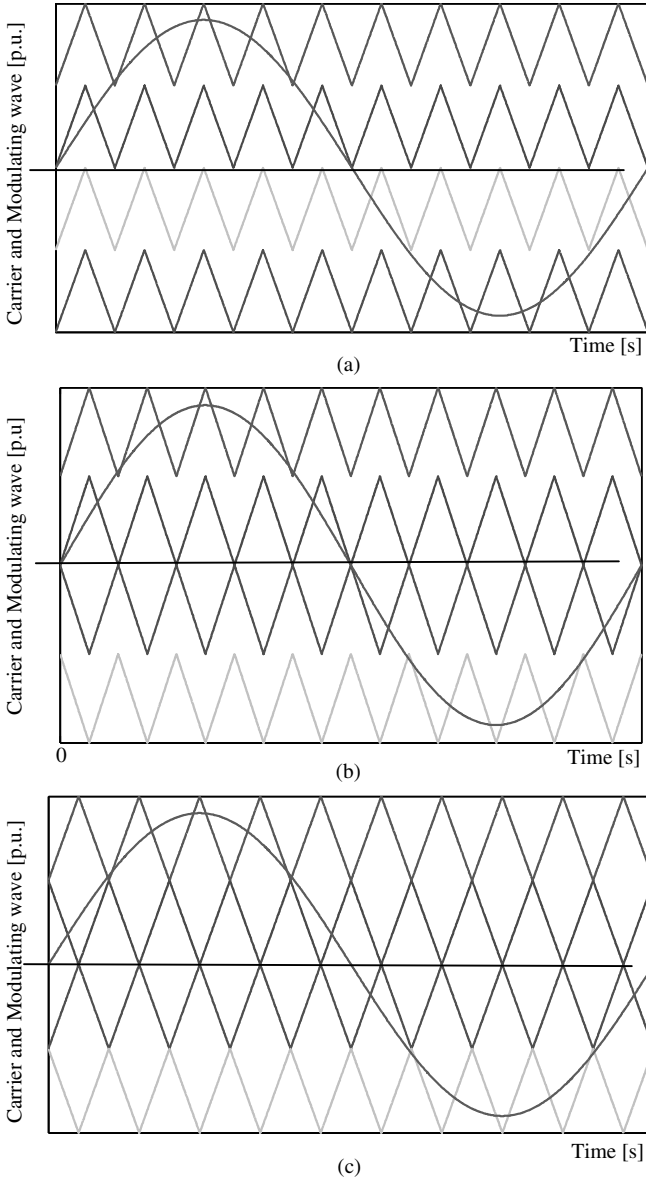


**Figure 3.53** Principle of SPWM for a five-level diode clamped inverter: (a) IPD; (b) POD; and (c) APOD

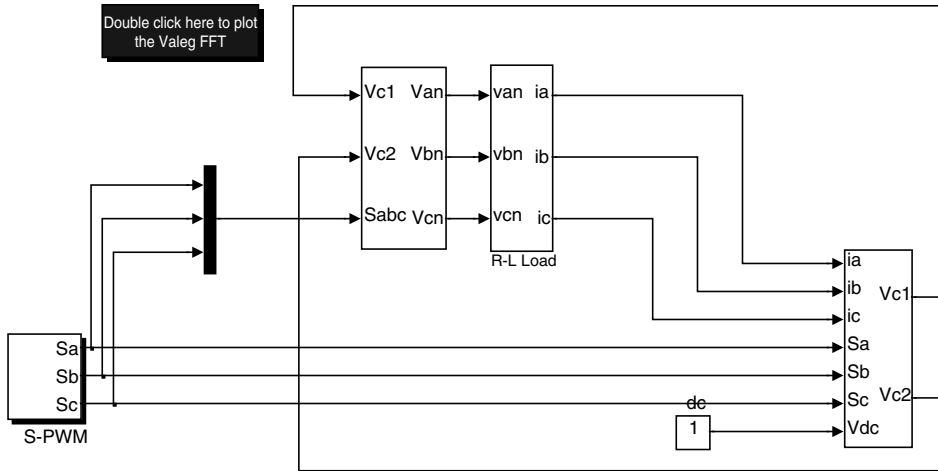


**Figure 3.54** MATLAB/Simulink model of SPWM for a three-level NPC (*File name: NPC\_3\_phase\_3\_level.mdl*)

upper and third from the top power switches are complimentary. Similarly, the second from the top and the bottom-most switches are complimentary in operation.

### 3.6.1.2 MATLAB/Simulink Model of Carrier-based PWM Scheme for Three-level NPC

MATLAB/Simulink model of a three-level NPC inverter is shown in Figure 3.54. The simulation model is developed using the mathematical model of the inverter. The DC link voltage is assumed as unity, the fundamental output frequency is chosen as 50 Hz, and the switching frequency is kept at 2 kHz. The carrier signals are chosen such that they are in phase disposition (IPD).

The resulting waveforms obtained from the simulation are shown in Figure 3.55. Seven-level phase voltages are obtained, while three-level line voltages are generated. More number of step leads to lower THD. Spectrum of phase voltage is also shown in the figure.

### 3.6.2 Flying Capacitor Type Multi-level Inverter

The flying capacitor or capacitor clamped topology has some distinct advantages over other topologies of multi-level inverters, for example, the redundancies of the voltage levels, which means that more than one switch combination can create same output voltage and hence freedom exists in the choice of the appropriate switching combination. The flying level capacitor inverter has phase redundancies, unlike the NPC that has only line-to-line redundancies [40–48]. This feature allows charging and discharging of particular capacitors in a way that may be integrated within the control algorithm for balancing the voltages. Other advantage of this inverter is that the active and reactive power flow can be controlled. Also, the large number of capacitors enables an operation through short duration outages and significant voltage sags.

Flying capacitor multilevel topology is a good approach, particularly for more than three voltage levels. A negative aspect of using a Flying Capacitor is that the output current changes

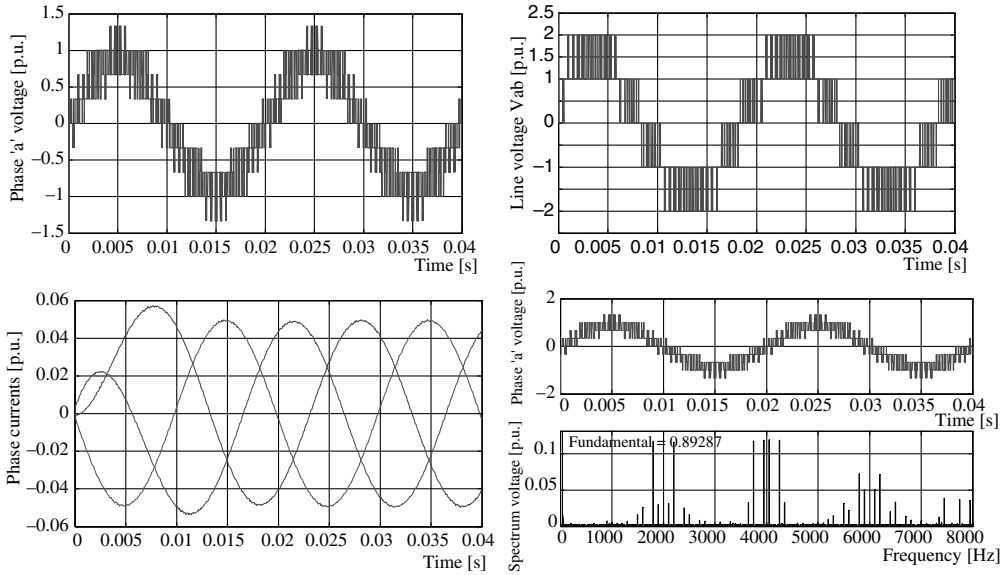


**Figure 3.55** Response of a three-level NPC

the voltage of the capacitors. In general, the capacitance must be selected as high to make the changes as low as possible. Therefore, the size of the capacitors increases as an inverse of the switching frequency. This topology is therefore not practical for low switching frequency applications [40]. Another important shortcoming of this topology is the starting/excitation of the inverter. The capacitor must be charged to the appropriate voltage level before operating of the inverter. Hence, a special starting procedure is required for this type of multi-level inverter.

The flying capacitor voltage balancing is a tedious task in the flying capacitor topology [40–42]. Numerous techniques have been presented in the literature to balance the voltage across the clamping capacitors [41–48]. These include the SPWM, as well as the SVPWM, using switching vector redundancies. Among the carrier-based techniques, three methods are most popular, namely phase shifted PWM, modified carrier redistribution PWM, and sawtooth rotation PWM. A comprehensive comparison of these methods are presented in [46] for a three-phase system. It is concluded that the modified carrier redistribution PWM offers the optimum performance. This technique is further used in [14,17]. Hence, the same technique is elaborated on in this chapter.

### 3.6.2.1 Operation of Three-level Flying Capacitor Inverter

The power circuit topology of a five-phase three-level flying capacitor type voltage source inverter is shown in Figure 3.56. In this topology of a multi-level inverter, the floating capacitors are employed to clamp the node voltages of the series connected power switching devices. Four power switching devices are connected in series to form one leg of the inverter. The complimentary switches are indicated in the Figure 3.56  $((s_{n1}, s'_{n1}), (s_{n2}, s'_{n2}); n \in a, b, c)$ ; the top and the bottom switches and the two middle switches are

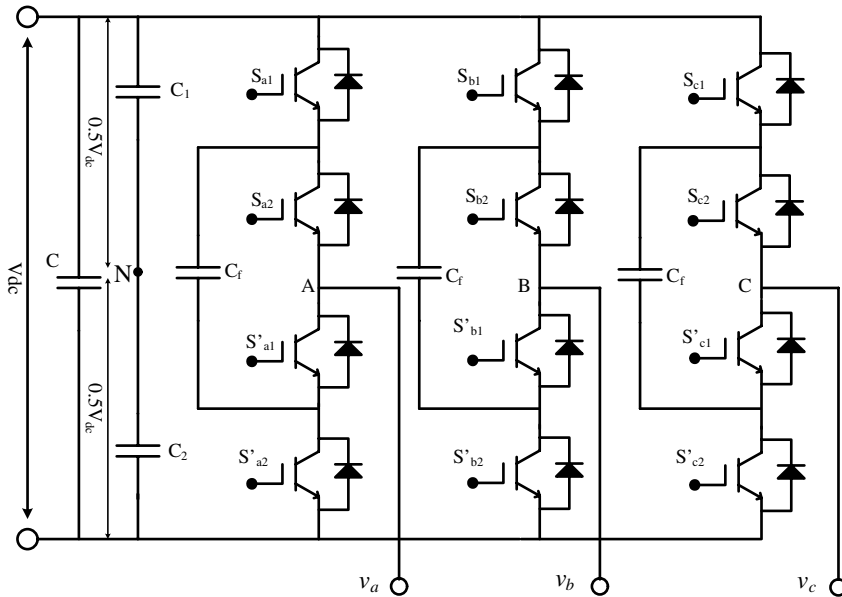


**Figure 3.56** Power circuit of a three-level three-phase flying capacitor type inverter

complimentary. Two power switching devices are turned on simultaneously to provide three different voltage levels at the output phase,  $0.5V_{dc}$ ,  $-0.5V_{dc}$ , and 0. Since the voltage across the flying capacitors is limited to  $0.5V_{dc}$ , the same voltage stress will be borne by each switch. As the number of levels increases the required voltage, the blocking value reduces, thus lower rating switches can be used or alternatively higher voltage can be achieved. The relationship between the pole voltage and the output phase voltage remains the same as that of an NPC three-level inverter.

One cycle of the operation of one leg of the flying capacitor inverter is depicted in Figures 3.57 a–h. The path of the current is shown as a dotted line. The pole voltage is  $0.5V_{dc}$  and the current either flows to or from the load in Figures 3.57a and b. The capacitor state remains unchanged.

The flying capacitor charges during the switching state of Figures 3.57c and f. The charging current is equal to the load current. Hence the design of flying capacitor should take into account the maximum load current. The pole voltage is zero during this operation. The flying capacitor discharges during the switching state of Figures 3.57d and e. Once again the current flow through the capacitor is equal to the load current. The pole voltage remains zero during this switching state. Figures 3.57g and h show the switching state when the pole voltage attains the value of  $-0.5V_{dc}$  and the flying capacitor conditions remains unchanged.

It is evident from the above discussion that the capacitor charging state changes throughout Figures 3.57c–f. Thus, to balance the flying capacitor voltage, these switching states need special attention. Thus the PWM technique described in the next section optimally exploits these redundant switching states.

### 3.6.2.2 PWM Technique to Balance Flying Capacitor Voltage [44,46]

The major goal of the PWM scheme is to balance the flying capacitor voltage and keep it constant at half of the DC link voltage, irrespective of the load condition. The basic idea behind voltage balancing is equal charging and discharging time of the flying capacitor. From the switching diagram (Figure 3.57) it is clear that for switch states of Figures 3.57c and f, the output pole voltage remains the same (zero), thus these states are redundant states. However, the flying capacitor charges in the state of Figures 3.57c and f and discharges to the load in state of Figures 3.57d and e. Therefore, states (Figures 3.57c and f) and (Figures 3.57d and e) should persist for the same time for equal charging and discharging of the flying capacitor. To accomplish this, the carrier signal should be formulated, as shown in Figures 3.58 and 3.59, for switch  $S_{n1}$  and  $S_{n2}$ , respectively. The upper carrier is used when the reference voltage lies between  $0.5V_{dc}$  and  $V_{dc}$ , while the lower carrier is used when reference voltage lies between 0 and  $0.5V_{dc}$ . The gate signals are shown in Figures 3.60 and 3.61 for the two different values of the reference voltages. The carrier signal for four sampling periods are shown. It is evident that the redundant switching state is active in the first sample and then in the third sample in Figure 3.60. Hence, the flying capacitor charges in the first sampling time and discharges in the third sampling time, keeping the same charging and discharging time in four sample periods. The switching time of each power switch will be equal to  $2T_s$  as evident from Figures 3.60 and 3.61. The similar observation can be made from Figure 3.61. Thus it is seen that for all the values of the reference voltages, the charge and discharge time of the flying capacitors remains the same. Thus the voltage is balanced at the flying capacitor terminals as an average in four sample time. This average balancing time will be higher for higher level numbers.

### 3.6.2.3 Start-up/Excitation Procedure of FLC

One of the important requirements of a flying capacitor inverter is its start-up procedure. This problem still persists in a five-phase inverter as in a three-phase inverter. At the start, the flying capacitor needs to be charged equal to  $0.5 V_{dc}$ . Thus the gating signal is provided in such a way that the switch  $S_{n1}$  and  $S_{n1}'$  remains 'ON' to charge the capacitor and the switches  $S_{n2}$  and  $S_{n2}'$  remain 'OFF'. Once the voltage of the flying capacitor builds up to the required voltage level (i.e.  $0.5 V_{dc}$ ), all the switches are kept off so that the flying capacitor voltage floats at  $0.5 V_{dc}$ . Then the normal PWM inverter operation is implemented.

### 3.6.2.4 MATLAB/Simulink Model of Three-level Capacitor Clamped or FLC Inverter

The MATLAB/Simulink model for implementing the three-level FLC inverter is shown in Figure 3.62. The model is shown using the simpower system block-sets. SPWM is further illustrated in Figures 3.60 and 3.61, which are used in this model.

DC link voltage of 100 V is retained and the switching frequency remains at 2.5 kHz, the flying capacitor is chosen as  $100 \mu\text{F}$ , and the load parameters are  $R = 5 \Omega$  and  $L = 0.5 \text{ mH}$ . The resulting output line and phase voltages are shown in Figure 3.63. The output line voltage assumes three levels and the phase voltage has seven levels.

### 3.6.3 Cascaded H-Bridge Multi-level Inverter

Several units of the H-bridge inverters are connected in series to form a cascaded H-bridge topology that outputs multi-level voltages. This is a highly modular configuration, where by

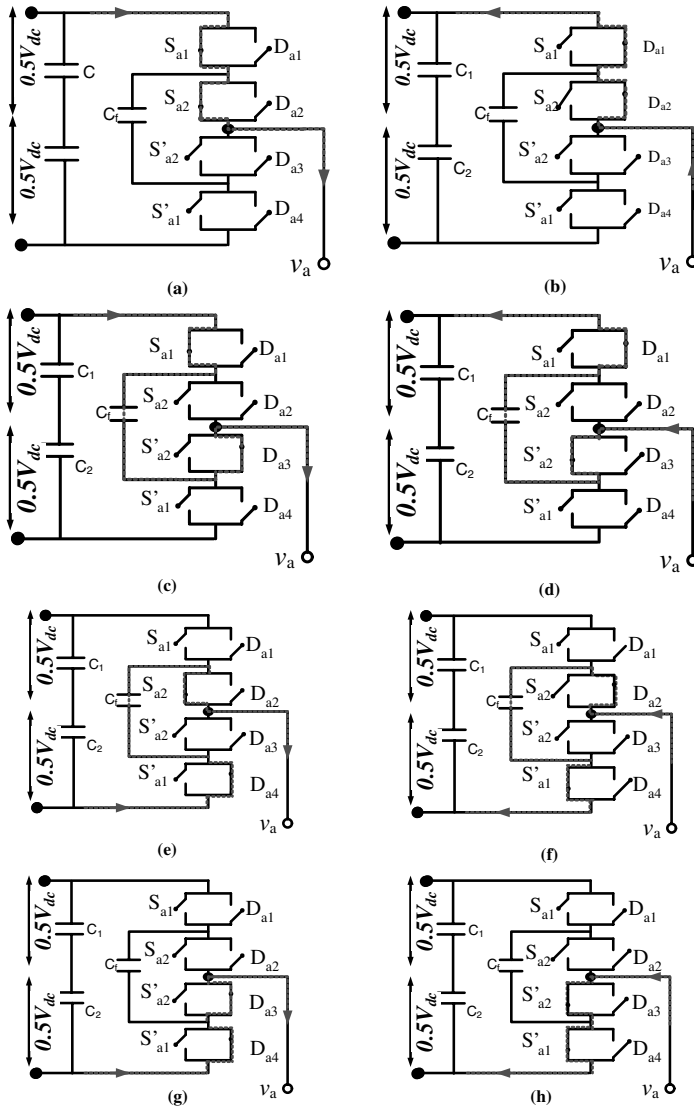


**Figure 3.57** (a) Switch State 1100 with positive current flow; (b) Switch state 1100 with negative current flow; (c) Switch state 1010 with positive current flow (Flying capacitor charges); (d) Switch state 1010 with negative current flow (Flying capacitor discharges); (e) Switch state 0101 with positive current flow (Flying capacitor discharges); (f) Switch state 0101 with negative current flow (Flying capacitor charges); (g) Switch state 0011 with positive current flow; (h) Switch state 0011 with negative current flow

adding each H-bridge cell increases the level of the output voltages. Each H-bridge unit requires isolated DC supplies. The number of units to be connected in series to obtain an L level (odd) of the output voltages is given as

$$N = \frac{L - 1}{2} \tag{3.65}$$

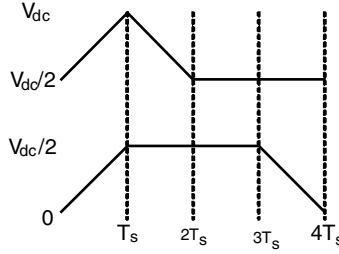


**Figure 3.58** Carrier wave for  $S_{n1}$  and  $S_{n1}'$  in FLC inverter

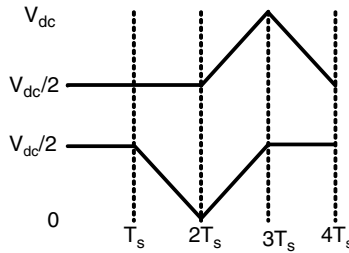


**Figure 3.59** Carrier wave for  $S_{n2}$  and  $S_{n2}'$  in FLC inverter

where  $L$  is the number of output levels and  $N$  is the number of H-bridge unit. The number of output voltage levels can only be odd. Hence, to obtain a five-level output, two H-bridge units are connected in series.

If two units are connected in series, they form a five-level output, as shown in Figure 3.64. The switching states and the possible output voltages for this configuration are given in Table 3.7. The output phase voltages can acquire four different voltage levels,  $-2V_{dc}$ ,  $-V_{dc}$ ,  $0$ ,  $V_{dc}$ ,  $2V_{dc}$ . It is further noted that the switching redundancy exists in the same way as the output voltage level is obtained from different switching combination. This redundancy can be exploited in a SVPWM to choose the best possible vectors to generate the reduced common mode voltages.

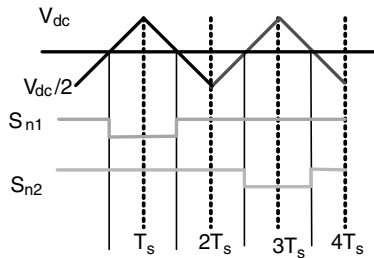


**Figure 3.60** Gate signal generation when  $V_{dc}/2 \leq |v_{ref}| \leq V_{dc}$

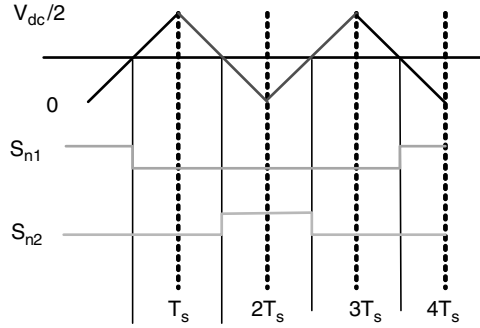


Figure 3.61 Gate signal generation when  $0 \leq |v_{ref}| \leq V_{dc}/2$

3.6.3.1 Carrier-based PWM Technique for a Multi-level CHB Inverter

The SPWM technique can be broadly classified into two types, phase shifted and level shifted. In the phase shifted SPWM technique, the phase shift angle between two adjacent carrier signals is given by equation (3.64). Hence, in a five-level cascaded H-bridge inverter, four carrier waves are required with the phase shift between the two carriers at 90 degrees. The modulating signals are three-phase sinusoids. In a five-level inverter, the carrier with a 0-degree phase shift will control the switching of the cell-1 upper power switch  $S_{a11}$  and the 90-degree phase shifted carrier signal controls the switching of the cell-2 upper power switch  $S_{a12}$ . The 180-degree phase shifted carrier signal controls the switching of  $S_{a22}$  and the 270-degree phase shifted carrier controls the switching of  $S_{a21}$  of cell-2 (Figure 3.64). The gating signals are generated at the intersection of the triangular carrier signals and the

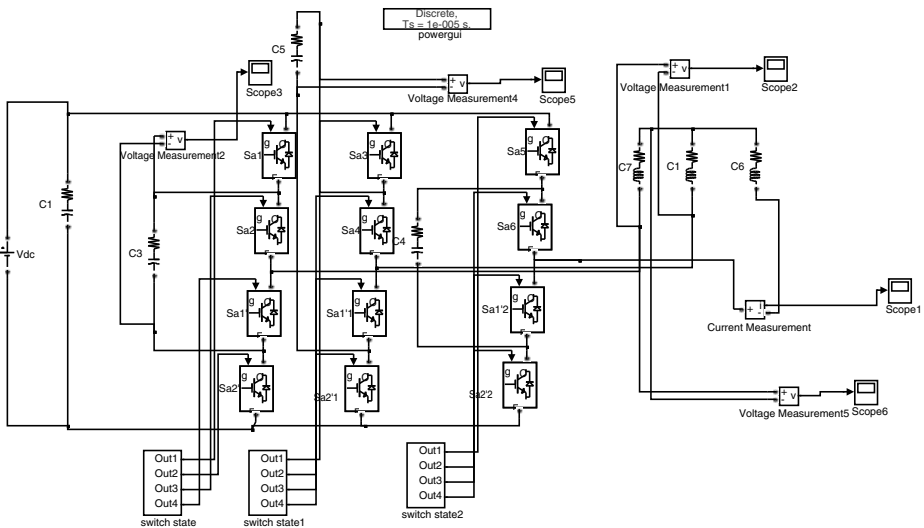


Figure 3.62 MATLAB/Simulink model of three-level flying capacitor inverter (File name: ftc\_3ph.mdl)



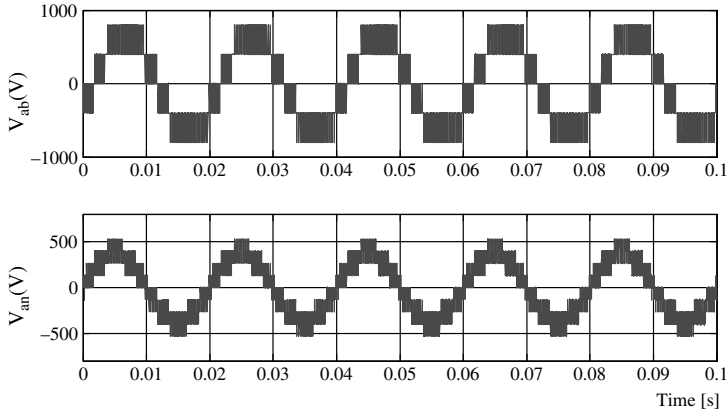


Figure 3.63 Output line and phase voltages from three-level FLC inverter

modulating signals. The inverter switching frequency and the device switching frequency is related by

$$f_{s,inverter} = (L - 1)f_{s,device} \tag{3.66}$$

In level-shifted SPWM technique,  $(L - 1)$  level shifted carriers are required. The carriers are arranged vertically between  $-V_{dc}$  and  $V_{dc}$  and the amplitude of the carrier depends upon their number, for example, in the case of a five-level inverter, four carrier signals are required. The amplitude of the carrier signals will then be  $0.5V_{dc}$  to  $V_{dc}$ ,  $0$  to  $0.5V_{dc}$ ,  $-0.5V_{dc}$  to  $-V_{dc}$ , and  $-0.5V_{dc}$  to  $0$ . The inverter switching frequency and the carrier frequency is the same in the case of level-shifted PWM. The device switching frequency and the inverter switching frequency is related, as shown in equation (3.65).

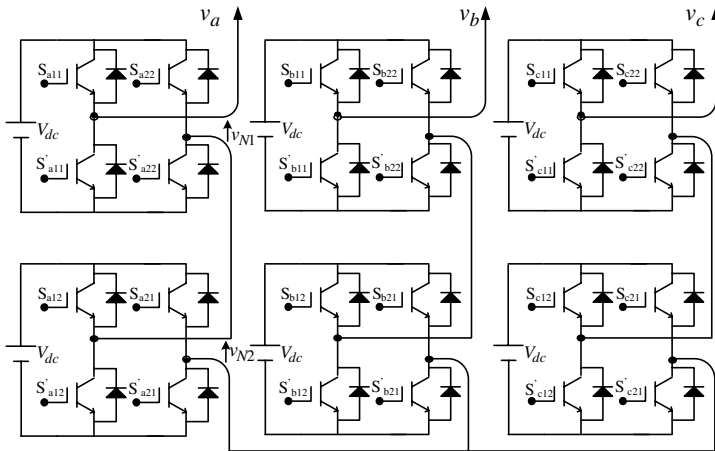


Figure 3.64 Power circuit topology of a five-level cascaded H-bridge inverter

**Table 3.7** Switching states and output voltages in a five-level CHB inverter

$S_{a11}$	$S_{a22}$	$S_{a12}$	$S_{a21}$	$v_{N1}$	$v_{N2}$	$v_a$
1	0	1	0	$V_{dc}$	$V_{dc}$	$2V_{dc}$
1	0	1	1	$V_{dc}$	0	$V_{dc}$
1	0	0	0	$V_{dc}$	0	$V_{dc}$
1	1	1	0	0	$V_{dc}$	$V_{dc}$
0	0	1	0	0	$V_{dc}$	$V_{dc}$
0	0	0	0	0	0	0
0	0	1	1	0	0	0
1	1	0	0	0	0	0
1	1	1	1	0	0	0
1	0	0	1	$V_{dc}$	$-V_{dc}$	0
0	1	1	0	$-V_{dc}$	$V_{dc}$	0
0	1	1	1	$-V_{dc}$	0	$-V_{dc}$
0	1	0	0	$-V_{dc}$	0	$-V_{dc}$
1	1	0	1	0	$-V_{dc}$	$-V_{dc}$
0	0	0	1	0	$-V_{dc}$	$-V_{dc}$
0	1	0	1	$-V_{dc}$	$-V_{dc}$	$-2V_{dc}$

### 3.6.3.2 MATLAB/Simulink Model of Five-level CHB Inverter

A MATLAB/Simulink model for a five-level cascaded H-bridge inverter is shown in Figure 3.65. The model is formulated using Simpower system block-sets. The phase-shifted SPWM technique is employed and the resulting waveforms are shown in Figure 3.66.

## 3.7 Impedance Source or Z-source Inverter

The impedance source or Z-source inverters are special types of inverters that provide the voltage boost capability in conventional inverters. The conventional inverters work as a buck converter only, because the output voltage is always lower than the DC input voltage. Moreover, the upper and lower power switch cannot conduct simultaneously, otherwise the DC source will short circuit. Hence, a dead band is provided intentionally between the switching on and switching off of the complimentary power switches of the same leg. This dead band causes distortion in the output current. These shortcomings are overcome in the Z-source inverter. Two inductors of equal value and two capacitors of equal value, arranged in the form of a letter X with series inductors and diagonal capacitors, are inserted between the DC source and inverter six power switches. This intermediate stage offers the advantage of boosting the DC source voltage, which is a highly attractive solution for renewable energy interface such as Photovoltaic system, Fuel Cells, etc., where the generated voltage is low and the load demand voltage is high. Detailed discussions on the Z-source inverters are given in [49–58]. The concept of impedance source is equally applicable to AC-DC, DC-DC, AC-AC, and DC-AC power converter topology. This section introduces this new class of inverters (DC-AC converter) and will elaborate the basic principle of operation and control power circuit

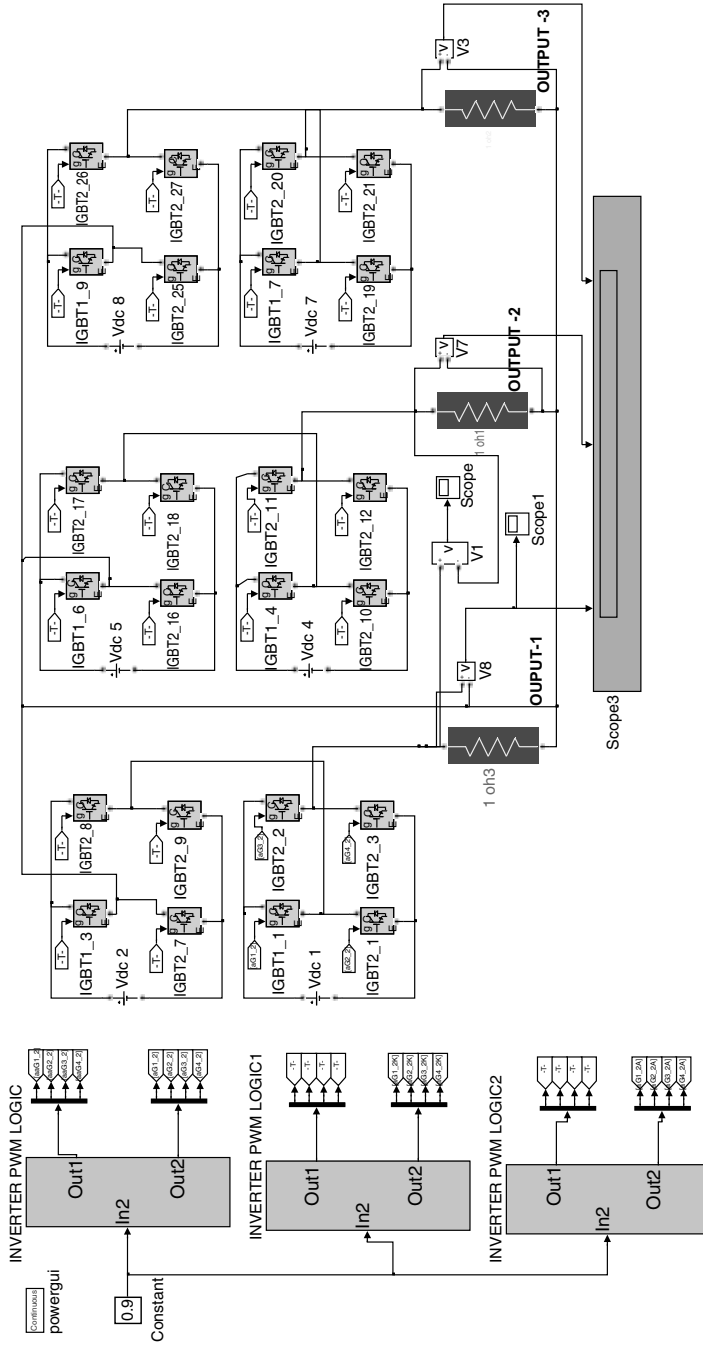
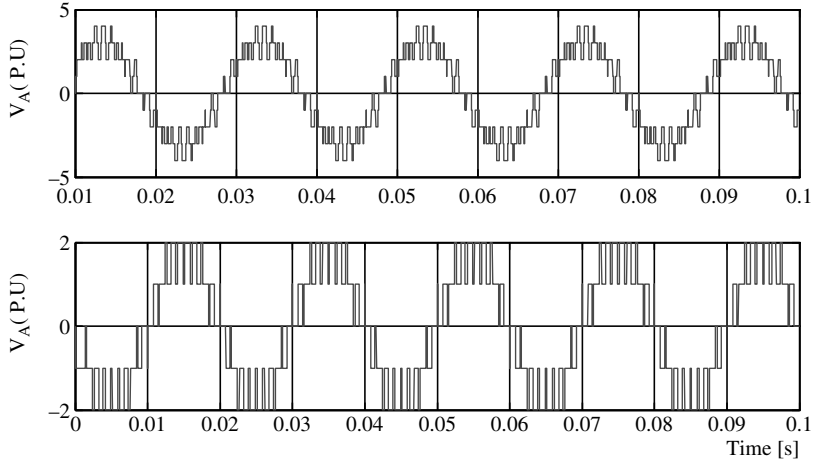


Figure 3.65 MATLAB/Simulink of five-level three-phase CHB (File Name: CHB\_5\_level.mdl)



**Figure 3.66** Output line and phase voltages from five-level CHB inverter

topology of a Z-source inverter, as shown in Figure 3.67. The DC source obtained from the renewable energy sources or a diode rectifier is connected to the conventional three-leg inverter through an intermediate impedance network.

The switching of a Z-source inverter produces seven additional states when compared with a conventional inverter where only eight states are possible (six active and two zero). This is because the operation of the power switch of the same leg is permitted in this type of inverters. When one or more leg is conducting with both power switches being ‘ON’ simultaneously, this leads to these additional switching states, called ‘shoot-through’ states and operation of the inverter in these states causes voltage boost. During ‘shoot-through’ states, the output voltage at the load terminal is zero, while the voltage at the input of the inverter or output DC from the impedance network increases. The switching table, with additional shoot-through states, is presented in Table 3.8

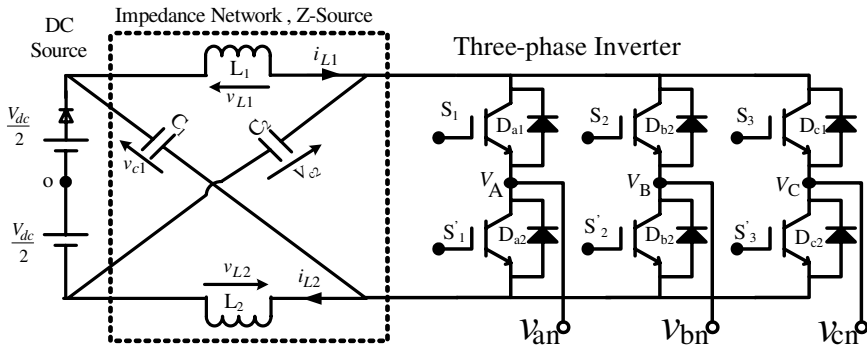


**Figure 3.67** Power circuit topology of a Z-source inverter

**Table 3.8** Shoot-through states in a three-phase Z-source Inverter

Switching State Name	Conducting Switches
Shoot-through 1 (E1)	$S_1, S_1'$
Shoot-through 2 (E2)	$S_2, S_2'$
Shoot-through 3 (E3)	$S_3, S_3'$
Shoot-through 4 (E4)	$S_1, S_1', S_2, S_2'$
Shoot-through 5 (E5)	$S_1, S_1', S_3, S_3'$
Shoot-through 6 (E6)	$S_2, S_2', S_3, S_3'$
Shoot-through 7 (E7)	$S_1, S_1', S_2, S_2', S_3, S_3'$

### 3.7.1 Circuit Analysis

The equivalent circuit of a Z-source inverter is shown in Figure 3.68. The inverter behaves as a constant current source when looked at from the impedance source to the inverter side, as shown in Figure 3.68a, where the inverter is operating in normal ‘non-shoot-through’ mode. The inverter is a short circuit and the equivalent diode at the DC side is off when the inverter operates in the ‘shoot-through’ mode, as shown in Figure 3.68b.

For the circuit analysis, the following assumptions are made; the inductance values are assumed to be the same, i.e.  $L_1 = L_2 = L$ , as are the capacitor values, i.e.  $C_1 = C_2 = C$ . The inductor current is assumed to be large and constant. If the switching period is  $T_s$ , the shoot-through period is  $T_{sh}$  and non-shoot-through period is  $T_{nsh}$ , where

$$T_s = T_{sh} + T_{nsh} \tag{3.67}$$

Due to the symmetrical impedance network, the following relation holds true:

$$v_{c1} = v_{c2} = V_c \tag{3.68}$$

$$v_{L1} = v_{L2} = V_L \tag{3.69}$$

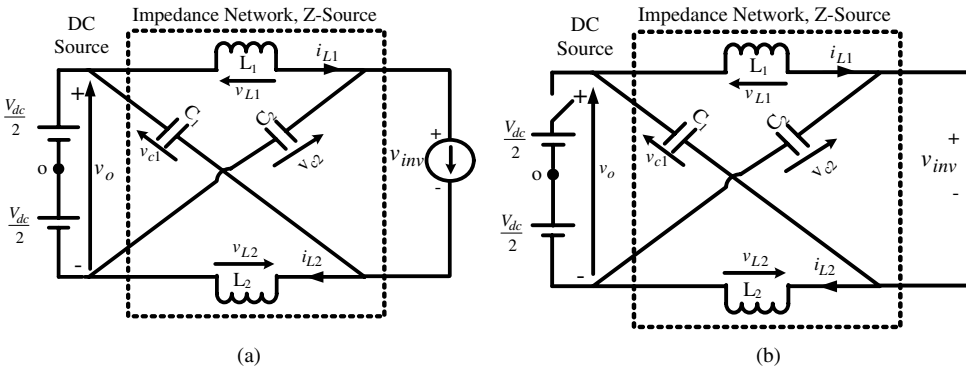


**Figure 3.68** Equivalent circuit of a Z-source inverter: (a) non-shoot-through mode; (b) shoot-through mode

During the non-shoot-through state, the following relations hold true from the equivalent circuit (Figure 3.68a):

$$v_{L-nsh} = V_L = V_{dc} - V_c \quad (3.70)$$

$$v_{inv} = V_c - V_L = 2V_c - v_o \quad (3.71)$$

$$v_o = V_{dc} \quad (3.72)$$

During the shoot-through period, the following relation is obtained from Figure 3.68b:

$$v_o = 2V_c \quad (3.73)$$

$$v_{L-sh} = V_L = V_c \quad (3.74)$$

$$v_{inv} = 0 \quad (3.75)$$

The average voltage across the inductor over one switching period should be zero in steady state and hence, from volt-second principle, the following relation can be written as

$$\begin{aligned} V_L T &= v_{L-sh} T_{sh} + v_{L-nsh} T_{nsh} = 0 \\ V_L T &= V_c T_{sh} + (V_{dc} - V_c) T_{nsh} = 0 \end{aligned} \quad (3.76)$$

From equation (3.76), the following relation is obtained:

$$\frac{V_c}{V_{dc}} = \frac{T_{nsh}}{T_{nsh} - T_{sh}} \quad (3.77)$$

The peak DC link voltage across the inverter bridge is obtained using equations (3.71) and (3.77):

$$\begin{aligned} \hat{v}_{inv} &= 2V_c - V_{dc} = \frac{2V_c - V_{dc}}{V_{dc}} V_{dc} = \left(2 \frac{V_c}{V_{dc}} - 1\right) V_{dc} = \left(2 \frac{T_{nsh}}{T_{nsh} - T_{sh}} - 1\right) V_{dc} \\ &= \frac{T_s}{T_{nsh} - T_{sh}} V_{dc} = g V_{dc} \end{aligned} \quad (3.78)$$

where

$$g = \frac{T_s}{T_{nsh} - T_{sh}} = \frac{1}{1 - 2 \frac{T_{sh}}{T_s}} = \frac{1}{1 - 2\delta} \geq 1 \quad (3.79)$$

where  $g$  is boost factor. The output peak AC voltage from a conventional inverter is

$$\hat{v} = M \frac{V_{dc}}{2} \quad (3.80)$$

The peak output voltage in a Z-source inverter is

$$\hat{v} = M\hat{v}_{inv}/2 = Mg \frac{V_{dc}}{2} \tag{3.81}$$

where  $M$  is the modulation index. It is thus seen that the output AC peak voltage from a Z-source inverter is  $g$  (boost factor) times the conventional inverter output. The value  $g$  is always more than unity and hence gain in the output voltage is achieved. It is seen from equation (3.79) that the boost factor  $g$  is zero if the shoot-through period  $T_{sh} = 0$ . Hence, it can be said that the boost in the output voltage is obtained due to the shoot-through in the switching state.

### 3.7.2 Carrier-based Simple Boost PWM Control of a Z-source Inverter

Conventional PWM schemes, such as sinusoidal carrier-based and SVPWM, are equally applicable to a Z-source inverter. The only difference is seen when voltage boost is required and shoot-through state operation is needed. In the conventional PWM, two zero states and two active states are used. The shoot-through state is inserted within the conventional zero states, as shown in Figure 3.69. The triangular carrier signal is shown along with the sampled modulating signals. Two additional constant signals are used, namely  $V_p^*$ ,  $V_N^*$ , to modulate the shoot-through duty ratio. Hence, by controlling the amplitude of the two additional signals, the output voltage from the Z-source inverter is controlled. It is seen that the zero vector time only is altered, the active vector time remaining the same.

The shoot-through duty ratio ( $\delta$ ) decreases with the increase in the modulation index  $M$ . The maximum duty ratio is  $1 - M$  and hence reaches zero for modulation index of unity. The voltage gain reduces with the increase in the modulation index. The voltage gain due to the boost becomes zero for  $M = 1$ . The gain is high for a low modulation index, hence to obtain a higher gain the modulation index must be kept low.

The overall gain  $G$  in the output voltage using the simple boost PWM method is

$$G = M \cdot g = \frac{\hat{v}}{V_{dc}/2} = \frac{M}{2M - 1} \tag{3.82}$$

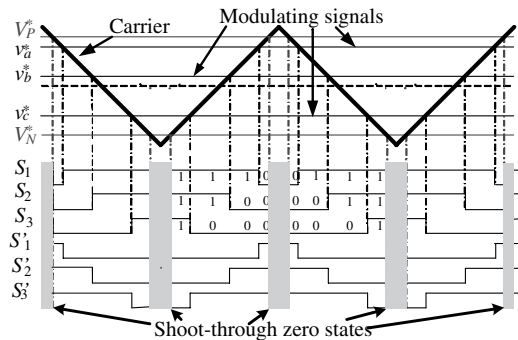


**Figure 3.69** Principle of carrier-based simple boost PWM for a Z-source inverter

The maximum modulation for given  $g$  is

$$M = \frac{G}{2G - 1} \tag{3.83}$$

The voltage stress across the power semiconductor switch using the carrier-based simple boost PWM method is

$$V_{stress} = gV_{dc} = (2G - 1)V_{dc} \tag{3.84}$$

Higher gain at the output of inverter leads to high stress on the power semiconductor power switch.

### 3.7.3 Carrier-based Maximum Boost PWM Control of a Z-source Inverter

The limitation of the simple boost control method is that the stress across the power switches is higher for higher voltage gain, since the voltage gain is given as  $M.g$  and the voltage stress across the switch is  $g.V_{dc}$ . In order to minimize the stress of the power switch, the boost factor  $g$  should be minimized and do simultaneously maximize the modulation index  $M$ , keeping the output voltage gain at a desired value. However, in order to increase the voltage gain, the boost factor  $g$  should be enhanced. To meet these conflicting requirements, the zero states are all converted into the shoot-through period. The active states remain unchanged, as shown in Figure 3.70.

The average duty ratio of the shoot-through is [50]:

$$\delta = \frac{T_{sh}}{T_s} = \frac{2\pi - 3\sqrt{3}M}{2\pi} \tag{3.85}$$

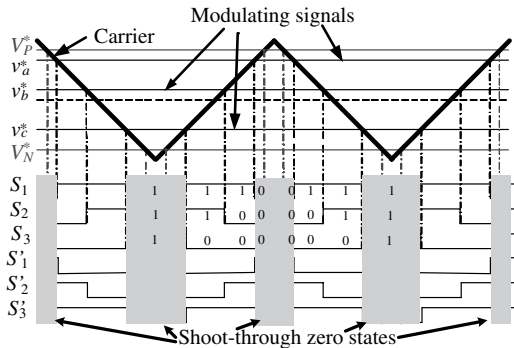


**Figure 3.70** Principle of carrier-based maximum boost PWM for a Z-source inverter



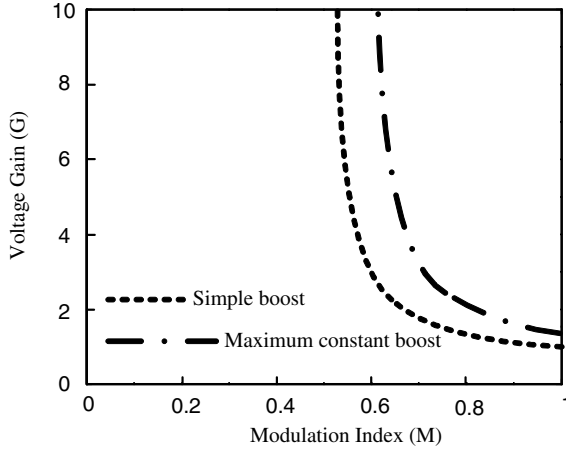


**Figure 3.71** Voltage gain versus modulation index for Z-source inverter

The boost factor is given by

$$g = \frac{1}{1 - 2\delta} = \frac{\pi}{3\sqrt{3}M - \pi} \quad (3.86)$$

The output voltage gain is given by

$$G = Mg = \frac{\pi M}{3\sqrt{3}M - \pi} \quad (3.87)$$

The voltage stress across the power switches are

$$V_{stress} = gV_{dc} = \frac{3\sqrt{3}G - \pi}{\pi} V_{dc} \quad (3.88)$$

The voltage stress in a PWM scheme is considerably lower than the simple boost PWM method. Hence, a higher gain can be achieved with this maximum constant boost PWM method.

The variation of the voltage gain  $G$  versus the modulation index for simple boost PWM and maximum constant boost PWM is shown in Figure 3.71.

To increase the modulation index  $M$  to  $1/\sqrt{3}$ , the third-harmonic injection method can be adopted. The modulating signal consists of a sinusoidal signal plus the one-fourth or one-sixth third harmonic.

### 3.7.4 MATLAB/Simulink Model of Z-source Inverter

The MATLAB/Simulink model of a Z-source inverter controlled using a simple SPWM scheme is shown in Figure 3.72. The switching frequency of the inverter is kept at 2 kHz, the

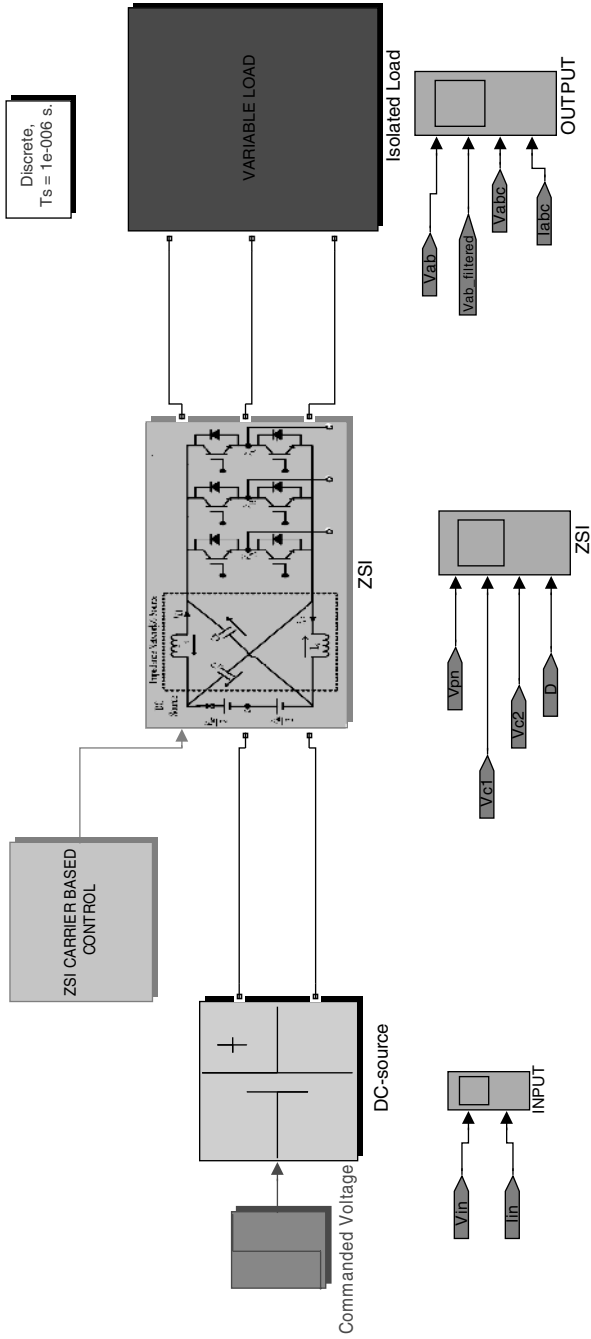
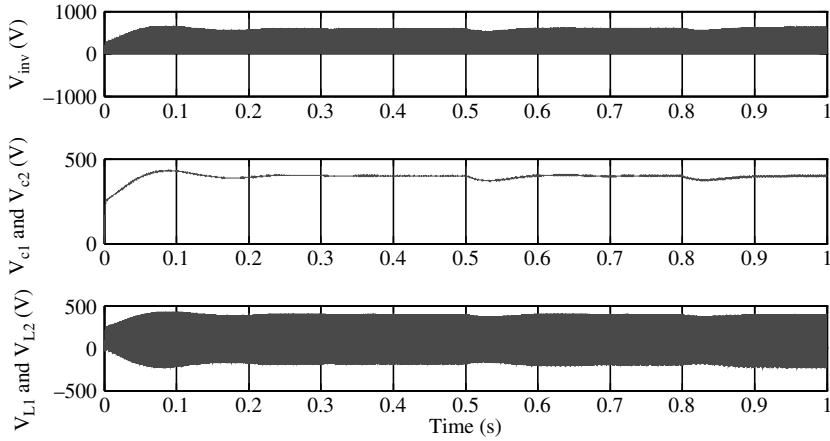
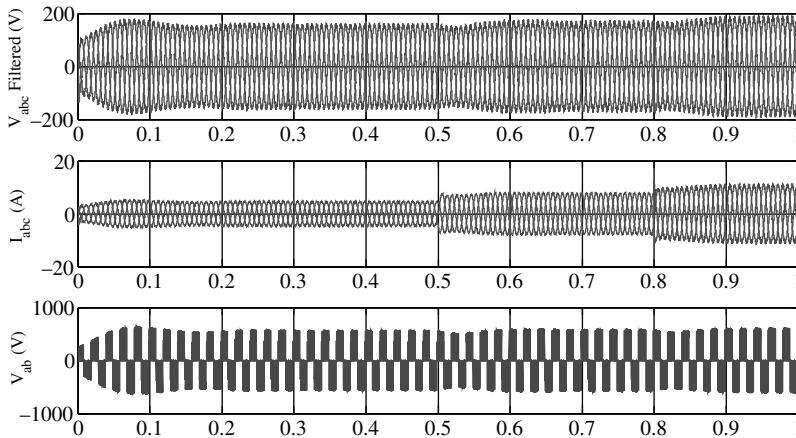


Figure 3.72 MATLAB/Simulink model of Z-source inverter



**Figure 3.73** Voltages at the source side: (a) at the input of the bridge inverter; (b) across two capacitors; and (c) across two inductors

fundamental frequency is chosen as 50 Hz, the impedance network parameters are  $L = 500 \mu\text{H}$  and  $C = 400 \mu\text{F}$ , and the output filter parameters are  $L_v = 0.01 \text{ H}$ ,  $C_v = 110 \mu\text{F}$ . The load is chosen as variable with different requirements of active and reactive powers. The load is changed at the instant of  $t = 0.5 \text{ s}$  and  $t = 0.8 \text{ s}$ , the modulation index is kept at 0.75, the output phase voltage requirement is 249 V rms, and the DC link voltage is kept at 400 V. The resulting waveforms are shown in Figures 3.73 and 3.74.



**Figure 3.74** Outputs from Z-source inverter: (a) filtered three-phase voltages; (b) three-phase load current; and (c) line voltage

### 3.8 Quasi Impedance Source or qZSI Inverter

The impedance source or Z-source inverter, described in Section (3.7) suffers from the drawback of discontinuous input (DC) current during boost mode, high voltages across the capacitors, and higher stress on power switches. These shortcomings are overcome by a different topology of inverter called qZSI [58–61]. The qZSI topology is derived from the original Z-source inverter. The advantages of a qZSI are:

- draws continuous current from DC source;
- the voltage across the capacitor C2 is reduced;
- lower component count and hence higher reliability and higher efficiency; and
- lower voltage stress on the power switches.

There are several topologies of qZSI reported in the literature [59]. This section elaborates on the voltage fed qZSI with continuous input current, as shown in Figure 3.75. The two operating modes of the inverter are the shoot-through and non-shoot-through modes, and the equivalent circuits during the modes of operation are shown in Figure 3.75. From the circuit (Figure 3.76a), the voltage relations during the non-shoot-through period ( $T_{nsh}$ ) are

$$v_{L1} = V_{dc} - v_{C1}, \quad v_{L2} = -v_{C2}, \tag{3.89}$$

$$v_{inv} = v_{C1} - v_{L2} = v_{C1} + v_{C2}, \quad v_{diode} = 0. \tag{3.90}$$

From the circuit (Figure 3.76b), the voltage relations during the shoot-through period ( $T_{sh}$ ) are

$$v_{L1} = v_{C2} + V_{in}, \quad v_{L2} = v_{C1} \tag{3.91}$$

$$v_{inv} = 0, \quad v_{diode} = -(v_{C1} + v_{C2}) \tag{3.92}$$

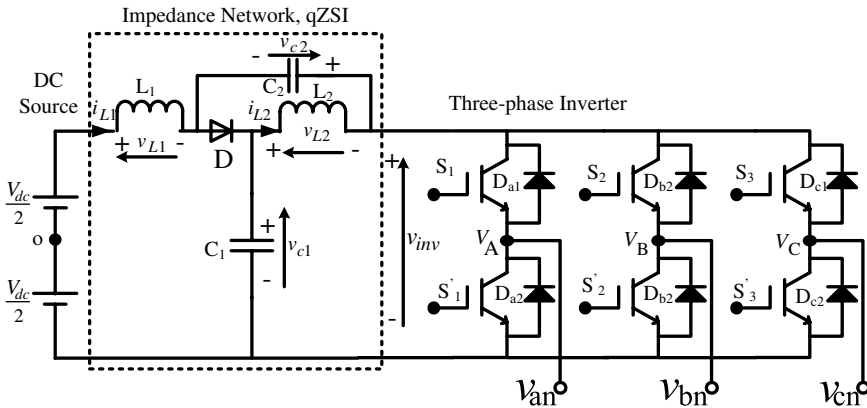
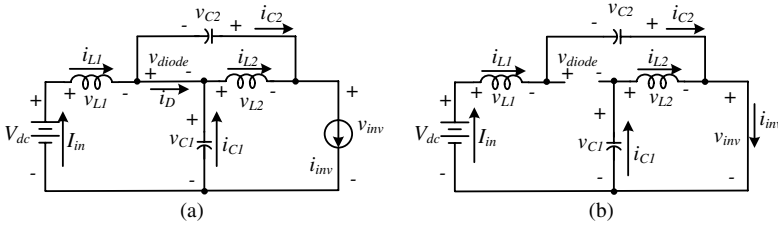


Figure 3.75 Power circuit topology of the voltage fed qZSI



**Figure 3.76** Equivalent circuit of the qZSI; a non-shoot-through state, b. shoot-through state

The average voltage across inductor over one switching period should be zero in steady state and hence, from volt-second principle, the following relation can be written from equations (3.89) and (3.91):

$$V_{L1} = \bar{v}_{L1}T_s = T_{sh}(V_{C2} + V_{dc}) + T_{nsh}(V_{dc} - V_{C1}) = 0 \quad (3.93)$$

$$V_{L2} = \bar{v}_{L2}T_s = T_{sh}(V_{C1}) + T_{nsh}(-V_{C2}) = 0 \quad (3.94)$$

Thus, the following relations are

$$V_{C1} = \frac{1 - \delta}{1 - 2\delta} V_{dc}, \quad V_{C2} = \frac{\delta}{1 - 2\delta} V_{dc} \quad (3.95)$$

From equations (3.90), (3.92), and (3.1046), the peak DC-link voltage across the inverter bridge is

$$v_{inv} = V_{C1} + V_{C2} = \frac{T_s}{T_{nsh} - T_{sh}} V_{dc} = \frac{1}{1 - 2\delta} V_{dc} = gV_{dc} \quad (3.96)$$

where  $g$  is the boost factor of the qZSI. The average currents through the two inductors  $L_1$  and  $L_2$  can be calculated by the system power rating  $P$ :

$$I_{L1} = I_{L2} = I_{in} = P/V_{dc} \quad (3.97)$$

According to Kirchoff's current law and equation (3.97), the following current relations are obtained:

$$I_{C1} = I_{C2} = I_{inv} - I_{L1}, \quad I_D = 2I_{L1} - I_{inv} \quad (3.98)$$

Defining the following terms:

1.  $M$  is the modulation index;  $\hat{v}$  is the ac peak phase voltage or output peak voltage of the inverter;
2.  $p = (1 - \delta)/(1 - 2\delta)$ ;  $k = \delta/(1 - 2\delta)$ ;  $g = 1/(1 - 2\delta)$ .

**Table 3.9** Comparison of average quantities of ZSI and qZSI [60]

	$v_{L1} = v_{L2}$		$v_{inv}$		$v_{diode}$		$V_{C1}$	$V_{C2}$	$\hat{v}$	$I_{in} = I_{L1} = I_{L2}$	$I_{C1} = I_{C2}$	$I_D$
	$T_{sh}$	$T_{nsh}$	$T_{sh}$	$T_{nsh}$	$T_{sh}$	$T_{nsh}$						
ZSI	$pV_{dc}$	$-kV_{dc}$	0	$gV_{dc}$	$gV_{dc}$	0	$pV_{dc}$	$pV_{dc}$	$GV_{dc}/2$	$P/V_{dc}$	$I_{inv} - I_{L1}$	$2I_{L1} - I_{inv}$
qZSI	$pV_{dc}$	$-kV_{dc}$	0	$gV_{dc}$	$gV_{dc}$	0	$pV_{dc}$	$kV_{dc}$	$GV_{dc}/2$	$P/V_{dc}$	$I_{inv} - I_{L1}$	$2I_{L1} - I_{inv}$

A comparison between the Z-source and quasi Z-source inverter average parameters are given in Table 3.9.

The qZSI and Z-source inverter have the same features. The advantage of boosting the input DC voltage in a single-stage configuration is also available with the qZSI. There is no need to provide dead time between the switching on and off of the power switches of the same leg.

### 3.8.1 MATLAB/Simulink Model of qZ-source Inverter

The MATLAB/Simulink model of the qZSI is shown in Figure 3.77. The inverter is controlled using a simple SPWM technique. The simulation parameters are the same as that of the ZSI. The resulting waveforms are shown in Figures 3.78 and 3.79.

## 3.9 Dead Time Effect in a Multi-phase Inverter

This section further elaborates on the effect of introducing dead time (time lag between the switching ‘ON’ and switching ‘OFF’ of the two power semiconductor switches of the same leg of an inverter). The two power switches of the same leg should not be turned on simultaneously, in order to avoid the source side short circuit and uncontrolled flow of current through inverter switches and subsequent failure of the inverter; the time delay thus to be introduced between the

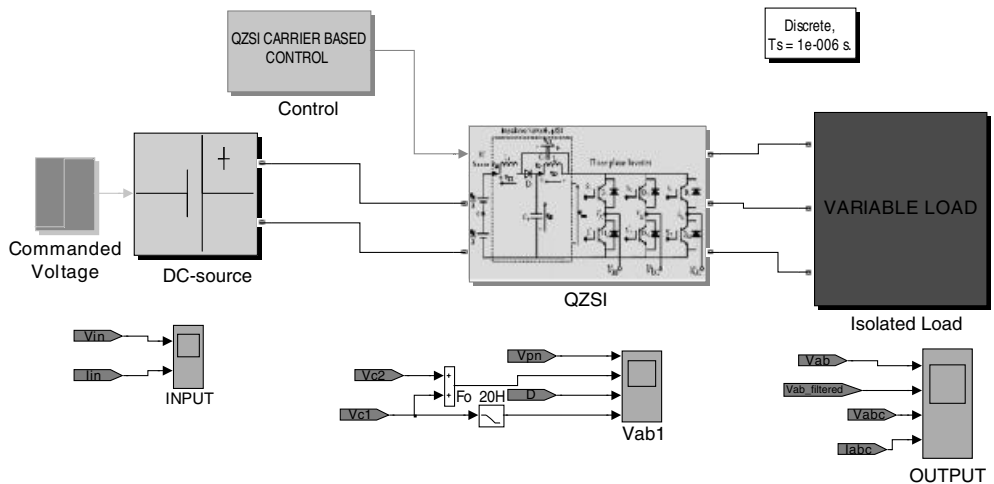


**Figure 3.77** MATLAB/Simulink model of Z-source inverter

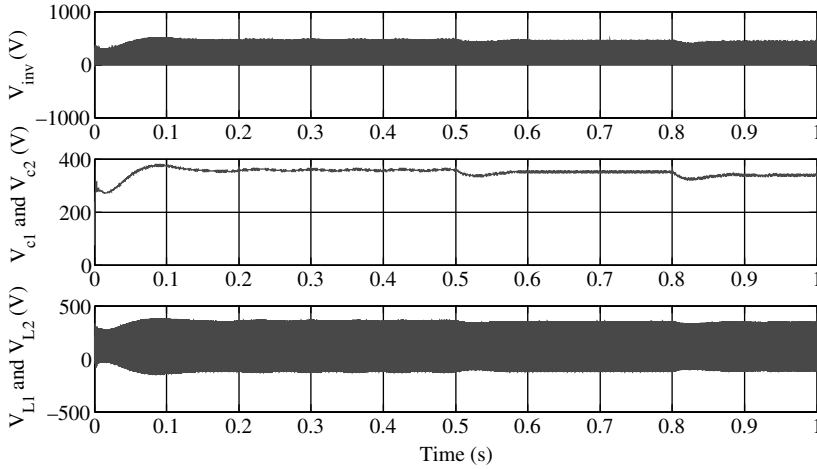


**Figure 3.78** Voltages at the source side: (a) at the input of the bridge inverter; (b) across two capacitors; (c) across two inductors

turning on and turning off of the two switches of the same leg. The power semiconductor switch turn-on and turn-off time depend upon several factors, such as the power rating of the switch, the operating temperature, and gate drive current [62]. The required dead time is a function of the power rating of the device, considering one leg of a multi-phase inverter with gate signal supplied from a gate drive circuit. The waveforms associated with Figure 3.80 are shown in Figure 3.81.

Figure 3.80 shows one of the legs of the basic multiphase PWM inverter with RL load.  $V_c(t)$  and  $V_i(t)$  are carrier and modulating signals, respectively, which are compared in a comparator.

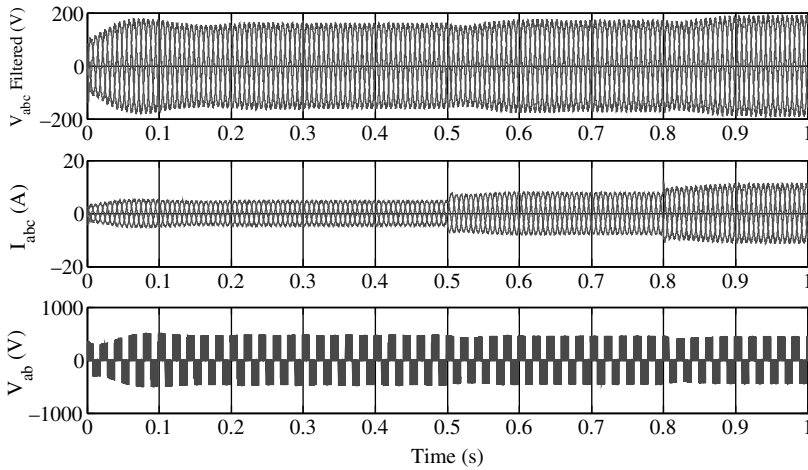


**Figure 3.79** Outputs from qZ-source inverter: (a) filtered three-phase voltages; (b) three-phase load current; (c) line voltage

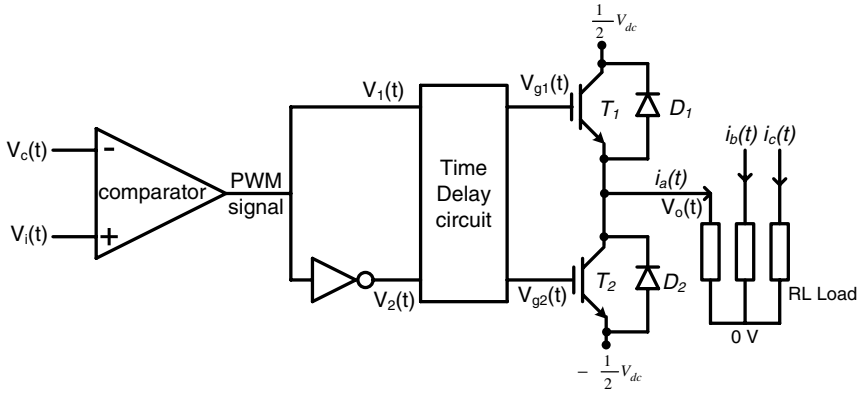


**Figure 3.80** One leg of multiphase PWM inverter with time delay circuit

Output of the comparator is  $V_1(t)$ . This output signal and its complement signal ( $V_2(t)$ ) are fed to the gates of upper ( $T_1$ ) and lower ( $T_2$ ) IGBTs of one leg through a time delay circuit. Time delay between upper and lower IGBTs switching is required to avoid shoot-through conditions and subsequently to avoid the source short circuit. The waveforms of the PWM inverter in Figure 3.80 are shown in Figure 3.81 for positive phase current  $i_a > 0$  and negative phase current  $i_a < 0$ . Figure 3.81 also shows the duration at which  $D_1$ ,  $D_2$ ,  $T_1$ , and  $T_2$  are conducting.  $V_{D1}$ ,  $V_{D2}$ ,  $V_{T1}$ , and  $V_{T2}$  are the voltage drops across  $D_1$ ,  $D_2$ ,  $T_1$ , and  $T_2$ , respectively.  $D_1$  and  $D_2$  are the free wheeling diodes. Here it is assumed that the delay time  $t_d$  includes  $t_{on}$  and  $t_{off}$  of the devices. The shaded portion for  $i_a > 0$  is responsible for the decrease of output voltage, whereas the shaded portion for  $i_a < 0$  is responsible for the increase of output voltage.

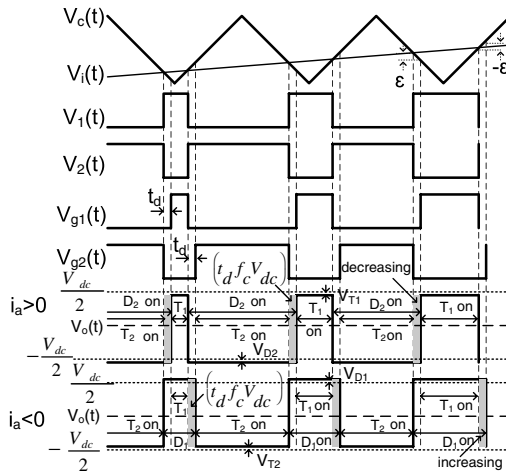


**Figure 3.81** Gate control signals  $V_{g1}$  and  $V_{g2}$ , and output voltages at  $i_a > 0$  and  $i_a < 0$ , showing IGBTs ( $T_1$ ,  $T_2$ ) and diode ( $D_1$ ,  $D_2$ ) ON conditions



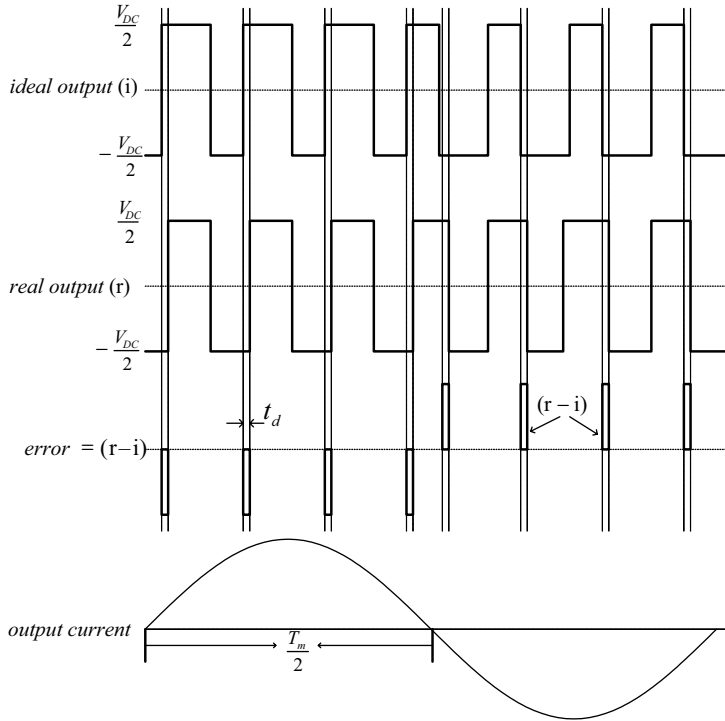


**Figure 3.82** Dead time effect on output voltage

The voltage deviation  $\varepsilon$  depends on the delay time  $t_d$  and slope of the carrier wave  $V_c(t)$ . Therefore:

$$\frac{-\varepsilon}{t_d} = \frac{-2V_c}{(T_c/2)} \text{ or } \varepsilon = t_d \frac{2V_c}{(T_c/2)} = 4f_c t_d V_c \tag{3.99}$$

where  $V_c$ ,  $f_c$ , and  $T_c$  are the amplitude, frequency, and time period of the carrier signal, respectively.

Figure 3.82 depicts ideal, real, and error output voltages waveforms. Here it is assumed that the IGBTs switch instantly. The error pulses, whose height and width are equal to  $\frac{V_{DC}}{2}$  and  $t_d$ , respectively, are in opposition to the output current.

The area of each pulse is

$$\Delta e = \frac{V_{DC}}{2} \times t_d \tag{3.100}$$

where the number of pulses is

$$n_p = \frac{\left(\frac{T_m}{2}\right)}{T_c} \tag{3.101}$$

The pulses due to dead time effect can be summed to form a square wave whose height and width are 'h' volt and  $\frac{T_m}{2}$  s, respectively and  $T_c$  is the period of the triangular wave or the inverter switching period. Therefore, the area of the resulting square wave is

$$h \times \frac{T_m}{2} = n_p \times \frac{V_{DC}}{2} \times t_d \text{ or } h = \Delta V = n_p \times \frac{V_{DC}}{T_m} \times t_d = f_c \times \frac{V_{DC}}{2} \times t_d \quad (3.102)$$

where  $\Delta V$  is the amplitude.

In the ideal PWM waveform, the predominant harmonics are shifted to the switching frequency and the low-order harmonics are either suppressed or cancelled. However, due to switching dead time,  $t_d$ , the presence of the error voltage can introduce low frequency components such as the 5th and 7th, especially at very high switching frequencies. The rectangular pulses can be approximated to a square wave with a frequency equal to that of the output fundamental frequency. If 'h' is the height of the square wave, then

$$h \times \frac{T_m}{2} = n_p \times V_{DC} \times t_d \quad (3.103)$$

i.e.:

$$h \frac{T_m}{2} = \frac{\left(\frac{T_m}{2}\right)}{T_c} \times V_{DC} \times t_d \quad (3.104)$$

$$h = f_c \times V_{DC} \times t_d \quad (3.105)$$

where  $f_c$  is the frequency of the carrier wave or the inverter switching frequency. Using the Fourier series expression for the square wave, the nth harmonic of the error voltage is

$$V_n = \frac{4h}{\pi n} = \frac{4f_c \times V_{DC} \times t_d}{\pi n} \quad (3.106)$$

The above equation shows that the more  $f_c$  increases, the more  $V_n$  rises. Therefore the upper limitation of carrier frequency exists when using the high frequency carrier waveform and the product of  $f_c$  and  $t_d$  should be selected to a minimum value to avoid waveform distortion due to low frequency harmonics introduced by switching lag times.

The effect of dead time is compensated in real time implementation using several open-loop and closed-loop techniques. Some of the important references related to the dead time compensation are [2,63–66].

### 3.10 Summary

This chapter discusses the PWM control of a three-phase two-level and multi-level voltage source inverter. The basic structure of the inverter is discussed starting from half-bridge to full-bridge and then three-phase inverter is elaborated on. A simple SPWM scheme is discussed followed by a third-harmonic injection and offset addition-based PWM. SVPWM is presented

and a general simulation model is given that can be modified to implement both continuous and discontinuous SVPWM. An over-modulation region is also presented along with its MATLAB/Simulink implementation. The use of the artificial intelligence technique for implementing SVPWM is described. The effect of dead banding is also discussed. Basic topologies of the multi-level inverter are presented and their SPWM is elaborated on. Special inverters (Z-source and quasi Z-source) that have the capability of boosting the voltage are discussed in detail.

### 3.11 Problems

- 3.1: A single-phase half-bridge voltage source inverter is supplied from a center-tapped dc input voltage 120 V. The inverter supplies a resistive load of  $20\ \Omega$ . Calculate;
  - (a) The fundamental output peak and rms voltage
  - (b) First three harmonics of the output voltage
  - (c) Power consumed by the load
- 3.2: A single-phase full-bridge voltage source inverter is supplied from a dc input voltage of 300 V. The inverter supplies a resistive load of  $20\ \Omega$ . Calculate;
  - (a) The fundamental output peak and rms voltage
  - (b) First three harmonics of the output voltage
  - (c) Power consumed by the load
- 3.3: A single-phase half bridge inverter is controlled using bipolar PWM method and supplied from a center tapped 120 V dc supply. The fundamental output voltage is of 50 Hz frequency. The triangular carrier signal's frequency is 5 kHz. For a modulation index of 0.9, determine;
  - (a) Frequency modulation ratio
  - (b) Fundamental output peak and rms voltage
  - (c) First three significant harmonic order produced in the output voltage
- 3.4: A single-phase full-bridge voltage source is supplied by a dc source of 300 V and controlled using unipolar PWM technique. The modulation index is 0.9, the fundamental output frequency is 50 Hz and the carrier signal frequency is 2 kHz. Compute the following:
  - (a) Fundamental output voltage peak value
  - (b) First three dominant harmonic components
- 3.5: A three-phase voltage source inverter is operating in  $180^\circ$  conduction mode and supplied from a 600 V dc link voltage. Calculate;
  - (a) The peak and rms value of the output fundamental phase and line voltages
  - (b) Three most significant harmonic component of phase peak value
- 3.6: A three-phase voltage source inverter is controlled using Carrier-based sinusoidal PWM technique. The frequency of the fundamental output voltage is to be kept at 50 Hz and the switching frequency of the inverter is 2 kHz. The inverter is supplied from a dc link voltage of 600 V. The modulation index is 0.9. Compute the fundamental output phase RMS voltage value.
 

To enhance the output voltage third harmonic components are injected. Compute the value of the peak value of the third harmonic component required to raise the output voltage by 15.47%.
- 3.7: A three-phase induction machine is supplied from a three-phase voltage source inverter. The three-phase VSI is controlled using space vector PWM technique and

sinusoidal supply is to be given to the motor. The inverter switching frequency is 5 kHz and the DC bus voltage at the inverter input is 300 V. The inverter output frequency is 50 Hz. The reference phase voltage rms is 100 V. Identify the space vectors that will be applied and their time of application for the time instants: 1 ms, 5 ms, and 10.5 ms.

## References

1. Kazmierkowski, M. P., Krishnan, R., and Blaabjerg, F. (2002) *Control in Power Electronics: Selected Problems*. Academic Press, USA.
2. Holmes, D. G. and Lipo, T. A. (2003) *Pulse Width Modulation for Power Converters: Principles and Practice*. IEEE Power Engineering Series, Wiley Interscience, USA.
3. Mohan, N., Undeland, T. M., and Robbins, W. P. (1995) *Power Electronics-Converters, Applications and Design*, 2nd edn. John Wiley & Sons, Ltd., USA.
4. Holtz, J. (1992) Pulse width modulation: A survey. *IEEE Trans. Ind. Elect.*, **39**(5), 410–420.
5. Wu, B. (2006) *High Power Converters and AC Drives*. IEEE Power Engineering Series, Wiley Interscience, USA.
6. Chen, Y. M. and Cheng, Y. M. (1999) PWM control using a modified triangle signal. *IEEE Trans. Ind. Elect.*, **1**(29), 312–317.
7. Boost, M. A. and Ziogas, P. D. (1998) State-of-art-carrier PWM techniques: A critical evaluation. *IEEE Trans. Ind. Appl.*, **24**(2), 271–280.
8. Van der Broeck, H. W., Skudenly, H., and Stanke, G. (1988) Analysis and realization of a pulse width modulator based on voltage space vectors. *IEEE Trans. Ind. Elect.*, **24**(1), 142–150.
9. Hava, A. M., Kerkman, R. S., and Lipo, T. A. (1997), A high performance generalized discontinuous PWM algorithm. *IEEE APEC*, **2**, 886–891.
10. Ojo, O. (2004) The generalized discontinuous PWM scheme for three-phase voltage source inverters. *IEEE Trans. Ind. Elect.*, **51**(6), 1280–1289.
11. Iqbal, A., Lamine, A., Ashraf, I., and Mohibullah (2006) MATLAB/Simulink model for space vector modulation of three-phase VSI. *IEEE UPEC 2006*, 6–8 September, Newcastle, UK, Vol. **3**, pp. 1096–1100.
12. Iqbal, A., Ahmed, M., Khan, M. A., and Abu-Rub, H. (2010) Generalised Simulation and experimental implementation of space vector PWM techniques of a three-phase voltage source inverter. *Int. J. Eng. Sci. Tech. (IJEST)*, **2**(1), 1–12.
13. Holtz, J., Khamabdkone, A. M., and Lotzkat, W. (1993) On continuous control of PWM inverters in the over modulation range including the six-step mode. *IEEE Trans. Power Elect.*, **8**(4), 546–553.
14. Lee, D. C. and Lee, G. M. (1998) A novel over-modulation technique for space vector PWM inverter. *IEEE Trans. Power Elect.*, **13**(6), 1144–1151.
15. Have, A. M. (1998) Carrier-based PWM voltage source inverter in the over-modulation range. PhD thesis, University of Wisconsin.
16. Kerkman, R. J., Leggate, D., Seibel, B. J., and Rowan, T. M. (1996) Operation of PWM voltage source-inverters in the over-modulation region. *IEEE Trans. Ind. Elect.*, **43**(1), 132–140.
17. Bose, B. K. (2007) Neural network applications in power electronics and motor drives: an introduction and perspective. *IEEE Trans. Ind. Elect.*, **54**(1), 14–33.
18. Fen, H. S., Zhi, Y. L., An, T. P., Ju, L., Cheng, P.H., and Mei, P. H. (2008) Research on space vector PWM inverter based on the neural network. *Proc. Int. Conf. on Elect. Mach.Syst.* pp. 1802–1805.
19. Kashif, S. A. R., Saqib, M. A., Zia, S., and Kaleem, A. (2009) Implementation of neural network based space vector pulse width modulation inverter-induction motor drive system. *Proc. 3rd Int. Conf. Elerc. Eng., ICEE* pp. 1–6.

20. Mondal, S. K., Pinto, O. P., and Bose, B. K. (2002) A neural-network-based space-vector PWM controller for a three-level voltage-fed inverter induction motor drive. *IEEE Trans. Ind. Appl.*, **38**(3), 660–669.
21. Xiang, G. and Huang, D. (2007) A neural network based space vector PWM for permanent magnet synchronous motor drive. *Proc. Int. Conf. Mech. Autom., ICMA* pp. 3673–3678.
22. Zhou, K. and Wang, D. (2002) Relationship between space vector modulation and three-phase carrier-based PWM: A comprehensive analysis. *IEEE Trans. Ind. Elect.*, **49**(1), 186–196.
23. Lai, J. S. and Zheng Peng, F. (1985) Multilevel converters a new breed of power converters. *IEEE Trans. Ind. Appl.*, **32**(3), 509–517.
24. Meynard, T. A., Fadel, M., and Aouda, N. (1997) Modeling of multilevel converters. *IEEE Tran. Ind. Elec.*, **4**(3), 356–364.
25. Tolbert, L. M., Peng, F. Z., and Habetler, T. (1999) Multilevel converters for large electric drives. *IEEE Trans. Ind. Appl.*, **35**, 36–44.
26. Rodriguez, J., Lai, J.-S., and Peng, R. Z. (2002) Multilevel inverters: A survey of topologies, controls, and applications. *IEEE Trans. Ind. Elect.*, **49**(4), 724–738.
27. Abu-Rub, H., Lewicki, A., Iqbal, A., and Guzinski, J. (2010) Medium voltage drives-challenges and requirements. *Proc. IEEE ISIE-2010 Bari, Italy*, pp. 1372–1377.
28. Abu-Rub, H., Holtz, J., Rodriguez, J., and Boaming, G. (2010) Medium voltage multilevel converter-state of the art, challenges and requirements in industrial applications. *IEEE Trans. Ind. Elect.*, **57**(8), 2581–2596.
29. Krug, D., Bernet, S., Fazel, S. S., Jalili, K., and Malinowski, M. (2007) Comparison of 2.3-kV medium-voltage multi-level converters for industrial medium-voltage drives. *IEEE Trans. Ind. Elect.*, **54**(6), 2979–2992.
30. Franquelo, L. G., Rodriguez, J., Leon, J. I., Kouro, S., Portillo, R., and Prats, M. A. M., (2008) The age of multi-level converters arrives. *IEEE Ind. Elect. Mag.*, **2**(2), 28–39.
31. Lin, L., Zou, Y., Wang, Z., and Jin, H. (2005) Modeling and control of neutral point voltage balancing problem in three-level NPC PWM inverters. *Proc. 36th IEEE PESC, Recife, Brazil*, pp. 861–866.
32. Ojo, O. and Konduru, S. (2005) A discontinuous carrier-based PWM modulation method for the control of neutral point voltage of three phase three-level diode clamped converters. *Proc. 36th IEEE Annu. Power Electron. Spec. Conf., Recife, Brazil*, pp. 1652–1658.
33. Bernet, S. (2006) State of the art and developments of medium voltage converters: An overview. *Prz. Elektrotech. (Elect. Rev.)* **82**(5), 1–10.
34. Peng, F. (2001) A generalized multilevel inverter topology with self voltage balancing. *IEEE Trans. Ind. Appl.*, **37**(2), 611–618.
35. Fracchia, M., Ghiara, T., Marchesoni, M., and Mazzucchelli, M. (1992) Optimized modulation techniques for the generalized N-level converter. *Proc. IEEE Power Elect. Spec. Conf.*, **2**, 1205–1213.
36. Mukherjee, S. and Poddar, G. (2010) Series-connected three-level inverter topology for medium-voltage squirrel-cage motor drive applications. *IEEE Trans. Ind. Appl.*, **46**(1), 179–186.
37. Du, Z., Tolbert, L. M., Chiasson, J. N., Ozpineci, B., Li, H., and Huang, A. Q. (2006) Hybrid cascaded H-bridges multilevel motor drive control for electric vehicles. *Proc. 37th IEEE Power Elect. Spec. Conf.* pp. 1–6.
38. Sirisukprasert, S., Xu, Z., Zhang, B., Lai, J. S., and Huang, A. Q. (2002) A high frequency 1.5 MVA H-bridge building block for cascaded multilevel converters using emitter turn-off thyristor. *Proc. IEEE Appl. Power Elect. Conf.* pp. 27–32.
39. Nabae, A., Takahashi, I., and Akagi, H. (1981) A new neutral point clamped PWM inverter. *IEEE Trans. Ind. Appl.*, **IA-17**(5) 518–523.
40. Escalante, M. F., Vannier, J. C. and Arzande, A. (2002) Flying capacitor multilevel inverters and DTC motor drive applications, *IEEE Trans. Ind. Elect.*, **49**(4), 809–815.

41. Fazel, S. S., Bernet, S., Krug, D., and Jalili, K. (2007) Design and comparison of 4 kV Neutral-point-clamped, flying capacitor and series-connected H-bridge multilevel converters. *IEEE Trans. Ind. Appl.*, **43**(4), 1032–1040.
42. Shukla, A., Ghosh, A., and Joshi, A. (2007) Capacitor voltage balancing schemes in flying capacitor multilevel inverters. *Proc. IEEE Power Elect. Spec. Conf. PESC-2007*, 17–21 June, Orlando, FL pp. 2367–2372.
43. Jin, B. S., Lee, W. K., Kim, T. J., Kang, D. W., and Hyun, D. S. (2005) A study on the multi-carrier PWM methods for voltage balancing of flying capacitor in the flying capacitor multilevel inverter. *Proc. 31st IEEE Ind. Elect. Conf. IECON*, 6–10 November, North Carolina, pp. 721–726.
44. Lee, S. G., Kang, D. W., Lee, W. H., and Hyun, D. S. (2001) The carrier-based PWM method for voltage balance of flying capacitor multilevel inverter. *Proc. 3rd IEEE Power Elect. Spec. Conf.*, **1**, 126–131.
45. Shukla, A., Ghosh, A., and Joshi, A. (2008) Improved multilevel hysteresis current regulation and capacitor voltage balancing schemes for flying capacitor multilevel inverter. *IEEE Trans. Power Elect.*, **23**(2), 518–529.
46. Lee, W. K., Kim, S. Y., Yoon, J. S., and Baek, D. H. (2006) A comparison of the carrier-base PWM techniques for voltage balance of flying capacitor in the the flying capacitor multilevel inverter. *Proc. 21st IEEE Appl. Power Elect. Conf. Exp.*, 19–23 March, Dallas, TX pp. 1653–1659.
47. Xin, M. C., Ping, S. L., Xu, W. T., and Bao, C. C. (2009) Flying capacitor multilevel inverters with novel PWM methods. *Procedia Earth and Planet. Sci.*, **1**, 1554–1560.
48. Khazraei, M., Sapahvand, H., Corzine, K., and Fredowski, M. (2010) A generalized capacitor voltage balancing scheme for flying capacitor multilevel converters. *Proc. 25th Appl. Power Elect. Conf. Exp.*, 6–10 March, Dallas, TX pp. 58–62.
49. Peng, F. Z. (2003) Z-source inverter. *IEEE Trans. Ind. Appl.*, **39**(2), 504–510.
50. Peng, F. Z., Shen, M., and Qian, Z. (2005) Maximum boost control of the Z-source inverter. *IEEE Trans. Power Elect.*, **20**(4), 833–838.
51. Shen, M., Wang, J., Joseph, A., Peng, F. Z., Tolbert, L. M., and Adams, D. J. (2006) Constant boost control of the Z-source inverter to minimize current ripple and voltage stress. *IEEE Trans. Ind. Appl.*, **42**(3), 770–778.
52. Badin, R., Huang, Y., Peng, F. Z., and Kim, H. G. (2007) Grid interconnected Z-source PV system. *Proc. IEEE PESC'07*, Orlando, FL, June, pp. 2328–2333.
53. Shen, M. and Peng, F. Z. (2008) Operation modes and characteristics of the Z-source inverter with small inductance or low power factor. *IEEE Trans. Ind. Elect.*, **55**(1), 89–96.
54. Peng, F. Z. (2008) Z-source networks for power conversion. *23rd Ann. IEEE App. Power Elect. Conf. Exp., APEC2008*, 24–28 February, Austin, TX, pp. 1258–1265.
55. Peng, F. Z. (2008) Recent advances and applications of power electronics and motor drives: Power converters. *34th Ann. Conf. IEEE Ind. Elect., IECON*, 10–13 November, Orlando, FL, pp. 10–13.
56. Peng, F. Z., Shen, M., and Holland, K. (2007) Application of Z-source inverter for traction drive of fuel cell-battery hybrid electric vehicles. *IEEE Trans. Power Elect.*, **22**(3), 1054–1061.
57. Peng, F. Z., Yuan, X., Fang, X., and Qian, Z. (2003) Z-source inverter for adjustable speed drives. *IEEE Power Elect. Lett.*, **1**(2), 33–35.
58. Peng, F. Z., Joseph, A., Wang, J. *et al.* (2005) Z-Source inverter for motor drives. *IEEE Trans. Power Elect.*, **20**(4), 857–863.
59. Anderson, J. and Peng, F. Z. (2008) A class of quasi-Z-source inverters. *IEEE Ind. Appl. Soc. Ann. Mtg., IAS '08*, 5–9 October., Edmonton, Alta, pp. 1–7.
60. Li, Y., Anderson, J., Peng, F. Z., and Liu, D. (2009) Quasi-Z-source inverter for photovoltaic power generation systems. *24th Ann. IEEE Appl. Power Elect. Conf. Exp., APEC 2009*, 15–19 February, Washington, DC pp. 918–924.

61. Park, J., Kim, H., Nho, E., Chun, T., and Choi, J. (2009) Grid-connected PV system using a quasi-Z-source inverter. *24th Ann. IEEE Appl. Power Elect. Conf. Exp., APEC 2009*, 15–19 February, Washington, DC pp. 925–929.
62. Murai, Y., Watanabe, T. and Iwasaki, H. (1987) Waveform distortion and correction circuit for PWM inverters with switching lag-times. *IEEE Trans. Ind. Appl.*, **1A-23** 881–886.
63. Jeong, S. G. and Park, M. H. (1991) The analysis and compensation of dead-time effects in PWM inverters. *IEEE Trans. Ind. Elect.*, **38**, 108–114.
64. Lin, J. L. (2002) A new approach of dead time compensation for PWM voltage inverters. *IEEE Trans. Circ. Syst. I-Fund. Theory Appl.*, **49**(4), 476–483.
65. Munoz, A. R. and Lipo, T. A. (1999) On-line dead time compensation technique for open-loop PWM VSI drives. *IEEE Trans. Power Elect.*, **14**(4), 683–689.
66. Victor G., Cgrdenas, M., Horta, S. M., and Echavarría, S. R. (2006) Elimination of dead time effects in three-phase inverters. *Proc. CIEP*, 14–17 October, Mexico, pp. 258–262.

# 4

## Field Oriented Control of AC Machines

### 4.1 Introduction

This chapter focuses on vector control of AC machines, particularly IM, PMSM, and DFIG. We consider these machines to be the most interesting for modern electric drives, and so the focus will be on their control and simulation. The control of AC machines can be classified into ‘scalar’ and ‘vector’ controls. Scalar controls are simple to implement and offer good steady-state response; however, the dynamics are slow because the transients are not controlled. To obtain high precision and good dynamics, vector control schemes have been invented for use with closed-loop feedback controls. Thus, this chapter focuses on the ‘vector control’ schemes of AC machines after a brief description of the scalar control method.

Adjustable speed drives offer significant energy savings and fast and precise responses in industrial applications. At the beginning of the 1970s [1–9], the principles of torque and flux control were introduced and called ‘field oriented control’ or ‘vector control’ for squirrel cage induction machines and later for synchronous machines. The vector control idea relies on the control of stator current space vectors in a similar, but more complicated, way to a DC machine. The advancement in adjustable speed AC drives was slow until the 1980s, when the microprocessor revolution made it possible to implement complex control algorithms, which made AC machines the dominating machine in the drives market.

The research on vector control of AC machines is active and up to date. The new advancements are high precision and include the use of novel solutions, such as the sensorless operation.

### 4.2 Induction Machines Control

Squirrel cage types of Induction Motors (IM) have been considered for a long time as the workhorse in industry [2]. It has been claimed that 90% of installed motors are of this type.



Among the reasons for their popularity are robustness, reliability, low price, and relatively high efficiency.

Different control methods are popular in the industry (e.g. scalar method (named V/f), vector control, direct torque control, etc.). In this chapter, we will first describe the V/f method, and then focus on the vector control approach.

#### 4.2.1 Control of Induction Motor using V/f Method

The aim of this section is to model a scalar control method for IM, named V/f = constant. This method is the simplest way for controlling this type of machine.

In this type of control, a constant ratio between the voltage magnitude and frequency is maintained. This is to keep it constant and is the optimal flux in the machine.

A well-known machine model is presented in Chapter 2 and can be rewritten as [1–8]:

$$u_{sx} = R_s i_{sx} + \frac{d\psi_{sx}}{d\tau} - \omega_a \psi_{sy} \quad (4.1)$$

$$u_{sy} = R_s i_{sy} + \frac{d\psi_{sy}}{d\tau} + \omega_a \psi_{sx} \quad (4.2)$$

It is assumed that the co-ordinate system is connected with stator current, hence:

$$\psi_{sx} = |\psi_s| \quad (4.3)$$

$$\psi_{sy} = 0 \quad (4.4)$$

which in a steady state would be

$$\frac{d\psi_{sx}}{d\tau} = 0 \quad (4.5)$$

Therefore:

$$u_{sx} = R_s i_{sx} \quad (4.6)$$

$$u_{sy} = R_s i_{sy} + \omega_a \psi_{sx} \quad (4.7)$$

The voltage vector magnitude is

$$|u_s| = \sqrt{u_{sx}^2 + u_{sy}^2} \quad (4.8)$$

$$|u_s| = \sqrt{(R_s i_{sx})^2 + (R_s i_{sy})^2 + (\omega_a \psi_{sx})^2 + 2 \cdot R_s i_{sy} \cdot \omega_a \psi_{sx}} \quad (4.9)$$

Neglecting stator resistance, the following is achieved:

$$|u_s| = \sqrt{(\omega_a \psi_{sx})^2} \tag{4.10}$$

Keeping constant motor flux magnitude at rated value (in per unit, this is 1), the following is correct:

$$|\psi_s| = 1 \text{ (rated value in per unit)} \tag{4.11}$$

Therefore, equation (4.13) becomes

$$|u_s| = \sqrt{(\omega_a)^2} \tag{4.12}$$

where

$$\omega_a = 2\pi f \tag{4.13}$$

Thus, in V/f control, a constant ratio between the voltage magnitude and frequency is maintained. This is to keep constant and optimal flux in the machine. The V/f control of the IM model is shown in Figure 4.1. It consists of the motor model and the control system model, as shown in Figure 4.2. All the models are described per unit unless otherwise specified. The Simulink software file of V/f control of the IM model is [IM\_Vbyf\_control]. The motor parameters are located in the [IM\_Vbyf\_param], which should be first executed.

### 4.2.1.1 Current and Flux Computation

The magnitude of current and flux can be calculated from the real and imaginary parts, as follows, and are also shown in Figure 4.3:

$$|I_s| = \sqrt{I_{s\alpha}^2 + I_{s\beta}^2} \tag{4.14}$$

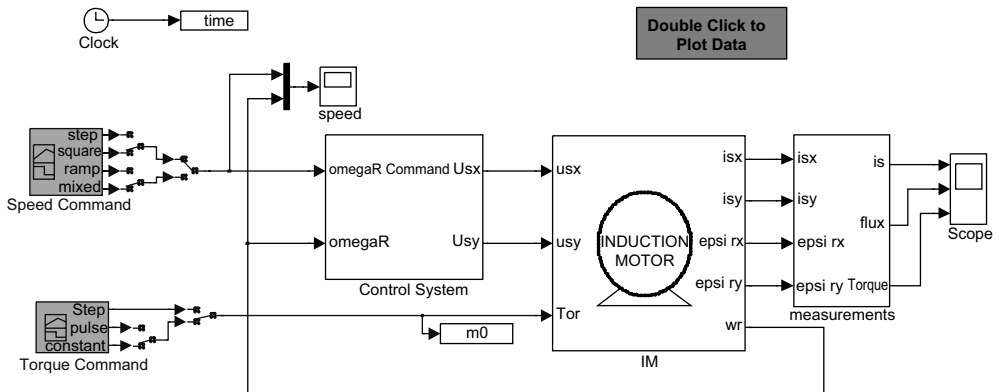


Figure 4.1 V/f control of an induction motor

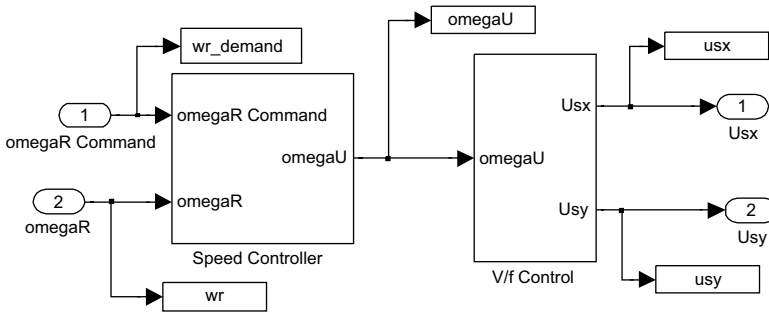


Figure 4.2 V/f control system model

$$|\psi_s| = \sqrt{\psi_{s\alpha}^2 + \psi_{s\beta}^2} \tag{4.15}$$

The motor torque is given by [1–7]

$$M_e = \frac{L_m}{JL_r} (\psi_{r\alpha} i_{s\beta} - \psi_{r\beta} i_{s\alpha}) \tag{4.16}$$

### 4.2.1.2 Control System

The control system model is a PI speed controller that calculates the stator voltage. The PI speed controller is shown in Figure 4.4. The integrator is only active when the error is within 0.4 per unit.

The V/f control calculates the real and imaginary parts of the stator voltage, based on constant V/f formulation (Figure 4.5). The magnitude of the stator voltage is calculated from

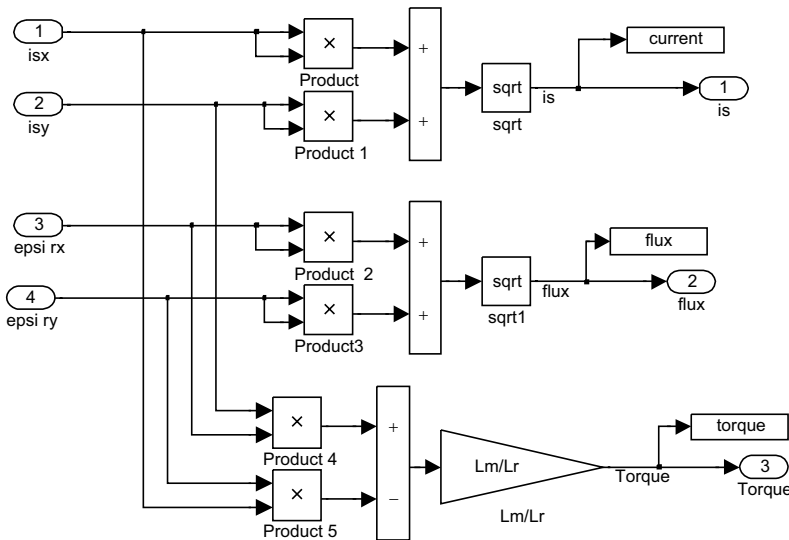
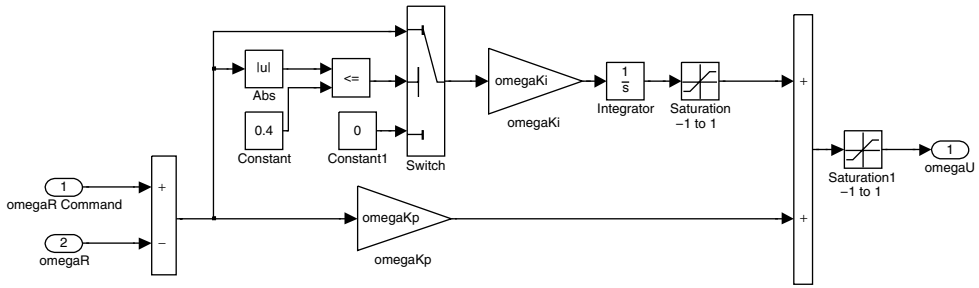


Figure 4.3 Current, flux, and motor torque calculations



**Figure 4.4** Limited authority PI control systems model

the absolute value of the PI controller output and the angle is calculated by integrating the PI controller output.

**4.2.1.3 Simulation Results**

The simulation result for square pulse command in speed is shown in Figure 4.6. The given results are selected examples of machine response.

*4.2.2 Vector Control of Induction Motor [1–16]*

Squirrel cage IM (and other types of AC machines) cannot be controlled as easily as they can be in the case of separately excited DC motor. For all types of control, the magnetic flux and produced torque should be decoupled for maintaining linearity between input and output and for achieving high dynamic drive. In the case of AC machines, the dynamic models are non-linear and more complex than those in DC machines.

Overcoming this problem became possible by using space vector representations of AC machines. The flux oriented control methods allow representation of the mathematically complicated induction machine in a similar manner to DC machines for obtaining control linearity, decoupling, and high performance AC drives.

Proper control of motor speed and produced electromagnetic torque is needed in high performance adjustable speed drives. The torque production depends on the armature current and machine flux. The magnetic field should be kept at the optimal level (rated flux) for producing maximum torque, while protecting against entering the saturation level. Keeping

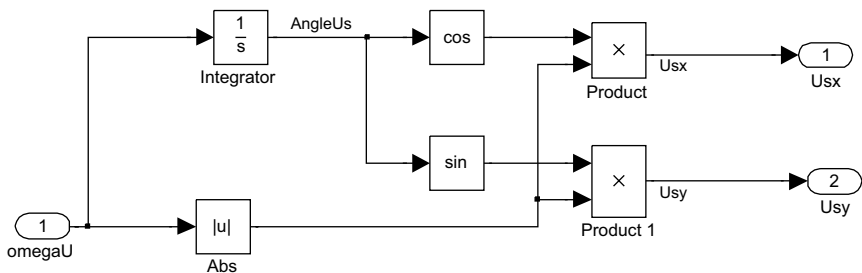


**Figure 4.5** V/f control

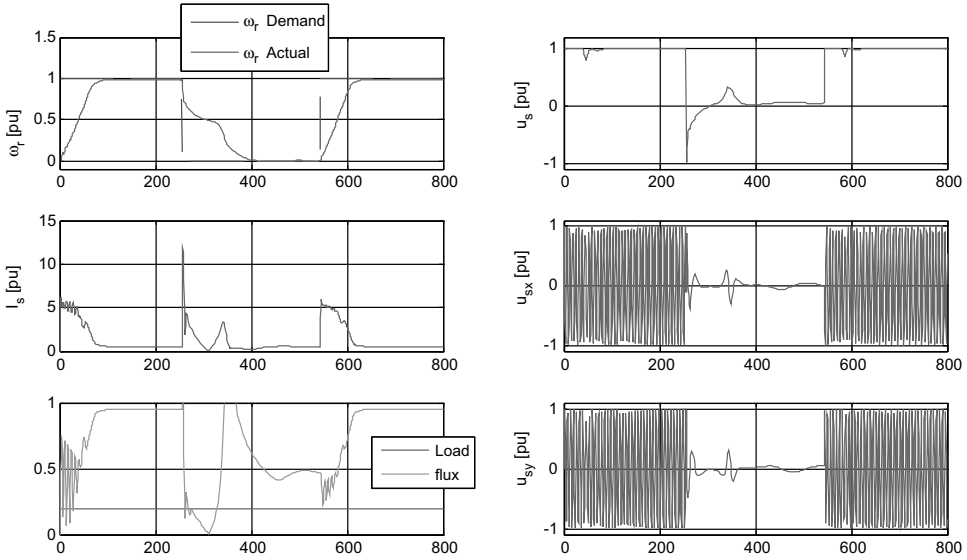


**Figure 4.6** Simulation results

constant flux allows for obtaining a linear relationship between motor torque and armature current. In this way, linear control is achieved with high machine dynamics.

Decoupled control between flux and torque is easily achieved in the case of separately excited DC motors, but it is not so simple for AC drives. In squirrel cage motors, the controlled signal is only the stator current because the rotor current is inaccessible. In such a way, the torque equation is not linear, so linear control with maximum torque production is difficult to achieve.

The vector control approach was first formulated by Blaschke [9] to overcome this problem. The principle of field-oriented control was introduced and decoupled control between torque and flux was possible.

In summary, by using vector representation, it is possible to present the variables in an arbitrary co-ordinate system. If the co-ordinate system rotates together with a flux space vector, then we use different terminology: flux-oriented control, rotor-oriented, etc.

Relationships of motor models presented in Chapter 2 can be described in frame  $d$ - $q$ , rotating with rotor flux on the  $d$  axis (the  $q$  flux component is zero  $\psi_{sq} = 0$ ), as

$$\frac{di_{sd}}{dt} = a_1 \cdot i_{sd} + a_2 \cdot 0 + \omega_{\psi r} \cdot i_{sq} + \omega_r \cdot a_3 \cdot 0 + a_4 \cdot u_{sd} \quad (4.17)$$

$$\frac{di_{sq}}{dt} = a_1 \cdot i_{sd} + a_2 \cdot 0 - \omega_{\psi r} \cdot i_{sd} - \omega_r \cdot a_3 \cdot \Psi_r + a_4 \cdot u_{sq} \quad (4.18)$$

$$\frac{d\Psi_r}{dt} = a_5 \cdot \Psi_{rd} + (\omega_{\psi r} - \omega_r) \cdot 0 + a_6 \cdot i_{sd} \quad (4.19)$$

$$0 = a_5 \cdot 0 - (\omega_{\psi r} - \omega_r) \cdot \Psi_r + a_6 \cdot i_{sq} \quad (4.20)$$

$$\frac{d\omega_r}{dt} = \frac{L_m}{L_r J} (\Psi_r i_{sq} - 0 \cdot i_{sd}) - \frac{1}{J} m_o \quad (4.21)$$

Hence:

$$M_{em} = \frac{L_m}{L_r} (\Psi_r i_{sq}) \tag{4.22}$$

In this way, it was possible to represent the electromagnetic torque as a product of a flux-producing current and a torque-producing current. Keeping constant flux, an induction machine may be controlled, like a separately excited DC machine.

Assuming that the flux is kept constant (at rated level):

$$0 = a_5 \cdot \Psi_{rd} + a_6 \cdot i_{sd} \tag{4.23}$$

which gives

$$i_{sd} = \frac{-a_5}{a_6} \cdot \Psi_{rd} \tag{4.24}$$

From the above equations, it is evident that in a quadrant co-ordinate system  $dq$ , the axis  $d$  is consistent with the direction of the rotor flux linkage vector and the component on axis  $q$  affects the quantity of electromagnetic torque.

#### 4.2.2.1 Basic Control Scheme

Figure 4.7 describes the basic scheme of vector control of an AC machine.

In typical AC drive systems, two motor phase currents and the DC bus voltage are measured. The measured currents are transformed using the Clarke transformation block into a stationary

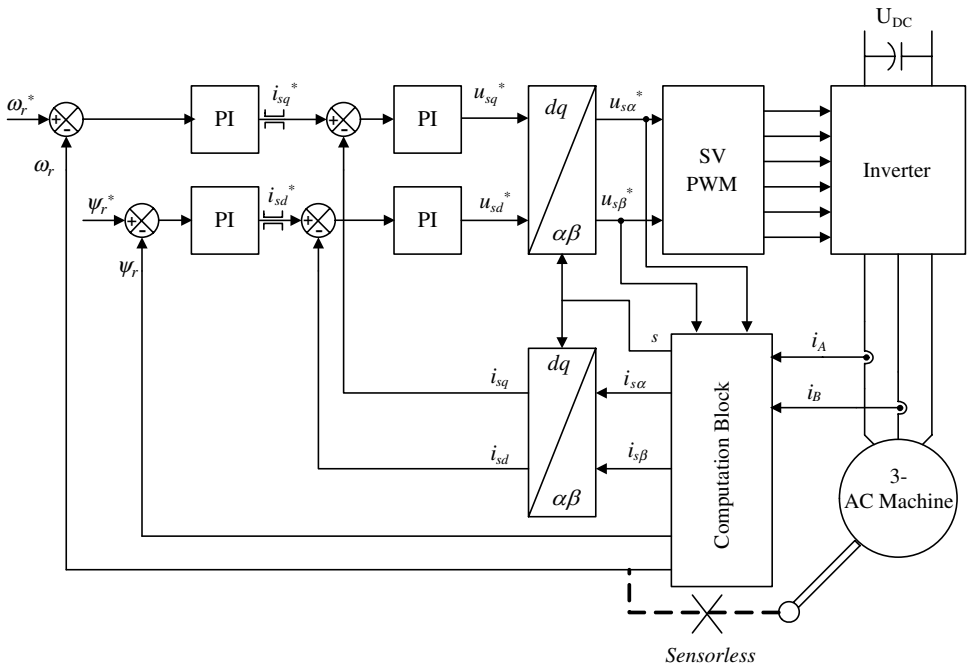


Figure 4.7 Basic scheme of FOC for the three-phase AC machine

frame ( $i_{s\alpha}$  and  $i_{s\beta}$ ). These last two components are further transformed, using the Park transformation, into rotating components ( $dq$ ). The PI controllers compare the command values with the measured components (after transformation) and command proper values to establish the desired condition.

The outputs of the controllers are transformed from a rotating to a stationary frame using the Park transformation. The commanded signals of the stator voltage are sent to the pulse width modulation (PWM) block.

#### 4.2.2.2 MATLAB/Simulink Model for Induction Motor Vector Control

The control scheme of an IM is shown in Figure 4.8. The control depends on vector transformation using Park/Clark transformations. The idea is to control this type of machine in a similar way to a separately excited DC motor, in which the torque is controlled separately from the flux. In this way, decoupled control between the two subsystems is achieved when the flux is kept constant.

For control purposes, the motor model is first transformed into the  $d-q$  axis model. It consists of a motor model, various transformations, and the control system model. All the models are in per unit unless otherwise specified. The Simulink software file of vector control of IM model in [IM\_vector\_control]. The motor parameters are located in the [IM\_param], which should be first executed.

The IM model in Simulink is described in Chapter 2. The motor current, flux magnitude are calculated in the following:

$$|I_s| = \sqrt{I_{s\alpha}^2 + I_{s\beta}^2} \tag{4.25}$$

$$|\psi_s| = \sqrt{\psi_{s\alpha}^2 + \psi_{s\beta}^2} \tag{4.26}$$

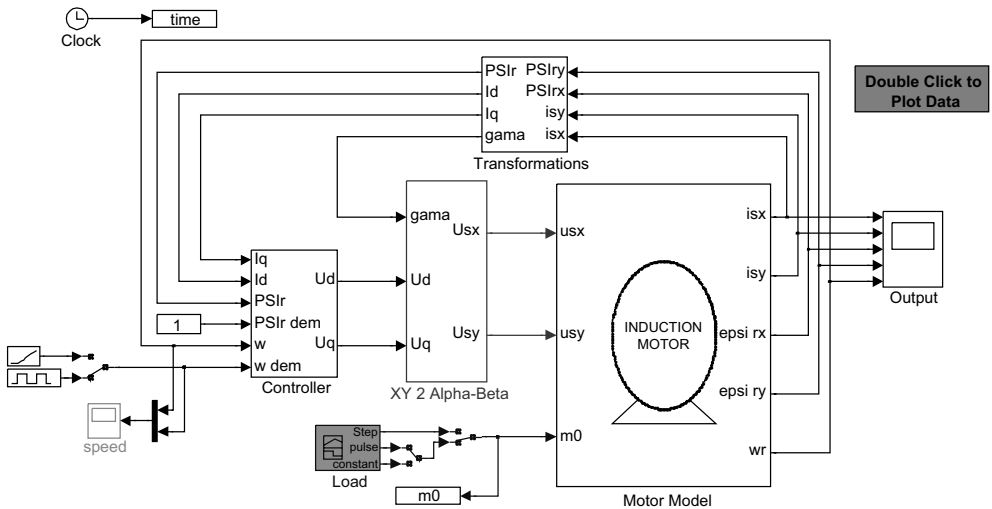
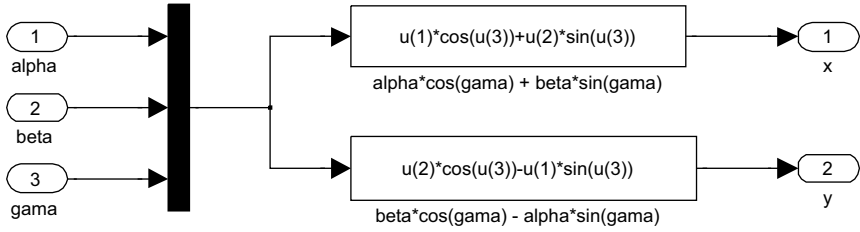
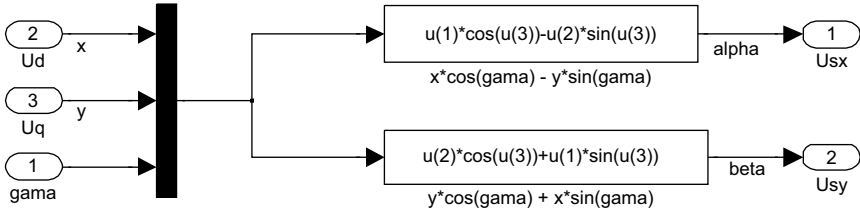


Figure 4.8 Induction motor control



**Figure 4.9**  $\alpha$ - $\beta$  to  $x$ - $y$  transformation



**Figure 4.10**  $x$ - $y$  to  $\alpha$ - $\beta$  transformation

**4.2.2.3 Variables Transformation**

The machine variables can be transformed into  $dq$  components by using the ‘ $\alpha$ - $\beta$  to  $x$ - $y$ ’ transformation, as shown in Figure 4.9. The block in Figure 4.9 calculates the voltages to be applied in the  $d$ - $q$  axis. The  $d$ - $q$  axis voltages are converted into the  $x$ - $y$  components by ‘ $x$ - $y$  to  $\alpha$ - $\beta$ ’ transformations, as shown in Figure 4.10. Both of these transformations require the rotor flux angle ( $\text{gama}$ ) and the rotor flux magnitude, which are calculated by using the transformation in Figure 4.11.

**4.2.2.4 Control Scheme**

The inner and outer loop control system model is shown in Figure 4.12. The inner loop controller works on the  $d$ - $q$  axis model. The outer loop controller works on the flux and speed to calculate the demand for  $I_d$  and  $I_q$  currents, respectively. The inner loop controller then controls the  $I_d$  and  $I_q$  currents.

**4.2.2.5 Simulation Results**

The simulation results for square pulse demand in speed are shown in Figure 4.13.

The given simulation results are selected examples of machine response.

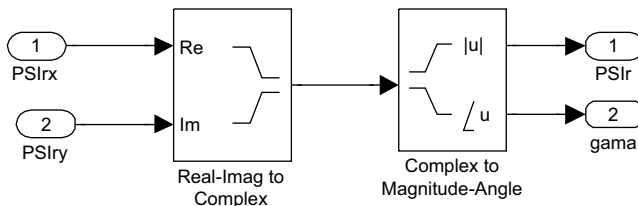


**Figure 4.11** Real-imaginary to magnitude-angle transformation



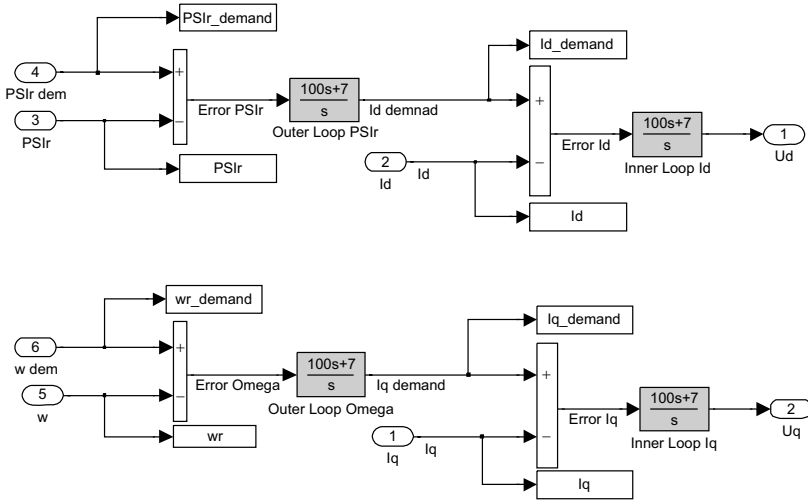


Figure 4.12 Two-loop control system for an induction motor

### 4.2.3 Direct and Indirect Field Oriented Control

Motor state variables may be identified using direct measurement or indirectly by using machine models or observers. In most control schemes, the optimal variables selected as state space are stator current components and rotor (or stator) flux components. In the direct, as well as indirect, control methods, the stator current is measured directly. In direct control schemes,

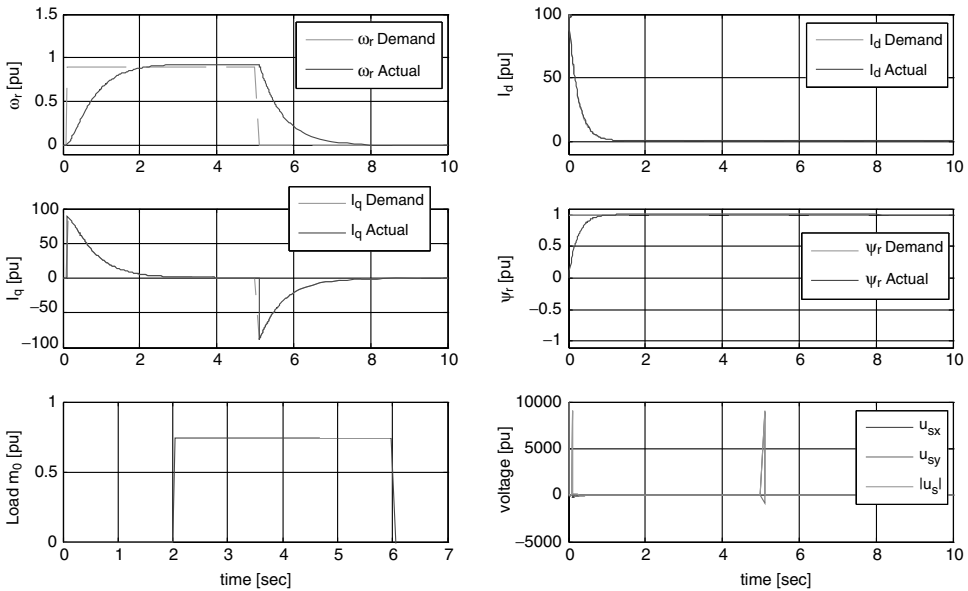


Figure 4.13 Simulation Results

the machine's magnetic field is measured using special sensors located in the machine air gap. This method is not practical and can be used for laboratory investigations; however, for practicality, the machine flux is computed using special methods.

These two basic advanced methods are used for flux computation and control purpose. A first method is based on modeling the AC machine by its state space equations. A sinusoidal magnetic field in the machine is assumed. The machine models are defined as open-loop (e.g. stator voltage model or as closed-loop adaptive observers [1–9,11–16]). The adaptive observers are receiving more attention than open loop models, because of their robustness against parameters variation and higher computation precision.

#### 4.2.4 Rotor and Stator Flux Computation

The stator flux vector could be computed from the next well-known voltage models [1–9,13,14]:

$$\bar{\psi}_s = \int (\bar{u}_s - R_s \bar{i}_s) dt \quad (4.27)$$

$$\bar{\psi}_s = L_s \bar{i}_s + L_m \bar{i}_r \quad (4.28)$$

The rotor flux vector is

$$\bar{\psi}_r = L_r \bar{i}_r + L_m \bar{i}_s \quad (4.29)$$

After some algebra, we get the next expressions of rotor flux vector components in the stationary co-ordinate system ( $\alpha\beta$ ):

$$\psi_{r\alpha} = \frac{L_r}{L_m} (\psi_{s\alpha} - \delta L_s i_{s\alpha}) \quad (4.30)$$

$$\psi_{r\beta} = \frac{L_r}{L_m} (\psi_{s\beta} - \delta L_s i_{s\beta}) \quad (4.31)$$

The rotor flux magnitude is computed as

$$|\psi_r| = \sqrt{\psi_\alpha^2 + \psi_\beta^2} \quad (4.32)$$

The angle of the rotor flux position  $\gamma_s$  is

$$\gamma_s = \tan^{-1} \left( \frac{\psi_{r\beta}}{\psi_{r\alpha}} \right) \quad (4.33)$$

The disadvantage of this method is that it is operationally limited at lower frequencies (below 3%), because of problems with integrating small signals at low frequencies.

An increase of lower speed operation range is possible using the current model [3,6]:

$$\hat{\tau}'_\sigma \frac{d\hat{i}_s}{d\tau} = \frac{k_r}{\hat{r}_\sigma \hat{\tau}_r} (1 - j\hat{\omega}_m \hat{\tau}_r) \hat{\psi}_r + \frac{1}{\hat{r}_\sigma} u_s \quad (4.34)$$

The model fails in operation at higher speeds, because of differentiating higher signals.

The control systems designed using those open models are sensitive to stator and rotor resistances. For the voltage model, the effect of stator resistance is particularly visible at lower speed range. The method is simple but needs significant modifications in order to increase the operation precision and cancel the DC drift for lower speed operation [12–15].

#### 4.2.5 Adaptive Flux Observers

In this section, we will discuss the basic description of flux closed loop observers. More examples will be given in Chapter 9.

The full-order observer used for estimating state variables (mostly stator current and rotor flux components) is described as [12]

$$\frac{d}{dt}\hat{x} = \hat{A}\hat{x} + Bu_s + G(\hat{i}_s - i_s) \quad (4.35)$$

In this,  $\hat{\phantom{x}}$  means the estimated value, and  $G$  is the feedback observer gain.

One of the commonly used observers is the Luenberger observer [16], which is mainly used for flux and stator current computation. The equations representing this type of observer are development of the machine model discussed in Chapter 2. The equations may be presented as [15]

$$\frac{d\hat{i}_{s\alpha}}{dt} = a_1 \cdot \hat{i}_{s\alpha} + a_2 \cdot \hat{\Psi}_{r\alpha} + \omega_r \cdot a_3 \cdot \hat{\Psi}_{r\beta} + a_4 \cdot u_{s\alpha} + k_i(i_{s\alpha} - \hat{i}_{s\alpha}) \quad (4.36)$$

$$\frac{d\hat{i}_{s\beta}}{dt} = a_1 \cdot \hat{i}_{s\beta} + a_2 \cdot \hat{\Psi}_{r\beta} - \omega_r \cdot a_3 \cdot \hat{\Psi}_{r\alpha} + a_4 \cdot u_{s\beta} + k_i(i_{s\beta} - \hat{i}_{s\beta}) \quad (4.37)$$

$$\frac{d\hat{\Psi}_{r\alpha}}{dt} = a_5 \cdot \hat{\Psi}_{r\alpha} - \omega_r \cdot \hat{\Psi}_{r\beta} + a_6 \cdot \hat{i}_{s\alpha} - k_{f1}(i_{s\alpha} - \hat{i}_{s\alpha}) - k_{f2}(i_{s\beta} - \hat{i}_{s\beta}) \quad (4.38)$$

$$\frac{d\hat{\Psi}_{r\beta}}{dt} = a_5 \cdot \hat{\Psi}_{r\beta} + a_6 \cdot \hat{i}_{s\beta} + \omega_r \hat{\Psi}_{r\alpha} + k_{f2}(i_{s\alpha} - \hat{i}_{s\alpha}) - k_{f1}(i_{s\beta} - \hat{i}_{s\beta}) \quad (4.39)$$

where

$$a_1 = -\frac{R_s L_r^2 + R_r L_m^2}{L_r w} \quad (4.40)$$

$$a_2 = \frac{R_r L_m}{L_r w} \quad (4.41)$$

$$a_3 = \frac{L_m}{w} \quad (4.42)$$

$$a_4 = \frac{L_r}{w} \quad (4.43)$$

$$a_5 = -\frac{R_r}{L_r} \quad (4.44)$$

$$a_6 = R_r \frac{L_m}{L_r} \tag{4.45}$$

$$w = \sigma L_r L_s = L_r L_s = L_r L_s - L_m^2 \tag{4.46}$$

$$\sigma = 1 - \frac{L_m^2}{L_s L_r} \tag{4.47}$$

Here,  $u_{s\alpha}, u_{s\beta}$  are voltage components;  $i_{s\alpha}, i_{s\beta}$  are measured current components;  $\hat{i}_{s\alpha}, \hat{i}_{s\beta}$  are estimated current components, with  $\hat{\Psi}_{r\alpha}, \hat{\Psi}_{r\beta}$  as estimated rotor flux components;  $R_s, R_r$  are motor resistances;  $L_s, L_r, L_m$  motor inductances;  $\omega_r$  is rotor angular speed; and  $k_i, k_{f1}, k_{f2}$  are constants. Based on the above differential equations, the Luenberger observer is shown in Figure 4.14.

The Simulink software file of vector control of IM model is [IM\_VC\_ Luenberger]. The motor parameters are located in the model initialization function.

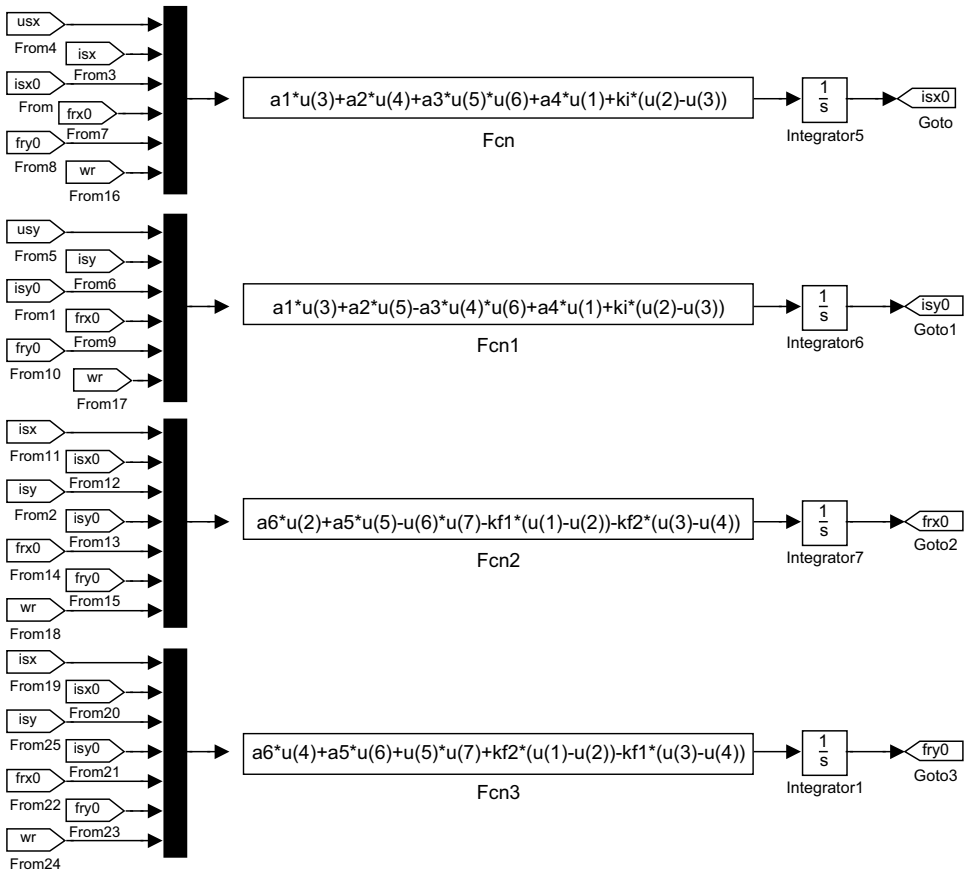
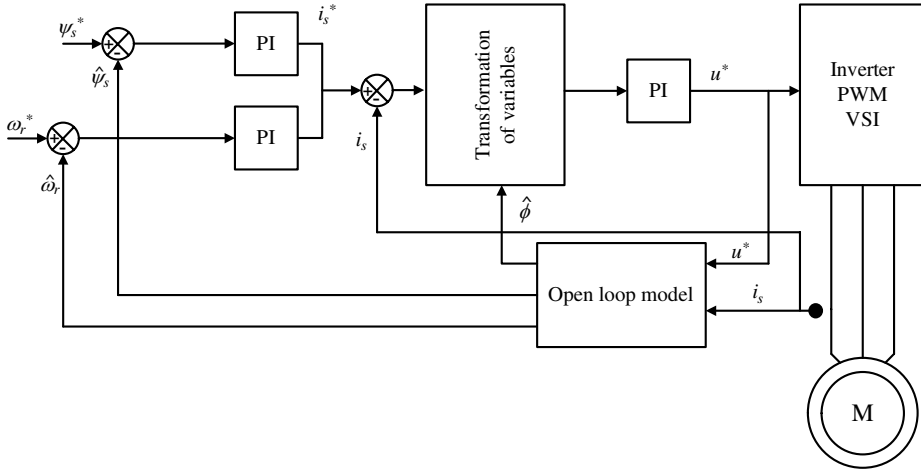


Figure 4.14 Simulink diagram of the Luenberger observer for stator currents and rotor fluxes estimator



**Figure 4.15** Stator flux oriented vector control

#### 4.2.6 Stator Flux Orientation

Stator flux oriented control (Figure 4.15) is less sensitive to machine parameters than rotor field orientation [11,13,17]. The usual method for computing stator flux is the open loop voltage model. Such equations are sensitive to stator resistance, which is dominant only at lower speeds [6]. The method enables producing more torque in the field weakening region than RFO, as will be discussed in the next section.

The use of the SFO scheme in field weakening is an excellent solution for many existing problems. This control principle gives a solution for decoupled control at field weakening. The operation at the absolute voltage limit of the inverter for maximum torque production eliminates the voltage margin required by the current controllers to adjust the respective current components  $i_d$  and  $i_q$ . Decoupled control of torque and flux would then become difficult in a classical vector control scheme [17,19].

#### 4.2.7 Field Weakening Control

One of the important applications of the machine is its running at the field weakening region, in which it operates at speeds higher than the rated one [17–24]. Such an operation is required in specific applications, such as spindle and traction drives.

The reason for flux weakening (decreasing) is that the magnetic field of the machine operating above rated speed level would be decreased due to the limit in the machine's voltage capability, which is imposed by a stator winding voltage limit and the DC link voltage [17–24].

To increase the produced torque to a maximum level in the field weakening region, it is essential to properly adjust the machine's magnetic field by maintaining the maximum voltage and maximum current. The loss of torque and power in the case of not properly adjusting the machine flux (e.g. in the case of  $1/\omega$  method) is up to 35% [18–23].

Therefore, the machine flux should be weakened to such a level that it would guarantee a maximum possible torque at the whole speed range.

Field weakening control can be categorized into three methods [17–24], including:

1. adjustment of the machine flux in inverse proportion to speed ( $1/\omega$ );
2. forward control of the flux based on simplified machine equations; and
3. closed loop control of the stator voltages to keep a maximum level.

For the conventional control method ( $1/\omega$ ), the flux is established inversely proportional to the motor speed. The DC link voltage cannot be fully utilized for maximum torque production, which means this method is not able to provide the maximum torque in the field weakening region. The reason is that enough of the voltage margin needed to control the stator current cannot be achieved [17,19].

The second method is based on simplified machine equations, making it parameter dependent. It gives reasonable results, assuming that machine parameters are known. Indeed, this type of control is not a preferable and optimal way for maximum torque control at the field weakening region.

The voltage control field weakening method ensures maximum torque production at the whole field weakening region when in a steady-state. The method provides maximum required torque during a steady state, and is not dependent on motor parameters and DC link voltage.

#### 4.2.7.1 Current and Voltage Limits for Maximum Torque Production

Current limiting during an overload condition in the field weakening must be controlled, in order to limit the torque producing current component  $i_q$ , while giving the priority to the flux producing component  $i_d$ . The  $i_q$  must be reduced to keep the total stator current within the maximum level imposed by the inverter and machine's capabilities. Hence, the optimum flux and maximum torque is achieved at field weakening [19].

The limit for the maximum voltage is reached when the system operates at maximum modulation index [19]. The inverter DC link voltage sets the maximum stator voltage limit. The priority in the voltage is for the  $d$  component  $u_d$ , responsible for machine excitation to insure the optimal flux and hence, the maximum possible torque. The limiting condition is  $u_a \leq \sqrt{u_{smax}^2 - u_d^2}$ , where  $u_{smax}$  is limited by inverter DC bus [19,20,22–24].

The block diagram for the control scheme at field weakening is shown in Figure 4.16 and is widely described in [19]. The system operates with a stator field or rotor field orientation. An open loop voltage model is used for estimating the machine flux components and transformation angle and even the rotor angular speed  $\omega$ .

### 4.3 Vector Control of Double Fed Induction Generator (DFIG)

#### 4.3.1 Introduction

The DFIG is a rotor-wound three-phase induction machine that is connected to the AC supply from both stator and rotor terminals (Figure 4.17). The stator windings of the machine are connected to the utility grid without using power converters, and the rotor windings are fed by an active front-end converter. The machine can be fed by current or voltage source inverters with controlled voltage magnitude and frequency [12,25–32].

In the control schemes of DFIM, two output variables in the stator side are generally defined and used for the control. These defined variables could be electromagnetic torque and reactive

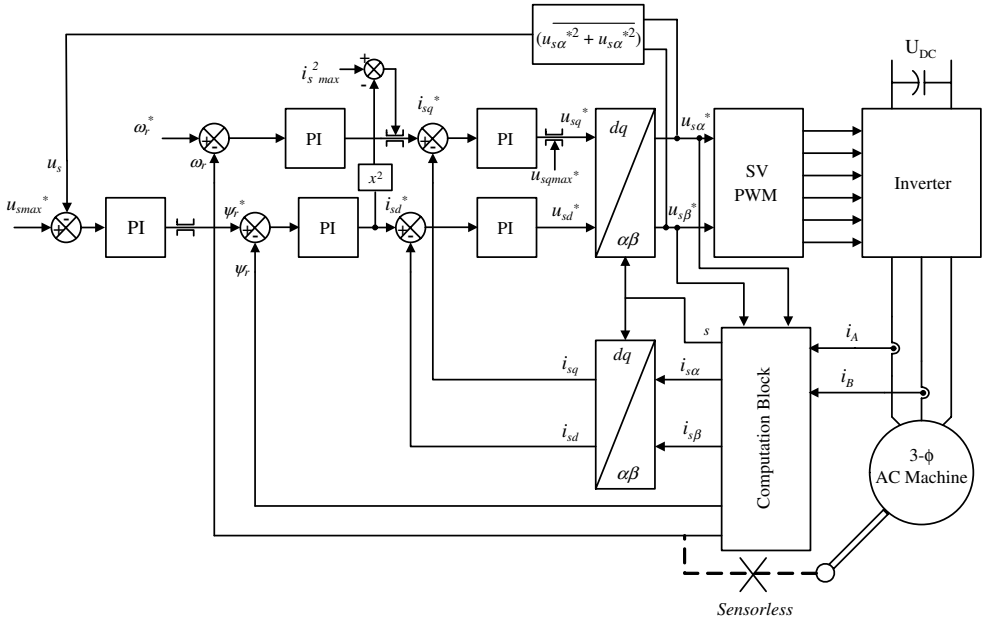


**Figure 4.16** Induction motor field weakening system

power, active and reactive powers, or stator voltage and its frequency. Different structures are used to control each pair of such variables.

The DFIM is popular and widely adopted for high power wind generation systems and other types of generators with similar variable speed high power sources (e.g. hydro systems). The advantage of using this type of machine is that the required converter capacity is much lower (up to three times lower) than those that connect the converter to the stator side [12,25–27,32]. Hence, the costs and losses in the conversion system are drastically reduced [1].

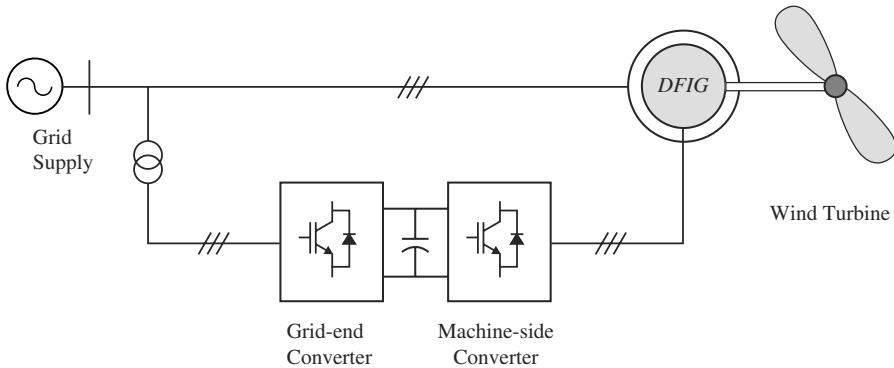


**Figure 4.17** General view of DFIG connected to wind system and utility grid

DFIG can be used either in an autonomous generation system (stand-alone), or in parallel with the grid. If the machine is working autonomously, the stator voltage and frequency are selected as the controlled signals. However, when the machine is connected to the infinite bus, the stator voltage and frequency are dictated by the system. In such situations, the controlled variables are the active and reactive powers [12,27–32]. Indeed, there are different types of control strategies for this type of machine; however, the most popular is vector control, which has different orientation frames similar to the squirrel cage IM, but the most popular of these is the stator orientation scheme.

### 4.3.2 Vector Control of DFIG Connected with the Grid ( $\alpha\beta$ Model)

The mathematical model of DFIM is similar to the squirrel cage induction machine, the only difference being that the rotor voltage is not zero. The machine model is presented in Chapter 2.

The active and reactive powers of stator and rotor circuits are needed in the control of DFIG and may be described in per unit as [32,38]

$$P_s = (v_{ds}i_{ds} + v_{qs}i_{qs}) \tag{4.48}$$

$$Q_s = (v_{qs}i_{ds} - v_{ds}i_{qs}) \tag{4.49}$$

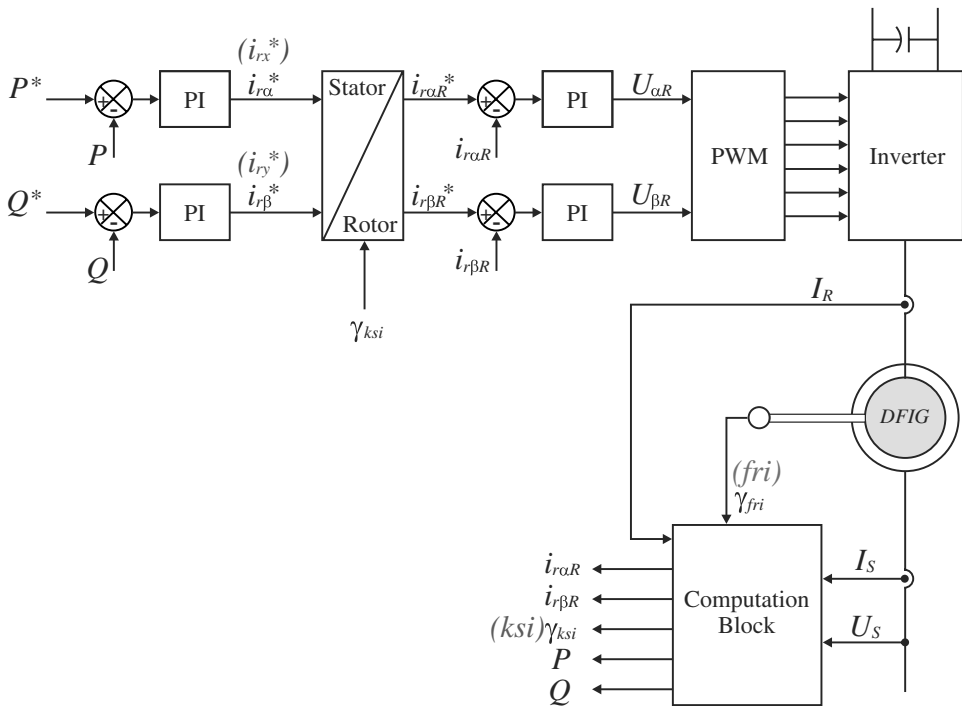


**Figure 4.18** Block diagram of the DFIG control system



$$P_r = (v_{dr}i_{dr} + v_{qr}i_{qr}) \tag{4.50}$$

$$Q_r = (v_{qr}i_{dr} - v_{dr}i_{qr}) \tag{4.51}$$

The DFIG system with vector control scheme is shown in Figure 4.18, and consists of a DFIG model presented in the  $\alpha\beta$  frame and control system part. All variables and parameters are in per unit unless otherwise specified. In practice, vector control of this machine is similar to the vector control of the squirrel cage IM with a difference in controlled variables. The control depends on vectors transformation from three-phase to rotating frame.

The control scheme was programmed in MATLAB/Simulink, as shown in Figure 4.19. The Simulink software file of vector control of double fed induction generator scheme is [DFIG\_VC\_model]. The scheme parameters are located in [DFIG\_VC\_init], which should be first executed.

The DFIG model consists of different blocks related to the machine model, computation blocks, and control part, as will be described below.

The machine model in the stationary frame is given in Chapter 2 (Figure 2.10).

### 4.3.3 Variables Transformation

#### 4.3.3.1 Stator to Rotor Transformation

The stator parameters (flux, current, and voltage) are converted into the rotor reference frame by using the following transformation:

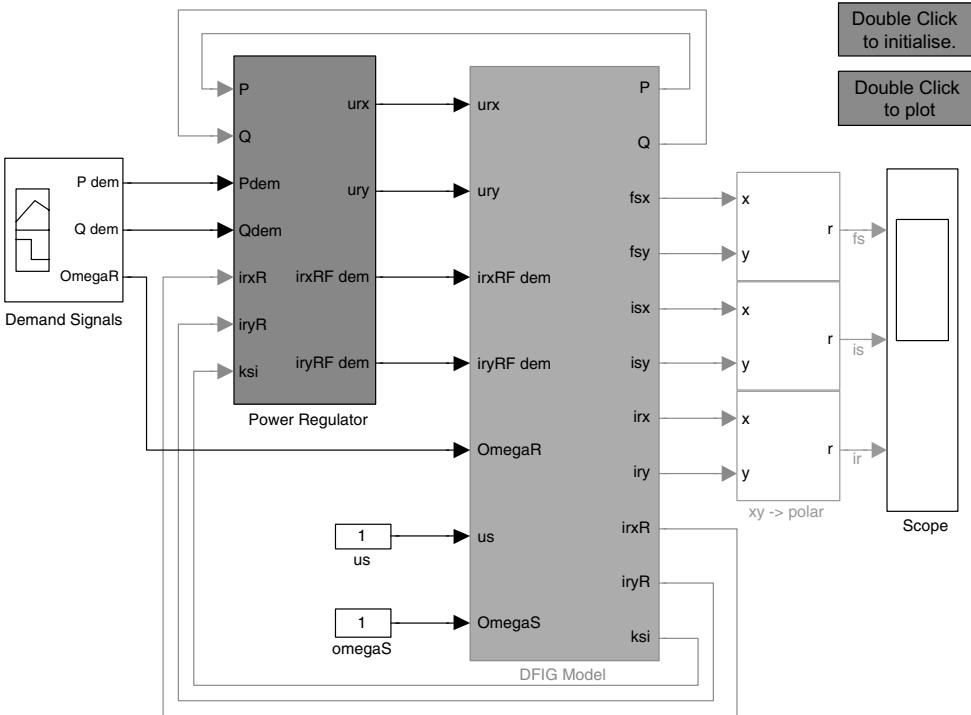
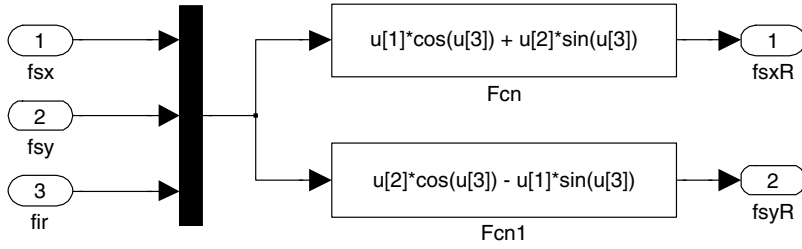


Figure 4.19 DFIG power regulation model



**Figure 4.20** Stator to rotor transformation

$$\phi_{sxR} = \phi_{sx} \cos \gamma_{fir} + \phi_{sy} \sin \gamma_{fir} \tag{4.52}$$

$$\phi_{syR} = \phi_{sy} \cos \gamma_{fir} + \phi_{sx} \sin \gamma_{fir} \tag{4.53}$$

These equations are modeled in Figure 4.20.

**4.3.3.2 Rotor to Stator Transformation**

The rotor parameters (flux, current, and voltage) are converted into the stator reference frame by using the following transformation:

$$i_{rx} = i_{rxR} \cos \gamma_{fir} - i_{ryR} \sin \gamma_{fir} \tag{4.54}$$

$$i_{ry} = i_{rxR} \sin \gamma_{fir} + i_{ryR} \cos \gamma_{fir} \tag{4.55}$$

The above equations are shown in Figure 4.21. The angle  $\gamma_{fir}$  is in the rotor angular position (fir in MATLAB/Simulink), is shown in Chapter 2.

**4.3.3.3 Stator Current Relationship**

The relationship between stator currents, stator flux, and rotor current is

$$i_{sx} = \frac{\phi_{sx}}{L_s} - \frac{L_m}{L_s} i_{rx} \tag{4.56}$$

$$i_{sy} = \frac{\phi_{sy}}{L_s} - \frac{L_m}{L_s} i_{ry} \tag{4.57}$$

These equations are programmed, as shown on Figure 4.22.

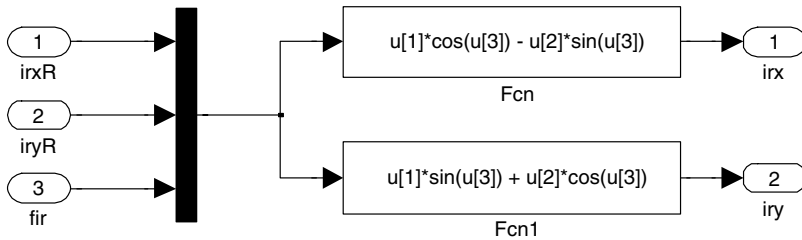


**Figure 4.21** Rotor to stator transformation

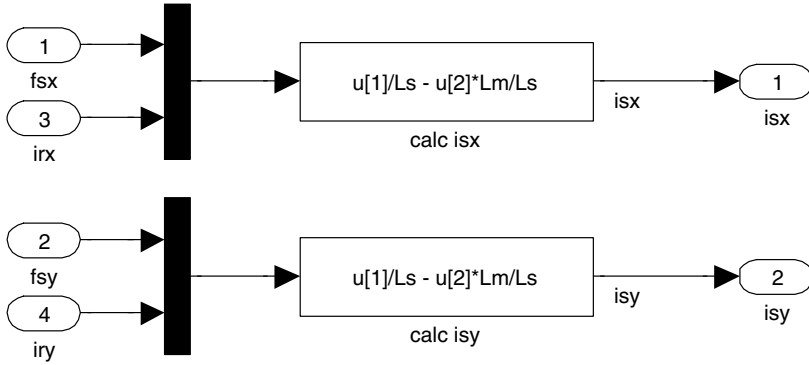


Figure 4.22 Stator current calculations

### 4.3.3.4 Power Calculations

The active and reactive power components are given as

$$P = u_{sx}i_{sxF} + u_{sy}i_{syF} \tag{4.58}$$

$$Q = u_{sy}i_{sxF} - u_{sx}i_{syF} \tag{4.59}$$

The index F denotes the filtered value. The filtration is not essential for the control; however, it provides smoother waveforms. Additional filters may be added to other variables if necessary. These equations are modeled, as shown in Figure 4.23.

### 4.3.3.5 Control System

Cascade control is used for power regulation. The PI control for active and reactive power provides the demand for an inner current loop, as shown in Figure 4.24. The active power controller commands the rotor current in the  $\alpha$  frame ( $i_{rx}$ ) in the stator reference frame. The

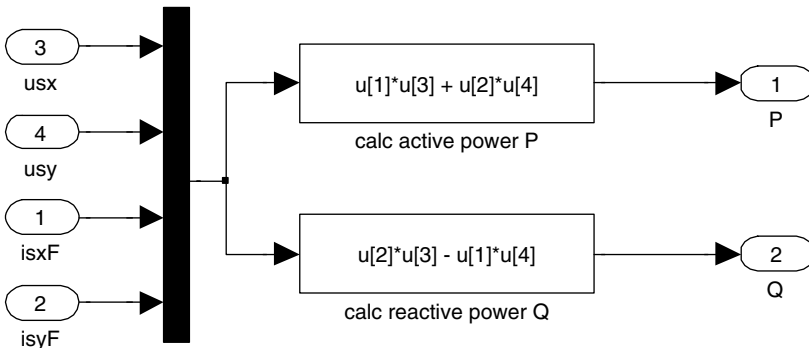
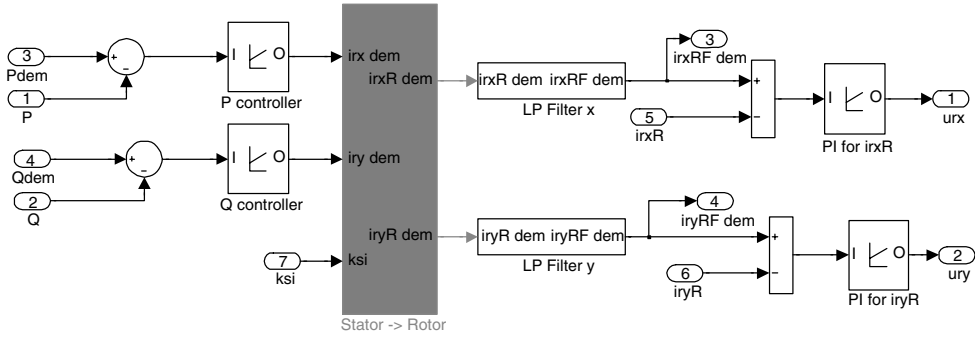


Figure 4.23 Active and reactive power calculations



**Figure 4.24** Cascaded control system model

reactive power controller commands the  $\beta$  component of this current. The angle  $\gamma_{ksi}$  is the angle between stator flux and rotor speed ( $\gamma_{ksi}$  in MATLAB/Simulink), as shown in Chapter 2. After transformation from stator flux reference frame to rotor speed frame, the  $\alpha\beta$  rotor current components  $i_{rxR}$  and  $i_{ryR}$  are obtained. Two additional PI controllers are used to generate the rotor voltage for the PWM voltage inverter. To simplify this, we neglect this inverter and command those two voltages directly to the DFIG model.

### 4.3.4 Simulation Results

The simulation result for power regulation with step changes in speed, which controls the active and reactive powers for different speeds, is shown in Figures 4.25 and 4.26.

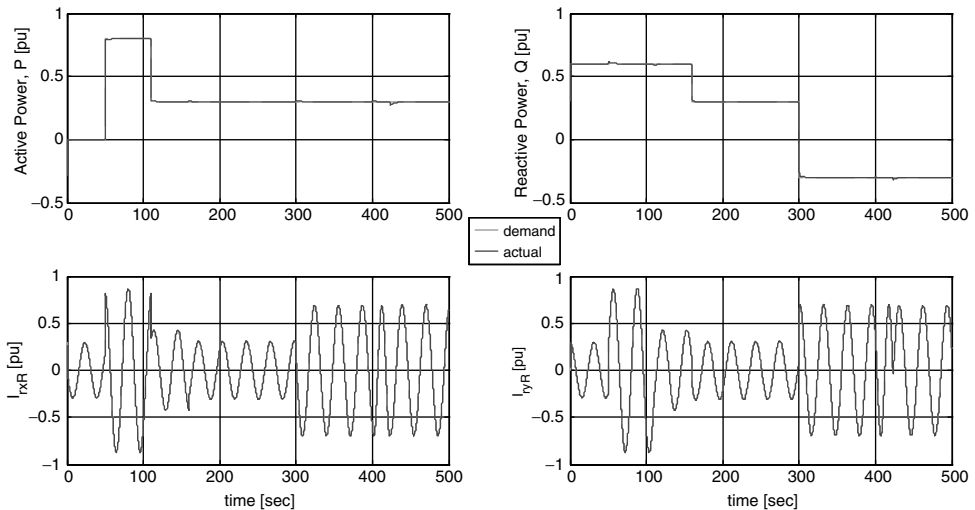


**Figure 4.25** Simulation results – tracking

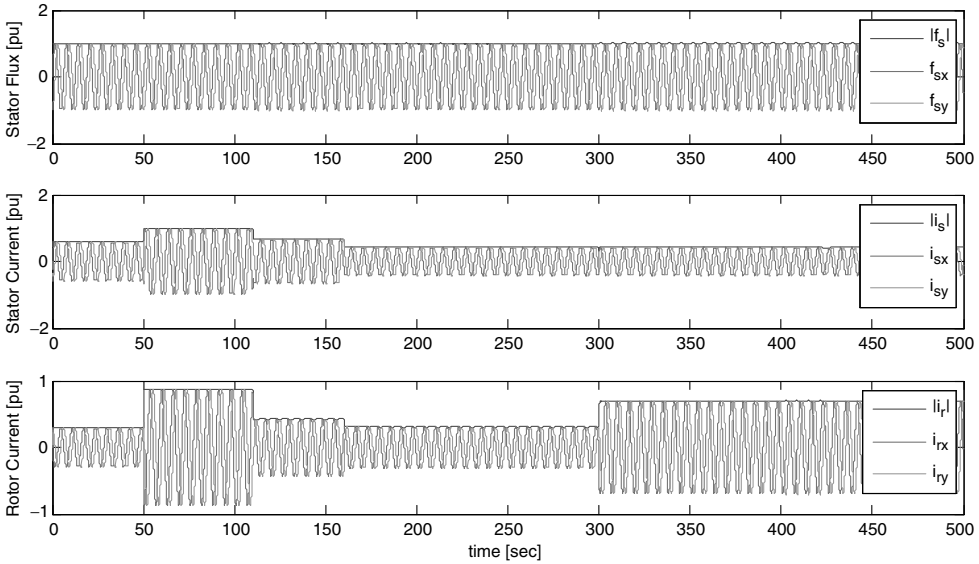


Figure 4.26 Other machine variables

## 4.4 Control of Permanent Magnet Synchronous Machine

### 4.4.1 Introduction

Permanent magnet synchronous motors (PMSM) have received increased attention in industry due to their mature material and design technology. Their high torque to inertia ratio, power density, and high efficiency make them an attractive alternative to industry's workhorse IM for many applications (Table 4.1).

Depending on the dynamic requirements and speed control precision, either brushless DC motor (BLDC) or PMSM are used. The former is mostly used with lower amounts of magnets. The latter is used for high requirements and has higher amounts of magnets. The BLDC is also named the Switched Permanent Magnet Motor (SPMM) or trapezoidal permanent magnet motor (TPMM). This type of motor is fed using a square current waveform; hence the character of the back emf is trapezoidal. The PMSM is fed by a sinusoidal current waveform and is widely used in industry.

In this chapter we will focus on controlling the motor without PWM. We will only be using PI controllers of the commanded currents.

Any reader interested in more details about the control and characteristics of this type of motor and drive is recommended to use the list of references given at the end of this chapter and in other chapters (particularly Chapters 2, 9, and 10).

### 4.4.2 Vector Control of PMSM in dq Axis

Using the vector of PMSM allows similar dealings with the motor as with a DC separately excited DC machine. Indeed, the idea is similar to the vector control of IM. The produced torque of the machine can be presented as [33–37]

**Table 4.1** Advantages and disadvantages of PMSM comparing with induction motor

Advantages	Disadvantages
<ul style="list-style-type: none"> <li>• Higher torque for the same dimension. For the same power, the dimension is lower by almost 25%;</li> <li>• Lower weight for the same power, around 25%;</li> <li>• Lower rotor losses, which results in higher efficiency of up to 3%;</li> <li>• Decreased motor noise by 3dB, which causes that the rotor to run smoother. This helps in reducing the harmonics that result from an irregularity of the air gap;</li> <li>• Higher inductance inside the magnetic path, around 1.2[T].</li> </ul>	<ul style="list-style-type: none"> <li>• In the case of inverter faults, it is not possible to reduce the magnetic field by reducing the torque surge, which forces a use of switch between the motor and the inverter;</li> <li>• It is possible to connect only one motor to the inverter; therefore group motor work is not possible;</li> <li>• The use of permanent magnet forces using enclosed motor housing complicates the cooling process;</li> <li>• Importance of using high switching frequency of the power transistors, which increases the switching losses and also the inverter structure, should be changed, e.g. trapezoidal inverter;</li> <li>• An increase of the inverter voltage in the case of inverter blocking during motor running. This results in the necessity of using chopper in the DC link;</li> <li>• Higher price of the motor (around 10–20%).</li> </ul>

$$t_e = \frac{3p}{2} [\Psi_f i_q + i_d i_q (L_d - L_q)] \quad (4.60)$$

and in per unit as

$$t_e = \psi_f i_q + (L_d - L_q) i_d i_q \quad (4.61)$$

For surface mounted PMSM, the  $d$  and  $q$  inductances are equal ( $L_d = L_q$ ). The produced torque in such a situation is

$$t_e = \psi_f i_q \quad (4.62)$$

Hence the torque can be expressed as

$$t_e = \psi_f i_s \sin \beta \quad (4.63)$$

The torque obtains maximum value for  $\beta$  (torque angle) equal to 90 degrees for a given value of stator current. This gives maximum torque per ampere and hence a higher efficiency [36].

A general scheme of the PMSM model in the  $dq$  axis is shown in Figure 4.27. It consists of a PMSM model and the control system in the  $dq$  axis connected with the rotor speed control loop. All the parameters and variables are presented in per unit unless otherwise specified.

Keeping zero  $i_{sd}$  is the most common control for permanent magnet machines. As explained earlier, this helps protect the machine against under- or over-excited conditions. Therefore, in the MATLAB/Simulink model, we start from commanding zero  $d$  axis stator current.

The Simulink model for the above scheme is shown in Figure 4.28. The Simulink software file of vector control of interior PMSM scheme is [PMSM\_VC\_dq]. The motor parameters are located in the model initialization function.

PMSM in stationary and rotating frame are given in Chapter 2.

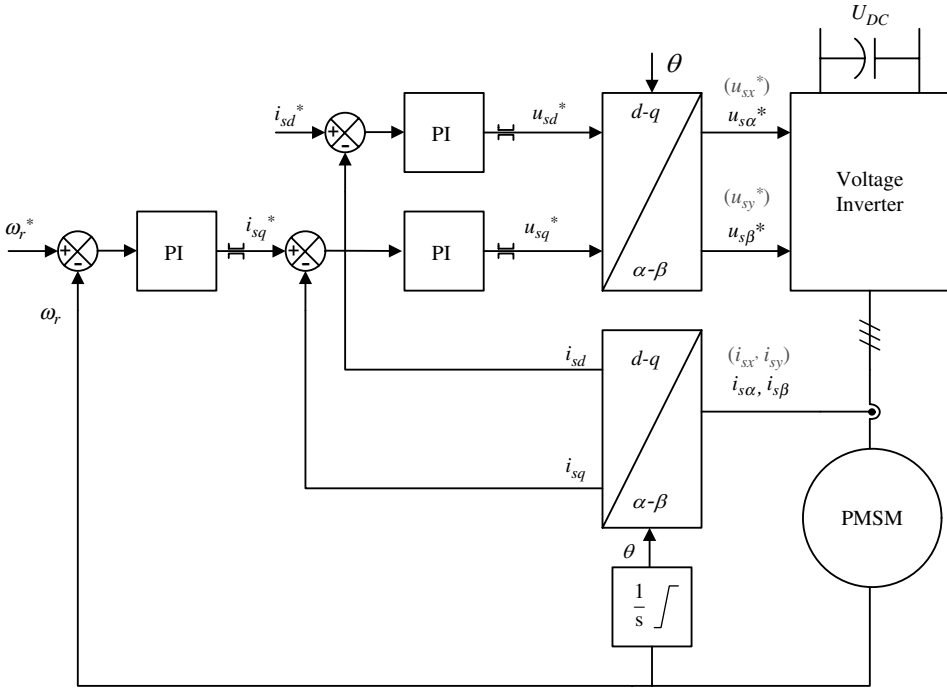


Figure 4.27 Vector control scheme of permanent magnet synchronous machine

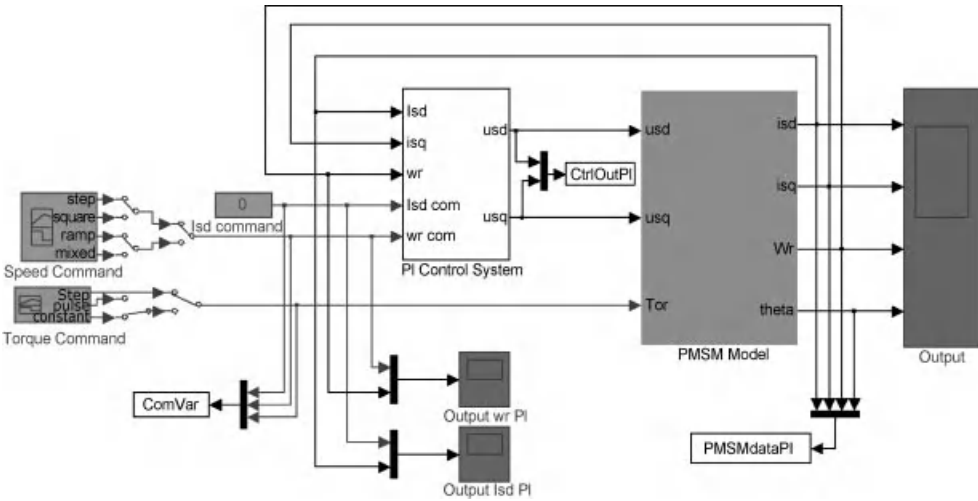


Figure 4.28 Vector control of PMSM

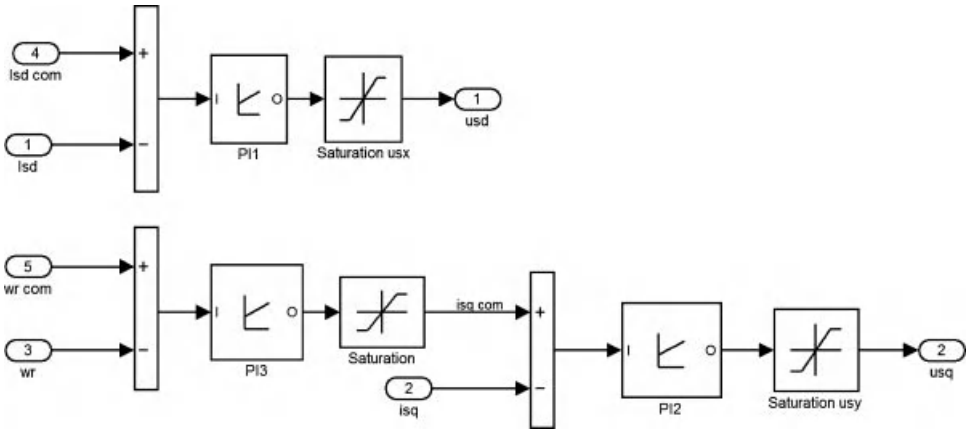


Figure 4.29 PI Control system for PMSM

4.4.2.1 Control System with Cascaded PI Controllers

PI control loop for  $d$ -current is used to provide the control input voltage  $u_{sd}$ , as shown in Figure 4.29. The rotor speed loop controller calculates the demand for  $q$ -current, which in turn provides the voltage component in axis  $q$  axis  $u_{sq}$ .

4.4.2.2 Simulation Results

Examples of simulation results for step changes in speed and load are shown in Figure 4.30.

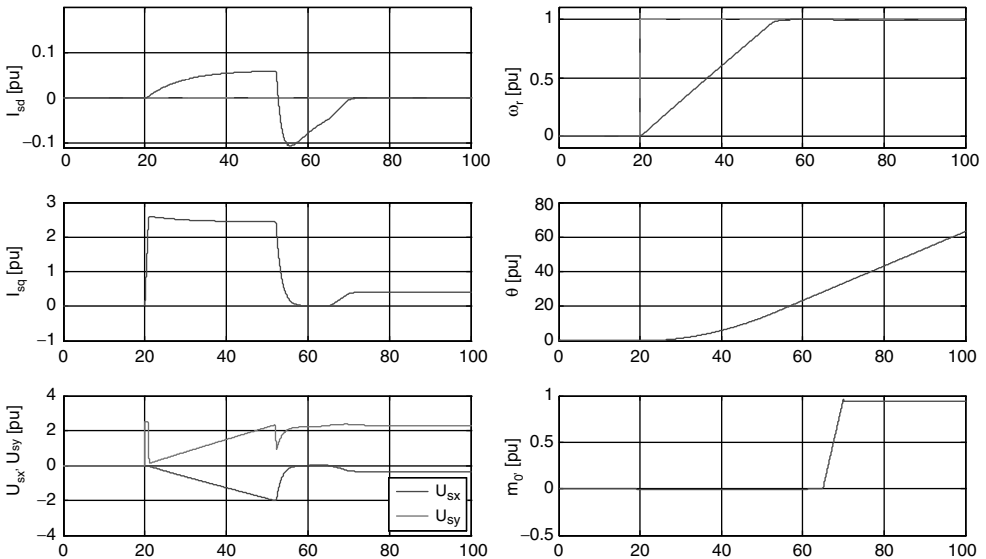


Figure 4.30 Simulation results



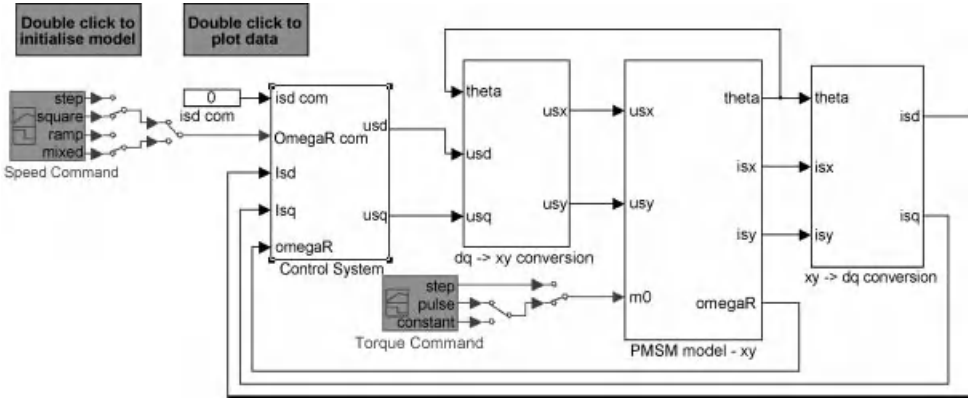


Figure 4.31 Vector control of PMSM

#### 4.4.3 Vector Control of PMSM in $\alpha$ - $\beta$ Axis using PI Controller

The control of the PMSM model in the  $\alpha$ - $\beta$  ( $x$ - $y$ ) axis is shown in Figure 4.31. It consists of the PMSM model and the control system model. All the models are in per unit unless otherwise specified. The machine model in stationary  $\alpha$ - $\beta$  reference frame is given in Chapter 2.

The Simulink software file of vector control of interior PMSM scheme is [PMSM\_VC\_alpha\_beta]. The scheme parameters are located in [PMSM\_param], which should be first executed.

##### 4.4.3.1 Variables Transformations

The currents in the  $x$ - $y$  ( $\alpha$ - $\beta$ ) axis are converted into the  $d$ - $q$  frame of reference by using the following transformation:

$$i_{sd} = i_{sx} \cos \theta + i_{sy} \sin \theta \tag{4.64}$$

$$i_{sq} = -i_{sx} \sin \theta + i_{sy} \cos \theta \tag{4.65}$$

These equations are modeled, as shown in Figure 4.20. The currents in the  $d$ - $q$  axis are used for control purposes. The controller provides control input in the  $d$ - $q$  axis.

The control voltage in the  $d$ - $q$  axis is then converted into the  $x$ - $y$  axis by using the following transformation and then applied to the machine in the  $x$ - $y$  reference frame:

$$u_{sx} = u_{sd} \cos \theta - u_{sq} \sin \theta \tag{4.66}$$

$$u_{sy} = u_{sd} \sin \theta + u_{sq} \cos \theta \tag{4.67}$$

These above equations are modeled, as shown in Figure 4.21.

##### 4.4.3.2 Control System

The control scheme is shown in Figure 4.34. The PI controller for the  $d$ -current provides the control input  $u_{sx}$  and a cascaded PI control for the speed is shown in Figures 4.35–4.37. The speed loop controller calculates the demand for the  $q$ -current loop, which in turn provides the other control input  $u_{sy}$ .

The transformation and individual PI controllers are shown in Figures 4.32 to 4.35.

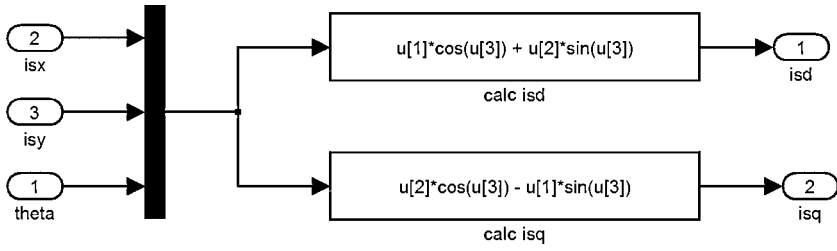


Figure 4.32 x-y to d-q transformation

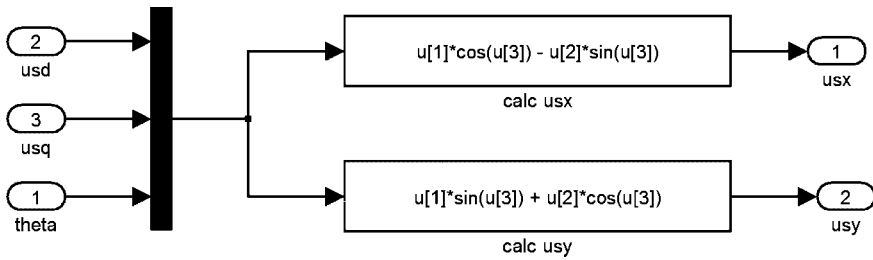


Figure 4.33 d-q to x-y transformation

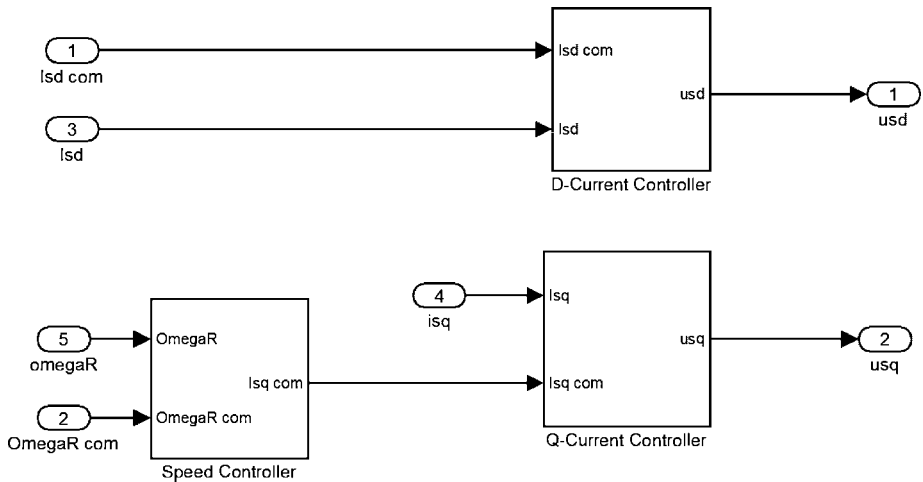


Figure 4.34 Control system model

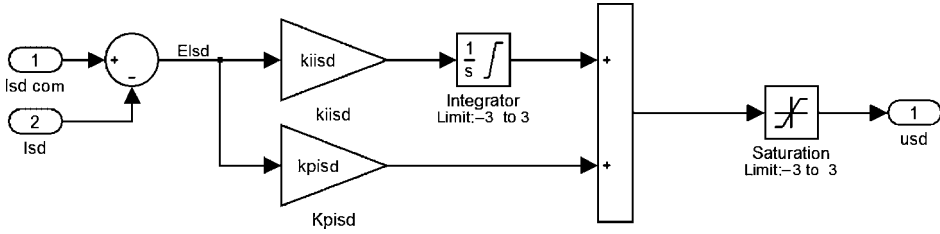


Figure 4.35 *d*-channel PI controller

4.4.3.3 Simulation Results

The simulation results for step demand in speed are shown in Figures 4.38 and 4.39.

4.4.4 Scalar Control of PMSM

Scalar control of PMSM is a simple way of controlling this type of machine; however, it is imprecise and has a slow response similar to the induction machine [33]. Hence, in this section we will not go into detailed equations, but will focus on the main characteristics and control scheme. The method is named constant volt per hertz or V by f (V/f), which is an open loop control method operating on the voltage magnitude rather than on the vectors. It is easy to perform, but results in a slow response and imprecise values. Nevertheless, this technique for PMSM offers a sensorless control scheme. The rotor angular speed can be computed using a stator voltage frequency [33].

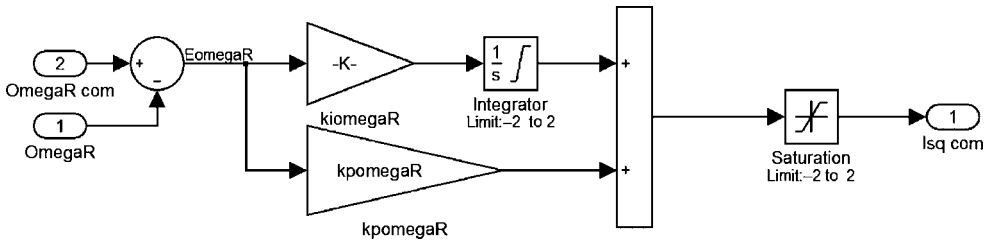


Figure 4.36 Outer loop PI controller for speed control

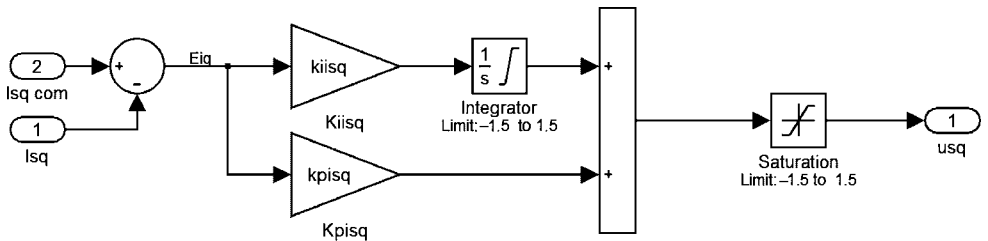
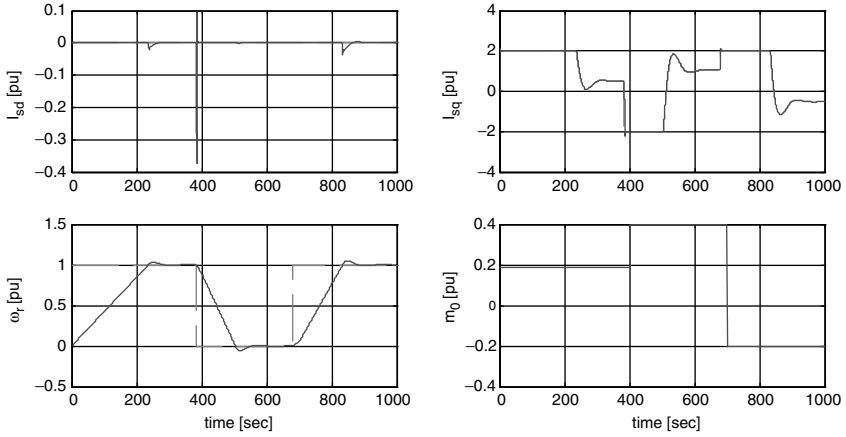


Figure 4.37 *q*-channel PI controller



**Figure 4.38** Simulation results – tracking

The voltage to frequency ratio should be constant ( $V/f = \text{const}$ ) to maintain constant flux in the machine. Otherwise the machine may reach under- or over-excitation conditions, which are not recommended from stability and economical points of view.

The method in principle is similar to the IM, which was explained earlier. The block diagram representing this method is shown in Figure 4.40. Stator resistance could not be neglected for lower frequencies; therefore, the speed is limited in the low frequency range.

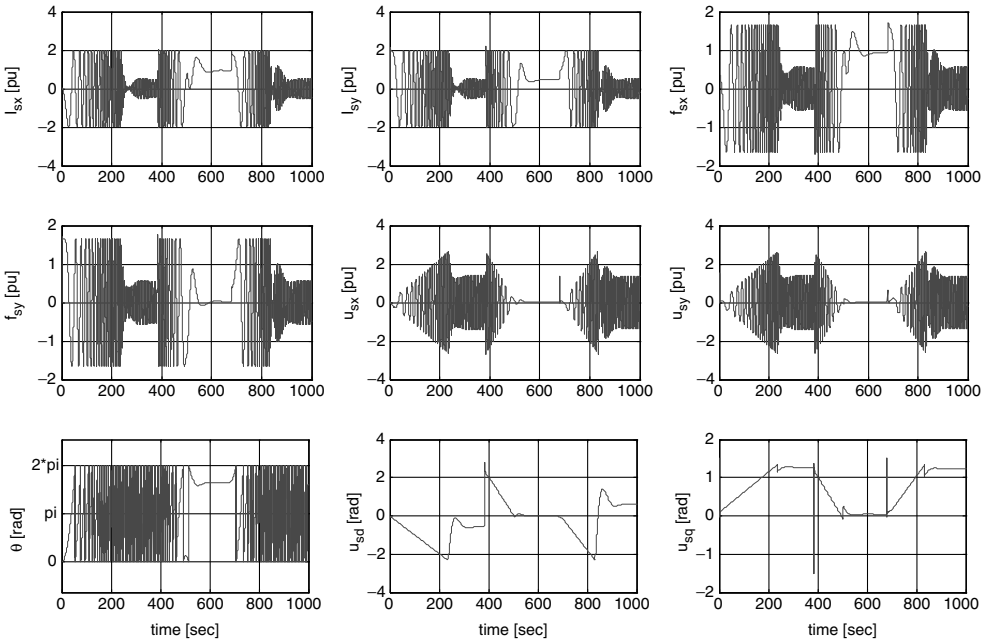


**Figure 4.39** Other machine variables

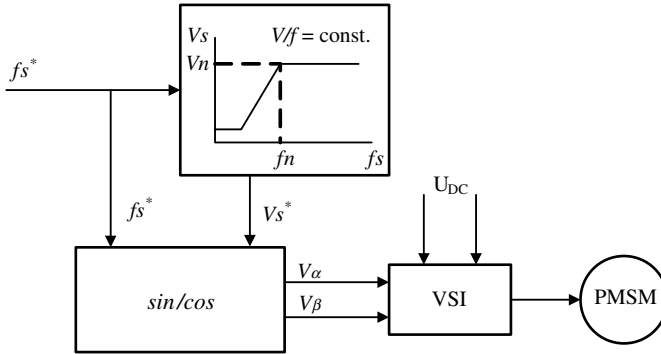


**Figure 4.40** Block diagram of constant volt by frequency control of PMSM

One disadvantage of using this method is that the stator current is not controlled. This allows changing of the main flux in the machine above the rated value.

## Exercises

1. Program the equation of the torque in all AC machines and give its value to the scope.
2. Calculate motor speed reverse and observe the current components and torque response?
3. See the effect of changing the parameters of PI controllers in all control schemes (hint: first change the proportional part and observe the response and then the integral time constant and observe the steady state error).
4. Observe what will happen if you command different values of  $i_d$  in motors control.
5. Program the scalar control scheme with speed control loop.

The Simulink software file of V by f vector control of interior PMSM scheme is [PMSM\_sca-  
lar]. The scheme parameters are located in [PMSM\_param], which should be first executed.

## Additional Tasks

1. Research a comparison study between stator flux and rotor flux field oriented control schemes.
2. Make a broad test of motors operation in term of starting, breaking, loading, reversing, etc.

## Possible Tasks for DFIG

1. Command different powers while changing the rotor speed around the rated value (up to 30% change). Observe the active and reactive powers, motor currents, voltages, and fluxes.
2. Obtain the unity power factor out of the DFIG (hint: the reactive power should be zero).
3. Observe the effect of changing controllers' parameters on the control performance. As an example, test the effect of changing the active power parameters.

## Questions

- Q1 What is scalar control of motors?
- Q2 What are a few drawbacks of scalar control?
- Q3 Why would one choose field oriented control over vector control?
- Q4 Classify field-oriented control (vector control) methods.
- Q5 State an advantage of using vector control.
- Q6 State some drawbacks of vector control.
- Q7 What are different types of reference frames used in vector control?

## References

1. Mohan, N. (2001) *Electric Drives an Integrative Approach*, 2nd en. MNPERE, Minneapolis.
2. Bose, B. K. (2006) *Power Electronics and Motor Drives: Advances and Trends*. Academic Press, Elsevier.
3. Vas, P. (1998) *Sensorless Vector and Direct Torque Control*. Oxford University Press Oxford,
4. Novotny, D. W. and Lipo, T. A. (1996) *Vector Control and Dynamics of AC Drive*. Oxford, Oxford University Press
5. Kazmierkowski, M. P., Krishnan R., and Blaabjerg, F. (2002) *Control in Power Electronics-Selected Problems*. Academic Press Elsevier.
6. Leonhard, W. (2001) *Control of Electrical Drives*. Springer
7. Krishnan, R. (2001) *Electric Motor Drives: Modeling, Analysis and Control*. Prentice Hall.
8. Chiasson, J. (2005) *Modeling and High Performance Control of Electric Machines*. John Wiley & Sons, Ltd.
9. Blaschke F. (1971) Das Prinzip der Feldorientierung, die Grundlage für Transvector-regelung von Drehfeld-maschine. *Siemens Z.* **45**, 757–760.
10. Kovacs, K. P. and Racz, I. (1959) *Transiente Vorgänge in Wechselstrommaschinen*. Budapest, Akad. Kiado.
11. Leonhard, W. (1991) 30 years of space vector, 20 years field orientation, 10 years digital signal processing with controlled AC drives: A review. *EPE Journal*, 1–2.
12. Bogdan, M. Wilamowski, J., and Irwin, D. (2011) *The Industrial Electronics Handbook – Power Electronics and Motor Drives*. Taylor and Francis Group, LLC.
13. Holtz, J. and Khambadkone, A. (1991) Vector controlled induction motor drive with a self-commissioning scheme. *IEEE Trans. Ind. Elect.*, **38**(5), 322–327.
14. Hu, J. and Wu, B. (1998) New integrations algorithms for estimating motor flux over a wide speed range. *IEEE Trans. Power Elect*, **13**(3), 969–977.
15. Krzeminski, Z. (2008) Observer of induction motor speed based on exact disturbance model. *Power Elect. Mot. Cont. Conf.*, EPE-PEMC pp. 2294–2299.
16. Khalil, H. K. (2002) *Nonlinear Systems*. Prentice Hall.
17. Xu, X. and Novotny, D. W. (1992) Selection of the flux reference for induction machine drive in the field weakening region. *IEEE Trans. Ind. Appl.*, **28**(6), 1353–1358.
18. Grotstollen, H. and Wiesing, J. (1995) Torque capability and control of a saturated induction motor over a wide range of flux weakening. *IEEE Trans. Ind. Elect.*, **42**(4), 374–381.
19. Abu-Rub, H., Schmirgel, H., and Holtz, J. (2006) Sensorless control of induction motors for maximum steady-state torque and fast dynamics at field weakening. *IEEE/IAS 41st Ann. Mtg.*, Tampa, FL.
20. Briz, F., Diez, A., Degner, M. W., and Lorenz, R. D. (2001) Current and flux regulation in field weakening operation of induction motors. *IEEE Trans. Ind. Appl.*, **37**(1), 42–50.
21. Harnefor, L. Pietilainen, K., and Gertmar, L. (2001) Torque-maximizing field-weakening control: design, analysis, and parameter selection. *IEEE Trans. Ind. Elect.*, **48**(1), 161–168.

22. Bünte, A., Grotstollen, H., and Krafska, P. (1996) Field weakening of induction motors in a very wide region with regard to parameter uncertainties. *27th Ann IEEE Power Elect. Spec. Conf.*, 23–27 June, vol. 1 pp. 944–950.
23. Bünte, A. (1998) Induction motor drive with a self-commissioning scheme and optimal torque adjustment (in German), PhD. Thesis, Paderborn University, Germany.
24. Kim, S. H. and Sul, S. K. (1997) Voltage control strategy for maximum torque operation of an induction machine in the field weakening region. *IEEE Trans. Ind. Elect.*, **44**(4), 512–518.
25. Lin, F-J. Hwang, J-C. Tan, K-H., Lu, Z-H., and Chang, Y-R. (2010) Control of doubly-fed induction generator system using PIDNNs. *2010 9th Int. Conf. Mach. Learn. Appl.* pp. 675–680.
26. Pena, R., Clare, J. C., and Asher, G. M. (1996) Doubly fed induction generator using back-to-back PWM converters and its application to variable-speed wind-energy generation. *IEEE Proc. Electr. Power Appl.*, **143**(3), 231–241, May.
27. Muller, S., Deicke, M., and De Doncker, R. W. (2002) Doubly-fed induction generator systems for wind turbines. *IEEE IAS Mag.*, **8**(3), 26–33.
28. Pena, R., Clare, J. C., and Asher, G. M. (1996) A doubly fed induction generator using back-to-back PWM converters supplying an isolated load from a variable speed wind turbine. *IEEE Proc. Electr. Power Appl.*, **143**(5), 380–387.
29. Forchetti, D., Garcia, G., and Valla, M. I. (2002) Vector control strategy for a doubly-fed stand-alone induction generator. *Proc. 28th IEEE Int. Conf., IECON*, vol. 2, pp. 991–995.
30. Jain, A. K. and Ranganathan, V. T. (2008) Wound rotor induction generator with sensorless control and integrated active filter for feeding nonlinear loads in a stand-alone grid. *IEEE Trans. Ind. Elect.*, **55**(1), 218–228.
31. Iwanski, G. and Koczara, W. (2008) DFIG-based power generation system with UPS function for variable-speed applications. *IEEE Trans. Ind. Elect.*, **55**(8), 3047–3054.
32. Bogalecka, E. (1993) Power control of a double fed induction generator without speed or position sensor. *Conf. Rec. EPE*, vol **377**, pt. 8, ch. 50, pp. 224–228.
33. Stulrajter, M. Hrabovcova, V., and Franko, M. (2007) Permanent magnets synchronous motor control theory. *J. Elect. Eng.*, **58**(2), 79–84.
34. Binns, K. J. and Shimmin, D. W. (1996) Relationship between rated torque and size of permanent magnet machines. *Elect. Mach. Drives IEE Proc. Electr. Power Appl.*, **143**(6), 417–422.
35. Pillay, P. and Knshnan, R. (1988) Modeling of permanent magnet motor drives. *IEEE Trans. Ind. Elect.*, **35**(4), 537–541.
36. Adamowicz, M. (2006) Observer of induction motor speed based on simplified dynamical equations of disturbance model. *Proc. Doct. Sch. of Energy and Geotech.*, 16–21 January, Kuressaare, Estonia, pp. 63–67.
37. Pajchrowski, T. and Zawirski, K. (2005) Robust speed control of Servodrives based on ANN. *IEEE ISIE 20–23 June*, Dubrovnik, Croatia.
38. Akagi, H., Kanazawa, Y., and Nabae, A. (1998) *Theory of the Instantaneous Reactive Power in Three-Phase Circuits*. IPEC, Tokyo.

# 5

## Direct Torque Control of AC Machines

Truc Phamdinh

### 5.1 Preliminary Remarks

Theoretical principles of direct torque control (DTC) for high performance drives were introduced in the second half of the 1980s [1–3]. Compared with field-oriented control, with origins that date back to the beginning of the 1970s, DTC is a significantly newer concept. It took almost 20 years for vector control to gain acceptance by industry. In contrast, the concept of DTC has been taken on board by industry relatively quickly in only ten years [4,5]. While vector control predominantly relies on mathematical modeling of an induction machine, DTC makes direct use of physical interactions that take place within the integrated system of the machine and its supply. The DTC scheme adopts simple signal processing methods and relies entirely on the non-ideal nature of the power source that is used to supply an induction machine within the variable speed drive system (two-level or three-level voltage source inverters, matrix converters, etc.). It can therefore be applied to power electronic converter-fed machines only. The on-off control of converter switches is used for the decoupling of the non-linear structure of the induction machine [6]. The most frequently discussed and used power electronic converter in DTC drives is a voltage source inverter.

DTC takes a different look at the induction machine and the associated power electronic converter. First, it recognizes that regardless of how the inverter is controlled, it is by default a voltage source rather than a current source. Next, it dispenses with one of the main characteristics of the vector control indirect flux and torque control by means of two stator current components. In essence, DTC recognizes that if flux and torque can be controlled indirectly by these two current components, then there is no reason why it should not be possible to control flux and torque directly, without intermediate current control loops.

The control part of a DTC drive consists of two parallel branches, similar to those of vector control. The references are the flux set point and the torque set point, which may or may not be



the output of the speed controller, depending on whether the drive is torque controlled or speed controlled. DTC asks for the estimation of stator flux and the motor torque, so that closed loop flux and torque control can be established. However, the errors between the set and the estimated flux and torque values are used in a completely different way when compared to the vector control. In vector control these errors would be used as inputs to the PI controllers, whose outputs are then set points for the stator  $d$ - $q$ -axis current references. The basic idea of DTC is that the existing errors in torque and flux can be used directly to drive the inverter without any intermediate current control loops or co-ordinate transformation. Flux and torque controllers are hysteresis types and their outputs are used to determine which of the possible inverter states should be applied to the machine terminals, so that the errors in the flux and torque remain within the prescribed hysteresis bands.

DTC is inherently sensorless. Information about an actual rotor speed is not necessary in the torque mode of operation, because of the absence of co-ordinate transformation. However, the correctness of the estimation of the stator flux and torque is important for the accurate operation of hysteresis controllers. An accurate mathematical model of an induction machine is therefore essential in DTC. Accuracy of DTC is also independent of variations of the rotor's parameters. Only variations of stator resistance, due to changes in thermal operating conditions, cause problems for high performance DTC at low speed.

In summary, the main features of DTC and differences compared to vector control are [7]:

- direct control of flux and torque;
- indirect control of stator currents and voltages;
- absence of co-ordinate transformation;
- absence of separate voltage modulation block, usually required in vector drives;
- requirement to know only the sector in which the stator flux linkage space vector is positioned, rather than the exact position of it (necessary in vector drives for co-ordinate transformation);
- absence of current controllers;
- inherently sensorless control, since speed information is never required in the torque mode of operation;
- in its basic form, the DTC scheme is only sensitive to variation in stator resistance.

## 5.2 Basic Concept and Principles of DTC

### 5.2.1 Basic Concept

The DTC principle was introduced in the late 1980s [11–13]. In contrast to vector control, which became accepted by drive manufacturers after 20 years of extensive research, DTC needed only just over a decade to really take off. A direct torque controlled induction motor drive has been manufactured commercially by ABB since the mid-1990s [5]. In the direct torque controller developed by ABB, the optimum inverter switching pattern is determined in every sampling period (25  $\mu$ s). The core of the control system in DTC is the sub-system containing torque and flux hysteresis controllers and optimal inverter switching logic. An accurate machine model is also important, since estimation of the stator flux and motor torque is based on the machine model and the measurement of the machine input stator voltages

and currents. The measurement of actual speed is not required [5]. A machine model in stationary reference frame is used to develop DTC theory. Detailed discussion regarding mathematical modeling of induction machines is presented in Chapter 6.

In the stationary reference frame, the stator flux linkage is the integral of the stator emf. If the stator voltage drop on stator resistance can be neglected, then the stator flux is the integral of the applied voltage. Hence, in a short period of time the increments of stator flux are proportional to the applied voltage. It therefore follows that the inverter output voltage space vector directly impresses on the stator flux and a desired locus of stator flux can be obtained by selecting the appropriate inverter output voltages [7]. The rotor time constant of induction machines is usually large; therefore the rotor flux linkage changes slowly compared to the stator flux linkage and can be assumed as constant in magnitude and in speed of rotation during short transients [7]. When the forward active voltage space vectors are applied, the stator flux linkage vector is moved away from the rotor flux linkage vector. This will increase the machine's torque, because the torque angle increases. However, if the zero or backward active voltage space vectors are applied, the torque angle is reduced. The torque is therefore reduced [6]. It can now be seen that torque can be controlled directly and increased or decreased almost instantly by moving the stator flux linkage space vector to the required position, being determined by torque demand. This in turn can be done quickly by selecting the appropriate voltage vector while the stator flux linkage magnitude is kept within the hysteresis band. This is the reason why the control scheme is called DTC [7].

DTC requires set points of flux and torque as independent inputs. The estimated values of these quantities are needed to establish closed loop control of the flux and torque. However, the errors between the estimates of actual quantities and set points are used in a completely different way compared to vector control. There is no utilization of current controllers in DTC. The torque and flux controllers are two-level or three-level hysteresis controllers, which determine whether an increase or a decrease of flux and/or torque is required, depending on whether or not torque or flux errors fall outside the predefined ranges. From this information, together with the knowledge of the position of the stator flux linkage space vector, an appropriate voltage vector will be selected based on the switching strategy. An accurate knowledge of the magnitude of the stator flux linkage space vector in the machine is needed. However, knowledge of the precise value of the stator flux space vector instantaneous position is not required. The control system only needs to know in which sector of the voltage vector space, which is a two-dimensional complex plane, the flux linkage space vector is. In the case of the standard two-level voltage source inverter, there are six sectors in the space vector plane corresponding to the six active voltage space vectors, with the voltage vectors positioned at the centers of the sectors. Each sector expands 60 degrees so that all six of them cover the voltage vector complex plane. DTC is inherently sensorless. Different structures of speed estimators can be incorporated into a direct torque controller for sensorless drive operation with closed loop speed control.

## 5.2.2 Principle of DTC

### 5.2.2.1 Torque Production in a Direct Torque Controlled Drive

In a direct torque controlled induction motor drive supplied by a voltage source inverter, it is possible to directly control the stator flux linkage and the electromagnetic torque by the

selection of the optimum stator voltage space vectors in the inverter. The selection of the most appropriate voltage vector is done in such a way that the flux and torque errors are restricted within the respective flux and torque hysteresis bands, fast torque response is obtained, and the inverter switching frequency is kept at the lowest possible level.

In the case of rotor flux oriented control of an induction motor, the electromagnetic torque developed by the motor is described by

$$T_e = (3/2)P(L_m/L_r)\psi_r i_{qs} \tag{5.1}$$

where the stator  $q$ -axis current is the imaginary component of the stator current space vector in the co-ordinate system fixed to the rotor flux space vector, as shown Figure 4.6a.

The torque equation (5.1) can be written in terms of the amplitude and phase of the stator current space vector with respect to the  $d$ -axis of the reference frame as

$$T_e = K\psi_r |i_s| \sin \lambda \tag{5.2}$$

Instantaneous change of the torque requires, according to equation (5.2), change in the amplitude and phase of the stator current space vector, such that the  $d$ -axis current component remains the same (so that rotor flux is constant), while the torque is stepped to the new appropriate value by the change in the stator  $q$ -axis current component.

An alternative expression for the torque uses the stator flux space vector and stator current space vector. Regardless of the applied method of control, the torque developed by the motor can be written as

$$T_e = \frac{3}{2}P |\psi_s| |i_s| \sin \alpha \tag{5.3}$$

where the angle  $\alpha$  is the instantaneous value of the angle between the stator current and stator flux space vectors. Figure 5.1b shows the stator current space vector and stator flux space vector's relative positions.

It can be shown [7] that at certain rotor speeds, if the amplitude of the stator flux is kept constant, an electromagnetic torque can be changed rapidly by altering its instantaneous position so that angle  $\alpha$  in equation (5.3) is rapidly changed. In other words, if such stator

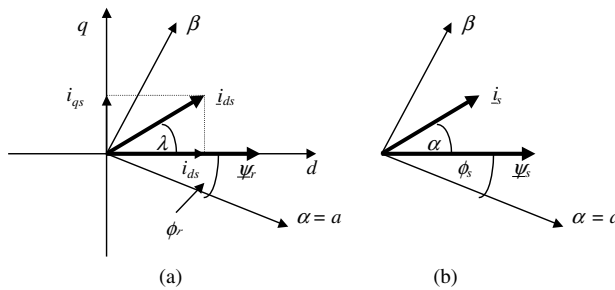


**Figure 5.1** (a) Stator current and rotor flux space vectors in a rotor flux oriented induction machine; (b) stator current and stator flux's relative position in an induction machine

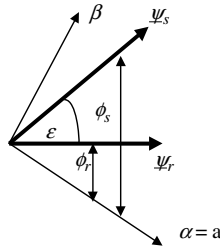


**Figure 5.2** Relative positions of stator flux and rotor flux space vectors

voltages are imposed on the motor, which keep the stator flux constant (at the set value), but which also quickly rotate the stator flux space vector into the required position (determined by the torque command), then fast torque control is obtained. It follows that if in the DTC drive the developed torque is smaller than the reference, the torque should be increased by using the maximum possible rate of change of the stator flux space vector position  $\phi_s$ . If the stator flux space vector is accelerated in the forward direction, an increase in torque is produced; however, when it is decelerated backwards, a decrease in torque results. The stator flux space vector can be adjusted by using the appropriate stator voltage space vectors, obtainable from the VSI operated in the PWM mode. Thus there is a direct stator flux and torque control achieved by means of the voltage source, hence the name ‘DTC.’ Another form of the torque equation (Figure 5.2) is the one given in terms of stator and rotor flux:

$$T_e = \frac{3}{2} P \frac{L_m}{\sigma L_s L_r} \left| \underline{\psi}_r \right| \left| \underline{\psi}_s \right| \sin \epsilon \quad (5.4)$$

where  $\epsilon$  is the angle between stator flux and rotor flux space vectors.

Rotor flux changes slowly because its rate of change depends on a relatively large rotor time constant; therefore, it can be assumed to be constant in a short period of time. The stator flux amplitude is also kept constant in the DTC control scheme; hence both the vectors in the equation (5.4) have constant amplitudes. Rapid change of torque can be obtained if instantaneous positions of the stator flux space vector are changed quickly so that  $\epsilon$  is quickly varied. This is the essence of DTC. The instantaneous change of  $\epsilon$  can be obtained by switching on the appropriate stator voltage space vector of the VSI.

If stator resistance voltage drop is neglected, the stator voltage equation in the stationary reference frame is

$$\underline{v}_s = d\underline{\psi}_s/dt \quad (5.5)$$

Hence the applied stator voltage directly impresses the stator flux. If the voltage abruptly changes, then stator flux will change accordingly to satisfy equation (5.5). The variation of the stator flux changes during a short period of time when the stator voltage is changed as  $\Delta\underline{\psi}_s = \underline{v}_s \Delta t$ . This shows that the stator flux space vector moves in the direction of the applied stator voltage space vector during this period. By selecting the appropriate stator voltage space vectors in subsequent time intervals, it is then possible to change the stator flux in the desired way. Decoupled control of the stator flux and torque is achieved by acting on the radial and

tangential components of the stator flux space vector. These two components are directly proportional to the components of the stator voltage space vector in the same directions.

The angle  $\varepsilon$  between stator and rotor flux space vectors is important in torque production. Assume that the rotor flux space vector is traveling at a given speed, at a certain point in the steady-state operation; this speed is initially equal to the average one of the stator flux space vector. The induction motor is accelerated. Appropriate stator voltage vector is applied to increase torque, and quick rotation of stator flux space vector occurs. However, rotor flux space vector amplitude does not change appreciably, because of the significant rotor time constant. The rotor flux space vector's speed of rotation is also not changed abruptly; recall that speed of rotation of this vector can be given in terms of rotor flux components and their derivatives; if rotor flux components do not change due to the large time constant, the angular speed of rotor flux space vector does not change either. This will result in an increase of  $\varepsilon$  that in return increases the motor's torque. If deceleration is required, an appropriate voltage vector will be applied to reduce the angle  $\varepsilon$  and therefore decrease the torque developed by the motor. The application of zero voltage vectors will almost stop the rotation of the stator flux space vector. If the angle  $\varepsilon$  becomes negative, the torque will change signs and a braking process takes place.

### 5.2.2.2 Inverter Switching Table

A number of methods for the selection of the optimum voltage space vectors for DTC have already been mentioned [1,8–12]. However, this book only discusses the classical method originally suggested by [1]. Space vectors of inverter output phase voltages are shown again in Figure 5.3 as further explanation. In addition, sections of the plane, identified with Roman numeral I to VI, are also included. The sectors are all of 60 degrees and are distributed  $\pm 30$  degrees around the corresponding voltage space vector. If the stator flux space vector lies in the  $k$ th sector, where  $k = 1, 2, 3, 4, 5, 6$ , its magnitude can be increased by using the voltage vectors  $k$ ,  $k + 1$ ,  $k - 1$ . Its magnitude can be decreased by using  $k + 2$ ,  $k - 2$ , and  $k + 3$  vectors. In other words, stator flux will be increased if either the voltage vector belonging to the sector or any of the two adjacent voltage vectors is applied. It will be decreased if the remaining three active voltage vectors are applied. Vectors  $k + 1$  and  $k + 2$  are called active forward voltage vectors, whereas vectors  $k - 1$  and  $k - 2$  are called active backward voltage vectors.

However, the selected voltage vector will also affect the torque production of the induction motor. In addition, the switching frequency will also be affected. The idea is to always keep the

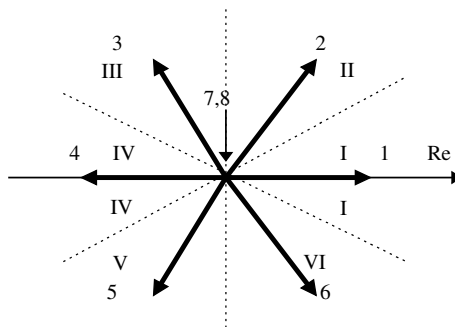


**Figure 5.3** Phase voltage space vectors and appropriate sectors

**Table 5.1** Phase to neutral voltages of three phase voltage inverter

Switching state	Switches on	Space vector	Phase voltage $v_a$	Phase voltage $v_b$	Phase voltage $v_c$
1	1,4,6	$\underline{v}_{1\text{phase}}$ (100)	$(2/3)V_{DC}$	$-(1/3)V_{DC}$	$-(1/3)V_{DC}$
2	1,3,6	$\underline{v}_{2\text{phase}}$ (110)	$(1/3)V_{DC}$	$(1/3)V_{DC}$	$-(2/3)V_{DC}$
3	2,3,6	$\underline{v}_{3\text{phase}}$ (010)	$-(1/3)V_{DC}$	$(2/3)V_{DC}$	$-(1/3)V_{DC}$
4	2,3,5	$\underline{v}_{4\text{phase}}$ (011)	$-(2/3)V_{DC}$	$(1/3)V_{DC}$	$(1/3)V_{DC}$
5	2,4,5	$\underline{v}_{5\text{phase}}$ (001)	$-(1/3)V_{DC}$	$-(1/3)V_{DC}$	$(2/3)V_{DC}$
6	1,4,5	$\underline{v}_{6\text{phase}}$ (101)	$(1/3)V_{DC}$	$-(2/3)V_{DC}$	$(1/3)V_{DC}$
7	1,3,5	$\underline{v}_{7\text{phase}}$ (111)	0	0	0
8	2,4,6	$\underline{v}_{8\text{phase}}$ (000)	0	0	0

switching frequency as low as possible so that the most appropriate voltage space vector is the one that requires the minimum number of switchings and simultaneously drives both the stator flux and the torque errors in the desired direction. From Table 5.1, where inverter switching states are defined as a set of binary signals for each of the six possible non-zero space vectors, we see that progressing from state one towards state six requires only switching one of three inverter legs. Hence, if the inverter operates with a vector whose state is 100, then the most appropriate subsequent vectors are 110, 101, and 000 (zero vector number 8), as these vectors require switching in a single inverter leg. Minimum switching frequency is achieved in this way. Which of the three possible vectors will be applied depends on the flux and torque errors.

An illustration of the switching process is given in Figure 5.4. Operation in the base speed region is assumed so that the stator flux reference is constant and equal to the rated stator flux. A deviation by a hysteresis band equal to  $\pm\Delta\psi_s$  is allowed for the actual flux with respect to the reference. It is assumed that in certain time instants, the stator flux is in the first sector and has just reached the outer boundary of the allowed deviation (point A). The inverter switching state therefore has to be changed, since the stator flux must be reduced. The direction of rotation is anticlockwise. If the stator flux is in sector one, then the application of voltage vectors 1, 2, and

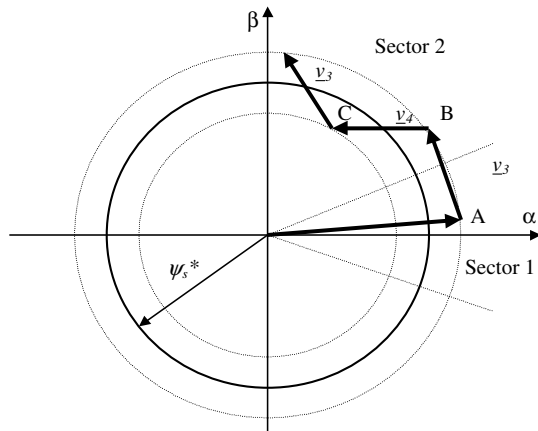


**Figure 5.4** Control of stator flux space vector by means of appropriate voltage vector application [7]

6 would further increase the flux. Reduction in the flux can be obtained using vectors 3, 4, and 5. Out of these three, vector 3 is the only one that asks for switching in only one of the inverter legs. Vector 3 is therefore applied, and drives the stator flux towards point B, where the stator flux once again reaches the upper hysteresis band. Since the stator flux is now in sector 2 and once again needs to be reduced, the possible voltage vectors that will lead to the reduction in the stator flux are vectors 4, 5, and 6. Vector 4 is the only one that asks for switching in a single inverter leg. Voltage vector 4 is therefore applied, and it drives stator flux towards the lower boundary of the allowed deviation (point C). In point C the stator flux is still in the second sector and needs to be increased. An increase can be obtained using vectors 1, 2, and 3. As vector 3 asks for a single switching, this vector will be applied again. The process continues over time.

Previous considerations did not take into account the impact of the torque error on the selection of the switching state. Stopping the rotation of the stator flux space vector corresponds to the case when the torque does not have to be changed (actual value of the torque is within the prescribed hysteresis bands). However, when the torque has to be changed in the clockwise or anticlockwise direction, corresponding to negative or positive torque variation, then the stator flux space vector has to be rotated in an appropriate direction. In general, if an increase in torque is required, then the torque is controlled by applying voltage vectors that advance the stator flux space vector in the direction of rotation. If a decrease is required, voltage vectors are applied to oppose the direction of rotation of stator flux space vector. If zero change in torque is required, then zero vectors are applied. It follows that the angle of the stator flux space vector is controlled indirectly through the flux amplitude and torque control. The torque demands are reduced to choices of increase, decrease, or zero. Similarly, the stator flux amplitude control is limited to the choice of increase and decrease. Figure 5.5 illustrates the selection of the optimum voltage vector as a function of the required change in flux and torque. The situation is shown for an anticlockwise direction of rotation of the stator flux space vector and for the initial position of the stator flux space vector in the first two sectors. Similar figures can be constructed for other sectors.

The result of these considerations can be represented in the optimum voltage vector selection table (Table 5.2) or inverter switching table. This gives the optimum selection of the voltage vectors for all the possible stator flux space vector positions (in terms of sectors) and the desired control inputs, which are the output of the torque and flux hysteresis comparator, respectively. The outputs will give commands of increase or decrease for torque and stator flux, in order to keep both of them within the respective hysteresis band. If a stator flux increase is required, then

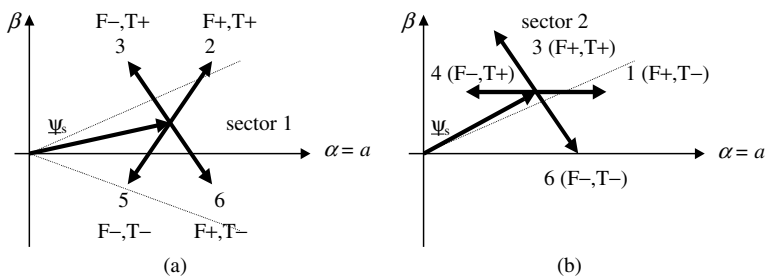


**Figure 5.5** Selection of the appropriate voltage vector for required changes in stator flux and torque: (a) when the stator flux is in sector 1; and (b) when the stator flux is in sector 2 ( $F \equiv$  flux,  $T \equiv$  torque)

**Table 5.2** Optimum voltage vector look-up table

$\Delta\psi_s$	$\Delta T_e$	Sector 1	Sector 2	Sector 3	Sector 4	Sector 5	Sector 6
1	1	$\underline{v}_2$	$\underline{v}_3$	$\underline{v}_4$	$\underline{v}_5$	$\underline{v}_6$	$\underline{v}_1$
	0	$\underline{v}_7$	$\underline{v}_8$	$\underline{v}_7$	$\underline{v}_8$	$\underline{v}_7$	$\underline{v}_8$
	-1	$\underline{v}_6$	$\underline{v}_1$	$\underline{v}_2$	$\underline{v}_3$	$\underline{v}_4$	$\underline{v}_5$
0	1	$\underline{v}_3$	$\underline{v}_4$	$\underline{v}_5$	$\underline{v}_6$	$\underline{v}_1$	$\underline{v}_2$
	0	$\underline{v}_8$	$\underline{v}_7$	$\underline{v}_8$	$\underline{v}_7$	$\underline{v}_8$	$\underline{v}_7$
	-1	$\underline{v}_5$	$\underline{v}_6$	$\underline{v}_1$	$\underline{v}_2$	$\underline{v}_3$	$\underline{v}_4$

Active voltage vectors: 1 (100), 2 (110), 3 (010), 4 (011), 5 (001), 6 (101).

Zero voltage vectors: 7 (111); 8 (000).

$\Delta\psi_s = 1$ , and if a stator flux decrease is required, then  $\Delta\psi_s = 0$ . This notation corresponds to the fact that the digital output signals of a two-level flux hysteresis comparator are

$$\begin{aligned} \Delta\psi_s = 1 & \quad \text{if} \quad \left| \underline{\psi}_s \right| \leq \left| \underline{\psi}_s^* \right| - |\text{hysteresis band}| \\ \Delta\psi_s = 0 & \quad \text{if} \quad \left| \underline{\psi}_s \right| \geq \left| \underline{\psi}_s^* \right| + |\text{hysteresis band}| \end{aligned} \quad (5.6)$$

Similarly, if a torque increase is required, then  $\Delta T_e = 1$ , if a torque decrease is required, then  $\Delta T_e = -1$ , and if no change in torque is required, then  $\Delta T_e = 0$ . The notation corresponds to the fact that the digital outputs of a three-level hysteresis comparator are

$$\begin{aligned} \Delta T_e = 1 & \quad \text{if} \quad T_e \leq T_e^* - |\text{hysteresis band}| \\ \Delta T_e = 0 & \quad \text{if} \quad T_e = T_e^* \\ \Delta T_e = -1 & \quad \text{if} \quad T_e \geq T_e^* + |\text{hysteresis band}| \end{aligned} \quad (5.7)$$

## 5.3 DTC of Induction Motor with Ideal Constant Machine Model

### 5.3.1 Ideal Constant Parameter Model of Induction Motors

#### 5.3.1.1 Induction Machine's Dynamic Model in $dq$ Rotating Reference Frame

An induction machine with a perfectly smoothed air gap is considered. The phase windings of the machine are assumed to be physically 120 degrees apart for both stator and rotor. Winding resistances and leakage inductances are assumed to be constant. All the parasitic phenomena, such as iron loss and main flux saturation, are ignored at this stage. The induction machine under consideration is therefore an ideal smooth air-gap machine with a sinusoidal distribution of windings, and all the effects of MMF harmonics are neglected [13,14]. A schematic representation of the machine is shown in Figure 5.6.

The notations in the figure above are:

1.  $\omega_r$ : angular rotor speed;
2.  $\omega_s$ : angular speed of stator flux space vector;



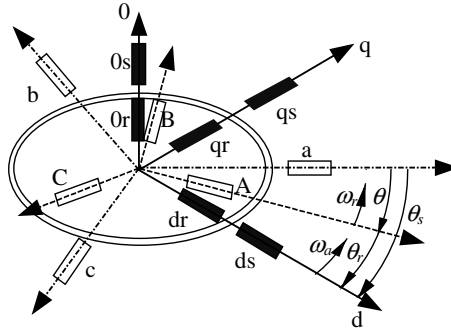


**Figure 5.6** Schematic representation of induction machine with reference frames in three-phase domain and common rotating  $d$ - $q$  reference frame

3.  $\theta$ : instantaneous rotor angular position with respect to phase  $a$  magnetic axis of stator;
4.  $\theta_s$ : instantaneous angular position of common rotating reference frame with respect to phase  $a$  magnetic axis of stator.
5.  $\theta_r$ : instantaneous angular position of common rotating reference frame with respect to phase  $a$  magnetic axis of rotor.

After the transformation from a three-phase domain to a common rotating reference frame with an arbitrary angular speed, the stator and rotor voltage equations of the induction machine are

$$\begin{aligned} v_{ds} &= R_s i_{ds} + \frac{d\psi_{ds}}{dt} - \omega_a \psi_{qs} \\ v_{qs} &= R_s i_{qs} + \frac{d\psi_{qs}}{dt} + \omega_a \psi_{ds} \end{aligned} \quad (5.8)$$

$$\begin{aligned} v_{dr} &= R_r i_{dr} + \frac{d\psi_{dr}}{dt} - (\omega_a - \omega_r) \psi_{qr} \\ v_{qr} &= R_r i_{qr} + \frac{d\psi_{qr}}{dt} + (\omega_a - \omega_r) \psi_{dr} \end{aligned} \quad (5.9)$$

The flux linkages are

$$\psi_{ds} = L_s i_{ds} + L_m i_{dr} \quad (5.10)$$

$$\psi_{qs} = L_s i_{qs} + L_m i_{qr}$$

$$\psi_{dr} = L_r i_{dr} + L_m i_{ds}$$

$$\psi_{qr} = L_r i_{qr} + L_m i_{qs} \quad (5.11)$$

Symbols  $L_s, L_r$  denote stator and rotor self-inductance respectively; while  $L_m$  is the magnetizing inductance.

The relationship between the stator, rotor, and magnetizing inductances and the three-phase model self and mutual inductances are

$$\begin{aligned} L_s &= L_{\sigma s} + L_m \\ L_r &= L_{\sigma r} + L_m \end{aligned} \quad (5.12)$$

where  $L_{\sigma s}$ ,  $L_{\sigma r}$  are stator and rotor leakage inductances, respectively. The equation of mechanical motion remains as

$$T_e - T_L = \frac{J}{P} \frac{d\omega_r}{dt} \quad (5.13)$$

where  $T_e$  is electromagnetic torque;  $T_L$  is load torque;  $J$  is inertia of the induction machine; and  $P$  is the number of pole pairs.

Electromagnetic torque can be expressed in terms of  $d$ - $q$  components of stator flux and stator current as

$$T_e = \frac{3}{2} P (\psi_{ds} i_{qs} - \psi_{qs} i_{ds}) \quad (5.14)$$

The per phase equivalent circuit of the ideal constant parameter machine mode in the  $d$ - $q$  rotating reference frame is shown in Figure 5.7.

### 5.3.1.2 Induction Machine's Dynamic Model in $\alpha$ - $\beta$ Stationary Reference Frame

The induction machine model that will be used later in this chapter for simulation purposes is the machine model in the stationary reference frame. Components of stator current, rotor current, and angular electrical speed  $\omega_r$  are used as state-space variables in the fifth-order differential equation system. The stator and rotor voltage equations with stator current,

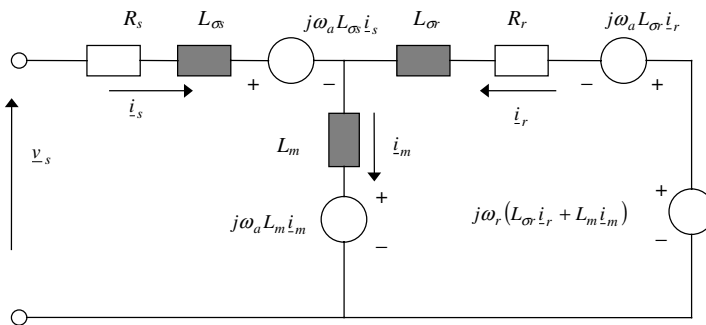


**Figure 5.7** Dynamic equivalent circuit of an IM in an arbitrary rotating common reference frame

rotor current, and rotor angular speed as state-space variables are obtained by using equations (5.8)–(5.11), and (5.13) as

$$\begin{aligned} v_{\alpha s} &= R_s i_{\alpha s} + L_s \frac{di_{\alpha s}}{dt} + L_m \frac{di_{\alpha r}}{dt} \\ v_{\beta s} &= R_s i_{\beta s} + L_s \frac{di_{\beta s}}{dt} + L_m \frac{di_{\beta r}}{dt} \end{aligned} \quad (5.15)$$

$$\begin{aligned} 0 &= L_m \frac{di_{\alpha s}}{dt} + \omega_r L_m i_{\beta s} + R_r i_{\alpha r} + L_r \frac{di_{\alpha r}}{dt} + \omega_r L_r i_{\beta r} \\ 0 &= -\omega_r L_m i_{\alpha s} + L_m \frac{di_{\beta s}}{dt} - \omega_r L_r i_{\alpha r} + R_r i_{\beta r} + L_r \frac{di_{\beta r}}{dt} \end{aligned} \quad (5.16)$$

$$\frac{J d\omega_r}{P dt} = \frac{3}{2} P [i_{\beta s} (L_s i_{\alpha s} + L_m i_{\alpha r}) - i_{\alpha s} (L_s i_{\beta s} + L_m i_{\beta r})] - T_L \quad (5.17)$$

These differential equations will be used to build the induction machine model in MATLAB/Simulink for the simulation of the performance of a DTC induction motor drive.

### 5.3.2 Direct Torque Control Scheme

#### 5.3.2.1 Basic Control Scheme of Direct Torque Controlled Induction Motor

Since  $\Delta\psi_s = \underline{v}_s \Delta t$ , then the stator flux space vector will move fast if non-zero voltage vectors are applied to the motor. It will almost stop if zero voltage vectors are applied. In DTC drives, at every sampling period the stator voltage vectors are selected on the basis of keeping the stator flux amplitude error and torque error within the prescribed hysteresis bands. The size of the hysteresis bands will significantly affect the inverter switching frequency. In general, the larger the hysteresis band, the lower the switching frequency and the poorer the response of the drive to change in reference. Because the stator flux space vector is the integral of the stator voltage vector, it will move in the direction of the stator voltage space vector for as long as this voltage vector is applied to the motor.

Basic control schemes of a DTC induction motor drive are shown in Figures 5.8 and 5.9 for torque mode and speed mode of operation, respectively. In each figure there are two parallel branches, one for stator flux amplitude and the other for the torque control. The torque reference is either an independent input (for a torque-controlled drive, Figure 5.8) or the output of the speed controller (in a speed-controlled drive, Figure 5.9). Both the stator flux and the torque controllers are of the hysteresis type. The drive requires appropriate measurements that will enable the estimation of the stator flux and torque for closed loop control of these two quantities. Stator currents and measured or reconstructed stator voltage are used for the estimation, as given by the equations (5.18) and (5.19):

$$\begin{aligned} \psi_{\alpha s} &= \int (v_{\alpha s} - R_s i_{\alpha s}) dt \\ \psi_{\beta s} &= \int (v_{\beta s} - R_s i_{\beta s}) dt \\ \psi_s &= \sqrt{\psi_{\alpha s}^2 + \psi_{\beta s}^2} \quad \cos \phi_s = \psi_{\alpha s} / \psi_s \quad \sin \phi_s = \psi_{\beta s} / \psi_s \end{aligned} \quad (5.18)$$

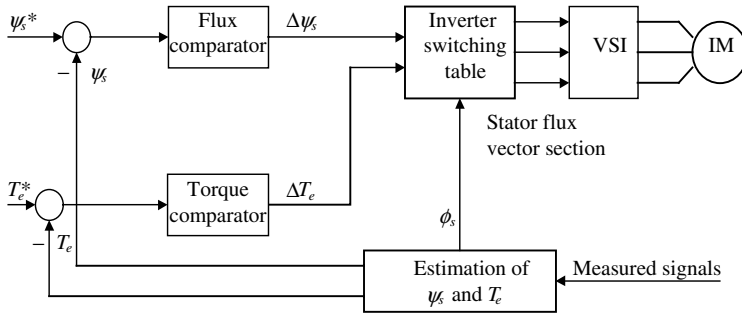


**Figure 5.8** Control scheme of a DTC induction motor drive for torque mode of operation

$$T_e = \frac{3}{2}P(\psi_{\alpha s}i_{\beta s} - \psi_{\beta s}i_{\alpha s}) \tag{5.19}$$

In addition, an estimate of the speed of rotation is required for closed loop speed control in sensorless DTC drives. Note that the DTC induction motor drive inherently lends itself to sensorless operation, since no co-ordinate transformation is involved and a speed signal is only needed for closing the speed loop.

**5.3.2.2 Stator Flux and Torque Estimation**

From the considerations of the previous sub-section, it follows that for successful operation of a DTC scheme, it is necessary to have accurate estimates of the stator flux amplitude and the electromagnetic torque. In addition, it is necessary to estimate in which sector of the complex plane the stator flux space vector is situated. As already shown in the sub-section above, the stator flux amplitude and torque can be obtained in a straightforward manner if stator currents are measured and stator voltages are reconstructed (or measured) according to equations (5.18) and (5.19).

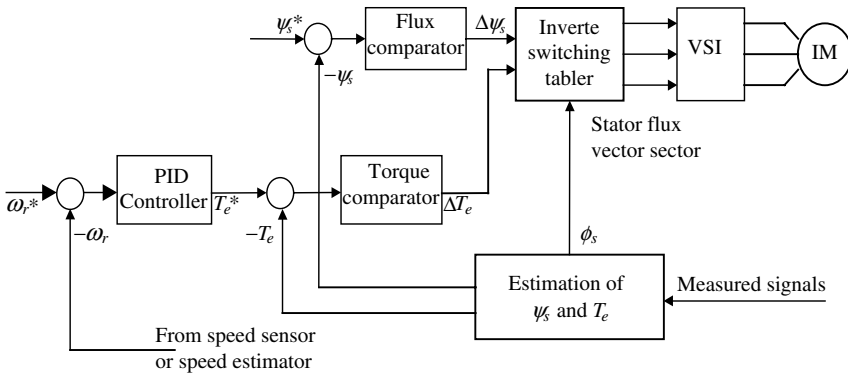


**Figure 5.9** Control scheme of DTC induction motor drive for speed mode of operation with or without speed sensor

The two problems encountered in the process of stator flux and torque estimation are the requirement for the pure integration and temperature related variation in stator resistance in equation (5.18). Stator resistance related voltage drop is significant at low speed of operation. The accuracy of the estimation at low frequency depends on the accuracy of stator resistance value. An open loop stator flux estimator can work well down to 1–2 Hz, but not below this frequency [7].

Equation (5.18) can also be used to find the location of the stator flux space vector in the complex plane:

$$\phi_s^e = \tan^{-1}(\psi_{\beta s} / \psi_{\alpha s}) \tag{5.20}$$

The exact position of the stator flux space vector is not needed in DTC induction motor drives. It is only necessary to know in which sector (out of six possible ones) of the complex plane the vector is located. Equation (5.20) will be used in the simulations for determining the sector containing the stator flux space vector. The determination of the sector of the complex plane containing the stator flux space vector can be done by using the algebraic signs of the stator flux  $\alpha$ - $\beta$  components obtained from equation (5.18) and the sign of the phase ‘b’ stator flux, which is obtained by using  $\psi_{b s} = -0.5\psi_{\alpha s} + 0.5\sqrt{3}\psi_{\beta s}$ , as discussed in [7].

### 5.3.3 Speed Control with DTC

The general speed control scheme is shown in Figure 5.9. A PID controller is used as a speed controller whose input is the error between the speed command and feedback speed. Feedback speed can be from the speed sensor or speed estimator. A PI controller is commonly used instead of a PID controller.

For better performance of speed responses (lower overshoot, faster time response, reduced or zero steady state-error), a PI controller with anti-wind up is used as a speed controller. Figure 5.10 shows the structure of a PID controller with anti-wind up in MATLAB/Simulink.

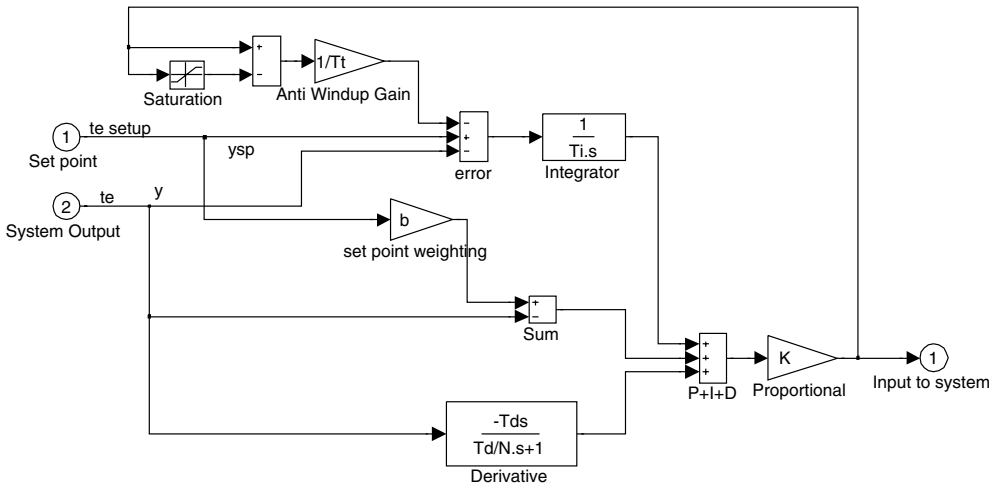


Figure 5.10 PID controller with anti-wind up

Simulation of the performance of the DTC of the induction motor using MATLAB/Simulink will be discussed in the next sub-section. The discussion will focus on both the torque control mode and the speed control mode. Structures of the simulation programs are also presented.

### 5.3.4 MATLAB/Simulink Simulation of Torque Control and Speed Control with DTC

#### 5.3.4.1 MATLAB/Simulink Simulation of Torque Control with DTC

This sub-section discusses the implementation of the simulation of the independent control of torque and stator flux with the DTC method suggested by [1]. The machine model does not consider iron losses, magnetic saturation, or stray losses. The machine's parameters are constant during the operation.

MATLAB/Simulink is used for the simulation. Figure 5.11 presents the overall layout of the simulation program.

Figure 5.12 shows the structure of the block that represents the dynamic mathematical model of the induction motor with constant parameters. Because the model is ideal, iron losses and magnetic saturation are not considered.

The parameters of the motor are listed in the dialog box, as shown in Figure 5.13.

The differential equations of the mathematical model are represented in the Simulink file, as shown in the Figure 5.14.

The machine model is represented in the  $\alpha$ - $\beta$  reference frame. The block 'Fcn' in Figure 5.14 is the expression of  $\frac{di_{\alpha s}}{dt}$  from all the variables  $i_{\alpha s}, i_{\beta s}, i_{\alpha r}, i_{\beta r}$  and the input voltage  $v_{\alpha s}, v_{\beta s}$ , as

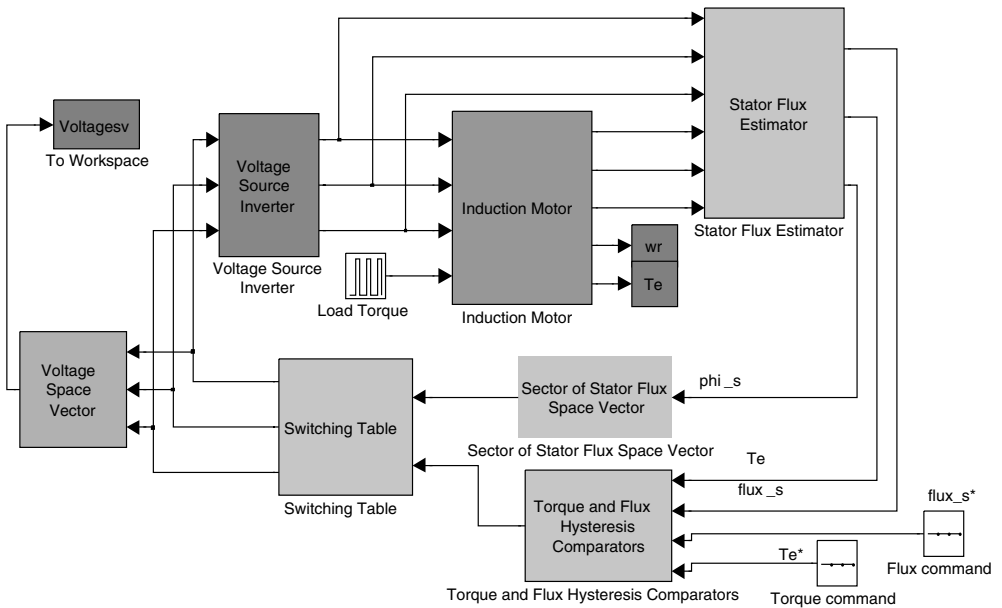


Figure 5.11 Simulation program of DTC of induction motor

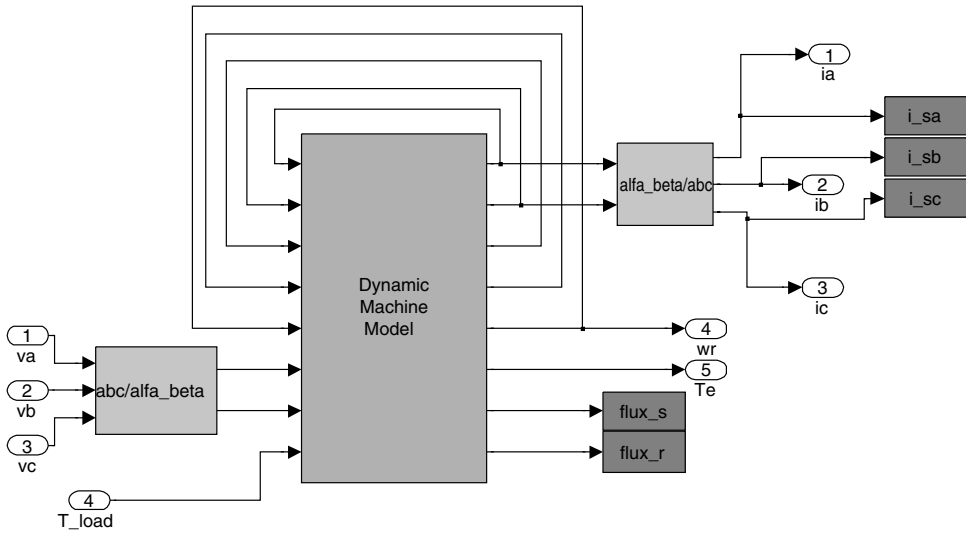


Figure 5.12 Simulink layout of the machine model

shown in Figure 5.15. Similarly, the block ‘Fcn1,’ ‘Fcn2,’ ‘Fcn3,’ and ‘Fcn4’ are the expressions for  $\frac{di_{\beta s}}{dt}$ ,  $\frac{di_{\alpha r}}{dt}$ ,  $\frac{di_{\beta r}}{dt}$ ,  $\frac{d\omega_r}{dt}$ , respectively. The block ‘Fcn5’ is the expression for the electromagnetic torque from the above variables.

The subsystem ‘Flux Calculator’ in Figure 5.14 contains the expression for the stator flux and rotor flux from the variables.

The layout of the subsystem ‘Stator Flux Estimator’ in Figure 5.11 is presented below in Figure 5.16.

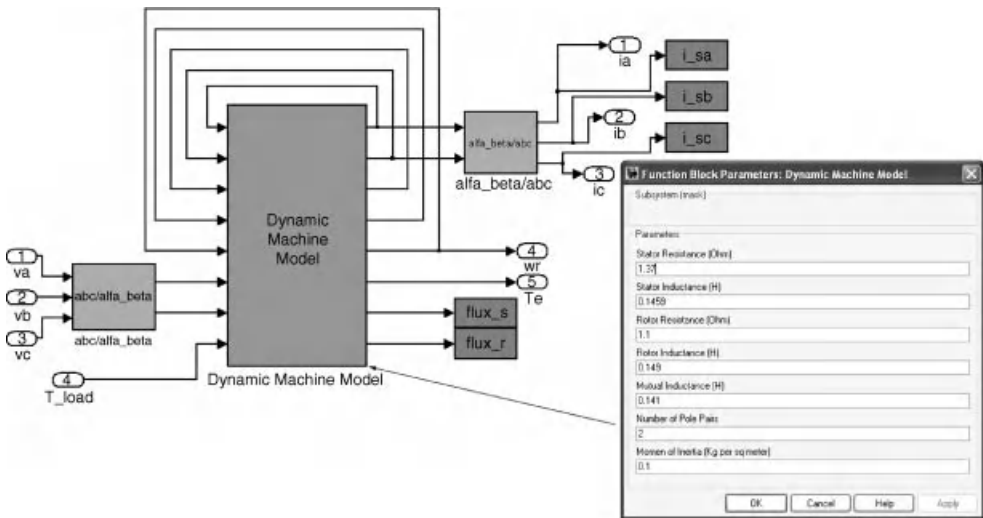
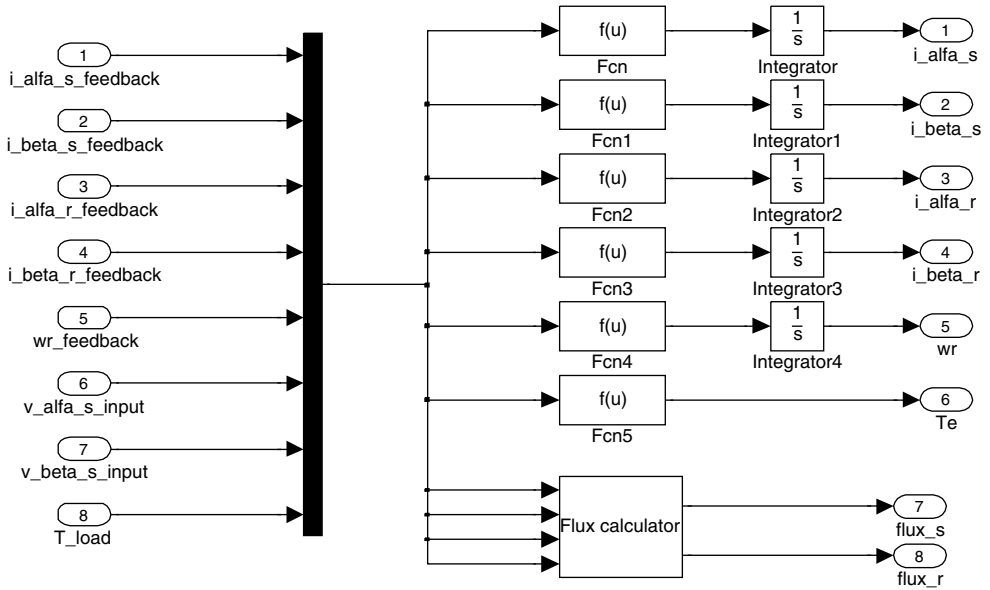


Figure 5.13 Parameters of the induction motor



**Figure 5.14** Representation of differential equations in the machine model

The location of the stator flux space vector in the complex plane is determined by the block ‘Sector of stator flux space vector’ block in the Figure 5.11. The structure of this block is shown in Figure 5.17.

The structure of the hysteresis comparators in the block ‘Torque and Flux Hysteresis Comparators’ are shown in Figure 5.18. Flux and torque hysteresis comparators are shown in Figures 5.19 and 5.20, respectively.

The structure of the switching table suggested in [1] is shown in Figure 5.21. Each ‘Look-up Table’ block represents the switching state of one leg of the three-phase voltage source inverter.

The block used to observe the voltage space vector applied to the induction motor is presented in Figure 5.22. The principle of operation of the three-phase voltage source inverter is illustrated in Figure 5.23. Each ‘Switch’ block represents a leg.

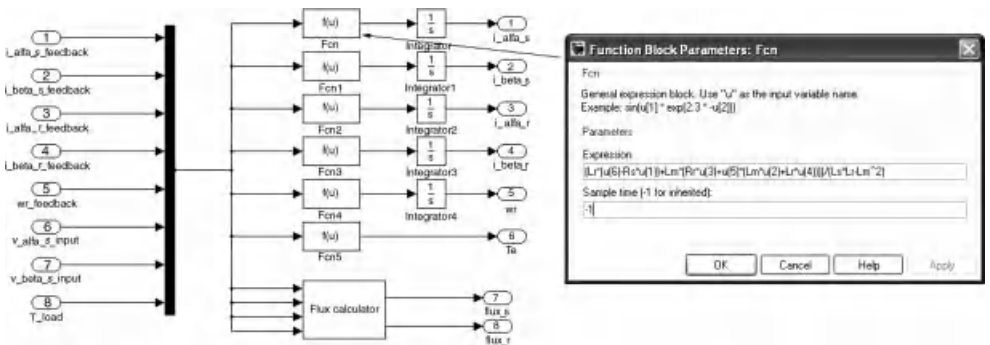


**Figure 5.15** Expression of differential equation in block ‘Fcn’



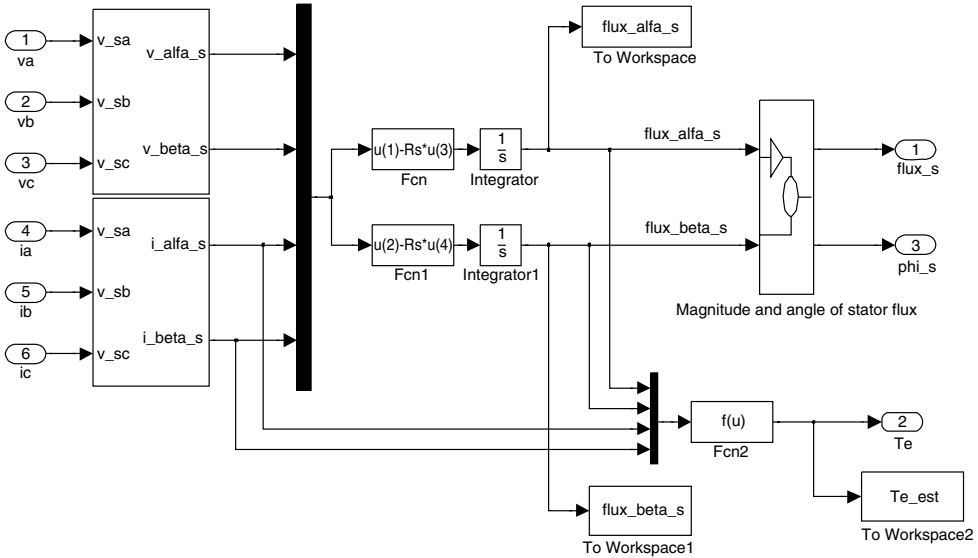


Figure 5.16 Schematic diagram of 'Stator Flux Estimator' block

The values of the flux command, torque command, and load torque of the DTC system are illustrated in Figure 5.24. The flux command is the rated flux, and the torque command is one and a half times of the rated torque. The load torque is equal to the rated value and applied instantaneously at the moment the rotor speed reaches the rated speed.

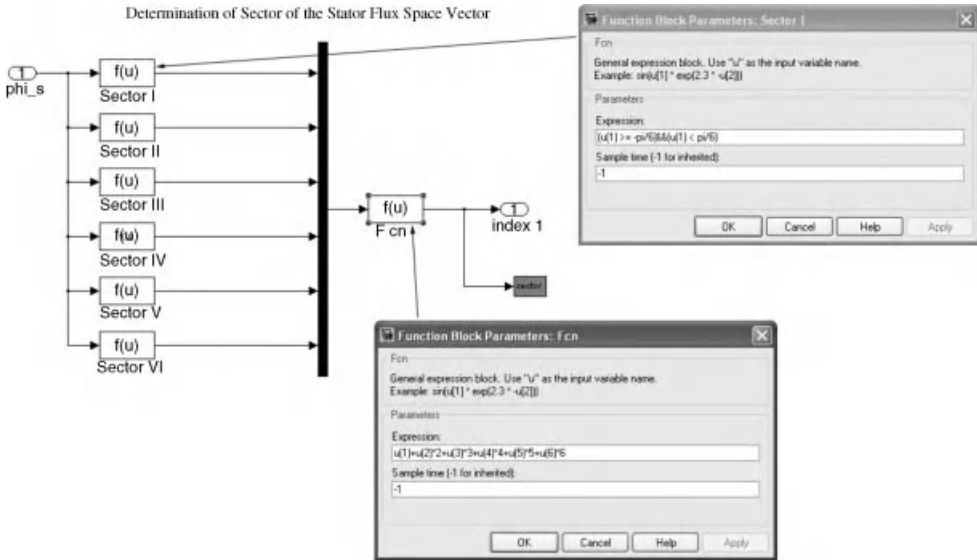


Figure 5.17 Structural diagram of 'Sector of stator flux space vector' block

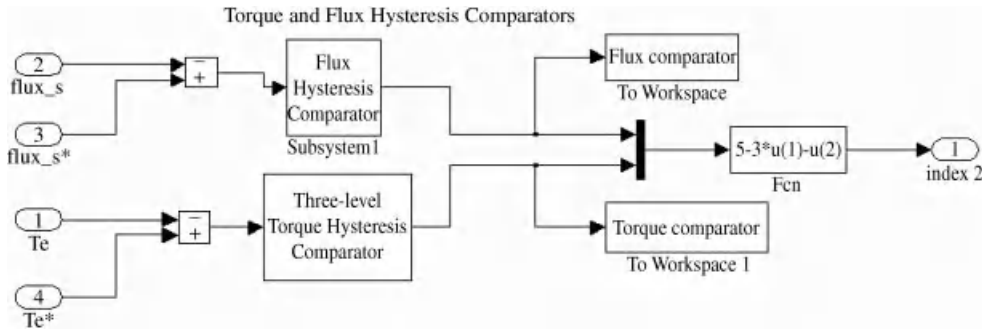


Figure 5.18 Structure of the 'Flux and Torque Hysteresis Comparators' block

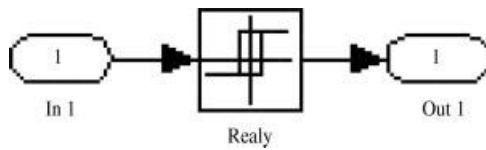


Figure 5.19 Flux hysteresis comparator

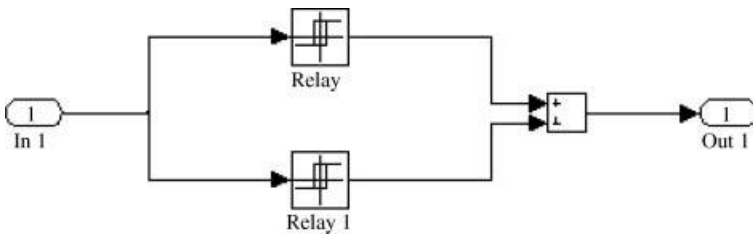


Figure 5.20 Torque hysteresis comparator

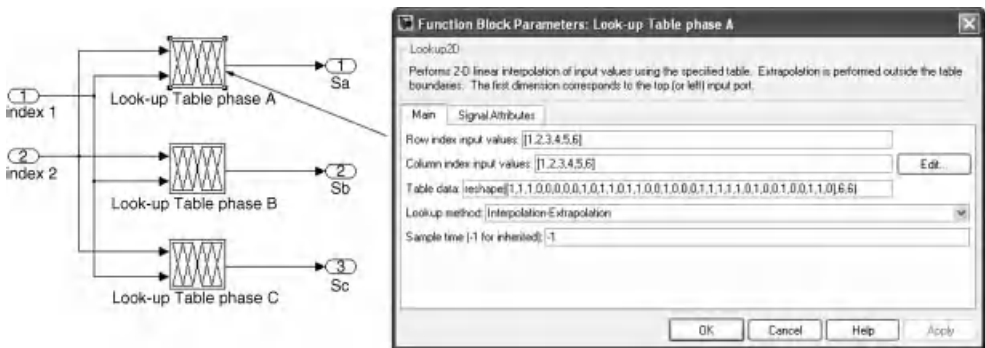


Figure 5.21 Simulink diagram of the DTC look-up table

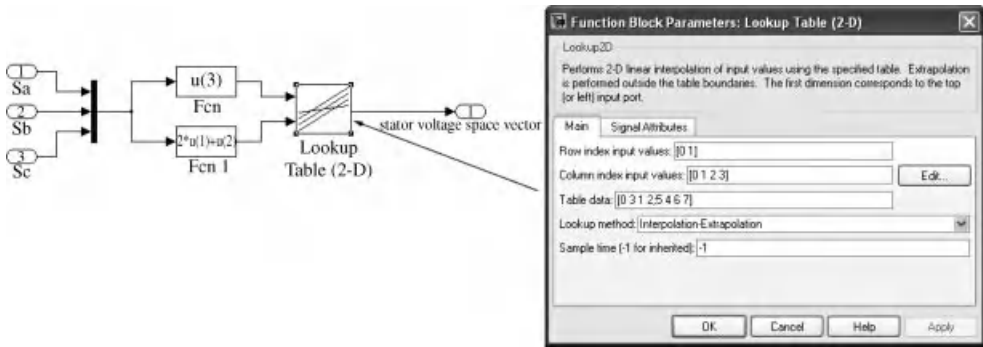


Figure 5.22 Simulink diagram for observation of the applied voltage space vectors

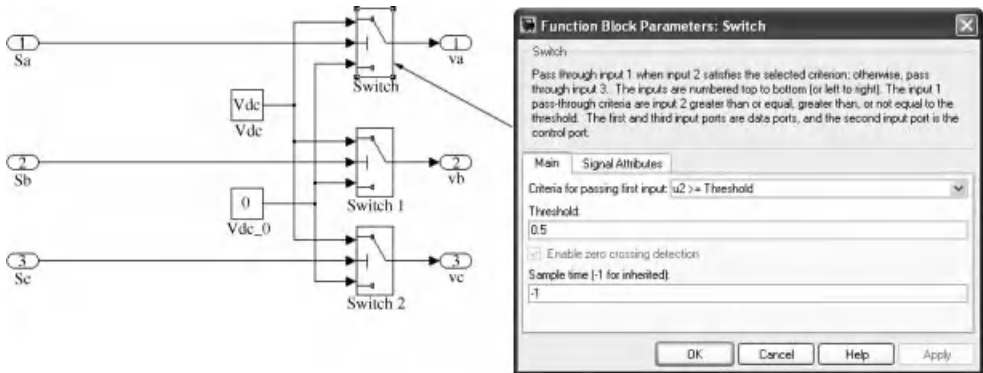


Figure 5.23 Simulink diagram of a three-phase voltage source inverter

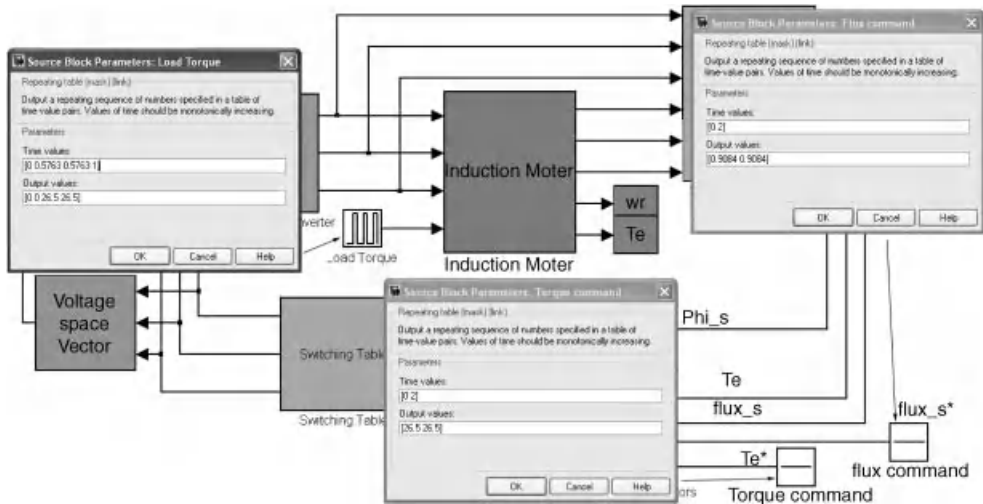
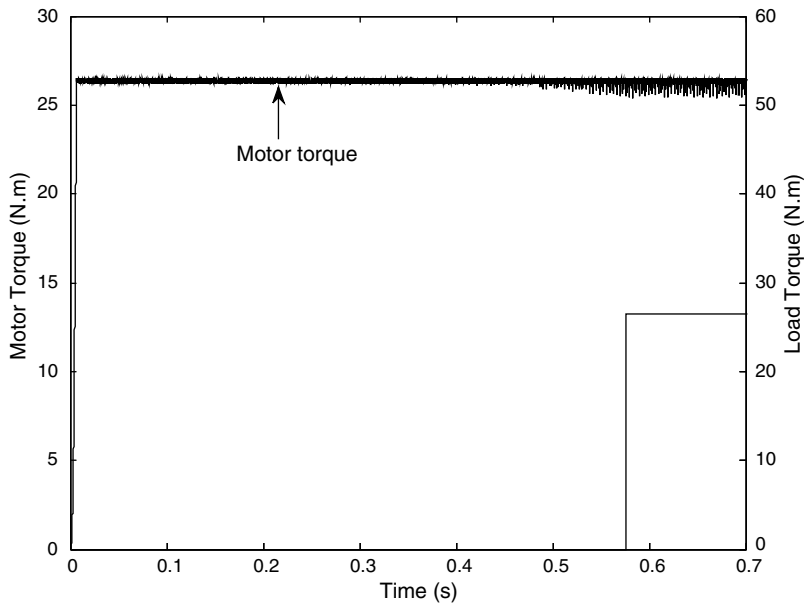


Figure 5.24 Values of flux command, torque command and load torque



**Figure 5.25** Induction motor's electromagnetic torque and load torque

Torque response in the control of torque and stator flux with DTC is shown in Figure 5.25. The load torque is not applied during the starting point, but the motor is fully loaded when it reaches the rated speed.

Stator flux and rotor speed are shown in Figure 5.26, and the stator current is illustrated in Figure 5.27.

The rotor speed in Figure 5.26 is slightly reduced with the progression of time. This is due to the fact that the average value of the motor's electromagnetic torque at high speed is slightly less than the load torque because of high torque ripples. The torque command and load torque are both at the rated values; therefore, the rate of change of speed with time is negative according to equation (5.13).

From the simulation results, the two significant weaknesses of DTC are high flux ripples at low speeds, and high torque ripple at high speeds.

#### 5.3.4.2 MATLAB/Simulink Simulation of Speed Control with DTC

Speed control can then be implemented after the development of independent control of electromagnetic torque and stator flux. A PID controller with an anti-wind up, whose structure is shown in Figure 5.10, is used for control of speed. The output of the controller is the torque command, which in turn is the input of the torque hysteresis comparator. The input of the speed controller is the error between the speed command and actual speed. Figure 5.28 shows the schematic structure of the speed control of an induction motor with DTC.

The speed control DTC system of the induction motor in Figure 5.28 is without load of the motor. The speed command goes from zero to the rated electrical speed. Details of the speed command signal and values of the PID controller's parameters are shown in Figure 5.29. Figure 5.30 shows the value of the load torque during the simulation. All other configurations

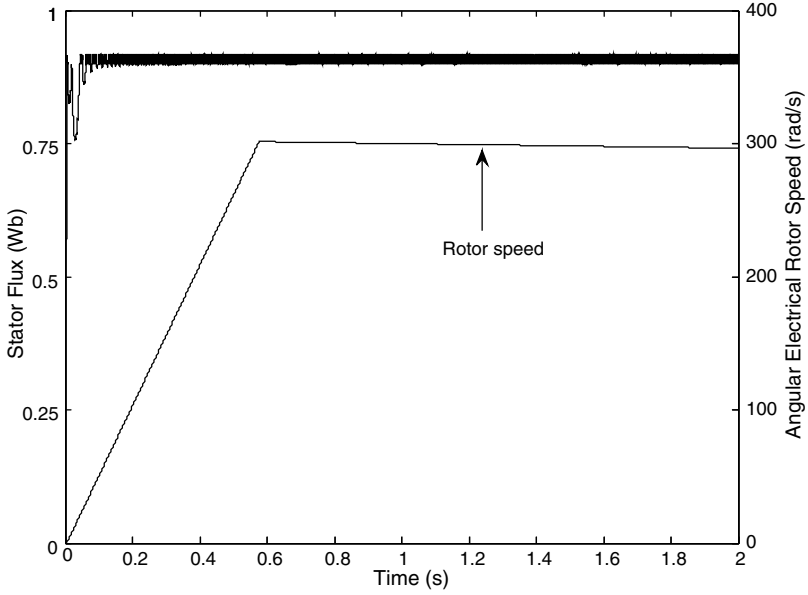


Figure 5.26 Stator flux and rotor speed in control of torque and stator flux with DTC

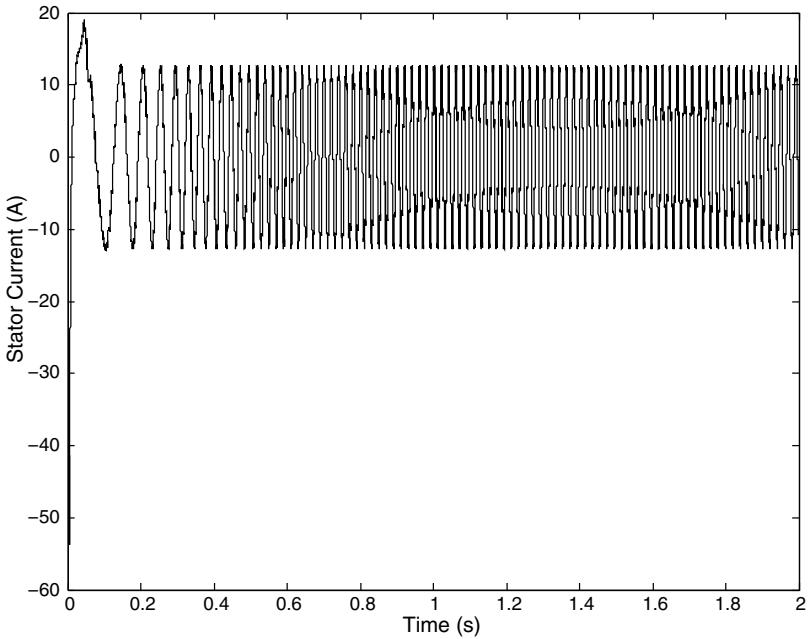
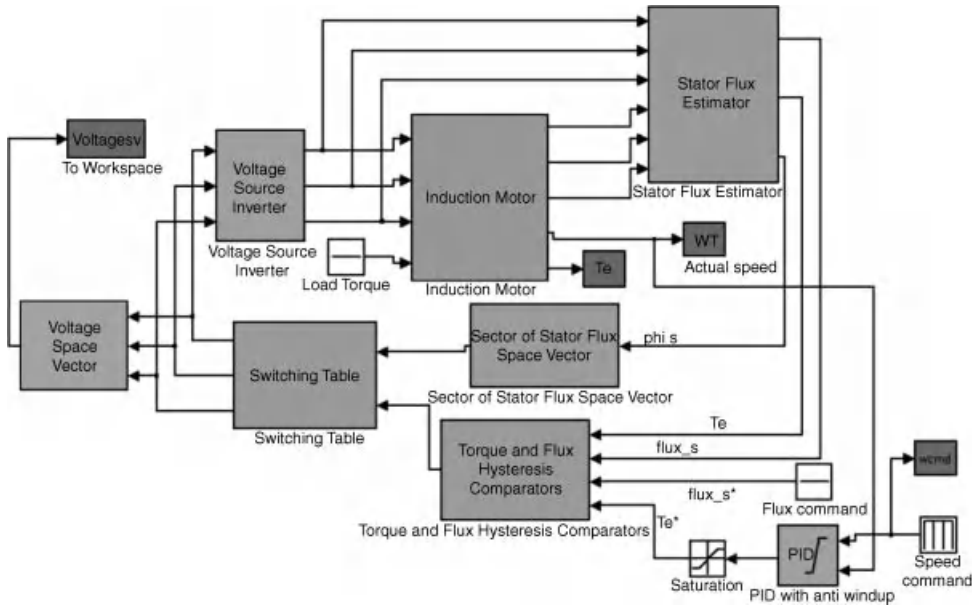
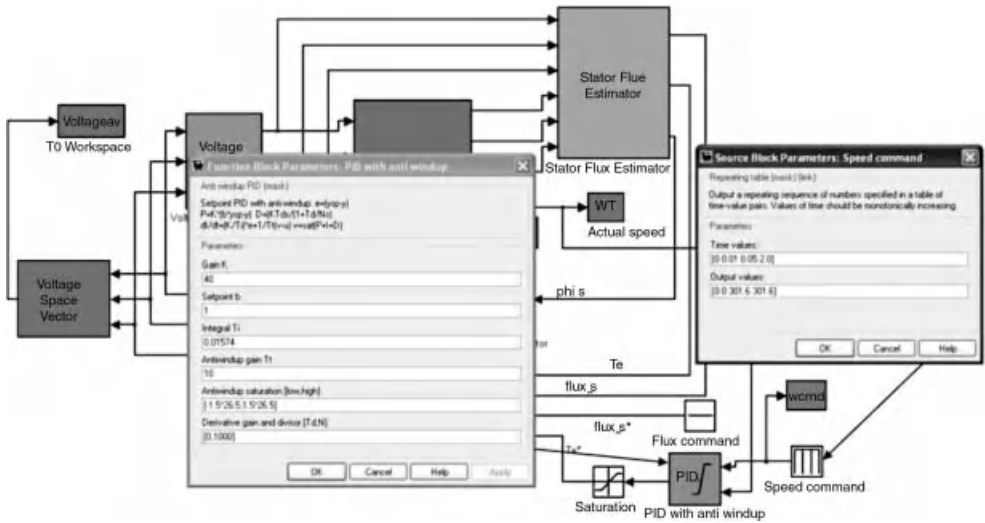


Figure 5.27 Stator current in control of torque and stator flux with DTC



**Figure 5.28** Simulation program of DTC of induction motor in speed control without load

of the simulation program are similar to the ones in the torque control program, except the values of the speed command and PID controller. Responses of the rotor speed, electromagnetic torque of the motor, stator flux, and phase current obtained from the simulation will be analyzed and presented in Figures 5.31–5.34.



**Figure 5.29** Speed command and values of PID controller’s parameters of the induction motor control system in Figure 5.28

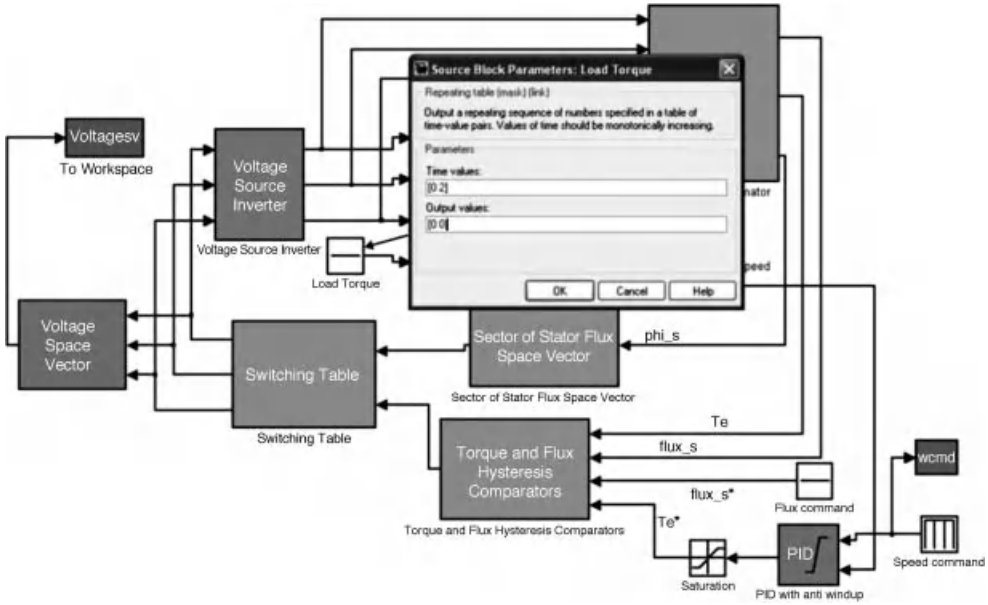


Figure 5.30 Load torque during the speed control simulation

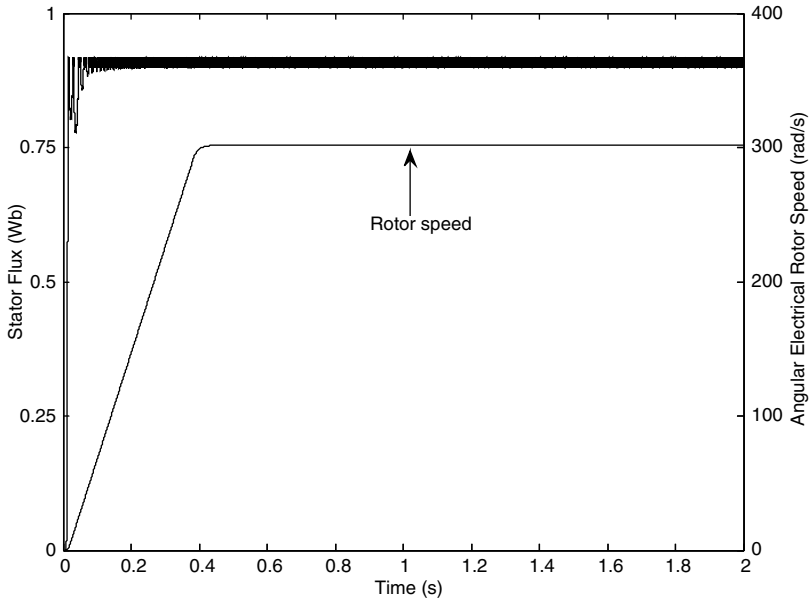
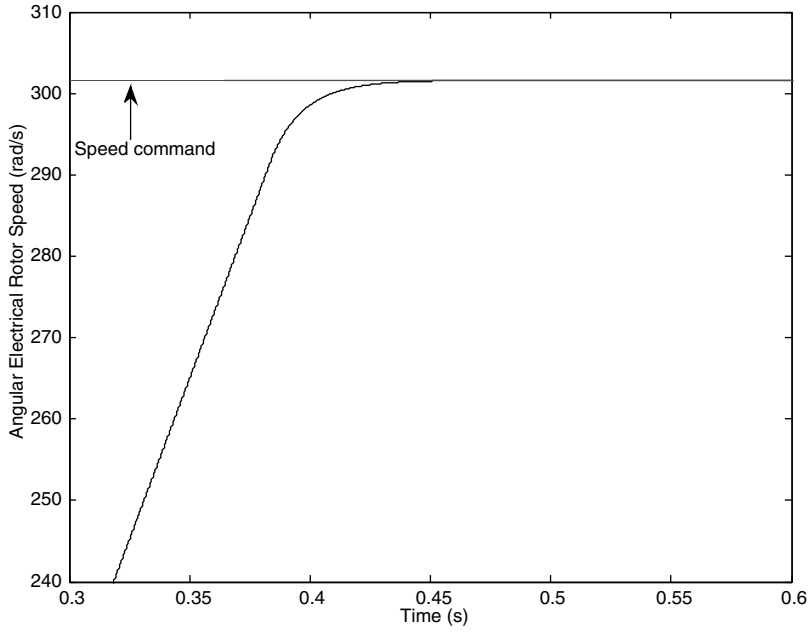
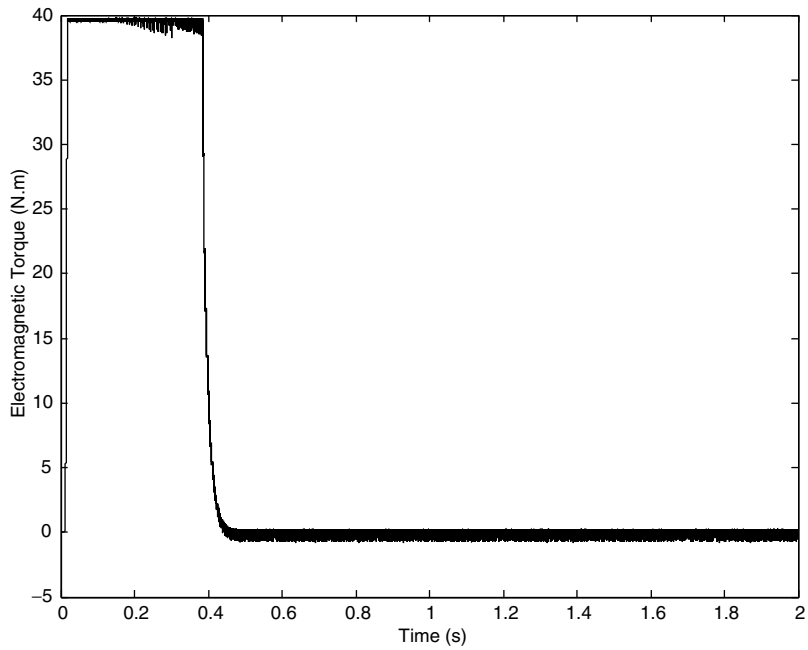


Figure 5.31 Stator flux and rotor speed of induction motor in DTC speed control without load



**Figure 5.32** Motor speed and speed command of induction motor in DTC speed control without load



**Figure 5.33** Torque response during no-load operation of DTC speed control



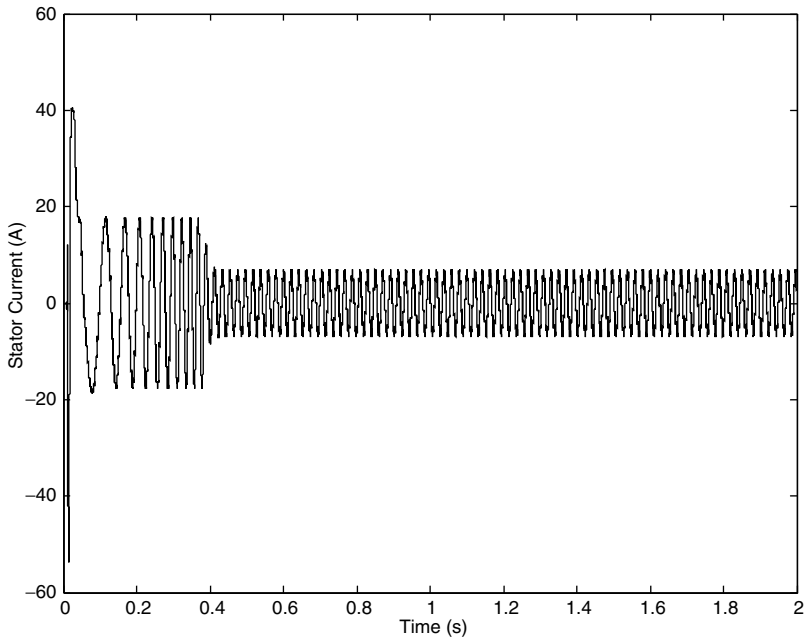


**Figure 5.34** Stator phase current during no-load operation of DTC speed control

The speed response in Figure 5.31 meets the requirement and is stable after reaching the command value. The obtained stator flux is similar to the one in the torque control and is not affected by the variation of speed. Figure 5.32 shows that the steady state error during no-load operation of the DTC speed control is insignificant.

The torque has been increased up to a maximum allowable value during the acceleration of the motor from standstill to commanded value. When the speed reaches and remains at the required value, the torque is reduced to proximity of zero. High torque ripples are still present due to the high speed of the rotor. Figure 5.34 shows the similarities between the current response versus the response obtained in torque control. In both cases the starting current is still high.

The motor is run again in the speed control mode without a load at starting point. Then a rated load torque is applied and removed step-wise; this is a highly hypothetical situation to test the noise removal capability of the controller. The load is suddenly applied after starting 1 s and also suddenly removed at the moment of 1.2 s from starting point. Speed, torque, flux, and stator phase current responses are shown in Figures 5.35–5.38, respectively.

When the load torque is applied, the speed drops, then quickly returns to the command value without steady state error. Similarly, the speed rises when the load torque is removed, then returns to speed command after a short period of time. The torque response shown in Figure 5.36 has demonstrated the dynamic of electromagnetic torque. The motor's torque cannot change abruptly to match the load torque. This is the reason for a dip in speed shown in Figure 5.35. However, the motor torque increases rapidly to bring the speed back to the required value and stabilize the speed response. Similar dynamic response of electromagnetic torque

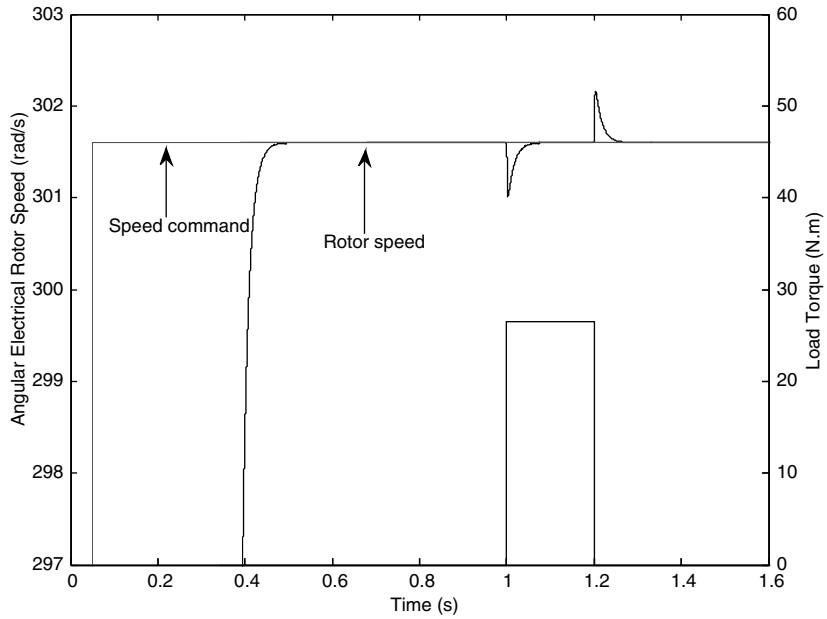


**Figure 5.35** Speed response and load torque when load is applied and removed during DTC speed control

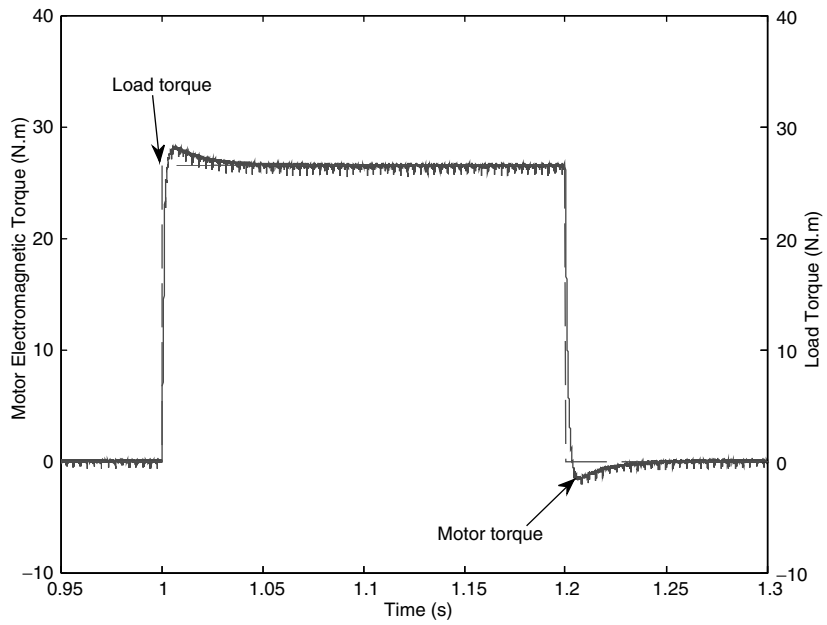


**Figure 5.36** Dynamic of motor's electromagnetic torque during the application and removal of rated load torque

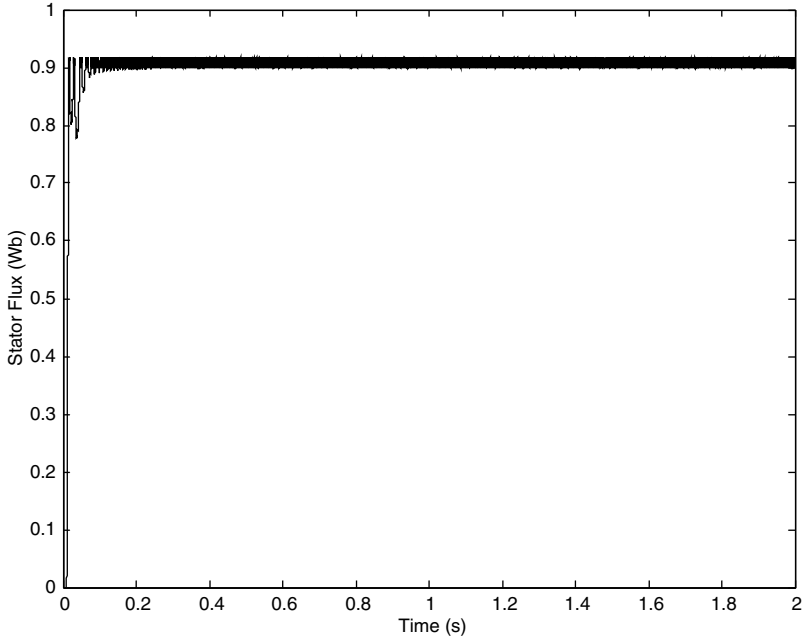


Figure 5.37 Stator flux response during the application and removal of rated load torque

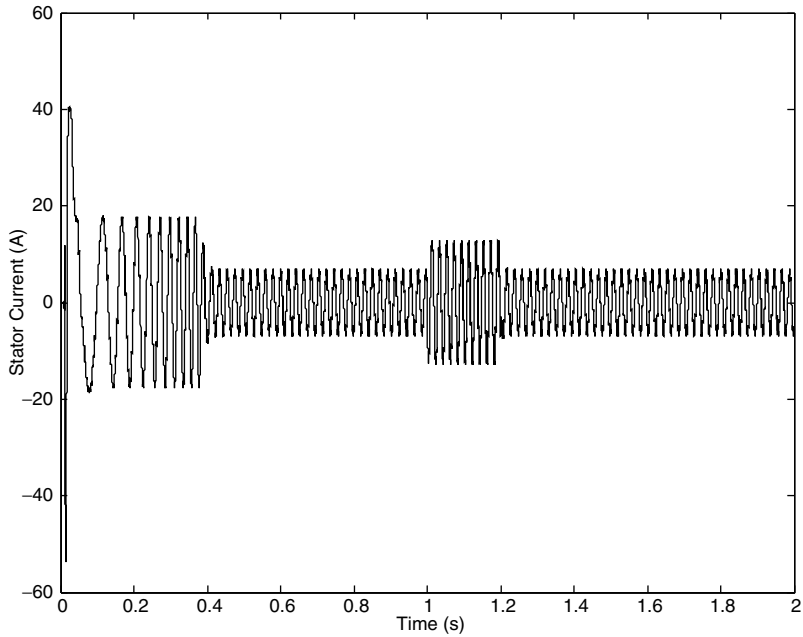


Figure 5.38 Stator phase current during the application and removal of rated load torque

occurs when the load torque is removed suddenly. This explains the variation of speed in Figure 5.35.

Stator flux is not affected during the application and removal of load torque, as shown in Figure 5.37, which causes the variation of the motor’s electromagnetic torque. This illustrates the ability of DTC to independently control the torque and flux in the induction motor.

Stator phase current is increased during the loading period of the motor, as shown in Figure 5.38. However, high overshoots are not detected during the transient period of loading and unloading. This demonstrates that the current is well controlled in DTC, except during the starting of the motor. The problem of high starting current can be overcome by the combination of soft starting and DTC.

In summary, DTC of induction motor with ideal constant parameter dynamic machine model in both torque control and speed control modes have been discussed in this section and have also been demonstrated with MATLAB/Simulink simulations. The DTC with dynamic machine model considering iron loss will be presented in the next section.

### 5.4 DTC of Induction Motor with Consideration of Iron Loss

#### 5.4.1 Induction Machine Model with Iron Loss Consideration

All the equations for this dynamic model are shown in an arbitrary, rotating common-reference frame. The equivalent iron loss resistance is placed in parallel to the magnetizing branch, as shown in Figure 5.39. The space vector equations for the new machine model in an arbitrary reference frame follow from Figure 5.39 in the form [15,16]:

$$\underline{v}_s = R_s \underline{i}_s + \frac{d\underline{\psi}_s}{dt} + j\omega_a \underline{\psi}_s \tag{5.21}$$

$$0 = R_r \underline{i}_r + \frac{d\underline{\psi}_r}{dt} + j(\omega_a - \omega_r) \underline{\psi}_r$$

$$\underline{\psi}_s = L_{\sigma s} \underline{i}_s + L_m \underline{i}_m = L_{\sigma s} \underline{i}_s + \underline{\psi}_m \tag{5.22}$$

$$\underline{\psi}_r = L_{\sigma r} \underline{i}_r + L_m \underline{i}_m = L_{\sigma r} \underline{i}_r + \underline{\psi}_m$$

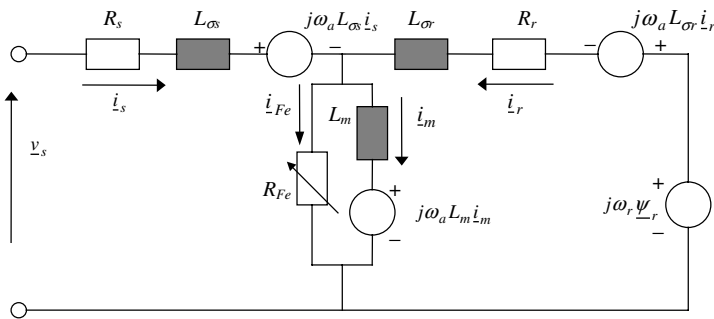


**Figure 5.39** Equivalent circuit of an induction machine with iron loss consideration in space vector form in an arbitrary rotating reference frame

$$R_{Fe} \dot{i}_{Fe} = L_m \frac{di_m}{dt} + j\omega_a L_m i_m \quad (5.23)$$

$$\dot{i}_m + \dot{i}_{Fe} = \dot{i}_s + \dot{i}_r \quad (5.24)$$

$$T_e = \frac{3}{2} P \frac{L_m}{L_{\sigma r}} (\psi_{dr} i_{qm} - \psi_{qr} i_{dm}) \quad (5.25)$$

The equivalent iron loss resistance is considered as a function of fundamental frequency only in the machine model above, where  $R_{Fe} = f(f)$ . In reality, equivalent iron loss resistance is a function of both flux density and frequency. However, the experimental method of its determination in [17] has already taken into account the dependency on flux density.

This dynamic model only takes into consideration the fundamental component of the actual iron loss, because the equivalent iron loss resistance in Figure 5.39 models only the fundamental component of the iron loss. The value of the equivalent iron loss resistance is calculated using a variable-frequency, no-load test where voltage magnitude is varied using the  $V/f = \text{const.}$  control law. The source used in the experiment can be either an ideal sinusoidal voltage source (e.g. a synchronous generator) or a PWM voltage source inverter, where measurement of the fundamental component of the input power and current is required. In real operation with PWM voltage source inverter, there will be higher-order voltage harmonics in the supply voltage. These harmonics will 'see' the fundamental equivalent iron loss resistance when the model of Figure 5.39 is used in dynamic simulation of a DTC induction motor drive, since the inverter model will be included. This is an inherent limitation of the model in equations (5.18)–(5.23), but is of no consequence when the vector control is considered. In simulation of the vector controlled drives, the voltage source can be assumed to be ideally sinusoidal without any loss of generality, so that the fundamental equivalent iron loss resistance suffices. However, this is not the case in DTC, where the inverter model has to be included in the study. Since use of the fundamental equivalent iron loss resistance for higher order voltage harmonics is of questionable accuracy, simulation results obtained with the model of Figure 5.39 will exhibit a change in the torque ripple characteristic. Unfortunately, there appears to be no better solution to the problem. We would ideally need to use the theory of multiple reference frames, in which an appropriate circuit, similar to the one of Figure 5.39, would be devised for each voltage harmonic. Equivalent iron loss resistance values in these harmonic equivalent circuits could be obtained using the extension of the iron loss identification procedure proposed in [17]. However, since DTC relies on hysteresis control, voltage harmonics that will be present in the inverter output voltage cannot be determined in advance; moreover, output voltage spectrum is continuous, so application of the multiple reference frame theory is not possible.

The complete model in the stationary reference frame, convenient for dynamic simulation, is obtained from equations (5.19) to (5.25) in the following forms:

$$\begin{aligned} v_{\alpha s} &= R_s i_{\alpha s} + L_{\sigma s} \frac{di_{\alpha s}}{dt} + L_m \frac{di_{\alpha m}}{dt} \\ v_{\beta s} &= R_s i_{\beta s} + L_{\sigma s} \frac{di_{\beta s}}{dt} + L_m \frac{di_{\beta m}}{dt} \end{aligned} \quad (5.26)$$

$$0 = R_r i_{\alpha r} + L_{\sigma r} \frac{di_{\alpha r}}{dt} + L_m \frac{di_{\alpha m}}{dt} + \omega_r (L_{\sigma r} i_{\beta r} + L_m i_{\beta m})$$

$$0 = R_r i_{\beta r} + L_{\sigma r} \frac{di_{\beta r}}{dt} + L_m \frac{di_{\beta m}}{dt} - \omega_r (L_{\sigma r} i_{\alpha r} + L_m i_{\alpha m})$$
(5.27)

$$i_{\alpha m} + i_{\alpha Fe} = i_{\alpha s} + i_{\alpha r} \quad i_{\beta m} + i_{\beta Fe} = i_{\beta s} + i_{\beta r}$$
(5.28)

$$R_{Fe} i_{\alpha Fe} = L_m \frac{di_{\alpha m}}{dt} \quad R_{Fe} i_{\beta Fe} = L_m \frac{di_{\beta m}}{dt}$$
(5.29)

$$T_e = \frac{3}{2} P \frac{L_m}{L_{\sigma r}} [i_{\beta m} (L_{\sigma r} i_{\alpha r} + L_m i_{\alpha m}) - i_{\alpha m} (L_{\sigma r} i_{\beta r} + L_m i_{\beta m})]$$
(5.30)

$$T_e - T_L = \frac{J}{P} \frac{d\omega_r}{dt}$$
(5.31)

The state-space variables of the differential equations are selected as  $\alpha$ - $\beta$  components of stator current, rotor current, and magnetizing current, as well as angular electrical speed of rotor. The final set of differential equations is derived from the equations (5.26) to (5.31) in a straightforward manner, by eliminating iron loss current components from equation (5.29) using equation (5.27).

Actual variation of the equivalent iron loss resistance with fundamental frequency is given in equation (5.32) for a three-phase squirrel cage, 4 kW, 380 V, 8.7 A, 4-pole, 50 Hz, 1440 rpm induction motor. The fundamental iron loss component was determined experimentally, using the procedure of [17]. The testing was performed in the frequency range from 10 Hz up to 100 Hz. The base speed region, relevant for the analysis and simulation in this chapter, encompasses frequencies up to 50 Hz. When the fundamental iron loss component, as function of the operating frequency, is known, the equivalent iron loss resistance of Figure 5.39 can be easily calculated. Figure 5.40 presents the measurement results related to the fundamental iron loss component (Figure 5.40a) and corresponding equivalent iron loss resistance

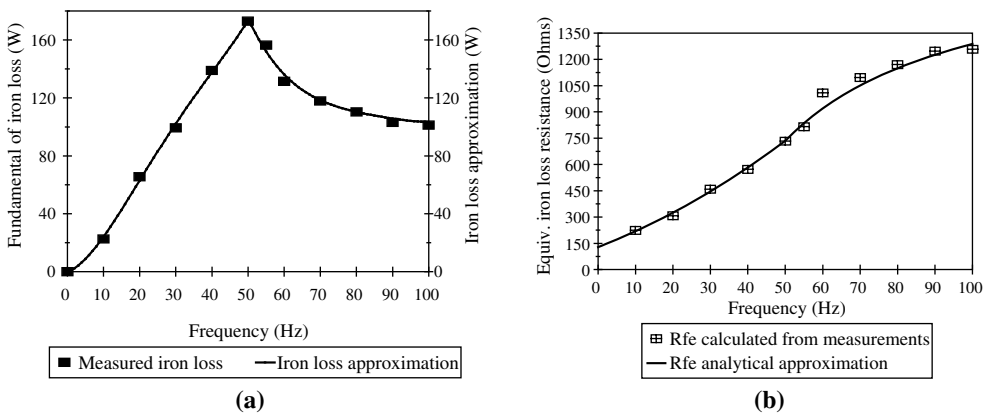


**Figure 5.40** Fundamental iron loss component: (a) calculated equivalent iron loss resistance; and (b) experimentally identified points and corresponding analytical approximations

(Figure 5.40b). The appropriate analytical approximation of the equivalent iron loss resistance, required for the circuit of Figure 5.39, is also shown in Figure 5.40b. Analytical approximation of the fundamental iron loss, included in Figure 5.40a, will be required later for compensation purposes. These analytical functions, obtained using least squares fitting, are given with the following expressions, in terms of fundamental frequency:

$$P_{Fe}(W) = \begin{cases} 0.00003808f^4 - 0.004585f^3 + 0.183f^2 + 1.0254f - 0.2784 & f \leq 50 \text{ Hz} \\ 0.00002087f^4 - 0.0073f^3 + 0.9658f^2 - 57.684f + 1468.3 & f > 50 \text{ Hz} \end{cases}$$

$$R_{Fe}(\Omega) = \begin{cases} 128.92 + 8.242f + 0.0788f^2 & f \leq 50 \text{ Hz} \\ 1841 - 55275/f & f > 50 \text{ Hz} \end{cases} \quad (5.32)$$

### 5.4.2 MATLAB/SIMULINK Simulation of the Effects of Iron Losses in Torque Control and Speed Control

#### 5.4.2.1 Dynamic Machine Model with Consideration of Iron Losses

A new MATLAB/SIMULINK model based on a dynamic machine model with iron loss consideration is developed. This new simulation model will then replace the model of ideal machine in simulation of DTC in torque control mode and speed control mode. Figure 5.41 below shows this new model for an induction machine with iron losses in a DTC torque control MATLAB/SIMULINK program. Figure 5.42 illustrates the block diagram of the model.

The details of the block ‘Induction Motor Dynamic Model’ in Figure 5.42 is shown below in Figure 5.43. Details of the differential equations are demonstrated in Figures 5.44–5.46.

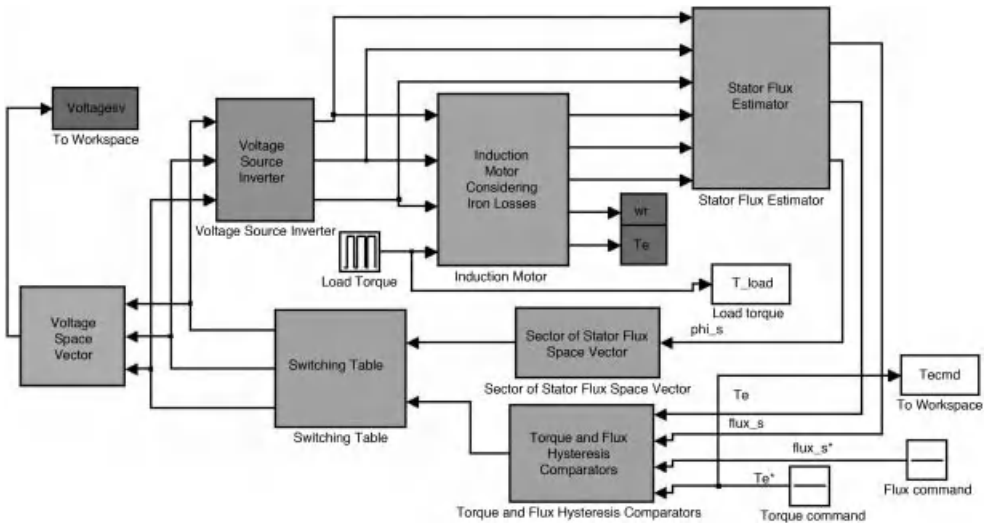


Figure 5.41 Simulation of an induction motor with iron losses consideration

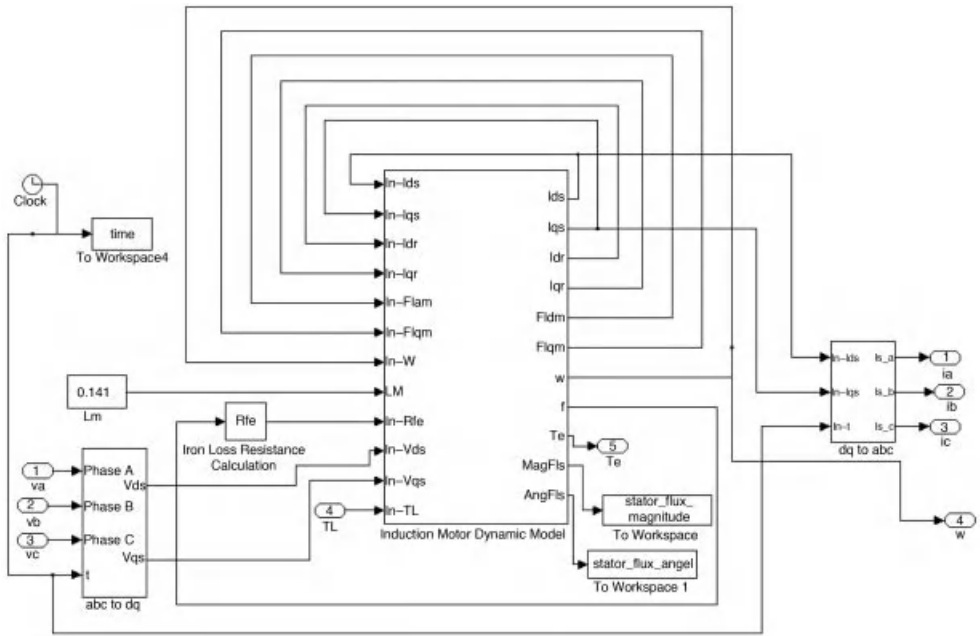


Figure 5.42 Block diagram model for an induction motor with iron losses

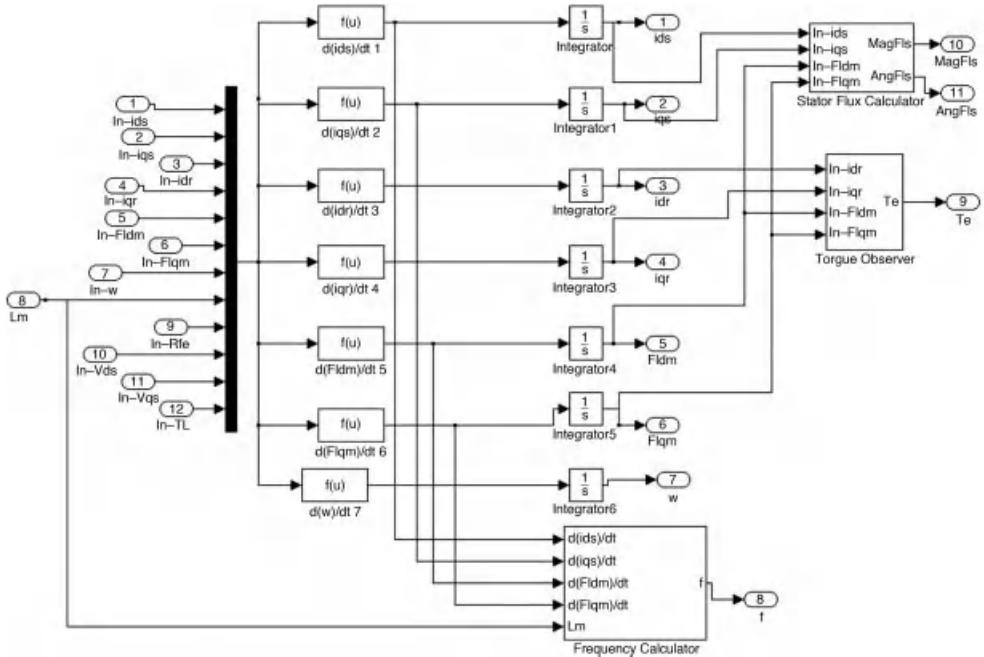


Figure 5.43 Representation of differential equations in a model with iron losses



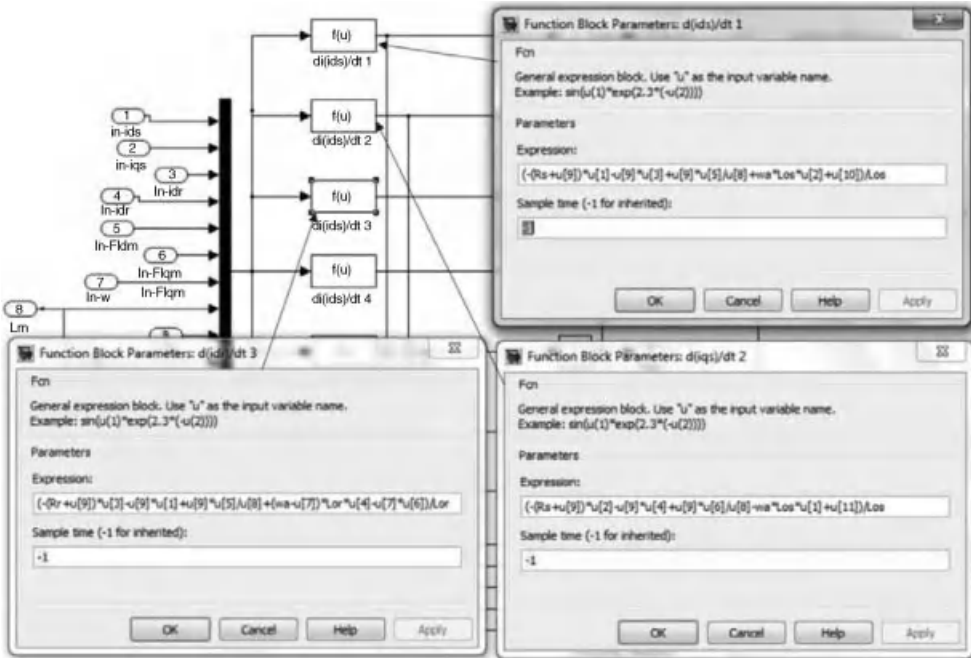


Figure 5.44 Expressions for the blocks ‘d(ids)/dt,’ ‘d(iqs)/dt,’ and ‘d(idr)/dt’

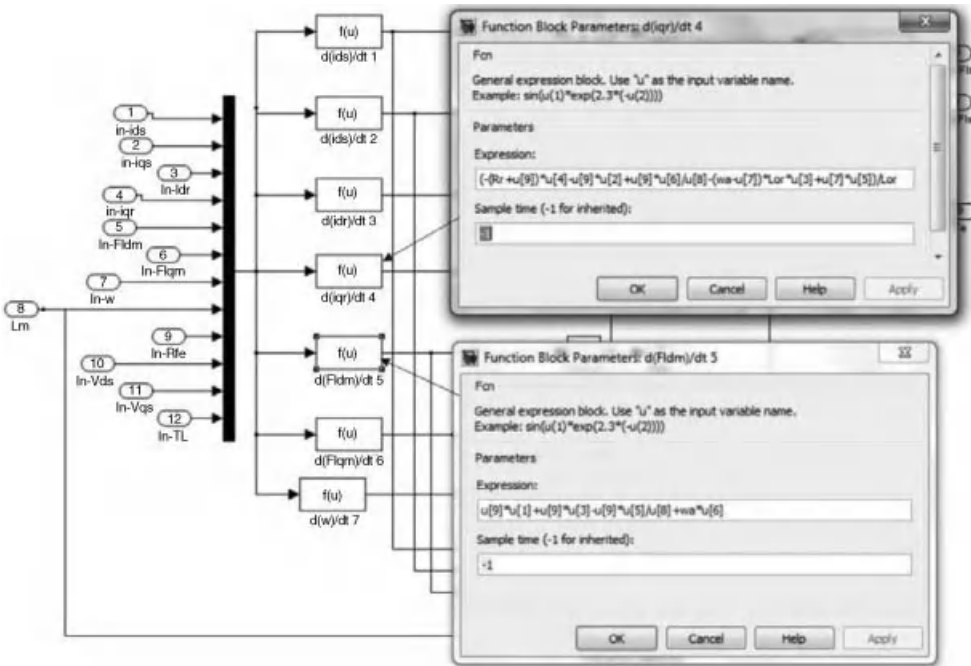


Figure 5.45 Expressions for the blocks ‘d(iqr)/dt’ and ‘d(Fldm)/dt’

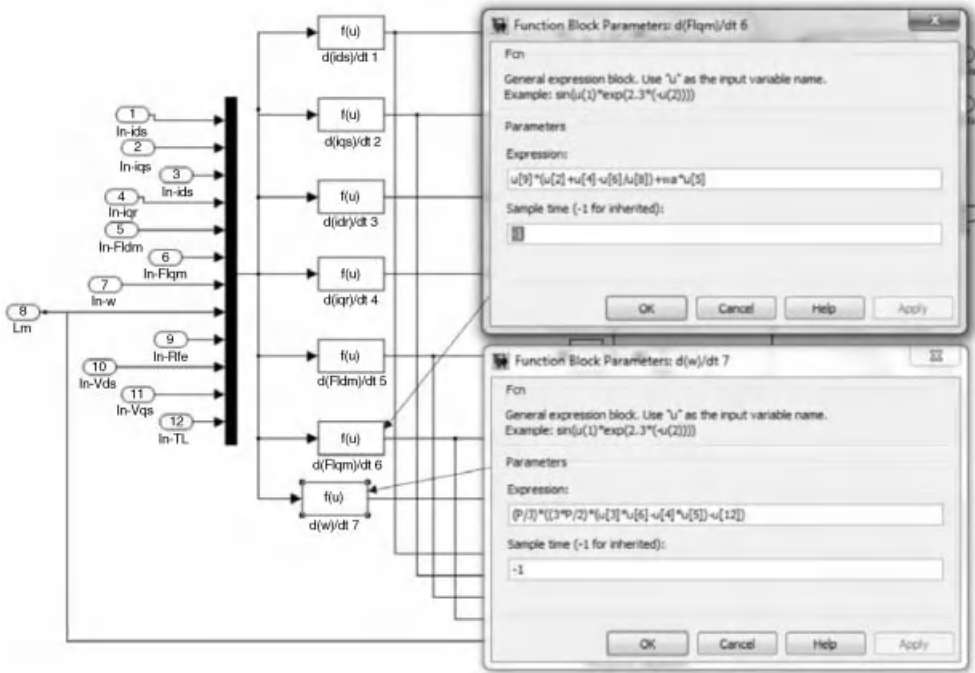


Figure 5.46 Expressions for the blocks ‘d(Flqm)/dt’ and ‘d(w)/dt’

The variables in the differential equations in the above figures are components of stator current, rotor current, air-gap flux, and rotor speed.

The structural diagram of the block ‘Frequency Calculator’ is shown in Figure 5.47. The frequency is calculated from the components of stator flux. The components of stator

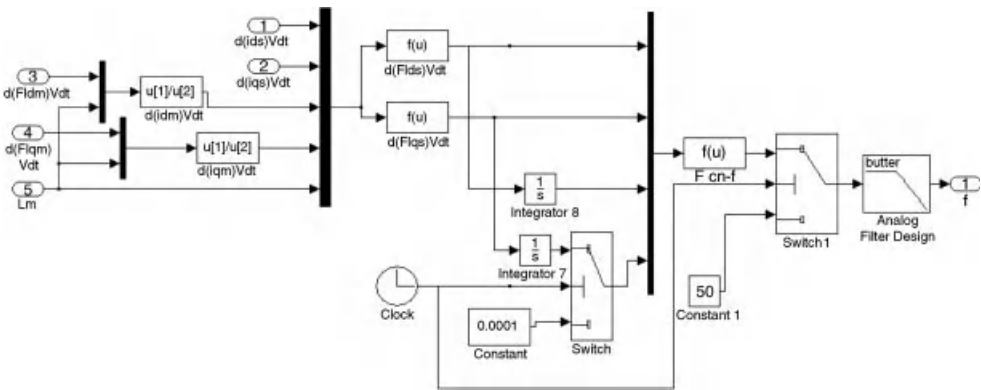


Figure 5.47 Structural diagram of the block ‘Frequency Calculator’

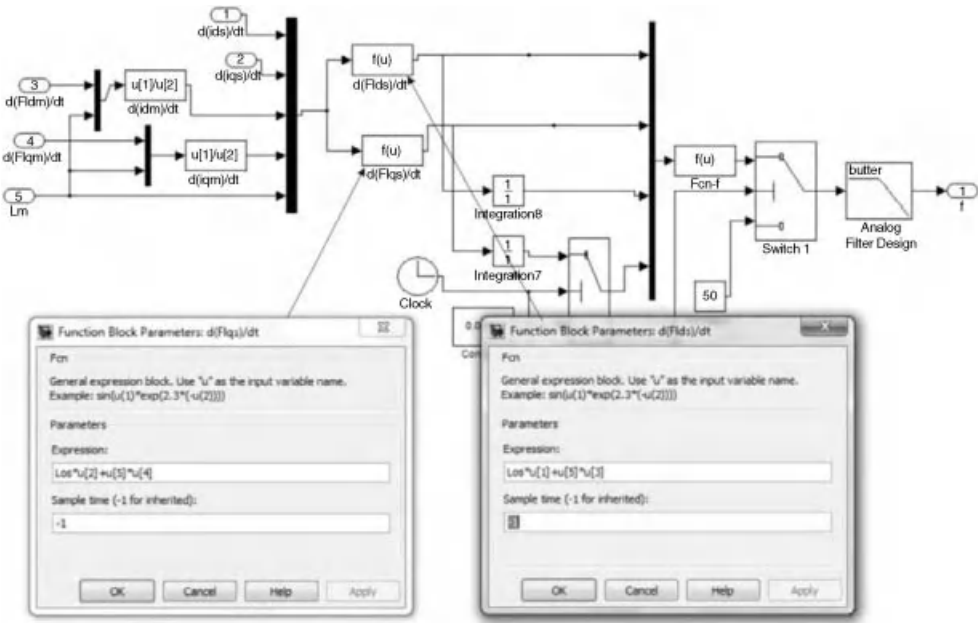


Figure 5.48 Equations for derivatives of  $\alpha$  and  $\beta$  components of stator flux

flux are determined from the components of stator current and air-gap flux. The equation for frequency determination is

$$f = \frac{1}{2\pi} \frac{\psi_{\alpha s} \frac{d\psi_{\beta s}}{dt} - \psi_{\beta s} \frac{d\psi_{\alpha s}}{dt}}{\psi_{\alpha s}^2 + \psi_{\beta s}^2} \tag{5.33}$$

Because the values of the denominator in equation (5.33) are small when the simulation starts running, the values of the variables are artificially kept for the first few step-sizes of the simulation to avoid the error ‘NaN’ (not a number). The frequency is also kept at 50 Hz during this period. Due to the small step-size of the simulation, this constant value does not affect the results of the simulation process. The calculated frequency then goes through a Butterworth low-pass filter before being used to determine the iron loss equivalent resistance.

Equations for calculating the derivatives of  $\alpha$  and  $\beta$  components of stator flux to be used in equation (5.33) are shown in Figure 5.48. Figure 5.49 demonstrates implementation of equation (5.33). The parameters of the Butterworth filter are also presented in Figure 5.49.

The selecting value for the switches is  $5 \mu s$ , as shown in Figure 5.50.

Figure 5.51 shows the block diagram and expression in ‘Stator Flux Calculator’ in Figure 5.43. Figure 5.52 illustrates the diagram and expression for electromagnetic torque estimation in the ‘Torque Observer’ block of Figure 5.43.

**5.4.2.2 Simulation of DTC with Iron Losses Consideration in Torque Control Mode**

The torque response obtained from the simulation of DTC in the torque control mode, when iron losses are considered, is illustrated in Figure 5.53. The torque command is still the same as the one in the simulations of Section 5.3 (26.5 Nm). Similarly, flux command remains at

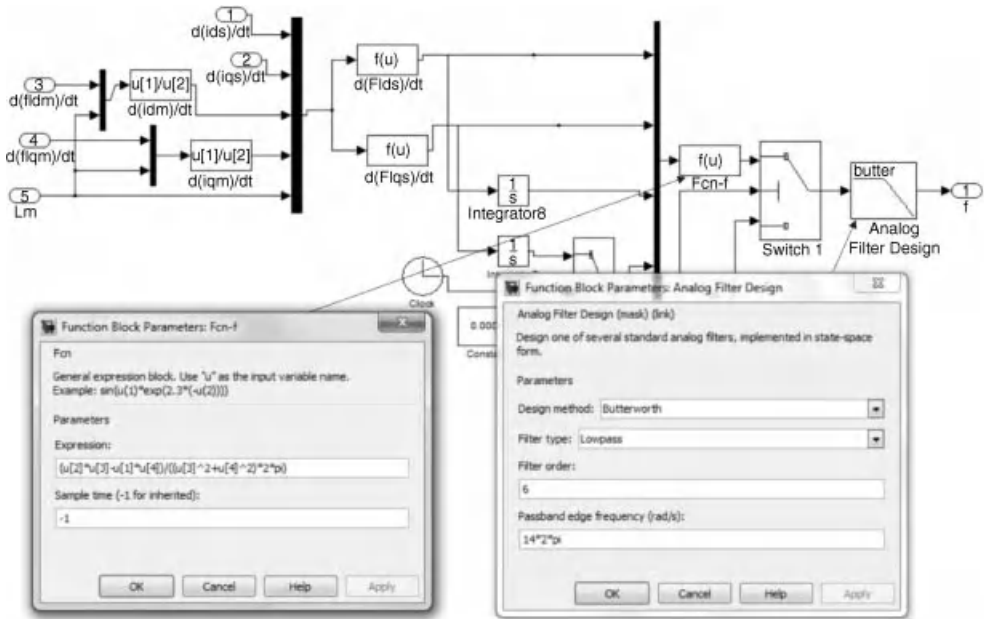


Figure 5.49 Expression in ‘Fcn-f’ block and parameters for Butterworth filter

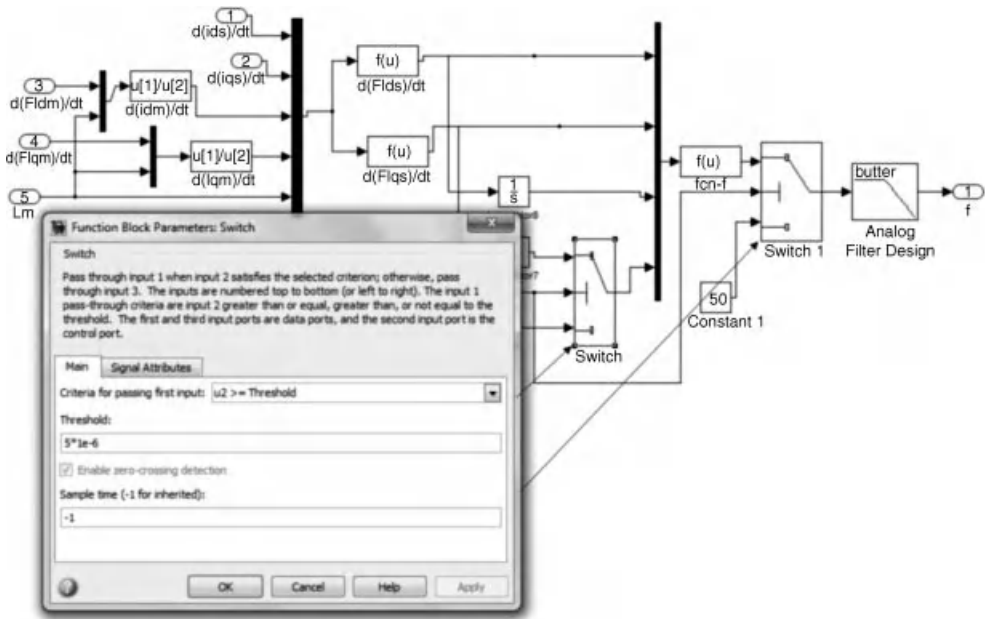


Figure 5.50 Selecting a value for the switches in Figure 5.47

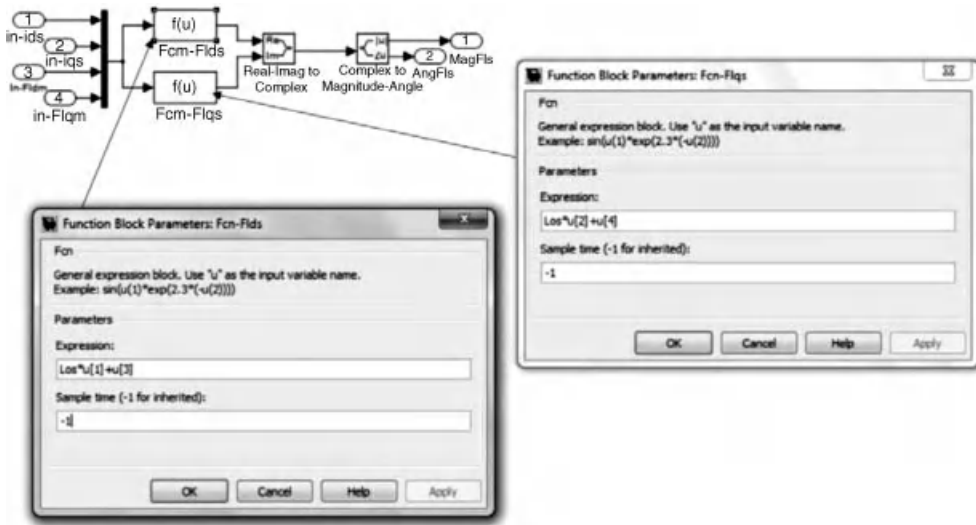


Figure 5.51 Diagram and expression for the stator flux calculation

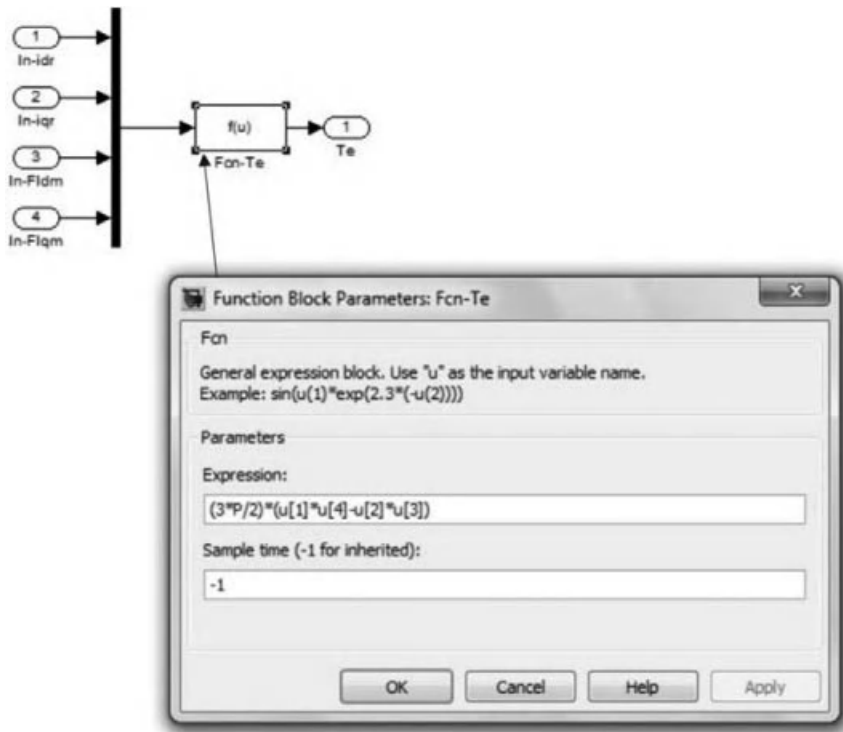
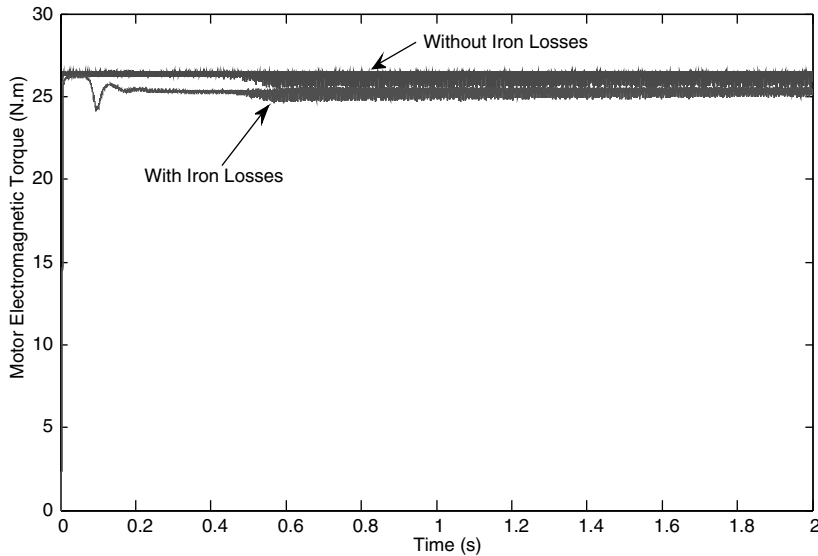


Figure 5.52 Diagram and expression for the electromagnetic torque observation



**Figure 5.53** Electromagnetic torque responses for the both cases, without iron losses and with iron losses consideration

0.9084. The induction motor is still the same, only changing the dynamic model from one with constant parameter and no iron loss consideration to one that includes iron losses as a function of frequency.

As can be seen in Figure 5.53 that the electromagnetic torque of the motor cannot reach the commanded value as it does in the case of ideal machine model due to the iron losses. Therefore, the actual torque created by the motor is lower than the expected value from the ideal machine model. This deficiency of the electromagnetic torque will cause inaccuracy in speed response, as shown in Figure 5.54. In this figure, the speed response of the ideal motor reaches the rated electrical speed when the rated load torque is applied. However, the rotor speed does not reach that rated value when iron losses are considered in the machine model, because of the deficiency of torque, as explained above and shown in Figure 5.55. The difference in torque responses during the steady state in Figure 5.55 result in a quick decrease of rotor speed, in Figure 5.54, when iron losses are included. Stator flux and phase current responses are not affected by the inclusion of iron losses in the machine model, as demonstrated in Figures 5.56 and 5.57.

#### 5.4.2.3 Simulation of DTC with Iron Losses Consideration in Speed Control Mode

The ideal constant parameter machine model in the MATLAB/Simulink program for speed control of DTC in Section 5.3.4.1 is replaced with the machine model considering iron loss, as presented in Section 5.4.2.1. The parameters of the PID speed controller are also adjusted to get a good response of the rotor speed. Figure 5.58 shows the response of the rotor speed during the start-up, application, and removal of load torque.

The speed response, when iron losses are included, is a little slower than the one obtained with an ideal constant machine model. This is due to the lower actual electromagnetic torque produced by the motor when output power is reduced by iron losses. However, the steady state response of the speed is acceptable. The rotor speed reaches the commanded value.

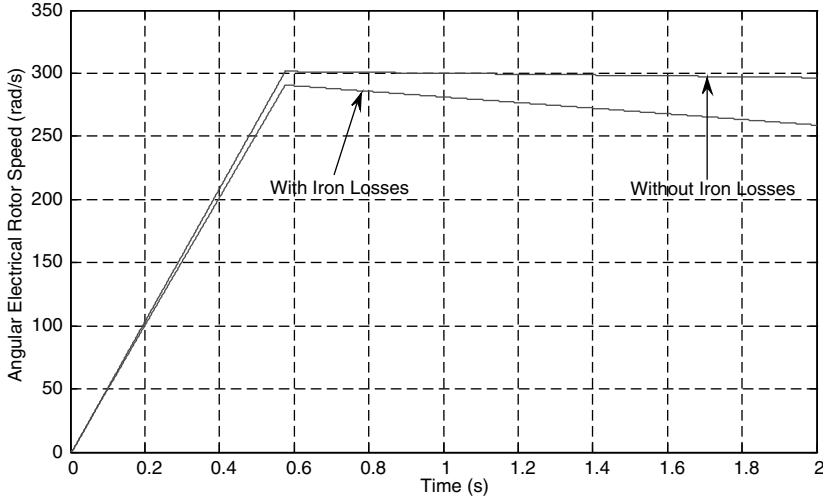


**Figure 5.54** Rotor speed responses for the both cases, without iron losses and with iron losses consideration

When the load torque is applied instantaneously, the speed goes down deeper for the case with iron loss. The recovering period of the speed response is therefore slightly longer for the case with iron loss. The steady state error of speed response is the same for both cases; rotor speed returns to commanded value in both cases. A similar difference between the two cases is observed when load torque is removed instantaneously.

Figures 5.59 and 5.60 show the responses of the motor’s electromagnetic torque when load torque is applied and removed respectively. In both figures, the torque responses, when iron

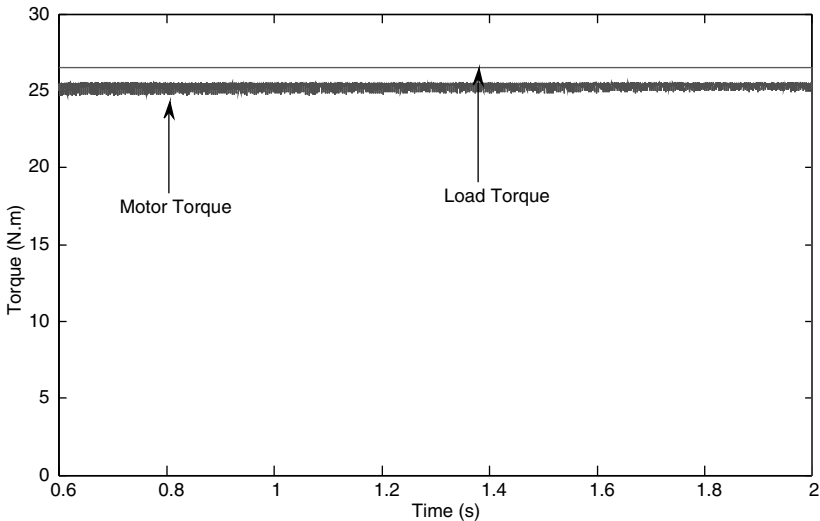


**Figure 5.55** Load torque and electromagnetic torque of the induction motor with iron losses consideration during steady state

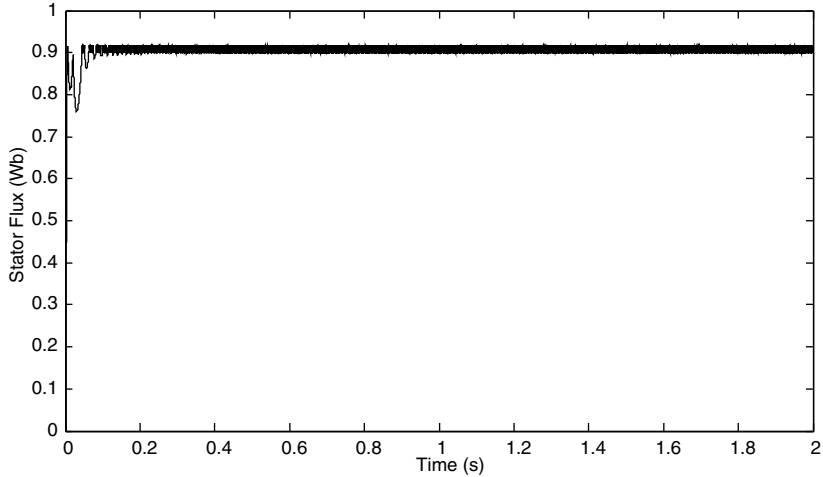


**Figure 5.56** Stator flux response when iron losses are considered

losses are ignored and included, are presented. From Figure 5.59, torque response in the case of iron losses has higher torque ripple in steady state and longer response time compared with the case when iron losses are not considered. Similar deficiency is also observed when load torque is removed.

The performance of speed control in DTC of induction motor is generally not affected seriously by the presence of iron losses. The transient response of speed is affected by the deficiency in torque response. Simple compensation schemes for torque deficiency are recommended. More complex compensation schemes can give more accurate torque response during transient state; however, they require more computing capabilities of the systems. The next sub-section will discuss a simple compensation scheme for torque response.

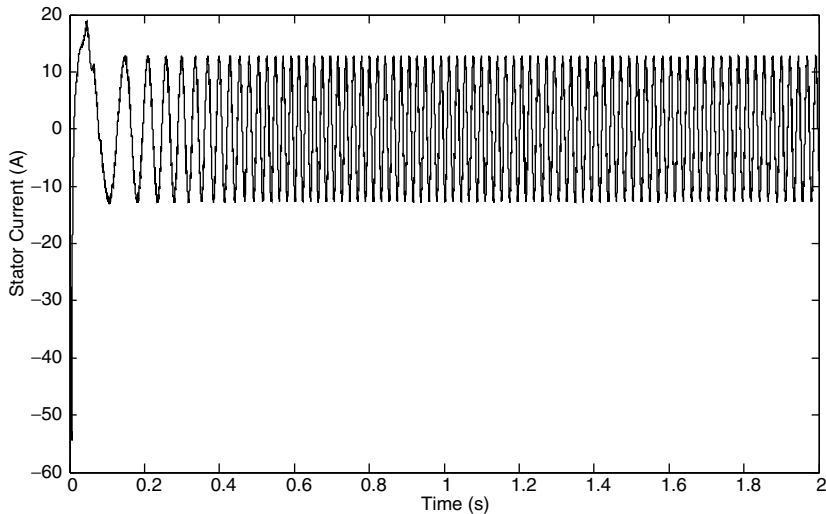


**Figure 5.57** Stator phase current of the induction motor with iron losses



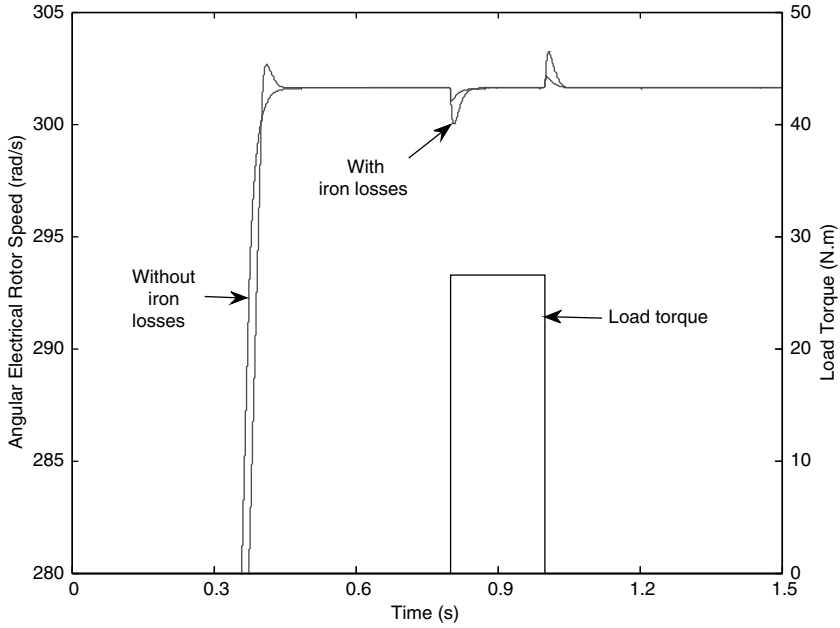


Figure 5.58 Speed response of DTC in speed control mode with machine model considering iron losses

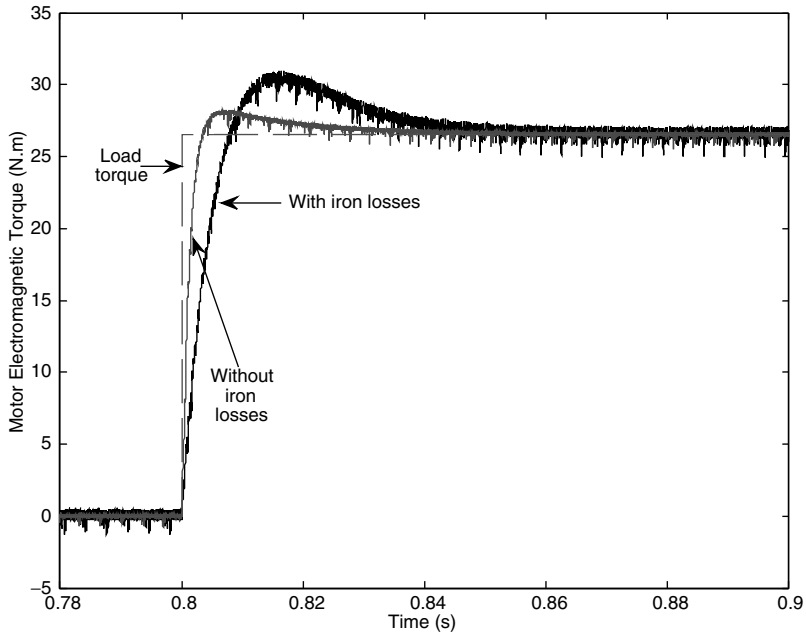
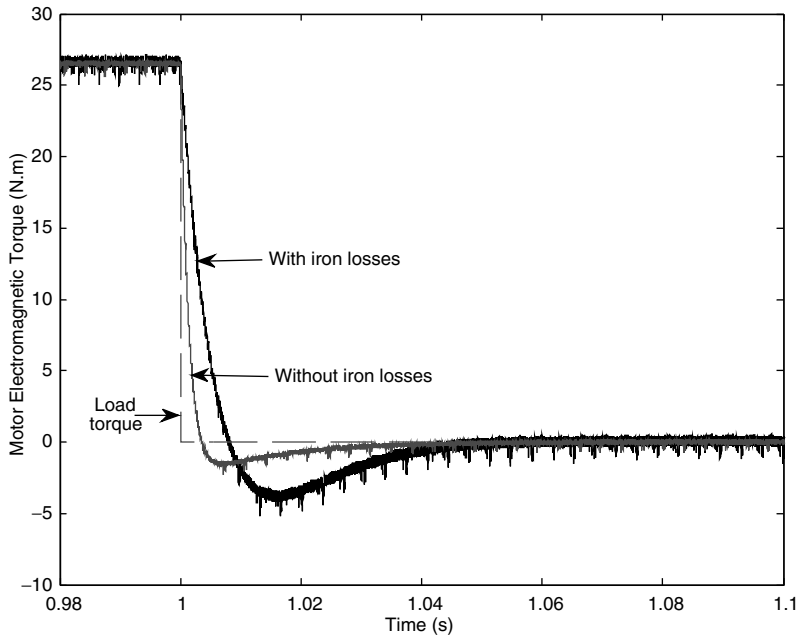


Figure 5.59 Responses of motor's electromagnetic torque when load torque is applied



**Figure 5.60** Responses of motor's electromagnetic torque when load torque is removed

### 5.4.3 Modified Direct Torque Control Scheme for Iron Loss Compensation

It has been shown that iron losses affect only the performance of electromagnetic torque response of the motor. Stator flux response is unchanged when iron losses are considered. Therefore, only compensation for iron losses is discussed. Equation (5.19), used for torque estimation in DTC, is based on the ideal machine model, therefore it does not realize the power deficiency by the existence of iron losses. The estimated value of electromagnetic torque is higher than the actual one. A reduction of estimated torque is introduced in [18], and is expressed by

$$T_e' = (3/2)P(\psi_{\alpha s}i_{\beta s} - \psi_{\beta s}i_{\alpha s}) - \Delta T_{Fe} \quad (5.34)$$

The mechanical power produced by the motor is theoretically assumed as  $T_e\omega_m$ , while the actual output power is  $T_e'\omega_m$  [18], and  $\omega_m$  is the mechanical angular speed of rotor rotation ( $\omega_m = \omega_r/P$ ). The torque compensation  $\Delta T_{Fe}$  in equation (5.34) can be obtained from the following equations [18]:

$$\begin{aligned} T_e\omega_m &= T_e'\omega_m + P_{Fe} \\ \Delta T_{Fe} &= P_{Fe}/\omega_m \\ P_{Fe} &= \Delta T_{Fe}\omega_m \end{aligned} \quad (5.35)$$

The symbol  $P_{Fe}$  stands for the fundamental component of the iron losses. Equation (5.34) holds true for both modes of operation of the motor, braking and motoring. The iron losses will lower the output torque in motoring, while the torque is higher in magnitude than the value obtained by equation (5.19) during braking.

The iron losses, as shown in equation (5.32), are a function of frequency. However, stator frequency is generally not available in DTC. The angular electrical speed of rotor can be used instead to approximate the iron losses. The difference between stator angular frequency and angular electrical speed of the rotor is a small slip frequency, and rotor speed is usually measured or estimated. The torque compensation now can be calculated as [19]

$$\Delta T_{Fe} = \frac{P_{Fe}(f)}{\omega_m} \quad \text{or} \quad \Delta T_{Fe} = \frac{P_{Fe}(P\omega_m/2\pi)}{\omega_m} \quad (5.36)$$

Experimentally identified fundamental component of iron losses often vary almost linearly with the stator frequency [20–22]. From Figure 5.40, the variation of the fundamental iron loss with frequency in the range from 0 to 50 Hz for the motor considered here is almost linear. By approximating the iron loss in the base speed region with a linear dependence on frequency, the simplest method of constant compensation for iron losses is suggested by [19]

$$\Delta T_{Fe} = \frac{P_{Fen}}{P_n} T_{en} = \text{const.} \quad (5.37)$$

As the fundamental iron loss at 50 Hz equals 173.4 W, while rated motor power and torque are 4 kW and 26.5 Nm, respectively, the constant torque compensation is 1.15 Nm.

The simulation results of DTC with constant compensation for iron losses in torque control mode are demonstrated in Figures 5.61 and 5.62.

The proposed improvement has over-compensated the power lost by the presence of iron losses by a small amount. The speed response with iron losses compensation is even better than the one without consideration of iron losses, as shown in Figure 5.61. The over-compensation in electromagnetic torque of the motor is clearly shown in Figure 5.62, especially during the start-up of the motor. This is because the actual iron losses are almost a linear function of the stator frequency in the low speed region and are much less than the compensated value during the start-up.

The simulation results of DTC with constant compensation for iron losses in speed control mode are demonstrated in Figures 5.63 and 5.64. During start-up of the motor, as shown in Figure 5.63, response time of the speed with compensation is slightly more than the one with ideal machine model. Slightly higher overshoot is also observed when compensation is included. However, there is a clear difference between the responses with and without compensation when iron losses are included.

When load torque is applied and removed instantaneously, compensation of iron losses does not improve the performance of speed, as shown in Figure 5.64. The responses are similar for the cases with and without compensation when iron losses are considered.

In summary, iron losses consideration for DTC of induction motor has been discussed in this sub-section. Simulation of the effects of iron losses on performance of DTC in both torque and

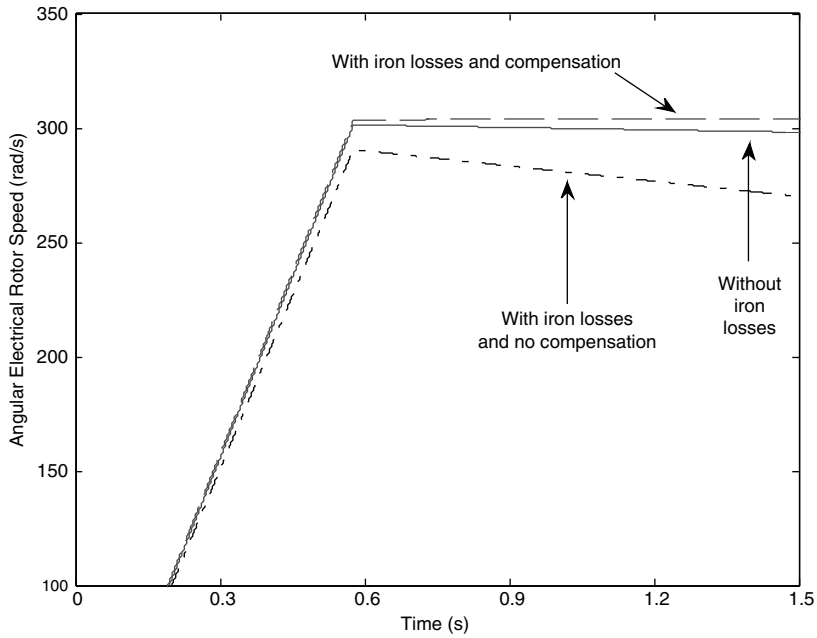


**Figure 5.61** Rotor speed responses of DTC in torque control mode for the three cases: without iron losses; with iron losses but no compensation; with iron losses and constant compensation

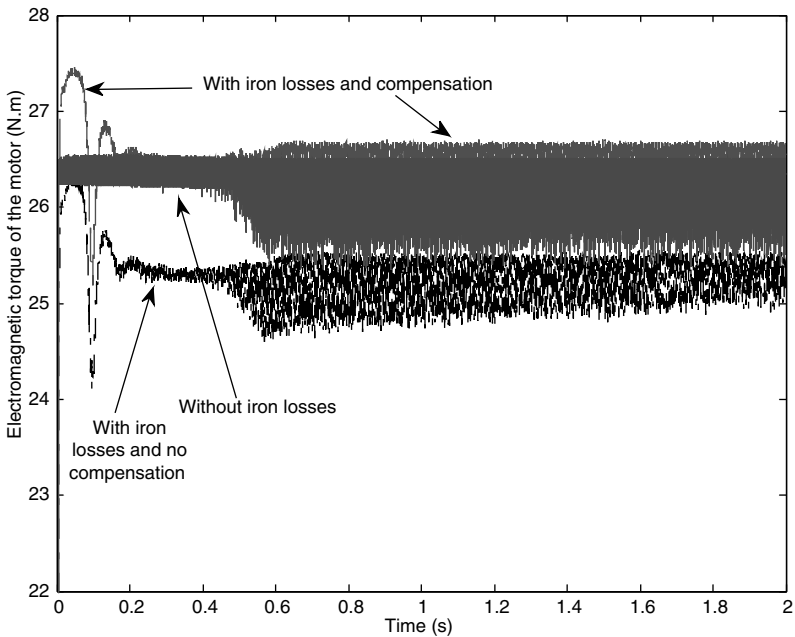


**Figure 5.62** Torque responses of DTC in torque control mode for the three cases: without iron losses; with iron losses but no compensation; with iron losses and constant compensation

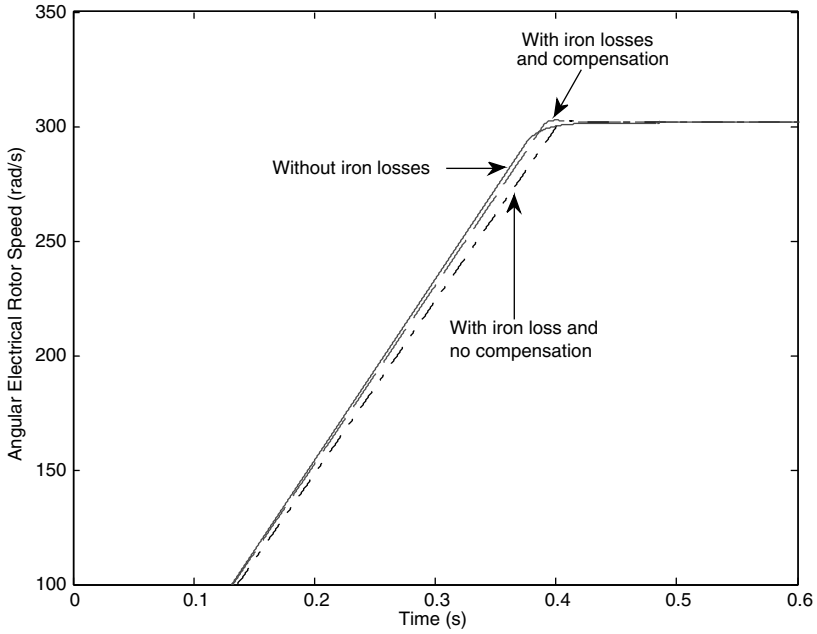


Figure 5.63 Rotor speed responses of DTC in speed control mode for the three cases

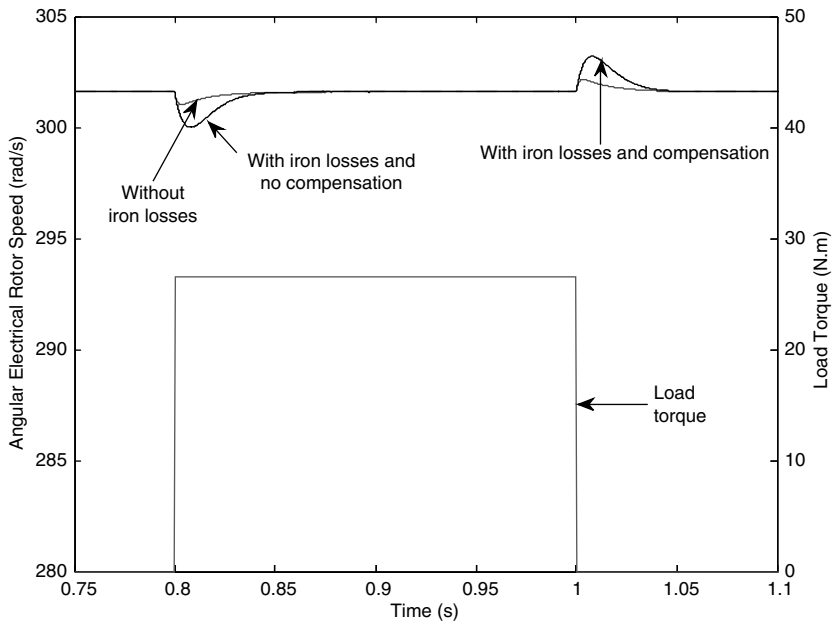


Figure 5.64 Speed responses of the three cases when load torque is applied and removed

speed control mode has been demonstrated. The results have also been analyzed. From the analysis, compensation methods have been discussed and simulation of the simplest one has been presented. The next section of this chapter will discuss the consideration of both iron losses and magnetic saturation in DTC.

### 5.5 DTC of Induction Motor with Consideration of both Iron Losses and Magnetic Saturation

#### 5.5.1 Induction Machine Model with Consideration of Iron Losses and Magnetic Saturation

Representations of iron losses and magnetic saturation in dynamic space vector equivalent circuit of induction machines in an arbitrary frame of reference rotating at angular speed  $\omega_a$  are shown in Figure 5.65.

Differential equations of the machine model are [23]

$$\begin{aligned}
 v_{\alpha s} &= R_s i_{\alpha s} + L_{\sigma s} \frac{di_{\alpha s}}{dt} + \frac{d\psi_{\alpha m}}{dt} \\
 v_{\beta s} &= R_s i_{\beta s} + L_{\sigma s} \frac{di_{\beta s}}{dt} + \frac{d\psi_{\beta m}}{dt}
 \end{aligned}
 \tag{5.38}$$

$$\begin{aligned}
 0 &= R_r i_{\alpha r} + L_{\sigma r} \frac{di_{\alpha r}}{dt} + \frac{d\psi_{\alpha m}}{dt} + \omega(L_{\sigma r} i_{\beta r} + \psi_{\beta m}) \\
 0 &= R_r i_{\beta r} + L_{\sigma r} \frac{di_{\beta r}}{dt} + \frac{d\psi_{\beta m}}{dt} + \omega(L_{\sigma r} i_{\alpha r} + \psi_{\alpha m})
 \end{aligned}
 \tag{5.39}$$

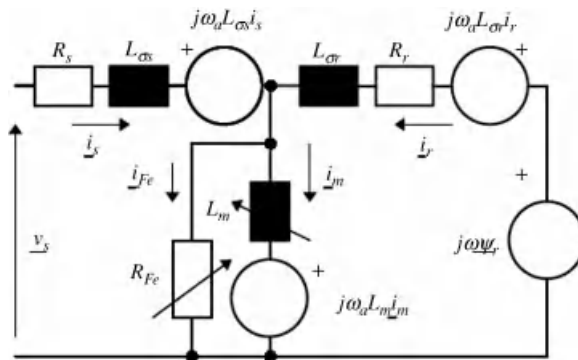


**Figure 5.65** Space vector dynamic equivalent circuit of induction machine in an arbitrary reference frame [23]

$$\begin{aligned}
0 &= \frac{d\psi_{\alpha m}}{dt} - R_{Fe}i_{\alpha s} - R_{Fe}i_{\alpha r} + \frac{R_{Fe}}{L_m}\psi_{\alpha m} \\
0 &= \frac{d\psi_{\beta m}}{dt} - R_{Fe}i_{\beta s} - R_{Fe}i_{\beta r} + \frac{R_{Fe}}{L_m}\psi_{\beta m}
\end{aligned} \tag{5.40}$$

$$\begin{aligned}
\psi_{\alpha s} &= L_{\sigma s}i_{\alpha s} + L_m i_{\alpha m} \\
\psi_{\beta s} &= L_{\sigma s}i_{\beta s} + L_m i_{\beta m} \\
\psi_{\alpha r} &= L_{\sigma r}i_{\alpha r} + L_m i_{\alpha m} \\
\psi_{\beta r} &= L_{\sigma r}i_{\beta r} + L_m i_{\beta m}
\end{aligned} \tag{5.41}$$

$$\frac{d\omega}{dt} = \frac{P}{J} \left[ \frac{3}{2} P (i_{\alpha r} \psi_{\beta m} - i_{\beta r} \psi_{\alpha m}) - T_L \right] \tag{5.42}$$

$$T_e = \frac{3}{2} P (i_{\alpha r} \psi_{\beta m} - i_{\beta r} \psi_{\alpha m}) \tag{5.43}$$

The equivalent iron loss resistance as a function of stator frequency is [23]

$$R_{Fe} = \begin{cases} 128.92 + 8.242f + 0.0788f^2 & (\Omega); f \leq 50 \text{ Hz} \\ 1841 - 55272/f & (\Omega); f \geq 50 \text{ Hz} \end{cases} \tag{5.44}$$

The equivalent magnetizing inductance is considered as a non-linear function of main flux:

$$L_m = f(\psi_m); \text{ where } L_m = \frac{\psi_m}{i_m} \tag{5.45}$$

Magnetizing curve approximation (rms values) is [23]

$$\psi_m = \begin{cases} 0.1964285i_m; & i_m < 2.2A \\ 0.8374 + 0.0067i_m - 0.924/i_m; & i_m > 2.2A \end{cases} \tag{5.46}$$

The indices  $s$  and  $r$  denote stator and rotor parameters and variable, respectively; index  $\sigma$  stands for leakage inductances; index  $m$  defines parameters and variables associated with magnetizing flux, magnetizing current, and magnetizing inductances;  $P$  is the number of pole pairs;  $J$  is the inertia constant; and  $\omega$  is the electrical angular speed of rotor.

## 5.5.2 MATLAB/Simulink Simulation of Effects of both Iron Losses and Magnetic Saturation in Torque Control and Speed Control

### 5.5.2.1 Effects of Iron Losses and Magnetic Saturation in Torque Control Mode

The ideal constant parameter machine model of the induction motor is replaced by the machine model considering iron losses and magnetic saturation in the MATLAB/Simulink program for torque control simulation using DTC, as shown in the Figure 5.66.

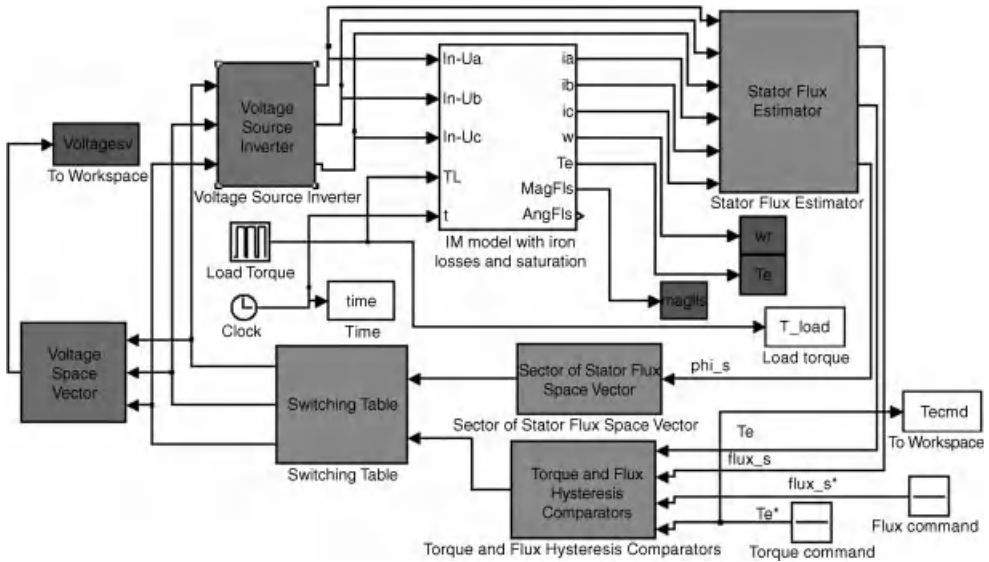


Figure 5.66 DTC of induction machine with iron losses and saturation

The other sub-systems of the DTC control system are essentially the same as those shown in Figures 5.11 and 5.41. The structure inside the block ‘IM model with iron losses and saturation’ is shown in Figure 5.67.

In addition to the blocks for transformation of reference frame, there are also blocks for calculation of instantaneous values of magnetizing inductance and equivalent resistance of

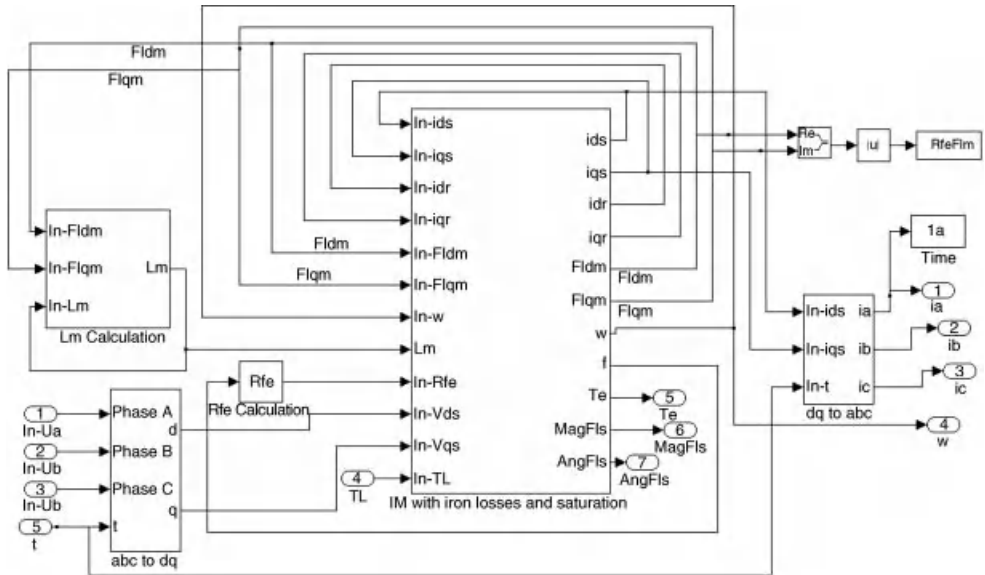
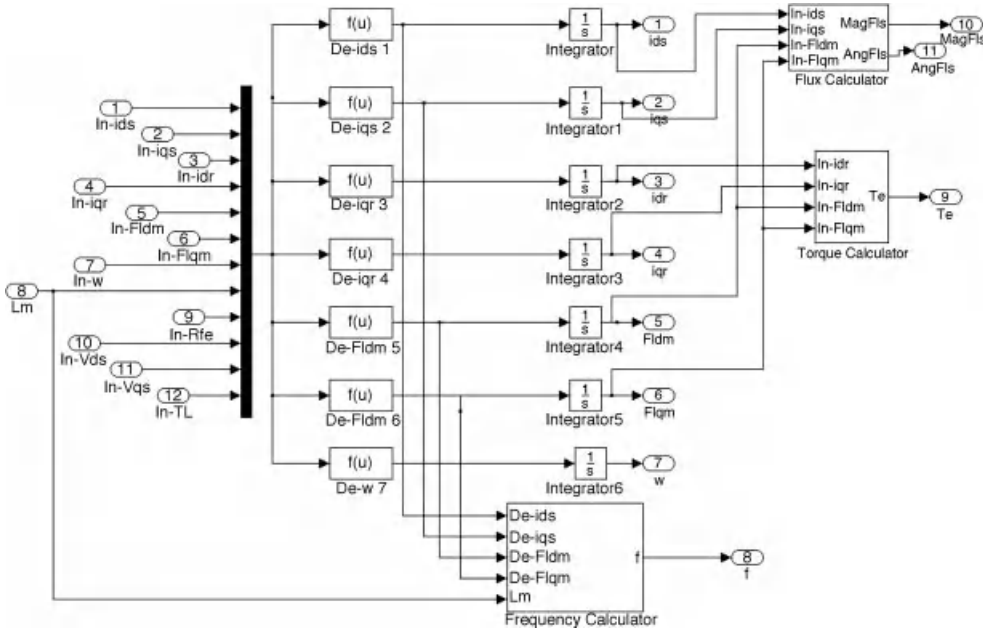


Figure 5.67 Diagram of the block ‘IM model with iron losses and saturation’





**Figure 5.68** Blocks for differential equations of the dynamic machine model

iron losses. The differential equations of the dynamic machine model inside the block ‘IM with iron losses and saturation’ are shown in Figure 5.68.

Details of the blocks expressing the differential equations are shown in the Figures 5.69–5.71.

The structure of the block ‘Frequency Calculator’ in Figure 5.68 is presented in the Figures 5.72–5.74.

Structures of the blocks used for stator flux and torque calculation in Figure 5.68 are illustrated in the Figures 5.75 and 5.76.

The instantaneous value of the magnetizing inductance is deduced from equations (5.45) and (5.46). The implementation of this calculation is presented in Figures 5.77 and 5.78.

The equivalent resistance for iron losses varies with frequency and the implementation of the calculation of instantaneous resistance is shown in Figure 5.79.

The parameters of the induction motor with consideration of iron losses and saturation are presented in Figure 5.80.

Simulation of torque control and flux control with DTC, when iron losses and magnetic saturation are included in the machine model, is carried out with rated values for both torque and flux commands. The obtained speed is shown in Figure 5.81, together with speeds of the motor when only iron losses are considered and the constant parameter machine model is used.

The responses of speed with only iron losses and with both iron losses and saturation are almost identical. The speeds decrease when rated load torque is applied due to the high ripples in torque responses, which result in lower average value of electromagnetic torque of

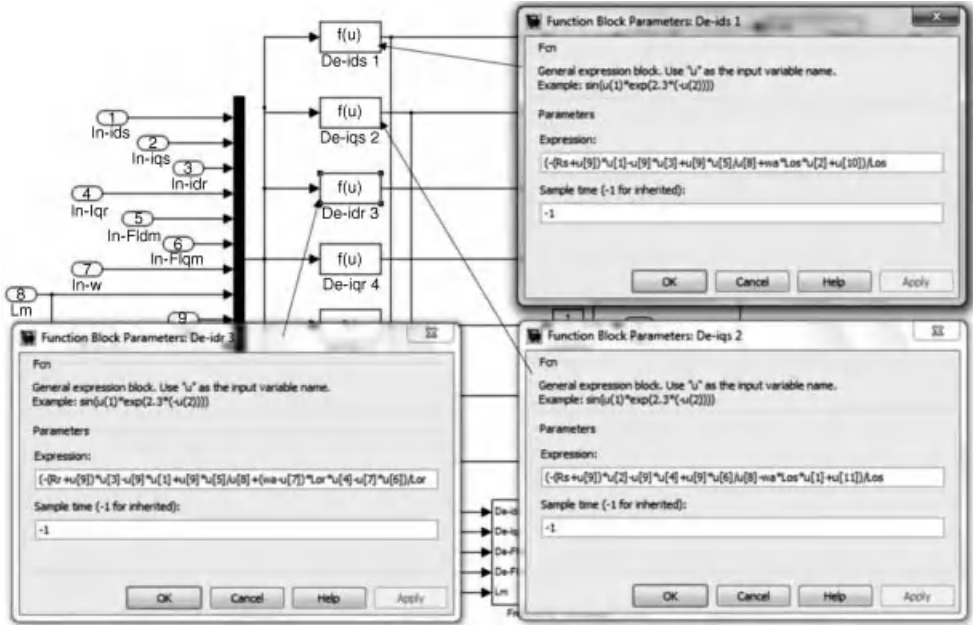


Figure 5.69 Expressions for differential equations of  $i_{ds}$ ,  $i_{dr}$ , and  $i_{dr}$

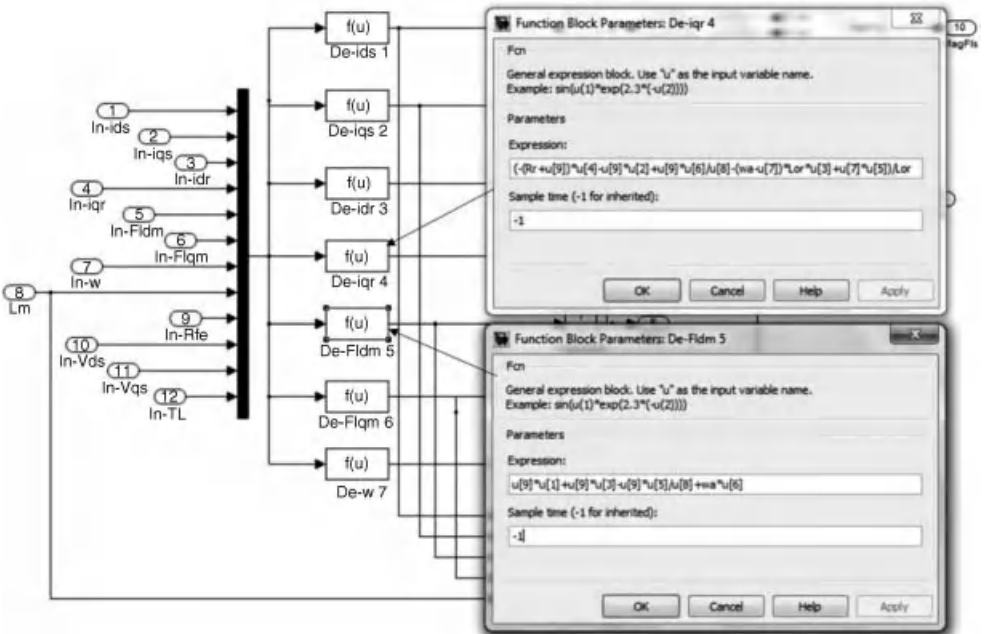


Figure 5.70 Expressions for differential equations of  $i_{qr}$  and  $\psi_{dm}$

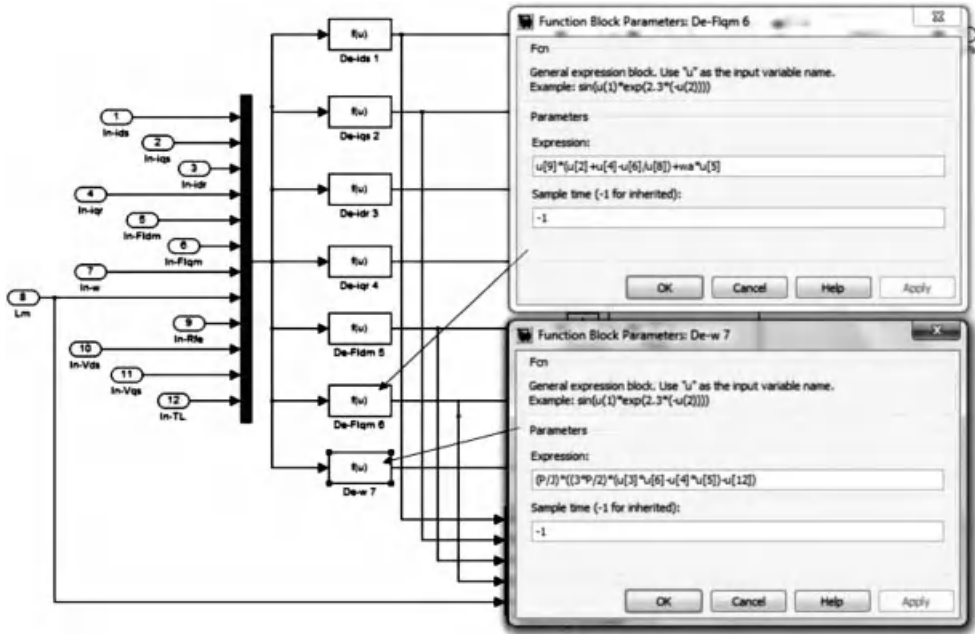


Figure 5.71 Expressions for differential equations of  $\psi_{dqm}$  and  $\omega$

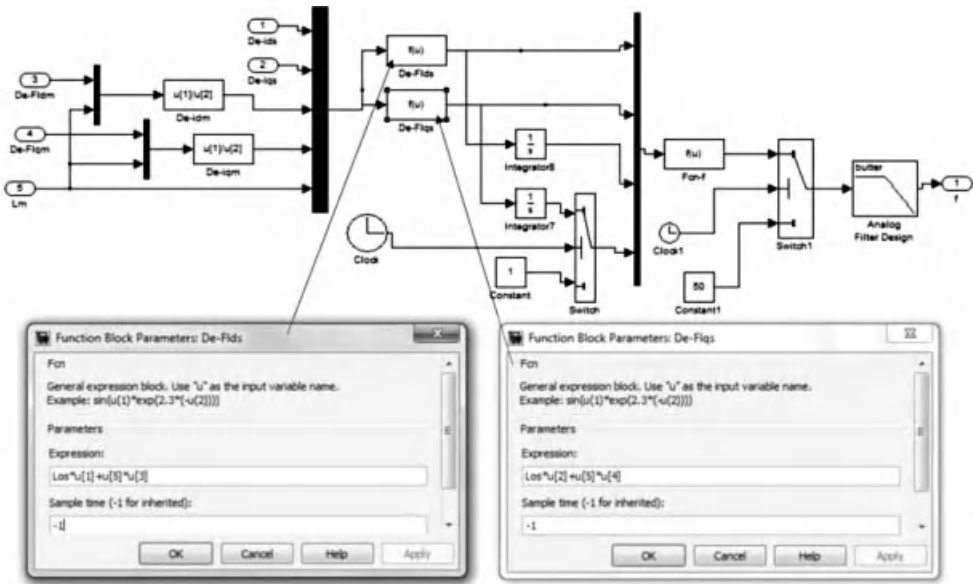


Figure 5.72 Expressions for  $d$ - $q$  components of stator flux used to calculate the stator frequency

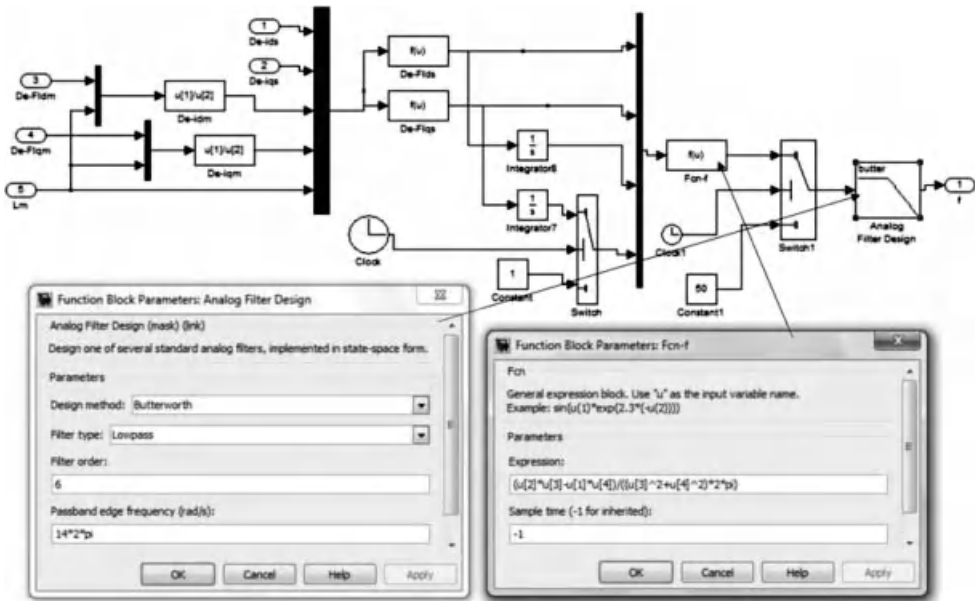


Figure 5.73 Expression for frequency calculation and design of Butterworth filter to obtain the fundamental component of stator frequency

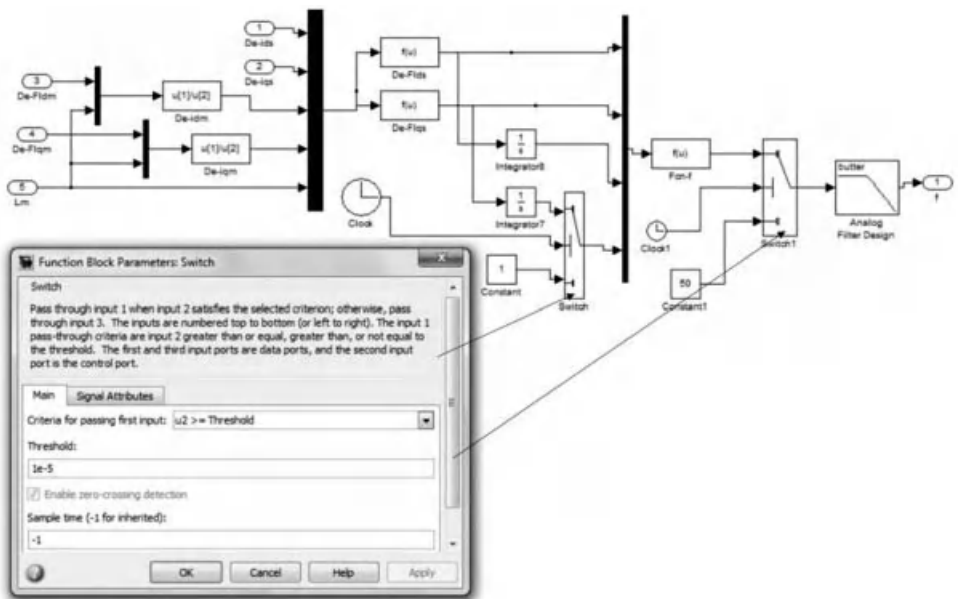


Figure 5.74 Designs of the 'Switch' blocks in Figure 5.72

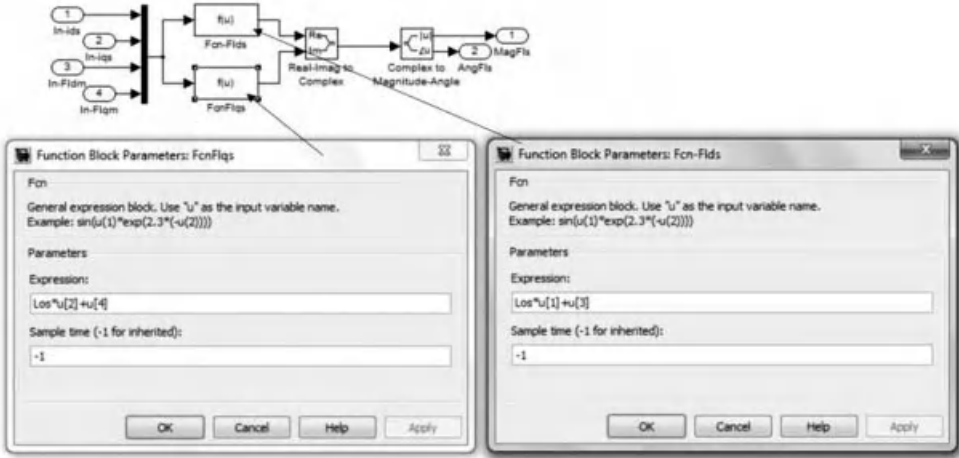


Figure 5.75 Stator flux calculation in induction machine model with iron losses and magnetic saturation

the motor. Magnetic saturation does not affect the speed response in this region of operation of the motor.

Torque responses are shown in Figure 5.82. Again, the additional inclusion of magnetic saturation does not change significantly torque response. Discrepancies between load torque

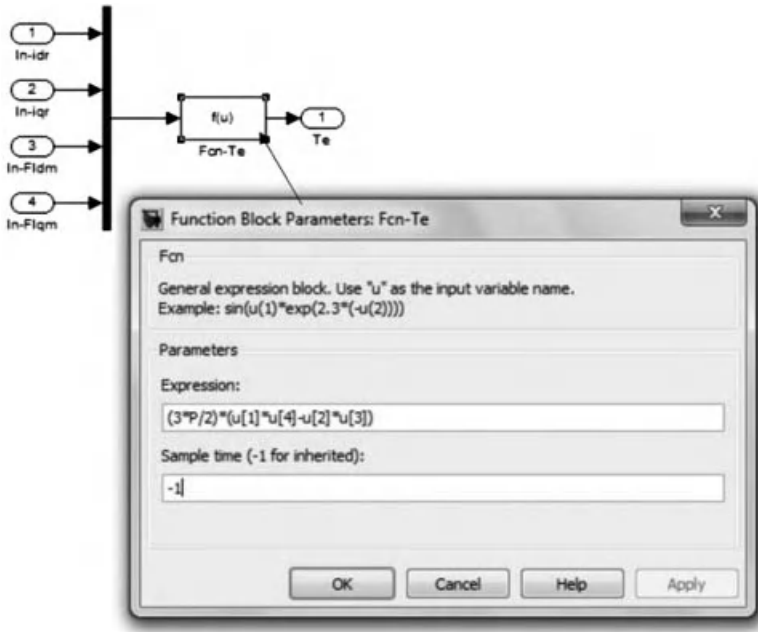
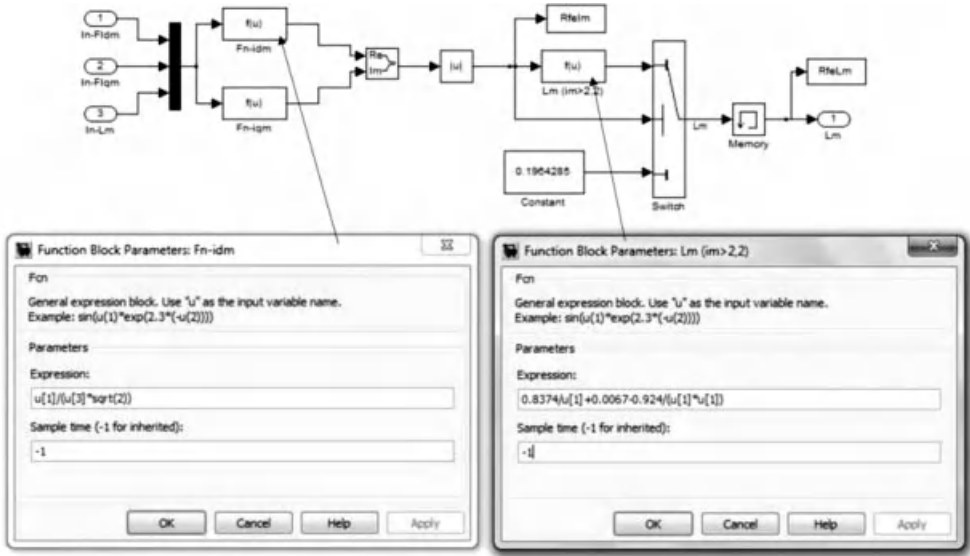
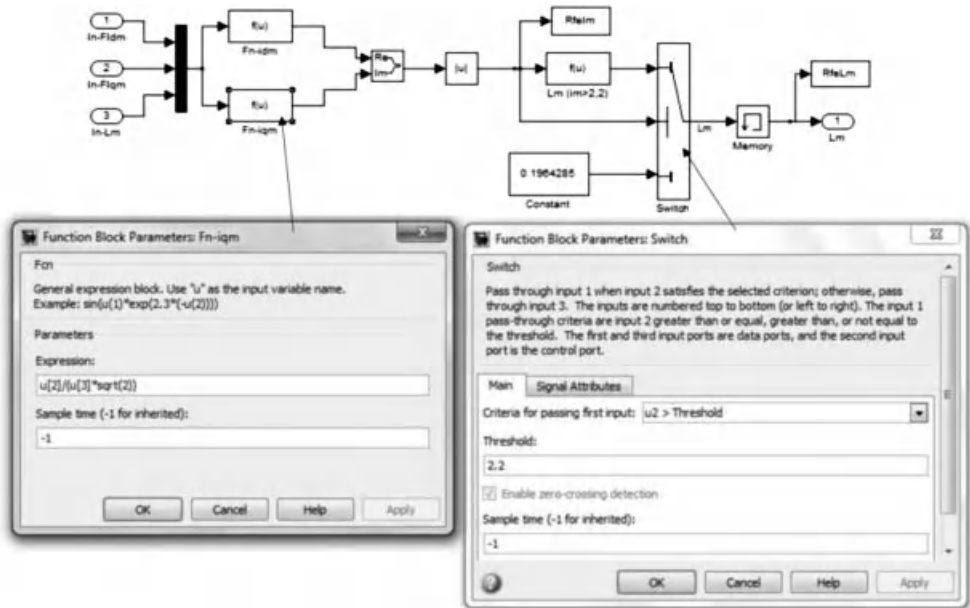


Figure 5.76 Electromagnetic torque calculation in the induction machine model



**Figure 5.77** Expressions for  $i_{dm}$  and  $L_m$  (when  $i_{dm}$  is  $>2.2$  A) in calculation of instantaneous value of the magnetizing inductance



**Figure 5.78** Expression of  $i_{qm}$  and values of 'Switch' block in Figure 5.77

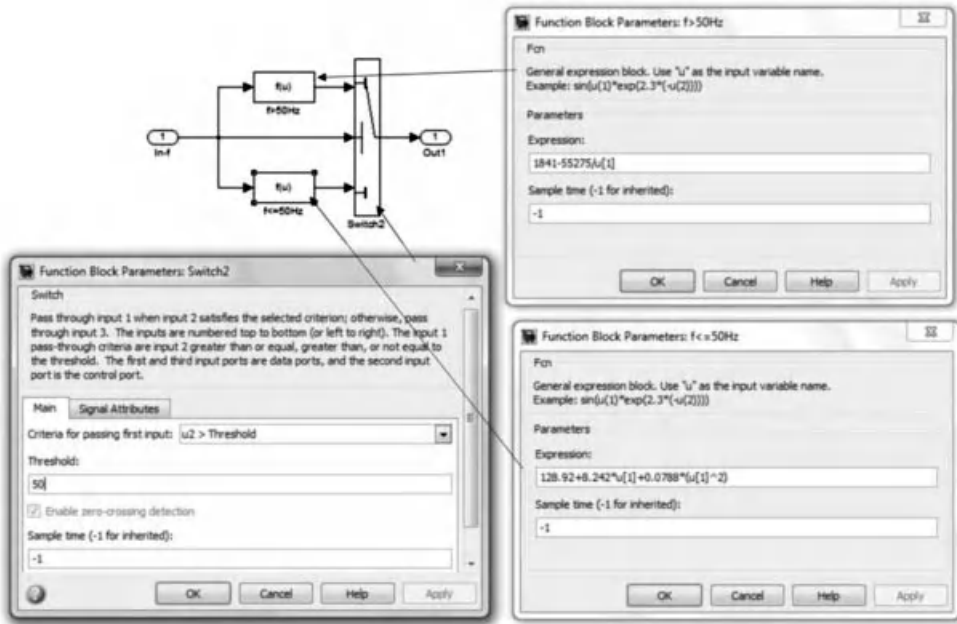


Figure 5.79 Calculation of the equivalent resistance for iron losses with frequency

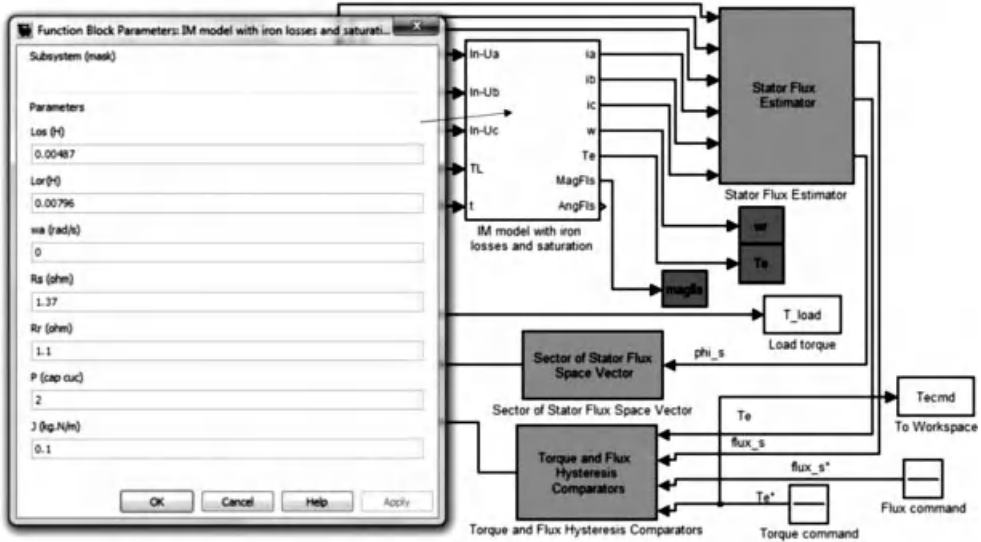


Figure 5.80 Parameters of the induction motor

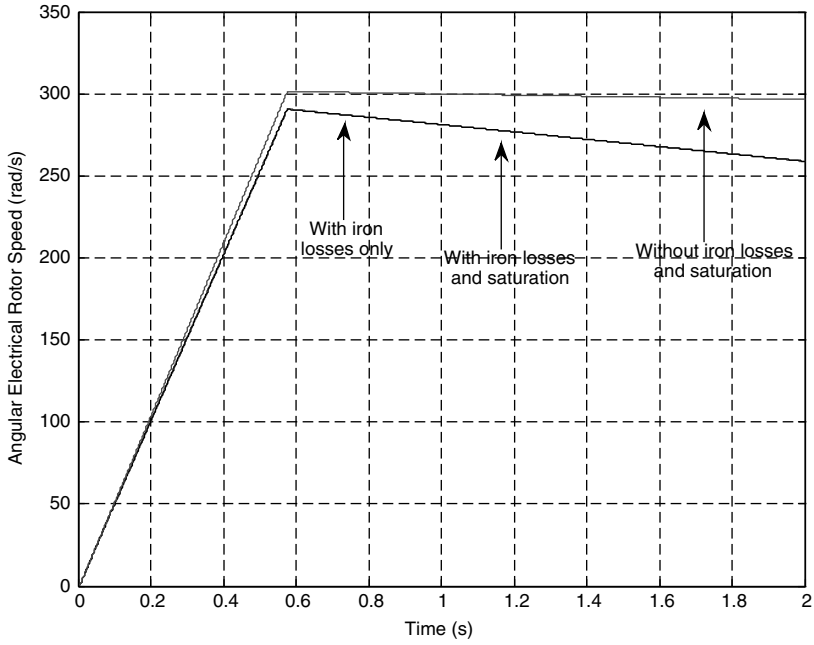


Figure 5.81 Speed responses in torque control mode of DTC

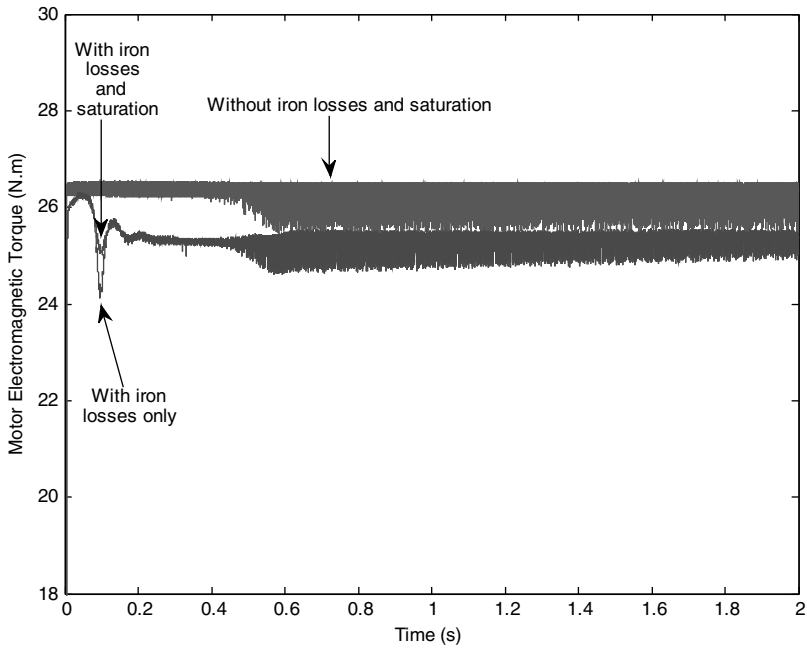
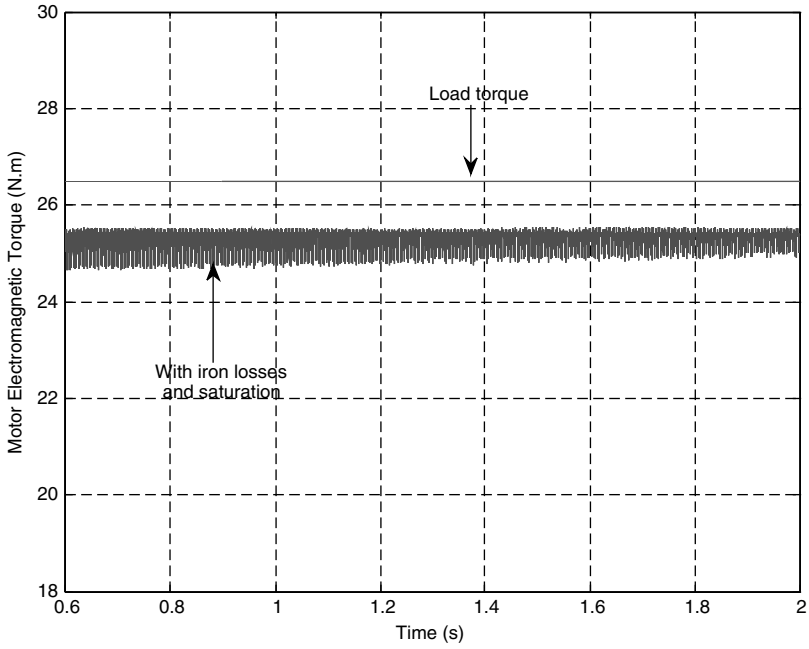
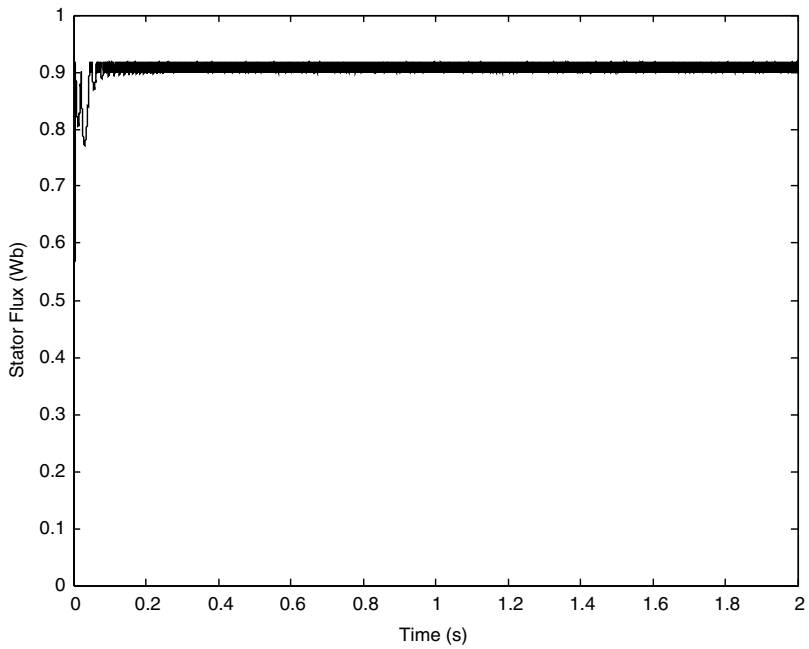


Figure 5.82 Torque responses in torque control mode of DTC





**Figure 5.83** Steady state response of torque when both iron losses and magnetic saturation are included



**Figure 5.84** Flux response with iron losses and magnetic saturation in torque control mode

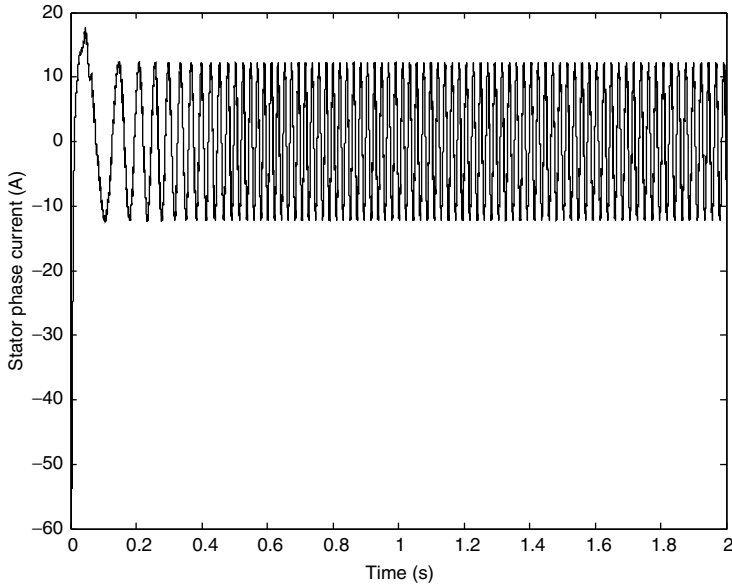


**Figure 5.85** Stator current response with iron losses and magnetic saturation in torque control mode

and the actual torque of the motor in steady state are shown in Figure 5.83. This difference is the cause of the decrease in speed.

Flux and stator current responses are demonstrated in Figures 5.84 and 5.85. The inclusion of magnetic saturation and iron losses does not cause significant changes in the responses.

### 5.5.2.2 Effects of Iron Losses and Magnetic Saturation in Speed Control Mode

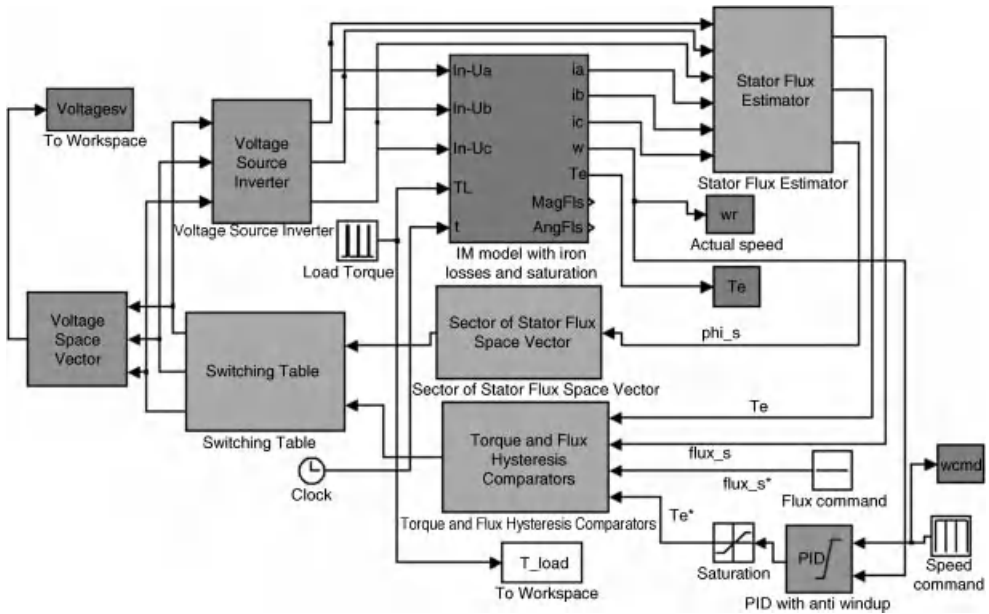
The simulation program of DTC in speed control mode is essentially the same as that shown in sub-section 5.3.4.1; only the Simulink block for the induction motor is changed to include iron losses and magnetic saturation. Figures 5.86 and 5.87 show the schematic diagram of the program and parameters of the PID controller, respectively.

Figure 5.88 shows the response of speed during the acceleration, applying and removing of rated load torque, and the speed response with the ideal machine model is also presented. Figure 5.89 shows the respective torque response when the iron losses and magnetic saturation are included.

The responses of the motor's electromagnetic torque during the application and removal of rated load torque are presented in Figures 5.90 and 5.91, respectively. The electromagnetic torque with the ideal constant parameter machine model is also demonstrated for comparison.

The difference between the speed responses with and without the inclusion of iron losses and magnetic saturation is not significant, as shown in Figure 5.88. The transient response of speed is slightly bit slower with iron losses and magnetic saturation due to the power losses, which reduce the actual electromagnetic torque. The torque response is essentially the same with torque response with only iron losses consideration (Figure 5.89).

When load torque is suddenly applied, the responses of electromagnetic torque are almost identical for all the cases, as shown in Figures 5.90 and 5.91.



**Figure 5.86** Simulation of DTC in speed control mode with the inclusion of both iron losses and magnetic saturation

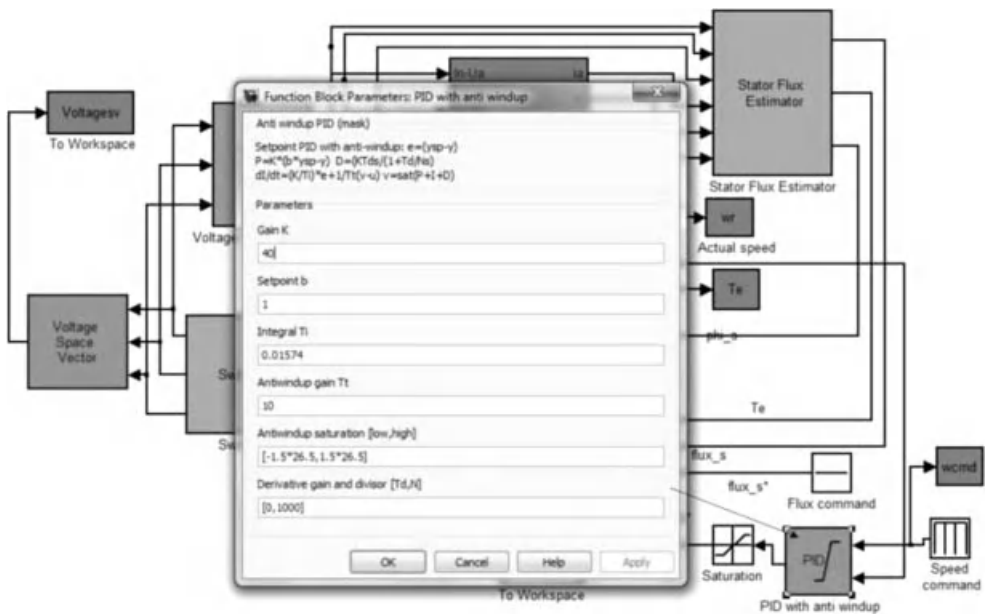


**Figure 5.87** Parameters of the PID controller in speed control mode

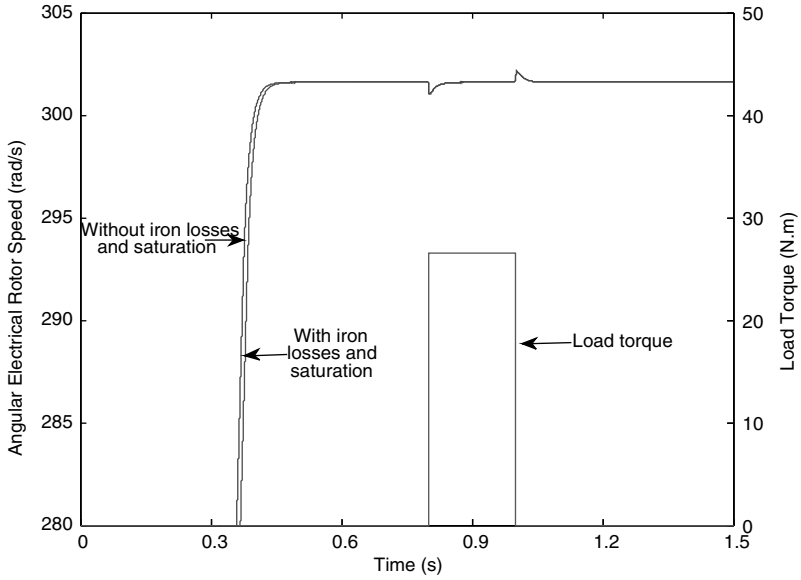


Figure 5.88 Speed responses when iron losses and saturation is included

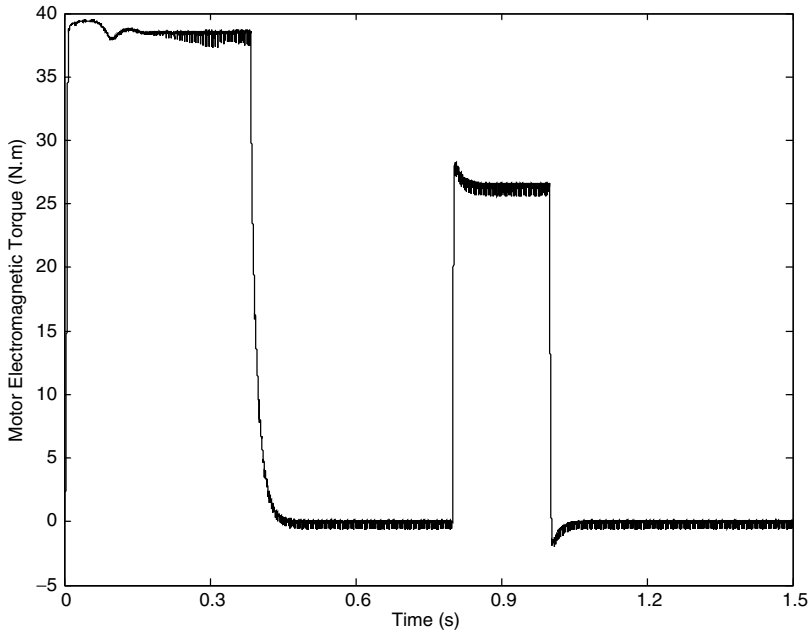


Figure 5.89 Torque responses during acceleration, loading, and unloading

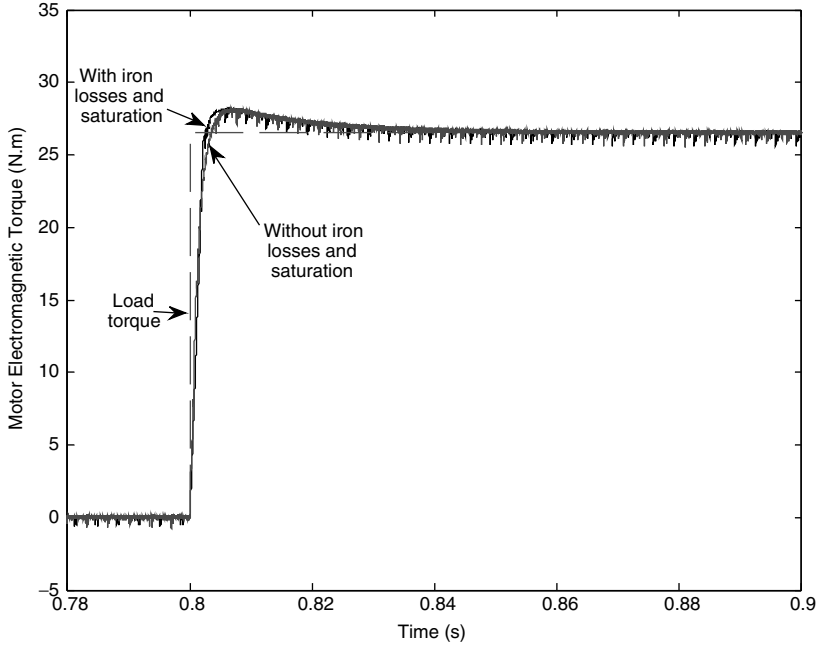


Figure 5.90 Motor torque response during the application of rated load torque

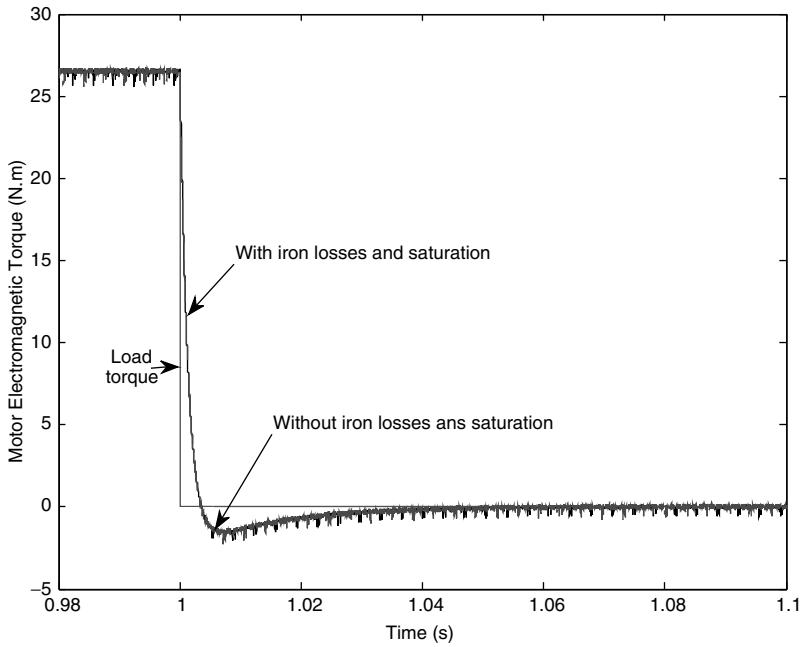


Figure 5.91 Motor torque response during the removal of rated load torque

## 5.6 Modified Direct Torque Control of Induction Machine with Constant Switching Frequency

From the discussion and simulation of Direct Torque Control of induction motors in previous sub-sessions, DTC has several major disadvantages such as [7]:

- problems during starting due to the absence of current controllers;
- operation in low-speed region due to high flux ripples;
- necessity of accurate estimation of stator flux and electromagnetic torque;
- changing switching frequency, because of hysteresis band-based control of torque; and
- high torque ripples in high-speed operation due to the utilization of zero voltage space vectors.

Variation of switching frequency in DTC is one of the major drawbacks in many industrial applications.

There have been many modifications suggested for constant switching frequency with DTC. These modifications include DTC with space vector modulation and deadbeat control for directly calculation of switching pattern to achieve constant switching period [24], DTC with predictive control, which calculates the optimal switching instant at each cycle on the basis of RMS torque-ripple equation during one switching period obtained from the instantaneous torque variation equation [9], and Direct Self Control with fuzzy controller for choosing switching states to reduce the flux and torque errors, while still achieving fast torque response and constant switching frequency [25]. However, these modifications have resulted in the increased sophistication of the control systems, which require more computational capabilities than the traditional DTC.

The concept of DTC is also extended to introduce the new control method called Stator Flux Vector Control, which delivers fast torque response and constant switching frequency without using current controller [26]. This new concept focuses on torque control using variations of the stator flux angular velocity and stator flux control for obtaining fixed rotor flux amplitude in a feed-forward manner. The new control method also improves the sensitivities to the induction motor's parameters and stabilities, even at low-speed operation [26].

Space vector pulse width modulation (SVPWM) with two-level and three-level inverter to obtain constant switching frequency in DTC has also been proposed for the applications in electric vehicle drive [27]. Furthermore, constant frequency torque controller is introduced to achieve both constant switching frequency and reduction of torque ripples, especially when DTC is implemented with a low speed processor, which results in low sampling frequency [28].

## 5.7 Direct Torque Control of Sinusoidal Permanent Magnet Synchronous Motors (SPMSM)

### 5.7.1 Introduction

Permanent magnet synchronous machines (SPMSMs) are categorized on the basis of the waveform of the induced electromotive force; they are either sinusoidal or trapezoidal. The SPMSMs with sinusoidal wave-shape of emf are called PMSMs, and the PMSMs with

trapezoidal wave-shape of emf are known as Brushless DC Machines (BLDCs) [29]. This sub-section discusses the DTC of SPMSMs, which has a sinusoidal distribution of air-gap flux.

The machines are of surface magnet structure, where the magnets are placed in the grooves of the outer periphery of the rotor lamination to provide high flux density in the air gap and also uniform cylindrical surface of the rotor for the mechanical robustness [29].

Mathematical equations for dynamic models of the SPMSMs are presented in the next sub-section.

### 5.7.2 Mathematical Model of Sinusoidal PMSM

The mathematical model for SPMSMs are shown in equations (5.47) to (5.52). The dynamic model is in the rotor flux oriented reference frame. The rotating speed of rotor and rotor flux space vector are the same for the synchronous motor, and they are also equal to the rotating speed of the reference frame  $\omega_a = \omega_r = \omega$ :

$$\begin{aligned} v_{ds} &= R_s i_{ds} + \frac{d\psi_{ds}}{dt} - \omega_r \psi_{qs} \\ v_{qs} &= R_s i_{qs} + \frac{d\psi_{qs}}{dt} + \omega_r \psi_{ds} \end{aligned} \quad (5.47)$$

$$v_f = R_f i_f + \frac{d\psi_f}{dt} \quad (5.48)$$

$$T_e - T_L = \frac{J}{P} \frac{d\omega_r}{dt} \quad (5.49)$$

$$\psi_{ds} = L_s i_{ds} + L_m i_f \quad (5.50)$$

$$\psi_{qs} = L_s i_{qs}$$

$$\psi_f = L_f i_f + L_m i_{ds} \quad (5.51)$$

$$T_e = \frac{3}{2} P (\psi_{ds} i_{qs} - \psi_{qs} i_{ds}) \quad (5.52)$$

Transformation equations for stator voltage and stator current are shown in equations (5.53) to (5.55), where  $\theta$  is the instantaneous angle of the rotor:

$$v_{ds} = \frac{2}{3} \left[ v_a \cos \theta + v_b \cos \left( \theta - \frac{2\pi}{3} \right) + v_c \cos \left( \theta - \frac{4\pi}{3} \right) \right] \quad (5.53)$$

$$v_{qs} = -\frac{2}{3} \left[ v_a \sin \theta + v_b \sin \left( \theta - \frac{2\pi}{3} \right) + v_c \sin \left( \theta - \frac{4\pi}{3} \right) \right]$$

$$i_a = i_{ds} \cos \theta - i_{qs} \sin \theta$$

$$i_b = i_{ds} \cos \left( \theta - \frac{2\pi}{3} \right) - i_{qs} \sin \left( \theta - \frac{2\pi}{3} \right)$$
(5.54)

$$i_c = i_{ds} \cos \left( \theta - \frac{4\pi}{3} \right) - i_{qs} \sin \left( \theta - \frac{4\pi}{3} \right)$$

$$\theta = \int_0^t \omega_r(\tau) d\tau + \theta(0)$$
(5.55)

When the rotor of the synchronous motor is a permanent magnet, the magnetizing flux linkage produced by the magnet can be expressed in terms of a fictitious field current  $i_f$  as [30]

$$\psi_m = L_m i_f$$
(5.56)

The mathematical model in an arbitrary rotating reference frame can be rewritten by applying the equation (5.56) into the equations (5.47) to (5.52):

$$v_{ds} = R_s i_{ds} + \frac{d\psi_{ds}}{dt} - \omega_a \psi_{qs}$$
(5.57)

$$v_{qs} = R_s i_{qs} + \frac{d\psi_{qs}}{dt} + \omega_a \psi_{ds}$$

$$\psi_{ds} = L_s i_{ds} + \psi_m$$
(5.58)

$$\psi_{qs} = L_s i_{qs}$$

$$T_e - T_L = \frac{J}{P} \frac{d\omega}{dt}$$
(5.59)

$$T_e = \frac{3}{2} P (\psi_{ds} i_{qs} - \psi_{qs} i_{ds}) = \frac{3}{2} P \psi_m i_{qs}$$
(5.60)

Because of the design of SPMSMs, the machines cannot be used for main operations as with traditional synchronous motors. Due to the absence of damper winding, the SPMSMs cannot be started [30]. They are mainly used for variable speed drives, which require power electronic conversions for power supplies. Therefore, it is always necessary to measure or estimate the position of the rotor for the feedback to the control system. However, this is not a disadvantage for SPMSM-based drives, because the information about rotor position is always needed in the applications of the drive systems.

The cost of BLDC machines are usually lower than the cost of SPMSMs. However, the performances of SPMSM are much better. The selection of which of the machines depends very much on the particular applications [30].



### 5.7.3 Direct Torque Control Scheme of PMSM

The mathematical model in equations (5.57) to (5.60) is expressed in the stationary reference frame as

$$\begin{aligned} v_{\alpha s} &= R_s i_{\alpha s} + \frac{d\psi_{\alpha s}}{dt} \\ v_{\beta s} &= R_s i_{\beta s} + \frac{d\psi_{\beta s}}{dt} \end{aligned} \quad (5.61)$$

$$\begin{aligned} \psi_{\alpha s} &= L_s i_{\beta s} + \psi_m \\ \psi_{\beta s} &= L_s i_{\beta s} \end{aligned} \quad (5.62)$$

$$T_e - T_L = \frac{J}{P} \frac{d\omega}{dt} \quad (5.63)$$

$$T_e = \frac{3}{2} P (\psi_{\alpha s} i_{\beta s} - \psi_{\beta s} i_{\alpha s}) = \frac{3}{2} P \psi_m i_{\beta s} \quad (5.64)$$

The DTC scheme for SPMSMs, which directly controls the stator flux linkage and electromagnetic torque by optimum switching table for voltage fed inverter, is discussed in this sub-section. Equations (5.61) to (5.64) are used to estimate the stator flux linkage and electromagnetic torque [7].

Comparisons between reference and estimated values of stator flux linkage and electromagnetic torque by comparators are carried out. Stator flux comparator is two-level and torque comparator is three-level, as expressed in equations (5.6) and (5.7), respectively.

The inputs of the optimum switching table are outputs from the comparators and the sector in the complex, which contains the estimated stator flux space vector. The complex plane is shown in Figure 5.3. The optimum switching table for DTC of SPMSMs in this sub-section is the one suggested by [1] and is shown in Table 5.2.

The next sub-section discusses the simulation of DTC of SPMSMs.

### 5.7.4 MATLAB/Simulink Simulation of SPMSM with DTC

#### 5.7.4.1 Development of MATLAB/Simulink Program

The simulation program for DTC of SPMSMs is developed on the basic of the scheme presented in previous the sub-section. The structural diagram is shown in Figure 5.92.

The PID controller in Figure 5.92 is identical to the controller in Figure 5.10. The Simulink diagram for a machine model of SPMSM inside the block 'SPMSM' in the above figure is shown in Figure 5.93.

Expressions for differential equations in equations (5.61) to (5.63) in MATLAB/Simulink are demonstrated in Figure 5.94.

Transformation from rotor flux oriented reference frame to stationary co-ordinators in a machine model is demonstrated in Figure 5.95.

Transformation from stationary reference frame to rotor flux oriented  $d$ - $q$  axes in a machine model is presented in Figure 5.96.

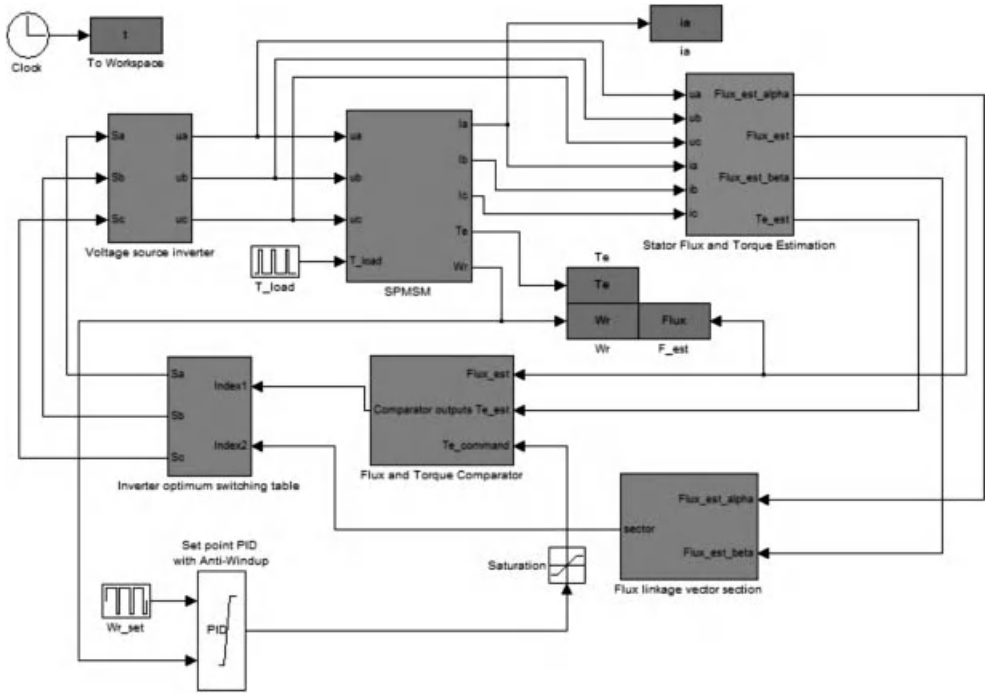


Figure 5.92 Simulation program for DTC of SPMSM

Block diagrams for estimation of stator flux linkage and electromagnetic torque of SPMSMs for DTC is shown in Figure 5.97

Block diagrams for transformation from phase stator voltage to  $\alpha$  and  $\beta$  components of stationary reference frame are demonstrated in Figure 5.98. The same structure can be used in the case of transformation for stator current.

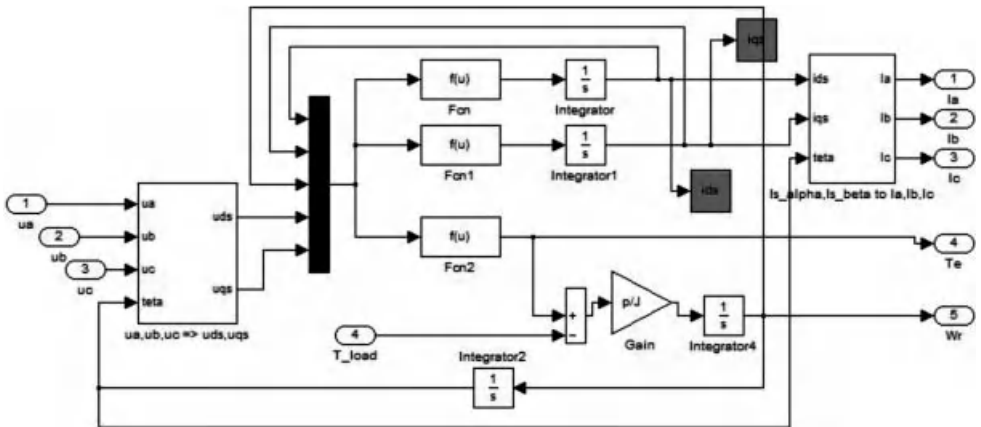


Figure 5.93 Simulink diagram of the SPMSM machine model

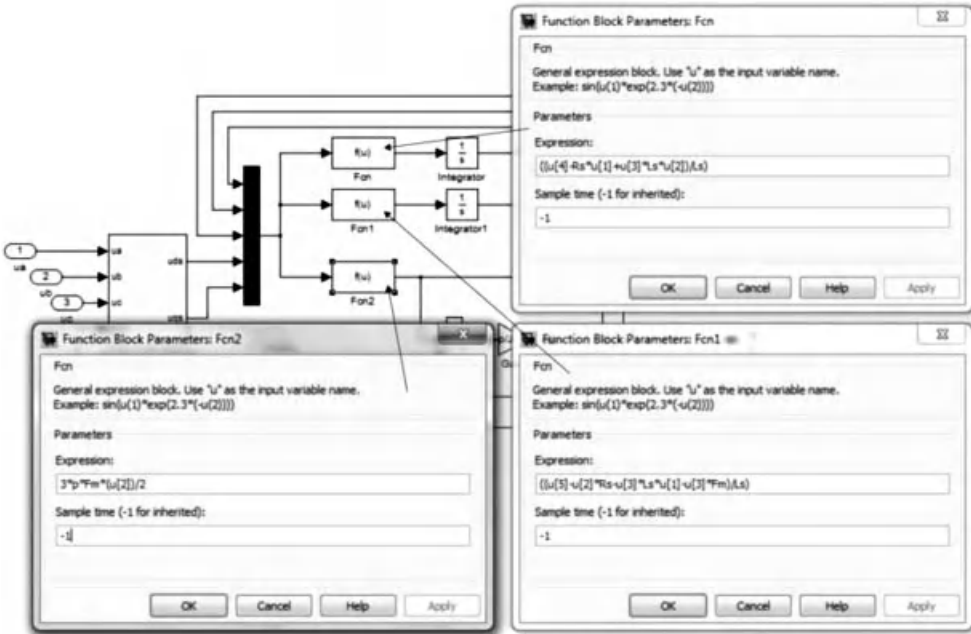


Figure 5.94 Differential equations of machine model in simulation program

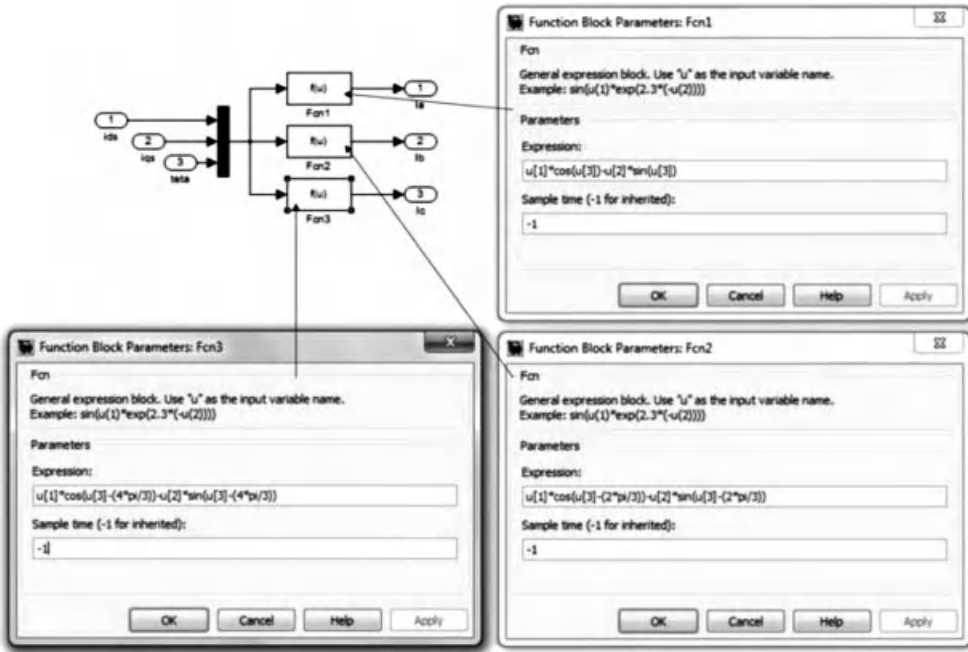


Figure 5.95 Transformation of reference frames from rotating to stationary

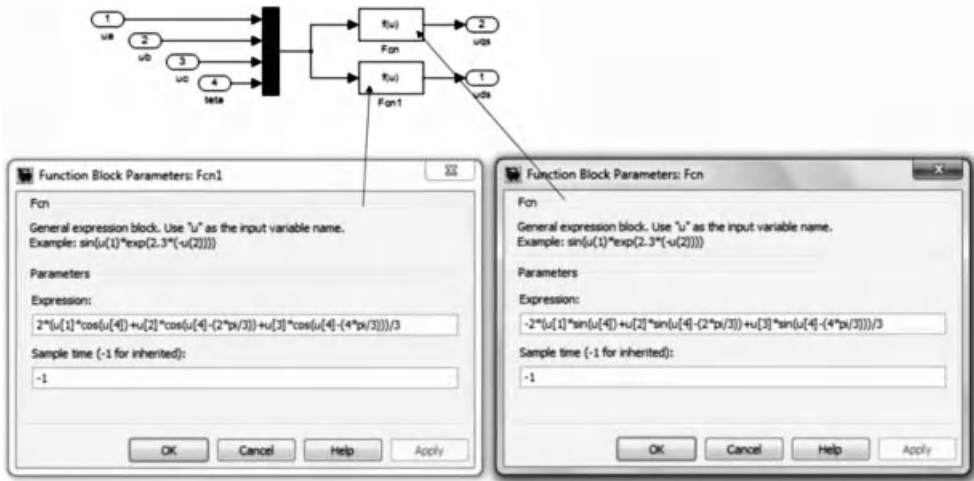


Figure 5.96 Transformation of reference frames from stationary to rotating

Block diagrams inside the sub-system ‘Flux linkage vector section,’ for determination of the section of complex plane containing instantaneous stator flux space vector, are shown in Figure 5.99.

The logical expressions for identifying the correct sector are similar to the ones in Figure 5.17 and shown again here for convenience in Figure 5.100.

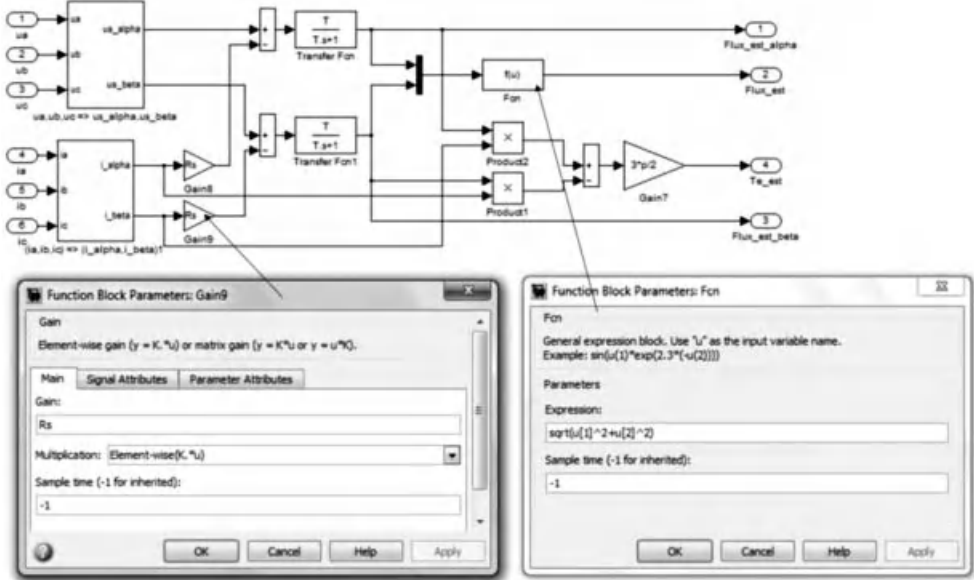


Figure 5.97 Estimation of SPMSM's stator flux linkage and electromagnetic torque

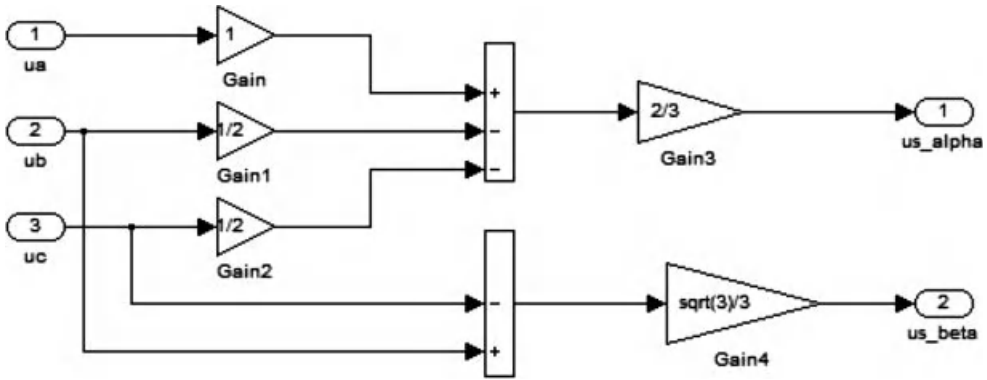


Figure 5.98 Conversion from phase voltage to  $\alpha$  and  $\beta$  components in stationary reference frame

Block diagrams in the sub-system ‘Flux and Torque Comparator,’ to determine the incremental or decreasing changes of the actual stator flux linkage and electromagnetic torque compared to the reference values, are illustrated in Figure 5.101.

The hysteresis band for flux comparator is 1% of rated value of stator flux linkage. Similarly, the hysteresis band for torque comparator is 1% of the rated torque. These are shown in Figure 5.102.

The two levels of flux comparator and three levels of torque comparator are also shown in Figures 5.103 and 5.104.

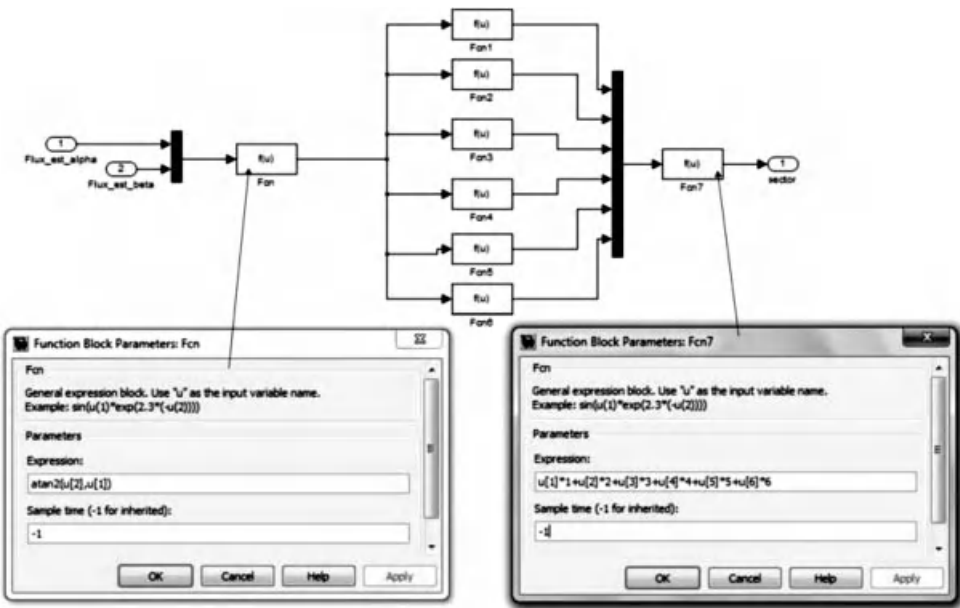


Figure 5.99 Determination of the complex plane’s sector for stator flux space vector

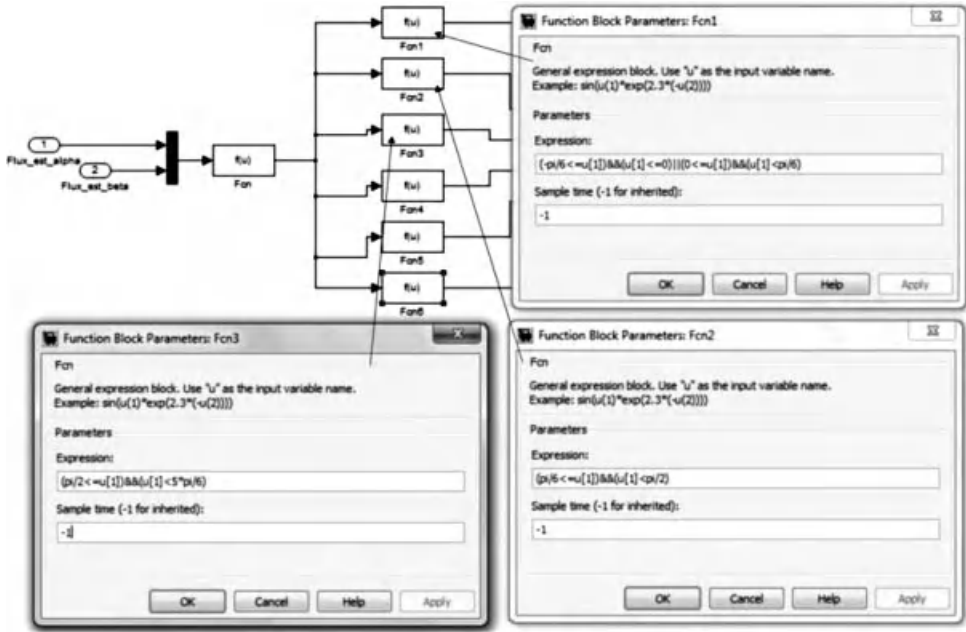


Figure 5.100 Logical expressions for identifying the sector of stator flux space vector

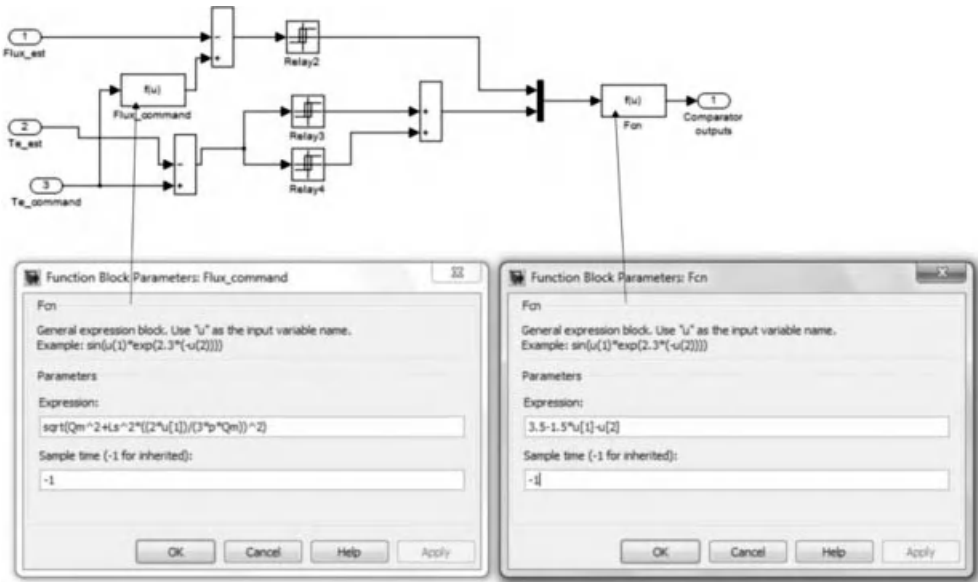


Figure 5.101 Stator flux and electromagnetic torque comparators

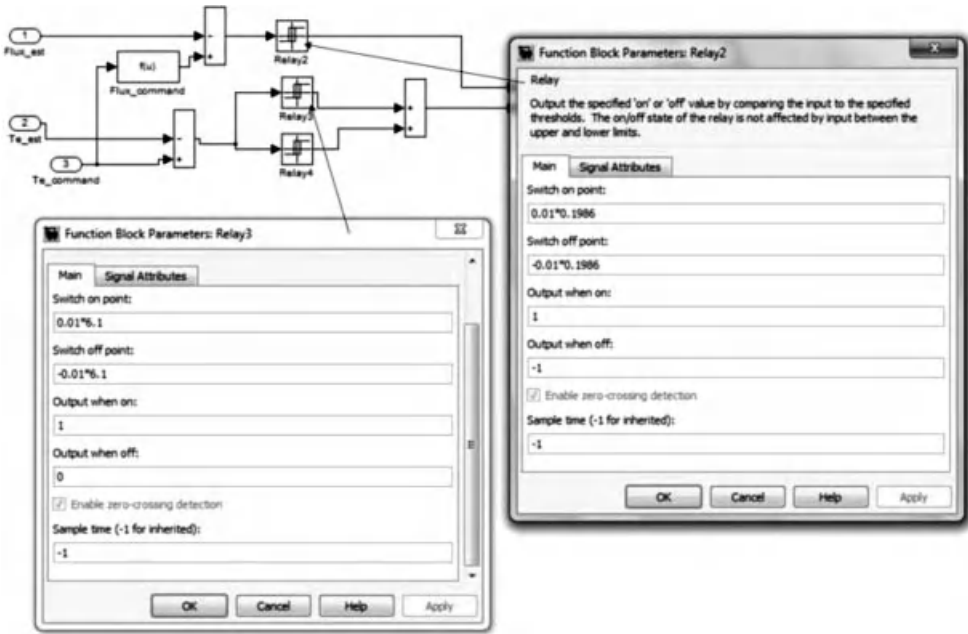


Figure 5.102 Hysteresis band for flux and torque comparators

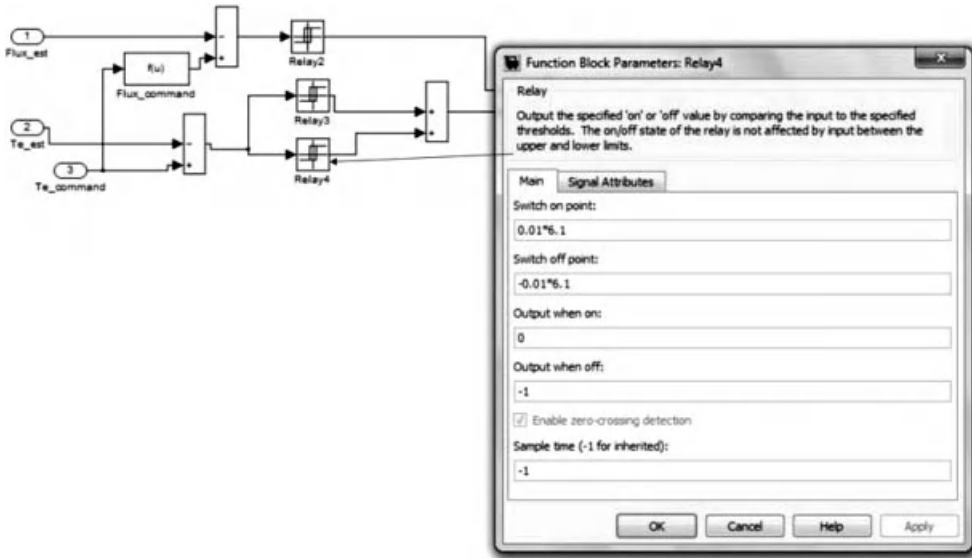


Figure 5.103 Three-level torque comparator

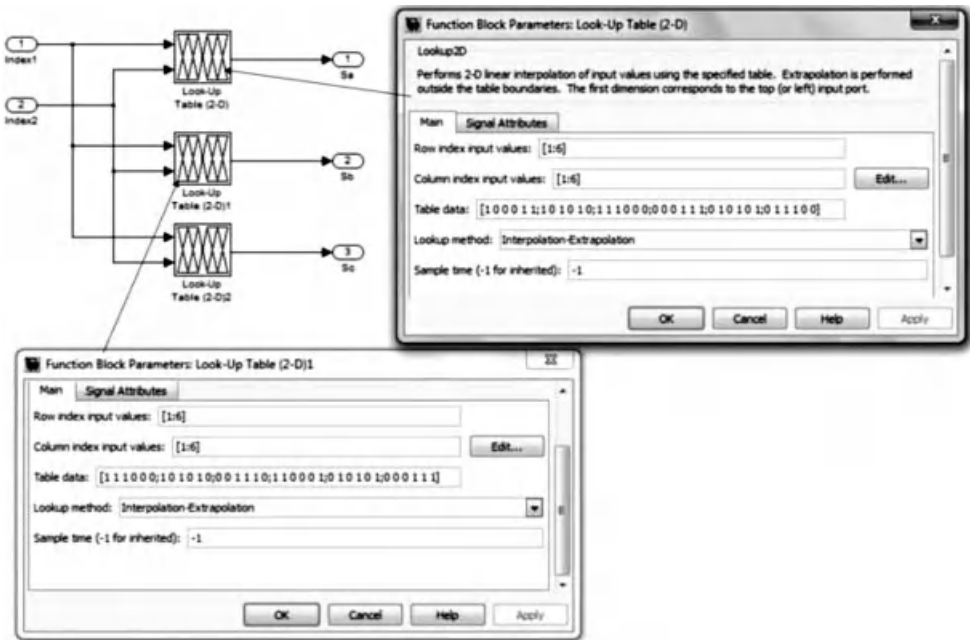


Figure 5.104 Optimum switching table for DTC of SPMSMs in MATLAB/Simulink

Optimum switching table suggested by [1] is presented in Figure 5.104. The three blocks ‘Look-Up Table (2-D)’ are used for coding the switching states of the three legs of the voltage source inverter.

The block diagrams for voltage source inverter are shown in Figure 5.105, with equations for calculation of phase voltage from the leg voltage of the inverter and Figure 5.106, with setting of the blocks ‘Switch.’

Speed command for DTC of SPMSM in speed control mode is shown in Figure 5.107, together with the parameters of the PID controller with anti-wind up, as shown in Figure 5.10. The motor is accelerated forward to rated speed and then reversed to the same speed in the opposite direction. The upper and lower limits of the PID controller’s output, which is the torque command, is 20 Nm and  $-20$  Nm, respectively.

Parameters of the SPMSM are shown in Figure 5.108, together with the application and removal of the load torque during the operation.

#### 5.7.4.2 Simulation of DTC of SPMSM

The simulation program developed in sub-section 5.7.4.2 is run with a fixed step size of  $10 \mu\text{s}$  for solver option of Runge-Kutta in MATLAB/Simulink. The SPMSM is accelerated, then reversed with the speed command shown in Figure 5.107. When the motor has settled after the acceleration, the load torque is suddenly applied and removed in a step-wise approach.

Figures 5.109–5.112 show rotor speed, stator flux linkage, electromagnetic torque, and stator phase current, respectively during start-up and acceleration. The actual rotor speed quickly meets the commanded speed after 0.05 s. The stator flux is fluctuated during the



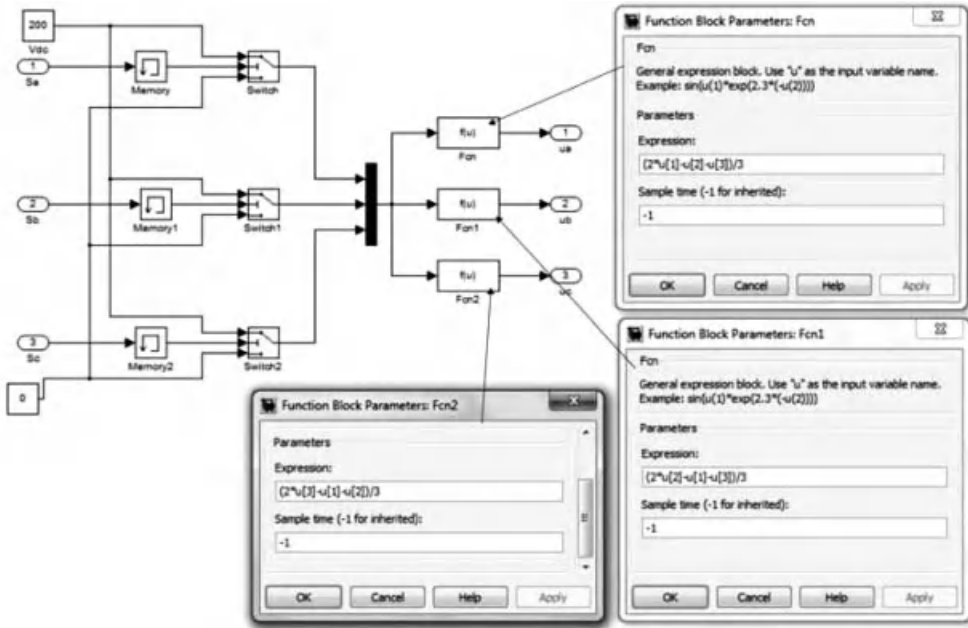


Figure 5.105 Voltage source inverter for DTC of SPMSMs

start-up then steady at the rated value. Torque overshoot is high during the start-up and up to the maximum limit set up by the limiter of the torque command at the output of the PID controller in Figure 5.92. Due to the high starting torque, the starting current’s overshoot is also high.

Responses of actual rotor speed, motor’s torque, and stator phase current during the application of load torque are shown in Figures 5.112–5.114.

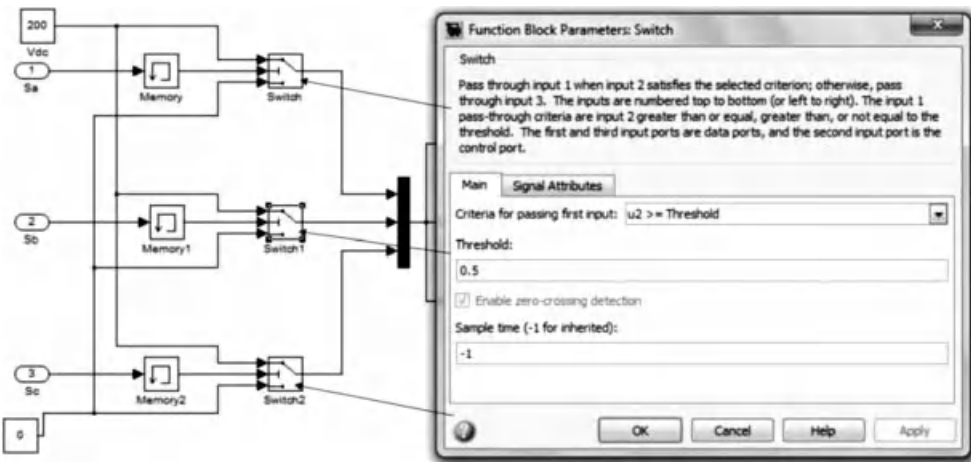


Figure 5.106 Setting of the blocks ‘Switch’ in sub-system ‘Voltage source inverter’



Figure 5.107 Speed command and parameters of PID controller

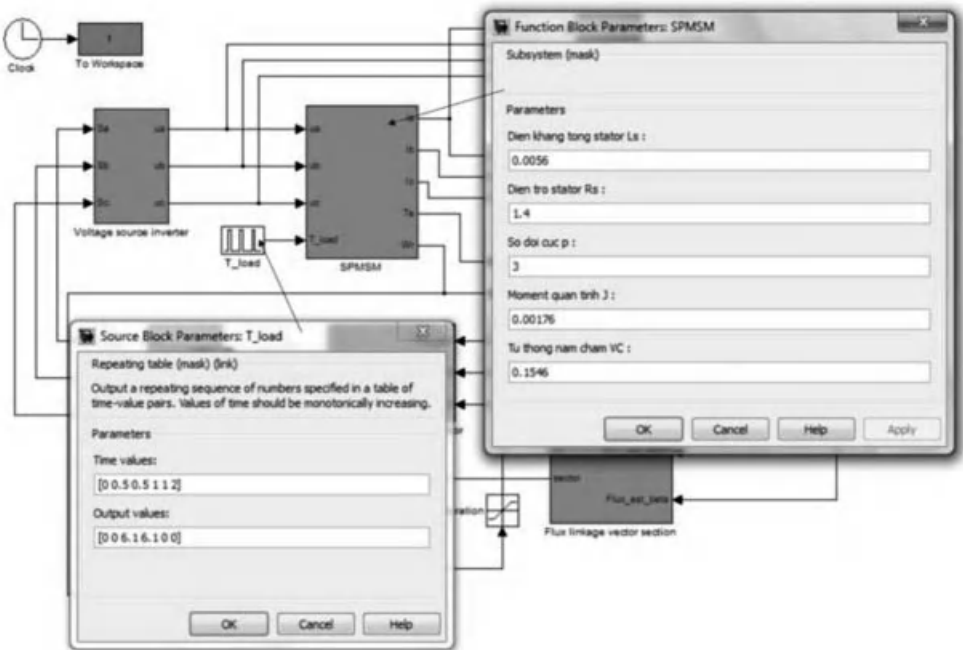
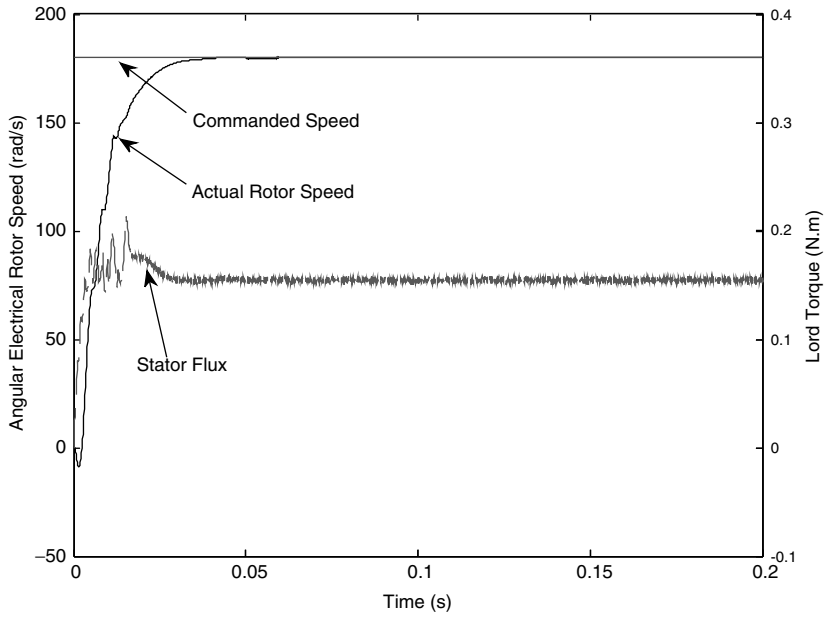
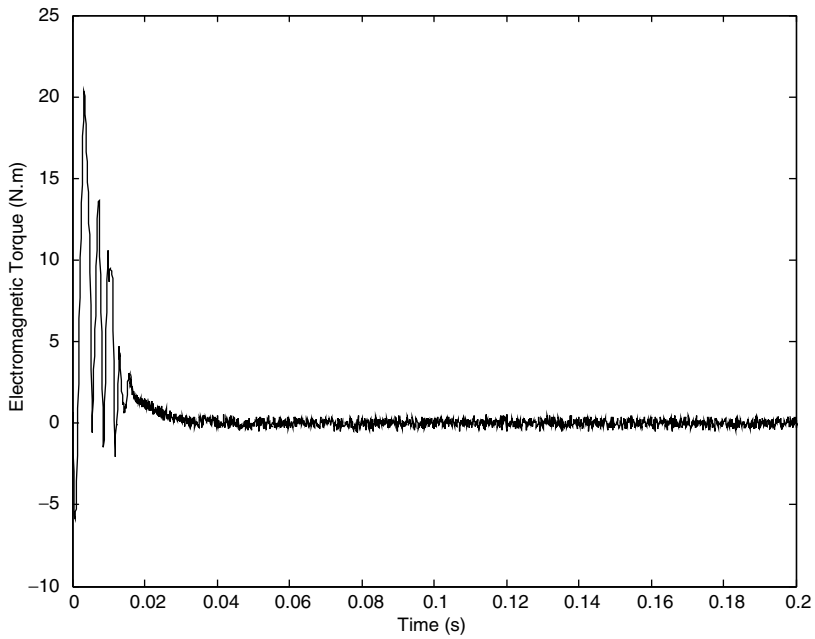


Figure 5.108 Parameters of the SPMSM



**Figure 5.109** SPMSM's rotor speed and stator flux linkage during start-up and acceleration



**Figure 5.110** Electromagnetic torque of SPMSM during start-up and acceleration

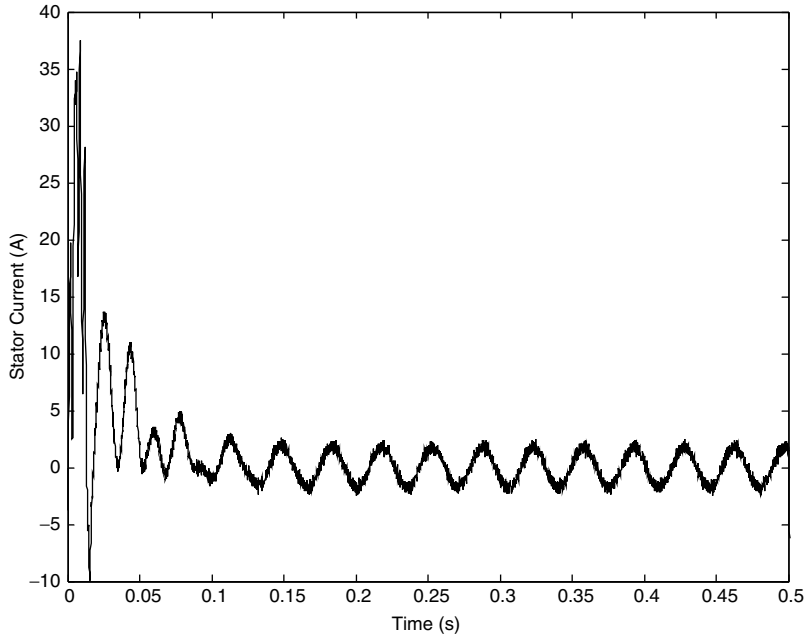


**Figure 5.111** Stator phase current of the SPMSM during start-up and acceleration

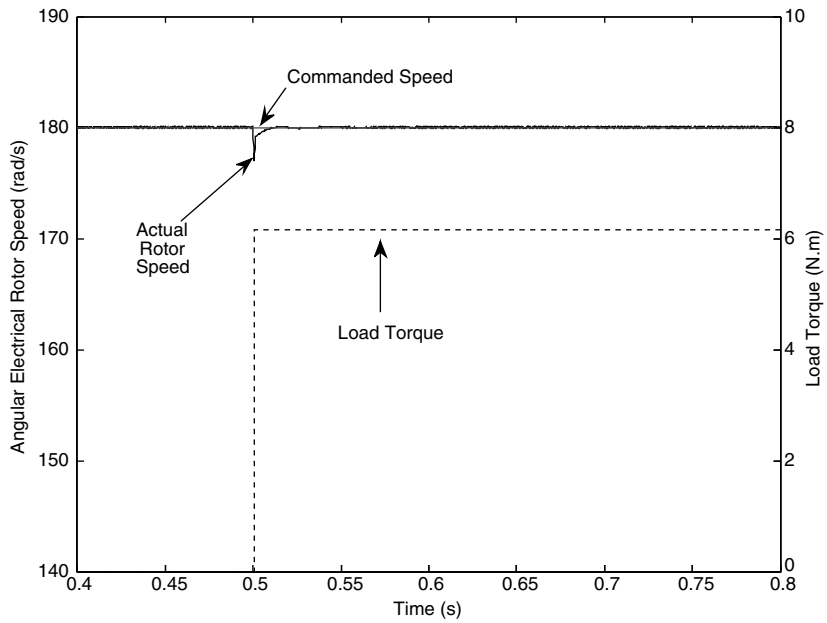


**Figure 5.112** Commanded speed, actual rotor speed during the application of load torque

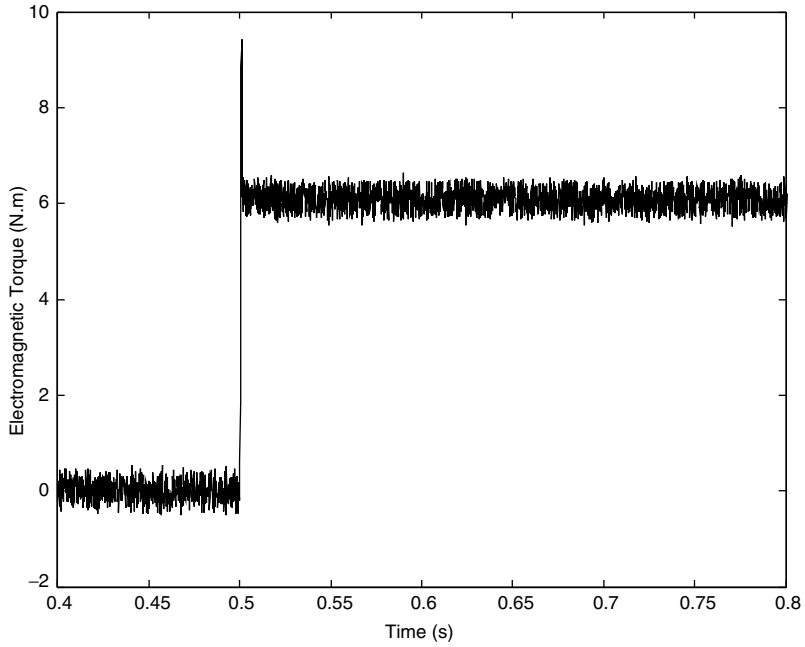


**Figure 5.113** Response of SPMSM's electromagnetic torque during load torque application

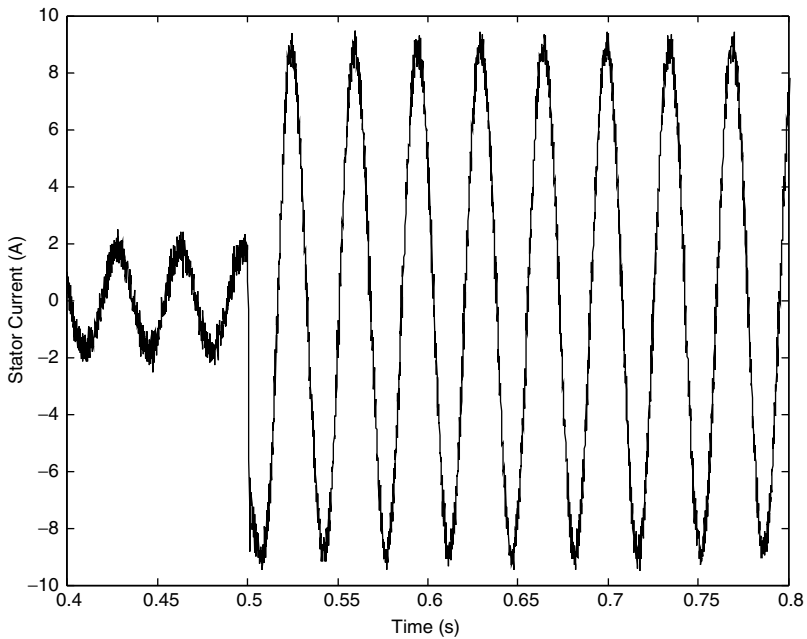


**Figure 5.114** Stator phase current when load torque is applied

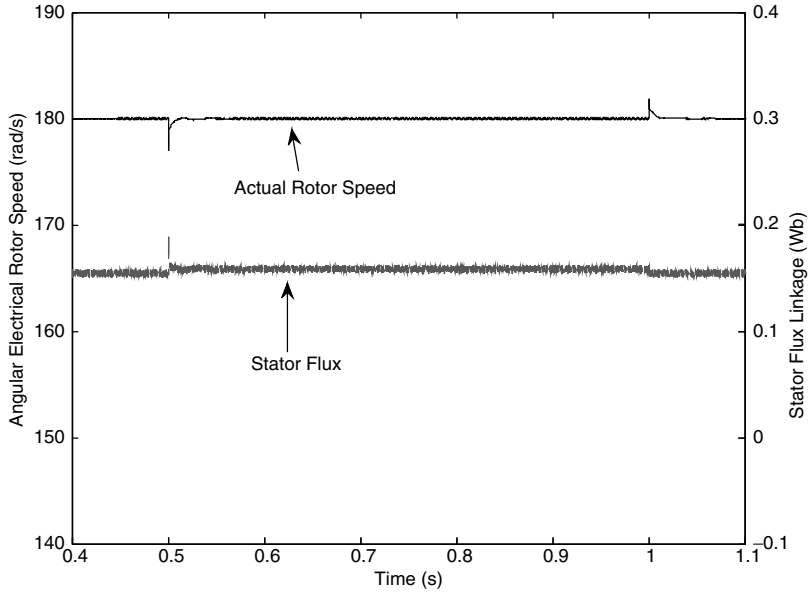


Figure 5.115 Response of stator flux linkage during application and removal of load torque

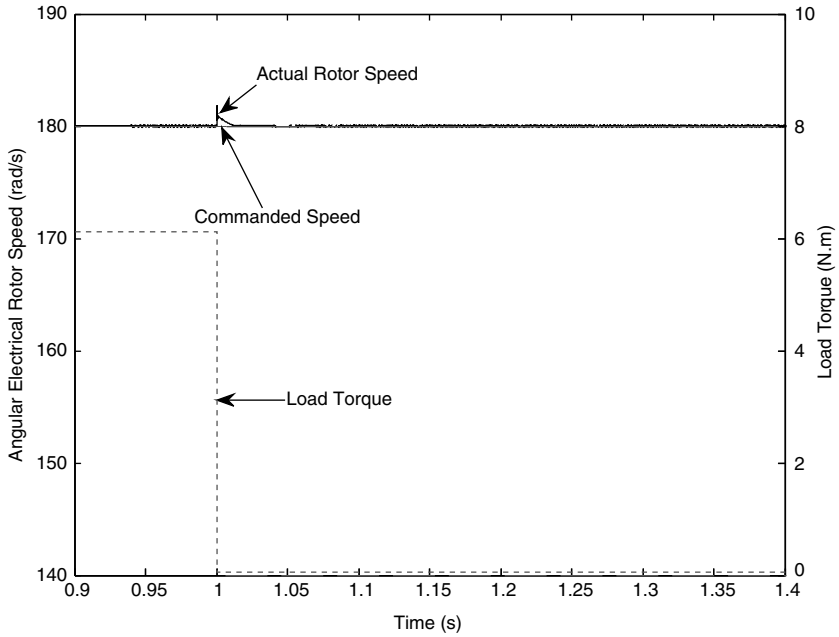
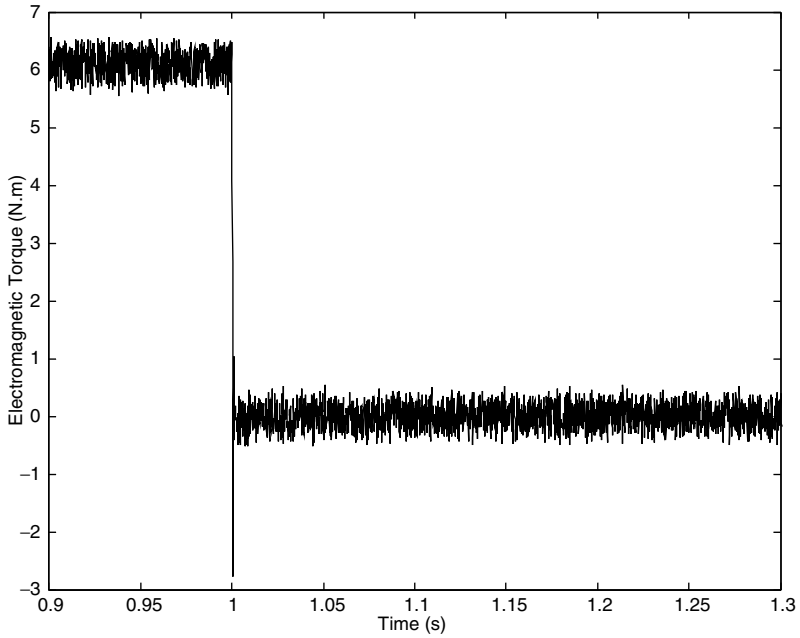
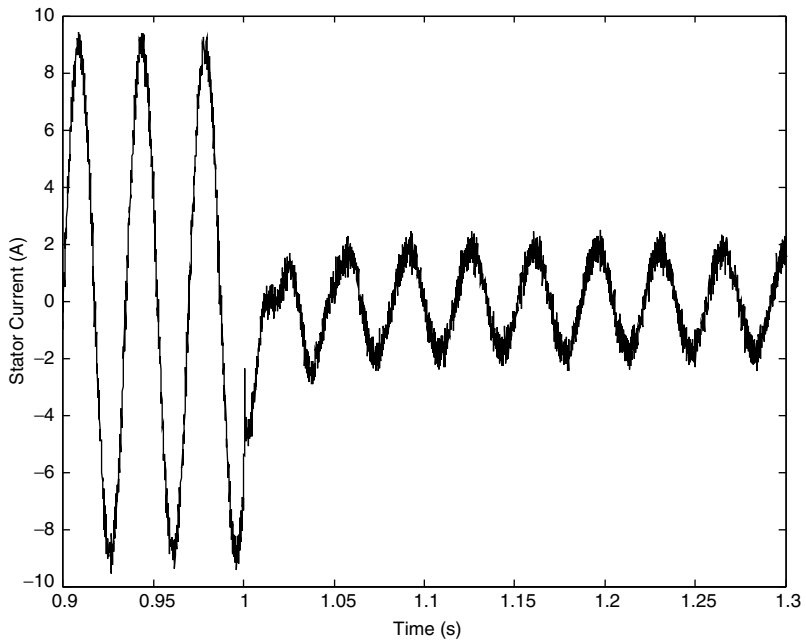


Figure 5.116 Commanded speed, actual rotor speed during the removal of load torque



**Figure 5.117** Response of the SPMSM's electromagnetic torque during load torque removal



**Figure 5.118** Stator current during the removal of load torque

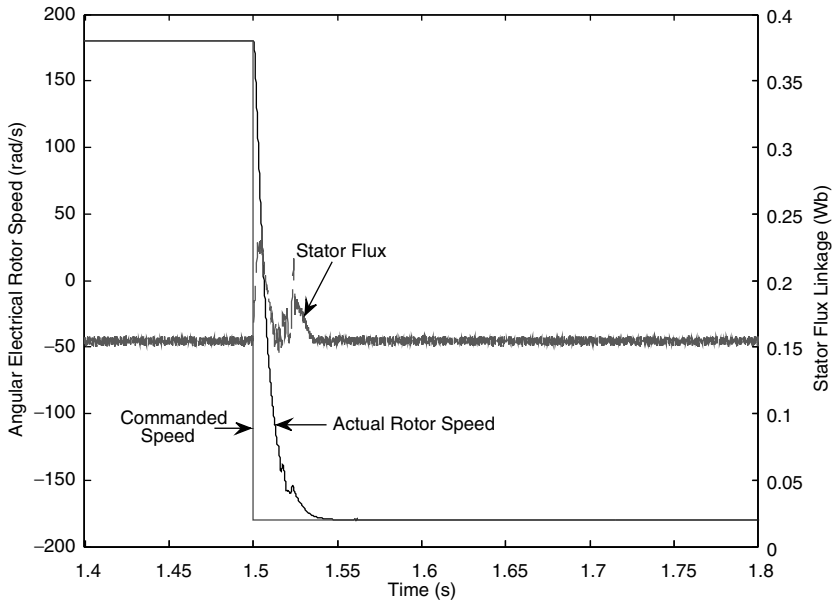


**Figure 5.119** Commanded speed, actual rotor speed, and stator flux during the reversal of speed

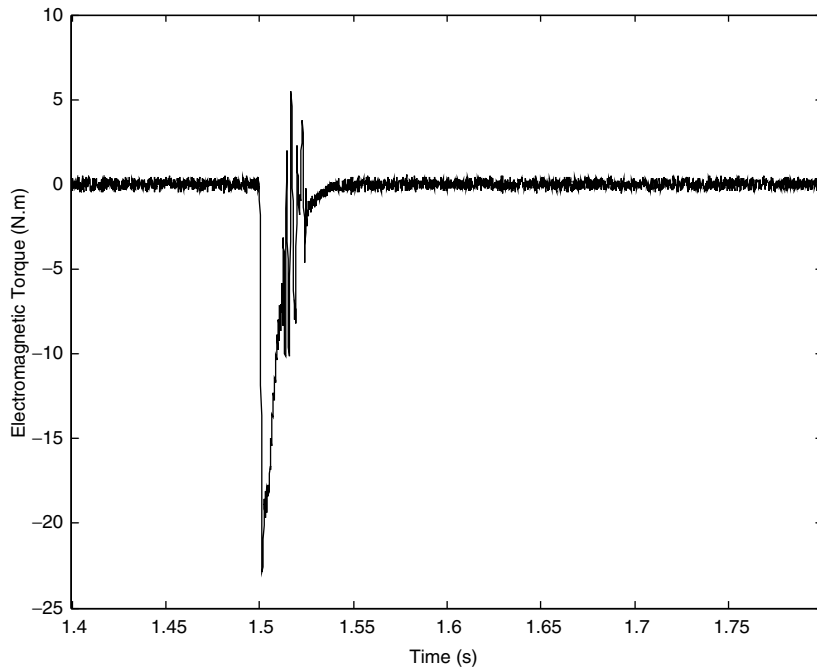


**Figure 5.120** Electromagnetic torque of SPMSM during reversal of speed



Rotor speed of the SPMSM is not significantly affected when the rated load torque is suddenly applied in a step-wise approach. The speed drops slightly then quickly returns to the commanded value, as shown in Figure 5.112.

Transient response of electromagnetic torque is also fast. Electromagnetic torque of the SPMSM quickly stabilized within the hysteresis bands around the commanded torque, as shown in Figure 5.113. Figure 5.114 also shows fast response of stator current during the application of load torque.

Stator flux linkage is slightly affected when the load torque is present, as shown in Figure 5.115.

Responses of actual rotor speed, motor's torque, and stator phase current during the removal of load torque are shown in Figures 5.116–5.118. The response of speed is also slightly affected when the load torque is removed. Fast transient responses are observed for electromagnetic torque and stator current. Rotor speed, stator flux, electromagnetic torque, and stator current of the SPMSM during reversal of speed are shown in Figures 5.119–5.121, respectively.

Stator flux of the SPMSM is affected significantly during deceleration in the forward direction of speed, as well as acceleration in the backward direction. This observation is consistent with the results shown in Figure 5.109. The actual rotor speed quickly follows the commanded values, as shown in Figure 5.119. The steady state error of speed is insignificant.

Electromagnetic torque does slightly cross the lower limit set by the limiter at the output of the PID speed controller, as shown in Figure 5.120. Stator current has high overshoot during the speed reversal, as demonstrated in Figure 5.121.

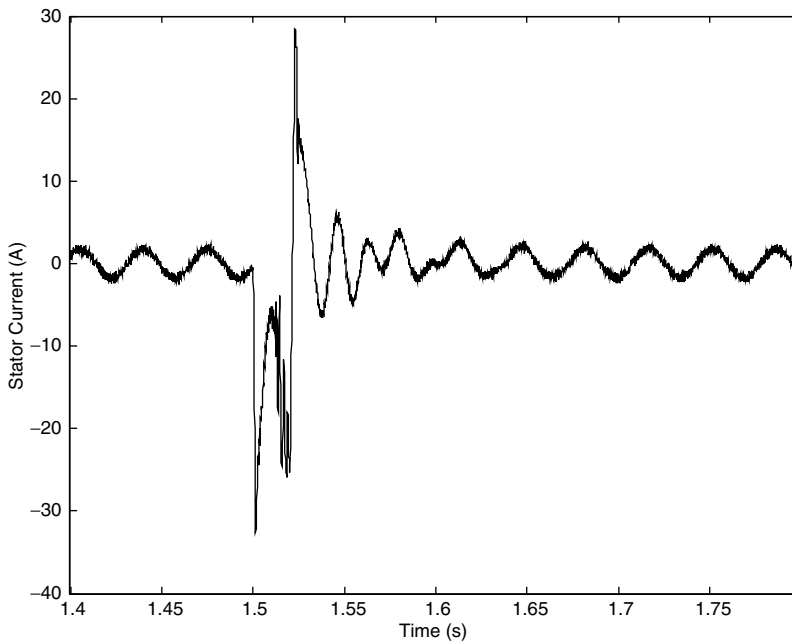


**Figure 5.121** Stator current of SPMSM during reversal of speed

## References

1. Takahashi, I. and Noguchi, T. (1986) A new quick-response and high-efficiency control strategy of an induction motor. *IEEE Trans. Ind. Appl.*, **IA-22(5)**, 820–827.
2. Depenbrock, M. (1985) Direkte Selbstregelung (DSR) für hochdynamische Drehfeldantriebe mit Stromrichterschaltung. *Etz Archiv.*, **7(7)**, 211–218.
3. Depenbrock, M. (1988) Direct self-control (DSC) of inverter-fed induction motors. *IEEE Trans. Power Elect.*, **3(4)**, 420–429.
4. Schofield, J. R. G. (1998); Variable speed drives using induction motors and direct torque control. *Dig. IEE Colloq. 'Vector Control Revisited'*, London, pp. 5/1–5/7.
5. Tiitinen, P., Pohjalainen, P., and Lalu, J. (1995) The next generation motor control method: Direct torque control (DTC). *Europ. Power Elect. J.*, **5(1)**, 14–18.
6. Kazmierkowski, M. P. and Tunia, H. (1994) *Auto. Cont. Conv. Drive*. Elsevier, New York.
7. Vas, P. (1998) *Sensorless Vector and Direct Torque Control*. Oxford University Press, New York.
8. Chen, J. and Li, Y. (1999) Virtual vectors based predictive control of torque and flux of induction motor and speed sensorless drives. *IEEE Ind. App. Soc. Ann. Mtg., IAS'99*, Phoenix, AZ, CD-ROM, paper No. 59\_3.
9. Kang, J. K. and Sul, S. K. (1999) New direct torque control of induction motor for minimum torque ripple and constant switching frequency. *IEEE Trans. Ind. Appl.*, **35(5)**, 1076–1082.
10. Alfonso, D., Gianluca, G., Ignazio, M., and Aldo, P. (1999) An improved look-up table for zero speed control in DTC drives. *Europ. Conf. Power Elect. Appl. EPE'99*, Lausanne, Switzerland, CD-ROM.
11. Casadei, D., Grandi, G., Serra, G., and Tani, A. (1994) Switching strategies in direct torque control of induction machines. *Int. Conf. Elect. Mach. IECM'94*. Paris, pp. 204–209.
12. Casadei, D., Grandi, G., Serra, G., and Tani, A. (1998a) The use of matrix converters in direct torque control of induction machines. *IEEE Ann. Mtg. Ind. Elect. Soc., IECON'98*. Aachen, Germany, pp. 744–749.
13. Vas, P. (1992) *Electrical Machines and Drives: A Space-vector Theory Approach*. Oxford, Clarendon Press.
14. Boldea, I. and Nasar, S. A. (1992) *Vector Control of AC Drives*. Boca Raton, Florida CRC Press.
15. Levi, E. (1994) Impact of iron loss on behaviour of vector controlled induction machines. *IEEE Ind. App. Soc. Ann. Mtg., IAS'94*, Denver, CO, pp. 74–80.
16. Levi, E. (1995) Impact of iron loss on behaviour of vector controlled induction machines. *IEEE Trans. Ind. App.* **31(6)**, 1287–1296.
17. Levi, E. (1996) Rotor flux oriented control of induction machines considering the core loss. *Elect. Mach. Power Syst.*, **24(1)**, 37–50.
18. Levi, E. and Pham-Dihn, T. (2002) DTC of induction machines considering the iron loss. *Elect. Power Comp. Syst.*, **30(5)**, May 2002.
19. Pham-Dihn, T. (2003) Direct torque control of induction machines considering the iron losses, PhD thesis, Liverpool John Moores University, UK.
20. Dittrich, A. (1998) Model based identification of the iron loss resistance of an induction machine. *Int. Conf. Power Elect. Var. Speed Drives, PEVD'98* London, IEE Conference Publication No. 456, pp. 500–503.
21. Noguchi, T., Nakmahachalasint, P., and Watanakul, N. (1997) Precise torque control of induction motor with on-line parameter identification in consideration of core loss. *Proc. Power Conv. Conf., PCC'97*, Nagaoka, Japan, pp. 113–118.
22. Wieser, R. S. (1998) Some clarifications on the impact of AC machine iron properties on space phasor models and field oriented control. *Int. Conf. Elect. Mach., IECM'98*, Istanbul, pp. 1510–1515.
23. Sokola, M and Levi, E. (2000) A novel induction machine model and its application in the development of an advanced vector control scheme. *Int. J. Elect. Eng. Educ.*, **37(3)**, 233–248.

24. Habetler, T. G., Profumo, F., Pastorelli, M., and Tolbert, L. M. (1992) Direct torque control of induction machines using space vector modulation. *IEEE Trans. Ind. Appl.*, **28**(5).
25. Mir, S. A., Elbuluk, M. E., and Zinger, D. S. (1994) Fuzzy implementation of direct self control of induction machines. *IEEE Trans. Ind. Appl.*, **30**(3), 729–735.
26. Stojic, M. D. and Vukosavic, N. S. (2005) A new induction motor drive based on the flux vector acceleration method. *IEEE Trans. Ener. Conv.*, **20**(1), 173–180.
27. Swarupa, L. M., Das, T. R. J., and Gopal, R. V. P. (2009) Simulaiton and analysis of SVPWM based 2-level and 3-level inverters for direct torque of induction motor. *Int. J. Elect. Eng. Res.*, **1**(3), 169–184.
28. Jidin, A., Idris, N. R. N, Jatim, N. H. A, Sutikno, T., and Elbuluk, E. M. (2011) Extending switching frequency of torque ripple reduction utilizing a contant frequency torque controller in DTC of induction motors. *J. Power Elect.*, **11**(2), 148–155.
29. Krishnan, R. (2010) *Permanent Magnet Synchronous and Brushless DC Drives*. CRC Press, Taylor & Francis Group.
30. Levi, E. (2001) *High Performance Drives*. Course note for the Subject ENGN3028, School of Engineering, Liverpool John Moores University, UK.

# 6

## Non-Linear Control of Electrical Machines Using Non-Linear Feedback

Zbigniew Krzeminski and Haitham Abu-Rub

### 6.1 Introduction

A recent trend in advanced drives control has enabled an AC motor to behavior like a separately excited DC motor. This goal has been almost achieved since introducing the vector control principle. The main disadvantage of vector control methods is the presence of non-linearity in the mechanical part of the equation during the changing of rotor flux linkage.

Although good results from field-oriented control have been observed, attempts to obtain new control methods are being made. Non-linear control of induction motors was first presented in [1]. It introduced a novel mathematical model for induction motors, which made it possible to avoid using sin/cos transformation of state variables. The model consists of two completely decoupled subsystems, mechanical and electromagnetic. It has been shown that in such a situation it is possible to have non-linear control and decoupling between electromagnetic torque and the rotor linkage flux. Decoupling between torque and the square of rotor flux has been obtained, after assuming some simplification [1,2,25,26]. Works that discuss non-linear control of dynamic systems include [1–28].

When a motor is fed by voltage source inverters, and when the rotor flux linkage magnitude is kept constant, the non-linear control system control is equivalent to the vector control method. In many other situations, this new idea gives simplicity of the structure and good response [2,25,26].

The main disadvantage of vector control methods is the presence of non-linearity in the mechanical part of the equation while changing the rotor flux linkage. Direct use of vector methods to control an induction machine fed by a current inverter, or to control a double-fed

machine, provides high complexity of the machine model, which is necessary to obtain precise control systems.

The use of variables transformation to obtain non-linear model variables makes the control strategy easy to perform, because only four state variables have been obtained with relatively simple non-linearity form. This means it possible to use this method in the case of flux vector changing and to obtain simple system structures. In such systems, it is possible to change the rotor flux linkage with operating point without affecting the dynamics of the system. The relations occurring between the new variables make it possible to obtain novel control structures that guarantee a good response from the drive system. This is convenient for the economical operation of drive systems in which this flux is reduced if the load is decreased.

It is possible to decouple the drive system into two parts using field oriented control (FOC), followed by an introduction to a new variable. However, this operation provides a more complicated non-linear feedback form than those used in the non-linear control approach. In addition, the use of new variable further complicates the control system.

## 6.2 Dynamic System Linearization using Non-Linear Feedback

The linearity of the control system using non-linear feedback requires the accessibility to all state variables. It is assumed that all necessary variables are measured and directly calculated or estimated using a model or observer system.

The linearization process of non-linear systems is widely discussed in [2,3,8,26,27]. To use non-linear feedback, it is desirable to obtain a mathematical description of the non-linear dynamic system as a system of differential equations. It is assumed that the dynamic system is described by equations [2,3,8,19]:

$$\dot{\mathbf{x}} = \mathbf{f}(\mathbf{x}) = \sum_{i=1}^m \mathbf{g}_i(\mathbf{x})\mathbf{u}_i \quad (6.1)$$

where

$\mathbf{u} = [u_1, u_2, \dots, u_m]^T$ ;  $\mathbf{x} \in \mathbf{R}^n$ ,  $u \in \mathbf{R}^m$ ,  $m \leq n$ ,  $\mathbf{f}(\cdot)$ ,  $\mathbf{g}_i(\cdot)$  are vector functions.

Methods of differential geometry [8] make it possible to convert the above-described system by using a non-linear change of variables and non-linear feedback to the next form:

$$\dot{\mathbf{y}} = \mathbf{A}\mathbf{y} + \mathbf{B}\mathbf{v} \quad (6.2)$$

where  $\mathbf{A}$  and  $\mathbf{B}$  are constant **matrices**, so that a pair  $(\mathbf{A}, \mathbf{B})$  is controllable.

Linearization of the system using variables transformation and non-linear feedback may be realized, as in [8] The first step of linearization is to choose new variables:

$$\mathbf{z} = \mathbf{z}(\mathbf{x}) \quad (6.3)$$

such that the differential equations take the form:

$$\dot{\mathbf{z}}_1 = \mathbf{A}_1\mathbf{z} \quad (6.4)$$

$$\dot{\mathbf{z}}_2 = \mathbf{A}_2 \mathbf{z}_2 + \mathbf{f}_2(\mathbf{z}) + \mathbf{g}_2(\mathbf{z})\mathbf{u} \tag{6.5}$$

where  $\mathbf{A}_1, \mathbf{A}_2$  are constant matrices; and  $\mathbf{f}_2(\cdot)$ ; and  $\mathbf{g}_2(\cdot)$  are non-linear vector functions; and  $\mathbf{z}_1 \in \mathbf{R}^{(n-m)}$ ;  $\mathbf{z}_2 \in \mathbf{R}^m$

In the next step of linearization, it is assumed that when using non-linear feedback, the non-linearity in equation (6.4) will be compensated for. This leads to

$$\mathbf{B}_2 \mathbf{v} = \mathbf{f}_2(\mathbf{z}) + \mathbf{g}_2(\mathbf{z})\mathbf{u} \tag{6.6}$$

where  $\mathbf{B}_2$  is the adopted constant matrix and  $\mathbf{v}$  is the new control signal.

If there is an inverse function to  $\mathbf{g}_2(\mathbf{z})$ , then the control signal used for linearization is calculated from [2,3,8,27]

$$\mathbf{u} = [\mathbf{g}_2(\mathbf{z})]^{-1} [\mathbf{B}_2 \mathbf{v} - \mathbf{f}_2(\mathbf{z})] \tag{6.7}$$

After the suggestion of the non-linear control described above, the dynamic system may be obtained as

$$\dot{\mathbf{z}}_1 = \mathbf{A}_1 \mathbf{z}_1 \tag{6.8}$$

$$\dot{\mathbf{z}}_2 = \mathbf{A}_2 \mathbf{z}_2 + \mathbf{B}_2 \mathbf{v} \tag{6.9}$$

Linearization of a drive system with an induction motor using non-linear feedback requires, in general, accesses to all state variables.

Figure 6.1 summarizes the idea of system linearization using non-linear feedback [26]. Combining non-linear feedback with the non-linear model, and then making variables transformations, converts the highly non-linear dynamic system, such as an induction motor, into a linear object. This will be shown step-by-step in this chapter.

After obtaining a linear structure of the dynamic system, it will be possible to use a simple cascaded structure of PI controllers, as shown in the next section.

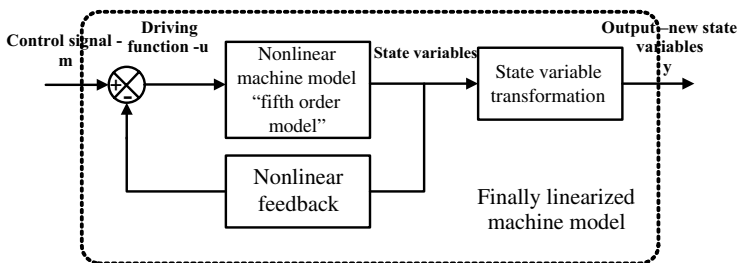


**Figure 6.1** Linearization of dynamic system using non-linear feedback:  $m$  – driving function of the linearized system;  $y$  – state variable of the linearized system;  $u$ –driving function of the non-linear system;  $x$  – state variable of the non-linear system

### 6.3 Non-Linear Control of Separately Excited DC Motors

Because the separately excited DC motor has the best mechanical characteristics, and it is one of most widely used DC motors, we will limit our explanation of the control of this motor to our introduction to the topic. Although the DC motor is not being used for advanced drives at this time, presenting this type of motor is beneficial from an educational point of view.

For realizing a linearization of the non-linearity in the mathematical model, a new variable is introduced, proportional to the motor torque [20]:

$$m = i_a \cdot i_f \quad (6.10)$$

After taking the derivative of the new variable and making some mathematical arrangements, the following model is derived [18]:

$$\frac{dm}{dt} = \left( \frac{1}{T_f} + \frac{1}{T_a} \right) m + \frac{1}{T_a} v1 \quad (6.11)$$

$$\frac{di_f}{dt} = -\frac{i_f}{T_f} + \frac{1}{T_f} v2 \quad (6.12)$$

$$J \frac{d\omega_r}{dt} = \frac{m}{T_m} - \frac{m_o}{T_m} \quad (6.13)$$

The new model allows us to use linear and cascaded controllers for motor control. The output signals of the controllers are the new variables  $v1$  and  $v2$ , which are described from the model as

$$v1 = K_1 \cdot u_a \cdot i_f + \frac{T_a \cdot K_2 \cdot u_f \cdot i_a}{T_f} - K_3 \cdot i_f^2 \cdot \omega_r \quad (6.14)$$

$$v2 = K_2 \cdot u_f \quad (6.15)$$

The control scheme of the motor using the above procedure is shown on Figure 6.2. The speed controller commands the variable  $m$  that is proportional to the motor torque. This value is limited by the product of the actual value of the field current and the maximum value of the armature current. The torque controller commands the variable  $v2$ , while the controller of the field current commands the control signal  $v1$ . These two variables, along with other signals, are used in the decoupling block to compute the command values of the armature and field voltages.

#### 6.3.1 MATLAB/Simulink Non-Linear Control Model

The separately excited DC motor control model shown in Figure 6.3 consists of two blocks; a control system model and a separately excited DC motor model are shown in Figure 6.4. All the models are in per unit unless otherwise specified. The Simulink software file of separately

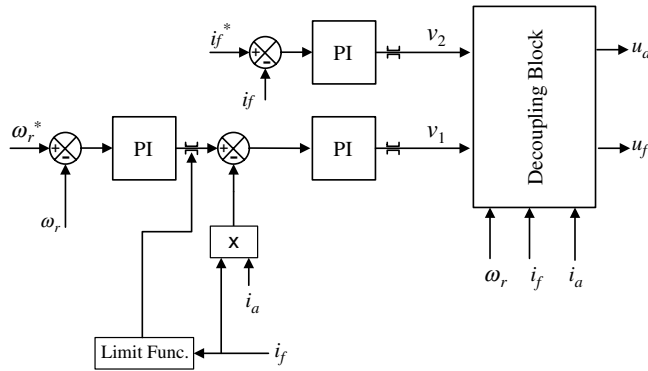


Figure 6.2 Separately excited DC motor control scheme

excited DC motor model is [DCmotor\_non-linear]. The motor parameters are located in [DCmotor\_non-linear\_init], which should be first initialized.

### 6.3.2 Non-Linear Control Systems

The motor model is linearized by a non-linear input transformation with new input variables  $v_1$  and  $v_2$ . The transformation is

$$v_1 = K_1 \cdot u_a + \frac{T_a \cdot K_2 \cdot u_f \cdot I_a}{T_f} - K_3 \cdot I_a^2 \cdot \omega_r \tag{6.16}$$

$$v_2 = K_2 \cdot u_f \tag{6.17}$$

These equations are modeled in the transformation blocks shown in Figures 6.5 and 6.6.

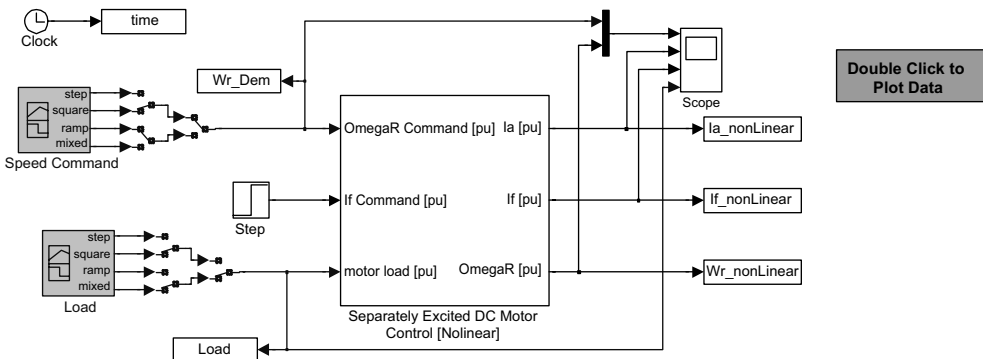
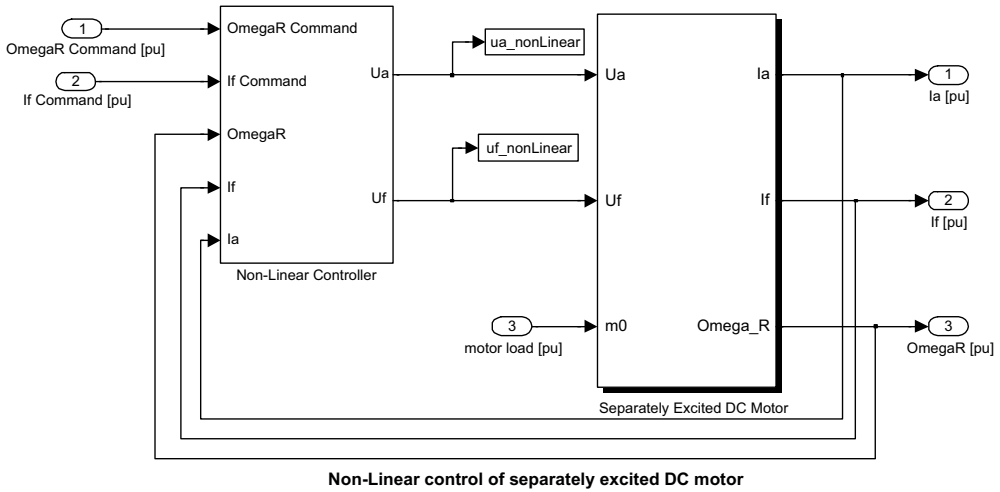


Figure 6.3 Separately excited DC motor control model





**Figure 6.4** Components of separately excited DC motor control model

### 6.3.3 Speed Controller

The speed controller is a PI controller, which calculated the demand for variable  $m$ , as shown in Figure 6.7. The armature current demand is calculated by solving the following equations:

$$m_{command} = U_{int} + K_{p1}(\omega_{r_{command}} - \omega_r) \tag{6.18}$$

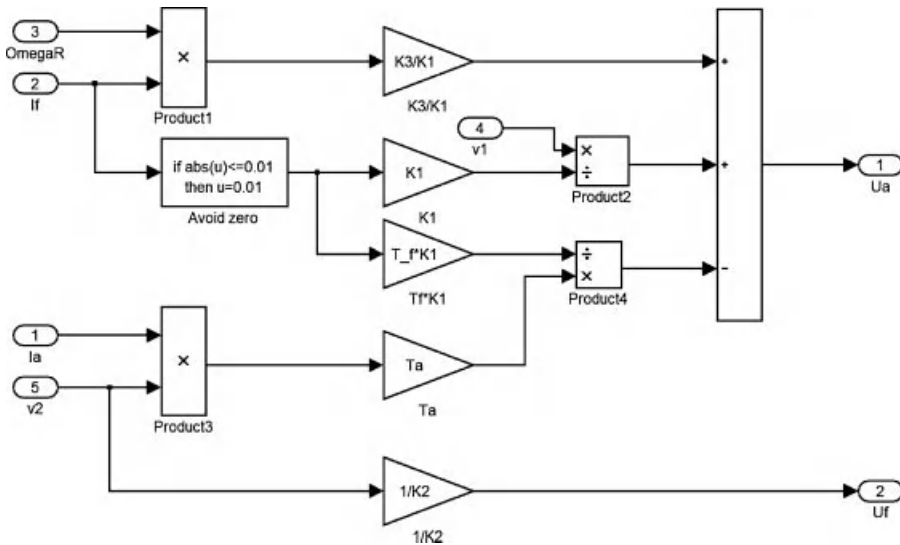


**Figure 6.5** Transformation block

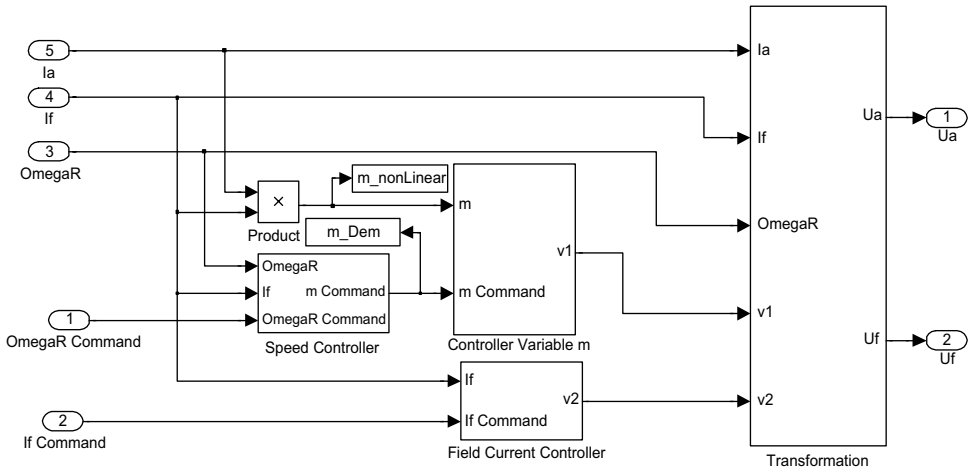


Figure 6.6 Non-linear controller

$$\frac{dU_{int}}{dt} = +K_{i1}(\omega_{rcommand} - \omega_r) \tag{6.19}$$

where  $|U_{int}| \leq I_f I_{a_{max}}$  and  $|m_{command}| \leq I_f I_{a_{max}}$

### 6.3.4 Controller for Variable $m$

The variable  $m$  controller is a PI, as shown in the Figure 6.8. The input  $v_1$  is calculated by solving the following equations:

$$v_1 = m_{int} + K_{p2}(m_{command} - m) \tag{6.20}$$

$$\frac{dm_{int}}{dt} = K_{i2}(m_{command} - m) \tag{6.21}$$

where  $|m_{int}| \leq 3$  and  $|v_1| \leq 3$

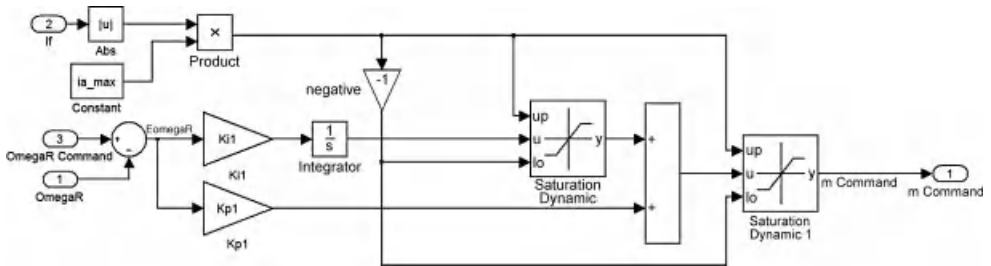
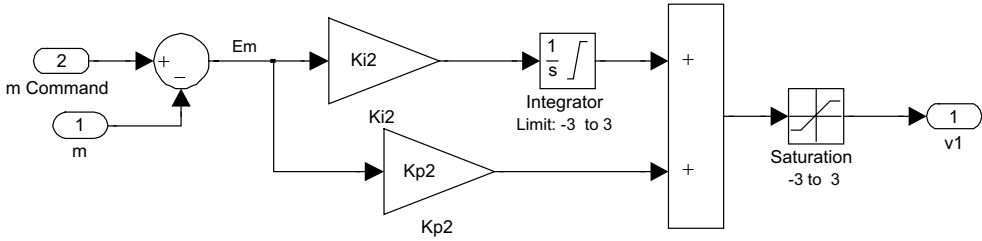


Figure 6.7 Speed controller



**Figure 6.8** Variable m controller

### 6.3.5 Field Current Controller

The field controller is also a PI type. The control variable  $v_2$  is calculated by solving the following equations (Figure 6.9):

$$v_2 = U_{f_{int}} + K_{p3} (I_{f_{command}} - I_f) \tag{6.22}$$

$$\frac{dU_{f_{int}}}{dt} = K_{i3} (I_{f_{command}} - I_f) \tag{6.23}$$

where,  $|U_f| \leq 1$  and  $|v_2| \leq 1$

### 6.3.6 Simulation Results

The simulation results for various steps in the speed demand with varying loads are shown in Figure 6.10. The controller tracks the demand well.

## 6.4 Multiscalar model (MM) of Induction Motor

An induction motor is a higher-order, non-linear object, as shown in Chapter 2. An internal coupling appears between mechanical and electromagnetic variables. Therefore, it is especially beneficial to use the idea of non-linear control for induction motor control.

### 6.4.1 Multiscalar Variables

The non-linear control idea using non-linear feedback was first time presented in [1]. It creates a new model of the machine with fewer state variables, which may be linked with the rotor,

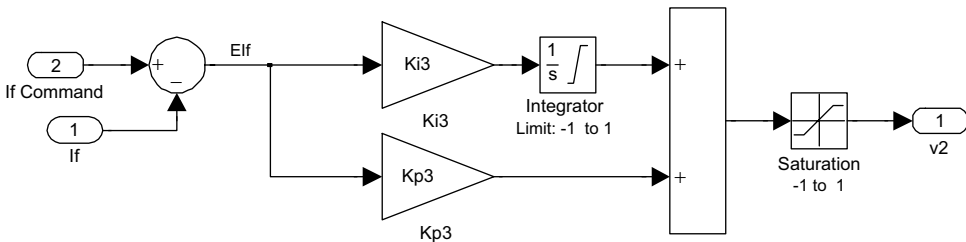


**Figure 6.9** Variable  $v_2$  controller

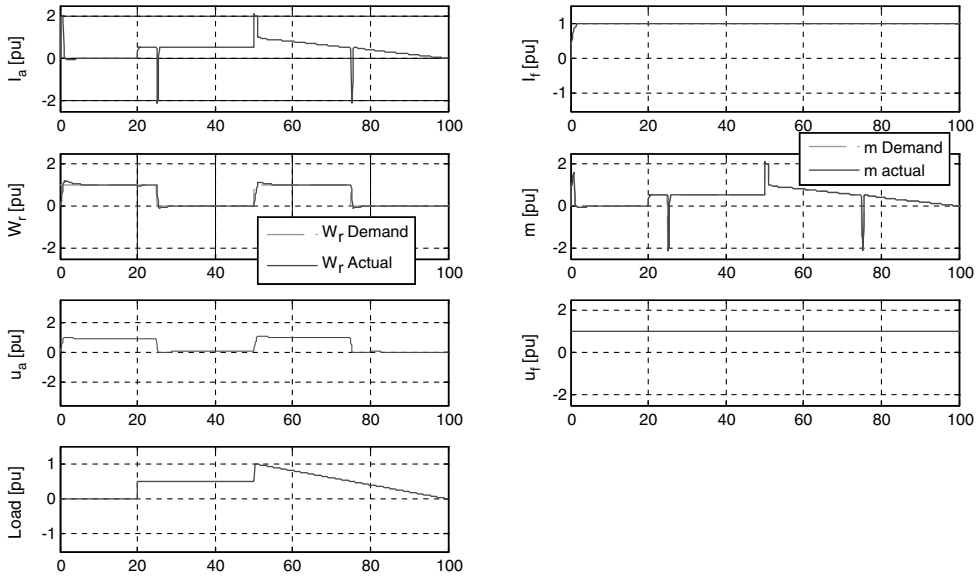


Figure 6.10 Simulation results

stator, main flux, etc. If the variables are a function of the rotor flux, then a terminology of non-linear rotor-oriented control systems is presented ( $i_s, \psi_r$ ). Other options, such as ( $i_s, \psi_s$ ), ( $i_s, \psi_m$ ), may also be used. In this book, we will focus on the first option because of its popularity and less complicated decoupling system; however, for extra work, other options could be derived and examined.

The new state variables for the ( $i_s, \psi_r$ ) option may be interpreted as rotor angular speed, scalar, and vector products of the stator current and rotor flux vectors, and the square of the rotor linkage flux presented in an arbitrary reference frame (i.e. XY) as [1,2,26]

$$x_{11} = \omega_r \tag{6.24}$$

$$x_{12} = \psi_{rx} i_{sy} - \psi_{ry} i_{sx} \tag{6.25}$$

$$x_{21} = \psi_{rx}^2 + \psi_{ry}^2 \tag{6.26}$$

$$x_{22} = \psi_{rx} i_{sx} + \psi_{ry} i_{sy} \tag{6.27}$$

In these equations,  $\psi_{rx}, \psi_{ry}, i_{sx}, i_{sy}$  are the rotor flux and stator current vectors in the co-ordinate system XY, rotating with arbitrary speed, and  $\omega_r$  is the angular speed of the rotor shaft. Subscript  $x$  denotes the real frame and  $y$  the imaginary frame; therefore, the variables could be presented in a stationary  $\alpha\beta$  frame or any other rotating co-ordinate system.

The state variable  $x_{11}$  is the rotor speed;  $x_{12}$  is proportional to the motor torque;  $x_{21}$  is the square of the rotor flux; and  $x_{22}$  is somehow proportional to the energy; the physical meaning of this variable, however, is not related to our idea of control, so we have not elaborated upon it here.

### 6.4.2 Non-Linear Linearization of Induction Motor Fed by Voltage Controlled VSI

A mathematical model of a dynamic system is presented as differential equations of the state variables. In the conventional induction motor model from Chapter 2, the model was shown as a derivative of five state variables. In the non-linear control approach, we have four state variables that should be differentiated to gain the new model. Therefore, the first step of obtaining the new mathematical model of the machine is differentiating the four state variables (equations), which leads to [1,2,26]

$$\frac{dx_{11}}{dt} = \frac{d\omega_r}{dt} \quad (6.28)$$

$$\frac{dx_{12}}{dt} = \psi_{rx} \frac{di_{sy}}{dt} + i_{sy} \frac{d\psi_{rx}}{dt} - \psi_{ry} \frac{di_{sx}}{dt} - i_{sx} \frac{d\psi_{ry}}{dt} \quad (6.29)$$

$$\frac{dx_{21}}{dt} = 2\psi_{rx} \frac{d\psi_{rx}}{dt} + 2\psi_{ry} \frac{d\psi_{ry}}{dt} \quad (6.30)$$

$$\frac{dx_{22}}{dt} = \psi_{rx} \frac{di_{sx}}{dt} + i_{sx} \frac{d\psi_{rx}}{dt} + \psi_{ry} \frac{di_{sy}}{dt} + i_{sy} \frac{d\psi_{ry}}{dt} \quad (6.31)$$

The next step is to substitute derivatives for the currents and fluxes from the motor model (equations) in the derivatives of new variables (in equations). After using such substitutions and taking into account the relationships of the new state variables (equations), we obtain the next model of the system [1,2,26]:

$$\frac{dx_{11}}{d\tau} = \frac{x_{12}L_m}{JL_r} - \frac{m_o}{J} \quad (6.32)$$

$$\frac{dx_{12}}{d\tau} = -\frac{1}{T_v}x_{12} - x_{11}\left(x_{22} + \frac{L_m}{w_\sigma}x_{21}\right) + \frac{L_r}{w_\sigma}u_1 \quad (6.33)$$

$$\frac{dx_{21}}{d\tau} = -2\frac{R_r}{L_r}x_{21} + 2R_r\frac{L_m}{L_r}x_{22} \quad (6.34)$$

$$\frac{dx_{22}}{d\tau} = -\frac{x_{22}}{T_v} + x_{11}x_{12} + \frac{R_rL_m}{L_rw_\sigma}x_{21} + \frac{R_rL_m}{L_r}\frac{x_{12}^2 + x_{22}^2}{x_{21}} + \frac{L_r}{w_\sigma}u_2 \quad (6.35)$$

when  $T_v$  is motor electromagnetic time constant:

$$T_v = \frac{w_\sigma L_r}{R_r w_\sigma + R_s L_r^2 + R_r L_m^2} \quad (6.36)$$

$$w_\sigma = L_r L_s - L_m^2 \quad (6.37)$$

$$u_1 = \psi_{rx} u_{sy} - \psi_{ry} u_{sx} \quad (6.38)$$

$$u_2 = \psi_{rx} u_{sx} + \psi_{ry} u_{sy} \quad (6.39)$$

The above model has significantly less non-linearities than the conventional model presented in Chapter 2. Equations (6.9) and (6.11) are linear, though non-linearities still exist in equations (6.10) and (6.12). To linearize these two equations, a new signal ( $m$ ) is used in the feedback of the system according to the definitions in equations (6.10 and 6.12). The two signals are defined to replace the non-linearities in the above equations, as can be seen from [1,2,26]

$$m_1 = -x_{11} \left( x_{22} + \frac{L_m}{w_\sigma} x_{21} \right) + \frac{L_r}{w_\sigma} u_1 \quad (6.40)$$

$$m_2 = x_{11} x_{12} + \frac{R_r L_m}{L_r w_\sigma} x_{21} + \frac{R_r L_m}{L_r} \frac{x_{12}^2 + x_{22}^2}{x_{21}} + \frac{L_r}{w_\sigma} u_2 \quad (6.41)$$

Therefore, the new mathematical model of induction motors is described as [1,2,26]  
Mechanical subsystem:

$$\frac{dx_{11}}{d\tau} = \frac{x_{12} L_m}{J L_r} - \frac{m_o}{J} \quad (6.42)$$

$$\frac{dx_{12}}{d\tau} = -\frac{1}{T_v} x_{12} - m_1 \quad (6.43)$$

Electromagnetic subsystem:

$$\frac{dx_{21}}{d\tau} = -2 \frac{R_r}{L_r} x_{21} + 2 R_r \frac{L_m}{L_r} x_{22} \quad (6.44)$$

$$\frac{dx_{22}}{d\tau} = -\frac{x_{22}}{T_v} + m_2 \quad (6.45)$$

The above model is linear and fully decoupled, which makes it possible to use a linear cascaded controller, as shown in Figure 6.11.

In the control system, the control signals  $m_1$  and  $m_2$  are generated by the PI controller of the state variables  $x_{12}$  and  $x_{21}$  respectively. Having generated these two signals, the signals  $u_1$  and  $u_2$  can be then computed as [1,62,26]

$$u_1 = \frac{w_\sigma}{L_r} \left[ x_{11} \left( x_{22} + \frac{L_m}{w_\sigma} x_{21} \right) + m_1 \right] \quad (6.46)$$

$$u_2 = \frac{w_\sigma}{L_r} \left( -x_{11} x_{12} + \frac{R_r L_m}{L_r w_\sigma} x_{21} - \frac{R_r L_m}{L_r} \frac{x_{12}^2 + x_{22}^2}{x_{21}} + m_2 \right) \quad (6.47)$$

The voltage components ( $u_{s\alpha}$  and  $u_{s\beta}$ ) to be sent for the PVM algorithm are defined as [1,2,26]

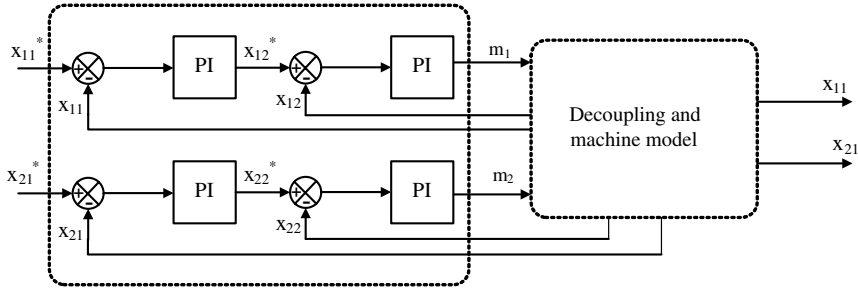


**Figure 6.11** Cascaded structure for the multiscalar model control method [2]

$$u_{s\alpha} = \frac{\psi_{r\alpha}u_2 - \psi_{r\beta}u_1}{\psi_r^2} \tag{6.48}$$

$$u_{s\beta} = \frac{\psi_{r\beta}u_2 - \psi_{r\alpha}u_1}{\psi_r^2} \tag{6.49}$$

where  $\psi_r$  is the module of rotor flux linkage.

In the new space variables, the current is not directly controlled; nevertheless, it should be limited for motor protection. The current magnitude may be computed as

$$\frac{x_{12}^2 + x_{22}^2}{x_{21}} = I_s^2 \tag{6.50}$$

Therefore, the output signals of the controllers should be limited to assure that the motor current does not exceed the specific maximum current,  $I_{s \max}$ . The torque, then, is limited according to

$$I_s^2 < \frac{x_{12}^2 + x_{22}^2}{x_{21}} \tag{6.51}$$

$$x_{12}^{limit} = \sqrt{I_{s \max}^2 x_{21} - x_{22}^2} \tag{6.52}$$

### 6.4.3 Design of System Control

When using an MM, the torque produced by an induction motor is proportional only to one state variable ( $x_{12}$ ), which is present in the mechanical part of the control system. The rotor flux linkage is stabilized in the electromagnetic part of the system, and its command value may be described by assuming such criterion as the minimization of energy losses in the system, or the minimization of response time in the mechanical part of the system when commands are limited [2].

The mechanical part consists of a first-order delay connected with an integral element in series. Because of the necessity for torque limiting, it is convenient to use a cascaded control structure for this subsystem. The disturbance in the mechanical sub-system is the load torque.

The electromagnetic sub-system consists of two first-order delay elements connected in a series. To limit the square of rotor flux in this situation, it is also convenient to use a cascade control structure.

Therefore, in the control system when using MM, cascaded controllers of the PI type may be applied with constant parameters that are tuned in accordance with the well-known control theory of linear systems.

In Figure 6.12, the fully decoupled system control of induction, in the case of using voltage controlled PWM, is shown [2].

### 6.4.4 Non-Linear Linearization of Induction Motor Fed by Current Controlled VSI

Although we operate on a stationary reference frame of initial analysis and new model derivation, we assume that our frame is the stator current in the  $x$ -axis (here  $x$  denotes the rotating, not stationary, frame with stator current). In a co-ordinate system, rotating with the stator current vector in the  $x$ -axis, the imaginary component equals zero ( $i_{sy} = 0$ ). After introducing the first-order delay with a time constant  $T$  in the stator current set value channel, the differential equations of the induction motor are [2,25]

$$\frac{di_{sx}}{dt} = -\frac{1}{T}(-i_{sx} + I_s) \tag{6.53}$$

$$\frac{d\Psi_{rx}}{dt} = -\frac{R_r}{L_r}\Psi_{rx} + (\omega_i - \omega_r)\Psi_{ry} + R_r \frac{L_m}{L_r} i_{sx} \tag{6.54}$$

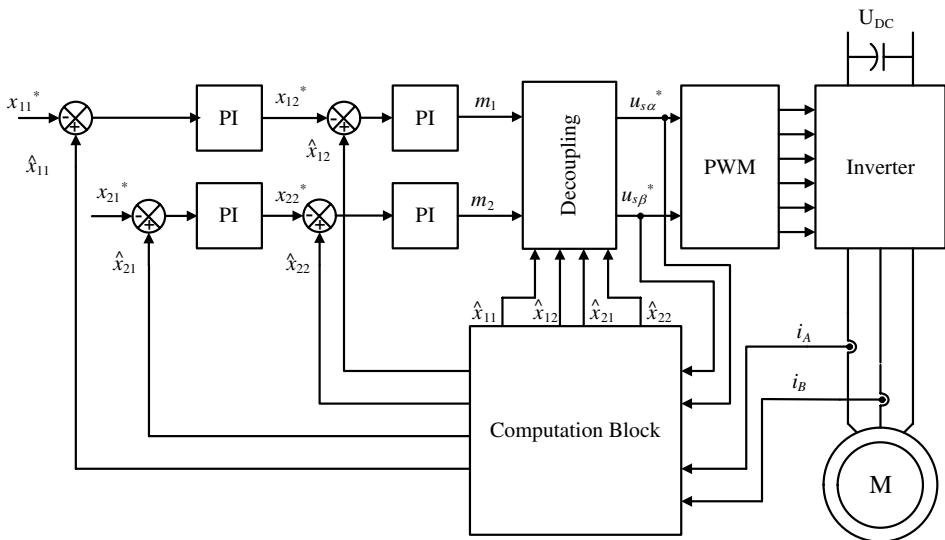


Figure 6.12 System control of an induction motor fed by voltage controlled VSI



$$\frac{d\Psi_{ry}}{dt} = -\frac{R_r}{L_r}\Psi_{ry} - (\omega_i - \omega_r)\Psi_{rx} \quad (6.55)$$

$$\frac{d\omega_r}{dt} = \frac{L_m}{L_r J} (-\Psi_{ry} i_{sx}) - \frac{1}{J} m_o \quad (6.56)$$

$R_r$ , and  $L_r$  are rotor resistance and inductance, respectively;  $L_m$  is the mutual inductance;  $\omega_r$  the rotor angular speed;  $\omega_s$  the angular speed of co-ordinate system;  $J$  the inertia; and  $m_o$  the load torque.

The multiscalar model of induction motor is further determined from the derivations of the new MM state variables (equations), and while taking into account the above differential equations of stator current and rotor flux vectors (equations) that are similar to previous sections, we obtain the next model with less non-linearities than a conventional one [2,26]:

$$\frac{dx_{11}}{dt} = \frac{L_m}{JL_r} x_{12} - \frac{1}{J} m_o \quad (6.57)$$

$$\frac{dx_{12}}{dt} = -\frac{1}{L_i} x_{12} + v_1 \quad (6.58)$$

$$\frac{dx_{21}}{dt} = -2\frac{R_r}{L_r} x_{21} + 2R_r \frac{L_m}{L_r} x_{22} \quad (6.59)$$

$$\frac{dx_{22}}{dt} = -\frac{1}{T_i} x_{22} - \frac{R_r L_m}{L_r} i_{sx}^2 + v'_2 \quad (6.60)$$

where  $\frac{1}{T_i} = \frac{1}{T} + \frac{R_r}{L_r}$ ; and  $T$  is a used time constant in the channel of current set value; and  $v_1$  and  $v'_2$  are control signals:

$$v_1 = -\frac{1}{T} I_s \Psi_{rx} + i_{sx} \Psi_{rx} s_i \quad (6.61)$$

$$v'_2 = \frac{1}{T} I_s \Psi_{rx} + i_{sx} \Psi_{ry} s_i \quad (6.62)$$

In this new model, there is a simple non-linearity in only one differential equation. Using non-linear feedback can compensate the non-linearity presented in equation (6.60). This non-linear feedback has the expression [2,25]:

$$v_2 = v'_2 - \frac{R_r L_m}{L_r} i_{sx}^2 \quad (6.63)$$

The quantity of the stator current amplitude is

$$I_s = T \frac{\Psi_{rx} v_2 - \Psi_{ry} v_1}{\Psi_r^2} \quad (6.64)$$

and the next relationship is

$$\frac{x_{12}^2 + x_{22}^2}{x_{21}} = I_s^2 \quad (6.65)$$

The slip frequency is

$$s_i = \frac{\Psi_{ry}v_2 + \Psi_{rx}v_1}{i_{sx}\Psi_r^2} \quad (6.66)$$

After introducing non-linear feedback, it is possible to obtain two linear fully-decoupled sub-systems, mechanical and electromagnetic. Such properties do not depend on the feeding system of the motor. The final MM has the form:

Mechanical subsystem [2,26]:

$$\frac{dx_{11}}{dt} = \frac{L_m}{JL_r}x_{12} - \frac{1}{J}m_o \quad (6.67)$$

$$\frac{dx_{12}}{dt} = -\frac{1}{T_i}x_{12} + v_1 \quad (6.68)$$

Electromagnetic subsystem:

$$\frac{dx_{21}}{dt} = -2\frac{R_r}{L_r}x_{21} + 2\frac{R_rL_m}{L_r}x_{22} \quad (6.69)$$

$$\frac{dx_{22}}{dt} = -\frac{1}{T_i}x_{22} + v_2 \quad (6.70)$$

The multiscalar variables are not connected with the co-ordinate system. Therefore, it is not necessary to make the variables transform from the specified co-ordinate system to variables in the other co-ordinate system, which is selected in accordance with dynamic description or system control synthesis. This is essential for the practical realization of systems control, because it gives significant simplification to the drive system.

The fully decoupled subsystems make it possible to use this method in the case of a changing flux vector and to obtain simple systems structures. It is possible to use the cascade structure of PI controllers in the decoupled control subsystems, making it possible to limit the reference quantities of the variables  $x_{12}$  and  $x_{22}$ , such that the following relationship is fulfilled:

$$\frac{x_{12}^2 + x_{22}^2}{x_{21}} \leq I_{smax}^2 \quad (6.71)$$

where  $I_{smax}$  is the maximum allowed output current.

Also, it is possible, when using this method, to limit the inverter output voltage of the voltage inverter, cycloconverter, and the voltage in the DC bus of current inverter. This can be done by limiting the output quantities of controllers.

The final control system of an induction motor is shown in Figure 6.13. The stator current components are controlled using current controllers (e.g. hysteresis controllers). Instantaneous quantities of stator currents and voltages are used in the calculation block to compute the motor variables. To control the variables  $x_{12}$  and  $x_{22}$ , two PI controllers are used. The command value for the  $x_{12}$  controller is the output signal of the speed controller. The angular speed  $x_{11}$  is measured or calculated and used in the control feedback. The command value for the  $x_{22}$  controller is the output signal of the controller for the square of the rotor flux.

In the control system, the stator voltages are determined from the DC link voltage, with knowledge of the pulse width modulation algorithm or directly from commanded voltage in case of using voltage modulator. This method simplifies the total drive system and decreases the cost.

### 6.4.5 Stator Oriented Non-Linear Control System (based on $\Psi_s, i_s$ )

The steady state and transient electromagnetic behaviors of an induction motor can be described by the following equations in the stationary reference frame [25,26]:

$$\frac{di_{sx}}{d\tau} = -\frac{L_r R_s + L_s R_r}{w_\sigma} i_{sx} + \frac{R_r}{w_\sigma} \psi_{sx} - \omega_r i_{sy} + \omega_r \frac{L_r}{w_\sigma} \psi_{sy} + \frac{L_r}{w_\sigma} u_{sx} \tag{6.72}$$

$$\frac{di_{sy}}{d\tau} = -\frac{L_r R_s + L_s R_r}{w_\sigma} i_{sy} + \frac{R_r}{w_\sigma} \psi_{sy} + \omega_r i_{sx} - \omega_r \frac{L_r}{w_\sigma} \psi_{sx} + \frac{L_r}{w_\sigma} u_{sy} \tag{6.73}$$

$$\frac{d\psi_{sx}}{d\tau} = -R_s i_{sx} + u_{sx} \tag{6.74}$$

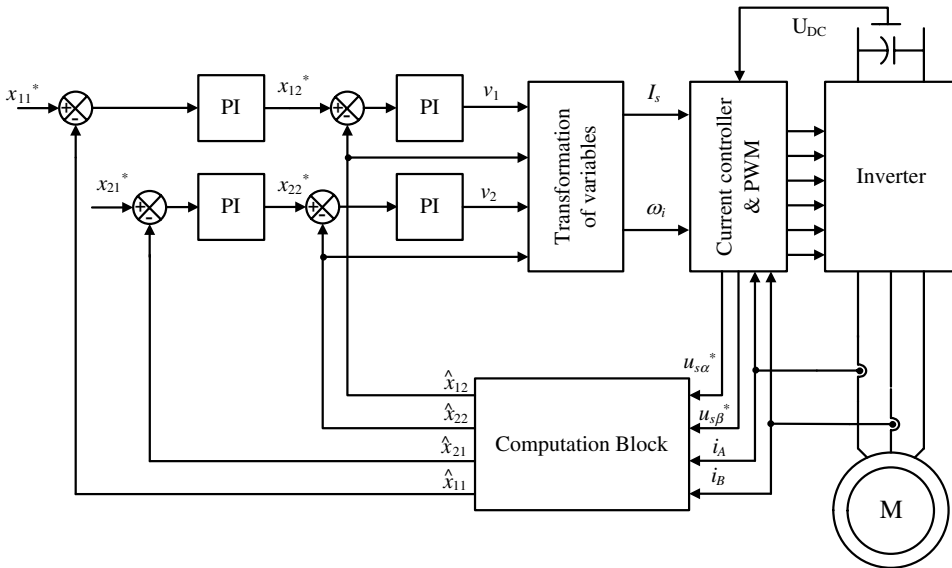


Figure 6.13 System control of an induction motor fed by current controlled VSI

$$\frac{d\psi_{sy}}{d\tau} = -R_s i_{sy} + u_{sy} \quad (6.75)$$

$$\frac{d\omega_r}{d\tau} = \frac{L_m}{JL_r} (\psi_{rx} i_{sy} - \psi_{ry} i_{sx}) - \frac{1}{J} m_o \quad (6.76)$$

where  $i_{sxy}$ ,  $\psi_{sxy}$ ,  $u_{sxy}$  denotes vectors of stator current, stator flux, and stator voltage, respectively, and  $\omega_r$  is the rotor speed. In addition, the mechanical behavior of an induction motor can be described by the rotor speed equation:

$$\frac{d\omega_r}{d\tau} = \frac{1}{J} (\psi_{sx} i_{sy} - \psi_{sy} i_{sx}) - \frac{1}{J} m_o \quad (6.77)$$

where the parameter  $w_\sigma$  is defined by:

$$w_\sigma = L_s L_r - L_m^2 \quad (6.78)$$

and  $L_s$ ,  $L_r$ ,  $L_m$  are stator, rotor, and mutual inductances, respectively;  $R_s$ ,  $R_r$  are stator and rotor resistances;  $m_o$  is the load torque; and  $J$  is the moment of inertia. All variables and parameters are expressed in the p.u. system. A stationary  $x$ - $y$  reference frame is recommended for simplifications of measurements.

#### 6.4.6 Rotor-Stator Fluxes-based Model

The multiscale model may be modified by selecting other motor variables other than rotor flux and stator current. Here, stator flux  $\psi_s$  and rotor flux  $\psi_r$  components could be selected to represent the motor [25,26,29]:

$$\frac{d\psi_{sx}}{d\tau} = -\frac{R_s}{w_\sigma} (L_r \psi_{sx} - L_m \psi_{rx}) + \omega_a \psi_{sy} + u_{sx} \quad (6.79)$$

$$\frac{d\psi_{sy}}{d\tau} = -\frac{R_s}{w_\sigma} (L_r \psi_{sy} - L_m \psi_{ry}) - \omega_a \psi_{sx} + u_{sy} \quad (6.80)$$

$$\frac{d\psi_{rx}}{d\tau} = -\frac{R_r}{w_\sigma} (L_s \psi_{rx} - L_m \psi_{sx}) + (\omega_a - \omega_r) \psi_{ry} \quad (6.81)$$

$$\frac{d\psi_{ry}}{d\tau} = -\frac{R_r}{w_\sigma} (L_s \psi_{ry} - L_m \psi_{sy}) + (\omega_a - \omega_r) \psi_{rx} \quad (6.82)$$

$$\frac{d\omega_r}{d\tau} = \frac{L_m}{Jw_\sigma} (\psi_{sx} \psi_{ry} - \psi_{sy} \psi_{rx}) - \frac{1}{J} m_o \quad (6.83)$$

The MM state variables could be then selected as [25,26,29]

$$q_{11} = \omega_r \quad (6.84)$$

$$q_{12} = \psi_{sx}\psi_{ry} - \psi_{sy}\psi_{rx} \quad (6.85)$$

$$q_{21} = \psi_{rx}^2 - \psi_{ry}^2 \quad (6.86)$$

$$q_{22} = \psi_{sx}\psi_{rx} + \psi_{sy}\psi_{ry} \quad (6.87)$$

Then, the derivatives of the above state variables, while taking into account the motor model from equations (6.79) to 6.83, yields [25,26,29]

$$\frac{dq_{11}}{d\tau} = \frac{L_m}{Jw_\sigma} q_{12} - \frac{m_0}{J} \quad (6.88)$$

$$\frac{dq_{12}}{d\tau} = -\frac{1}{T_v} q_{12} + q_{11}q_{22} + w_1 \quad (6.89)$$

$$\frac{dq_{21}}{d\tau} = -2\frac{R_r L_s}{w_\sigma} q_{21} + 2R_r \frac{L_m}{w_\sigma} q_{22} \quad (6.90)$$

$$\frac{dq_{22}}{d\tau} = -\frac{q_{22}}{T_v} + (R_r + R_s) \frac{L_m}{w_\sigma} q_{21} - q_{11}q_{12} + w_2 \quad (6.91)$$

where  $T_v$  represents machine electromagnetic time constant:

$$w_1 = u_{sx}\psi_{ry} - u_{sy}\psi_{rx} \quad (6.92)$$

$$w_2 = u_{sx}\psi_{rx} + u_{sy}\psi_{ry} \quad (6.93)$$

Though this model is simple, it requires an access to rotor and stator fluxes.

*(Student work: design the control system and run it on MATLAB/Simulink) for this system.*

### 6.4.7 Stator Oriented Multiscalar Model

The first set of variables for the description of the induction motor dynamics was defined in [2]:

$$x_{11} = \omega_r \quad (6.94)$$

$$x_{12} = \psi_{sx}i_{sy} - \psi_{sy}i_{sx} \quad (6.95)$$

$$x_{21} = \psi_{sx}^2 - \psi_{sy}^2 \quad (6.96)$$

$$x_{22} = \psi_{sx}i_{sx} + \psi_{sy}i_{sy} \quad (6.97)$$

The differential equations for these variables form the multiscalar model of induction motor [25,26,29]:

$$\frac{dx_{11}}{d\tau} = \frac{1}{J} x_{12} - \frac{m_o}{J} \quad (6.98)$$

$$\frac{dx_{12}}{d\tau} = -\frac{1}{T_v}x_{12} + x_{11}\left(x_{22} - \frac{L_r}{w_\sigma}x_{21}\right) + \frac{L_m}{w_\sigma}u_1 \quad (6.99)$$

$$\frac{dx_{21}}{d\tau} = -2R_s x_{22} + 2u_2 \quad (6.100)$$

$$\frac{dx_{22}}{d\tau} = -\frac{1}{T_v}x_{22} - x_{11}x_{12} + \frac{R_r}{w_\sigma}x_{21} - \frac{x_{12}^2 + x_{22}^2}{x_{21}} + 2\frac{L_r}{w_\sigma}u_2 - \frac{L_m}{w_\sigma}u'_1 \quad (6.101)$$

where

$$u_1 = u_{sy}\psi_{rx} - u_{sx}\psi_{ry} \quad (6.102)$$

$$u_2 = u_{sx}\psi_{sx} + u_{sy}\psi_{sy} \quad (6.103)$$

$$u'_1 = u_{sx}\psi_{rx} + u_{sy}\psi_{ry} \quad (6.104)$$

$$T_v = \frac{w_\sigma L_r}{R_r w_\sigma + R_s L_r^2 + R_r L_m^2} \quad (6.105)$$

The non-linear feedback decoupling of the form is

$$u_1 = \frac{w_\sigma}{L_r} \left[ m_1 - x_{11} \left( x_{22} - \frac{L_r}{w_\sigma} x_{21} \right) \right] \quad (6.106)$$

$$u_2 = \frac{1}{2} \left( m_2 - \frac{1}{T} x_{21} \right) + R_s x_{22} \quad (6.107)$$

Then transform the system equations (6.98–101) to the linear systems of the following forms [25,26,29]:

Mechanical subsystem:

$$\frac{dx_{11}}{d\tau} = \frac{1}{J}x_{12} - \frac{m_o}{J} \quad (6.108)$$

$$\frac{dx_{12}}{d\tau} = -\frac{1}{T_v}x_{12} + m_1 \quad (6.109)$$

Electromechanical subsystem:

$$\frac{dx_{21}}{d\tau} = -\frac{1}{T_v}x_{21} + m_2 \quad (6.110)$$

where  $m_1$  and  $m_2$  are new inputs in the linear system and  $T$  time constant. The control variables  $u_1$  and  $u_2$ , appearing in the multiscalar model of induction motor, are transformed on stator voltage components in the following way [25,26,29]:

$$u_{sx} = \frac{u_2 \psi_{rx} - u_1 \psi_{sy}}{\psi_{sx} \psi_{rx} + \psi_{ry} \psi_{sy}} \tag{6.111}$$

$$u_{sy} = \frac{u_2 \psi_{ry} - u_1 \psi_{sx}}{\psi_{sx} \psi_{rx} + \psi_{ry} \psi_{sy}} \tag{6.112}$$

A scheme of the system with non-linear control based on stator flux and current is presented in Figure 6.14. This system, which consists of two linear subsystems, may be controlled by means of cascaded controllers of mechanical subsystem, but only one controller of flux. The new state variables do not depend on the system co-ordinate. This is essential for the practical realization of control systems, because it significantly simplifies the drive system. Sign ^ denotes variables estimated in the speed observer presented in [3,4].

### 6.4.8 Multiscalar Control of Induction Motor

The control of induction motor model is shown in Figure 6.14. For control purpose, the motor model is decoupled by non-linear state and input transformations. The model consists of motor model, various transformations, and the control system model. All the models are in per unit unless otherwise specified.

The Simulink software file of multiscalar control of induction motor model is [MM\_voltage\_control]. The motor parameters are located in [IM\_param], which should be first initialized.

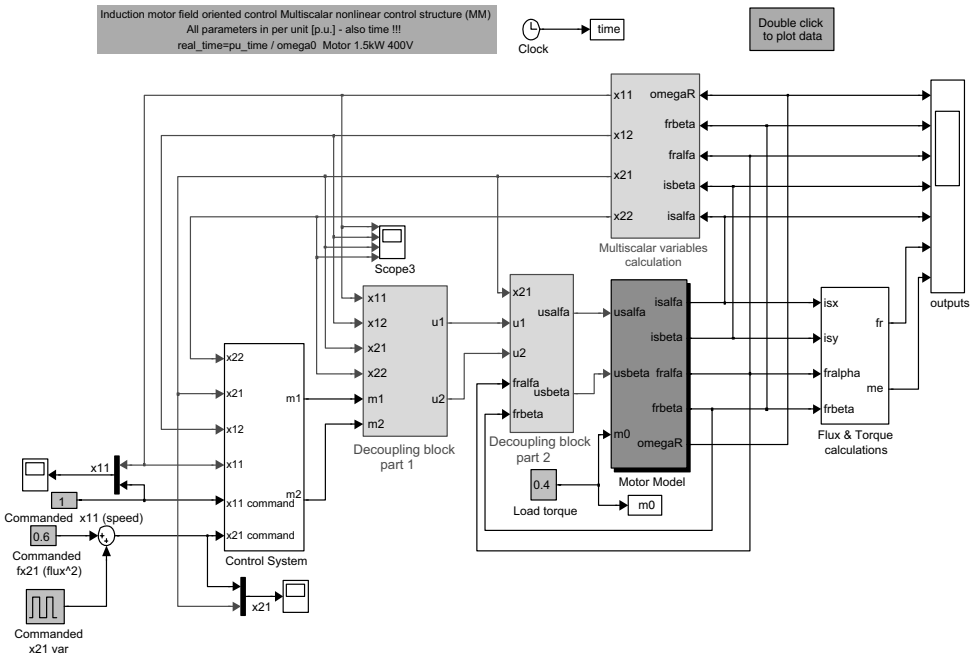


Figure 6.14 Induction motor control

### 6.4.9 Induction Motor Model

The induction motor (IM) model presented in per unit in a rotating frame with arbitrary speed ( $\omega_a$ ) is given in Chapter 2, and modeled in Figure 6.15.

The motor current and flux magnitude are calculated as

$$|I_s| = \sqrt{I_{s\alpha}^2 + I_{s\beta}^2} \tag{6.113}$$

$$|\psi_s| = \sqrt{\psi_{s\alpha}^2 + \psi_{s\beta}^2} \tag{6.114}$$

The motor torque is given by

$$M_e = \frac{L_m}{JL_r} (\psi_{r\alpha} i_{s\beta} - \psi_{r\beta} i_{s\alpha}) \tag{6.115}$$

### 6.4.10 State Transformations

The following non-linear state transformation is adopted to convert a system into a form where non-linearity only appears in the control channel:

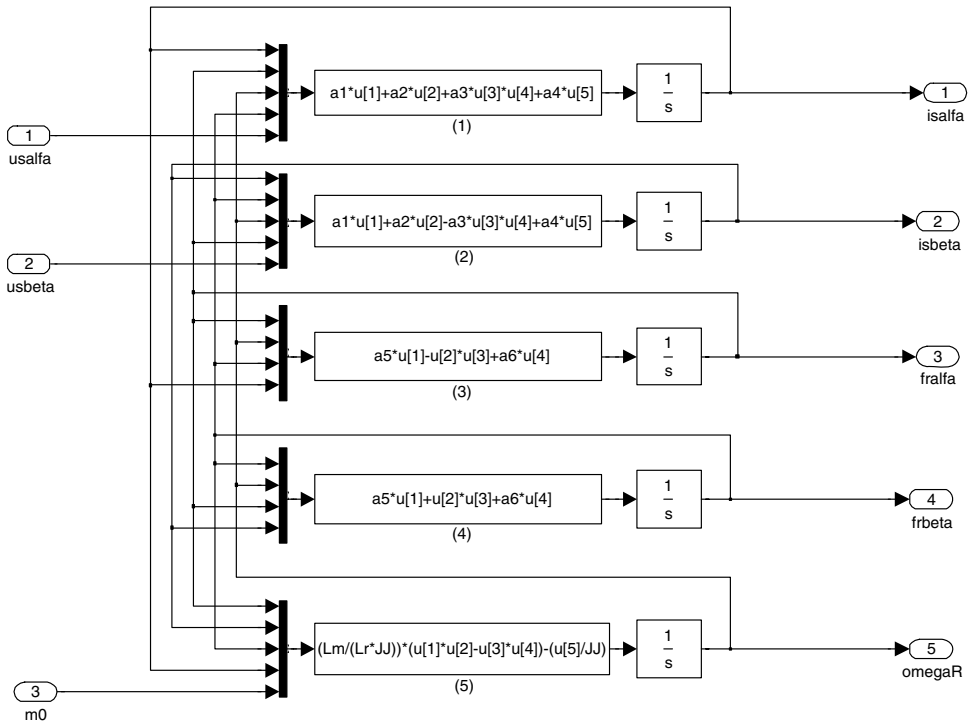


Figure 6.15 Induction motor model



$$x_{11} = \omega_r \tag{6.116}$$

$$x_{12} = \psi_{r\alpha} i_{s\beta} - \psi_{r\beta} i_{s\alpha} = t_e \tag{6.117}$$

$$x_{21} = \psi_{r\alpha}^2 + \psi_{r\beta}^2 = \psi_r^2 \tag{6.118}$$

$$x_{22} = \psi_{r\alpha} i_{s\alpha} + \psi_{r\beta} i_{s\beta} \tag{6.119}$$

The above transformation is modeled in Figure 6.16.

With the new inputs  $m_1$  and  $m_2$ , using following input transformation, the non-linear induction motor can be completely decoupled [2]:

$$u_{s\alpha} = \frac{\psi_{r\alpha} u_2 - \psi_{r\beta} u_1}{x_{21}} \tag{6.120}$$

$$u_{s\beta} = \frac{\psi_{r\alpha} u_1 + \psi_{r\beta} u_2}{x_{21}} \tag{6.121}$$

$$u_1 = \frac{w_\sigma}{L_r} \left( x_{11} \left( x_{22} + \frac{L_m}{w_\sigma} x_{21} \right) + m_1 \right) \tag{6.122}$$

$$u_2 = \frac{w_\sigma}{L_r} \left( -x_{11} x_{12} - \frac{R_r L_m}{L_r w_\sigma} x_{21} - \frac{R_r L_m}{L_r} \frac{x_{12}^2 x_{22}^2}{x_{21}} + m_2 \right) \tag{6.123}$$

These equations are modeled in Figures 6.17 and 6.18.

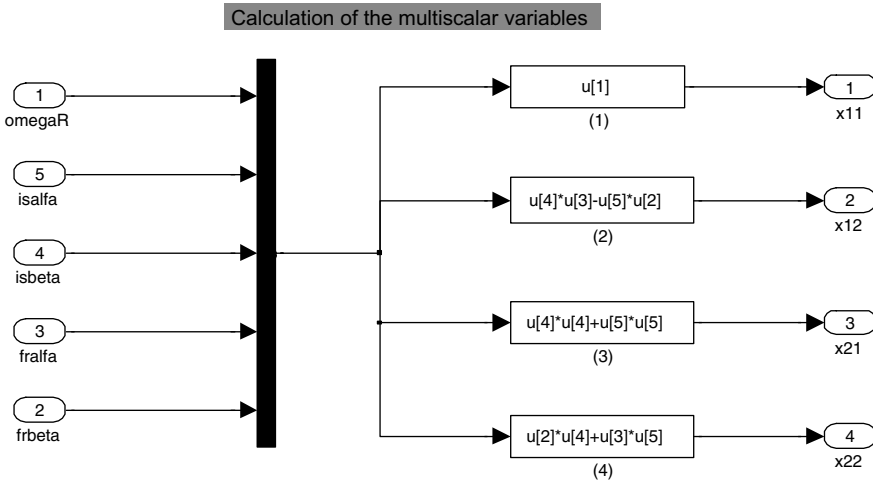


Figure 6.16 Non-linear state transformation

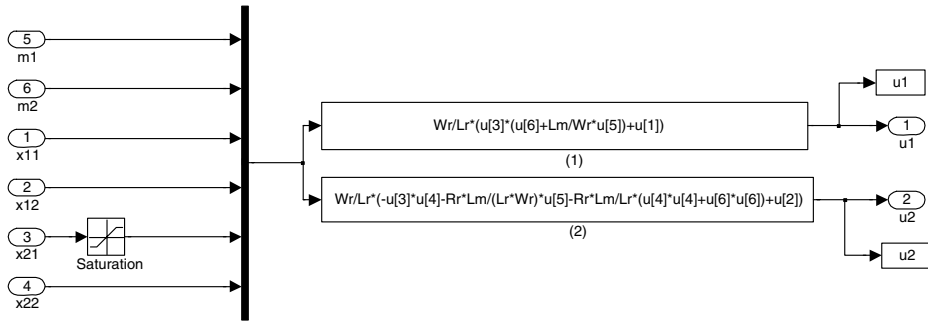


Figure 6.17 Non-linear mapping between  $m_1, m_2,$  and  $u_1, u_2$

### 6.4.11 Decoupled IM Model

The decoupled IM model between new multiscalar states and inputs  $m_1$  and  $m_2$  can be given as [2,25,26,29]

$$\frac{dx_{11}}{d\tau} = \frac{L_m}{JL_r} x_{12} - \frac{1}{J} m_o \tag{6.124}$$

$$\frac{dx_{12}}{d\tau} = -\frac{1}{T_v} x_{12} + m_1 \tag{6.125}$$

$$\frac{dx_{21}}{d\tau} = -2 \frac{R_r}{L_r} x_{21} + 2 \frac{R_r L_m}{L_r} x_{22} \tag{6.126}$$

$$\frac{dx_{22}}{d\tau} = -\frac{1}{T_v} x_{22} + m_2 \tag{6.127}$$

where  $T_v = \frac{w_\sigma L_r}{R_r w_\sigma + R_s L_r^2 + R_r L_m^2}$

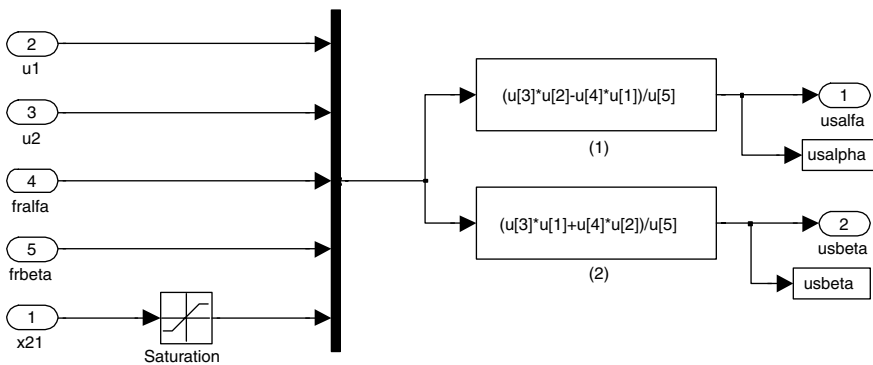


Figure 6.18 Non-linear mapping between  $u_1, u_2$  and  $usalfa, usbeta$

### 6.4.11.1 Control System

As the system model is decoupled, the simple cascade control can be designed, which is also easy to tune. The cascade control system model is shown in Figure 6.19. The outer loop control works on system states  $x_{11}$  and  $x_{21}$  to provide demand for  $x_{12}$  and  $x_{22}$ . The inner loop controller works on the  $x_{12}$  and  $x_{22}$  to achieve the required values.

### 6.4.11.2 Simulation Results

The simulation result for square pulse demand in speed is shown in Figures 6.20 and 6.21.

## 6.5 MM of Double Fed Induction Machine (DFIM)

The mathematical model of DFIM can be derived as differential equations of five state variables. In addition to the rotor speed  $\omega_r$ , stator flux  $\psi_s$  and rotor current  $i_r$ , vectors are selected to represent the machine in [25,26]

$$\frac{d\psi_{sx}}{d\tau} = -\frac{R_s}{L_s} \cdot \psi_{sx} + R_s \frac{L_m}{L_s} \cdot i_{rx} + \omega_a \psi_{sy} + u_{sx} \tag{6.128}$$

$$\frac{d\psi_{sy}}{d\tau} = -\frac{R_s}{L_s} \cdot \psi_{sy} + R_s \frac{L_m}{L_s} \cdot i_{ry} - \omega_a \psi_{sx} + u_{sy} \tag{6.129}$$

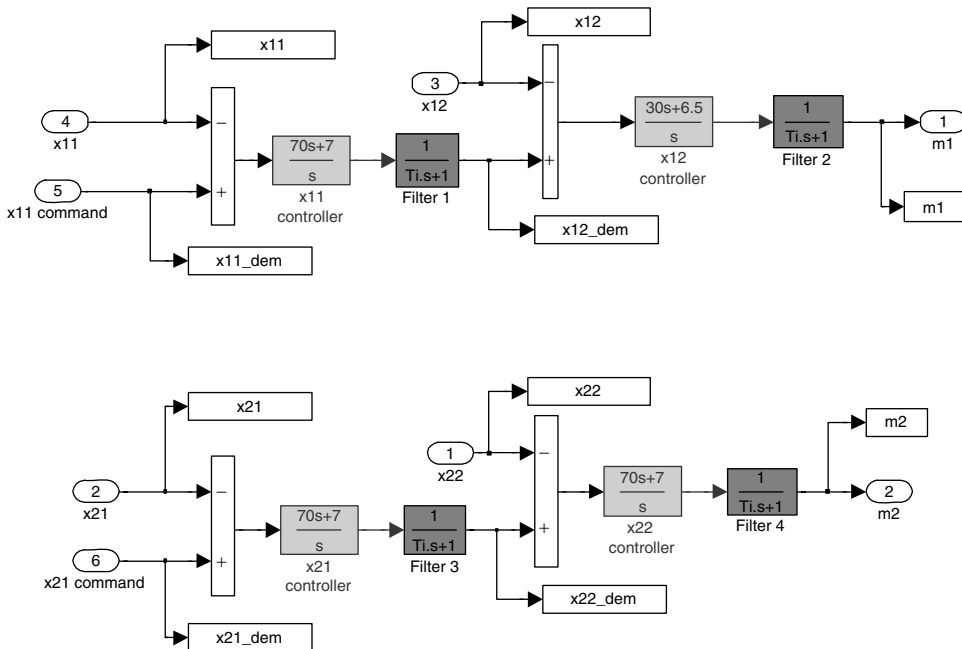


Figure 6.19 Cascaded control system for induction motor

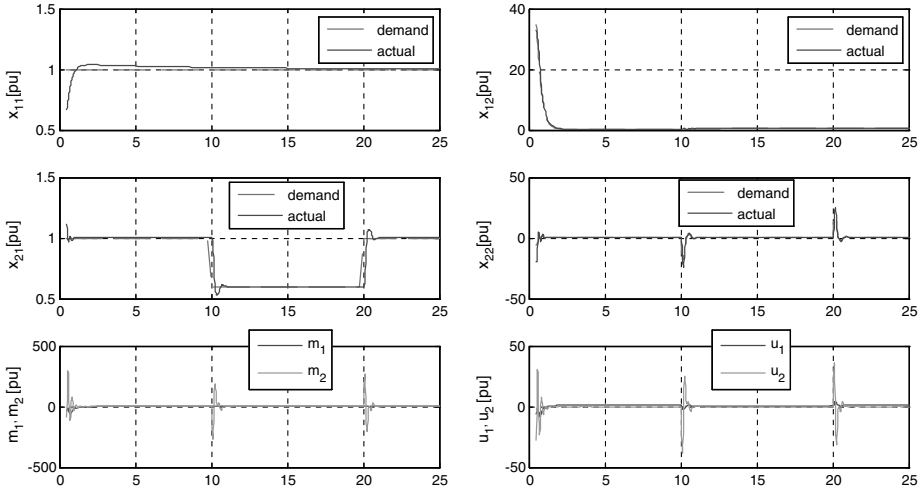


Figure 6.20 Simulation results – 1

$$\frac{di_{rx}}{d\tau} = -\frac{R_r L_r^2 + R_s L_m^2}{L_s w_\sigma} i_{rx} + \frac{R_s L_m}{L_s w_\sigma} \psi_{sx} + (\omega_a - \omega_r) i_{ry} - \omega_r \frac{L_m}{w_\sigma} \psi_{sy} + \frac{L_s}{w_\sigma} u_{rx} - \frac{L_m}{w_\sigma} u_{sx} \tag{6.130}$$

$$\frac{di_{ry}}{d\tau} = -\frac{R_r L_r^2 + R_s L_m^2}{L_s w_\sigma} i_{ry} + \frac{R_s L_m}{L_s w_\sigma} \psi_{sy} - (\omega_a - \omega_r) i_{rx} + \omega_r \frac{L_m}{w_\sigma} \psi_{sx} + \frac{L_s}{w_\sigma} u_{ry} - \frac{L_m}{w_\sigma} u_{sy} \tag{6.131}$$

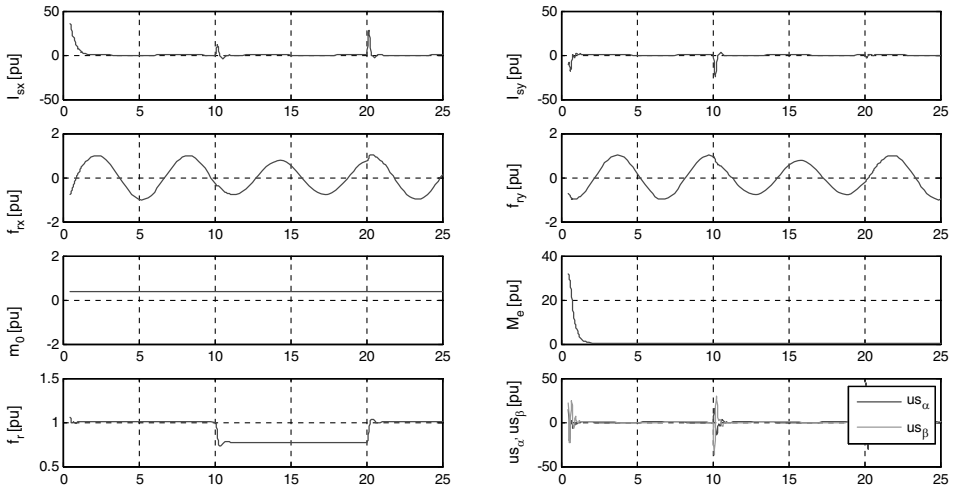


Figure 6.21 Simulation results – 2

$$\frac{d\omega_r}{d\tau} = \frac{L_m}{L_s J} (\psi_{sx} i_{ry} - \Psi_{sy} i_{rx}) - \frac{1}{J} m_o \quad (6.132)$$

For stationary reference, frame  $\omega_a$  is zero. For the machine working as generator, the speed  $\omega_r$  is an input to the model.

The multiscalar variables for DFIM can be selected as stators flux and rotor current, represented as [25,26]

$$x_{11} = \omega_r \quad (6.133)$$

$$x_{12} = \psi_{sx} i_{ry} - \psi_{sy} i_{rx} \quad (6.134)$$

$$x_{21} = \psi_{sx}^2 + \psi_{sy}^2 \quad (6.135)$$

$$x_{22} = \psi_{sx} i_{rx} + \psi_{sy} i_{ry} \quad (6.136)$$

where  $\psi_{sx}, \psi_{sy}, i_{rx}, i_{ry}$  are the stator flux and rotor current vectors in the co-ordinate system XY, rotating with arbitrary speed and  $\omega_r$  is the angular speed of the rotor shaft.

After deriving the new state variables, and substituting the current and flux derivatives using the machine model, a new multiscalar model of this machine can be presented as [25,26]

$$\frac{dx_{11}}{d\tau} = \frac{L_m}{J L_s} x_{12} - \frac{m_o}{J} \quad (6.137)$$

$$\frac{dx_{12}}{d\tau} = -\frac{1}{T_v} x_{12} + x_{11} x_{22} + \frac{L_m}{w_\sigma} x_{11} x_{21} + \frac{L_s}{w_\sigma} u_{r1} - \frac{L_m}{w_\sigma} u_{sf1} + u_{si1} \quad (6.138)$$

$$\frac{dx_{21}}{d\tau} = -2 \frac{R_s}{L_s} x_{21} + 2 R_s \frac{L_m}{L_s} x_{22} + 2 u_{sf2} \quad (6.139)$$

$$\frac{dx_{22}}{d\tau} = -\frac{x_{22}}{T_v} - x_{11} x_{12} + \frac{R_s L_m}{L_s w_\sigma} x_{21} + \frac{R_s L_m}{L_s} \frac{x_{12}^2 + x_{22}^2}{x_{21}} - \frac{L_s}{w_\sigma} u_{r2} - \frac{L_m}{w_\sigma} u_{sf2} + u_{si2} \quad (6.140)$$

where

$$u_{r1} = u_{ry} \psi_{sx} - u_{rx} \psi_{sy} \quad (6.141)$$

$$u_{r2} = u_{rx} \psi_{sx} + u_{ry} \psi_{sy} \quad (6.142)$$

$$u_{sf1} = u_{sy} \psi_{sx} - u_{sx} \psi_{sy} \quad (6.143)$$

$$u_{sf2} = u_{sx} \psi_{sx} + u_{sy} \psi_{sy} \quad (6.144)$$

$$u_{si1} = u_{sx} i_{ry} - u_{sy} i_{rx} \quad (6.145)$$

$$u_{si2} = u_{sx} i_{rx} + u_{sy} i_{ry} \quad (6.146)$$

In the non-linear control method, as well as in the vector control method, the angle between the stator and the rotor is needed either by measurement or estimation.

After using non-linear feedback, the new linearized machine model is [25,26]

$$\frac{dx_{11}}{d\tau} = \frac{L_m}{JL_s} x_{12} - \frac{1}{J} m_o \quad (6.147)$$

$$\frac{dx_{12}}{d\tau} = \frac{1}{T_v} (-x_{12} + m_1) \quad (6.148)$$

$$\frac{dx_{21}}{d\tau} = -2 \frac{R_s}{L_s} x_{21} + 2 \frac{R_s L_m}{L_s} x_{22} + 2u_{sf2} \quad (6.149)$$

$$\frac{dx_{22}}{d\tau} = \frac{1}{T_v} (-x_{22} + m_2) \quad (6.150)$$

Where  $T_v$  is time constant and

$$u_{r1} = u_{ry}\psi_{sx} - u_{rx}\psi_{sy} \quad (6.151)$$

$$u_{r2} = u_{rx}\psi_{sx} + u_{ry}\psi_{sy} \quad (6.152)$$

$$u_{r1} = \frac{w_\sigma}{L_s} \left( -x_{11} \left( x_{22} + \frac{L_m}{w_\sigma} x_{21} \right) + \frac{L_m}{w_\sigma} u_{sf1} - u_{si1} + \frac{1}{T_v} m_1 \right) \quad (6.153)$$

$$u_{r2} = \frac{w_\sigma}{L_s} \left( -\frac{R_s L_m}{L_s w_\sigma} x_{21} - \frac{R_s L_m}{L_s} i_r^2 + x_{11} x_{12} + \frac{L_m}{w_\sigma} u_{sf2} - u_{si2} + \frac{1}{T_v} m_2 \right) \quad (6.154)$$

The rotor voltage components to be sent for the PVM algorithm are defined as:

$$u_{rx} = \frac{\psi_{sy} u_{r1} + \psi_{sx} u_{r2}}{x_{21}} \quad (6.155)$$

$$u_{ry} = \frac{\psi_{sy} u_{r2} - \psi_{sx} u_{r1}}{x_{21}} \quad (6.156)$$

## 6.6 Non-Linear Control of Permanent Magnet Synchronous Machine

The mathematical model of Permanent Magnet Synchronous Machine (PMSM) in stationary reference frame appears as [17]

$$\frac{di_\alpha}{dt} = -\frac{R_s}{L_s} i_\alpha + \frac{1}{L_s} e_\alpha + \frac{1}{L_s} u_{s\alpha} \quad (6.157)$$

$$\frac{di_\beta}{dt} = -\frac{R_s}{L_s} i_\beta + \frac{1}{L_s} e_\beta + \frac{1}{L_s} u_{s\beta} \quad (6.158)$$

$$\frac{d\psi_r}{dt} = \frac{1}{J} (\psi_{s\alpha} i_\beta - \psi_{s\beta} i_\alpha) - \frac{1}{J} m_o \quad (6.159)$$

and

$$\psi_{f\alpha} = \psi_f \cos\theta \quad (6.160)$$

$$\psi_{f\beta} = \psi_f \sin\theta \quad (6.161)$$

$$e_\alpha = \frac{d\psi_{f\alpha}}{dt} = -\psi_f \omega_r \sin\theta = -\omega_r \psi_{f\beta} \quad (6.162)$$

$$e_\beta = \frac{d\psi_{f\beta}}{dt} = +\psi_f \omega_r \cos\theta = \omega_r \psi_{f\alpha} \quad (6.163)$$

For  $\psi_s = \psi_f$  :

$$\frac{d\omega_r}{dt} = \frac{1}{J} (\psi_{f\alpha} i_\beta - \psi_{f\beta} i_\alpha) - \frac{1}{J} m_o \quad (6.164)$$

The multiscalar motor variables are [17]

$$x_{12} = i_\beta \psi_{f\alpha} - i_\alpha \psi_{f\beta} \quad (6.165)$$

$$x_{22} = i_\alpha \psi_{f\alpha} + i_\beta \psi_{f\beta} \quad (6.166)$$

Taking the derivatives of those two state variables, and substituting the derivatives of motor currents and fluxes, the next model is [17]

$$\frac{dx_{12}}{dt} = -\frac{R_s}{L_s} (i_\beta \psi_{f\alpha} - i_\alpha \psi_{f\beta}) + e_\alpha i_\beta + \frac{1}{L_s} e_\beta \psi_{f\alpha} - e_\beta i_\alpha - \frac{1}{L_s} e_\alpha \psi_{f\beta} + \frac{1}{L_s} u_\beta \psi_{f\alpha} - \frac{1}{L_s} u_\alpha \psi_{f\beta} \quad (6.167)$$

$$\begin{aligned} \frac{dx_{12}}{dt} = & -\frac{R_s}{L_s} (i_\beta \psi_{f\alpha} - i_\alpha \psi_{f\beta}) - \omega_r \psi_{f\beta} i_\beta - \omega_r \psi_{f\alpha} i_\alpha + \frac{1}{L_s} \omega_r \psi_{f\alpha}^2 - \frac{1}{L_s} \omega_r \psi_{f\beta}^2 \\ & + \frac{1}{L_s} u_\beta \psi_{f\alpha} - \frac{1}{L_s} u_\alpha \psi_{f\beta} \end{aligned} \quad (6.168)$$

$$\frac{dx_{12}}{dt} = -\frac{R_s}{L_s} x_{12} - x_{11} x_{22} + \frac{1}{L_s} x_{11} x_{21} + V_1 \quad (6.169)$$

$$\begin{aligned} \frac{dx_{22}}{dt} = & -\frac{R_s}{L_s} (i_\alpha \psi_{f\alpha} + i_\beta \psi_{f\beta}) + \omega_r (\psi_{f\alpha} i_\beta - \psi_{f\beta} i_\alpha) - \frac{1}{L_s} \omega_r \psi_{f\alpha} \psi_{f\beta} + \frac{1}{L_s} \omega_r \psi_{f\alpha} \psi_{f\beta} \\ & + \frac{1}{L_s} u_\beta \psi_{f\alpha} + \frac{1}{L_s} u_\alpha \psi_{f\beta} \end{aligned} \quad (6.170)$$

$$\frac{dx_{22}}{dt} = -\frac{R_s}{L_s} x_{22} + x_{11} x_{12} + V_2 \quad (6.171)$$

This is equivalent to [17]

$$\frac{dx_{12}}{dt} = -\frac{R_s}{L_s}x_{12} - x_{11}x_{22} + \frac{1}{L_s}x_{11}x_{21} + V_1 \quad (6.172)$$

$$\frac{dx_{22}}{dt} = -\frac{R_s}{L_s}x_{22} + x_{11}x_{12} + V_2 \quad (6.173)$$

$$V_1 = \frac{1}{L_s}u_\beta\psi_{f\alpha} - \frac{1}{L_s}u_\alpha\psi_{f\beta} \quad (6.174)$$

$$V_2 = \frac{1}{L_s}u_\beta\psi_{f\beta} + \frac{1}{L_s}u_\alpha\psi_{f\alpha} \quad (6.175)$$

The final decoupled model of the machine is [17]

$$\frac{dx_{12}}{dt} = \frac{1}{T_i}(-x_{12} + m_1) \quad (6.176)$$

$$\frac{dx_{22}}{dt} = \frac{1}{T_i}(-x_{22} + m_2) \quad (6.177)$$

where

$$V_1 = x_{11}x_{22} - \frac{1}{L_s}x_{11}x_{21} + \frac{1}{T_i}m_1 \quad (6.178)$$

$$V_2 = -x_{11}x_{12} + \frac{1}{T_i}m_2 \quad (6.179)$$

From this, the control signals are obtained as [17]

$$u_\alpha = L_s \frac{V_2\psi_{f\alpha} - V_1\psi_{f\beta}}{x_{21}} \quad (6.180)$$

$$u_\beta = L_s \frac{V_2\psi_{f\beta} + V_1\psi_{f\alpha}}{x_{21}} \quad (6.181)$$

The block diagram of the control part is shown in Figure 6.22

### 6.6.1 Non-Linear Control of PMSM for a $dq$ Motor Model

For a better description of the non-linear control, we again present the motor model [17]:

$$\frac{di_d}{dt} = -\frac{R_s}{L_d}i_d + \frac{L_q}{L_d}\omega_r i_q + \frac{1}{L_d}u_d \quad (6.182)$$



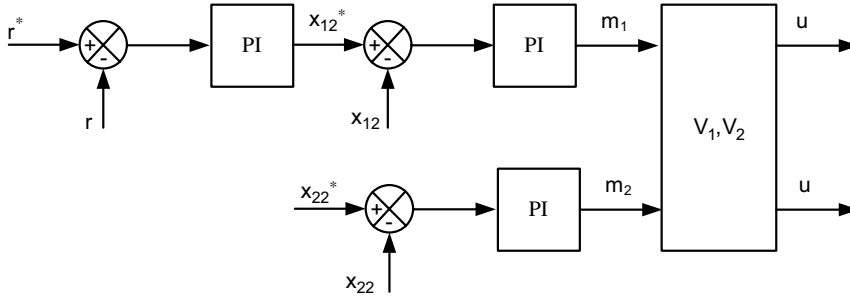


**Figure 6.22** Block diagram of the PMSM with non-linear decoupling

$$\frac{di_q}{dt} = -\frac{R_s}{L_q} i_q - \frac{L_d}{L_q} \omega_r i_d - \frac{1}{L_q} \omega_r \psi_f + \frac{1}{L_q} u_q \quad (6.183)$$

$$\frac{d\omega}{dt} = \frac{1}{T_m} [\psi_f i_q + (L_d - L_q) i_d i_q - m_o] \quad (6.184)$$

$$\frac{d\theta}{dt} = \omega_r \quad (6.185)$$

The new driving functions are [17]

$$v_1 = \frac{L_q}{L_d} \omega_r i_q + \frac{1}{L_d} u_d \quad (6.186)$$

$$v_2 = -\frac{L_d}{L_q} \omega_r i_d - \frac{1}{L_q} \omega_r \psi_f + \frac{1}{L_q} u_q \quad (6.187)$$

Then, the motor model is [17]

$$\frac{di_d}{dt} = -\frac{R_s}{L_d} i_d + v_1 \quad (6.188)$$

$$\frac{di_q}{dt} = -\frac{R_s}{L_q} i_q + v_2 \quad (6.189)$$

$$\frac{d\omega}{dt} = \frac{1}{T_m} [\psi_f i_q + (L_d - L_q) i_d i_q - m_o] \quad (6.190)$$

$$\frac{d\theta}{dt} = \omega_r \quad (6.191)$$

The command voltage components could be used from the decoupling block by using  $v_1$  and  $v_2$  in the following way [17]:



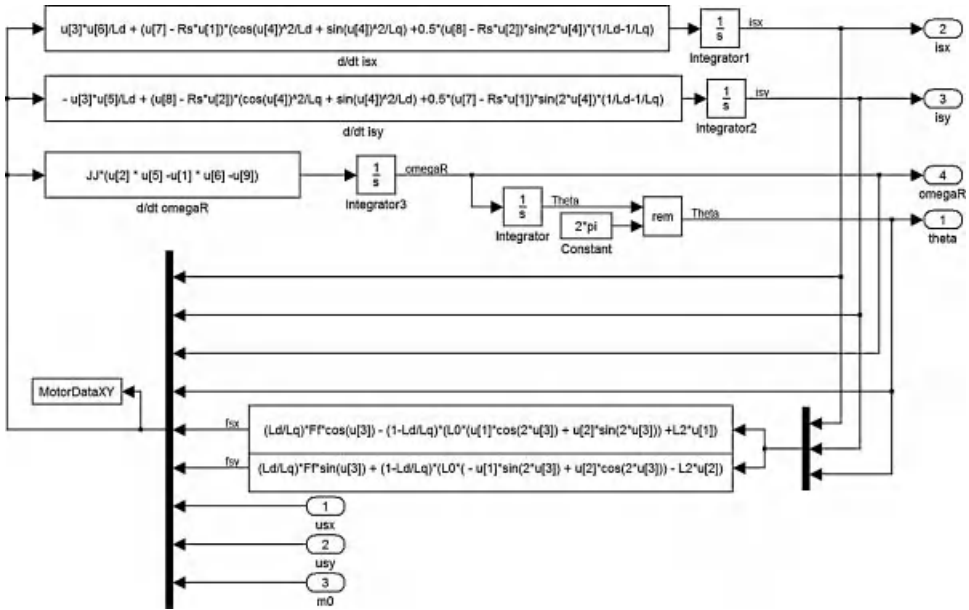


Figure 6.24 PMSM model in  $\alpha$ - $\beta$  axis

$$i_{sq} = -i_{sx}\sin\theta + i_{sy}\cos\theta \tag{6.195}$$

These equations are modeled in Figure 6.25. The currents in the  $d$ - $q$  axis are used for control purposes. The controller provides control input in the  $d$ - $q$  axis.

The control voltage in  $d$ - $q$  axis is then converted into the  $x$ - $y$  axis by using the following transformation and then applying it to the machine in the  $x$ - $y$  reference frame:

$$u_{sx} = u_{sd}\cos\theta - u_{sq}\sin\theta \tag{6.196}$$

$$i_{sy} = u_{sd}\sin\theta + u_{sq}\cos\theta \tag{6.197}$$

These above equations are modeled in Figure 6.26.

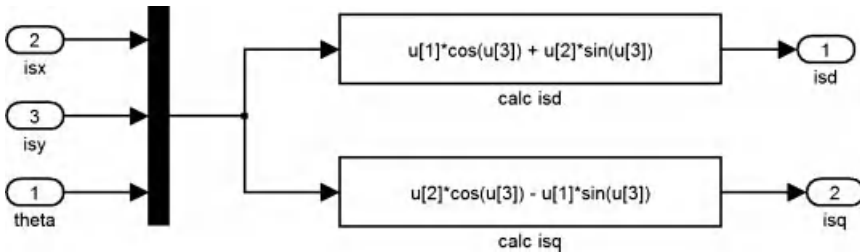


Figure 6.25  $x$ - $y$  to  $d$ - $q$  transformation

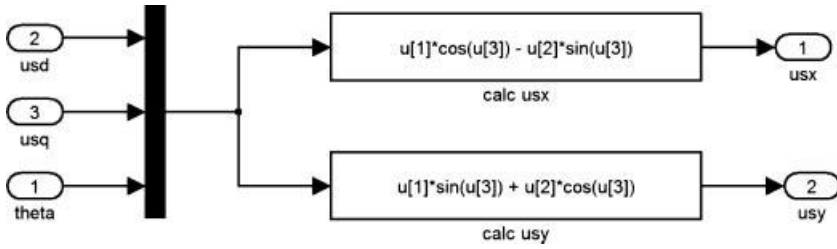


Figure 6.26 *d-q* to *x-y* transformation

### 6.6.4.1 State and Input Transformations

The PMSM model is linearized by non-linear state and input transformations. The model is linear between multiscale inputs  $m_1, m_2$  and states  $x_{11}, x_{12}, x_{22}$ . The transformations are given as the following:

### 6.6.4.2 State Transformation

The non-linear multiscale states are calculated as

$$x_{11} = \omega_r \tag{6.198}$$

$$x_{12} = ((L_d - L_q)i_{sd} + F_f)i_{sq} \tag{6.199}$$

$$x_{22} = i_{sd} \tag{6.200}$$

### 6.6.4.3 Input Transformation

$$FF = (L_d - L_q)i_{sd} + F_f \tag{6.201}$$

$$U_1 = \left[ -L_q \left( \frac{1}{L_d} - \frac{1}{L_q} \right) R_s i_{sd} i_{sd} + x_{11} \left( \frac{1}{L_q} FF^2 + i_{sd} FF \right) + x_{11} \left( \frac{1}{L_d} - \frac{1}{L_q} \right) L_q^2 i_{sq}^2 \right] + \frac{R_s}{L_q} m_1 \tag{6.202}$$

$$U_2 = -\frac{1}{L_d} x_{11} L_q i_{sq} + \frac{R_s}{L_d} m_2 \tag{6.203}$$

$$u_{sq} = \frac{L_q (U_1 - (L_d - L_q) i_{sq} U_2)}{FF} \tag{6.204}$$

$$u_{sd} = L_d U_2 \tag{6.205}$$

### 6.6.5 Control System

PI control for the  $x_{22}$  channel provides the control input  $m_2$  and a cascaded PI control for the  $x_{11}$  channel is shown in Figure 6.27. The  $x_{11}$  loop controller calculates the demand for the  $x_{12}$  loop, which in turn provides the control input  $m_1$ .

The PI controller structure is shown in the Figure 6.28.

### 6.6.6 Simulation Results

The simulation results for speed tracking are shown in Figures 6.29 and 6.30.

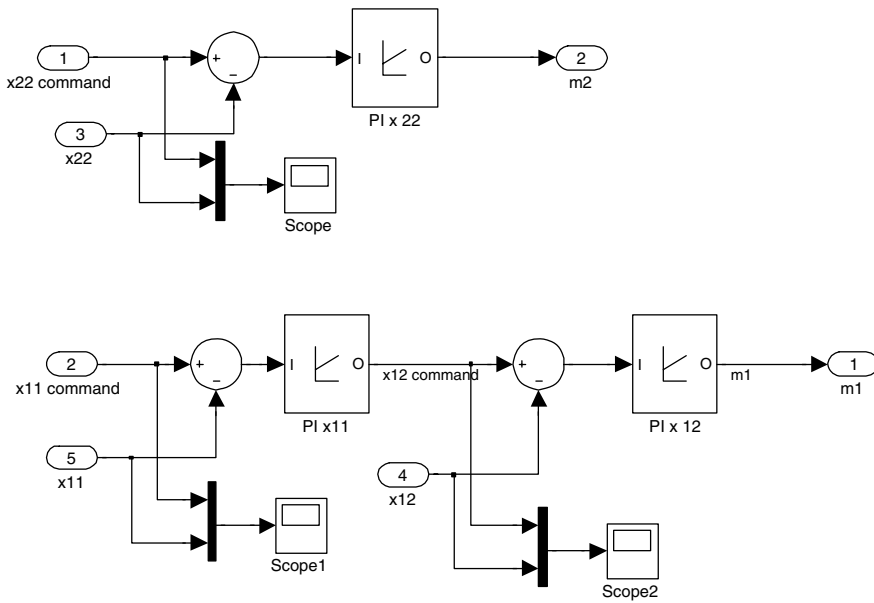


Figure 6.27 Control system model

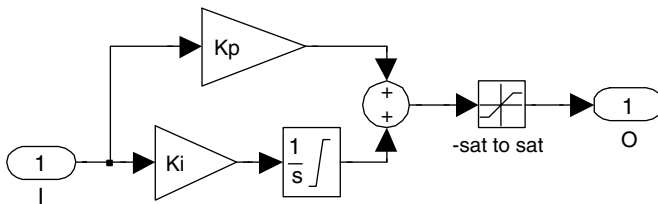


Figure 6.28 Generic PI controller

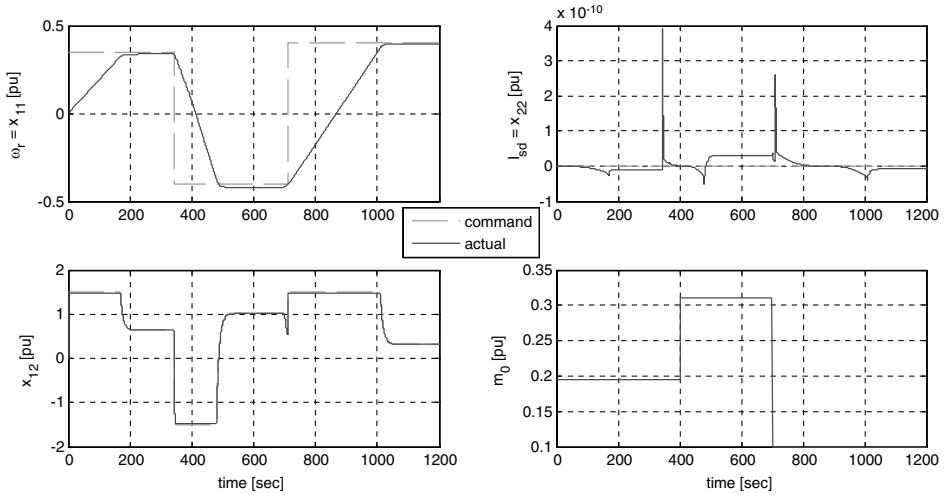


Figure 6.29 Simulation results – tracking

## 6.7 Problems

### 6.1 Select the parameters of the PI controllers.

Realize the simulation by commanding different voltages and field currents. Investigate the motor response.

### 6.2 Program the two control schemes of separately excited DC motors, with linear and with non-linear control approaches in one Simulink file. This will give you the possibility for comparison.

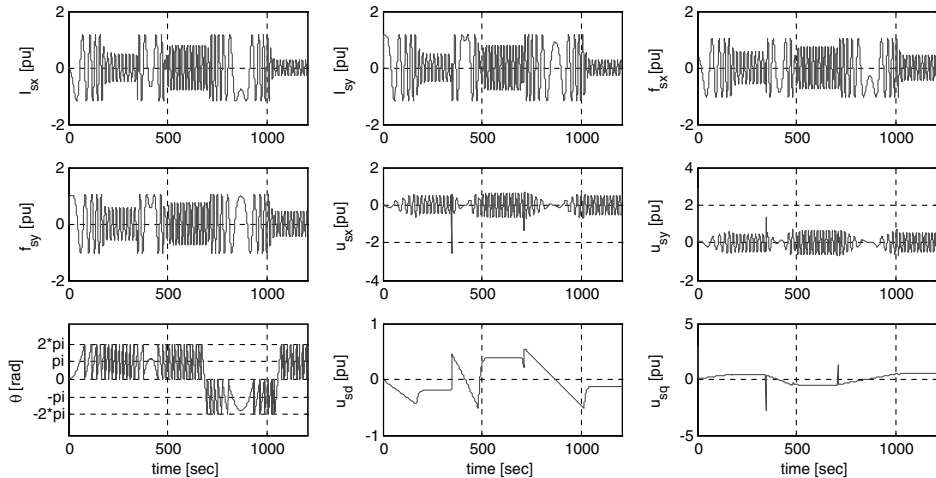


Figure 6.30 Other machine variables

**6.3** Program in Simulink the multiscalar current control scheme of induction motor (*hint: use the block from Figure 6.13 as an example*)

## References

1. Krzeminski, Z. (1987) Non-linear Control of Induction Motor. *IFAC 10th World Congr. Auto. Contr.*, Munich, pp. 349–354.
2. Krzeminski, Z. (1991) *Structures of Non-Linear Systems Control of Asynchronous Machine*. Technical University of Czestochowa, Book No 23, Poland (in Polish).
3. Isidori, A. (1995) *Non-linear Control Systems*, 3rd en. Springer Verlag.
4. Bellini, A. and Figali, G. (1993) An adaptive control for induction motor drives based on a fully linearized model, *EPE 5th Europ. Conf. on Pow. Elec. Applic.* Brighton, UK, pp. 196–201.
5. Chen, B., Ruan, Y., Xu, Y., and Liang, Q. (1990) Non-linear decoupling control of inverter-fed induction motor system with feedback linearization, *IFAC 11th World Congress*, Tallin, pp. 191–196.
6. De Luca, A. and Ulivi, G. (1989) Design of an exact non-linear controller for induction motor. *IEEE Trans. Aut. Contr.*, **34**(12), 1304–1307.
7. Georgiu, G. (1989) Adaptive feedback linearization and tracking for induction motors, *Proc. IFAC Congr.*, Tbilisi, Russia, pp. 255–260.
8. Jakubczyk, B. and Respondek, W. (1980) On linearization of control systems. *Bull. Acad. Polon. Sci. Ser. Ind. Appl. Math. Astron. Phys.*, **28**(9–10), 517–522.
9. Kim, G., Ha, I., Ko, M., and Park, J. (1989) Speed and efficiency control of induction motors via asymptotic decoupling, *20th Ann IEEE Power Elect. Spe. Conf.*, Milwaukee, WI, pp. 931–938.
10. Abu-Rub, H., Guzinski, J., Krzeminski, K., and Toliyat, H. (2003) Speed observer system for advanced sensorless control of induction motor, *IEEE Trans. Ener. Conv. . .*, **18**(2), 219–224.
11. Abu-Rub, H., Guzinski, J., Ahmed, S., and Toliyat, H. (2001) Sensorless torque control of induction motors, *IECON'01*, Denver, CO.
12. Krzemiński, Z. (2000) Sensorless control of the induction motor based on new observer. *PCIM*, Nürnberg.
13. Marino, R., Peresada, S. and Valigi, P. (1993) Adaptive input-output linearizing control of induction motors, *IEEE Trans. on Auto. Cont.*, **38**.
14. Morici, R., Rossi, C., and Tonielli, A. (1993) Discrete-time non-linear controller for induction motor, *IECON'93*, Hawaje.
15. Pires, A. J. and Esteves, J. (1994) Non-linear control methodology application on variable speed AC drives, *PEMC*, Warszawa, pp. 652–657.
16. Yan, W., Dianguo, X., Yongjun, D., and Jinggi, L. (1988) Non-linear feedback decoupling control of induction motor servosystem. *2nd Int. Conf. Elect. Drives*, Poiana Brasov (Rumania), pp. C.211–217.
17. Morawiec, M., Krzemiński, Z., and Lewicki, A. (2009) The control system of PMSM with the Speer Observer, *Przegląd Elektrotechniczny (Electrical Review)* (in Polish), pp. 48–51.
18. Baran, J. and Krzemiński, Z. (1987) Simulation of non-linear controlled DC drive, *SPD-4*, Polana Chocholowska, (in Polish).
19. Krzemiński, Z. and Guziński, J. (1995) Non-linear control of DC drives, *II Polish Nat. Conf. Pover Elect. Electr. Drives Cont.*, Łódź, (in Polish).
20. Krause, P. C. and Wasynczuk, O. (1989) *Electromechanical Motion Devices*. McGraw-Hill.
21. Buxbaum, A., Straughen, A. and Schierau, K. (1990) *Design of Control Systems for DC Drives*. Springer-Verlag.
22. Baran, J. and Szweczyk, K. (1994) Synthesis of a non-linear control system of a chopper. *Conf. Elect. Drives Power Electron., EDPE'94*, The High Tatras, Slovakia.

23. Alexandridis, A. T and Iracleous, D. P. (1994) Non-linear controllers for series-connected DC motor drive, *PEMC'94*, Warsaw.
24. Vukosavić, S. N. (2007) *Digital Control of Electrical Drives*. Springer Science + Business Media, LLC.
25. Krzemiński, Z. (2001) *Digital Control of AC Machines*. Gdańsk University of Technology Publishers, Gdańsk, (in Polish).
26. Bogdan, M., Wilamowski, J., and Irwin, D. (2011) *The Industrial Electronics Handbook: Power Electronics and Motor Drives* (Chapters 22-I and 27-I), Taylor and Francis Group, LLC.
27. Khalil, H. K. (2002) *Non-linear Systems*, 3rd edition, Prentice Hall, Upper Saddle River, NJ.
28. Abu-Rub, H., Krzeminski, Z., and Guzinski, J. (2000) Non-linear control of induction motor: Idea and application. *EPE-PEMC, 9th Inter. Power Elect. Motion Cont. Conf.*, vol. 6, pp. 213-218, Kosice/Slovak Republic.
29. Krzemiński, Z., Lewicki, A., and Włas, M. (2006) Properties of control systems based on non-linear models of the induction motor, *COMPEL Int. J. Comp. Math. Elect. Electr. Eng.*, **25**(1), 0332–1649.



# 7

## Five-Phase Induction Motor Drive System

### 7.1 Preliminary Remarks

The term ‘multi-phase’ in this chapter refers to a phase number greater than three. Three-phase electrical power is readily available as the power is generated, transmitted, and distributed in three phases. This is the most optimal number of phases for generation and transmission, as the trade off exists between the complexity and power handling capability of the three-phase system. The variable speed electric drive is also developed for three-phase AC machines. However, a power electronic converter, most commonly a voltage source or current source inverter, is invariably used to supply such three-phase drives. The power electronic converters do not pose any limit on their number of legs. The number of output phases in an inverter is the same as their respective number of legs. Hence, adding an additional leg to an inverter increases the number of output phases. This degree of freedom lead to interest in developing variable speed electric drives with more than three phases. The first proposal of a variable speed five-phase induction motor drive is believed to have been made in 1969 [1]. The five-phase inverter used initially operated in the square wave mode; however, later the pulse width modulation (PWM) mode of operation was used. Six-phase drives have attracted much attention in the literature, after their advantages were revealed in 1983 [2]. The research on high phase order motor drives remained steady until the end of the 19th century. The multi-phase drive attracted much attention from researchers after the advent of cheap and reliable power switching devices, as well as powerful digital signal processors. Since this chapter is dedicated to the five-phase system, the discussion is focused on five-phase drives only.

The PWM techniques of multi-phase inverters are developed as a part of the control of advanced multi-phase drive systems. Sinusoidal PWM controls, applied to three-phase inverters, are also extended to five-phase inverters [2]. A selective harmonic elimination technique is employed, in addition to sinusoidal PWM. Later, space vector PWM (SVPWM) techniques were developed and implemented in multi-phase voltage source inverters [3–14]. The initial approach was to use the simple extension of the SVPWM of the three-phase VSI for the five-phase system. Then it was realized that more elaborate schemes were needed to generate sinusoidal output and hence several schemes were developed and reported in the literature. The research on the five-phase drive system is active with a large number of publications on this subject [5–16].

This chapter describes the fundamental concept of a five-phase drive system. A typical five-phase drive system consists of a five-phase power converter, a five-phase motor, and their associated control, which is nowadays implemented in advanced digital signal processors interfaced with the PC. First, the model of the five-phase inverter is elaborated on, followed by the simple control in square wave mode known as a ten-step operation. The theoretical concept is supported by their simulation and experimental validation. More advanced control techniques, such as SVPWM, are next described. The mathematical model of the complete drive in field oriented control (FOC) mode is also presented. The simulation model is given subsequently for each control algorithm. Readers are encouraged to simulate the given drive system and implement their own algorithms. For further details on the five-phase drive systems and other higher-order systems, a large literature is available. A comprehensive review of the development in this area is encompassed in [17–21].

## 7.2 Advantages and Applications of Multi-Phase Drives

Multi-phase drives offer some distinct advantages over their three-phase drive counterparts. The major advantages of using a multi-phase machine instead of a three-phase machine are described in [17–42]:

- higher torque density [22–26];
- reduced torque pulsations [1,27];
- greater fault tolerance [27–38];
- reduction in the required rating per inverter leg (and therefore simpler and more reliable power conditioning equipment) [39,40]; and
- better noise characteristics, higher phase, number yield smoother torque due to the simultaneous increase of the frequency of the torque pulsation, and reduction of the torque ripple magnitude [41,42].

Multi-phase drives are still unsuitable for general purpose drives application and thus their application areas are restricted to some critical domains such as ship propulsion, more-electric aircraft, hybrid electric vehicles, electric traction, and battery-powered electric vehicles [43–48]. The reasons behind this are primarily two-fold. In high power applications (i.e. ship propulsion), the use of multi-phase drives enables reduction of the required power rating per inverter leg (phase). This is a major advantage over the converter end side, as lower switch ratings can handle reduced per-phase power. In high power applications, series and/or parallel combinations of power electronics switches are required to process large amounts of

power. The series/parallel combination of switches poses the problem of static and dynamic voltage and current sharing. Thus reduced per-phase power is very attractive in this application. In safety-critical applications (i.e. more-electric aircraft), the use of multi-phase drives enables greater fault tolerance, which is of paramount importance. It has been shown that the loss of one or two phases has little impact on drive behavior. Finally, in electric vehicles and hybrid electric vehicle applications, use of multi-phase drives for propulsion enables reduction of the required semiconductor switch current rating; although these drives are not characterized by high power, low voltage availability in vehicles makes the current high.

### 7.3 Modeling and Simulation of a Five-Phase Induction Motor Drive

A five-phase drive system consists of a five-phase AC machine, a five-phase power converter, and a controller based on microcontroller/digital signal processors/field programmable gate arrays that are controlled using a PC. The following section describes the modeling procedure of these components. At first the model of a five-phase induction motor is presented, followed by the model development of a five-phase voltage source inverter. The simulation using MATLAB/Simulink of motor and inverter is also discussed.

#### 7.3.1 Five-Phase Induction Motor Model

The model of a five-phase induction motor described, is developed initially in phase variable form. In order to simplify the model by removing the time variation of inductance terms, a transformation is applied and a so-called  $d-q-x-y-0$  model of the machine is constructed. It is assumed that the spatial distribution of all the magneto-motive forces (fields) in the machine is sinusoidal, since only torque production due to the 1st harmonic of the field is considered. However, in a five-phase machine with concentrated type of winding, the 3rd harmonic component of the current is also used together with the fundamental to enhance the torque production [5]. This special feature of a five-phase machine is not considered in this book. All the other standard assumptions of the general theory of electrical machines apply (Chapter 4). A more detailed discussion of the modeling procedure is available in [49].

##### 7.3.1.1 Phase Variable Model

A five-phase induction machine is constructed using ten phase belts, each of 36 degrees, along the circumference of the stator. The spatial displacement between phases is therefore 72 degrees. The rotor winding is treated as an equivalent five-phase winding, with the same properties as the stator winding. It is assumed that the rotor winding has already been referred to as stator winding, using the winding transformation ratio. A five-phase induction machine can then be described with the following voltage equilibrium and flux linkage equations in matrix form (underlined symbols):

$$\begin{aligned} \underline{v}_{abcde}^s &= \underline{R}_s \underline{i}_{abcde}^s + \frac{d\underline{\psi}_{abcde}^s}{dt} \\ \underline{\psi}_{abcde}^s &= \underline{L}_s \underline{i}_{abcde}^s + \underline{L}_{sr} \underline{i}_{abcde}^r \end{aligned} \quad (7.1)$$

$$\begin{aligned}\underline{v}_{abcde}^r &= \underline{R}_r \underline{i}_{abcde}^r + \frac{d\underline{\psi}_{abcde}^r}{dt} \\ \underline{\psi}_{abcde}^r &= \underline{L}_r \underline{i}_{abcde}^r + \underline{L}_{rs} \underline{i}_{abcde}^s\end{aligned}\quad (7.2)$$

The following definition of phase voltages, currents, and flux linkages applies to equations (7.1) and (7.2):

$$\begin{aligned}\underline{v}_{abcde}^s &= [v_{as} \ v_{bs} \ v_{cs} \ v_{ds} \ v_{es}]^T \\ \underline{i}_{abcde}^s &= [i_{as} \ i_{bs} \ i_{cs} \ i_{ds} \ i_{es}]^T \\ \underline{\psi}_{abcde}^s &= [\psi_{as} \ \psi_{bs} \ \psi_{cs} \ \psi_{ds} \ \psi_{es}]^T \\ \underline{v}_{abcde}^r &= [v_{ar} \ v_{br} \ v_{cr} \ v_{dr} \ v_{er}]^T \\ \underline{i}_{abcde}^r &= [i_{ar} \ i_{br} \ i_{cr} \ i_{dr} \ i_{er}]^T \\ \underline{\psi}_{abcde}^r &= [\psi_{ar} \ \psi_{br} \ \psi_{cr} \ \psi_{dr} \ \psi_{er}]^T\end{aligned}\quad (7.3)$$

The matrices of stator and rotor inductances are given with ( $\alpha = 2\pi/5$ ):

$$\underline{L}_s = \begin{bmatrix} L_{aas} & L_{abs} & L_{acs} & L_{ads} & L_{aes} \\ L_{abs} & L_{bbs} & L_{bcs} & L_{bds} & L_{bes} \\ L_{acs} & L_{bcs} & L_{ccs} & L_{c ds} & L_{ces} \\ L_{ads} & L_{bds} & L_{c ds} & L_{dds} & L_{des} \\ L_{aes} & L_{bes} & L_{ces} & L_{des} & L_{ees} \end{bmatrix}\quad (7.4)$$

$$\underline{L}_s = \begin{bmatrix} L_{ls} + M & M \cos \alpha & M \cos 2\alpha & M \cos 2\alpha & M \cos \alpha \\ M \cos \alpha & L_{ls} + M & M \cos \alpha & M \cos 2\alpha & M \cos 2\alpha \\ M \cos 2\alpha & M \cos \alpha & L_{ls} + M & M \cos \alpha & M \cos 2\alpha \\ M \cos 2\alpha & M \cos 2\alpha & M \cos \alpha & L_{ls} + M & M \cos \alpha \\ M \cos \alpha & M \cos 2\alpha & M \cos 2\alpha & M \cos \alpha & L_{ls} + M \end{bmatrix}$$

$$\underline{L}_r = \begin{bmatrix} L_{aar} & L_{abr} & L_{acr} & L_{adr} & L_{aer} \\ L_{abr} & L_{bbr} & L_{bcr} & L_{bdr} & L_{ber} \\ L_{acr} & L_{bcr} & L_{ccr} & L_{cdr} & L_{cer} \\ L_{adr} & L_{bdr} & L_{cdr} & L_{ddr} & L_{der} \\ L_{aer} & L_{ber} & L_{cer} & L_{der} & L_{eer} \end{bmatrix}\quad (7.5)$$

$$\underline{L}_r = \begin{bmatrix} L_{lr} + M & M \cos \alpha & M \cos 2\alpha & M \cos 2\alpha & M \cos \alpha \\ M \cos \alpha & L_{lr} + M & M \cos \alpha & M \cos 2\alpha & M \cos 2\alpha \\ M \cos 2\alpha & M \cos \alpha & L_{lr} + M & M \cos \alpha & M \cos 2\alpha \\ M \cos 2\alpha & M \cos 2\alpha & M \cos \alpha & L_{lr} + M & M \cos \alpha \\ M \cos \alpha & M \cos 2\alpha & M \cos 2\alpha & M \cos \alpha & L_{lr} + M \end{bmatrix}$$

Mutual inductances between stator and rotor windings are given with

$$\underline{L}_{sr} = M \begin{bmatrix} \cos \theta & \cos(\theta + \alpha) & \cos(\theta + 2\alpha) & \cos(\theta - 2\alpha) & \cos(\theta - \alpha) \\ \cos(\theta - \alpha) & \cos \theta & \cos(\theta + \alpha) & \cos(\theta + 2\alpha) & \cos(\theta - 2\alpha) \\ \cos(\theta - 2\alpha) & \cos(\theta - \alpha) & \cos \theta & \cos(\theta + \alpha) & \cos(\theta + 2\alpha) \\ \cos(\theta + 2\alpha) & \cos(\theta - 2\alpha) & \cos(\theta - \alpha) & \cos \theta & \cos(\theta + \alpha) \\ \cos(\theta + \alpha) & \cos(\theta + 2\alpha) & \cos(\theta - 2\alpha) & \cos(\theta - \alpha) & \cos \theta \end{bmatrix} \quad (7.6)$$

$$\underline{L}_{rs} = \underline{L}_{sr}^T$$

The angle  $\theta$  denotes the instantaneous position of the magnetic axis of the rotor phase 'a' with respect to the stationary stator phase 'a' magnetic axis (i.e. the instantaneous position of the rotor with respect to stator). Stator and rotor resistance matrices are  $5 \times 5$  diagonal matrices:

$$\begin{aligned} \underline{R}_s &= \text{diag}(R_s \ R_s \ R_s \ R_s \ R_s) \\ \underline{R}_r &= \text{diag}(R_r \ R_r \ R_r \ R_r \ R_r) \end{aligned} \quad (7.7)$$

Motor torque can be expressed in terms of phase variables as

$$T_e = \frac{P}{2} \underline{i}^T \frac{d\underline{L}_{abcde}}{d\theta} \underline{i} = \frac{P}{2} \begin{bmatrix} \underline{i}_{abcde}^{sT} & \underline{i}_{abcde}^{rT} \end{bmatrix} \frac{d\underline{L}_{abcde}}{d\theta} \begin{bmatrix} \underline{i}_{abcde}^s \\ \underline{i}_{abcde}^r \end{bmatrix} \quad (7.8a)$$

$$T_e = P \underline{i}_{abcde}^{sT} \frac{d\underline{L}_{sr}}{d\theta} \underline{i}_{abcde}^r \quad (7.8b)$$

Substitution of stator and rotor currents from equations (7.2) to (7.3) and equation (7.6) into equation (7.8b) yields the torque equation in developed form:

$$T_e = -PM \left\{ \begin{aligned} &(i_{as}i_{ar} + i_{bs}i_{br} + i_{cs}i_{cr} + i_{ds}i_{dr} + i_{es}i_{er})\sin \theta + (i_{es}i_{ar} + i_{as}i_{br} + i_{bs}i_{cr} + i_{cs}i_{dr} + i_{ds}i_{er})\sin(\theta + \alpha) + \\ &(i_{ds}i_{ar} + i_{es}i_{br} + i_{as}i_{cr} + i_{bs}i_{dr} + i_{cs}i_{er})\sin(\theta + 2\alpha) + (i_{cs}i_{ar} + i_{ds}i_{br} + i_{es}i_{cr} + i_{as}i_{dr} + i_{bs}i_{er}) \\ &\sin(\theta - 2\alpha) + (i_{bs}i_{ar} + i_{cs}i_{br} + i_{ds}i_{cr} + i_{es}i_{dr} + i_{as}i_{er})\sin(\theta - \alpha) \end{aligned} \right\} \quad (7.9)$$

### 7.3.1.2 Model Transformation

In order to simplify the model, it is necessary to apply a co-ordinate transformation, which will remove the time varying inductances. The co-ordinate transformation is used in the power invariant form. The following transformation matrix is therefore applied to the stator five-phase winding:

$$\underline{A}_s = \sqrt{\frac{2}{5}} \begin{bmatrix} \cos \theta_s & \cos(\theta_s - \alpha) & \cos(\theta_s - 2\alpha) & \cos(\theta_s + 2\alpha) & \cos(\theta_s + \alpha) \\ -\sin \theta_s & -\sin(\theta_s - \alpha) & -\sin(\theta_s - 2\alpha) & -\sin(\theta_s + 2\alpha) & -\sin(\theta_s + \alpha) \\ 1 & \cos(2\alpha) & \cos(4\alpha) & \cos(4\alpha) & \cos(2\alpha) \\ 0 & \sin(2\alpha) & \sin(4\alpha) & -\sin(4\alpha) & -\sin(2\alpha) \\ \frac{1}{\sqrt{2}} & \frac{1}{\sqrt{2}} & \frac{1}{\sqrt{2}} & \frac{1}{\sqrt{2}} & \frac{1}{\sqrt{2}} \end{bmatrix} \quad (7.10)$$

Transformation of the rotor variables is performed using the same transformation expression, except that  $\theta_s$  is replaced by  $\beta$ , where  $\beta = \theta_s - \theta$ . Here,  $\theta_s$  is the instantaneous angular position of the  $d$ -axis of the common reference frame with respect to the phase 'a' magnetic axis of the stator, while  $\beta$  is the instantaneous angular position of the  $d$ -axis of the common reference frame with respect to the phase 'a' magnetic axis of the rotor. Hence the transformation matrix for rotor is

$$\underline{A}_r = \sqrt{\frac{2}{5}} \begin{bmatrix} \cos \beta & \cos(\beta - \alpha) & \cos(\beta - 2\alpha) & \cos(\beta + 2\alpha) & \cos(\beta + \alpha) \\ -\sin \beta & -\sin(\beta - \alpha) & -\sin(\beta - 2\alpha) & -\sin(\beta + 2\alpha) & -\sin(\beta + \alpha) \\ 1 & \cos(2\alpha) & \cos(4\alpha) & \cos(4\alpha) & \cos(2\alpha) \\ 0 & \sin(2\alpha) & \sin(4\alpha) & -\sin(4\alpha) & -\sin(2\alpha) \\ \frac{1}{\sqrt{2}} & \frac{1}{\sqrt{2}} & \frac{1}{\sqrt{2}} & \frac{1}{\sqrt{2}} & \frac{1}{\sqrt{2}} \end{bmatrix} \quad (7.11)$$

The angles of transformation for stator quantities and for rotor quantities are related to the arbitrary speed of the selected common reference frame through

$$\begin{aligned} \theta_s &= \int \omega_a dt \\ \beta &= \theta_s - \theta = \int (\omega_a - \omega) dt \end{aligned} \quad (7.12)$$

where  $\omega$  is the instantaneous electrical angular speed of rotation of the rotor.

### 7.3.1.3 Machine Model in an Arbitrary Common Reference Frame

Correlation between original phase variables and new variables in the transformed domain is governed by the following transformation expressions:

$$\begin{aligned} \underline{v}_{dq}^s &= \underline{A}_s \underline{v}_{abcde}^s & \underline{i}_{dq}^s &= \underline{A}_s \underline{i}_{abcde}^s & \underline{\psi}_{dq}^s &= \underline{A}_s \underline{\psi}_{abcde}^s \\ \underline{v}_{dq}^r &= \underline{A}_r \underline{v}_{abcde}^r & \underline{i}_{dq}^r &= \underline{A}_r \underline{i}_{abcde}^r & \underline{\psi}_{dq}^r &= \underline{A}_r \underline{\psi}_{abcde}^r \end{aligned} \quad (7.13)$$

Substituting equations (7.1) and (7.2) into equation (7.13) and the application of equations (7.10) and (7.11) yield the machine's voltage equations in the common reference frame where  $p = d/dt$ :

$$\begin{aligned} v_{ds} &= R_s i_{ds} - \omega_a \psi_{qs} + p \psi_{ds} & v_{dr} &= R_r i_{dr} - (\omega_a - \omega) \psi_{qr} + p \psi_{dr} \\ v_{qs} &= R_s i_{qs} + \omega_a \psi_{ds} + p \psi_{qs} & v_{qr} &= R_r i_{qr} + (\omega_a - \omega) \psi_{dr} + p \psi_{qr} \\ v_{xs} &= R_s i_{xs} + p \psi_{xs} & v_{xr} &= R_r i_{xr} + p \psi_{xr} \\ v_{ys} &= R_s i_{ys} + p \psi_{ys} & v_{yr} &= R_r i_{yr} + p \psi_{yr} \\ v_{0s} &= R_s i_{0s} + p \psi_{0s} & v_{0r} &= R_r i_{0r} + p \psi_{0r} \end{aligned} \quad (7.14)$$

Transformation of flux linkage equations (7.1) and (7.2) results in

$$\begin{aligned}
 \psi_{ds} &= (L_{ls} + 2.5M)i_{ds} + 2.5Mi_{dr} & \psi_{dr} &= (L_{lr} + 2.5M)i_{dr} + 2.5Mi_{ds} \\
 \psi_{qs} &= (L_{ls} + 2.5M)i_{qs} + 2.5Mi_{qr} & \psi_{qr} &= (L_{lr} + 2.5M)i_{qr} + 2.5Mi_{qs} \\
 \psi_{xs} &= L_{ls}i_{xs} & \psi_{xr} &= L_{lr}i_{xr} \\
 \psi_{ys} &= L_{ls}i_{ys} & \psi_{yr} &= L_{lr}i_{yr} \\
 \psi_{0s} &= L_{ls}i_{0s} & \psi_{0r} &= L_{lr}i_{0r}
 \end{aligned} \tag{7.15}$$

Introduction of the magnetizing inductance  $L_m = 2.5M$  enables equation (7.15) to be written in the following form:

$$\begin{aligned}
 \psi_{ds} &= (L_{ls} + L_m)i_{ds} + L_mi_{dr} & \psi_{dr} &= (L_{lr} + L_m)i_{dr} + L_mi_{ds} \\
 \psi_{qs} &= (L_{ls} + L_m)i_{qs} + L_mi_{qr} & \psi_{qr} &= (L_{lr} + L_m)i_{qr} + L_mi_{qs} \\
 \psi_{xs} &= L_{ls}i_{xs} & \psi_{xr} &= L_{lr}i_{xr} \\
 \psi_{ys} &= L_{ls}i_{ys} & \psi_{yr} &= L_{lr}i_{yr} \\
 \psi_{0s} &= L_{ls}i_{0s} & \psi_{0r} &= L_{lr}i_{0r}
 \end{aligned} \tag{7.16}$$

Finally, transformation of the original torque equation (7.8b) yields

$$\begin{aligned}
 T_e &= \frac{5P}{2}M[i_{dr}i_{qs} - i_{ds}i_{qr}] \\
 T_e &= PL_m[i_{dr}i_{qs} - i_{ds}i_{qr}]
 \end{aligned} \tag{7.17}$$

The mechanical equation of rotor motion is invariant under the transformation and is

$$T_e - T_L = \frac{J}{P} \frac{d\omega}{dt} \tag{7.18}$$

Where  $J$  is the inertia and  $P$  is the number of poles in machine. The difference between a three-phase machine model and a five-phase machine model lies in the extra  $x$ - $y$  set of components that exist only in a five-phase machine. However, this extra set are non-flux and non-torque producing components. They simply add to the extra losses in the machine. The steady state equivalent circuit of a five-phase induction machine can be obtained by replacing  $d/dt$  term by  $j\omega_e$ , where  $\omega_e$  is the fundamental operating frequency of the machine, as shown in Figure 7.1.

In a five-phase machine, the  $x$ - $y$  components are decoupled from  $d$ - $q$  components; also there is no coupling of  $x$ - $y$  with the rotor circuit. This is true for an  $n$ -phase AC machine with sinusoidal distributed MMF and hence only one pair of components, i.e.  $d$ - $q$  produces torque and the remaining component simply causes losses in the machine. Different harmonics of the stator voltage/current map into either the  $d$ - $q$  or  $x$ - $y$  planes of the stationary reference frame, depending on the harmonic order, as shown in Table 7.1. This is a general property of multi-phase systems, which lead to distinctions with respect to control of a multi-phase machine.

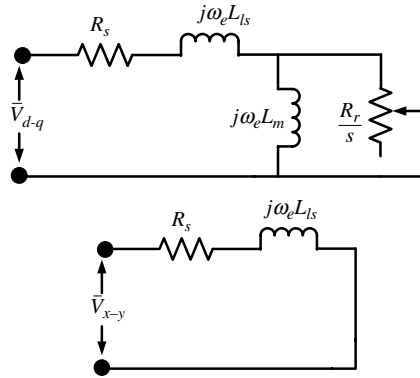


**Figure 7.1** Steady-state equivalent circuit of a five-phase induction machine

Thus the fundamental, 9th, 11th . . . are produced due to *d-q* components, while 3rd, 7th, 13th . . . are generated due to *x-y* components and a multiple of the 5th harmonic is produced due to zero-sequence components.

**7.3.1.4 MATLAB/Simulink Model of Main Fed Five-Phase Induction Motor Drive**

The MATLAB/Simulink model of a five-phase induction machine fed by a pure five-phase sine wave is illustrated in Figure 7.2. The five-phase sine wave is generated using a ‘sine wave’ from the source library of Simulink. All the five phases are generated from one block, by providing the appropriate phase shift of 72 degrees  $[0 \quad \frac{2\pi}{5} \quad \frac{4\pi}{5} \quad -\frac{4\pi}{5} \quad -\frac{2\pi}{5}]$ . The model can be used either in the phase variable form of equations (7.1–7.9) or in the transformed domain of equations (7.14–7.18); here the latter approach is given. The input source voltages are transformed to *d-q-x-y* and given to the machine model. The outputs of the machine models are taken as currents, speed, torque, and rotor flux. The sub-blocks are presented in Figures 7.2b and 7.2c.

A five-phase sinusoidal supply is given to the five-phase induction motor under no-load and loaded conditions. The resulting waveforms are presented in Figures 7.3–7.11.

**7.3.1.5 No-Load Condition**

The response of a five-phase motor under no-load conditions is presented in Figures 7.3–7.7. Rated voltage of value  $220\sqrt{2}$  and frequency of 50 Hz is applied to the stator of a

**Table 7.1** Harmonic mapping for five-phase machine

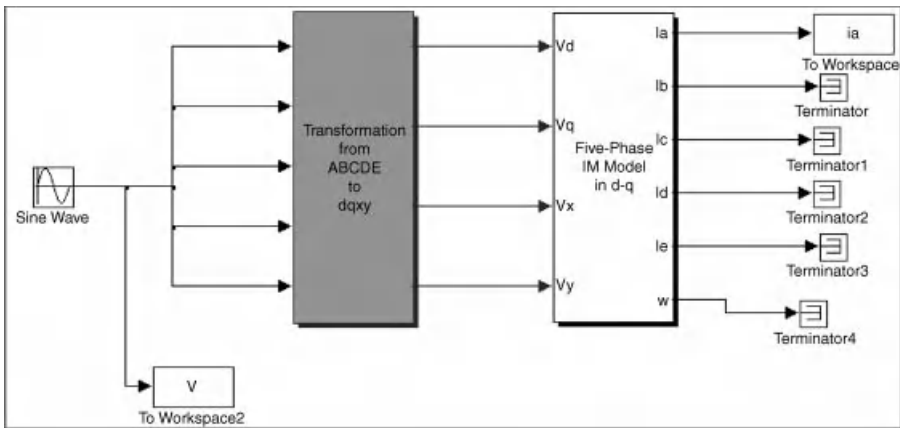
Component	Five-phase system
<i>d-q</i>	$10j \pm 1$ ( $j=0, 1, 2, \dots$ )
<i>x-y</i>	$10j \pm 3$ ( $j=0, 1, 2, \dots$ )
Zero sequence	$10j + 5$ ( $j=0, 1, 2, \dots$ )



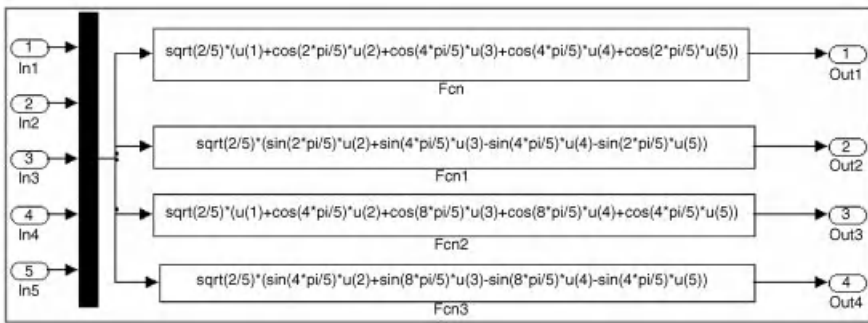
five-phase motor and is allowed to accelerate to its rated speed of 1500 rpm. The supply voltage for two cycles is shown in Figure 7.3. The response of the motor is similar to that obtained with a three-phase induction motor.

**7.3.1.6 Rated Load Condition**

To observe the behavior of the machine under loaded conditions, a rated load of 8.33 Nm is applied to the motor shaft at a time instant of 1 sec. The load is applied once the motor reaches a steady-state condition after excitation and acceleration transients. The resulting waveforms are shown in Figures 7.8–7.11. It is evident from Figure 7.8 that the motor follows the load torque well. The speed response presented in Figure 7.9 clearly shows a drop in the speed of the motor, as the motor settles to a new speed of nearly 1428 rpm. Since no corrective action is incorporated into the drive, the motor continues to rotate at the reduced speed. Normally a



a



b

**Figure 7.2** (a) Simulink block of five-phase motor fed using ideal five-phase supply (*File Name Ideal\_5\_Motor.mdl*); (b) Sub-blocks of transformation from five-phase to four orthogonal phases; and (c) Five-phase induction motor simulation model

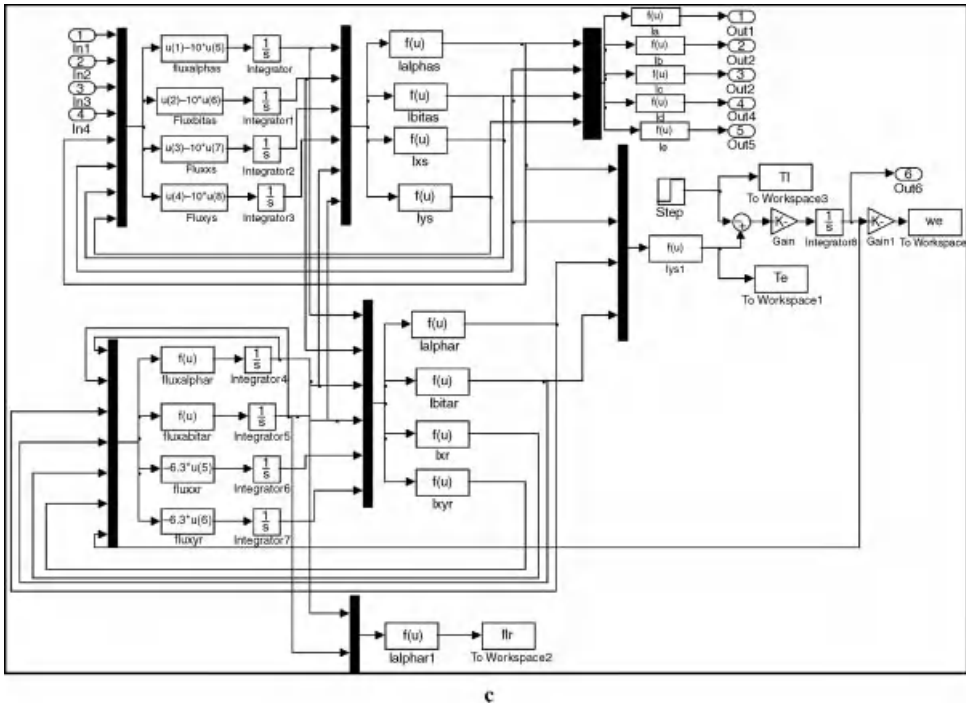


Figure 7.2 (Continued)

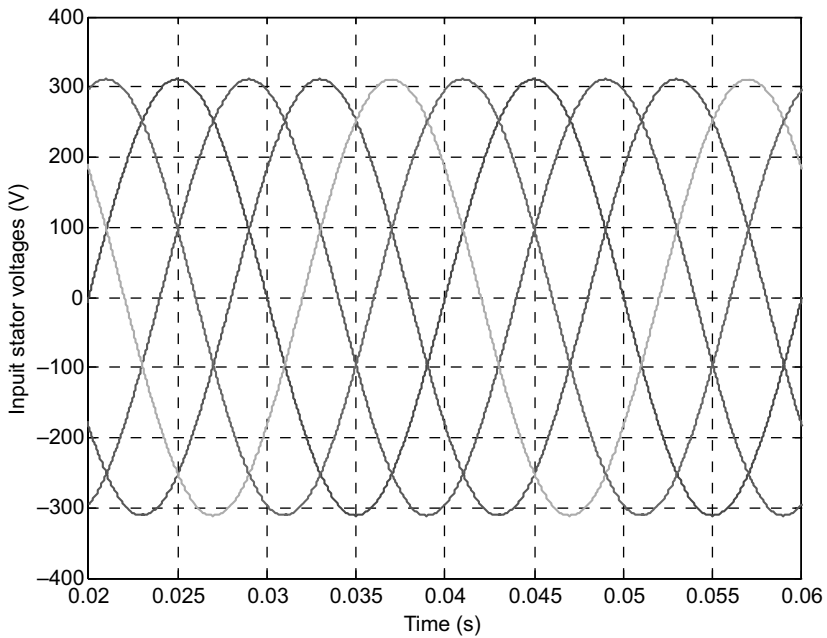
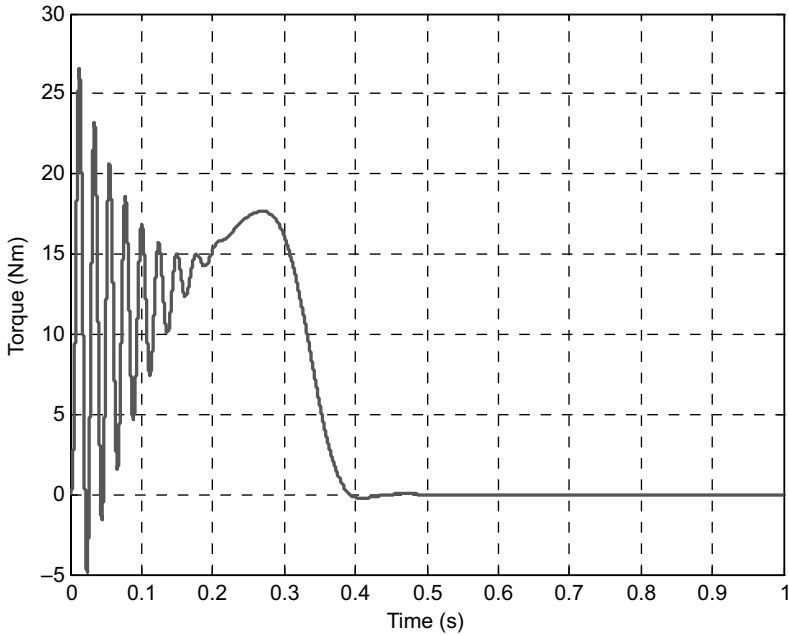
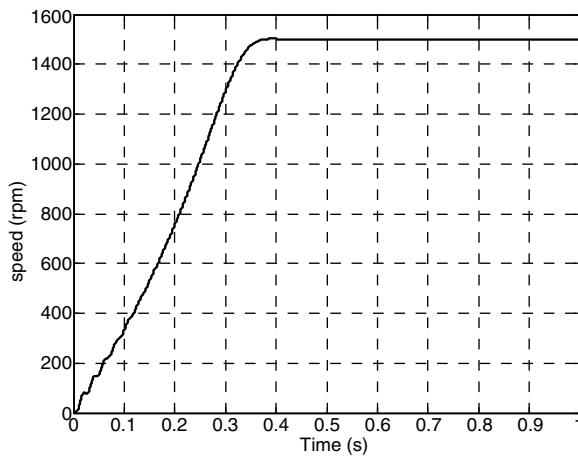


Figure 7.3 Input five-phase voltage to the stator of machine



**Figure 7.4** Torque response of a five-phase motor under no-load

PI controller is used for closed-loop operation to correct the speed error, but this is not taken up here. The rotor flux for the complete duration of simulation is presented in Figure 7.11. It shows a drop in the flux due to application of load. Thus, conclusively, it can be said that a five-phase motor shows similar behavior as that of a three-phase induction motor.



**Figure 7.5** Speed response of five-phase motor under no-load

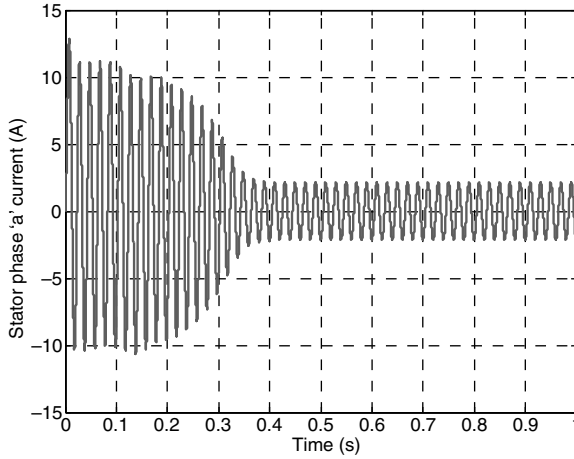


**Figure 7.6** Stator phase 'a' current of five-phase motor under no-load

### 7.3.2 Five-Phase Two-Level Voltage Source Inverter Model

This section describes the modeling procedure of a five-phase voltage source inverter. A five-phase inverter has a similar front-side converter structure to that of a three-phase voltage source inverter. The fixed voltage and fixed frequency grid supply voltage is converted to DC by using either controlled (thyristor based or power transistor based) or uncontrolled rectifier (diode based). The output of the rectifier (AC-DC converter) is filtered to remove the ripple in the output voltage signal. The rectified and filtered DC voltage is fed to the inverter (DC-AC) block. The inverter block outputs five-phase variable voltage and variable frequency supply to feed motor drives or other applications as desired. The five-phase inverter has two additional legs

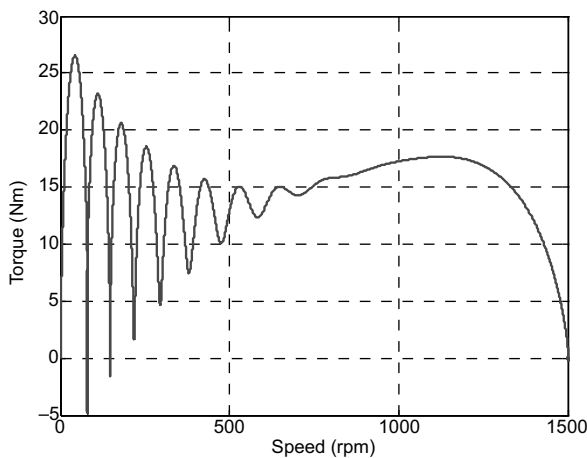


**Figure 7.7** Torque versus speed response of five-phase motor under no-load

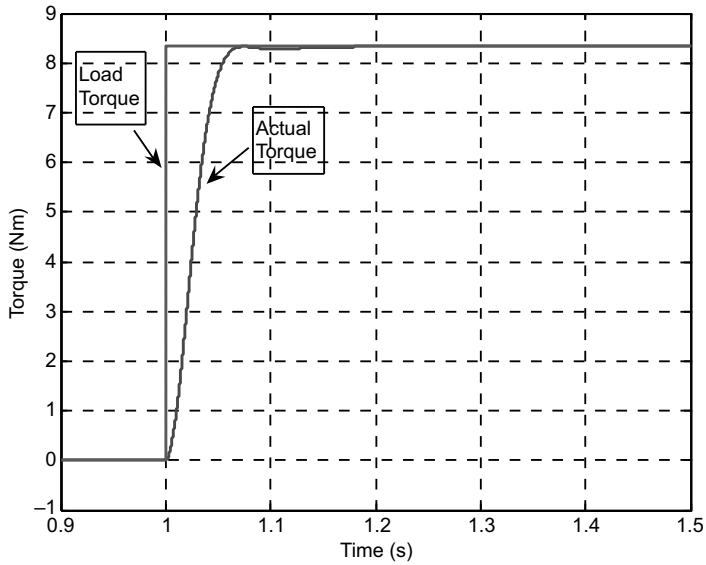


**Figure 7.8** Torque response of a five-phase motor under rated load condition

when compared to a three-phase inverter. The block diagram of this arrangement is shown in Figure 7.12, where the inverter is feeding a five-phase induction motor. The rectifier, filter, and five-phase inverter constitute the complete three-phase fixed voltage and fixed frequency to five-phase variable voltage and variable frequency supply system. The DC link side or the front

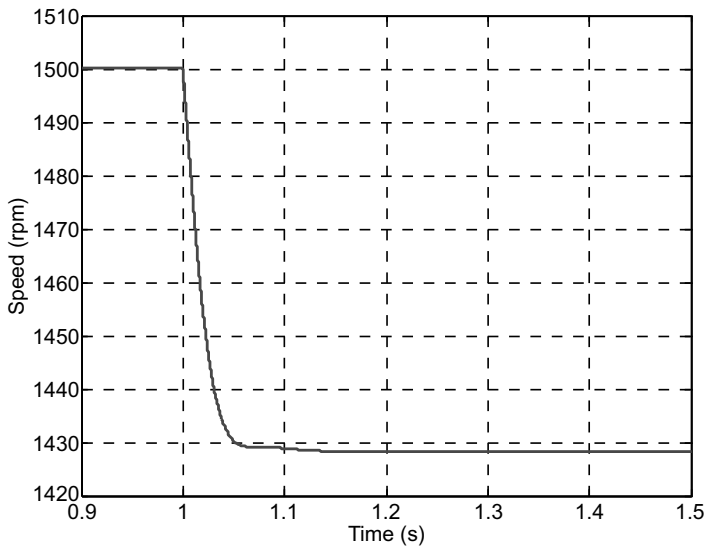


**Figure 7.9** Speed response of five-phase motor under rated load condition

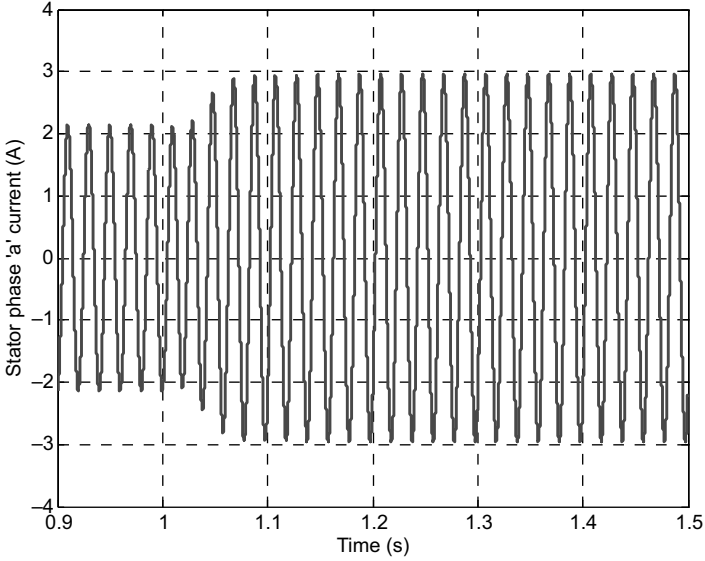


**Figure 7.10** Stator phase ‘a’ current in a five-phase motor under rated load condition

side will be omitted from further discussion. The five-phase inverter block will be discussed in detail in the subsequent section.

The power circuit topology of a five-phase voltage source inverter is shown in Figure 7.2; this was first proposed by [1]. Each switch in the circuit consists of two power semiconductor devices connected in anti-parallel. One of these is a fully controllable semiconductor, such as a

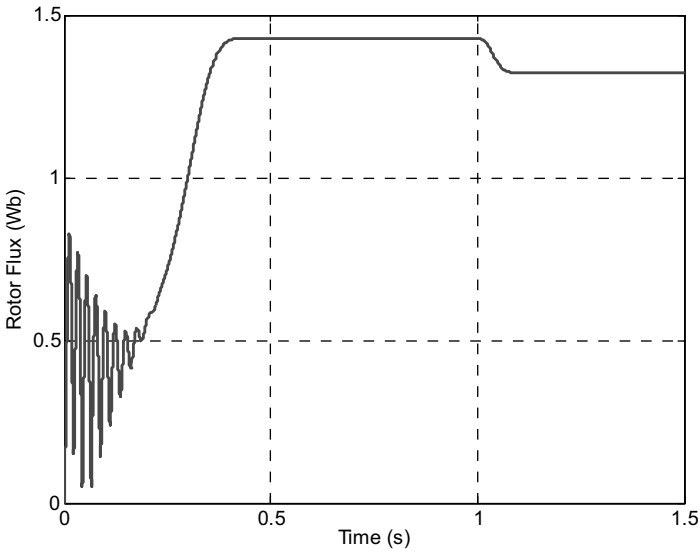


**Figure 7.11** Rotor flux in a five-phase motor

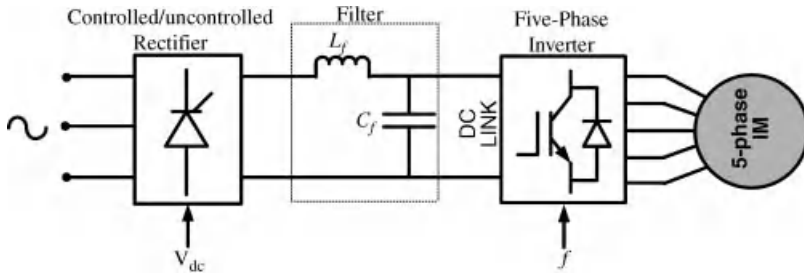


**Figure 7.12** Block diagram of five-phase induction motor drive

bipolar transistor, MOSFET, or IGBT, while the second is a diode. The input of the inverter is a DC voltage, which is regarded as constant. The inverter outputs are denoted in Figure 7.13 with lower-case letters (*a, b, c, d, e*), while the points of connection of the outputs to the inverter legs have symbols in capital letters (*A, B, C, D, E*). The voltage of this point of connection is called the ‘Pole voltage’ or ‘Leg voltage.’ The voltage between the terminal of the output of the inverter and the neutral of the load is called the ‘Phase voltage’. The voltage between the neutral of the load and the neutral of the DC link is called ‘Common mode voltage’. The voltage across the two output terminals of the load is called the ‘Line voltages’. However, in a five-phase system, there exists two different line voltages, called non-adjacent and adjacent line voltages, contrary to a three-phase system where only one line voltage is defined. This is further discussed in the next section.

The basic operating principles of the five-phase VSI are developed as follows, assuming ideal commutation and zero forward voltage drop. The upper and lower power switches of the same leg are complimentary in operation, i.e. if the upper switch is ‘ON,’ the lower must be ‘OFF,’ and vice-versa. This is done to avoid shorting the DC supply. Complimentary operation of the switches is obtained by providing a 180-degree phase shifted gate drive signal to the two upper and lower switches. However, it is important to provide a time delay between turning ‘ON’ and turning ‘OFF’ of the two complimentary switches. This time delay is called ‘Dead time,’ as both the power switches remain ‘OFF’ simultaneously for a small duration of time. Thus the ‘ON’ time of each power switch is smaller compared to their corresponding ‘OFF’ time, which is illustrated in Figure 7.14. The upper trace shows the gate drive signal for upper

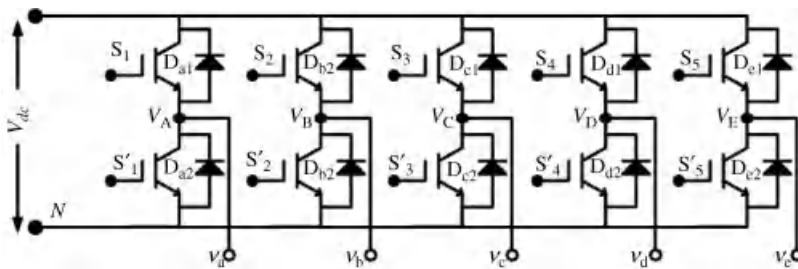


**Figure 7.13** Power circuit topology of a five-phase voltage source inverter

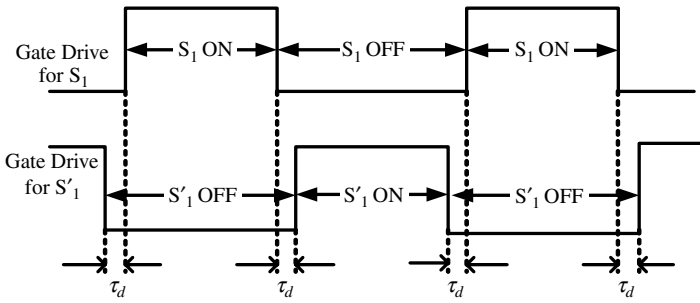


Figure 7.14 Illustration for dead time

switch  $S_1$  and the lower trace shows the gate drive signal for lower switch  $S'_1$ . When switch  $S_1$  goes 'OFF,' the Switch  $S'_1$  turns off after a delay of  $\tau_d$  (dead time). The Power module from Semikron and other manufacturers have built-in hardware for providing this dead time. In software realization, there are also options in Digital Signal Processors to incorporate and change the dead time. In practice, the delay time can be set between 5 and 50  $\mu\text{sec}$ .

To simulate the dead time for inverter leg switching in MATLAB/Simulink, the block of Figure 7.15 can be used. The input to the block is the gate driving signal, where one signal is passed directly and the second signal is processed through 'Discrete Edge Detector' (from 'Discrete Control blocks' of 'Extra Library' of 'SimPowerSystem' block-sets), then multiplied by  $-1$  (to make a complimentary signal) using a 'Gain' block. The outputs of the block of Figure 7.15 are two complimentary gate drive signals with the desired dead time. The 'Discrete Edge Detector' block is used to provide the desired dead time. This block is used when the inverter is modeled using 'SimPowerSystems block-sets,' using actual components.

The inclusion of dead time in the simulation model affects the output waveform and will be illustrated using a simulation example in the next section.

The relationship between pole voltage and switching signals is given as

$$V_k = S_k V_{dc}; \quad k \in A, B, C, D, E \tag{7.19}$$

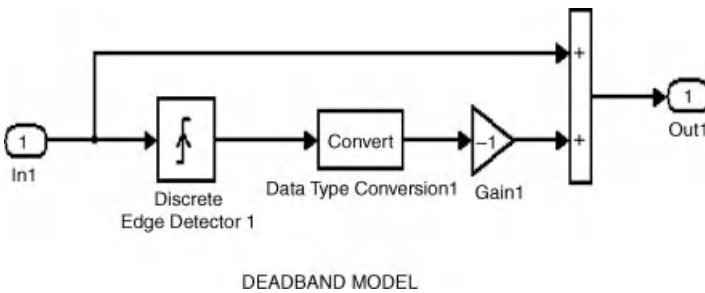


Figure 7.15 Simulink model to create dead time



where  $S_k = 1$  when the upper power switch is ‘ON’ and  $S_k = 0$  when the lower switch is ‘ON.’ If the load is assumed to be a star connected five-phase, then the relation between the phase-to-neutral load voltage and the pole voltages can be written as

$$\begin{aligned} V_A(t) &= v_a(t) + v_{nN}(t) \\ V_B(t) &= v_b(t) + v_{nN}(t) \\ V_C(t) &= v_c(t) + v_{nN}(t) \\ V_D(t) &= v_d(t) + v_{nN}(t) \\ V_E(t) &= v_e(t) + v_{nN}(t) \end{aligned} \quad (7.20)$$

where  $v_{nN}$  is the voltage difference between the star point  $n$  of the load and the negative rail of the DC bus  $N$ , called the ‘Common mode voltage.’ This common mode voltage or neutral voltage is responsible of leakage bearing currents and their subsequent failure [50–53]. The PWM techniques should take into account the minimization or elimination of common mode voltage.

By adding each term of the equation (7.20), and putting the sum of phase-to-neutral voltage zero (assuming a balanced five-phase voltage whose instantaneous sum is always zero), we obtain

$$v_{nN}(t) = (1/5)(V_A(t) + V_B(t) + V_C(t) + V_D(t) + V_E(t)) \quad (7.21)$$

Substituting equation (7.21) back into equation (7.20), the following expressions for the phase-to-neutral voltage are obtained

$$\begin{aligned} v_a(t) &= (4/5)V_A(t) - (1/5)(V_B(t) + V_C(t) + V_D(t) + V_E(t)) \\ v_b(t) &= (4/5)V_B(t) - (1/5)(V_A(t) + V_C(t) + V_D(t) + V_E(t)) \\ v_c(t) &= (4/5)V_C(t) - (1/5)(V_B(t) + V_A(t) + V_D(t) + V_E(t)) \\ v_d(t) &= (4/5)V_D(t) - (1/5)(V_B(t) + V_C(t) + V_A(t) + V_E(t)) \\ v_e(t) &= (4/5)V_E(t) - (1/5)(V_B(t) + V_C(t) + V_D(t) + V_A(t)) \end{aligned} \quad (7.22)$$

Equation (7.22) can also be written using the switching function definition of equation (7.19):

$$\begin{aligned} v_a(t) &= \left(\frac{V_{dc}}{5}\right)[4S_A - S_B - S_C - S_D - S_E] \\ v_b(t) &= \left(\frac{V_{dc}}{5}\right)[4S_B - S_A - S_C - S_D - S_E] \\ v_c(t) &= \left(\frac{V_{dc}}{5}\right)[4S_C - S_B - S_A - S_D - S_E] \\ v_d(t) &= \left(\frac{V_{dc}}{5}\right)[4S_D - S_B - S_C - S_A - S_E] \\ v_e(t) &= \left(\frac{V_{dc}}{5}\right)[4S_E - S_B - S_C - S_D - S_A] \end{aligned} \quad (7.23)$$

7.3.2.1 Ten-Step Mode of Operation

This mode of operation is an extension of the six-step operation of a three-phase voltage source inverter. The output phase voltage assumes ten different values, so is called the ‘Ten-step mode.’ The switching frequency of the power switches in this mode is equal to the fundamental output voltage frequency. Each power switch operates for half of the fundamental cycle and so is called the 180-degree conduction mode. Thus each power switch turns ‘ON’ and turns ‘OFF’ only once in the whole fundamental cycle. The output in maximum in this mode and switching losses are minimal. However, the output in mode contains a considerable amount of low-order harmonics, which decreases the performance of the load. The upper power switch is ‘ON’ when the load current is positive (current flowing from inverter to the load) and the pole voltage is positive, and the anti-parallel diode across the upper switch is turned ‘ON’ when the load current is negative while the pole voltage is also positive. The lower power switch is turned ‘ON’ when the load current is positive and the pole voltage is zero or negative (depending upon the choice of DC link, i.e.  $+V_{dc}$  and  $0$  or  $+0.5V_{dc}$  and  $-0.5V_{dc}$ ) and the lower anti-parallel diode is turned on for a negative load current. This is illustrated in Figure 7.16. The possible pole voltages during the step operation of the five-phase VSI and the corresponding switches that are ‘ON’ are listed in Table 7.2.

The switching signal for the ten-step mode of operation is given in Figure 7.17. The delay in switching between the two consecutive phases are  $360^\circ/5 = 72^\circ$  or  $\pi/5$ . The complementary gate drive signals are also shown. The ‘dead time’ is not considered here.

To determine the phase-to-neutral voltages for a ten-step mode, the leg voltages from Table 7.2 is substituted into equation (7.3), and the corresponding values are listed in Table 7.3

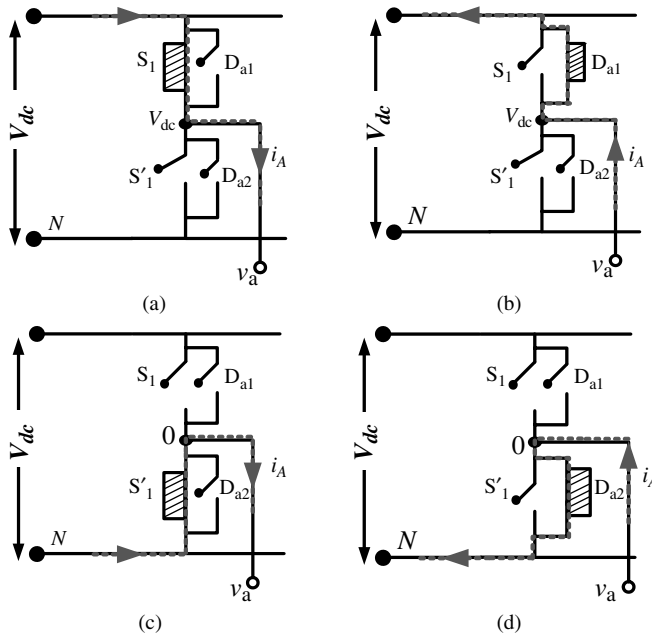


Figure 7.16 Switching state for leg A in a five-phase VSI: (a and c)  $i_A > 0$ ; (b and d)  $i_A < 0$

**Table 7.2** Pole voltages of the five-phase VSI during step mode of operation

Switching mode	Switches ON	Pole voltage $V_A$	Pole voltage $V_B$	Pole voltage $V_C$	Pole voltage $V_D$	Pole voltage $V_E$
1	$S_1, S_2, S'_3, S'_4, S_5$	$V_{dc}$	$V_{dc}$	0	0	$V_{dc}$
2	$S_1, S_2, S'_3, S'_4, S'_5$	$V_{dc}$	$V_{dc}$	0	0	0
3	$S_1, S_2, S_3, S'_4, S_5$	$V_{dc}$	$V_{dc}$	$V_{dc}$	0	0
4	$S'_1, S_2, S_3, S'_4, S'_5$	0	$V_{dc}$	$V_{dc}$	0	0
5	$S'_1, S_2, S_3, S_4, S'_5$	0	$V_{dc}$	$V_{dc}$	$V_{dc}$	0
6	$S'_1, S'_2, S_3, S_4, S'_5$	0	0	$V_{dc}$	$V_{dc}$	0
7	$S'_1, S'_2, S_3, S_4, S_5$	0	0	$V_{dc}$	$V_{dc}$	$V_{dc}$
8	$S'_1, S'_2, S'_3, S_4, S_5$	0	0	0	$V_{dc}$	$V_{dc}$
9	$S_1, S'_2, S'_3, S_4, S_5$	$V_{dc}$	0	0	$V_{dc}$	$V_{dc}$
10	$S_1, S'_2, S'_3, S'_4, S_5$	$V_{dc}$	0	0	0	$V_{dc}$

for a star connected load. The corresponding waveform is given in Figure 7.18. It is evident that the phase-to-neutral voltage takes on four different values/levels and ten steps in one fundamental cycle.

Line-to-line voltages are now discussed for a star-connected load. In a five-phase system, there exist two different systems of line voltages, termed ‘Adjacent line-to-line voltage’ and ‘Non-adjacent line-to-line voltage,’ as illustrated in Figure 7.19. The phase voltages are represented as  $(v_a, v_b, v_c, v_d, v_e)$ , the adjacent line voltages are denoted as  $(v_{ab}, v_{bc}, v_{cd}, v_{de}, v_{ea})$ , and the non-adjacent line voltages are given as  $(v_{ac}, v_{bd}, v_{ce}, v_{da}, v_{eb})$ . The relationship between the adjacent, non-adjacent, and phase voltages are elaborated upon by using a numerical example.

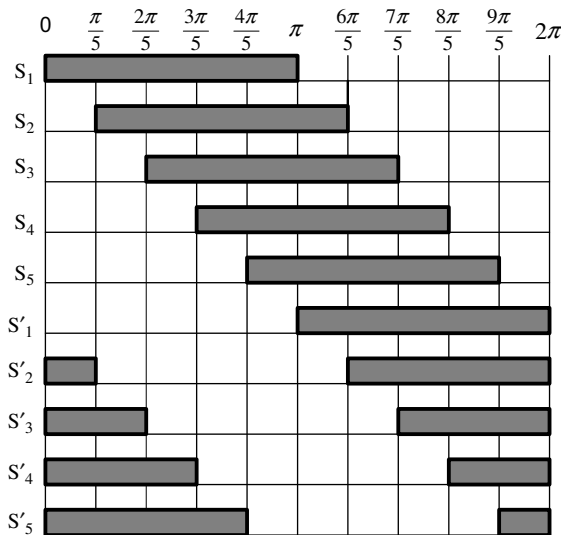


**Figure 7.17** Gate drive signal for a ten-step mode of operation

**Table 7.3** Phase-to-neutral voltages of a star connected load supplied from a five-phase VSI

Mode	Switches ON	$v_a$	$v_b$	$v_c$	$v_d$	$v_e$
1	$S_1, S_2, S'_3, S'_4, S_5$	$2/5 V_{dc}$	$2/5 V_{dc}$	$-3/5 V_{dc}$	$-3/5 V_{dc}$	$2/5 V_{dc}$
2	$S_1, S_2, S'_3, S'_4, S'_5$	$3/5 V_{dc}$	$3/5 V_{dc}$	$-2/5 V_{dc}$	$-2/5 V_{dc}$	$-2/5 V_{dc}$
3	$S_1, S_2, S_3, S'_4, S_5$	$2/5 V_{dc}$	$2/5 V_{dc}$	$2/5 V_{dc}$	$-3/5 V_{dc}$	$-3/5 V_{dc}$
4	$S'_1, S_2, S_3, S'_4, S'_5$	$-2/5 V_{dc}$	$3/5 V_{dc}$	$3/5 V_{dc}$	$-2/5 V_{dc}$	$-2/5 V_{dc}$
5	$S'_1, S_2, S_3, S_4, S'_5$	$-3/5 V_{dc}$	$2/5 V_{dc}$	$2/5 V_{dc}$	$2/5 V_{dc}$	$-3/5 V_{dc}$
6	$S'_1, S'_2, S_3, S_4, S'_5$	$-2/5 V_{dc}$	$-2/5 V_{dc}$	$3/5 V_{dc}$	$3/5 V_{dc}$	$-2/5 V_{dc}$
7	$S'_1, S'_2, S_3, S_4, S_5$	$-3/5 V_{dc}$	$-3/5 V_{dc}$	$2/5 V_{dc}$	$2/5 V_{dc}$	$2/5 V_{dc}$
8	$S'_1, S'_2, S'_3, S_4, S_5$	$-2/5 V_{dc}$	$-2/5 V_{dc}$	$-2/5 V_{dc}$	$3/5 V_{dc}$	$3/5 V_{dc}$
9	$S_1, S'_2, S'_3, S_4, S_5$	$2/5 V_{dc}$	$-3/5 V_{dc}$	$-3/5 V_{dc}$	$2/5 V_{dc}$	$2/5 V_{dc}$
10	$S_1, S'_2, S'_3, S'_4, S_5$	$3/5 V_{dc}$	$-2/5 V_{dc}$	$-2/5 V_{dc}$	$-2/5 V_{dc}$	$3/5 V_{dc}$

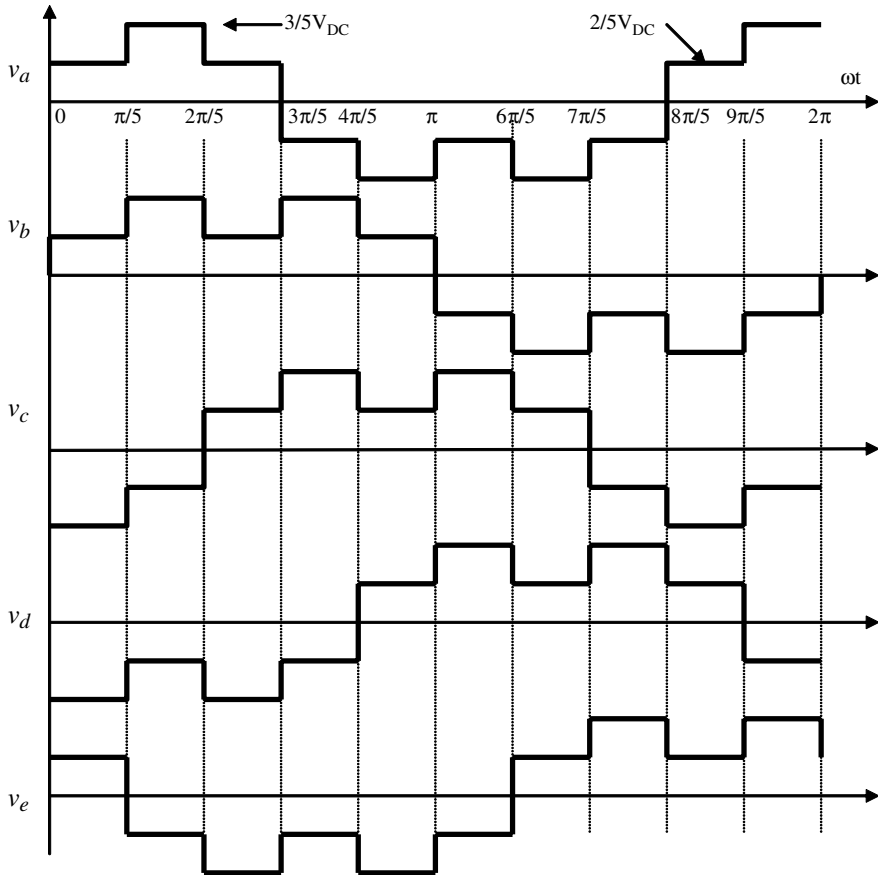


**Figure 7.18** Phase-to-neutral voltage of a five-phase VSI in ten-step mode

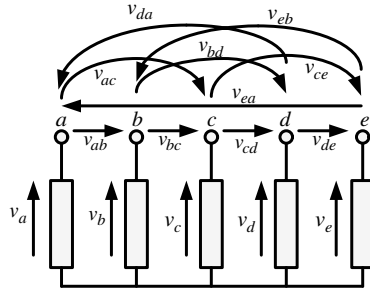


**Figure 7.19** Phase and line voltages in a five-phase system

The adjacent line voltages are calculated from the values of the phase voltages from Table 7.3, and the resulting values are listed in Table 7.4 for the ten-step mode of operation. Similarly, non-adjacent line voltages are obtained and listed in Table 7.5.

The pictorial representation of the adjacent and non-adjacent line voltages are given in Figures 7.20 and 7.21, respectively.

**7.3.2.2 Fourier Analysis of the Five-Phase Inverter Output Voltages**

In order to relate the input DC link voltage of the inverter with the output phase-to-neutral and line-to-line voltages, Fourier analysis of the voltage waveforms is undertaken. Out of the two sets of the line-to-line voltages, discussed in the preceding sub-section, only non-adjacent line-to-line voltages are analyzed, since they have higher fundamental harmonic values than the adjacent line-to-line voltages.

Using definition of the Fourier series for a periodic waveform:

$$v(t) = V_o + \sum_{k=1}^{\infty} (A_k \cos k\omega t + B_k \sin k\omega t) \tag{7.24}$$

**Table 7.4** Adjacent line-to-line voltages of the five-phase VSI

Mode	Switches ON	$v_{ab}$	$v_{bc}$	$v_{cd}$	$v_{de}$	$v_{ea}$
1	$S_1, S_2, S'_3, S'_4, S_5$	0	$V_{dc}$	0	$-V_{dc}$	0
2	$S_1, S_2, S'_3, S'_4, S'_5$	0	$V_{dc}$	0	0	$-V_{dc}$
3	$S_1, S_2, S_3, S'_4, S_5$	0	0	$V_{dc}$	0	$-V_{dc}$
4	$S'_1, S_2, S_3, S'_4, S'_5$	$-V_{dc}$	0	$V_{dc}$	0	0
5	$S'_1, S_2, S_3, S_4, S'_5$	$-V_{dc}$	0	0	$V_{dc}$	0
6	$S'_1, S'_2, S_3, S_4, S'_5$	0	$-V_{dc}$	0	$V_{dc}$	0
7	$S'_1, S'_2, S_3, S_4, S_5$	0	$-V_{dc}$	0	0	$V_{dc}$
8	$S'_1, S'_2, S'_3, S_4, S_5$	0	0	$-V_{dc}$	0	$V_{dc}$
9	$S_1, S'_2, S'_3, S_4, S_5$	$V_{dc}$	0	$-V_{dc}$	0	0
10	$S_1, S'_2, S'_3, S'_4, S_5$	$V_{dc}$	0	0	$-V_{dc}$	0

**Table 7.5** Non-adjacent line-to-line voltages of the five-phase VSI

Mode	Switches ON	$v_{ac}$	$v_{bd}$	$v_{ce}$	$v_{da}$	$v_{eb}$
1	$S_1, S_2, S'_3, S'_4, S_5$	$V_{dc}$	$V_{dc}$	$-V_{dc}$	$-V_{dc}$	0
2	$S_1, S_2, S'_3, S'_4, S'_5$	$V_{dc}$	$V_{dc}$	0	$-V_{dc}$	$-V_{dc}$
3	$S_1, S_2, S_3, S'_4, S_5$	0	$V_{dc}$	$V_{dc}$	$-V_{dc}$	$-V_{dc}$
4	$S'_1, S_2, S_3, S'_4, S'_5$	$-V_{dc}$	$V_{dc}$	$V_{dc}$	0	$-V_{dc}$
5	$S'_1, S_2, S_3, S_4, S'_5$	$-V_{dc}$	0	$V_{dc}$	$V_{dc}$	$-V_{dc}$
6	$S'_1, S'_2, S_3, S_4, S'_5$	$-V_{dc}$	$-V_{dc}$	$V_{dc}$	$V_{dc}$	0
7	$S'_1, S'_2, S_3, S_4, S_5$	$-V_{dc}$	$-V_{dc}$	0	$V_{dc}$	$V_{dc}$
8	$S'_1, S'_2, S'_3, S_4, S_5$	0	$-V_{dc}$	$-V_{dc}$	$V_{dc}$	$V_{dc}$
9	$S_1, S'_2, S'_3, S_4, S_5$	$V_{dc}$	$-V_{dc}$	$-V_{dc}$	0	$V_{dc}$
10	$S_1, S'_2, S'_3, S'_4, S_5$	$V_{dc}$	0	$-V_{dc}$	$-V_{dc}$	$V_{dc}$

where the coefficients of the Fourier series are given by

$$V_o = \frac{1}{T} \int_0^T v(t) dt = \frac{1}{2\pi} \int_0^{2\pi} v(\theta) d\theta$$

$$A_k = \frac{2}{T} \int_0^T v(t) \cos k\omega t dt = \frac{1}{\pi} \int_0^{2\pi} v(\theta) \cos k\theta d\theta \tag{7.25}$$

$$B_k = \frac{2}{T} \int_0^T v(t) \sin k\omega t dt = \frac{1}{\pi} \int_0^{2\pi} v(\theta) \sin k\theta d\theta$$

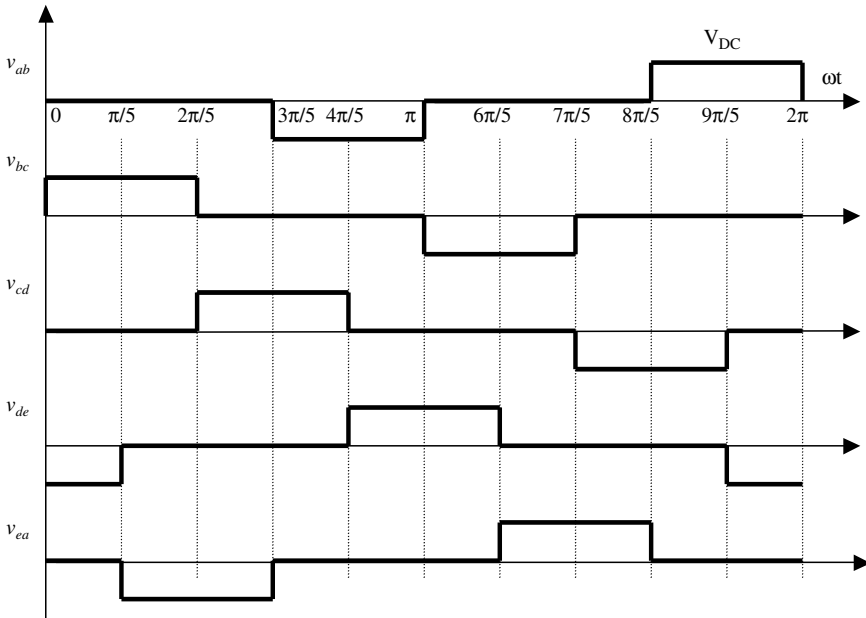


**Figure 7.20** Adjacent line-to-line voltages of the five-phase VSI

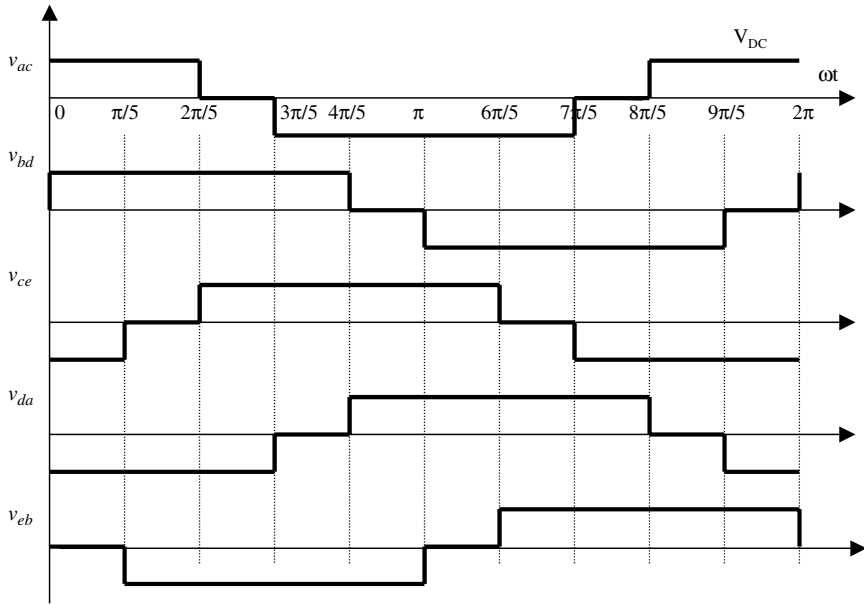


**Figure 7.21** Non-adjacent line-to-line voltages of the five-phase VSI

and observing that the waveforms possess quarter-wave symmetry and can be conveniently taken as odd functions, we can represent phase-to-neutral voltages and line-to-line voltages with the following expressions:

$$v(t) = \sum_{k=0}^{\infty} B_{2k+1} \sin(2k + 1)\omega t = \sqrt{2} \sum_{k=0}^{\infty} V_{2k+1} \sin(2k + 1)\omega t \tag{7.26}$$

$$B_{2k+1} = \sqrt{2} V_{2k+1} = \frac{1}{\pi} 4 \int_0^{\pi/2} v(\theta) \sin(2k + 1)\theta d\theta$$

In the case of the phase-to-neutral voltage  $v_b$ , shown in Figure 7.18, the coefficients of the Fourier series are

$$B_{2k+1} = \frac{1}{\pi} 4 V_{DC} \frac{1}{2k + 1} \left[ 2 + \cos(2k + 1) \frac{\pi}{5} - \cos(2k + 1) \frac{2\pi}{5} \right] \tag{7.27}$$

The expression in brackets in the second equation (7.27) equals zero for all harmonics whose order is divisible by five. For all the other harmonics, it equals 2.5. Hence, we can write the Fourier series of the phase-to-neutral voltage as

$$v(t) = \frac{2}{\pi} V_{DC} \left[ \sin \omega t + \frac{1}{3} \sin 3\omega t + \frac{1}{7} \sin 7\omega t + \frac{1}{9} \sin 9\omega t + \frac{1}{11} \sin 11\omega t + \frac{1}{13} \sin 13\omega t + \dots \right] \tag{7.28}$$

From equation (7.28) it follows that the fundamental component of the output phase-to-neutral voltage has an rms value of

$$V_1 = \frac{\sqrt{2}}{\pi} V_{DC} = 0.45V_{DC} \quad (7.29)$$

It is observed that the fundamental output of a five-phase voltage source inverter is the same as that of a three-phase voltage source inverter.

Fourier analysis of the non-adjacent line-to-line voltages is performed in the same manner. Fourier series remains to be given by equation (7.25). Taking the second voltage in Figure 7.20 and shifting the zero time instant by  $\pi/10$  degrees to the left, we have the following Fourier series coefficients:

$$B_{2k+1} = \frac{1}{\pi} 4 \int_{\pi/10}^{\pi/2} V_{DC} \sin(2k+1)\theta d\theta = \frac{1}{\pi} 4V_{DC} \frac{1}{2k+1} \cos(2k+1) \frac{\pi}{10} \quad (7.30)$$

Hence the Fourier series of the non-adjacent line-to-line voltage is

$$v(t) = \frac{4}{\pi} V_{DC} \left[ 0.95 \sin \omega t + \frac{0.59}{3} \sin 3\omega t - \frac{0.59}{7} \sin 7\omega t - \frac{0.95}{9} \sin 9\omega t - \frac{0.95}{11} \sin 11\omega t - \dots \right] \quad (7.31)$$

and the fundamental harmonic rms value of the non-adjacent line-to-line voltage is

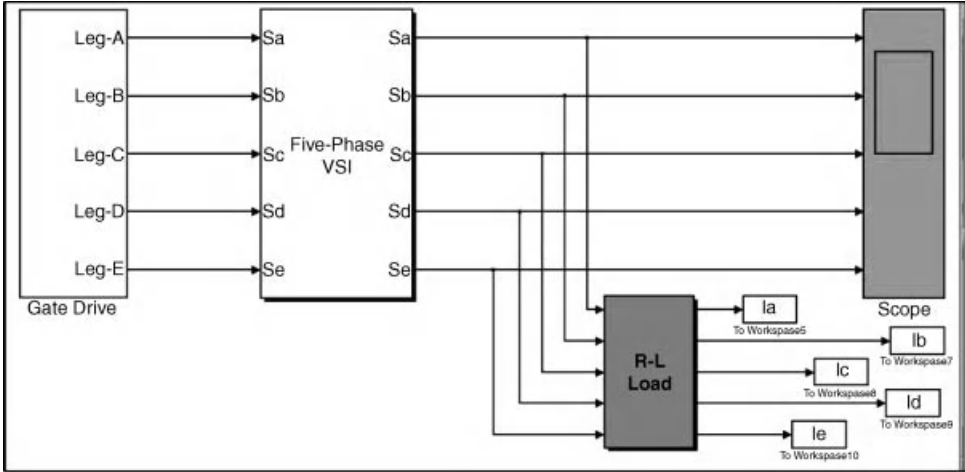
$$V_{1L} = \frac{2\sqrt{2}}{\pi} V_{DC} \cos \frac{\pi}{10} = 0.856V_{DC} = 1.902V_1 \quad (7.32)$$

### 7.3.2.3 MATLAB/Simulink Modeling for Ten-Step Mode

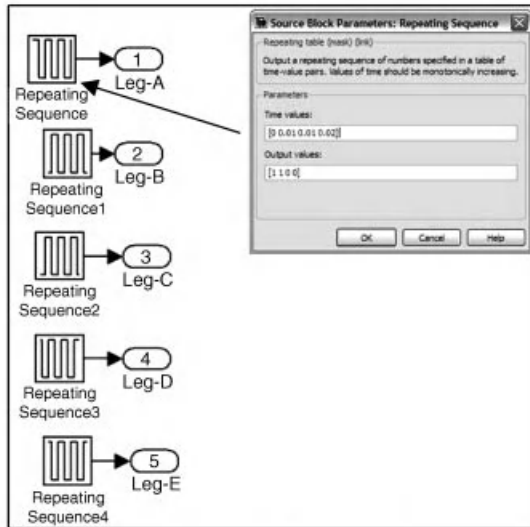
The MATLAB/Simulink model is shown in Figure 7.22. The model consists of a gate drive generator and the power circuit part of the five-phase inverter. The gate drive signal generator model, shown in Figure 7.22a, is developed using a ‘repeating’ block of Simulink, illustrated in Figure 7.22b. The inverter power circuit, shown in Figure 7.22c, is obtained using equation (7.5). The power circuit can also be modeled using an actual IGBT switch model from ‘simpowersystem’ block-sets of Simulink. The repeating block is generating a square wave gate drive signal of 50 Hz fundamental. This can be changed by changing the time axis values. The inverter equations are realized using the ‘function block’ of Simulink. The inverter power circuit, shown in Figure 7.22c, needs the value of the DC link voltage, which can be given from the main MATLAB command window or from the model initialisation. The R-L load is modeled using a first-order low pass filter, as shown in Figure 7.22d. The complete MATLAB/Simulink model is available in the CD-ROM provided with this book.



The simulation results for 50 Hz fundamental frequency and unit DC link voltage are given in Figure 7.23. The phase voltage, adjacent voltage, and non-adjacent voltage and resulting current obtained using simulation are shown. The output phase voltages exhibit ten steps and the remainder of the curves correspond to the theoretical waveforms. This is further verified by implementing this control in a prototype five-phase inverter experimentally and is shown in the next section.

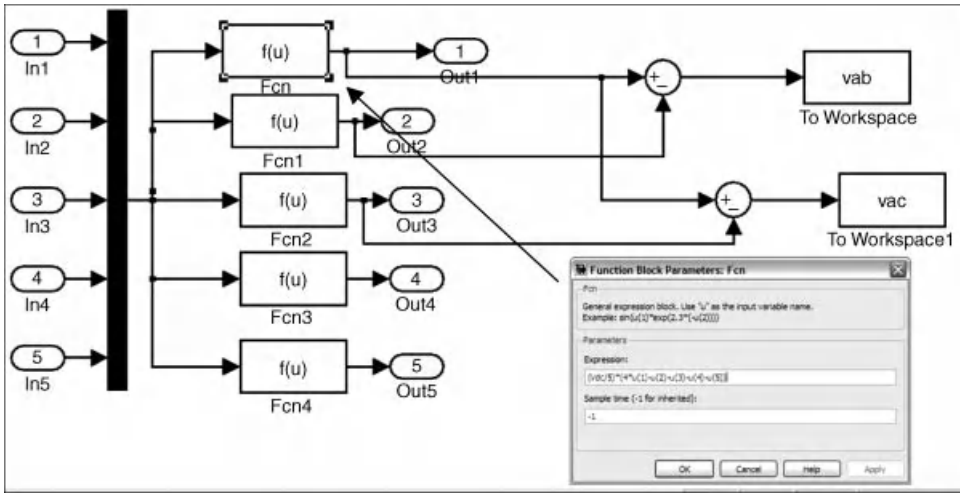


(a)

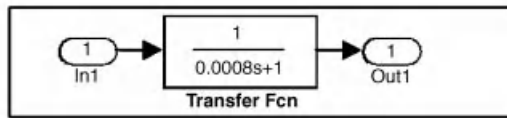


(b)

**Figure 7.22** (a) MATLAB/Simulink model of a five-phase voltage source inverter for ten-step operation (*File Name: Ten\_step\_mode.mdl*); (b) Gate drive signal generation for ten-step operation; (c) Simulink model of a five-phase VSI; and (d) R-L Load model



(c)



(d)

Figure 7.22 (Continued)

### 7.3.2.4 Prototype of a Five-Phase VSI for Ten-Step Operation

The inverters control logic can be implemented using an analog circuit and its complete block diagram is shown in Figure 7.24. The other method is by using advanced microprocessors, microcontrollers, and digital signal processor to implement the control schemes.

In Figure 7.24, the supply is taken from a single-phase power supply and converted to 9-0-9 V using a small transformer. This is fed to the phase shifting circuit, shown in Figure 7.25, to provide an appropriate phase shift for operation at various conduction angles. The phase shifted signal is then fed to the inverting/non-inverting Schmitt trigger circuit and wave-shaping circuit (Figures 7.26 and 7.27). The processed signal is then fed to the isolation and driver circuit shown in Figure 7.28, which is then finally given to the gate of IGBTs. There are two separate circuits for upper and lower legs of the inverter.

The power circuit can be made up of IGBT, with a snubber circuit consisting of a series combination of a resistance and a capacitor with a diode in parallel with the resistance.

### 7.3.2.5 Experimental Results for Ten-Step Mode

This section gives the experimental results obtained from the five-phase voltage source inverter for stepped operation of an inverter, with a 180-degree conduction modes leading to a ten-step output with a star connected load. A single-phase supply is given to the control circuit through

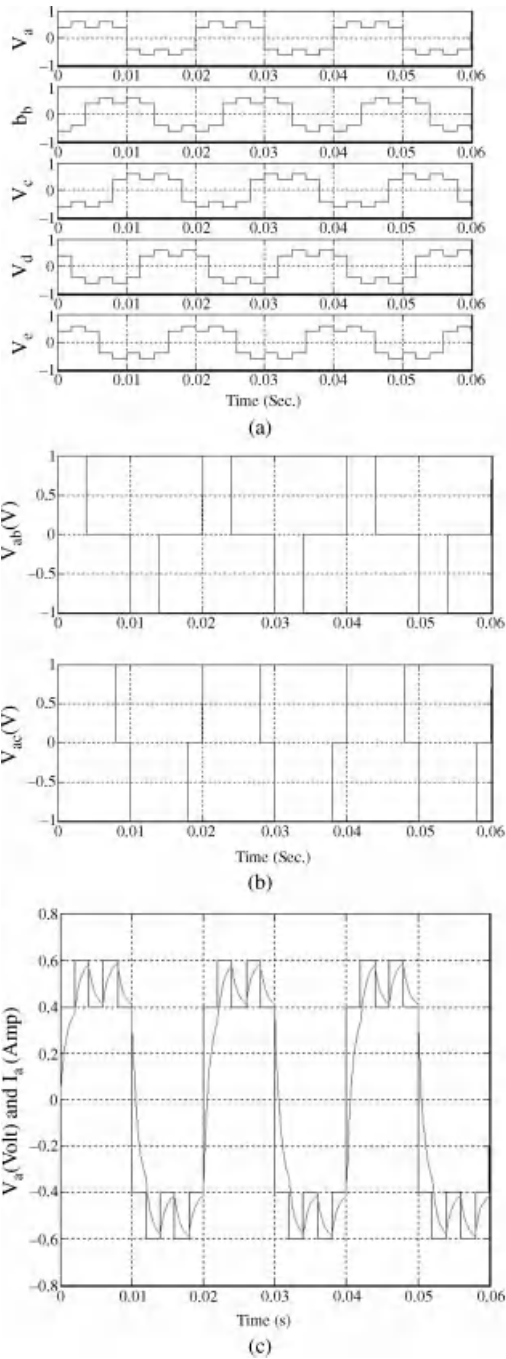


**Figure. 7.23** (a) Output phase-to-neutral voltage of a five-phase VSI in ten-step mode; (b) Output line voltages of a five-phase VSI in ten-step mode; and (c) Output phase 'a' voltage and phase 'a' current of a five-phase VSI in ten-step mode for R-L Load

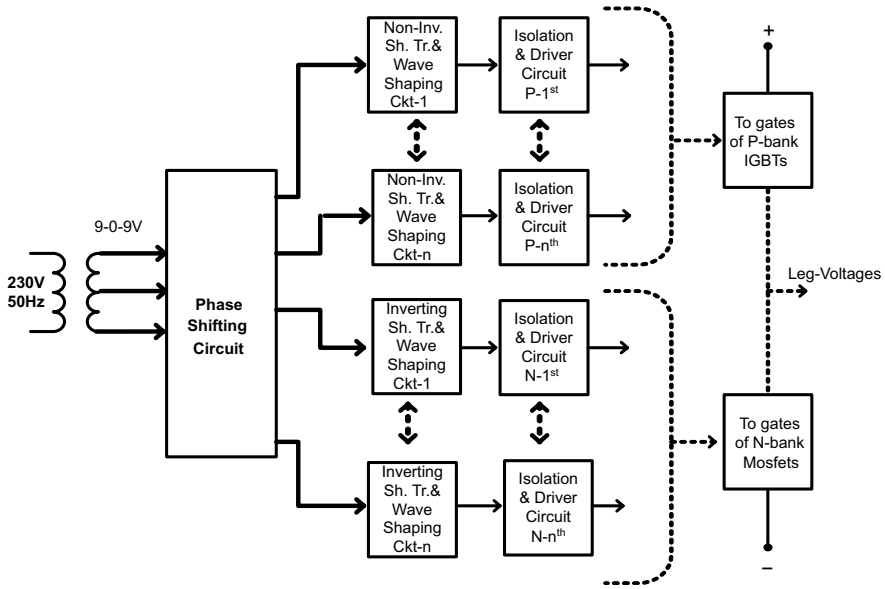


Figure 7.24 Block diagram of the complete inverter

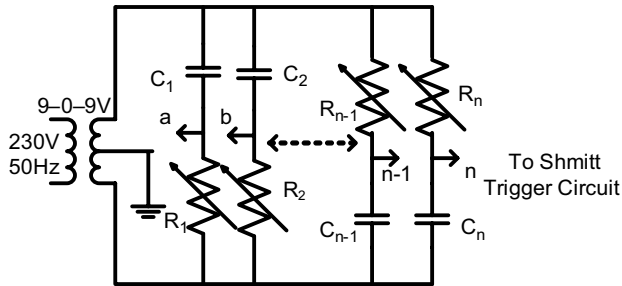


Figure 7.25 Phase shifting network

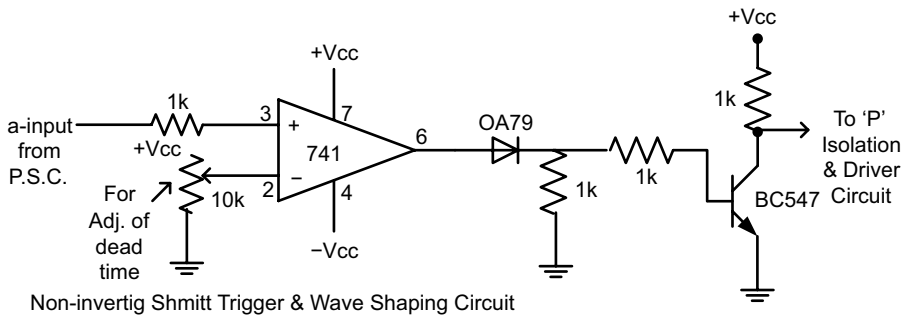
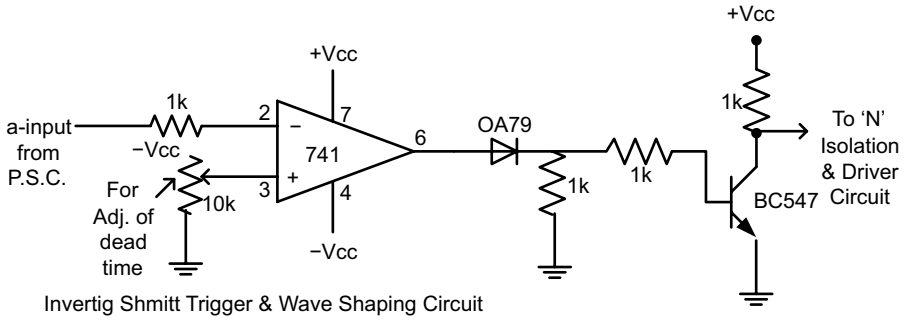


Figure 7.26 Non-inverting Schmitt trigger and wave shaping circuit



**Figure 7.27** Inverting Schmitt trigger and wave-shaping circuit

the phase shifting network. The output of the phase shifting circuit provides the required five-phase output voltage by appropriately tuning it. These five-phase signals are then further processed to generate the gate drive circuit.

The gate drive signal is given to the IGBTs and the corresponding phase-to-neutral voltages thus generated, as shown in Figure 7.29, keeping the DC link voltage at 60 V. It is seen that the phase-to-neutral voltages has ten steps with output voltage levels of  $\pm 0.2 V_{dc}$  and  $\pm 0.4 V_{dc}$ . Another experimental waveform is illustrated in Figure 7.30, for non-adjacent voltage and stator line current of a five-phase induction motor. The current shows a typical response of an induction machine.

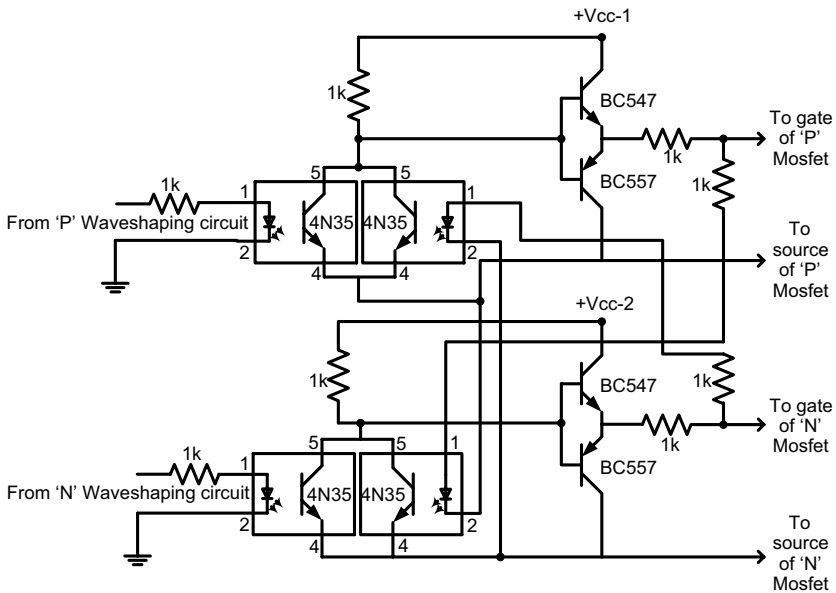


**Figure 7.28** Gate driver circuit

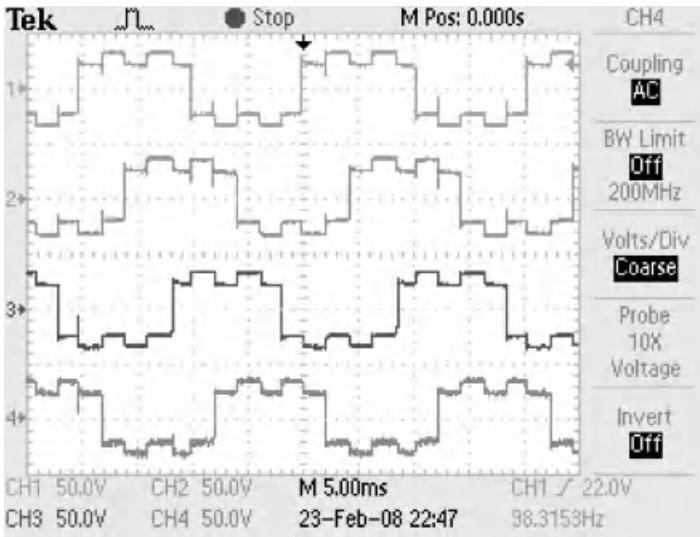


Figure 7.29 Output phase ‘a-d’ voltages for 180-degree conduction mode

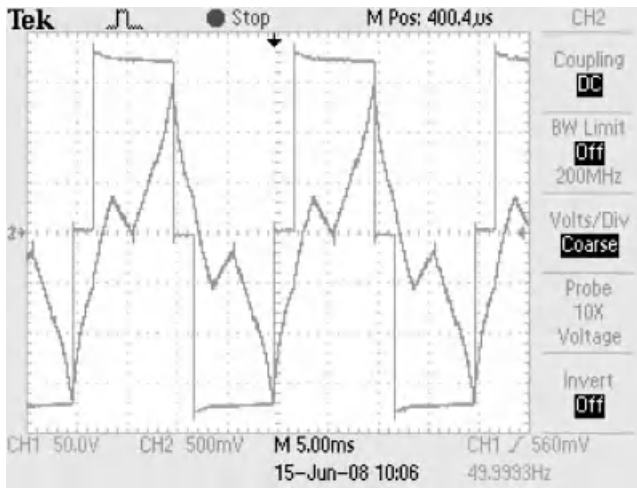


Figure 7.30 Non-adjacent line voltage and stator current

**Problem 7.1**

Assume a balanced five-phase system with 120 V rms as the phase voltages. Determine the adjacent and non-adjacent line voltages and derive their relationship.

**Solution:**

The five-phase voltage is given as

$$v_a = 120\sqrt{2}\sin(\omega t)$$

$$v_b = 120\sqrt{2}\sin\left(\omega t - 2\frac{\pi}{5}\right)$$

$$\begin{aligned}
 v_c &= 120\sqrt{2}\sin\left(\omega t - 4\frac{\pi}{5}\right) \\
 v_d &= 120\sqrt{2}\sin\left(\omega t + 4\frac{\pi}{5}\right) \\
 v_e &= 120\sqrt{2}\sin\left(\omega t + 2\frac{\pi}{5}\right)
 \end{aligned} \tag{7.33}$$

The adjacent line voltage is given as

$$v_{ab} = v_a - v_b = 120\sqrt{2}\sin(\omega t) - 120\sqrt{2}\sin\left(\omega t - 2\frac{\pi}{5}\right) \tag{7.34}$$

The adjacent line voltage can be written in polar form as

$$\begin{aligned}
 v_{ab} &= 120\sqrt{2} \angle 0 - 120\sqrt{2} \angle -72 = 120\sqrt{2} + j0.0 - 120\sqrt{2}\{\cos(-72) + j\sin(-72)\} \\
 v_{ab} &= 120\sqrt{2} + j0.0 - 120\sqrt{2}\{0.309 - j0.9511\} \\
 v_{ab} &= 82.92\sqrt{2} + j114.132\sqrt{2} = 199.5086 \angle 54
 \end{aligned}$$

Similarly we can determine other adjacent line voltages as

$$\begin{aligned}
 v_{bc} &= v_b - v_c = 199.5086 \angle -18 \\
 v_{cd} &= v_c - v_d = 199.5086 \angle -90 \\
 v_{de} &= v_d - v_e = 199.5086 \angle -162 \\
 v_{ea} &= v_e - v_a = 199.5086 \angle 126
 \end{aligned}$$

This calculation can also be shown using the graphical technique, as in Figures 7.31 and 7.32.

The relationship between the phase voltage and adjacent line voltage can be written as (assuming balanced voltages)

$$\begin{aligned}
 |v_{ab}| &= \sqrt{|v_a|^2 + |v_b|^2 + |v_a|^*|v_b|\cos\left(3\frac{\pi}{5}\right)} \\
 V_{adj-L} &= 1.1756V_{phase} \\
 |v_{ab}| &= V_{adj-L}; \quad |v_a| = |v_b| = V_{phase}
 \end{aligned} \tag{7.35}$$

The relationship between the phase voltage and non-adjacent line voltage can be written as (assuming balanced voltages)

$$\begin{aligned}
 |v_{ab}| &= \sqrt{|v_a|^2 + |v_b|^2 + |v_a|^*|v_b|\cos\left(\frac{\pi}{5}\right)} \\
 V_{non-adj-L} &= 1.9025V_{phase} \\
 |v_{ab}| &= V_{non-adj-L}; \quad |v_a| = |v_b| = V_{phase}
 \end{aligned} \tag{7.36}$$

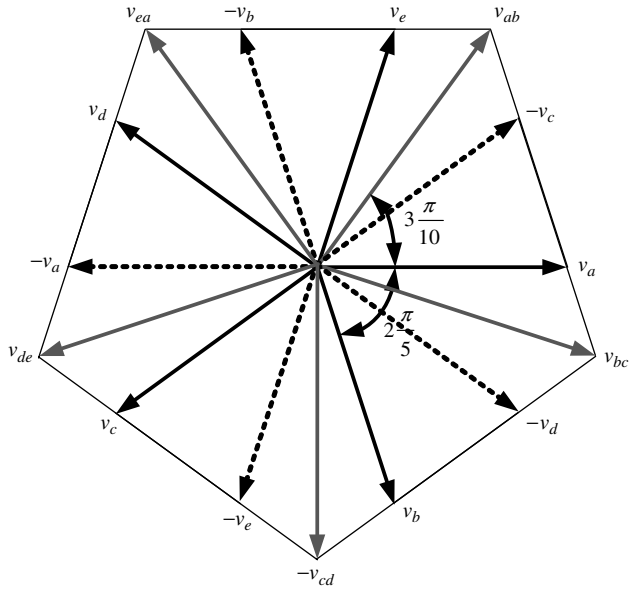


Figure 7.31 Phase and adjacent line voltage concept

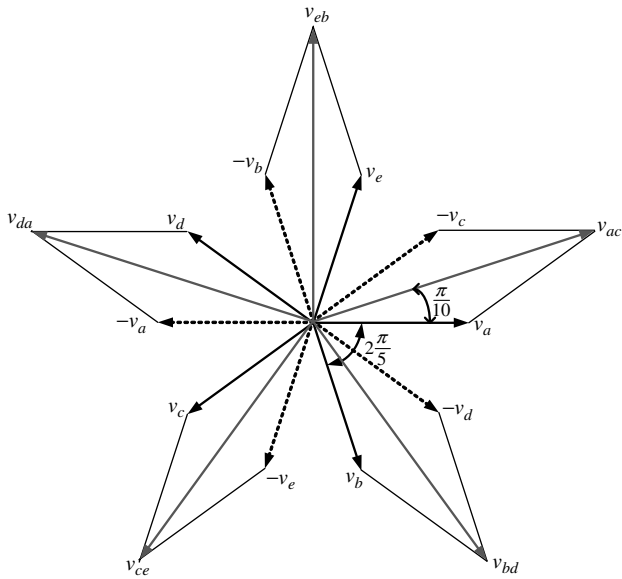


Figure 7.32 Phase and adjacent line voltage concept



**Problem 7.2**

Determine the relationship between the line voltages of a three-phase system and a five-phase system, given the phase voltage as  $V_{phase}$  for both three- and five-phase systems. Assume star-connected systems.

**Solution:**

The line-to-line voltage in a three-phase system is given as

$$V_{line} = \sqrt{3}V_{phase} = 1.7321V_{phase} \quad (7.37)$$

$$V_{adj-L} = \sqrt{1.382}V_{phase} = 1.1756V_{phase} \quad (7.38)$$

$$V_{non-adj-L} = 1.9025V_{phase} \quad (7.39)$$

$$\frac{\text{Adjacent Line Voltage Five-phase}}{\text{Line Voltage Three-phase}} = \frac{V_{adj-L}}{V_{line}} = \frac{1.1756V_{phase}}{1.7321V_{phase}} = 0.6787$$

$$\frac{\text{Non-Adjacent Line Voltage Five-phase}}{\text{Line Voltage Three-phase}} = \frac{V_{non-adj-L}}{V_{line}} = \frac{1.9025V_{phase}}{1.7321V_{phase}} = 1.0984$$

**Problem 7.3**

Determine the phase voltage of a five-phase star-connected load for obtaining same highest line-to-line voltage as that of a standard three-phase system. (*Hint: A standard three-phase system has 400 V line-to-line voltage.*) Also determine the ratio of phase voltage of the three-phase and the five-phase system

**Solution:**

Given the highest line-to-line voltage of a five-phase system as 400 V, i.e.  $V_{non-adj-L} = 400$  V

$$V_{non-adj-L} = 1.9025V_{phase} = 400$$

$$V_{phase-5} = \frac{400}{1.9025} = 210.25 \text{ V}$$

Thus the phase voltage of the five-phase load will be 210.25 V  
The phase voltage of three-phase system is

$$V_{phase-3} = \frac{400}{\sqrt{3}} = 230.94 \text{ V}$$

$$\frac{V_{phase-3}}{V_{phase-5}} = \frac{230.94}{210.25} = 1.0984$$

**Problem 7.4**

Draw the waveform of common-mode voltage generated in ten-step model of operation of a five-phase voltage source inverter. Assume  $V_{dc} = 1$  V.

**Solution:** Common mode voltage is given as

$$v_{nN}(t) = (1/5)(V_A(t) + V_B(t) + V_C(t) + V_D(t) + V_E(t)) \quad (7.40)$$

The leg voltage waveforms for the ten-step mode of operation are given in Figure 7.33. The magnitude of the voltage is  $V_{dc}$ . To determine the common mode voltage, the instantaneous values are added for all the five legs and the resulting waveform is given in Figure 7.33.

**7.3.2.6 PWM Mode of Operation of Five-Phase VSI**

If a five-phase VSI is operated in PWM mode, apart from the already described ten states, there will be an additional 22 switching states. This is because there are five inverter legs and each of them can be in two states, since the discussion is limited to two-level inverters. The number of states increases in the case of multi-level inverters. The number of possible switching states is in general equal to  $2^n$ , where  $n$  is the number of inverter legs (i.e. output phases). This correlation is valid for any two-level VSI. For a multi-level inverter, with  $m$  level and  $n$  output phases, the number of possible switching states is  $m^n$ .

The 22 possible switching states encompass three possible situations: all the states when four switches from the upper (or lower) half and one from the lower (or upper) half of the inverter are 'ON' (states 11–20); two states when either all the five upper (or lower) switches are 'ON'

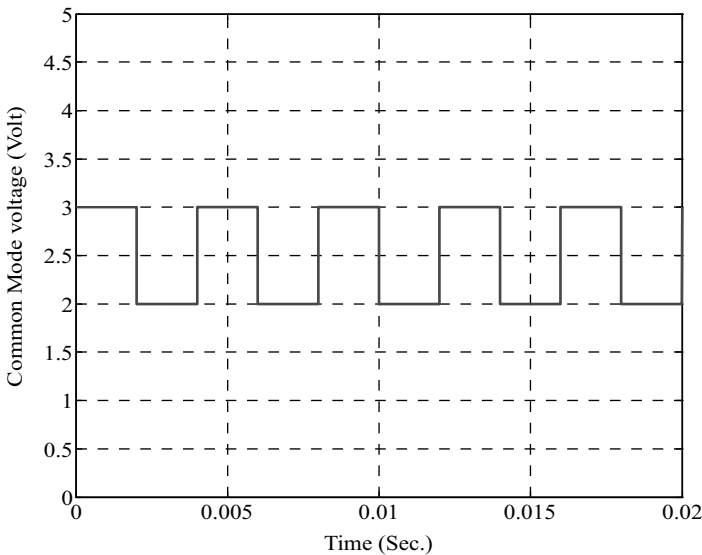


**Figure 7.33** Common mode voltage of Problem 7.4

(states 31 and 32); and the remaining states with three switches from the upper (lower) half and two switches from the lower (upper) half are in conduction mode (states 21–30). When all the upper or lower switches are ‘ON,’ they lead to zero output voltage and are termed as ‘zero states,’ similar to a three-phase VSI (Chapter 3). The remaining combination of switching states is termed ‘active states,’ as they lead to positive or negative output voltages. Phase-to-neutral voltages in these 22 switching states are listed in Table 7.6.

In order to introduce space vector representation of the five-phase inverter output voltages, an ideal sinusoidal five-phase supply source is considered. Let the phase voltages of a five-phase pure balanced sinusoidal supply be given with

$$\begin{aligned}
 v_a &= \sqrt{2}V\cos(\omega t) \\
 v_b &= \sqrt{2}V\cos(\omega t - 2\pi/5) \\
 v_c &= \sqrt{2}V\cos(\omega t - 4\pi/5) \\
 v_d &= \sqrt{2}V\cos(\omega t + 4\pi/5) \\
 v_e &= \sqrt{2}V\cos(\omega t + 2\pi/5)
 \end{aligned} \tag{7.41}$$

Since a five-phase system is under consideration, the vector needs to be analyzed in a five-dimensional space. Decoupling transformation leads to two orthogonal planes, namely  $dq$ ,  $xy$ ,

**Table 7.6** Phase-to-neutral voltage for PWM operation of five-phase VSI

State	Switches ON	$v_a$	$v_b$	$v_c$	$v_d$	$v_e$
11	$S_1, S_4', S_2', S_3'$	$4/5 V_{DC}$	$-1/5 V_{DC}$	$-1/5 V_{DC}$	$-1/5 V_{DC}$	$-1/5 V_{DC}$
12	$S_1, S_4', S_2, S_3, S_5$	$1/5 V_{DC}$	$1/5 V_{DC}$	$1/5 V_{DC}$	$-4/5 V_{DC}$	$1/5 V_{DC}$
13	$S_4'S_2, S_5', S_1', S_3'$	$-1/5 V_{DC}$	$4/5 V_{DC}$	$-1/5 V_{DC}$	$-1/5 V_{DC}$	$-1/5 V_{DC}$
14	$S_1, S_2, S_5', S_3, S_4$	$1/5 V_{DC}$	$1/5 V_{DC}$	$1/5 V_{DC}$	$1/5 V_{DC}$	$-4/5 V_{DC}$
15	$S_4', S_5', S_3, S_1', S_2'$	$-1/5 V_{DC}$	$-1/5 V_{DC}$	$4/5 V_{DC}$	$-1/5 V_{DC}$	$-1/5 V_{DC}$
16	$S_2, S_3, S_1', S_4, S_5$	$-4/5 V_{DC}$	$1/5 V_{DC}$	$1/5 V_{DC}$	$1/5 V_{DC}$	$1/5 V_{DC}$
17	$S_5', S_1', S_4, S_2', S_3'$	$-1/5 V_{DC}$	$-1/5 V_{DC}$	$-1/5 V_{DC}$	$4/5 V_{DC}$	$-1/5 V_{DC}$
18	$S_1, S_3, S_4, S_2', S_5$	$1/5 V_{DC}$	$-4/5 V_{DC}$	$1/5 V_{DC}$	$1/5 V_{DC}$	$1/5 V_{DC}$
19	$S_4', S_1', S_2', S_5, S_3'$	$-1/5 V_{DC}$	$-1/5 V_{DC}$	$-1/5 V_{DC}$	$-1/5 V_{DC}$	$4/5 V_{DC}$
20	$S_1, S_2, S_4, S_5, S_3'$	$1/5 V_{DC}$	$1/5 V_{DC}$	$-4/5 V_{DC}$	$1/5 V_{DC}$	$1/5 V_{DC}$
21	$S_4', S_2, S_1', S_5, S_3'$	$-2/5 V_{DC}$	$3/5 V_{DC}$	$-2/5 V_{DC}$	$-2/5 V_{DC}$	$3/5 V_{DC}$
22	1,3,4,7,10	$2/5 V_{DC}$	$2/5 V_{DC}$	$-3/5 V_{DC}$	$2/5 V_{DC}$	$-3/5 V_{DC}$
23	1,2,4,5,8	$3/5 V_{DC}$	$-2/5 V_{DC}$	$3/5 V_{DC}$	$-2/5 V_{DC}$	$-2/5 V_{DC}$
24	2,3,5,6,9	$-3/5 V_{DC}$	$2/5 V_{DC}$	$2/5 V_{DC}$	$-3/5 V_{DC}$	$2/5 V_{DC}$
25	3,4,6,7,10	$-2/5 V_{DC}$	$3/5 V_{DC}$	$-2/5 V_{DC}$	$3/5 V_{DC}$	$-2/5 V_{DC}$
26	1,4,5,7,8	$3/5 V_{DC}$	$-2/5 V_{DC}$	$3/5 V_{DC}$	$3/5 V_{DC}$	$-2/5 V_{DC}$
27	2,5,6,8,9	$-2/5 V_{DC}$	$-2/5 V_{DC}$	$3/5 V_{DC}$	$-2/5 V_{DC}$	$3/5 V_{DC}$
28	3,6,7,9,10	$-3/5 V_{DC}$	$2/5 V_{DC}$	$-3/5 V_{DC}$	$2/5 V_{DC}$	$2/5 V_{DC}$
29	1,2,4,7,8	$3/5 V_{DC}$	$-2/5 V_{DC}$	$-2/5 V_{DC}$	$3/5 V_{DC}$	$-2/5 V_{DC}$
30	1,2,5,8,9	$2/5 V_{DC}$	$-3/5 V_{DC}$	$2/5 V_{DC}$	$-3/5 V_{DC}$	$2/5 V_{DC}$

and a zero sequence component. The space vectors in the two orthogonal planes are defined as

$$\begin{aligned} \underline{v}_{\alpha-\beta} &= \frac{2}{5}(v_a + \underline{a}v_b + \underline{a}^2v_b + \underline{a}^4v_d + \underline{a}^6v_e) \\ \underline{v}_{xy} &= \frac{2}{5}(v_a + \underline{a}^2v_b + \underline{a}^4v_b + \underline{a}^8v_d + \underline{a}^{12}v_e) \end{aligned} \quad (7.42)$$

where  $\underline{a} = \exp(j2\pi/5)$ ,  $\underline{a}^2 = \exp(j4\pi/5)$ ,  $\underline{a}^n = \exp(jn\pi/5)$ .

The space vector is a complex quantity, which represents the five-phase balanced supply with a single complex variable. Substituting equation (7.42) into equation (7.41) yields an ideal sinusoidal source, the space vector:

$$\underline{v} = V \exp(j\omega t) \quad (7.43)$$

The space vector model of a five-phase voltage source inverter can be obtained by substituting the phase voltages in equation (7.42) and determining the corresponding space vectors in the  $\alpha$ - $\beta$  and  $x$ - $y$  planes, as given in Table 7.7.

Thus, it can be seen that the total of 32 space vectors, available in the PWM operation, fall into four distinct categories (three active lengths and one zero length) regarding the magnitude of the available output phase voltage. The phase voltage space vectors are summarised in Table 7.7. The ratio of phase voltage space vector magnitudes is 1:1.618:(1.618)<sup>2</sup>, from the smallest to the largest, respectively. All these vectors form ten sectors of 36 degrees each and one decagon. The mapping of the  $\alpha$ - $\beta$  plane vectors in the  $x$ - $y$  plane are such that the largest length vectors of  $\alpha$ - $\beta$  become the smallest length vectors of the  $x$ - $y$  plane and vice-versa. The medium vectors remain the same in both planes. Moreover, the  $x$ - $y$  plane vectors are the 3rd harmonic of the fundamental, as shown in Figures 7.34 and 7.35. These  $x$ - $y$  vectors produce losses in the system if remaining unattenuated. Thus, while developing PWM techniques, it is necessary to reduce or eliminate completely the  $x$ - $y$  components to yield sinusoidal output voltages.

### 7.3.3 PWM Schemes of a Five-Phase VSI

This section describes PWM schemes for a five-phase voltage source inverter. PWM techniques are the most basic method of energy processing in a power converter. The purpose is to obtain variable voltage and variable frequency voltages/currents at the output of the inverter. The basic idea is to modulate the pulse widths in order to alter the mean value of the voltages/currents. Several PWM schemes are developed in the literature for a five-phase VSI [6–16]; however, this chapter focuses only on the simple approaches that are extension of three-phase PWM. The popular and simple PWM schemes are elaborated on in the next sub-section, along with the MATLAB/Simulink model.

#### 7.3.3.1 Carrier-Based Sinusoidal PWM Scheme

Carrier-based sinusoidal PWM is the most popular and widely used PWM technique, because of its simple implementation in both analog and digital realization [54,55]. The principle of carrier-based PWM true for a three-phase VSI is also applicable to a multi-phase VSI.

**Table 7.7** Space vector table of phase voltages for a five-phase VSI

S. No.	Switching States	Space vectors in $\alpha$ - $\beta$ plane	Space vector in $x$ - $y$ plane
0	0 0 0 0 0	0	0
1	0 0 0 0 1	$2/5V_{DC}2\exp(j8\pi/5)$	$2/5V_{DC}2\exp(j6\pi/5)$
2	0 0 0 1 0	$2/5V_{DC}2\exp(j6\pi/5)$	$2/5V_{DC}2\exp(j2\pi/5)$
3	0 0 0 1 1	$2/5V_{DC}2\cos(\pi/5)\exp(j7\pi/5)$	$2/5V_{DC}4\cos(2\pi/5)\exp(j4\pi/5)$
4	0 0 1 0 0	$2/5V_{DC}2\exp(j4\pi/5)$	$2/5V_{DC}2\exp(j8\pi/5)$
5	0 0 1 0 1	$2/5V_{DC}4\cos(2\pi/5)\exp(j6\pi/5)$	$2/5V_{DC}2\cos(\pi/5)\exp(j7\pi/5)$
6	0 0 1 1 0	$2/5V_{DC}2\cos(\pi/5)\exp(j\pi)$	$2/5V_{DC}4\cos(2\pi/5)\exp(0)$
7	0 0 1 1 1	$2/5V_{DC}2\cos(\pi/5)\exp(j6\pi/5)$	$2/5V_{DC}4\cos(2\pi/5)\exp(j7\pi/5)$
8	0 1 0 0 0	$2/5V_{DC}2\exp(j2\pi/5)$	$2/5V_{DC}2\exp(j4\pi/5)$
9	0 1 0 0 1	$2/5V_{DC}4\cos(2\pi/5)\exp(0)$	$2/5V_{DC}2\cos(\pi/5)\exp(j\pi)$
10	0 1 0 1 0	$2/5V_{DC}4\cos(2\pi/5)\exp(j4\pi/5)$	$2/5V_{DC}2\cos(\pi/5)\exp(j3\pi/5)$
11	0 1 0 1 1	$2/5V_{DC}4\cos(2\pi/5)\exp(j7\pi/5)$	$2/5V_{DC}2\cos(\pi/5)\exp(j4\pi/5)$
12	0 1 1 0 0	$2/5V_{DC}2\cos(\pi/5)\exp(j3\pi/5)$	$2/5V_{DC}4\cos(2\pi/5)\exp(j6\pi/5)$
13	0 1 1 0 1	$2/5V_{DC}4\cos(2\pi/5)\exp(j3\pi/5)$	$2/5V_{DC}2\cos(\pi/5)\exp(j6\pi/5)$
14	0 1 1 1 0	$2/5V_{DC}2\cos(\pi/5)\exp(j4\pi/5)$	$2/5V_{DC}4\cos(2\pi/5)\exp(j3\pi/5)$
15	0 1 1 1 1	$2/5V_{DC}2\exp(j\pi)$	$2/5V_{DC}2\exp(j\pi)$
16	1 0 0 0 0	$2/5V_{DC}2\exp(j0)$	$2/5V_{DC}2\exp(j0)$
17	1 0 0 0 1	$2/5V_{DC}2\cos(\pi/5)\exp(j9\pi/5)$	$2/5V_{DC}4\cos(2\pi/5)\exp(j8\pi/5)$
18	1 0 0 1 0	$2/5V_{DC}4\cos(2\pi/5)\exp(j8\pi/5)$	$2/5V_{DC}2\cos(\pi/5)\exp(j\pi/5)$
19	1 0 0 1 1	$2/5V_{DC}2\cos(\pi/5)\exp(j7\pi/5)$	$2/5V_{DC}4\cos(2\pi/5)\exp(j\pi/5)$
20	1 0 1 0 0	$2/5V_{DC}4\cos(2\pi/5)\exp(j2\pi/5)$	$2/5V_{DC}2\cos(\pi/5)\exp(j9\pi/5)$
21	1 0 1 0 1	$2/5V_{DC}4\cos(2\pi/5)\exp(j9\pi/5)$	$2/5V_{DC}2\cos(\pi/5)\exp(j7\pi/5)$
22	1 0 1 1 0	$2/5V_{DC}4\cos(2\pi/5)\exp(j\pi)$	$2/5V_{DC}2\cos(\pi/5)\exp(j0)$
23	1 0 1 1 1	$2/5V_{DC}2\exp(j7\pi/5)$	$2/5V_{DC}2\exp(j9\pi/5)$
24	1 1 0 0 0	$2/5V_{DC}2\cos(\pi/5)\exp(j\pi/5)$	$2/5V_{DC}4\cos(2\pi/5)\exp(j2\pi/5)$
25	1 1 0 0 1	$2/5V_{DC}2\cos(\pi/5)\exp(j0)$	$2/5V_{DC}4\cos(2\pi/5)\exp(j\pi)$
26	1 1 0 1 0	$2/5V_{DC}4\cos(2\pi/5)\exp(j\pi/5)$	$2/5V_{DC}2\cos(\pi/5)\exp(j2\pi/5)$
27	1 1 0 1 1	$2/5V_{DC}2\exp(j9\pi/5)$	$2/5V_{DC}2\exp(j3\pi/5)$
28	1 1 1 0 0	$2/5V_{DC}2\cos(\pi/5)\exp(j2\pi/5)$	$2/5V_{DC}4\cos(2\pi/5)\exp(j9\pi/5)$
29	1 1 1 0 1	$2/5V_{DC}2\exp(j\pi/5)$	$2/5V_{DC}2\exp(j7\pi/5)$
30	1 1 1 1 0	$2/5V_{DC}2\exp(j3\pi/5)$	$2/5V_{DC}2\exp(j\pi/5)$
31	1 1 1 1 1	0	0

The PWM signal is generated by comparing a sinusoidal modulating signal with a triangular (double edge) or a saw-tooth (single edge) carrier signal. The frequency of the carrier is normally kept much higher compared to the modulating signal (10 to 12 times). The operation of a carrier-based PWM modulator is shown in Figure 7.36 and generation of a PWM waveform is illustrated in Figure 7.37. The reference voltage signals or modulating signals are compared with the high frequency carrier and the pulses are formed at the intersection of the modulation signals, which are five-phase fundamental sinusoidal signals (displaced in time by  $\alpha = 2\pi/5$ ). These modulation signals are compared with a high frequency carrier signal (saw-tooth or

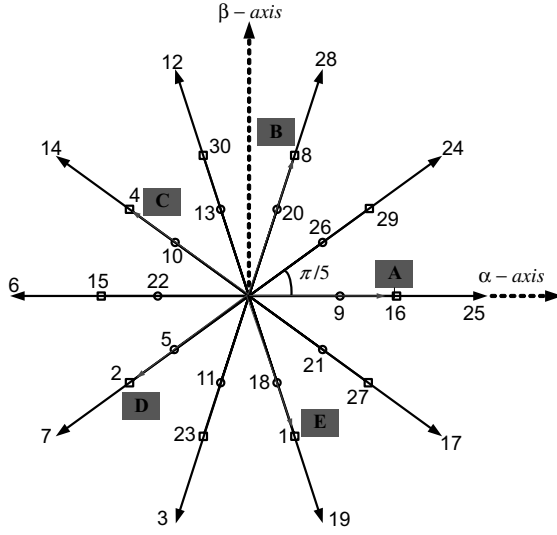


Figure 7.34 Phase voltage space vector  $\alpha$ - $\beta$  plane

triangular shape) and all five switching functions for inverter legs are obtained directly. In general, modulation signal can be expressed as

$$v_i(t) = v_i^*(t) + v_{mN}(t) \tag{7.44}$$

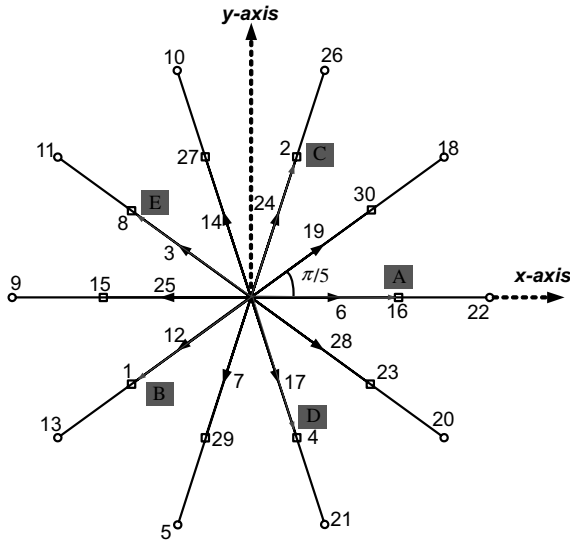


Figure 7.35 Phase voltage space vectors in  $x$ - $y$  plane

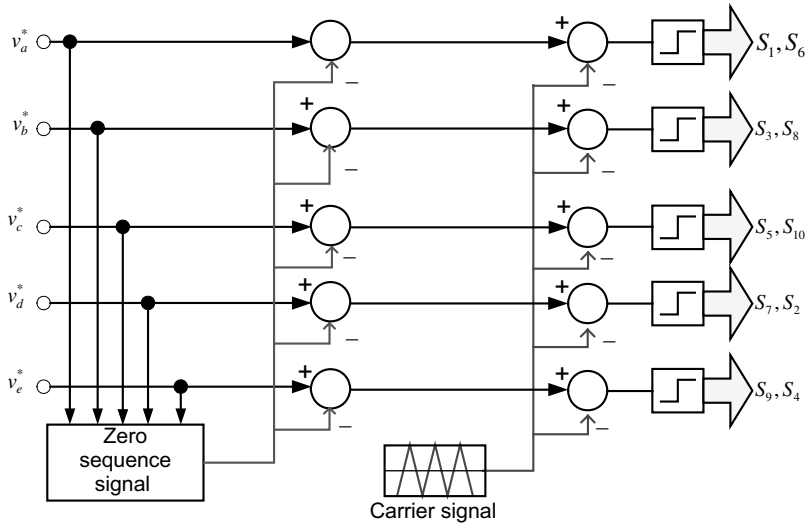


Figure 7.36 Principle of carrier-based PWM technique for a five-phase VSI

where  $i = a, b, c, d, e$  and  $v_{nN}$  represents zero-sequence signal and  $v_i^*$  are fundamental sinusoidal signals. Zero-sequence signal represents a degree of freedom that exists in the structure of a carrier-based modulator and is used to modify modulation signal waveforms and thus to obtain different modulation schemes. Continuous PWM schemes result, as long as the peak value of the modulation signal does not exceed the carrier magnitude. If the modulating signals peak exceeds the height of the carrier signals, it is termed a carrier dropping mode and leads to over-modulation.

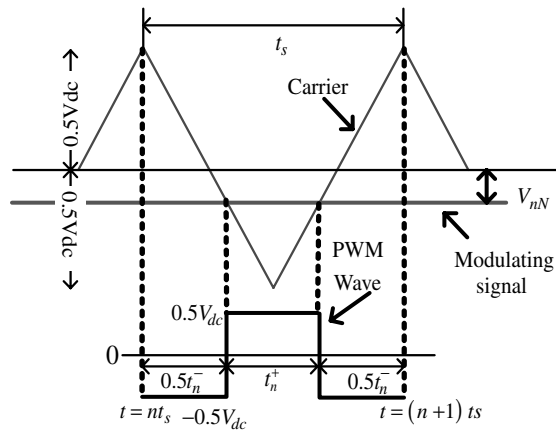


Figure 7.37 PWM waveform generation in carrier-based sinusoidal method

The following relationship holds true in Figure 7.37:

$$t_n^+ - t_n^- = v_n t_s \quad (7.45a)$$

where

$$t_n^+ = \left( \frac{1}{2} + v_n \right) t_s \quad (7.45b)$$

$$t_n^- = \left( \frac{1}{2} - v_n \right) t_s \quad (7.45c)$$

where  $t_n^+$  and  $t_n^-$  are the positive and negative pulse widths in the  $n$ th sampling interval, respectively, and  $v_n$  is the normalized amplitude of modulation signal. The normalization is done with respect to  $V_{dc}$ . Equation (7.37) is referred as the Equal volt-second principle, as applied to a three-phase inverter [54,55]. The normalized peak value of the triangular carrier wave is  $\pm 0.5$  in linear region of operation. Modulator gain has the unity value while operating in the linear region and the peak value of inverter output fundamental voltage is equal to the peak value of the fundamental sinusoidal signal. Thus the maximum output phase voltages from a five-phase VSI are limited to 0.5 p.u. Thus the output phase voltage from a three-phase and a five-phase VSI are the same when using carrier-based PWM [56].

### 7.3.3.2 MATLAB/Simulink Simulation of Carrier-Based Sinusoidal PWM

Developing the Simulink model, assuming an ideal DC bus and ideal inverter model, is very simple. It follows exactly Figures 7.36 and 7.37. The inverter can either be modeled using the actual IGBT switches from the ‘sim-power system’ block-sets or by using equation (7.23). The complete simulink model is shown in Figure 7.38, where equation (7.23) is used to model the inverter.

The five-phase sinusoidal source is generated from the ‘sin wave’ block from the ‘source’ sub-library, and the phase shifts are created by substituting appropriate phase differences in the ‘phase (rad)’ dialog box. The triangular carrier signal is generated using the ‘repetitive’ block from the ‘source’ sub-library. The switching frequency is kept at 5 kHz, the DC link voltage is assumed as 1, and the fundamental output frequency is assumed as 50 Hz. The resulting waveforms are presented in Figures 7.36 and 7.40. The output voltage magnitude is limited to 0.5 p.u. (typically it the same value as that of three-phase VSI), as evident from Figure 7.40 (spectrum). The filtered output voltages are also depicted to show their sinusoidal nature.

### 7.3.3.3 5th Harmonic Injection Based Pulse Width Modulation Scheme

The effect of addition of a harmonic with reverse polarity in any signal is to reduce the peak of the signal. The aim here is to bring the amplitude of the reference or modulating signal as low as possible, so that the reference can then be pushed to make it equal to the carrier, resulting in the higher output voltage and better DC bus utilization. Using this principle, 3rd-harmonic injection PWM scheme is used in a three-phase VSI, which results in an increase in the fundamental output voltage to  $0.575 V_{dc}$ , as discussed in Chapter 3. Third-harmonic voltages do not appear in the output phase voltages and are restricted to the leg voltages. Following the



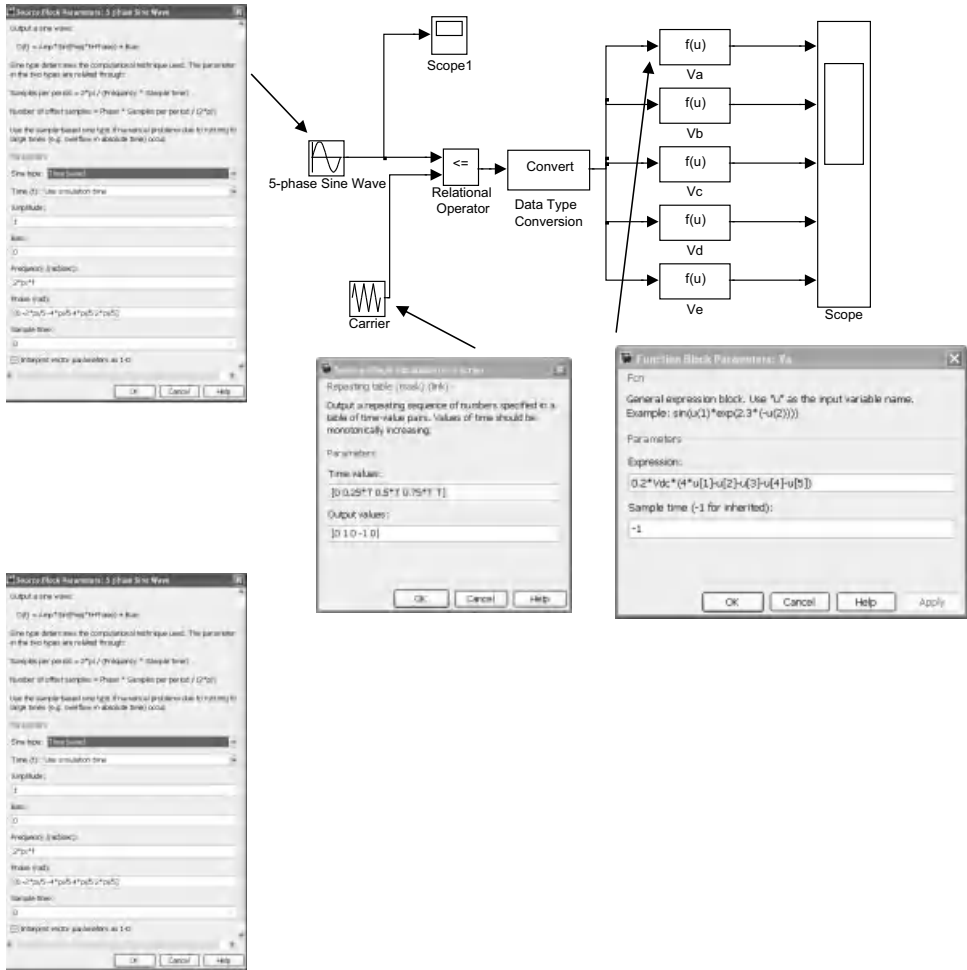


**Figure 7.38** Simulink for implementing carrier-based PWM (File Name: *Carrier\_PWM\_5\_phase\_VSI.mdl*)

same principle, 5th-harmonic injection PWM scheme is used to increase the modulation index of a five-phase VSI [57].

The reference leg voltages or modulating signals are given as

$$\begin{aligned}
 V_{ao}^* &= 0.5M_1 V_{dc} \cos(\omega t) + 0.5M_5 V_{dc} \cos(5\omega t) \\
 V_{bo}^* &= 0.5M_1 V_{dc} \cos(\omega t - 2\pi/5) + 0.5M_5 V_{dc} \cos(5\omega t) \\
 V_{co}^* &= 0.5M_1 V_{dc} \cos(\omega t - 4\pi/5) + 0.5M_5 V_{dc} \cos(5\omega t) \\
 V_{do}^* &= 0.5M_1 V_{dc} \cos(\omega t + 4\pi/5) + 0.5M_5 V_{dc} \cos(5\omega t) \\
 V_{eo}^* &= 0.5M_1 V_{dc} \cos(\omega t + 2\pi/5) + 0.5M_5 V_{dc} \cos(5\omega t)
 \end{aligned}
 \tag{7.46}$$

Here,  $M_1$  and  $M_5$  are the peaks of the fundamental and 5th harmonic, respectively. It is to be noted that the 5th harmonic has no effect on the value of the reference waveform when

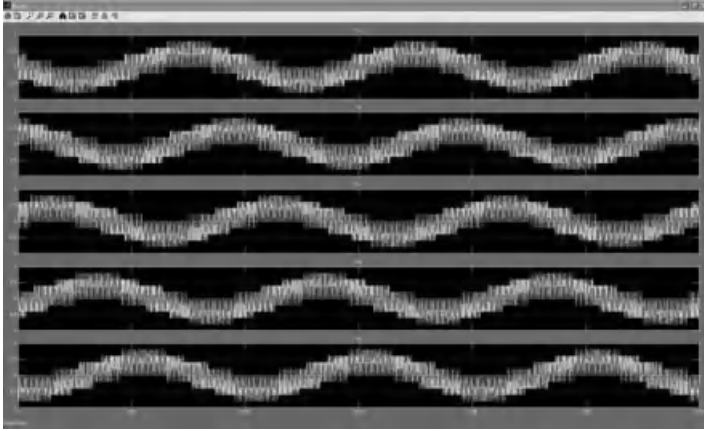


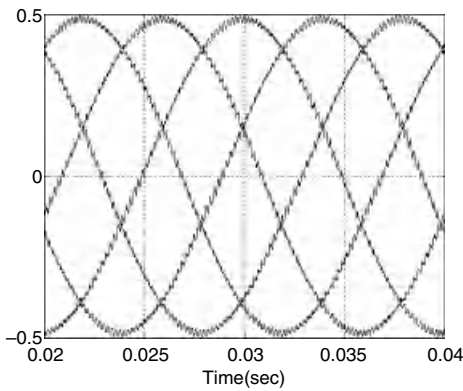
**Figure 7.39** Output phase voltages from carrier-based PWM scheme

$\omega t = (2k + 1)\pi/10$ , since  $\cos(5(2k + 1)\pi/10) = 0$  for all odd  $k$ . Thus  $M_5$  is chosen to make the peak magnitude of the reference of equation (7.46) occur where the 5th harmonic is zero. This ensures the maximum possible value of the fundamental component. The reference voltage reaches a maximum when

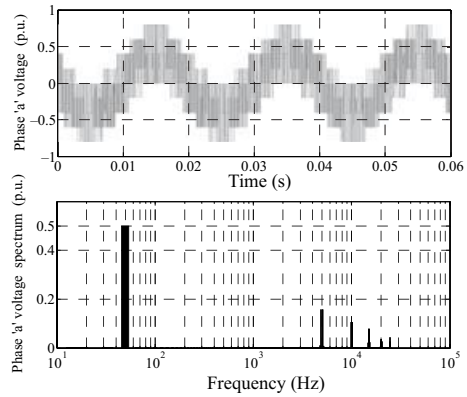
$$\frac{dV_{ao}^*}{dt} = -0.5M_1V_{dc}\sin\omega t - 0.5 \cdot 5M_5V_{dc}\sin 5\omega t = 0 \tag{7.47}$$

This yields:

$$M_5 = -M_1 \frac{\sin(\pi/10)}{5}; \quad \text{for } \omega t = \pi/10 \tag{7.48}$$



(a) Filtered output voltage



(b) Harmonic spectrum phase 'a' voltage

**Figure 7.40** Simulation results of the carrier based PWM scheme

Thus the maximum modulation index can be determined from

$$|V_{ao}^*| = \left| 0.5M_1V_{dc}\cos(\omega t) - 0.5\frac{\sin(\pi/10)}{5}M_1V_{dc}\cos(3\omega t) \right| = 0.5V_{dc} \quad (7.49)$$

The above equation gives

$$M_1 = \frac{1}{\cos(\pi/10)}; \quad \text{for } \omega t = \pi/10 \quad (7.50)$$

Thus the output fundamental voltage is increased to 5.15% higher than the value obtained using simple carrier-based PWM by injecting 6.18% 5th harmonic into the fundamental voltage. The output now reaches  $0.5257V_{dc}$ . The 5th harmonic is in opposite phase to that of the fundamental voltage. The effect of adding 5th harmonic in the sinusoidal reference is illustrated with the help of Figure 7.41. When 5th harmonic =  $0.0618^*$  fundamental voltage is injected into the sinusoidal reference, the modified signal's peak reduces, and its shape changes (Figure 7.41), providing more room for enhancing the reference and subsequently increasing the output of the inverter.

#### 7.3.3.4 MATLAB/Simulink Simulation of 5th Harmonic Injection PWM

The Simulink model for this PWM scheme is similar to the carrier-based PWM, except the generation of the modulating signal. In the five-phase reference signals, a 5th harmonic of 0.0618 p.u. is subtracted forming the resultant modulating or reference signal. The modified modulating signals are then compared with the high frequency carrier signal to generate the gating pulses, which are then given to the inverter model. The complete Simulink model is given in Figure 7.42. For the same simulation conditions as that of carrier-based PWM, the

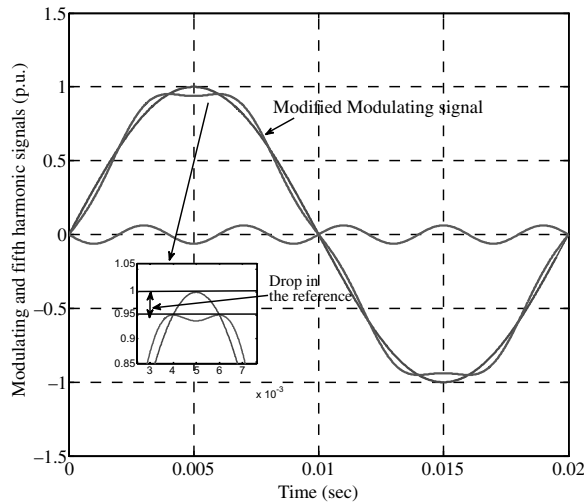


**Figure 7.41** 5th-harmonic injection PWM

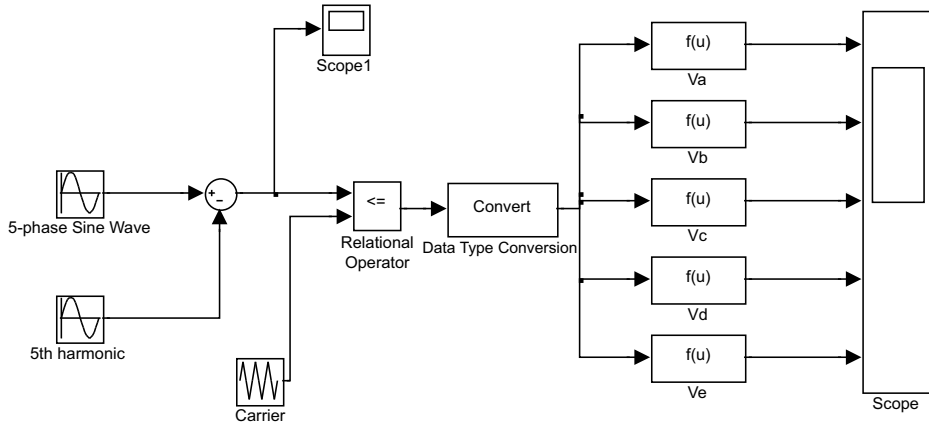


**Figure 7.42** Simulink model for 5th-harmonic injection PWM scheme (File Name: Carrier\_PWM\_5<sup>th</sup>\_harmonic\_5\_phase\_VSI.mdl)

output PWM voltage waveforms look similar to those in Figure 7.39 and so are not shown here. The filtered inverter output voltages and the spectrum of phase ‘a’ are presented in Figure 7.43 for the reference of 1.0515 p.u. The output voltage now increases to 0.5257  $V_{dc}$  without going into pulse dropping mode.

**7.3.3.5 Offset Addition Based Pulse Width Modulation Scheme**

Another way of increasing the modulation indices is to add an offset voltage to the references. The offset voltage addition is effectively adding  $3n$  ( $n = 1, 2, \dots$ ) harmonic in a three-phase

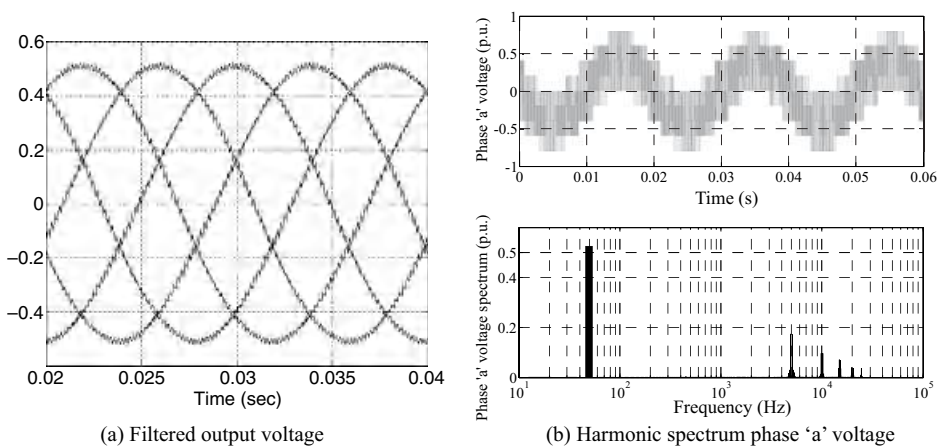


**Figure 7.43** Simulation results of the 5th harmonic injection based PWM scheme

case and  $5n$  ( $n = 1, 2, \dots$ ) in a five-phase case. This will effectively perform the same function as above. The offset voltage is given as

$$V_{offset} = -\frac{V_{max} + V_{min}}{2} \tag{7.51}$$

where  $v_{max} = \max(v_a, v_b, v_c, v_d, v_e)$  and  $v_{min} = \min(v_a, v_b, v_c, v_d, v_e)$ . Note that this is the same as for a three-phase inverter. In a five-phase VSI, the offset is found as the 5th-harmonic triangular wave of magnitude 9.55% of the fundamental input reference. This peak value has been established by simulations approach. Offset addition requires only addition operation and hence is suitable for practical implementation.

A generalized formula of offset voltage, which is to be injected along with the fundamental voltage in the case of five-phase VSI, is [58]

$$V_{no} = -0.5528(V_{max} - V_{min}) + 3/5(1 - 2\mu)V_{DC}/2 - 3/5(1 - 2\mu)(V_{max} - V_{min}) \tag{7.52}$$

where  $V_{max}$  is the maximum of the five-phase references;  $V_{min}$  is the minimum of the five-phase references; and  $\mu$  is the factor that decides the placement of the two zero vector states. If it is 0.5, then the two zero states are placed equally and this corresponds to symmetrical zero vector placement and conventional SVPWM. The modulating signal with and without offset addition and offset signals are shown in Figure 7.44. The reduction in the modified modulating signal is evident. The modulating signal can now be increased further to a yield higher output voltage by the inverter.

The Simulink model is shown in Figure 7.45. The simulation results are not shown for the offset addition method, as the nature remains the same as that of the 5th-harmonic injection method, except for improved switching harmonics.

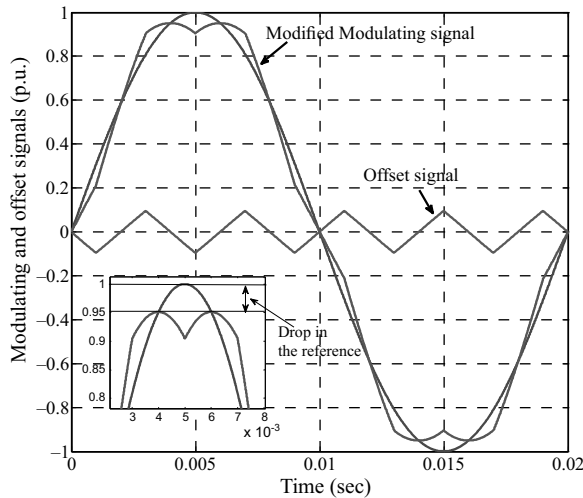


**Figure 7.44** Offset addition-based PWM

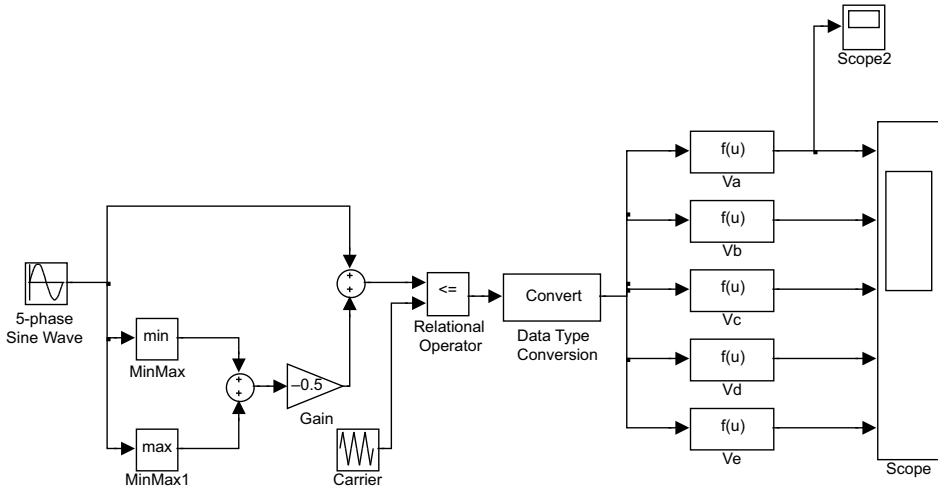


**Figure 7.45** Simulink model of offset addition based PWM (File Name: *Carrier\_PWM\_offset\_5\_phase\_VSI.mdl*)

### 7.3.3.6 Space Vector Pulse Width Modulation Scheme

SVPWM has become one of the most popular PWM techniques, because of its easier digital implementation and better DC bus utilization, when compared to the carrier-based sinusoidal PWM method. The principle of SVPWM lies in the switching of the inverter in a special way, so as to apply a set of space vectors for a specific time. As seen in the previous section, a five-phase VSI yields 32 space vectors spanning over 360 degrees, forming a decagon with 10 sectors of 36 degrees each. The reference voltage is synthesized by switching between the neighboring vectors, such that the volt-second balance is maintained. As seen in Chapter 3, two neighboring active vectors are employed to implement SVPWM, thus as an extension in a five-phase VSI, also two neighboring active space vector can be used. However, the next section shows that simple extension of SVPWM leads to distortion in the output voltage. Hence, it is realized that instead of two, four neighboring vectors when used to implement SVPWM will lead to sinusoidal output voltages. As a rule of thumb,  $n - 1$  ( $n$  phase number) numbers of active space vectors are needed to generate sinusoidal output in multi-phase voltage source inverters.

Thus there exists more than one method of implementing SVPWM in a multi-phase voltage source inverter. Nevertheless, an ideal SVPWM of a five-phase inverter should satisfy a number of requirements. First, in order to keep the switching frequency constant, each switch can change state only twice in the switching-period (once 'ON' to 'OFF' and once 'OFF' to 'ON', or vice-versa). Second, the rms value of the fundamental phase voltage of the output must equal the rms of the reference space vector. Third, the scheme must provide full utilization of the available DC bus voltage. Finally, since the inverter is aimed at supplying the load with sinusoidal voltages, the low-order harmonic content needs to be minimized (this especially applies to the 3rd and 7th harmonics). These criteria are used in assessing the merits and demerits of various SVPWMs. Two methods are elaborated here, one with two active space vectors and one with four active vectors.

In one case, two neighboring active space vectors and two zero space vectors are used in one switching period to synthesise the input reference voltage. There are five legs in a five-phase inverter, each with two power switches whose operations are complimentary. In one switching period, each power switch will change its state twice (from ‘OFF’ to ‘ON’ and then from ‘ON’ to ‘OFF’), hence in total, ten switchings take place in one switching period. The switching patterns are pre-formulated and stored in a look-up table. The switching is done in such a way that in the first switching half-period, the first zero vector is applied, followed by two active state vectors and then by the second zero state vector. The second switching half-period is the mirror image of the first. The symmetrical SVPWM is achieved in this way. This method is the simplest extension of space vector modulation of three-phase VSIs. The time of application of each active and zero space vector are obtained using the simple trigonometric relation considered in Figure 7.46.

Assuming the time of application of the right-hand side vector as  $t_a$  and the time of application of the left-hand side vector as  $t_b$ , and the time of application of zero space vector is  $t_o$  where the total switching period is  $t_s$ . From Figure 7.46, the following relation holds good:

$$\underline{v}_s^* t_s = \underline{v}_a t_a + \underline{v}_b t_b \tag{7.53}$$

In Cartesian form, this equation can be written as

$$|\underline{v}_s^*|(\cos(\alpha) + j \sin(\alpha))t_s = |\underline{v}_a|(\cos(0) + j \sin(0))t_a + |\underline{v}_b| \left( \cos\left(\frac{\pi}{5}\right) + j \sin\left(\frac{\pi}{5}\right) \right) t_b \tag{7.54}$$

Now equating the real and imaginary parts, the following relations are obtained:

$$t_a = \frac{|\underline{v}_s^*| \sin(k\pi/5 - \alpha)}{|\underline{v}_l| \sin(\pi/5)} t_s \tag{7.55a}$$

$$t_b = \frac{|\underline{v}_s^*| \sin(\alpha - (k - 1)\pi/5)}{|\underline{v}_l| \sin(\pi/5)} t_s \tag{7.55b}$$

$$t_o = t_s - t_a - t_b \tag{7.55c}$$

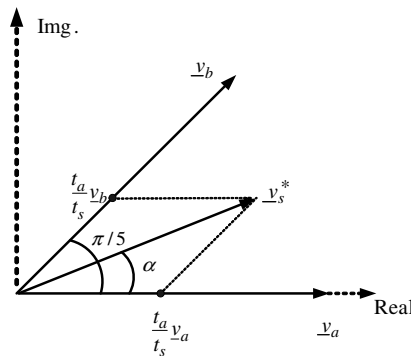
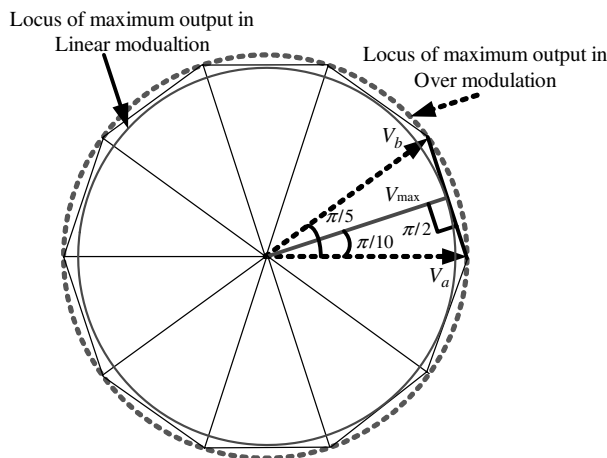


Figure 7.46 Principle of SVPWM for a five-phase VSI

Here  $k$  is the sector number ( $k = 1 - 10$ ), and large vector length is  $|v_{al}| = |v_{bl}| = |v_l| = \frac{2}{5}V_{DC} 2\cos(\pi/5)$ . The corresponding medium vector length, which will be needed in the subsequent expression, is  $|v_{am}| = |v_{bm}| = V_m = (2/5)V_{DC}$ . Symbol  $v_s^*$  denotes the reference space vector, while  $|x|$  is the modulus of a complex number  $x$ . The largest possible fundamental peak voltage magnitude that may be achieved using this scheme corresponds to the radius of the largest circle that can be inscribed within the decagon. The circle is tangential to the mid-point of the lines connecting the ends of the active space vectors, as shown in Figure 7.47. The trajectory of the output will follow the outermost circle if operating in the over-modulation region (not discussed here), and the trajectory will follow the inner circle when operating in maximum linear modulation. The trajectory will be along the decagon for the ten-step operation of the inverter. Thus the maximum fundamental peak output voltage  $V_{\max}$  is  $V_{\max} = |v_l|\cos(\pi/10)$ , and  $V_{\max} = (2/5)2\cos(\pi/5)\cos(\pi/10)V_{DC} = 0.61554V_{DC}$ . The maximum peak fundamental output in the ten-step mode is, from equation (7.29), given with  $V_{\max,10step} = \frac{2}{\pi}V_{DC}$ . Thus the ratio of the maximum possible fundamental output voltage with SVPWM and in the ten-step mode is  $V_{\max}/V_{\max,10step} = 0.96689$ .

The sequence of vectors applied in sectors I and II and corresponding switching patterns are shown in Figure 7.48, where states of five inverter legs take values of  $-1/2$  and  $1/2$  (referencing to the mid-point of the DC supply is applied) and the five traces illustrate, from top to bottom, legs A, B, C, D, and E, respectively. In odd sector numbers, the left-hand side (with respect to the reference) vector is applied first, followed by the right-hand side vector; while in even sectors, the right-hand side vector is applied first, followed by the left-hand side vector. For implementation of this scheme, these switching patterns are stored in a look-up table.

The above method leads to unwanted low-order harmonics in the output phase voltages of the inverter, as shown in the next section. The reason is the free flow of  $x$ - $y$  components. Application of two adjacent medium active space vectors, together with two large active space vectors in each switching period, makes it possible to maintain zero average values in the second plane ( $x$ - $y$ ) and consequently providing sinusoidal output. When using two large length



**Figure 7.47** Maximum possible output in SVPWM for a five-phase VSI



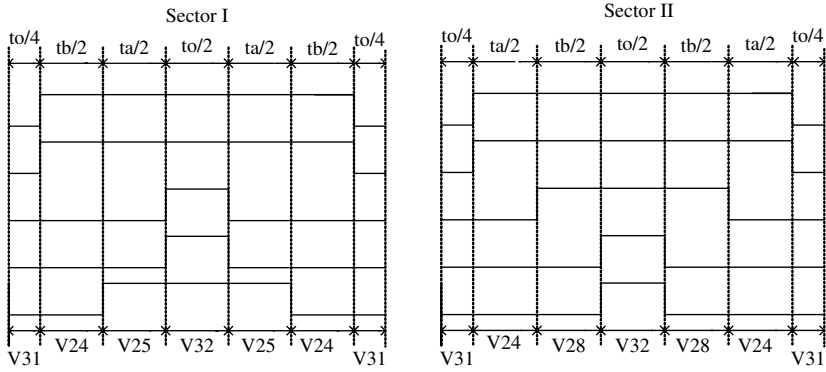


**Figure 7.48** Switching pattern for SVPWM using only two active vectors

and two medium length active vectors, their mapping in the  $x$ - $y$  plane is such that they cancel each other, as illustrated in Figure 7.49 for sector I and it follows for the rest of the sectors. Since vector numbers 16 and 25 are opposite to each other, and so are 24 and 29, their lengths are different (ratio of lengths of larger to smaller is 1.618). Thus if the time of application of the smaller vector is increased in the same proportion, they will have equal volt-second and will cancel each other, eliminating the  $x$ - $y$  components and generating sinusoidal output.

Use of four active space vectors per switching period requires the calculation of four application times, labeled here as  $t_{al}$ ,  $t_{bl}$ ,  $t_{am}$ ,  $t_{bm}$ . The expressions used for calculation of dwell times of various space vectors are [11]

$$\underline{v}_s^* t_s = \underline{v}_{al} t_{al} + \underline{v}_{bl} t_{bl} + \underline{v}_{am} t_{am} + \underline{v}_{bm} t_{bm}, \tag{7.56}$$

where

$$|\underline{v}_{al}| = |\underline{v}_{bl}| = |\underline{v}_l| = \frac{2}{5} V_{DC} 2 \cos(\pi/5) \tag{7.57a}$$

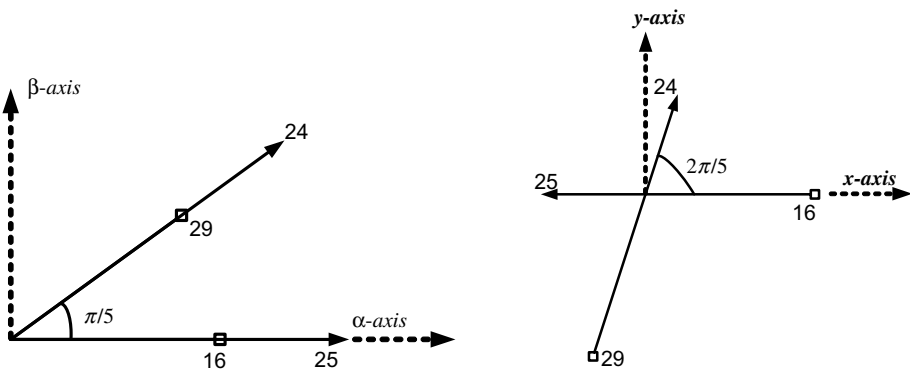


**Figure 7.49** Principle of SVPWM with four active vectors

$$|v_{am}| = |v_{bm}| = |v_m| = V_m = \frac{2}{5} V_{DC} \quad (7.57b)$$

and

$$\frac{t_{al}}{t_{am}} = \frac{t_{bl}}{t_{bm}} = \frac{|v_l|}{|v_m|} = \tau = 1.618 \quad (7.57c)$$

Separating the real and imaginary parts of equation (7.56) and substituting equation (7.57a), the following equations result:

$$t_{al} = \frac{|v_s^*|}{V_m \sin(\pi/5)} \left( \frac{\tau}{1 + \tau^2} \right) t_s \sin\left(\frac{\pi}{5}k - \alpha\right) \quad (7.58a)$$

$$t_{bl} = \frac{|v_s^*|}{V_m \sin(\pi/5)} \left( \frac{\tau}{1 + \tau^2} \right) t_s \sin\left(\alpha - (k-1)\frac{\pi}{5}\right) \quad (7.58b)$$

$$t_{am} = \frac{|v_s^*|}{V_m \sin(\pi/5)} \left( \frac{1}{1 + \tau^2} \right) t_s \sin\left(\frac{\pi}{5}k - \alpha\right) \quad (7.58c)$$

$$t_{bm} = \frac{|v_s^*|}{V_m \sin(\pi/5)} \left( \frac{1}{1 + \tau^2} \right) t_s \sin\left(\alpha - (k-1)\frac{\pi}{5}\right) \quad (7.58d)$$

$$t_0 = t_s - t_{al} - t_{bl} - t_{am} - t_{bm} \quad (7.58e)$$

where  $t_a = t_{al} + t_{am}$ ;  $t_b = t_{bl} + t_{bm}$ . This allocates 61.8% more dwell time to a large space vector compared to a medium space vector, thus satisfying the constraints of producing zero average voltage in the  $x$ - $y$  plane. The constraint imposed on the time of application of each vector is that they cannot be less than zero, and also the sum of time of application of active and zero vectors cannot exceed the switching time. With these constraints, the maximum possible output with this approach is  $0.5257 V_{DC}$ , which is almost 16% less than with the previous method. The switching patterns for the two sectors are shown in Figure 7.50. The switching pattern is a symmetrical PWM with two commutations per each inverter leg. The space vectors are applied in odd sectors using the sequence  $[v_{31}, v_{al}, v_{bm}, v_{am}, v_{bl}, v_{32}, v_{bl}, v_{am}, v_{bm}, v_{al}, v_{31}]$ , while the sequence is  $[v_{31}, v_{bl}, v_{am}, v_{bm}, v_{al}, v_{32}, v_{al}, v_{bm}, v_{am}, v_{bl}, v_{31}]$  in even sectors.

### 7.3.3.7 MATLAB/Simulink Model of SVPWM

The SVPWM can be developed in MATLAB/Simulink by using different approaches. The model presented here uses the Simulink and MATLAB function block. The MATLAB/Simulink model is presented in Figure 7.51. The five-phase voltage reference is generated using the 'sine wave' generator and then transformed into  $\alpha$ - $\beta$  and  $x$ - $y$  components. The reference space vector magnitude and angle is thus generated from the 'reference voltage generator' block. The magnitude is constant, while the angle changes from 0 to  $\pi$  and then  $-\pi$  to 0 as a sawtooth waveform. The angle is held for one sample time, so as to keep its value

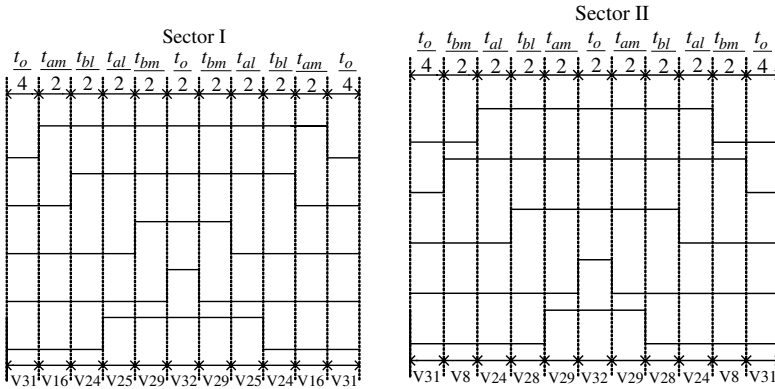


Figure 7.50 Switching pattern for SVPWM using four active vectors

constant during the calculation of times of application of vectors. Another repetitive signal (time [0 Ts], amplitude [0 Ts]) is used to compare with the angle to determine the location of the reference signal. The MATLAB function block contains the switching table and sector determination algorithm (given in the soft copy). The MATLAB function block outputs the switching functions and is given to the five-phase inverter model. The algorithm inside the MATLAB function block can be changed to implement two-vector or four-vector SVPWM. The inverter produces a space vector modulated voltage waveform that can be given to the five-phase load.

Simulation results are shown for two SVPWM techniques, using two active vectors (Figure 7.52) and using four active vectors (Figure 7.53). The fundamental frequency is kept at 50 Hz, the switching frequency is chosen as 5 kHz, the output is set at maximum value ( $0.6115 V_{dc}$  for two vectors case and  $0.5257 V_{dc}$  for four vectors case), and the DC link voltage

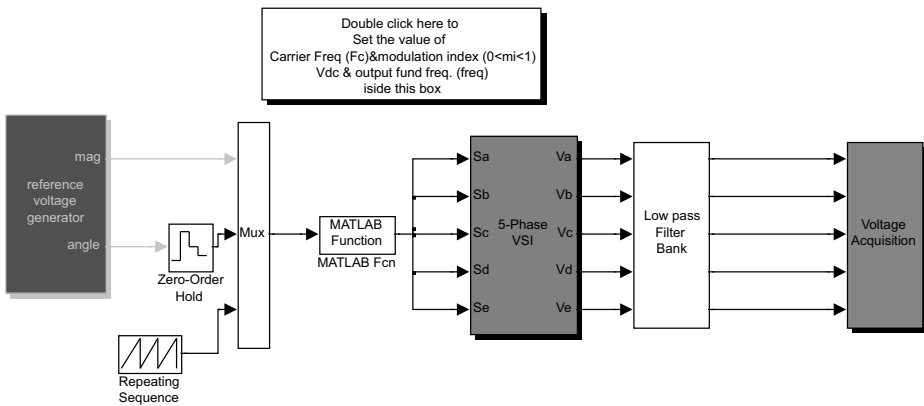
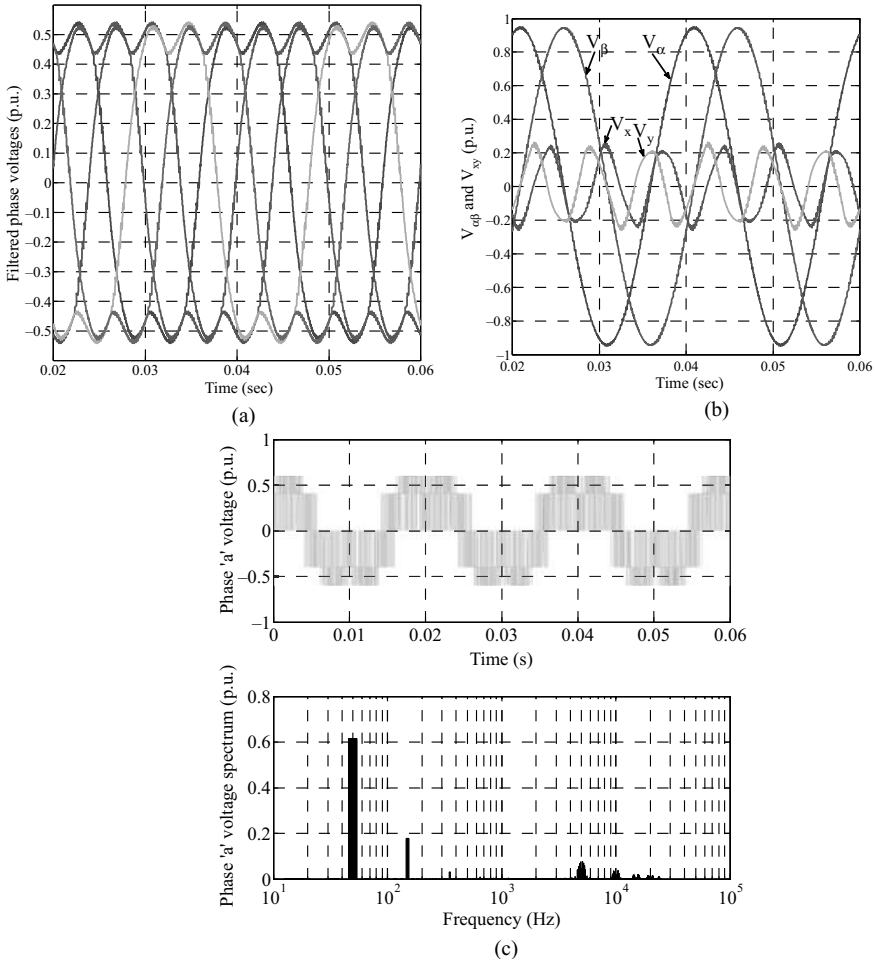


Figure 7.51 MATLAB/Simulink model for implementing SVPWM (File Name: Space5.mdl and Large5.m and SVM\_5\_sine.m)



**Figure 7.52** SVPWM simulation results for two active vectors: (a) phase voltages; (b)  $\alpha$ - $\beta$  and  $x$ - $y$  axes voltages; (c) phase ‘a’ voltage and its spectrum

$V_{dc}$  is set to 1 p.u. The output phase voltages are distorted if only two active vectors are employed for SVPWM. The distortion appears due to the presence of the  $x$ - $y$  plane vectors, as evident from Figure 7.52b. The phase voltages are completely sinusoidal when using four active vectors for the implementation of SVPWM. This is due to the fact that the  $x$ - $y$  components are completely eliminated.

### 7.4 Indirect Rotor Field Oriented Control of Five-Phase Induction Motor

Field oriented control refers to the control technique in which an induction machine emulates as a DC machine. The torque and flux producing currents are decoupled and controlled

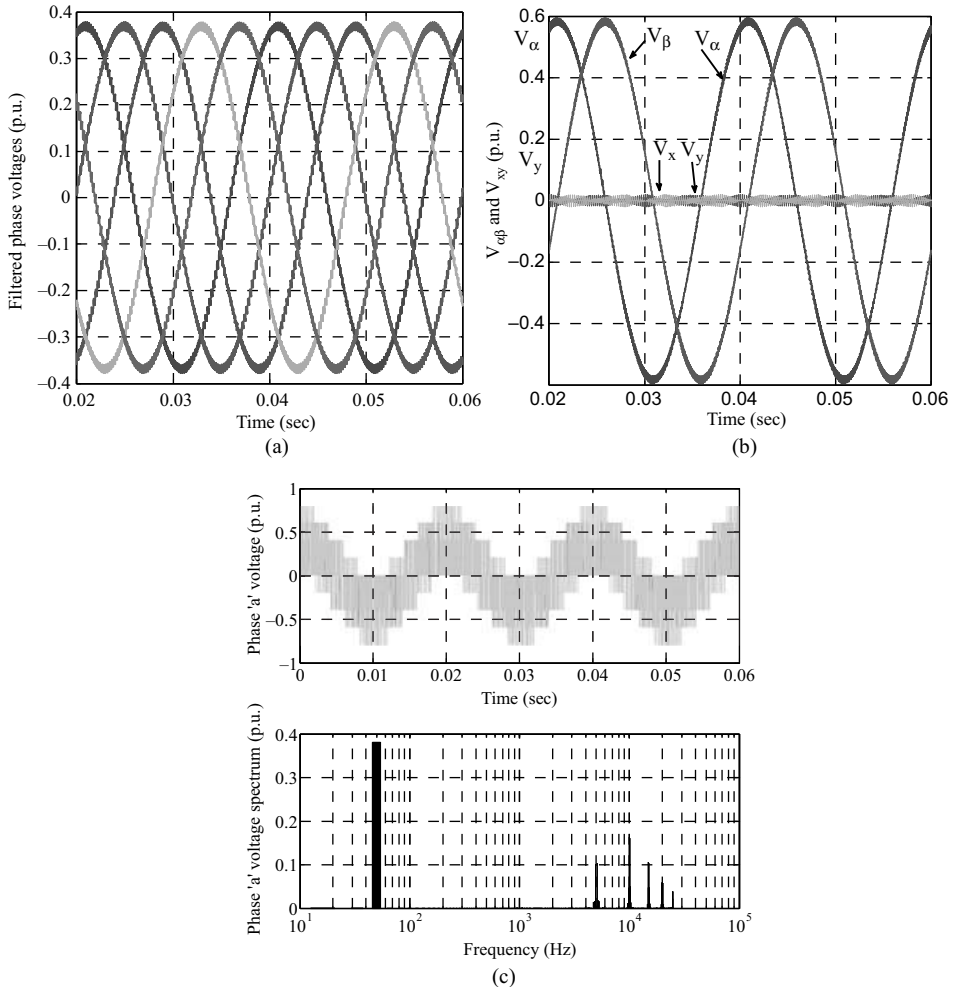


**Figure 7.53** SVPWM simulation results for four active vectors: (a) phase voltages; (b)  $\alpha$ - $\beta$  and  $x$ - $y$  axes voltages; and (c) phase 'a' voltage and its spectrum

independently, giving rise to fast dynamics of machine. This control technique is also called vector control, since the stator current space vector is controlled in this method. The detail description of field orientation and the vector control principle is discussed in Chapter 4. The purpose here is to distinguish between the control of a three-phase and a five-phase machine. Essentially, only two current components are required to produce torque in an induction machine, regardless of the phase number. In general, the  $d$ -axis current control of the flux in the machine is maintained constant for speed control in the base speed region and is reduced in appropriate proportion in the field weakening region (speed above the nominal or rated value). The  $q$ -axis current component controls the torque in the machine, since the  $d$ -axis current is kept constant (see equation (7.17)).

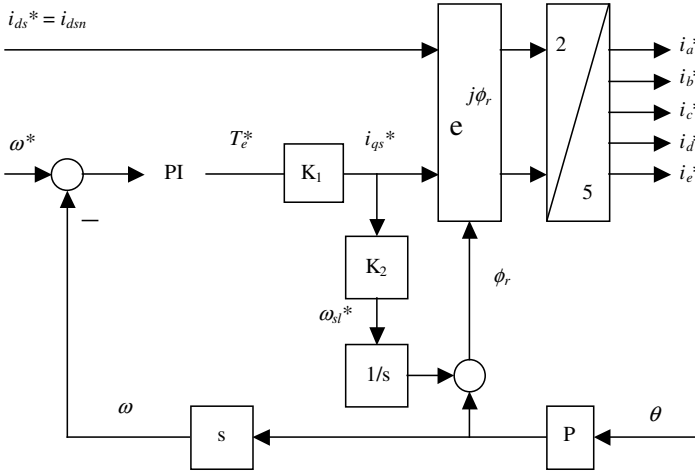
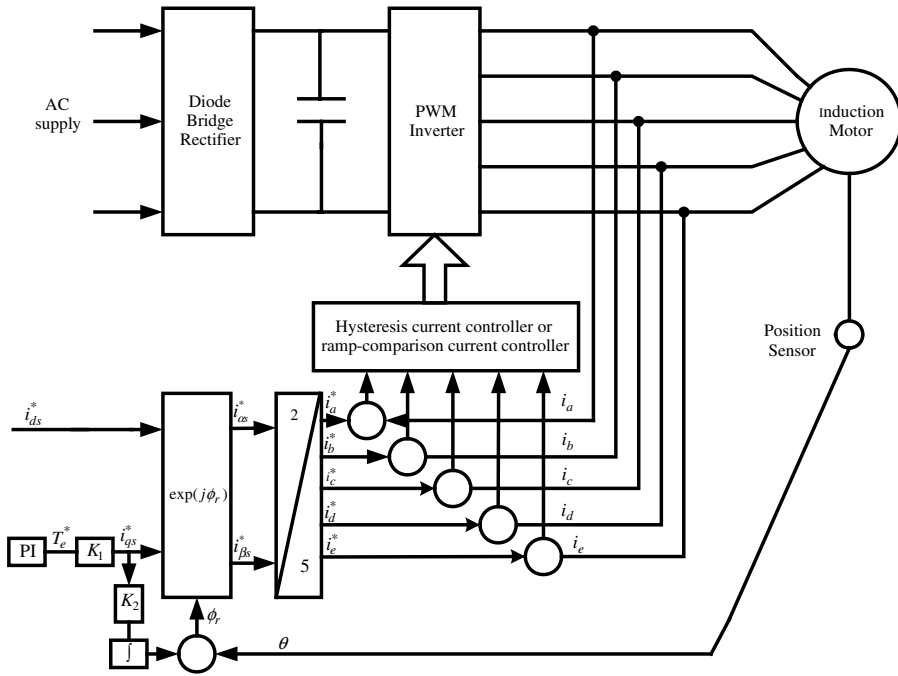


Figure 7.54 Vector controller of a five-phase machine

Since only two current components are needed for vector control, its principle remains the same for a multi-phase (more than three) machine as that of a three-phase machine. The only difference lies in the transformation of the current from two ( $\alpha$ - $\beta$ ) to three ( $i_a, i_b, i_c$ ) in the case of a three-phase machine and two ( $\alpha$ - $\beta$ ) to five ( $i_a, i_b, i_c, i_d, i_e$ ) in a five-phase machine, as illustrated in Figure 7.54 for speed control in the base speed region. The commanded speed and the actual speed (obtained from the speed sensor or speed observer in sensorless mode) are compared to determine the speed error, which is processed in a PI controller to determine the commanded torque. The output of the PI controller (commanded torque) is limited to rated torque or sometimes twice the rated torque (for fast acceleration). The commanded torque, when multiplied by constant  $K_1$ , gives the  $q$ -axis current component. This current component is multiplied by constant  $K_2$  to obtain slip speed. The expression for constants  $K_1$  and  $K_2$  are given as

$$K_1 = \frac{1}{P} \frac{L_r}{L_m} \frac{1}{\psi_r^*} = \frac{1}{P} \frac{L_r}{L_m^2} \frac{1}{i_{ds}^*} = 0.431 \quad K_2 = \omega_{sl}^* / i_{qs}^* = \frac{L_m}{T_r \psi_r^*} = \frac{1}{T_r i_{ds}^*} = 4.527 \quad (7.59)$$

Slip speed is integrated to obtain the position and then added to the rotor position, this gives the rotor flux position  $\phi_r$ . The letter ‘P’ in Figure 7.54 represents the number of pole pairs of the motor and  $\theta$  gives the mechanical rotor position. This is multiplied by the number of pole pairs of machine to obtain electrical rotor position. The vector rotator block  $j^{\phi_r}$  transforms the  $d$ - $q$ -axis current to the stationary  $\alpha$ - $\beta$ -axis current, which is finally transformed into five-phase currents. Thus generated are the reference five-phase currents, and are reconstructed by a current controlled five-phase PWM voltage source inverter. The current control can be performed using a simple hysteresis current controller or by using a ramp comparison current controller. A block schematic of indirect rotor FOC of a five-phase induction motor is given in Figure 7.55. In the block diagram, the torque reference is applied if the machine is in torque controlled mode. In case of speed control mode the reference torque is generated from the PI controller where the input is the speed error signal.



**Figure 7.55** Block schematic of indirect rotor field oriented control of a five-phase induction machine

### 7.4.1 MATLAB/Simulink Model of Field-Oriented Control of Five-Phase Induction Machine

MATLAB/Simulink model of a five-phase induction machine in indirect field oriented controlled mode for speed control in base speed region is shown in Figures 7.56 and 7.57. The vector controller block takes speed reference, the rotor flux reference, and actual speed as input; the rotor flux is kept constant in base speed region and is reduced in the field weakening region. The block shows only the actual speed as input, but inside the block, reference speed and reference rotor flux are provided. The vector controller generates the stator current references, which are compared with the actual stator current in the comparator block. The current errors thus generated are given to the hysteresis block that produces the gating signals for five-phase voltage source inverter. The phase voltages produced by the inverter is transformed using equation (7.10) (with  $\theta_s = 0$ , since the motor model is in the stationary reference frame) into  $\alpha$ - $\beta$  and  $x$ - $y$  components and is given as the input to the five-phase induction motor model.

The resulting waveforms for the five-phase vector controlled drive system are shown in Figure 7.58. Per-phase equivalent circuit parameters of the 50 Hz, five-phase induction machine are  $R_s = 10 \Omega$ ,  $R_r = 6.3 \Omega$ ,  $L_{ls} = L_{lr} = 0.04 \text{ H}$ ,  $L_m = 0.42 \text{ H}$ . Inertia and the number of pole pairs are equal to  $0.03 \text{ kgm}^2$  and 2, respectively. Rated phase current, phase-to-neutral voltage, and per-phase torque are 2.1 A, 220 V, and 1.67 Nm, respectively. Rated (rms) rotor flux is 0.5683 Wb. Parameters of the speed PI controller are obtained using standard tuning procedure. The hysteresis band is set to  $\pm 2.5\%$  of the rated peak phase current (i.e.  $\pm 0.07425 \text{ A}$ ). The torque limit is at all times equal to twice the rated motor torque (i.e. 16.67 Nm). DC link voltage equals

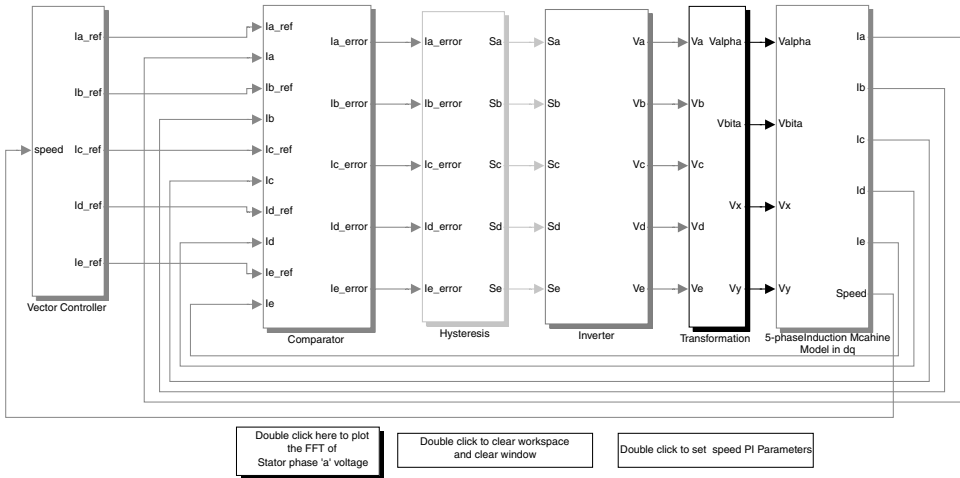


**Figure 7.56** Simulink model for indirect field oriented control of a five-phase induction motor (*File Name: Vector\_control\_5\_phase\_IM.mdl*)

587 V ( $= \sqrt{2} \times 415 \text{ V}$ ) and provides approximately 10% voltage reserve at rated frequency. The constants  $K_1$  and  $K_2$  of the vector controller are 0.431 and 4.527, respectively. Rotor flux reference (i.e. stator  $d$ -axis current reference) is ramped from  $t = 0$  to  $t = 0.01$  s to twice the rated value. In order to obtain a forced excitation, it is kept at twice the rated value from  $t = 0.01$  to  $t = 0.05$  seconds. Next, it is reduced from twice the rated value to the rated value in a linear fashion from  $t = 0.05$  to  $t = 0.06$  s and it is kept constant for the rest of the simulation period. Speed command of 1200 rpm is applied at  $t = 0.3$  s in a ramp-wise manner from  $t = 0.3$  to  $t = 0.35$  s and is further kept unchanged. Operation takes place under no-load conditions initially, followed by loading and then reversing. Reference and actual rotor flux, reference and actual torque, speed and stator phase 'a' reference, and actual current are shown in Figure 7.57. After the initial transient rotor flux settles to the reference value, it does not change any more, showing decoupled torque and flux control (vector control). Acceleration takes place with the maximum allowed value of the motor torque. The motor phase current tracks the reference well and consequently, torque response closely follows torque reference. Application of the load torque at  $t = 1$  s causes an inevitable dip in speed, of the order of 30 rpm in this case. Motor torque quickly follows the torque reference and enables rapid compensation of the speed dip ( $< 100$  ms). The motor torque settles at the value equal to the load torque after around 100 ms and the motor current becomes rated at the end of the transient. Reverse speed command is given at  $t = 1.3$  s and actual torque closely follows the reference, leading to the speed reversal, with torque in the limit, in the shortest possible time interval ( $\sim 350$  ms). Thus decoupled torque and flux control is achieved in a five-phase induction motor drive system.

## 7.5 Field Oriented Control of Five-Phase Induction Motor with Current Control in the Synchronous Reference Frame

The current control can be exercised either for phase current control (Section 7.4) or current control in the synchronous reference frame. Current references are generated by the vector



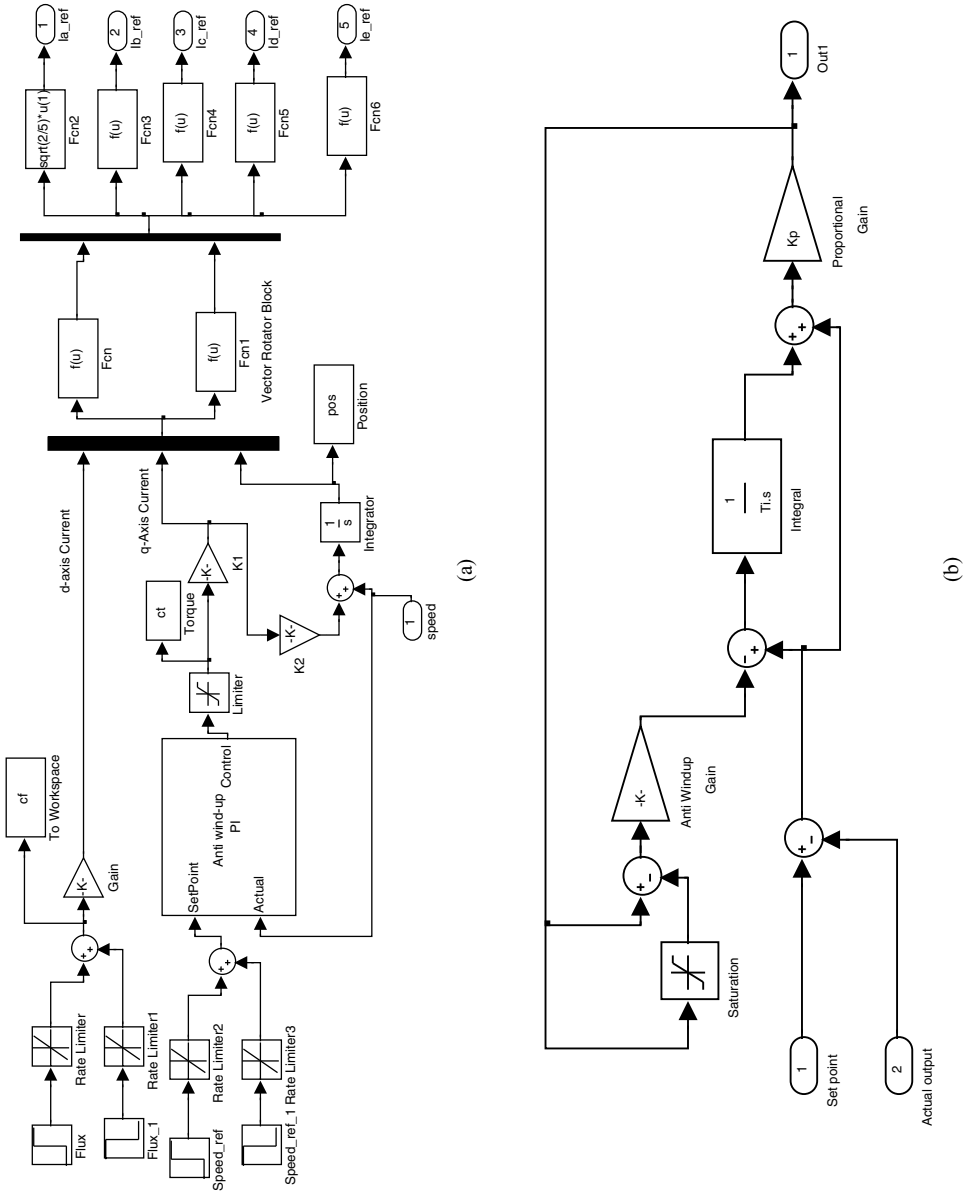


**Figure 7.57** (a) Simulink of vector controller to generate five-phase reference current; and (b) anti-wind up speed PI controller

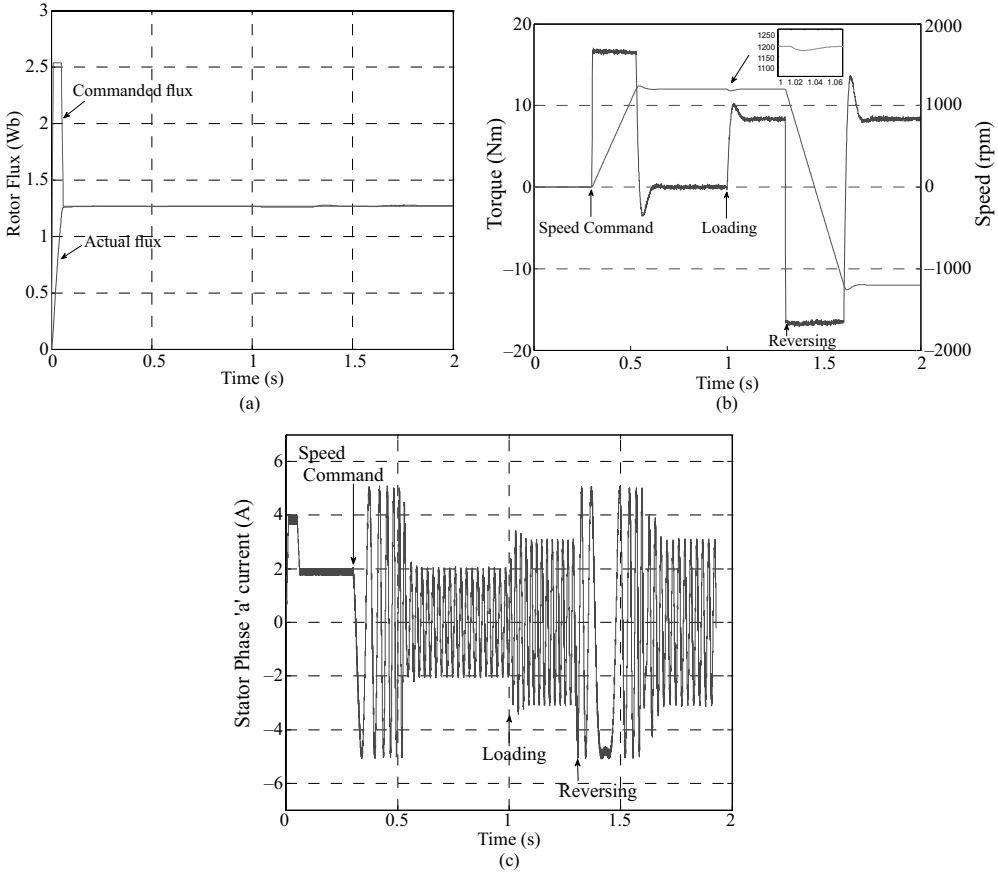


**Figure 7.58** Indirect rotor field oriented control of five-phase induction motor: (a) rotor flux; (b) speed and torque; (c) stator phase ‘a’ current

controller for phase current control, while voltage references are generated when current control in the synchronous reference frame is employed. The mathematical model of five-phase induction machine, obtained in the Section 7.2, is modified to incorporate the vector control using current control in the synchronous reference frame as follows.

Under the condition of rotor flux orientation, the stator flux is given by (the  $x$ - $y$  component is not considered as it is supposed to be zero for the sinusoidal supply condition)

$$\begin{aligned} \psi_{ds} &= \frac{L_m}{L_r} \psi_r + \sigma L_s i_{ds} \\ \psi_{qs} &= \frac{L_m}{L_r} \psi_r + \sigma L_s i_{qs} \end{aligned} \tag{7.60}$$

where  $\sigma = 1 - \frac{L_m^2}{L_s L_r}$  is the total leakage coefficient. Substituting equation (7.60) into the stator voltage equation (7.14) yields

$$v_{ds} = R_s i_{ds} + \sigma L_s \frac{di_{ds}}{dt} + \frac{L_m}{L_r} \frac{d\psi_r}{dt} - \omega_r \sigma L_s i_{qs} \quad (7.61)$$

$$v_{qs} = R_s i_{qs} + \sigma L_s \frac{di_{qs}}{dt} + \frac{L_m}{L_r} \frac{d\psi_r}{dt} - \omega_r \sigma L_s i_{ds}$$

$$i_{ds} + \frac{\sigma L_s}{R_s} \frac{di_{ds}}{dt} = \frac{1}{R_s} v_{ds} - \frac{L_m}{L_r R_s} \frac{d\psi_r}{dt} + \frac{\omega_r \sigma L_s}{R_s} i_{qs} \quad (7.62)$$

$$i_{qs} + \frac{\sigma L_s}{R_s} \frac{di_{qs}}{dt} = \frac{1}{R_s} v_{qs} + \frac{L_m}{L_r R_s} \frac{d\psi_r}{dt} + \frac{\omega_r \sigma L_s}{R_s} i_{ds}$$

As seen from equation (7.62), the two stator current components are not decoupled. Hence decoupling circuit needs to be introduced for true decoupled  $d$ - and  $q$ -axis currents. If the output variables of current controllers are defined as

$$v_{ds}^1 = R_s \left( i_{ds} + \frac{\sigma L_s}{R_s} \frac{di_{ds}}{dt} \right) \quad (7.63)$$

$$v_{qs}^1 = R_s \left( i_{qs} + \frac{\sigma L_s}{R_s} \frac{di_{qs}}{dt} \right)$$

then the required reference values of axis voltages  $v_{ds}^*$  and  $v_{qs}^*$  are

$$\begin{aligned} v_{ds}^* &= v_{ds}^1 + e_d \\ v_{qs}^* &= v_{qs}^1 + e_q \end{aligned} \quad (7.64)$$

where auxiliary variables are defined as

$$\begin{aligned} e_d &= R_s \left( \frac{L_m}{L_r R_s} \frac{d\psi_r}{dt} - \omega_r \frac{\sigma L_s}{R_s} i_{qs} \right) \\ e_q &= R_s \left( \frac{L_m}{L_r R_s} \frac{d\psi_r}{dt} + \omega_r \frac{\sigma L_s}{R_s} i_{ds} \right) \end{aligned} \quad (7.65)$$

Equation (7.65) describes the decoupling circuit which is used in conjunction with the voltage fed rotor flux oriented controlled five-phase induction motor drive. Usually the derivative of the rotor flux term is neglected for simplicity without compromising the dynamics of the machine. The structure of the vector controller is shown in Figure 7.59.

The constant in Figure 7.59a is given as  $\omega_{sl}^* = K_1 i_{qs}^* \Rightarrow K_1 = \omega_{sl}^* / i_{qs}^* = \frac{L_m}{T_r \psi_r} = \frac{1}{T_r i_{ds}^*}$ . Since the speed control in the base speed region is considered, the  $d$ -axis current is held constant equal to the rated value. The reference  $q$ -axis current is generated using the PI controller, which

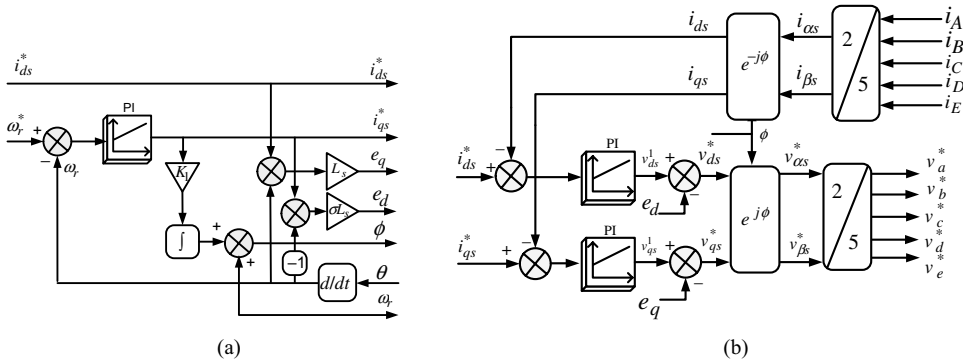


**Figure 7.59** Vector control of five-phase induction machine: (a) reference current generation; (b) reference voltage generation

processes the speed error. The  $d$ -axis current error and  $q$ -axis current error are further processed in the PI controller and the auxiliary variables are subtracted from the outputs to generate the required reference voltages in the rotational reference frame. These voltages are then transformed to the stationary reference frame and then transformed into five-phase voltage references. These five-phase voltage references are given to the PWM block. This block then generates the appropriate switching signals for the PWM voltage source inverter. The inverter finally produces the required voltages that are impressed at the stator of the five-phase induction machine. The PWM that can be used for generating the voltages can be carrier-based sinusoidal method or space vector method.

The simulation result for the indirect rotor FOC with current control in the synchronously rotating reference frame is given in [59]. It is evident from the results shown in [59] that the  $x$ - $y$  components of the stator current are still present, despite the use of the PWM method, which claims to completely eliminate the  $x$ - $y$  component. The presence of  $x$ - $y$  components of current is the consequence of the dead time in the switching signals of the IGBTs of the inverter. To eliminate completely the  $x$ - $y$  components of the current and consequently the distortion in the stator current, two additional current controllers need to be added in the vector controller of Figure 7.59, resulting in the modified vector control scheme, as shown in Figure 7.60. In the modified current control scheme, two extra pairs of current controllers are introduced that operate in the same reference frame as for the  $d$ - $q$  components and have the same gains. The reference currents for  $x$ - $y$  are set to zero. The  $d$ - $q$  current parameters are the same as in the previous case (Figure 7.59) and the rotor flux position calculation also remains the same. The simulation result of the modified current control scheme is also depicted in [59]. The current waveform now shows complete elimination of the  $x$ - $y$  components of current and the distortion in the stator current is minimized.

## 7.6 Model Predictive Control (MPC)

In the last 20 years, model predictive control (MPC) has achieved a significant level of acceptability and success in practical process control applications, and has been mainly applied in power plants and petroleum refineries. With the development of the modern micro-controller,

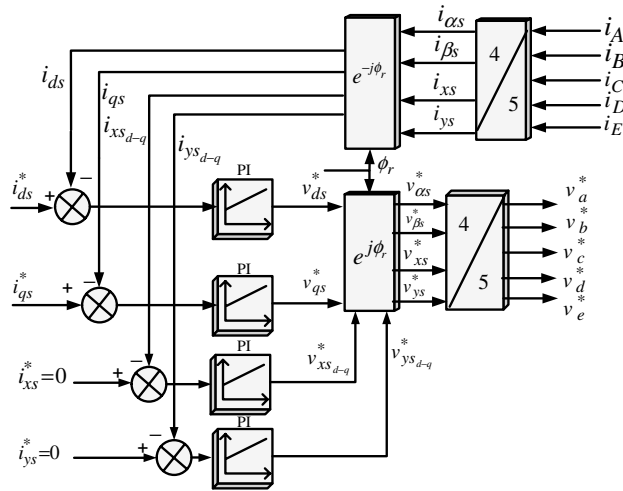


**Figure 7.60** Vector control scheme of a five-phase induction machine with four current controller in synchronous reference frame [59]

digital signal processors, and field programmable gate Arrays, MPC applications have been found in a variety of areas including chemicals, food processing, automotive and aerospace applications, and power electronics and drives [60–65].

MPC algorithms use an explicit process model to predict the future response of a process or plant. A cost function represents the desired behavior of the system. An optimization problem is formulated, where a sequence of future actuations is obtained by minimizing the cost function. The first element of the sequence is applied and all calculations are repeated for every sample period. The process model therefore plays a decisive role in the controller. The chosen model must be able to capture the process dynamics to precisely predict future outputs and be simple to implement and understand. Linear models have been widely used, as they can be easily obtained by system identification technique, or by linearization of first-principles non-linear models. The cost function, in consequence, is quadratic and the constraints are in the form of linear inequalities. For such quadratic programming (QP) problem, active set methods (AS), and interior point methods (IP) can provide the best performance. This formulation of linear MPC (LMPC) has been implemented successfully in several commercial predictive control products, such as AspenTech's DMC Plus, Honeywell's RMPCT, Adersa's PFC and HIECON, and ABB's 3DMPC. However, if the plant exhibits severe non-linearities, the usefulness of predictive control based on a linear model is limited, particularly if it is used to transfer the plant from one operating point to another [66]. Adopting a non-linear model in an MPC scheme is an obvious solution to improve the control performance. In fact, predictive control with non-linear internal models (NLMPC) has been one of the most relevant and challenging problems. Because the optimization problem to find control action has become non-linear, the convexity of the optimization problem in LMPC has been lost, which makes the online application extremely difficult. However, in order to obtain accurate predictions of process behavior, the application of NLMPC has been increasing by using powerful micro-controller and efficient optimization algorithms [67–69].

MPC is an attractive control methodology to modern industry, because it has the ability to handle both input and output constraints explicitly, which allows plant operation closer to constraints. If the controlled processes operate at output constraints, the most profitable operation can be obtained. In addition, input constraints in MPC take account of actuator limitations, which means safe operations on plant have been considered at the same time as its most profitable condition [66]. In addition, MPC handles multi-variable control problems naturally, which makes it easily meet the requirement of integrated control of complex plants in profit maximization. By monitoring the future behavior of many output variables, MPC can keep a process operating both economically and safely [70].

However, a widely recognized shortcoming of MPC is that it can usually only be used in applications with slow dynamics, where the sample time is measured in seconds or minutes. Hence, the development of a fast MPC to broaden its application in industry has been an active research field. One well-known technique for implementing a fast MPC is to compute the entire control law offline, in which case the online controller can be implemented as a look-up table [71,72]. This method works well for systems with small state and input dimensions (i.e. no more than five), few constraints, and short time horizons. On the other hand, optimization algorithms, such as QP re-formulations, warm-starting, and early termination in IP, have been investigated to speed up the computation of control action in MPC, and high-quality controls using these improved algorithms have been obtained [66,72].

### 7.6.1 MPC Applied to a Five-Phase Two-Level VSI

Since the power electronic converters have finite switching states, MPC can be effectively used in such converter systems for their current and power control, called ‘finite state MPC.’ This section elaborates on finite state MPC for a five-phase voltage source inverter for their current control [76,77].

The basic block schematic of the proposed strategy is illustrated in Figure 7.61. The discrete load model, called the ‘Predictive Model,’ is used to pre-calculate the behavior of the current in the next sampling interval. The pre-calculated current sample is then fed to the optimizer along with the reference current (obtained from the external loop). The optimizer calculates the cost function for all the possible switching combinations of the inverter. Thus, it generates the optimal switching state corresponding to the global minimum cost function in each sampling interval and passes it on to the gate drive of the inverter. This is how the optimal solution is obtained. This concept is entirely different from the conventional PWM techniques, where the symmetrical switching patterns are generated and ensures that each leg changes the state at

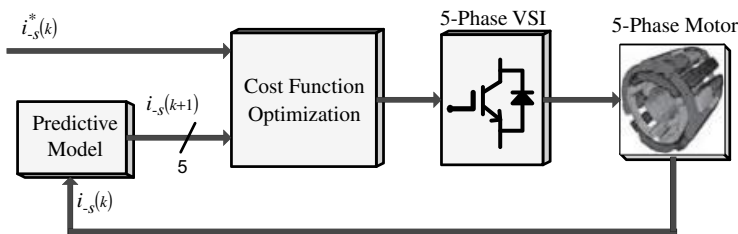


**Figure 7.61** Model predictive current controller for five-phase drive

least twice in the same switching interval, keeping constant the switching frequency spectrum. In contrast to the MPC, the two switchings of each leg are not guaranteed and hence the switching frequency is variable. However, this method is powerful owing to the fact that the concept is simple and intuitive. The controller can incorporate many desired features by simply modifying the cost function.

Owing to the fact that a five-phase inverter generates a large number of space vectors (30 active and 2 zero), many possible solutions can exist to implement MPC, as discussed in the latter section. Nevertheless in this section, few solutions are elaborated on and there still remains many more to explore.

The choice of the cost function is the most important aspect of the MPC. A judicious choice leads to the optimal solution of the control objective. Thus the cost function should include all the parameters to be optimized within the imposed constraints. In the current control, the most important variable is the current tracking error. Thus the most simple and straightforward choice is the absolute value of the current error. The other choices could be the square of the current error, integral of the current error, or the rate of change of error, etc. Specifically, in a five-phase drive system, there exist two orthogonal sub-spaces, namely  $\alpha$ - $\beta$  and  $x$ - $y$ . Thus, in the case of a five-phase drive system, the current errors in both planes have to be considered for devising a cost function. In general, for the square of current error, the cost function is given as

$$\begin{aligned}\hat{g}_{\alpha\beta} &= |i_{\alpha}^*(k) - \hat{i}_{\alpha}(k+1)| + |i_{\beta}^*(k) - \hat{i}_{\beta}(k+1)| \\ \hat{g}_{xy} &= |i_x^*(k) - \hat{i}_x(k+1)| + |i_y^*(k) - \hat{i}_y(k+1)|\end{aligned}\quad (7.66)$$

The final cost function can be expressed as

$$J_{\alpha\beta xy} = \|\hat{g}_{\alpha\beta}\|^2 + \gamma \|\hat{g}_{xy}\|^2 \quad (7.67)$$

where  $\|\cdot\|$  denote modulus and  $\gamma$  is a tuning parameter that offer degrees of freedom to put emphasis on  $\alpha$ - $\beta$  or  $x$ - $y$  sub-spaces. Comparative studies are made to emphasize the effect of the choice of the tuning parameter on the performance of the controller.

The load is assumed as a five-phase RLE (resistance, inductance, and back emf). The discrete time model of the load suitable for current prediction is obtained from [63]

$$\hat{i}(k+1) = \frac{T_s}{L}(\underline{v}(k) - \hat{\underline{e}}(k)) + \underline{i}(k) \left(1 - \frac{RT_s}{L}\right) \quad (7.68)$$

where  $R$  and  $L$  are the resistance and inductance of the load;  $T_s$  is the sampling interval;  $\underline{i}$  is the load current space vector;  $\underline{v}$  is the inverter voltage space vector used as a decision variable; and  $\hat{\underline{e}}$  is the estimated back emf obtained from [63]

$$\underline{i} = [i_a \quad i_b \quad i_c \quad i_d \quad i_e]^t, \quad \underline{v} = [v_a \quad v_b \quad v_c \quad v_d \quad v_e]^t \quad (7.69)$$

$$\hat{\underline{e}}(k) = \underline{v}(k) + \frac{L}{T_s} \underline{i}(k-1) - \underline{i}(k) \left(R + \frac{L}{T_s}\right) \quad (7.70)$$

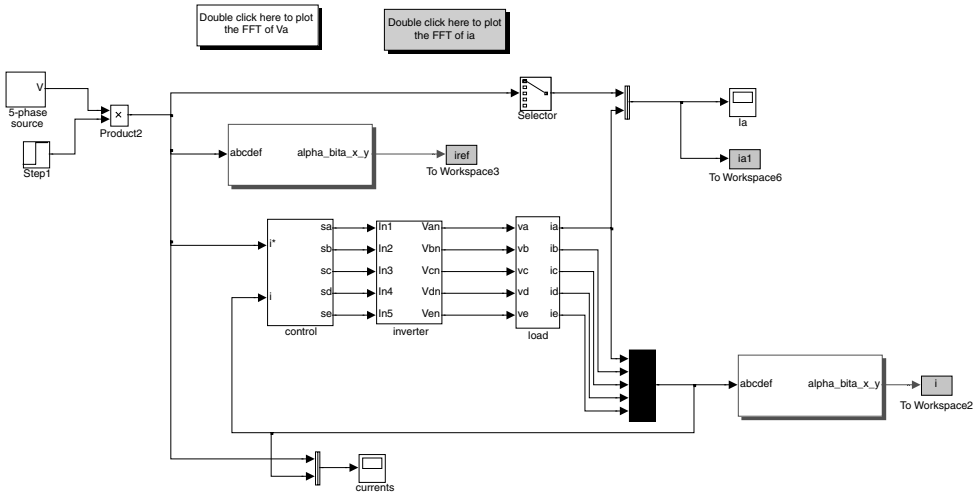


**Figure 7.62** Finite set MPC of a five-phase VSI (File Name: MPC\_5\_phase.mdl and control\_5\_phase\_Large.m)

where  $\hat{e}(k)$  is the estimated value of  $e(k)$ . However, for simulation purposes, the amplitude and frequency of back emf are assumed as constant.

### 7.6.2 MATLAB/Simulink of MPC for Five-Phase VSI

The MATLAB/Simulink model for current control of a five-phase VSI fed five-phase R-L load using finite set MPC is shown in Figure 7.62. The five-phase reference current is given as the commanded value and the actual five-phase current through the five-phase R-L load is recorded and compared.

Simulation results are presented first using the outer large vector set from Figure 7.34 and a zero vector, thus in total 11 vectors are used, and the cost function is such that it minimizes current tracking errors only in the  $\alpha$ - $\beta$  plane. This is followed by using cost function, which takes into account the current tracking error minimization in both the  $\alpha$ - $\beta$  and  $x$ - $y$  planes. The sampling time  $T_s$  is kept equal to  $50 \mu\text{sec}$ . The fundamental frequency of the sinusoidal reference current is chosen as 50 Hz. The other parameters are  $R = 10 \Omega$ ,  $L = 10 \text{ mH}$ , and  $V_{dc} = 200 \text{ V}$ . The five-phase reference current amplitude is at first kept at 4 A, then stepped up to 8 A in the first quarter of the second fundamental cycle. The optimization algorithm is implemented using the ‘s’ function of MATLAB.

### 7.6.3 Using Eleven Vectors with $\gamma = 0$

The resulting waveforms for using only ten outer large space vectors and one zero vector are shown in Figure 7.63. The current tracking error is forced to become zero only in the  $\alpha$ - $\beta$  plane. It is evident from Figure 7.63 that the  $\alpha$ - $\beta$  components of the current are sinusoidal, while there are extra  $x$ - $y$  components produced because of the vector of the  $x$ - $y$  plane, which are firmly tied to the vectors of the  $\alpha$ - $\beta$  plane. Moreover, the optimizer does not take into



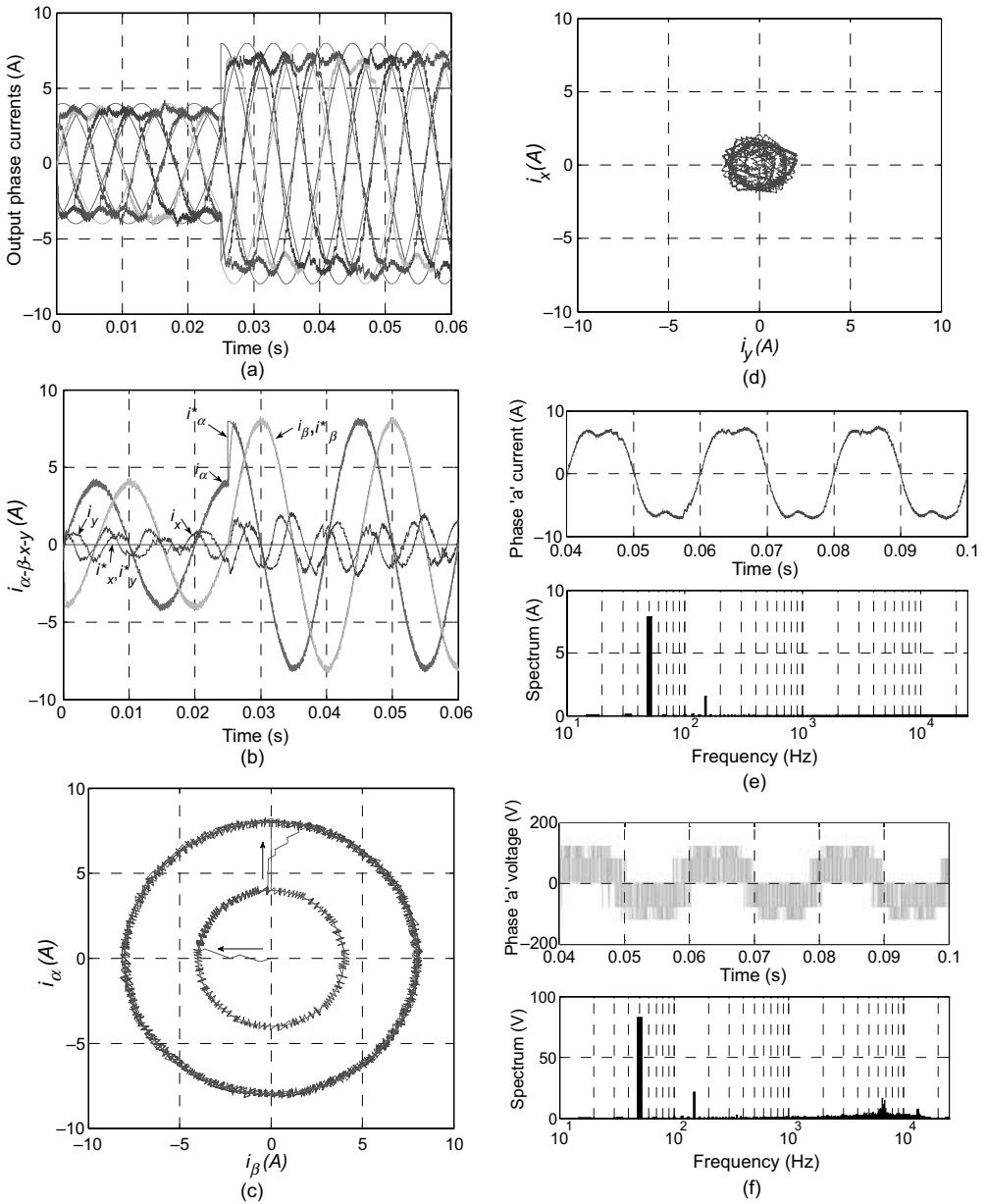


**Figure 7.63** MPC performance with  $\gamma = 0$ : (a) Actual and reference five-phase currents; (b) transformed current; (c) trajectory of  $\alpha$ -axis current; (d) trajectory of  $x$ -axis current; (e) spectrum of current; and (f) spectrum of voltage

account the tracking error in the second plane. The loci of the current in the two different planes are illustrated in Figure 7.63. The  $\alpha$ - $\beta$  plane shows circular trajectory, while the  $x$ - $y$  plane is irregular but close to the circle. To further explore the performance of the controller current and inverter voltage spectrum, they are depicted in Figure 7.63f. The THD is

calculated up to 500 harmonics for both voltage and current waveforms. The current waveform shows a THD of 19.67% and the highest lower-order harmonic is third equal to 19.55% of the fundamental (7.9 A). The voltage spectrum offers a THD of 42.36% and the highest lower-order harmonic is one-third with their magnitude equal to 25.82% of the fundamental (82.7 V). The switching harmonics are distributed and the average could be estimated around 7–8 kHz.

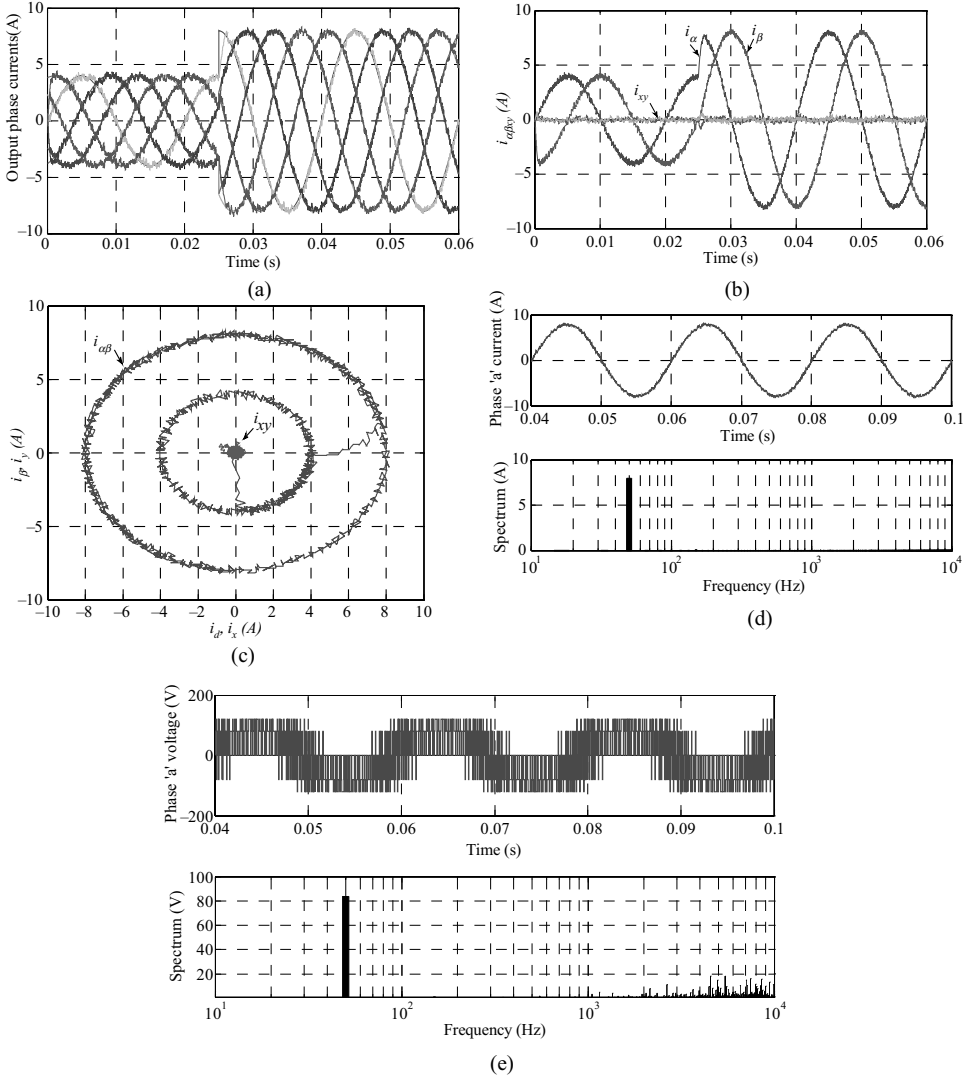


**Figure 7.64** MPC performance with  $\gamma = 1$ : (a) actual and reference phase currents; (b) transformed current; (c) trajectory of  $\alpha$ - $\beta$  and  $x$ - $y$  axis currents; (d) spectrum of current; and (e) spectrum of phase voltage

### 7.6.4 Using Eleven Vectors with $\gamma = 1$

The simulation results are further shown to eliminate the  $x$ - $y$  components of the currents, as they are undesirable for distributed winding AC machine drives (causing extra losses). The cost function thus includes the  $x$ - $y$  current tracking error, and the resulting waveforms are shown in Figure 7.64. The results obtained shows effective elimination of the  $x$ - $y$  components, leading to sinusoidal output voltages and currents. Hence, by using only 11 large outer space vector sets, sinusoidal output voltages and currents are obtained that were not possible with the SVPWM technique.

## 7.7 Summary

This chapter discussed the structure of a five-phase drive system and its control properties and elaborated the advantages and limitations of a five-phase induction motor drive system and identified its potential application areas. Modeling of a five-phase voltage source inverter was illustrated for step mode of operation and PWM mode of operation. FFT analysis was given for the step mode of operation of five-phase VSI. Experimental results were also given for step-mode of operation of the five-phase voltage source inverter. This was followed by the phase variable model of a five-phase induction machine. The model was then transformed into two orthogonal planes, namely  $d$ - $q$  and  $x$ - $y$  and the torque equation was obtained. The vector control principle was then presented for the five-phase induction motor drive system. The difference between the vector control principle applied to a three-phase system and a five-phase system was highlighted. The theoretical background was supported by the simulation model using MATLAB/Simulink software. The modern control technique such as Model predictive control is discussed with reference to the application for current control of a five-phase voltage source inverter.

## Problems

- D 7.1:** Calculate the rms voltage of the output phase voltage and adjacent line and non-adjacent line voltage for ten-step mode of operation of a five-phase voltage source inverter operating at 100 Hz fundamental frequency in terms of dc link voltage  $V_{dc}$ .
- D 7.2:** A Five-phase voltage source inverter is supplying a five-phase load and operating in ten-step mode of operation. The fundamental output frequency is assumed to be 25 Hz. Calculate the conduction period of each power switch of the inverter.
- D 7.3:** A five-phase induction machine is supplied from a five-phase voltage source inverter. The five-phase VSI is controlled using space vector PWM technique and sinusoidal supply is to be supplied to the motor. The inverter switching frequency is 5 kHz and the DC bus voltage at the inverter input is 300 V. The inverter output frequency is 50 Hz. The reference phase voltage rms is 100 V. Identify the space vectors that will be applied and their time of application for the time instants: 1 ms, 5 ms, and 10.5 ms.
- D 7.4:** A five-phase induction machine is supplied from a five-phase voltage source inverter and controlled in square wave mode with conduction angle as  $144^\circ$ . The dc link voltage is assumed as 1 p.u.,

- (a) Write down the switching state and corresponding leg voltage values and leg voltage space vectors in the stationary reference frame.
- (b) Calculate the phase-to-neutral voltages and determine the corresponding space vectors in both d-q and x-y planes.
- (c) Determine the possible line-to-line voltages and corresponding space vectors in d-q and x-y planes.
- D 7.5:** Determine the effect of dead time on the output phase-to-neutral voltage of a five-phase voltage source inverter operating in ten-step mode. Consider the dead time of  $20 \mu\text{s}$  and  $50 \mu\text{s}$ . (Hint: Develop the simulink model to solve this problem)
- Solution:** (file name: vs1\_ten\_step\_20\_micro\_delay.mdl)
- D 7.6:** A Five-phase induction machine rated at 200 V (adjacent line voltage) is supplied from a Five-phase PWM voltage source inverter operating at 5 kHz switching frequency and employing simple carrier-based sinusoidal PWM scheme. The motor is assumed to be operating with  $v/f = \text{constant}$  control law and the rated voltage is applied at 50 Hz. To enhance the output of the inverter, 5<sup>th</sup> harmonic injection PWM scheme is adopted. Determine the amplitude and frequency of the 5<sup>th</sup> harmonic components to be injected for motor operation at 50 Hz, 25 Hz, and 10 Hz.
- D 7.7:** A Five-phase induction machine is supplied from a Five-phase voltage source inverter and the inverter is modulated using space vector PWM with sinusoidal output. The operation of the five-phase motor is assumed in  $v/f = \text{constant}$  mode. The inverter switching frequency is 2 kHz and the DC bus voltage at the inverter input is 600 V.
- (a) Determine the maximum value of the inverter output phase to neutral fundamental rms voltage for this PWM mode. This is treated as the rated motor's voltage and the rated frequency of the motor is assumed as 60 Hz.
- (b) Find the set of the space vectors that will be applied and the time of their applications for the output frequency of 25 Hz, for the time instants of: 1.5 ms, 4 ms and 8 ms
- (c) The five-phase induction motor is now supplied from 120 Hz. Calculate the new reference space vector and determine which of the space vectors will be applied and for how long, for the time instants of 2 ms, 10 ms, 15 ms.
- D 7.8:** Develop a complete MATLAB/Simulink model of a 4-pole, 220 V rms, phase, Five-phase induction motor drive system for open-loop  $v/f = \text{constant}$  control mode. The Five-phase voltage source inverter may be simulated using IGBT model from 'simpower system' block sets. The inverter dead time may be given as  $50 \mu\text{sec}$  and the switching frequency of the inverter is assumed as 5 kHz. The same model should be implemented in real time with TMS320F2812 DSP and the voltage signal to the DSP, corresponding to rated speed is 3.3 V. The speed reference should be given as voltage signal to the control block. Per-phase equivalent circuit parameters of the 50 Hz, Five-phase induction machine, are  $R_s = 10 \Omega$ ,  $R_r = 6.3 \Omega$ ,  $L_{ls} = L_{lr} = 0.04 \text{ H}$ ,  $L_m = 0.42 \text{ H}$ . Inertia and the number of pole pairs are equal to  $0.03 \text{ kgm}^2$  and 2, respectively. Rated phase current, phase-to-neutral voltage and per-phase torque are 2.1 A, 220 V and 1.67 Nm, respectively.
- D 7.9:** Determine the voltages in the  $\alpha$ - $\beta$  and x-y plane for the following phase voltages in the stationary reference frame. Use the transformation matrix (assume star connected load and  $\alpha = 72^\circ$ ). You can use MATLAB/Simulink simulation and plot the voltages in the two orthogonal planes. (Assume  $V_3 = 0.5V_1$  and  $V_5 = 0.25V_1$ )

## References

1. Ward, E. E. and Harer, H. (1969) Preliminary investigation of an inverter-fed 5-phase induction motor. *Proc. Int. Elect. Eng.*, **116**(6), 980–984.
2. Klingshirn, E. A. (1983) High phase order induction motors (part I and II). *IEEE Trans. Power App. Sys.*, **PAS\_102**(1), 47–59.
3. Pavithran, K. N., Parimelalagan, R., and Krishnamurthy, M. R. (1988) Studies on inverter-fed five-phase induction motor drive. *IEEE Trans. On Power Elect.*, **3**(2), 224–233.
4. Xu, H., Toliyat, H. A., and Petersen, L. J. (2009) Five-phase induction motor drives with DSP-based control system. *Proc. IEEE Int. Elec. Mach. And Drives Conf. IEMDC2001*, Cambridge, MA, pp. 304–309.
5. Xu, H., Toliyat, H. A., and Petersen, L. J. (2001) Rotor field oriented control of a five-phase induction motor with the combined fundamental and third harmonic injection. *Proc. IEEE Applied Power Elec. Conf. APEC*, Anaheim, CA, pp. 608–614.
6. Iqbal, A. and Levi, E. (2005) Space vector modulation scheme for a five-phase voltage source inverter. *Proc. Europ. Power Elect. Appl. Conf., EPE*, Dresden, CD-ROM, paper 0006.
7. Ojo, O., Dong, G., and Wu, Z. (2006) Pulse width modulation for five-phase converters based on device turn-on times. *Proc. IEEE Ind. Appl. Soc. Ann. Mtg IAS*, Tampa, FL, CD-ROM, paper IAS15, p. 7.
8. Ryu, H. M., Kim, J. H., and Sul, S. K. (2005) Analysis of multi-phase space vector pulse width modulation based on multiple d-q space concept. *IEEE Trans. Power Elect.*, **20**(6), 1364–1371.
9. de Silva, P. S. N., Fletcher, J. E., and Williams, B. W. (2004) Development of space vector modulation strategies for five-phase voltage source inverters. *Proc. IEE Power Elect., Mach. Drives Conf., PEMD*, Edinburgh, pp. 650–655.
10. Dujic, D., Jones, M., and Levi, E. (2009) Generalised space vector PWM for sinusoidal output voltage generation with multiphase voltage source inverters. *Int. J. Ind. Elect. Drives*, **1**(1), 1–13.
11. de Silva, P. S. N., Fletcher, J. E., and Williams, B. W. (2004) Development of space vector Modulation strategies for five-phase voltage source inverters. *Proc. IEE Power Elect. Mach. Drives PEMD Conf.*, Edinburgh, pp. 650–655.
12. Iqbal, A. and Levi, E. (2006) Space vector PWM techniques for sinusoidal output voltage generation with a five-phase voltage source inverter. *Elect. Power Comp. Syst.*
13. Duran, M. J., Toral, S., Barrero, F., and Levi, E. (2007) Real time implementation of multi-dimensional five-phase space vector pulse width modulation. *Elect. Lett.* **43**(17), 949–950.
14. Ryu, H. M., Kim, J. H., and Sul, S. K. (2005) Analysis of multiphase space vector pulse-width modulation based on multiple d-q spaces concept. *IEEE Trans. Power Elec.*, **20**(6), 1364–1371.
15. Zheng, L., Fletcher, J., Williams, B., and He, X. (2010) A novel direct torque control scheme for a sensorless five-phase induction motor drive. *IEEE Trans. Ind. Elect.* Issue 99 (on-line version available).
16. Liliang, G. and Fletcher, J. E. (2010) A space vector switching strategy for a 3-level five-phase inverter drives. *IEEE Trans. Ind. Elect.* (On-line version available).
17. Singh, G. K. (2002) Multi-phase induction machine drive research: A survey. *Elect. Power Syst. Res.*, **61**, 139–147.
18. Jones, M. and E. Levi, E. (2002) A literature survey of state-of-the-art in multiphase AC drives, *Proc. 37th Int. Univ. Power Eng. Conf. UPEC*, Stafford, UK, pp. 505–510.
19. Levi, E., Bojoi, R., Profumo, F., Toliyat, H. A., and Williamson, S. (2007) Multi-phase induction motor drives: A technology status review. *IET Elect. Power Appl.*, **1**(4), 489–516.
20. Levi, E. (2008) Guest editorial. *IEEE Trans. Ind. Elect.*, **55**(5), 1891–1892.
21. Levi, E. (2008) Multi-phase machines for variable speed applications. *IEEE Trans. Ind. Elect.*, **55**(5), 1893–1909.
22. Toliyat, H. A., Rahimian, M. M., and Lipo, T. A. (1991) dq modeling of five-phase synchronous reluctance machines including third harmonic air-gap mmf. *Proc. IEEE Ind. Appl. Soc. Ann. Mtg*, pp. 231–237.

23. Toliyat, H. A., Rahmania, M. M., and Lipo, T. A. (1992) A five phase reluctance motor with high specific torque. *IEEE Trans. Ind. Appl.*, **28**(3), 659–667.
24. Xu, H., Toliyat, H. A., and Petersen, L. J. (2001) Rotor field oriented control of a five-phase induction motor with the combined fundamental and third harmonic injection. *Conf. Rec. IEEE Appl. Power Elect. Conf. APEC*, Anaheim, CA, pp. 608–614.
25. Duran, M. J., Salas, F., and Arahal, M. R. (2008) Bifurcation Analysis of five-phase induction motor drives with third-harmonic injection. *IEEE Trans. Ind. Elect.*, **55**(5), 2006–2014.
26. Shi, R., Toliyat, H. A., and El-Antably, A. (2001) Field oriented control of five-phase synchronous reluctance motor drive with flexible 3rd harmonic current injection for high specific torque. *Proc. 36th IEEE Ind. Appl. Conf.*, pp. 2097–2103.
27. Williamson, S. and Smith, S. (2003) Pulsating torques and losses in multiphase induction machines. *IEEE Trans. Ind. App.* **39**(4), 986–993.
28. Green, S., Atkinson, D. J., Jack, A. G., Mecrow, B. C., and King, A. (2003) Sensorless operation of a fault tolerant PM drive. *IEE Proc. Elect. Power Appl.*, **150**(2), 117–125.
29. Wang, J. B., Atallah, K., and Howe, D. (2003) Optimal torque control of fault-tolerant permanent magnet brushless machines. *IEEE Trans. Magn.*, **39**(5), 2962–2964.
30. Fu, J. R. and Lipo, T. A. (1994) Disturbance-free operation of a multiphase current-regulated motor drive with an opened phase. *IEEE Trans. Ind. Appl.*, **30**(5), 1267–1274.
31. Suman, D. and Parsa, L. (2008) Optimal current waveforms for five-phase permanent magnet motor drives under open-circuit fault. *Proc. IEEE Power Ener. Soc. Gen. Mtg: Conv. Del. Elect. Ener. 21st Cent.*, pp. 1–5.
32. Parsa, L. and Toliyat, H. A. (2004) Sensorless direct torque control of five-phase interior permanent magnet motor drives. *Proc. IEEE Ind. Appl. Soc. Mtg, IAS*, **2**, 992–999.
33. Chiricozzi, E. and Villani, M. (2008) Analysis of fault-tolerant five-phase IPM synchronous motor. *Proc. IEEE Int. Symp. Ind. Elect.*, pp. 759–763.
34. Toliyat, H. A. (1998) Analysis and simulation of five-phase variable speed induction motor drives under asymmetrical connections. *IEEE Trans. Power Elect.*, **13**(4), 748–756.
35. Husain, T., Ahmed, S. K. M., Iqbal, A., and Khan, M. R. (2008) Five-phase induction motor behaviour under faulted conditions. *Proc. INDICON*, pp. 509–513.
36. Casadei, D., Mengoni, M., Serra, G., Tani, A., and Zarri, L. (2008) Optimal fault-tolerant control strategy for multi-phase motor drives under an open circuit phase fault condition. *Proc. 18th Int. Conf. Elect. Mach., ICEM*, pp. 1–6.
37. Bianchi, N., Bologani, S., and Pre, M. D. (2007) Strategies for fault-to-lerant current control of a five-phase permanent magnet motor. *IEEE Trans. Ind. Appl.*, **43**(4), 960–970.
38. Jacobina, C. B., Freitas, I. S., Oloveira, T. M., da Silva, E. R. C., and Lima, A. M. N. (2004) Fault tolerant control of five-phase AC motor drive. *35th IEEE Power Elect. Spec. Conf.*, pp. 3486–3492.
39. Heising, C., Oettmeier, M., Bartlet, R., Fang, J., Staudt, V., and Steimel, A. (2009) Simulation of asymmetric faults of a five-phase induction machine used in naval applications. *Proc. 35th IEEE Ind. Elect. Conf. IECON*, pp. 1298–1303.
40. Parsa, L. and Toliyat, H. A. (2005) Five-phase permanent magnet motor drives for ship propulsion applications. *Proc. IEEE Electric Ship Technologies Symposium*, pp. 371–378.
41. Golubev, A. N. and Ignatenko, S. V. (2000) Influence of number of stator-winding phases on the noise characteristics of an asynchronous motor. *Russ. Elect. Eng.*, **71**(6), 41–46.
42. McCleer, P. J., Lawler, J. S., and Banerjee, B. (1993) Torque notch minimization for five-phase quasi square wave back emf PMSM with voltage source drives. *Proc. IEEE Int. Symp. Ind. Elect.*, pp. 25–32.
43. Zhang, X., Zhnag, C., Qiao, M., and Yu, F. (2008) Analysis and experiment of multi-phase induction motor drives for electrical propulsion. *Proc. Int. Conf. Elect. Mach., ICEM*, pp. 1251–1254.

44. Sadehgi, S. and Parsa, L. (2010) Design and dynamic simulation of five-phase IPM machine for series hybrid electric vehicles. *Proc. Green Tech. Conf.*, pp. 1–6.
45. Chan, C. C., Jiang, J. Z., Chen, G. H., Wang, X. Y., and Chau, K. T. (1994) A novel polyphase multipole square wave PM motor drive for electric vehicles. *IEEE Trans. Ind. Appl.*, **30**(5).
46. Jayasundara, J. and Munindradasa, D. (2006) Design of multi-phase in-wheel axial flux PM motor for electric vehicles. *Proc. Int. Conf. Ind. Info. Syst.*, pp. 510–512.
47. Abolhassani, M. T. (2005) A novel multiphase fault tolerant high torque density PM motor drive for traction application. *Proc. IEEE Int. Conf. Elect. Mach.*, pp. 728–734.
48. Sculler, F., Charpentier, J., Semail, E., and Clenet, S. (2007) Comparison of two 5-phase PM machine winding configurations, Application on naval propulsion specification. *Proc. Elect. Mach. Drives Conf. IEMDC*, pp. 34–39.
49. Jones, M. (2005) A novel concept of series-connected multi-phase multi-motor drive systems. PhD Thesis, School of Engineering, Liverpool John Moores University, Liverpool, UK.
50. Chen, S., Lipo, T. A., and Fitzgerald, D. (1996) Sources of induction motor gearing currents caused by PWM inverters. *IEEE Trans. Ener. Conv.*, **11**, 25–32.
51. Wang, F. (2000) Motor shaft voltages and bearing currents and their reduction in multi-level medium voltage PWM voltage source inverter drive applications. *IEEE Trans. Ind. Appl.*, **36**, 1645–1653.
52. Rodriguez, J., Moran, L., Pontt, J., Osorio, R., and Kouro, S. (2003) Modeling and analysis of common-mode voltages generated in medium voltage PWM-CSI drives. *IEEE Trans. Power Elect.*, **18**(3), 873–879.
53. Leonhard, W. (1985) *Control of Electrical Drives*. Springer-Verlag.
54. Grahame, D. and Lipo, T. A. (2003) *Pulse Width modulation for power converters*. IEEE Power Engineering Series by Wiley Inter-Science.
55. Kazmierkowski, M. P., Krishnan, R., and Blaabjerg, F. (2002) *Control in Power Electronics-Selected problems*. Academic Press, New York.
56. Iqbal, A. and Moinuddin, S. (2009) Comprehensive relationship between carrier-based PWM and space vector PWM in a five-phase VSI. *IEEE Trans. Power Elect.*, **24**(10), 2379–2390.
57. Iqbal, A., Levi, E., Jones, M., and Vukosavic, S. N. (2006) Generalised Sinusoidal PWM with harmonic injection for multi-phase VSIs. *IEEE 37th Power Elect. Spec. Conf. (PESC)*, Jeju, Korea, 18–22 June, CD\_ROM, paper no. ThB2-3, pp. 2871–2877.
58. Ojo, O. and Dong, G. (2005) Generalized discontinuous carrier-based PWM modulation scheme for multi-phase converter machine systems. *Proc. IEEE Ind. Appl. Soc. Ann. Mtg, IAS*, Hong Kong, CD-ROM, paper IAS 38, p 3.
59. Jones, M., Dujic, D., Levi, E., and Vukosavic, S. N. (2009) Dead-time effects in voltage source inverter fed multi-phase AC motor drives and their compensation. *Proc. 13th Int. Power Elect. Conf. EPE'09*, Barcelona, 5–8 September, pp. 1–10.
60. Rehalet, J. (1993) Industrial applications of model based predictive control. *Automatica*, **29**(5), 1251–1274.
61. Qin, S. J. and Badgwell, T. A. (2003) A survey of industrial model predictive control technology'. *Cont. Eng. Pract.*, **11**, 733–764.
62. Linder, A. and Kennel, R. (2005) Model Predictive control for electric Drives. *Proc. 36th An. IEEE PESC*, Recife, Brazil, pp. 1793–1799.
63. Kouro, S., Cortes, P., Vargas, R., Ammann, U., and Rodriguez, J. (2009) Model Predictive Control: A simple and powerful method to control power converters. *IEEE Trans Ind. Elect.*, **56**(6), 1826–1839.
64. Cortes, P., Kazmierkowski, P., Kennel, R. M., Quevedo, D. E., and Rodriguez, J. (2008) Predictive control in power electronics and drives. *IEEE Trans. Ind. Elect.*, **55**(12), 4312–4321.
65. Barrero, F., Arahal, M. R., Gregor, R., Toral, S., and Duran, M. J. (2009) A proof of concept study of predictive current control for VSI driven asymmetrical dual three-phase AC machines. *IEEE Tran. Ind. Elect.*, **56**(6), 1937–1954.

66. Arahal, M. R., Barrero, F., Toral, S., Duran, M., and Gregor, R. (2009) Multi-phase current control using finite state model predictive control. *Cont. Eng. Prac.*, **17**, 579–587.
67. Maciejowski, J. M. (2002) *'Predictive control with constraints'*, Prentice Hall.
68. Mayne, D. Q., Rawlings, J. B., Rao, C. V., and P.O.M. Scokaert, P. O. M. (2000) Constrained model predictive control: Stability and optimality. *Automation*, **36**(6), 789–814.
69. Lazar, M., Heemels, W., Bemporad, A., and Weiland, S. (2007) Discrete-time non-smooth NMPC: Stability and robustness. *Assess. Fut. Direc. NMPC*, LNCIS, **358**, 93–103. Springer, Heidelberg.
70. Magni, L. and Scattolini, R. (2007) Robustness and robust design of MPC for non-linear discrete time systems. *Assess. Fut. Dir. NMPC*. LNCIS, **358**, 239–254.
71. Franklin, G. F., Powell, J. D., and Emami-Naeini, A. (1994) *Feedback Control of Dynamics Systems*. 3rd edn. Addison-Wesley.
72. Bemporad, A., Morari, M., Dua, V., and Pistikopoulos, E. N. (2002) The explicit linear quadratic regulator for constrained systems. *Automatica*, **38**(1), 3–20.



# 8

## Sensorless Speed Control of AC Machines

### 8.1 Preliminary Remarks

Sensorless speed control of induction machine (IM) drives has, in the past decade, become a mature technology for a wide speed range [1–3].

The elimination of the rotor speed sensor, without affecting performance, is a major trend in advanced drives control systems [1]. The advantages of speed sensorless AC drives are reduced hardware complexity, lower costs, elimination of the sensor cable, better noise immunity, increased reliability, access to both sides of the shaft, less maintenance requirements, and higher robustness. An encoder is expensive and a problematic factor. The special motor shaft extension increases the drive's price. The use of encoders affects the reliability, particularly in hostile environments. In general, the operation in explosive, corrosive, or chemically aggressive environments requires a motor without a speed sensor.

A variety of different solutions for sensorless AC drives have been proposed, mostly in the past two decades. Their advantages and limits are reviewed in many survey papers [1–60].

Many methods are generally accepted as better solutions for high sensorless performance, for example, model reference adaptive system (MRAS), Kalman Filters, adaptive non-linear flux observer, sliding mode observers, and other improvements [7–14].

### 8.2 Sensorless Control of Induction Motor

Two basic approaches are used for sensorless control. The first includes methods that model the induction motor by its state equations [1]. A sinusoidal magnetic field in the air gap is assumed.

The models are either implemented as open-loop structures, like the stator model [1,11], or as closed-loop models, like adaptive observers [5,17]. The adaptive flux observers are now receiving considerable attention and many achieving new solutions because of their high precision and relative robustness against machine parameter deviation [1,10].

Open loop models and even adaptive observers have stability limits at very low stator frequencies. The rotor induced voltage at such operating points is then zero or close to zero, which renders the induction motor an unobservable system.

The basic limitation for sensorless operation is the DC offset components in the stator current and voltage acquisition channels at very low speeds [1]. At lower speeds, voltage distortions caused by the PWM inverter become significant.

The second approach used for low speed sensorless operation is the signal injection technique [1]. Carrier injection methods for sensorless control are sophisticated and the design must match the properties of the motor [1,4,18,41]. This makes the method unfeasible for practical application, so will not be discussed in this book.

Eliminating the speed sensor from the drive system requires estimation of the state variables, for example, motor speed and machine flux using stator variables. In this chapter we will discuss a few simple solutions for sensorless AC motor drives.

### 8.2.1 Speed Estimation using Open Loop Model and Slip Computation

The rotor speed in the vector control scheme can be computed from a difference between the synchronous speed and the slip speed, using the following known equation:

$$\hat{\omega} = \frac{\psi_{s\alpha}\psi_{s\beta(k)} - \psi_{s\beta}\psi_{s\alpha}}{\psi_s^2} - \hat{\omega}_{2r} \quad (8.1)$$

where

$$\omega_{si} = \frac{R_r(\psi_{s\alpha}i_{s\beta} - \psi_{s\beta}i_{s\alpha})}{\psi_s^2} \quad (8.2)$$

The stator flux components (or rotor flux in the rotor flux oriented system) can be computed using open loop models, as explained in earlier chapters, or by using closed loop observer systems. These observers can be used for speed computation in addition to the flux components, as will be discussed in the following sections.

### 8.2.2 Closed Loop Observers

The accuracy of the open loop models decreases as the mechanical speed decreases [1]. The performance depends on how the machine parameters can be identified. Those parameters have the largest influence on system operation at lower speeds. The robustness against parameter deviation can be significantly improved by using closed loop observers.

### 8.2.2.1 Observer 1

The Observer 1 is based on the voltage  $\psi_s, \psi_r$  model of the induction motor, with combination of the rotor and stator fluxes and stator current relationships [62]:

$$\tau'_s \frac{d\psi_s}{d\tau} + \psi_s = k_r \psi_r + \mathbf{u}_s \quad (8.3)$$

To prevent problems of voltage drift and to offset errors, instead of pure integrators, low pass filters are used. The limitation of the estimated stator flux is tuned to the stator flux nominal value. In addition, the extra compensation part is added, as presented in [61].

Based on equations (8.9)–(8.11), the rotor Observer 1 equations are [62]

$$\frac{d\hat{\psi}_{s\alpha}}{d\tau} = \frac{-\hat{\psi}_{s\alpha} + k_r \hat{\psi}_{r\alpha} + \hat{\mathbf{u}}_{s\alpha}}{\tau'_s} - k_{ab} (\mathbf{i}_1 - \hat{\mathbf{i}}_1) \quad (8.4)$$

$$\hat{\psi}_r = \frac{1}{k_r} (\hat{\psi}_s - \sigma L_s \mathbf{i}_s) \quad (8.5)$$

where  $k$  is observer gain.

The estimated value of the  $\mathbf{i}_s$  current appearing in equation (8.5) is

$$\hat{\mathbf{i}}_s = \frac{\hat{\psi}_s - k_r \hat{\psi}_r}{\sigma L_s} \quad (8.6)$$

The rotor flux Observer I structure is presented in Figure 8.1.

The rotor flux calculator receives the observed stator flux components and the measured stator current components, both in the stationary  $\alpha - \beta$  axis frame. These input signals require high precision, which is achieved by using the correcting error signal in equation (2.4) derived from the difference between the estimated and the measured stator current vectors. The stator current calculator in equation (2.6) receives the estimated stator flux and rotor flux. Any existing error may be further eliminated by providing the current error as a negative feedback signal in the stator flux observer system. The stator current error signal  $(\mathbf{i}_s - \hat{\mathbf{i}}_s)$  in the negative feedback of the flux observer is multiplied by a gain  $k$  to increase its robustness and its stability behavior, as well as to help eliminate additional disturbances related to the DC drift and computational and measurement errors.

Generally, the observer matrix gain  $k$  can be tuned experimentally and set at a constant real value. The tuning should be done for a wide range of operating speeds and varying load conditions. Finally, a behaviorally chosen optimum constant value of  $k$  should be selected. As was shown in the results sections, in spite of that simple tuning process, the described observer works properly, even for the low motor small voltage frequency supply.

The next calculation is of a rotor flux vector angle needed for transforming from the stationary to the rotating frame, and vice versa for a vector controller. The flux position

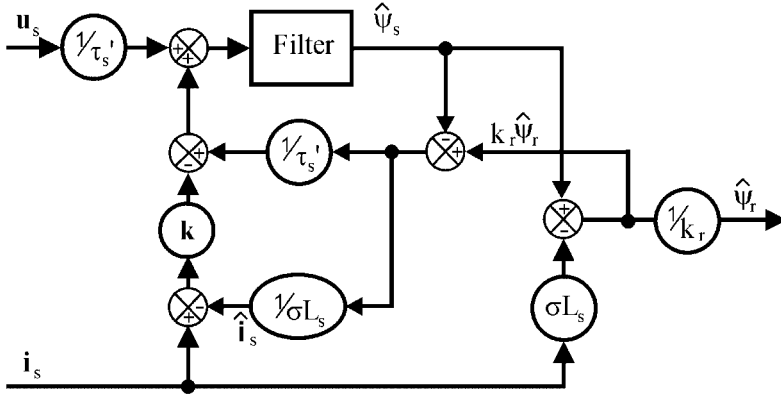


Figure 8.1 Structure of the proposed flux Observer I system

calculator receives stator flux components in the  $\alpha$ -axis and  $\beta$ -axis stationary frame. The derivative of this angle gives the rotor flux speed  $\omega_{\psi_r}$ .

Based on the estimated rotor flux components, the flux magnitude and angle position are

$$|\hat{\psi}_r| = \sqrt{\hat{\psi}_{r\alpha}^2 + \hat{\psi}_{r\beta}^2} \tag{8.7}$$

$$\hat{\rho}_{\psi_r} \text{arc tg} \frac{\hat{\psi}_{r\beta}}{\hat{\psi}_{r\alpha}} \tag{8.8}$$

If the main goal of the drive controller is to control the torque, then the drive system does not require a rotor speed signal. However, rotor velocity is required to perform closed-loop speed control. In the proposed estimation method, the motor mechanical speed signal is obtained by subtracting the slip from the rotor flux speed:

$$\hat{\omega}_r = \hat{\omega}_{\psi_r} - \hat{\omega}_2 \tag{8.9}$$

where the rotor flux pulsation is

$$\hat{\omega}_{\psi_r} = \frac{d\hat{\rho}_{\psi_r}}{d\tau} \tag{8.10}$$

and rotor slip pulsation is obtained from

$$\hat{\omega}_2 = \frac{(\hat{\psi}_{r\alpha} \hat{i}_{s\beta} - \hat{\psi}_{r\beta} \hat{i}_{s\alpha})}{|\hat{\psi}_r|^2} \tag{8.11}$$

The rotor flux magnitude, position, and mechanical speed estimation structure is presented in Figure 8.2.

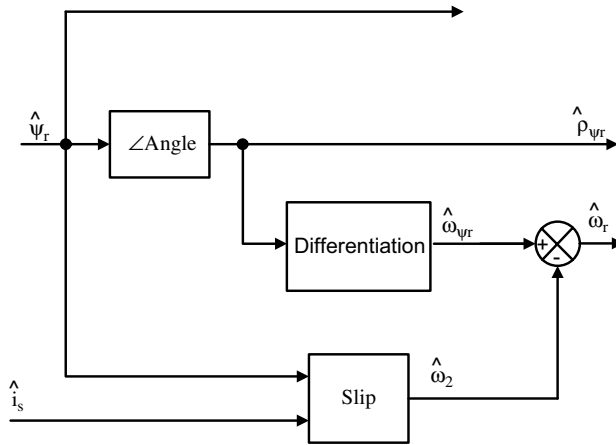


**Figure 8.2** Speed estimation calculation structure

The Observer I system in equations (8.4)–(8.6) does not contain information on rotor speed, therefore does not require computation or knowledge of its shaft position. Speed computation is performed in a separate block, as shown in equations (8.9)–(8.11), which does not affect the precision of the proposed observer. This eliminates any additional error associated with computing or even measuring such signals, particularly at extremely low frequencies. It is robust in that it does not require additional techniques for parameters tuning or DC drift elimination.

**Simulink Model of Observer 1**

The observer 1 for the estimation of stator and rotor fluxes is depicted by

$$\frac{d\hat{\psi}_{sx}}{d\tau} = \frac{1}{\tau'_s} (-\hat{\psi}_{sx} + k_r \hat{\psi}_{rx} + u_{sx}) - k(i_{sx} - \hat{i}_{sx}) \tag{8.12}$$

$$\frac{d\hat{\psi}_{sy}}{d\tau} = \frac{1}{\tau'_s} (-\hat{\psi}_{sy} + k_r \hat{\psi}_{ry} + u_{sy}) - k(i_{sy} - \hat{i}_{sy}) \tag{8.13}$$

$$\hat{\psi}_{rx} = \frac{\hat{\psi}_{sx} - \sigma L_s \hat{i}_{sx}}{k_r} \tag{8.14}$$

$$\hat{\psi}_{ry} = \frac{\hat{\psi}_{sy} - \sigma L_s \hat{i}_{sy}}{k_r} \tag{8.15}$$

The above equations are modeled in Figure 8.3.

**Stator Currents**

The stator current components can be computed from

$$\hat{i}_{sx} = \frac{\hat{\psi}_{sx} - k_r \hat{\psi}_{rx}}{\sigma L_s} \tag{8.16}$$

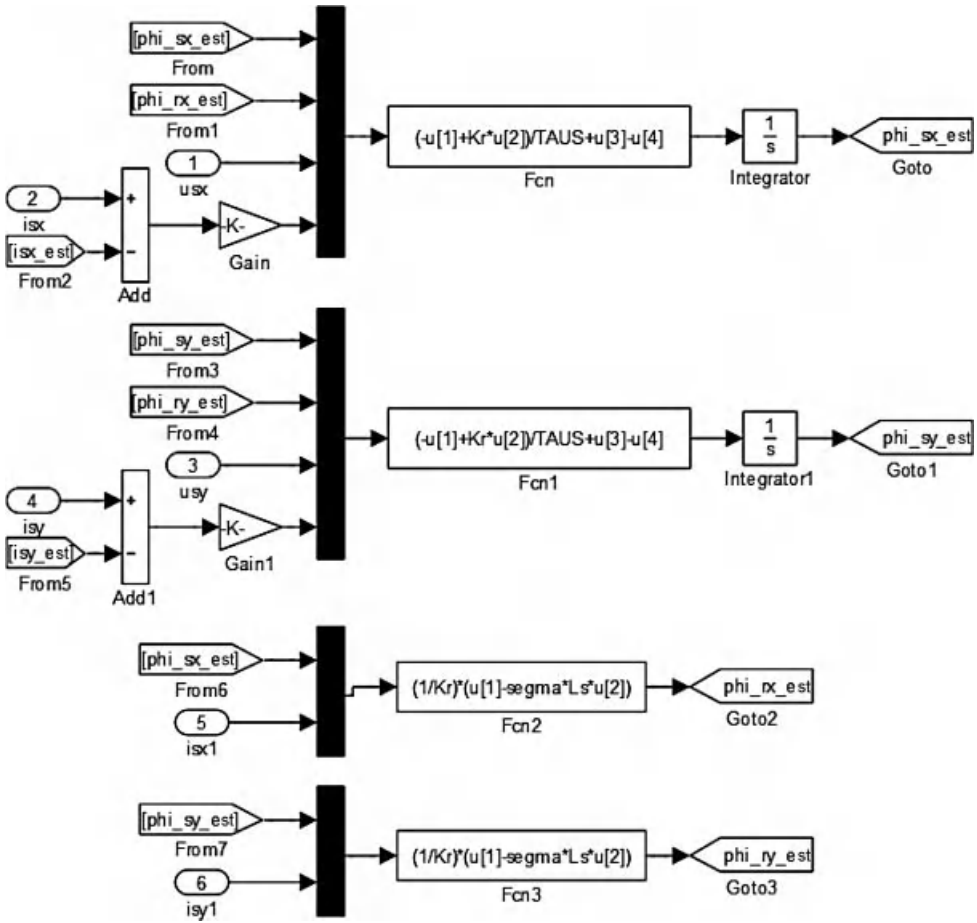


Figure 8.3 The stator and rotor flux observer system (Observer 1)

$$\hat{i}_{sy} = \frac{\hat{\psi}_{sy} - k_r \hat{\psi}_{ry}}{\sigma L_s} \tag{8.17}$$

The above equations are modeled in Figure 8.4.

### 8.2.2.2 Observer 2

The second flux observer system (Figure 8.5) was recently described in [20]; however, it was combined with an additional observer for speed computation. It is important to note that such a solution, as in [20], did not give satisfactory performance at low speed ranges. The approach in this paper is to compute the rotor speed, not from an additional speed observer, as in [20], but using slip computation (equations 8.1 and 8.2). This approach of speed computation extended the operating point of this observer significantly, more than that presented in [20]. In [20], it was possible to operate the motor down to 3% of rated speed, while in this procedure all observers

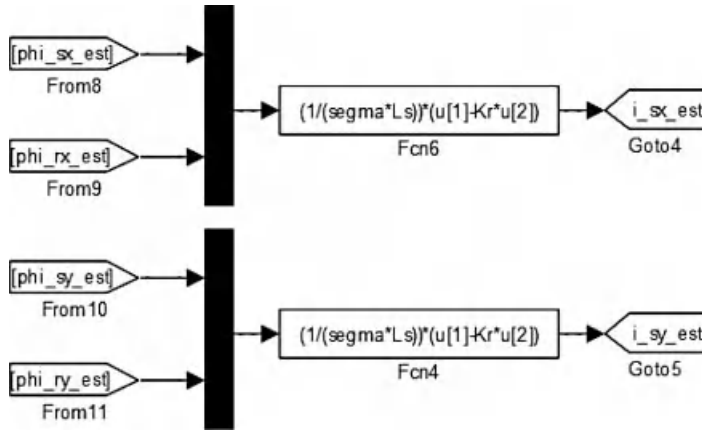


Figure 8.4 The observed stator currents

operated correctly, even around zero speed. The mathematical description of the third observer is given as [20]

$$\tau'_s \frac{d\hat{\psi}_s}{dt} + \hat{\psi}_s = k_r \hat{\psi}_r + u_s \tag{8.18}$$

$$\tau'_s \frac{d\hat{\psi}'_s}{dt} + \hat{\psi}'_s = k_r \hat{\psi}'_r + u_s \tag{8.19}$$

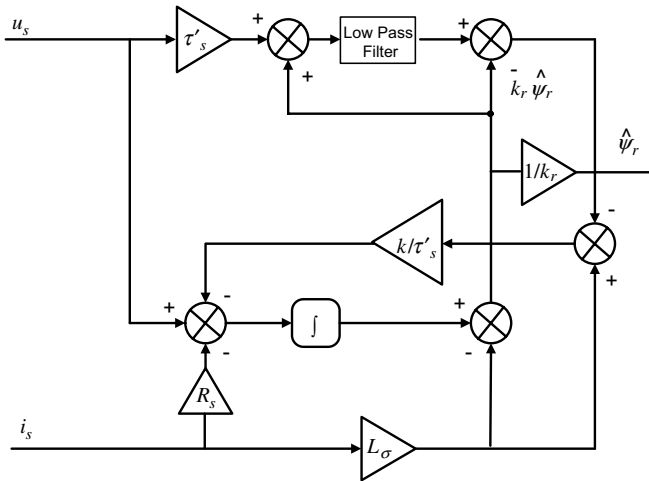


Figure 8.5 Version 2 of observer system

$$\frac{d\hat{\psi}_s''}{dt} = u_s - R_s i_s - k \Delta u_s \quad (8.20)$$

$$\hat{\psi}_r = \frac{1}{k_r} (\hat{\psi}_s'' - L_\sigma i_s) \quad (8.21)$$

$$\hat{\psi}_\sigma'' = L_\sigma i_s \quad (8.22)$$

$$\hat{\psi}'_\sigma = \hat{\psi}'_s - k_r \hat{\psi}_r \quad (8.23)$$

$$\Delta \psi_\sigma = \hat{\psi}_\sigma'' - \hat{\psi}'_\sigma \quad (8.24)$$

$$\Delta u_s = \frac{1}{\tau_s} \Delta \hat{\psi}_\sigma \quad (8.25)$$

which is

$$\Delta u_s = R_s \Delta i_s \quad (8.26)$$

Rotor speed and flux position are computed using the same procedure as earlier described systems (equations 8.1–8.8):

The observers' gains were selected experimentally and are shown in the following sections. Although a constant gain was used in our verifications, it was possible to run the controller around zero frequency with sufficient robustness against parameter variation. The influence of the selected gain on the accuracy and dynamics of the observer will be presented in the experimental section of this paper.

### 8.2.2.3 Observer 3

This kind of observer [68,69] is a speed observer and based on the Luenberger observer system (Figure 8.6). The observer may be used for rotor flux and speed estimation. It has been developed and discussed for almost 20 years. The differential equations of the speed observer are [68,69]

$$\frac{d\hat{i}_{sx}}{dt} = a_1 \hat{i}_{sx} + a_2 \hat{\psi}_{rx} + a_3 \omega_r \hat{\psi}_{ry} + a_4 u_{sx} + k_i (i_{sx} - \hat{i}_{sx}) \quad (8.27)$$

$$\frac{d\hat{i}_{sy}}{dt} = a_1 \hat{i}_{sy} + a_2 \hat{\psi}_{ry} - a_3 \omega_r \hat{\psi}_{rx} + a_4 u_{sy} + k_i (i_{sy} - \hat{i}_{sy}) \quad (8.28)$$

$$\frac{d\hat{\psi}_{rx}}{d\tau} = a_5 \hat{i}_{sx} + a_6 \hat{\psi}_{rx} - \zeta_y - k_2 (\hat{\omega}_r \hat{\psi}_{ry} - \zeta_y) \quad (8.29)$$



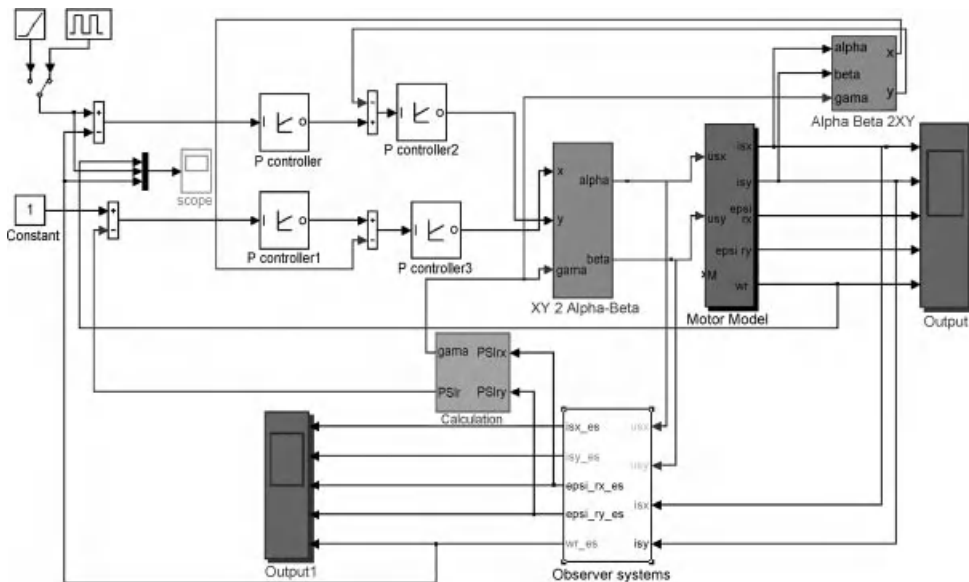


Figure 8.6 Control of induction motor model with the speed observer system [Observer\_three]

$$\frac{d\hat{\psi}_{ry}}{d\tau} = a_5 \hat{i}_{sy} + a_6 \hat{\psi}_{ry} + \zeta_x + k_2 (\hat{\omega}_r \hat{\psi}_{rx} - \zeta_x) \tag{8.30}$$

$$\frac{d\zeta_x}{d\tau} = k_1 (i_{sy} - \hat{i}_{sy}) \tag{8.31}$$

$$\frac{d\zeta_y}{d\tau} = -k_1 (i_{sx} - \hat{i}_{sx}) \tag{8.32}$$

$$\hat{\omega}_r = S \left( \sqrt{\frac{\zeta_x^2 + \zeta_y^2}{\hat{\psi}_{rx}^2 + \hat{\psi}_{ry}^2} + k_4 (V - V_f)} \right) \tag{8.33}$$

where  $\hat{\cdot}$  denotes estimated variables;  $k_1, k_2, k_3$  are the observer gains; and  $S$  is the sign of speed (Figures 8.7 and 8.8). The values  $\zeta_x, \zeta_y$  are the components of disturbance vector;  $V$  is the control signal obtained through experiments; and  $V_f$  is the filtered signal  $V$ . The observer coefficients  $k_1$  to  $k_4$  have small values and are selected experimentally. The coefficients depend on the operating point, for example, torque, speed, etc. The coefficient  $k_2$  depends on the rotor speed:

$$k_2 = a + b \cdot |\hat{\omega}_{rf}| \tag{8.34}$$

where  $a$  and  $b$  are constants and  $\hat{\omega}_{rf}$  is the absolute value of the estimated and filtered rotor speed.

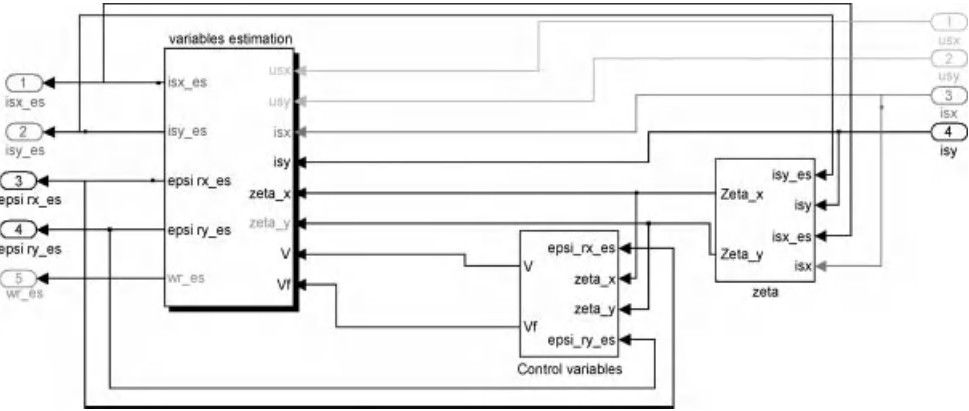


Figure 8.7 Observer 3 details

The control signals are defined as

$$V = \hat{\psi}_{rx}\zeta_y - \hat{\psi}_{ry}\zeta_x \tag{8.35}$$

$$\frac{dV_f}{d\tau} = \frac{1}{T_1} (V_1 - V_f) \tag{8.36}$$

This observer is appropriate for very low speed operations.

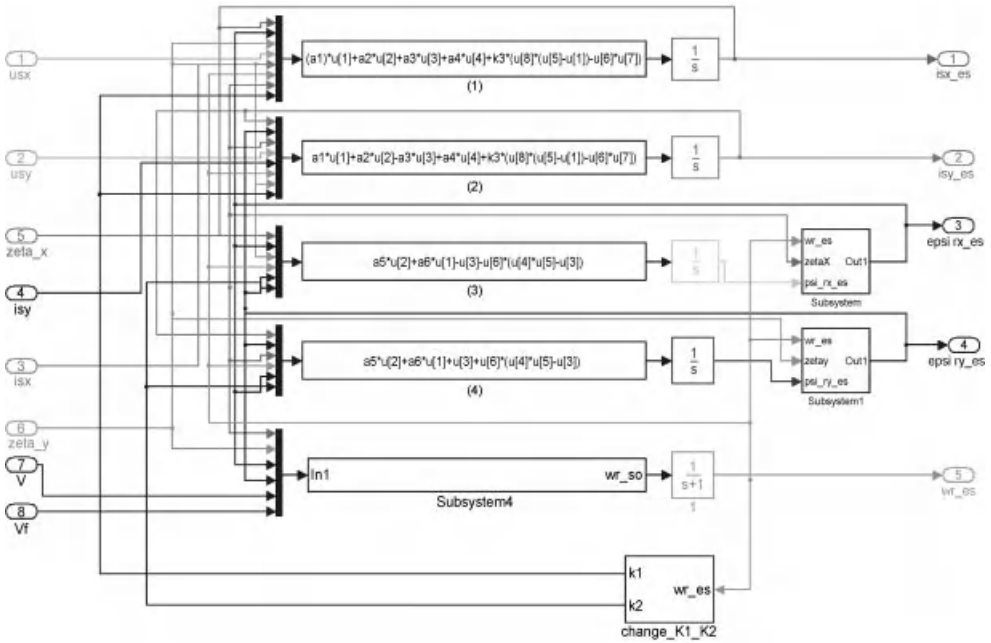


Figure 8.8 Variables estimation

The observer is simulated in Simulink in [70]. The Simulink software file of control of the induction motor model with the speed observer system is [*Observer\_three*]. The motor parameters are located in [*PAR\_AC*], which should be first executed.

### 8.2.3 MRAS (Closed-loop) Speed Estimator

Although several schemes are available for sensorless operation of a vector controlled drive, the MRAS is popular because of its simplicity [1,2,25–36]. The model reference approach takes advantage of using two independent machine models for estimating the same state variable [36–45,47,49]. The estimator that does not contain the speed to be computed is considered a reference model. The other block, which contains the estimated variable, is regarded as an adjustable model (Figure 8.9). The estimation error between the outputs of the two computational blocks is used to generate a proper mechanism for adapting the speed. The block diagram of the MRAS-based speed estimation is shown in Figure 8.9.

In this scheme, the outputs of the reference model and the adjustable model denoted in Figure 8.9 by  $\Psi_r^{(1)}$  and  $\Psi_r^{(2)}$  are two estimates of the rotor flux vectors.

The difference between the two estimated vectors is used to feed a PI controller (could be the only gain). The output of the controller is used to tune the adjustable model. The tuning signal actuates the rotor speed, which makes the error signal zero. The adaptation mechanism of MRAS is a simple gain, or in this example, a PI controller algorithm:

$$\omega^{est} = K_p \varepsilon + K_i \int \varepsilon dt \quad (8.37)$$

where the input of the PI controller is

$$\varepsilon = \psi_{\beta r}^{(1)} \psi_{\alpha r}^{(2)} - \psi_{\alpha r}^{(1)} \psi_{\beta r}^{(2)} \quad (8.38)$$

and  $K_p$  and  $K_i$  are the parameters of the PI controller.

#### 8.2.3.1 Simulink MRAS Model

The MRAS consists of two models, the reference one and the tuned one. Both models may be formed using the following equations.

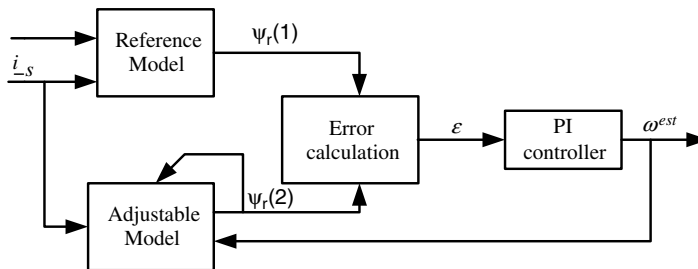


Figure 8.9 Block diagram of MRAS

By letting the reference frame speed  $\omega_a = 0$ , the motor basic equations are

$$\underline{v}_s = R_s \underline{i}_s + \frac{d\underline{\psi}_s}{dt} \quad (8.39)$$

$$0 = R_r \underline{i}_r + \frac{d\underline{\psi}_r}{dt} - j\omega_r \underline{\psi}_r \quad (8.40)$$

The extraction of the stator flux vector and rotor current vector enables the computation of the rotor flux vector using the following known equation:

$$\begin{aligned} \frac{d\underline{\psi}_r}{dt} &= \frac{L_r}{L_m} \left[ \underline{v}_s - R_s \underline{i}_s - \sigma L_s \frac{d\underline{i}_s}{dt} \right] \\ \frac{d\underline{\psi}_r}{dt} &= \left[ -\frac{1}{T_r} + j\omega_r \right] \underline{\psi}_r + \frac{L_m}{T_r} \underline{i}_s \end{aligned} \quad (8.41)$$

The first equation (8.41) can be used to calculate the rotor flux vector on the basis of the measured stator current and commanded voltage (or computed using PWM vectors). This first equation is independent of rotor speed, therefore it may represent the reference model of Figure 8.9. On the other hand, the second equation (8.41) requires stator currents only and is dependent on the rotor speed. Therefore, this equation may represent the adjustable (adaptive) model of Figure 8.9.

In matrix form those equations (models) appear as

$$\begin{aligned} p \begin{bmatrix} \underline{\psi}_{\alpha r} \\ \underline{\psi}_{\beta r} \end{bmatrix} &= \frac{L_r}{L_m} \left[ \begin{bmatrix} v_{\alpha s} \\ v_{\beta s} \end{bmatrix} - \begin{bmatrix} (R_s + \sigma L_s p) & 0 \\ 0 & (R_s + \sigma L_s p) \end{bmatrix} \begin{bmatrix} i_{\alpha s} \\ i_{\beta s} \end{bmatrix} \right] \\ p \begin{bmatrix} \underline{\psi}_{\alpha r} \\ \underline{\psi}_{\beta r} \end{bmatrix} &= \begin{bmatrix} -1/T_r & -\omega_r \\ \omega_r & -1/T_r \end{bmatrix} \begin{bmatrix} \underline{\psi}_{\alpha r} \\ \underline{\psi}_{\beta r} \end{bmatrix} + \frac{L_m}{T_r} \begin{bmatrix} i_{\alpha s} \\ i_{\beta s} \end{bmatrix} \end{aligned} \quad (8.42)$$

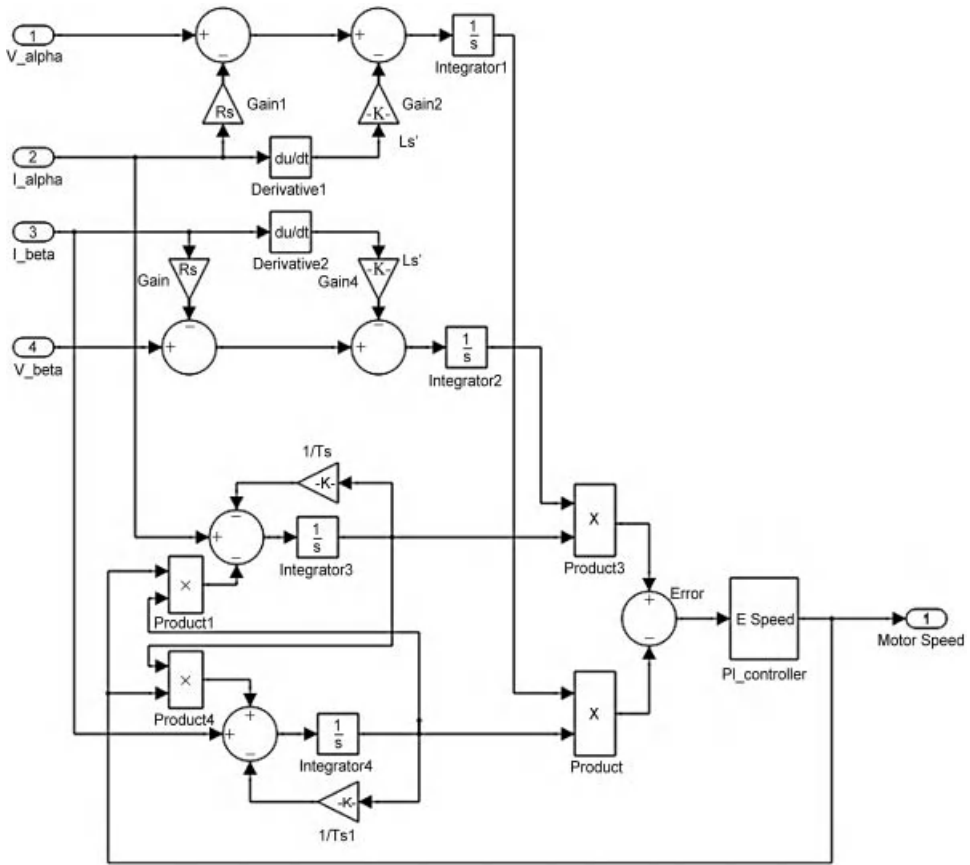
where  $\sigma = 1 - (L_m^2/L_s L_r)$  and  $p = \frac{d}{dt}$

Figure 8.10 describes the Simulink diagram of MRAS with both references (upper) and adaptive (lower) models used for motor speed estimation. The currents ( $i_\alpha$  and  $i_\beta$ ) and voltages ( $V_\alpha$  and  $V_\beta$ ) are taken from motor terminals for the speed estimation.

Indeed, it is possible to use different models either as a reference or adaptive system. Below is an additional example of the reference system in which Observer one is used as reference model. This is robust and not sensitive to motor parameters, which gives better results, even for very low frequencies.

### 8.2.3.2 MRAS with Observer 1

In this section, a complete and detail description of an induction motor model with MRAS and Observer one is explained. The induction motor model, induction motor controller,



**Figure 8.10** Simulink diagram of the MRAS estimator (both reference and adaptive models)

MRAS estimator, and the observer are illustrated in Figure 8.11. The Simulink software file of vector control of IM model is *[IM\_VC\_sensor\_less\_observer]*. The motor parameters are located in the file model properties within the initial function. Parameters should run automatically.

Description of induction motor with vector controller is given in an earlier chapter; therefore, will not be repeated.

The Simulink block of the observer is shown in Figure 8.12. The sensorless flux observer is used for the estimation of stator and rotor fluxes. The observer can also be used for other variable estimations.

As shown in Figure 8.12, the adaptive system is connected with inputs (fluxes) obtained from the sensorless observer, which is used as the reference model. The reference model is used for adjusting the speed in an adaptive model. By this method a robust scheme is possible to be designed, because the sensorless flux observer is insensitive to motor parameter deviation.

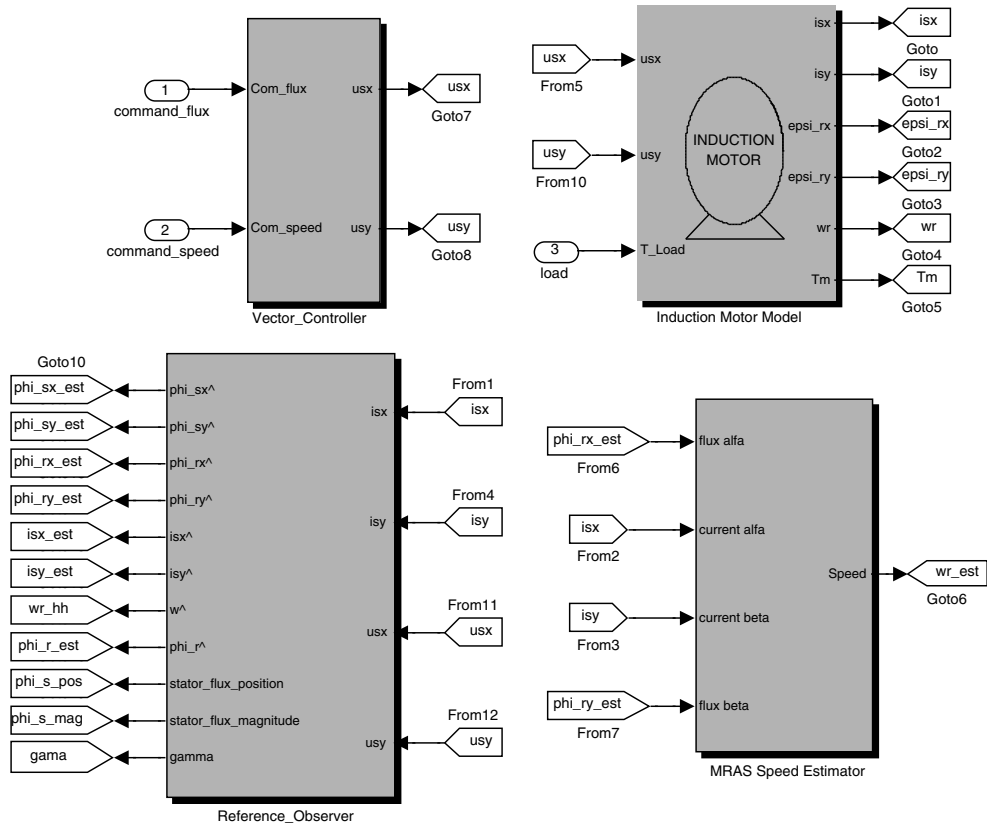


**Figure 8.11** Simulink blocks of induction motor, vector controller, reference observer, and MRAS observer

### 8.2.3.3 Simulation Results

The motor parameter for simulation are stator and rotor resistances  $R_s = R_r = 0.045$  p.u., stator and rotor inductances  $L_s = L_r = 1.927$  p.u., motor mutual inductance  $L_m = 1.85$  p.u., motor-load moment of inertia  $J = 5.9$  p.u., motor load torque, and  $m_o = 0.7$  p.u. The simulation result for a square pulse demand in speed is shown in Figure 8.13. The simulation time is set at 10 s. A step speed command of 0.9 p.u. magnitude is given at 0 s and then becomes zero at 5 s. A step load torque command is applied at 2 s and then makes  $t$  zero at 6 s The rotor flux command is set at 1 p.u. The corresponding simulation results of the motor speed  $\omega_r$ , currents  $I_d$  and  $I_q$ , rotor flux, load torque, and applied voltage in the p.u. system are shown in Figure 8.13. Proper limiting of the control variables is not provided. This should be taken into account for right control.

### 8.2.4 The Use of Power Measurements

The use of instantaneous reactive power and instantaneous active power provides a simplification of the speed estimation process [21,22].

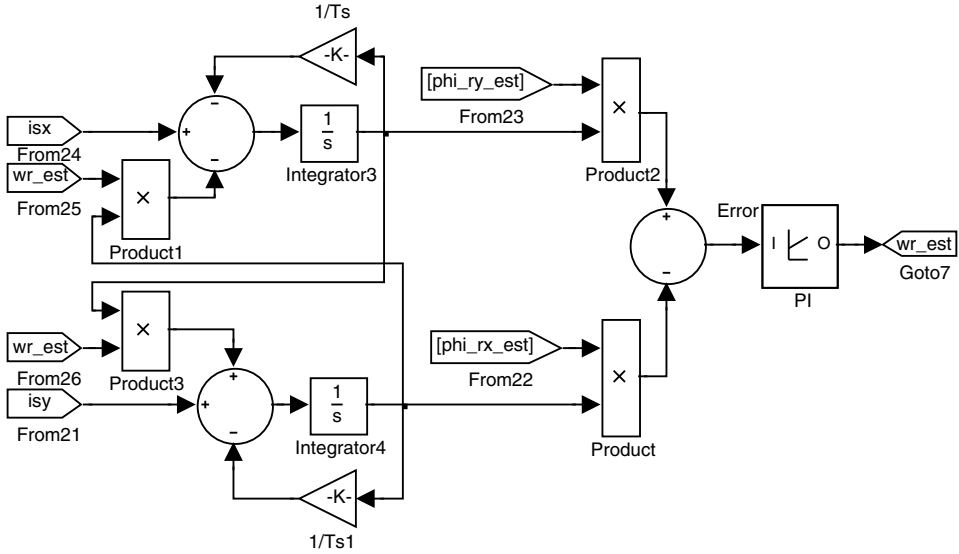


**Figure 8.12** Simulink diagram of adaptive system with input from sensorless observer

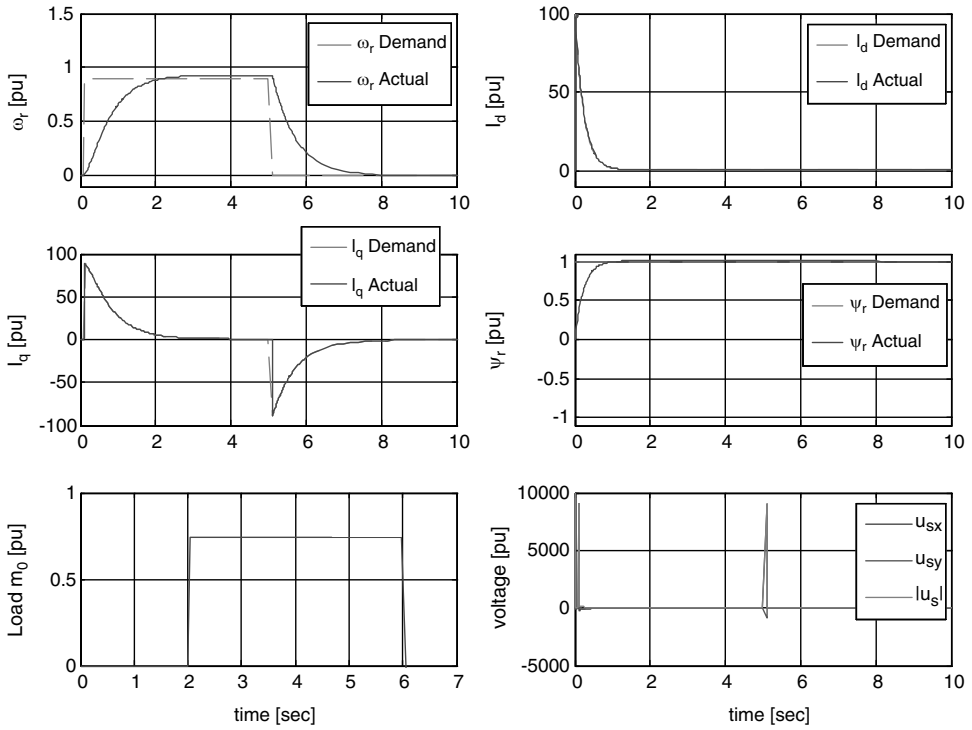


**Figure 8.13** Simulation results of motor speed  $w_r$ , currents  $I_d$  and  $I_q$ , rotor flux, load torque, and applied voltage in the p.u. system

Reference [62] provides new definitions of instantaneous powers in three-phase ( $\mathbf{p}$  and  $\mathbf{q}$ ) circuits, based on the instantaneous voltages and currents. The power definitions are

$$p = u_{sx}i_{sx} + u_{sy}i_{sy} \quad (8.43)$$

$$q = u_{sy}i_{sx} - u_{sx}i_{sy} \quad (8.44)$$

The used power  $\mathbf{P}$  and  $\mathbf{Q}$  for speed estimation are obtained after filtration (using a first-order filter) of  $\mathbf{p}$  and  $\mathbf{q}$  calculated from the above equations.

Rotor angular speed may be determined by using combinations between power equations, multiscalar variables, and the machine model (differential equations of stator current and rotor flux vector components) [21,22].

For simplification, the left-hand side of the machine model is equal to zero in steady state. Accordingly, the rotor speed can be computed in different ways [21,22]:

$$\omega_r = \frac{a_1 I_s^2 + a_2 z_3 + a_4 P}{a_3 z_2} \quad (8.45)$$

or

$$\omega_r = \frac{-a_2 z_2 - \omega_{si} I_s^2 + a_4 Q}{I_s^2 + a_3 z_3} \quad (8.46)$$

where

$$z_2 = \psi_{rx}i_{sy} - \psi_{ry}i_{sx} \quad (8.47)$$

$$z_3 = \psi_{rx}i_{sx} + \psi_{ry}i_{sy} \quad (8.48)$$

### 8.3 Sensorless Control of PMSM

The rotor speed and produced torque can be computed using the Luenberger back emf observer. Assuming that the dynamics of the mechanical system are much slower than the dynamics of the electric variables, we may assume that the motor back emf does not change during an observer sampling period, so that

$$\frac{de_\alpha}{dt} = 0 \quad (8.49)$$

$$\frac{de_\beta}{dt} = 0 \quad (8.50)$$

The used Luenberger observer for the PMSM back emf in the stationary  $\alpha\beta$  frame is described as [63,64,67]



$$\frac{d\hat{i}_\alpha}{dt} = \frac{1}{L_s} u_\alpha - \frac{R_s}{L_s} \hat{i}_\alpha + \frac{1}{L_s} \hat{e}_\alpha + K_{i\alpha} (i_\alpha - \hat{i}_\alpha) \quad (8.51)$$

$$\frac{d\hat{i}_\beta}{dt} = \frac{1}{L_s} u_\beta - \frac{R_s}{L_s} \hat{i}_\beta + \frac{1}{L_s} \hat{e}_\beta + K_{i\beta} (i_\beta - \hat{i}_\beta) \quad (8.52)$$

$$\frac{d\hat{e}_\alpha}{dt} = K_{e\alpha} (i_\alpha - \hat{i}_\alpha) \quad (8.53)$$

$$\frac{d\hat{e}_\beta}{dt} = K_{e\beta} (i_\beta - \hat{i}_\beta) \quad (8.54)$$

where  $\hat{\cdot}$  is the estimated value;  $L_s$  is the stator inductance, assuming that  $L_s = L_d$ ; and  $K_{i\alpha}$ ,  $K_{i\beta}$ ,  $K_{e\alpha}$ ,  $K_{e\beta}$ , are observer gains (when using symmetrical motor  $K_{i\alpha} = K_{i\beta} = K_i$ ,  $K_{e\alpha} = K_{e\beta} = K_e$ ).

The state variables in the observer are stator currents  $i_\alpha$ ,  $i_\beta$ ; however, the back emf signals  $e_\alpha$ ,  $e_\beta$  are disturbances that should be identified in the observer. The block showing such an operation is illustrated in Figure 8.14.

The rotor angle can be computed from the following:

$$\theta = -\arctan \frac{\hat{e}_\alpha}{\hat{e}_\beta} \quad (8.55)$$

where

$$\sin \hat{\theta} = -\frac{\hat{e}_\alpha}{|\hat{e}|} \quad (8.56)$$

$$\cos \hat{\theta} = \frac{\hat{e}_\beta}{|\hat{e}|} \quad (8.57)$$

$$|\hat{e}| = \sqrt{(\hat{e}_\alpha)^2 + (\hat{e}_\beta)^2} \quad (8.58)$$

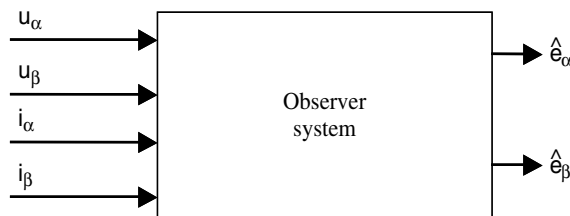


**Figure 8.14** emf observer

Rotor speed is identified by differentiating the rotor angle:

$$\hat{\omega}_r = \frac{d\hat{\theta}}{dt} \tag{8.59}$$

$$|\hat{\omega}_r| = \frac{|\hat{e}|}{k_e} \tag{8.60}$$

In this example, the sign of the speed needs to be additionally identified, for example, by verifying the sign of angle  $\theta$  derivative.

Motor electromagnetic torque can be computed by

$$\hat{t}_e = \frac{\hat{i}_\alpha \hat{e}_\beta - \hat{i}_\beta \hat{e}_\alpha}{\hat{\omega}_r} \tag{8.61}$$

The schematic of the back emf observer system is shown in Figure 8.15 [67].

### 8.3.1 Control system of PMSM

The schematic of the sensorless drive system with PMSM is shown in Figure 8.16.

The machine torque is obtained by

$$\hat{t}_e = \psi_f \hat{i}_q + (L_d - L_q) \hat{i}_d \hat{i}_q \tag{8.62}$$

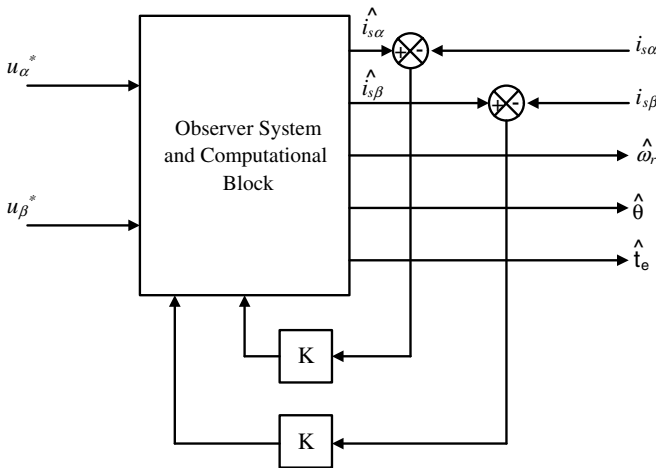


Figure 8.15 Schematic of the back emf observer system

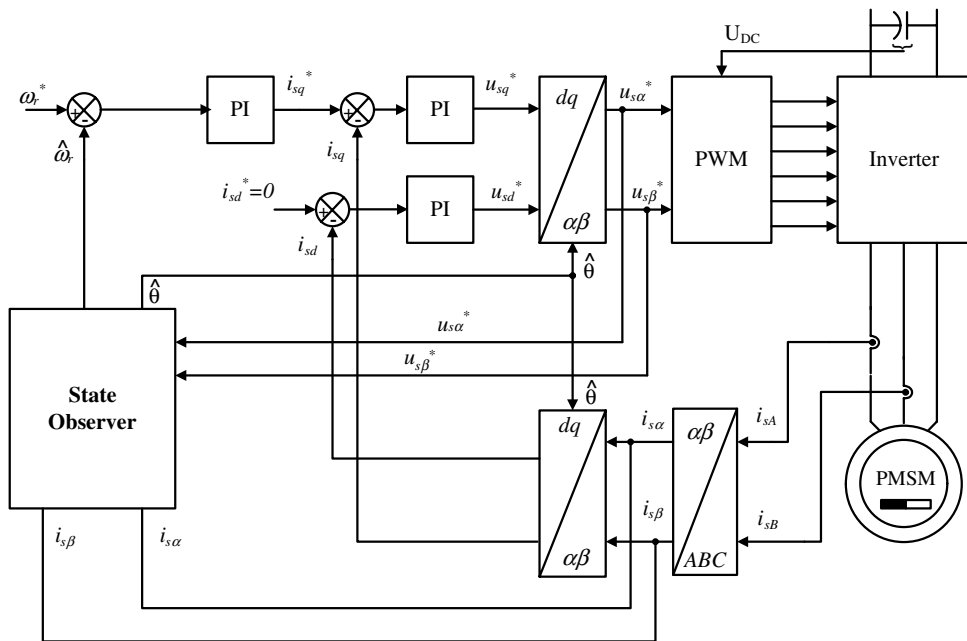


Figure 8.16 Schematic of the sensorless drive system with PMSM

### 8.3.2 Adaptive Backstepping Observer

The machine model in the rotating  $d$ - $q$  frame is [65,67]

$$u_d = R_s i_d + \frac{d\psi_{sd}}{dt} - \omega_{pr} \psi_{sq} \tag{8.63}$$

$$u_q = R_s i_q + \frac{d\psi_{sq}}{dt} + \omega_{pr} \psi_{sd} \tag{8.64}$$

$$\psi_{sd} = L_d i_d + \psi_f \tag{8.65}$$

$$\psi_{sq} = L_q i_q \tag{8.66}$$

It is possible to obtain [65,67]

$$\frac{d\psi_{sd}}{dt} = u_d - R_s i_d + \omega_{pr} \psi_{sq} = u_d - R_s \left( \frac{\psi_{sd} - \psi_f}{L_d} \right) + \omega_{pr} \psi_{sq} = -\frac{R_s}{L_d} \psi_{sd} + \omega_{pr} \psi_{sq} + \frac{R_s}{L_d} \psi_f + u_d \tag{8.67}$$

$$\frac{d\psi_{sq}}{dt} = u_q - R_s i_q - \omega_{pr} \psi_{sd} = u_q - R_s \frac{\psi_{sq}}{L_q} - \omega_{pr} \psi_{sd} = -\frac{R_s}{L_q} \psi_{sq} - \omega_{pr} \psi_{sd} + u_q \tag{8.68}$$

$$i_d = \frac{\psi_{sd}}{L_d} + \frac{\psi_f}{L_d} \quad (8.69)$$

$$i_q = \frac{\psi_{sq}}{L_q} \quad (8.70)$$

Hence, the observer equations may appear as [65,67]

$$\frac{d\hat{\psi}_{sd}}{dt} = -\frac{\hat{R}_s}{L_d}\hat{\psi}_{sd} + \hat{\omega}_{\psi r}\hat{\psi}_{sq} + \frac{\hat{R}_s}{L_d}\psi_f + u_d + k_d \quad (8.71)$$

$$\frac{d\hat{\psi}_{sq}}{dt} = -\frac{\hat{R}_s}{L_q}\hat{\psi}_{sq} - \hat{\omega}_{\psi r}\hat{\psi}_{sd} + u_q + k_q \quad (8.72)$$

$$i_d = \frac{\hat{\psi}_{sd}}{L_d} + \frac{\psi_f}{L_d} \quad (8.73)$$

$$i_q = \frac{\hat{\psi}_{sq}}{L_q} \quad (8.74)$$

where  $k_d$  and  $k_q$  are control signals designed according to the ‘backstepping’ theory [65]. The errors between the real and observed values can be written as

$$\tilde{\psi}_{sd} = \psi_{sd} - \hat{\psi}_{sd} \quad (8.75)$$

$$\tilde{\psi}_{sq} = \psi_{sq} - \hat{\psi}_{sq} \quad (8.76)$$

$$\tilde{\omega}_r = \omega_r - \hat{\omega}_r \quad (8.77)$$

$$\tilde{R}_s = R_s - \hat{R}_s \quad (8.78)$$

Then the response of the error can be represented by [65,67]

$$\frac{d\tilde{\psi}_{sd}}{dt} = -\frac{\tilde{R}_s}{L_d}\tilde{\psi}_{sd} + \hat{\omega}_{\psi r}\tilde{\psi}_{sq} + \frac{\tilde{R}_s}{L_d}\psi_f + u_d + k_d \quad (8.79)$$

$$\frac{d\tilde{\psi}_{sq}}{dt} = -\frac{\tilde{R}_s}{L_q}\tilde{\psi}_{sq} - \tilde{\omega}_{\psi r}\tilde{\psi}_{sd} + u_q + k_q \quad (8.80)$$

$$i_d = \frac{\tilde{\psi}_{sd}}{L_d} + \frac{\psi_f}{L_d} \tag{8.81}$$

$$i_q = \frac{\tilde{\psi}_{sq}}{L_q} \tag{8.82}$$

### 8.3.3 Model Reference Adaptive System for PMSM

Recently, the sensorless control of the Permanent Magnet Synchronous Motor (PMSM) has attracted wide attention due to their wide use in the industry. Several techniques have evolved in order to estimate the motor speed. Again, open-loop speed estimators, closed loop estimators, back emf based speed estimators, the high frequency signal injection method, and many others are used. Although several schemes are available for sensorless operation of vector controlled PMSM drives, one of the most popular schemes is the MRAS because of the ease of implementation [37–49]. The model reference approach makes use of two independent machine models of different structures to estimate the same state variable (back emf, rotor flux, reactive power, etc.) on the basis of different sets of input variables. The error between the outputs of the two estimators with the described earlier strategy is used to generate an adaptive mechanism for identifying rotor speed in the adjustable model. The schematic block of a MRAS for PMSM is illustrated in Figure 8.17.

The PMSM stator voltage equation in the stationary frame can be used as the reference model:

$$v_{\alpha s} = R_s i_{\alpha s} + L_s \frac{di_{\alpha s}}{dt} + e_{\alpha s} \tag{8.83}$$

$$v_{\beta s} = R_s i_{\beta s} + L_s \frac{di_{\beta s}}{dt} + e_{\beta s} \tag{8.84}$$

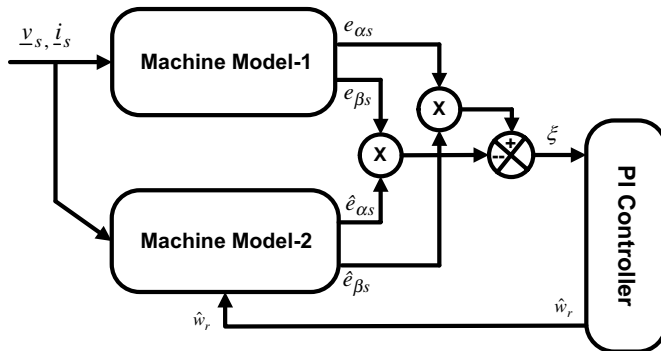


Figure 8.17 Block diagram of MRAS estimator for PMSM

where  $R_s$  and  $L_s$  are stator winding resistance and inductance per phase, respectively and  $e_s$  is the motor back emf.

The adaptive system contains a motor speed that is supposed to be identified in adaptive way according to Figure 8.12. In this scheme, the outputs of the motor model-1 and the motor model-2 are two estimates of the back emf’s.

The speed tuning signal actuates the rotor speed, which makes the error signal converge to zero. The adaptation mechanism of the MRAS-based speed estimation method is a PI controller algorithm:

$$\hat{\omega}_r = K_p \xi + K_i \int \xi dt \tag{8.85}$$

where the input of the PI controller is

$$\xi = e_{\alpha s} \hat{e}_{\beta s} - e_{\beta s} \hat{e}_{\alpha s} \tag{8.86}$$

and  $K_p$  and  $K_i$  are controller gains and  $\xi$  is the error signal.

The complete Simulink diagram of the MRAS block for the control of the PMSM is shown in Figure 8.18. The MRAS block takes currents and voltages from the motor terminals. The description of the MRAS block is explained in Figure 8.19. The Simulink software file of vector control of the PMSM model is [*PMSM\_FOC\_alfa\_beta*]. The motor parameters are located in [*PMSM\_param*], which should be first executed.

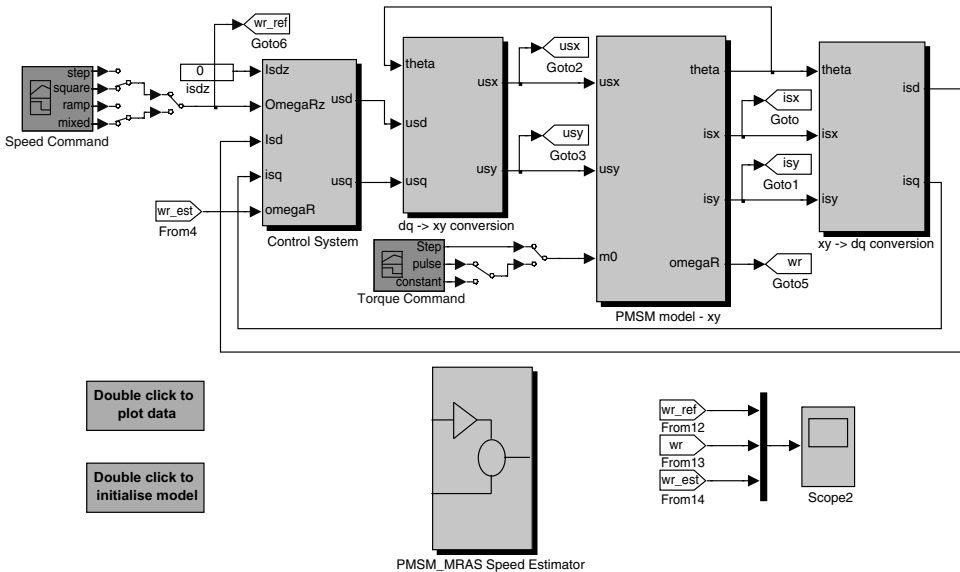


**Figure 8.18** Complete simulation block diagram of MRAS-based control of PMSM

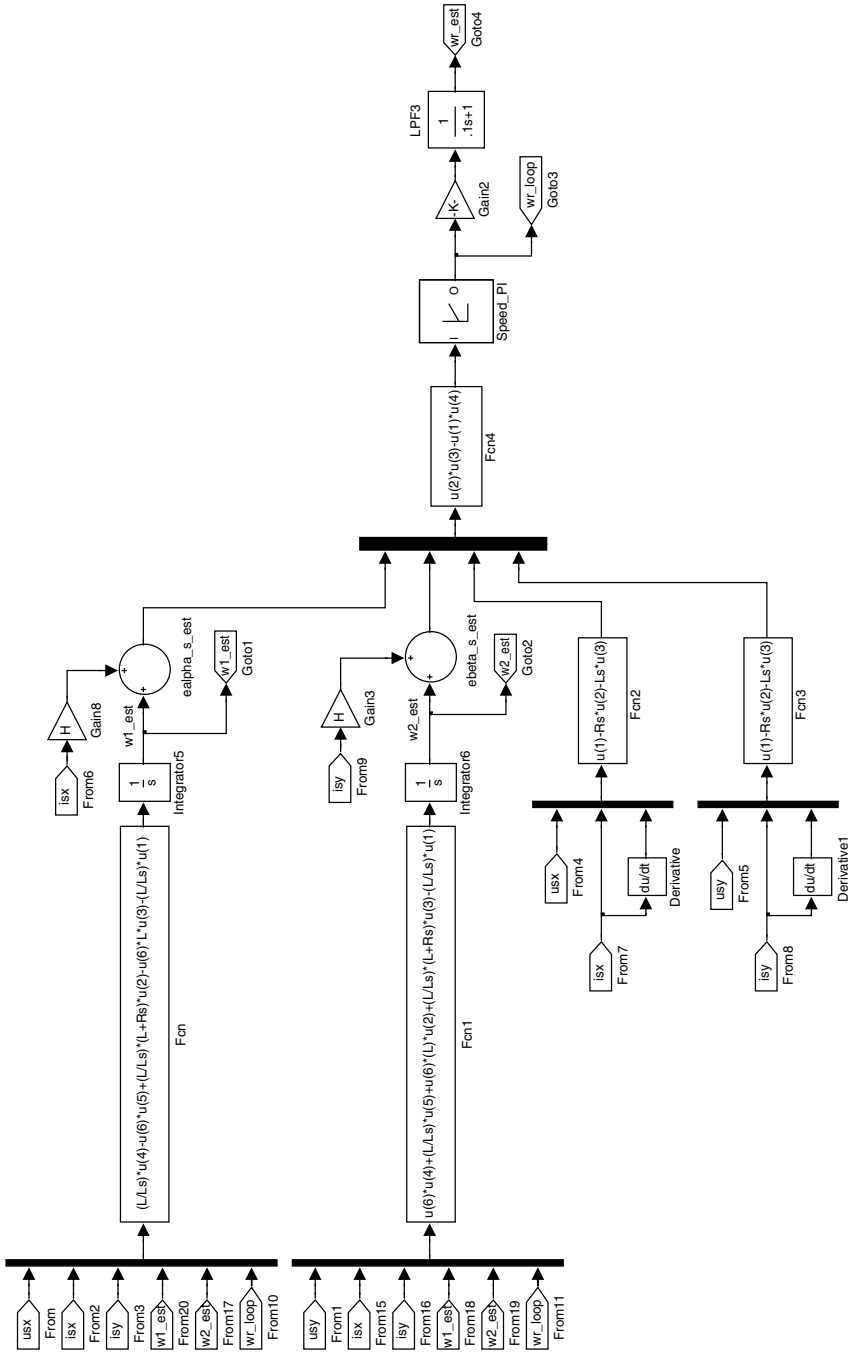
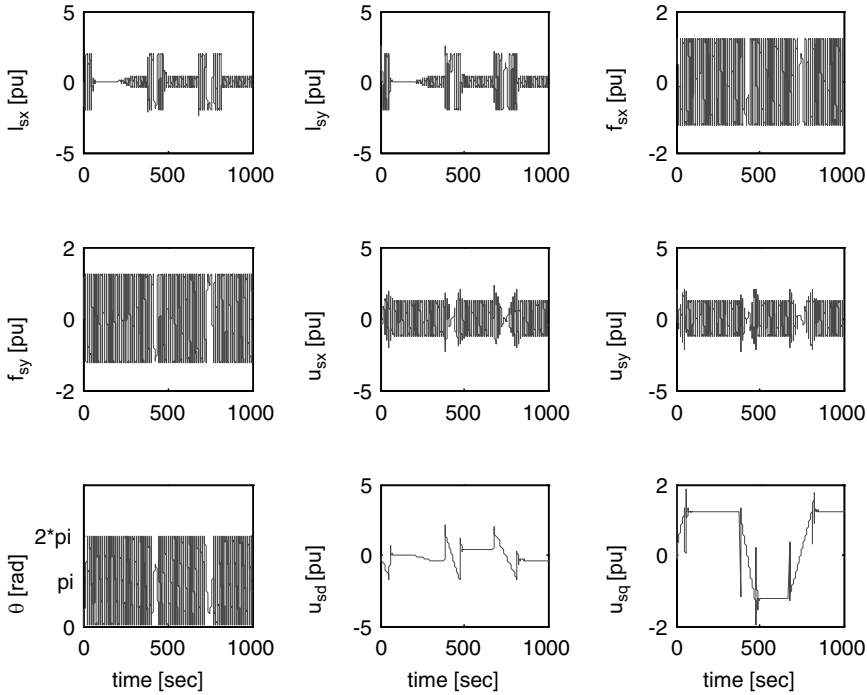


Figure 8.19 Simulink diagram of MRAS estimator for PMSM



**Figure 8.20** Simulation results of currents ( $I_{sx}$ ,  $I_{sy}$ ), field fluxes ( $f_{sx}$ ,  $f_{sy}$ ), and rotor angle and voltages ( $u_{sx}$ ,  $u_{sy}$ ,  $u_{sd}$ ,  $u_{sq}$ )

### 8.3.4 Simulation Results

Selected simulation results for an MRAS sensorless drive are shown in Figures 8.20 and 8.21.

## 8.4 MRAS-based Sensorless Control of Five-phase Induction Motor Drive

Sensorless operation of a vector controlled three-phase drive is widely discussed in the literature; however, this is not true for multi-phase AC machines, where a limited number of publications have appeared in the literature [25–27,59]. One of the most popular solutions is the MRAS, which is similar to three-phase drives [29–36].

As was shown in Chapter 6, multi-phase machine models can be transformed into an orthogonal frame of decoupled equations. The  $d$ - $q$  reference frame contributes to torque and flux production. Hence, in rotor field oriented control (FOC), the rotor flux linkage is kept in the  $d$ -axis so that the  $q$  component of the rotor flux is zero. Thus, the produced torque and the rotor flux can be controlled independently by the  $d$  and  $q$  components of the stator current. The decoupled control of the torque and flux using the rotor flux oriented control for a five-phase IM is illustrated in Chapter 6.

This section focuses on the MRAS-based sensorless control of a five-phase IM, with current control in the stationary reference frame. A PI controller is used to compensate the rotor speed in the adaptive model. Phase currents are controlled using the hysteresis current control method.



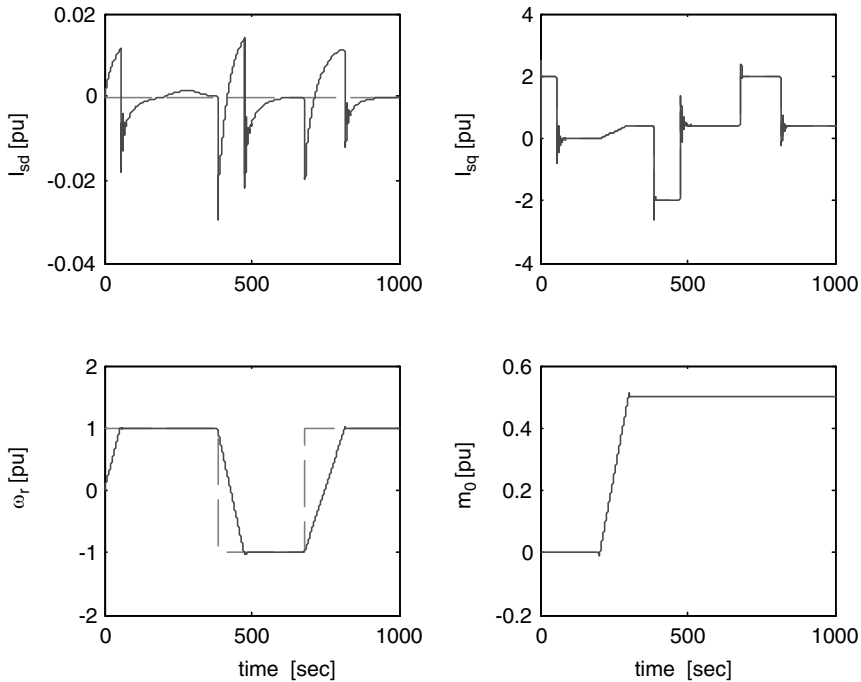


**Figure 8.21** Simulation results of currents ( $I_{sd}$  and  $I_{sq}$ ), rotor speed, and load torque.

The difference between the five-phase machine model, given in Chapter 6, and the three-phase machine model is the presence of  $x$ - $y$  component. Motor  $x$ - $y$  components are fully decoupled from  $d$ - $q$  components, in addition to the one decoupling from the other. Since the rotor winding of a squirrel cage motor is short-circuited, the  $x$ - $y$  components do not appear in the rotor winding. Since the stator  $x$ - $y$  components are fully decoupled from the  $d$ - $q$  components and one from the other, the equations for  $x$ - $y$  components do not need to be further considered. This means that the model of the five-phase IM in an arbitrary reference frame becomes identical to the model of a three-phase IM. Hence the same principles of RFOC can be used.

The mathematical model of a five-phase induction motor makes it possible that the MRAS used for a three-phase machine can be easily extended to a multi-phase machine. The MRAS for the five-phase induction motor drive in the stationary reference frame is shown in Figure 8.22.

#### 8.4.1 MRAS-based Speed Estimator

The schematic block of an MRAS based speed estimator is the same as that for IM or PMSM. In such a scheme, the outputs of the reference (motor model) and the adjustable models denoted by  $\psi_r$  and  $\hat{\psi}_r$  are two estimates of the rotor flux space vector, which are obtained from the machine model in the stationary reference frame. The rotor flux components in the stationary reference frame are obtained as

$$\frac{d\psi_{dr}}{dt} = \frac{L_r}{L_m} (v_{ds} - R_s i_{ds} - \sigma L_s \frac{di_{ds}}{dt}) \quad (8.87)$$

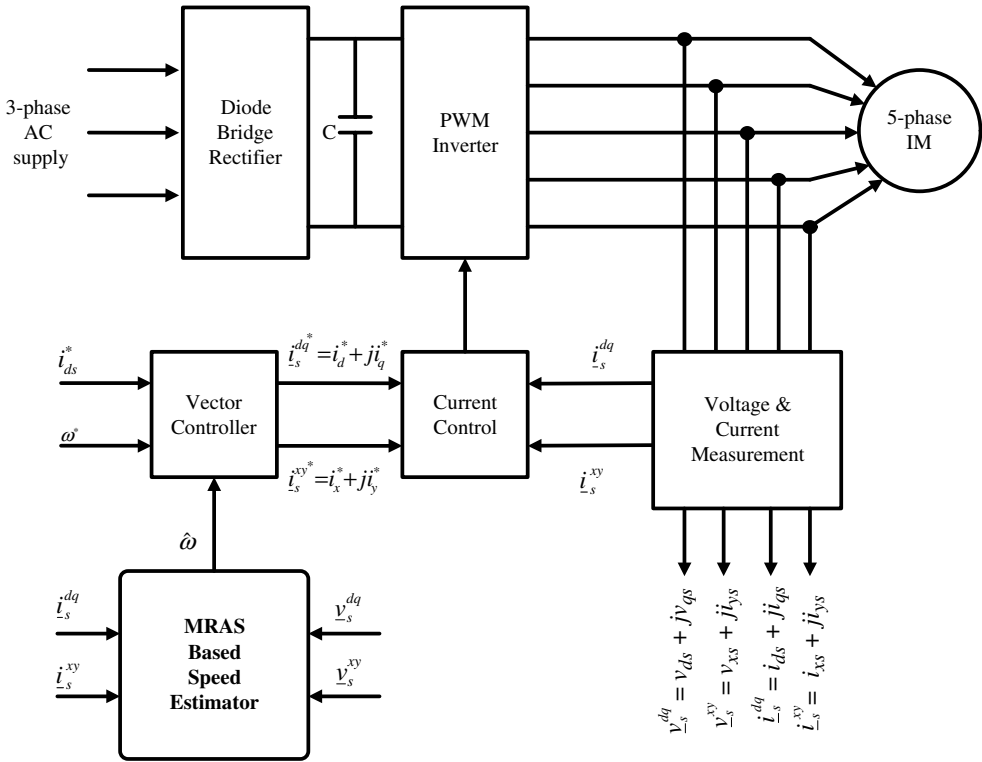


Figure 8.22 MRAS for five-phase induction motor drive

$$\frac{d\psi_{qr}}{dt} = \frac{L_r}{L_m} (v_{qs} - R_s i_{qs} - \sigma L_s \frac{di_{qs}}{dt}) \tag{8.88}$$

$$\frac{di_{xs}}{dt} = \frac{1}{L_{ls}} (v_{xs} - R_s i_{xs}) \tag{8.89}$$

$$\frac{di_{ys}}{dt} = \frac{1}{L_{ls}} (v_{ys} - R_s i_{ys}) \tag{8.90}$$

The adaptive model is based on the well-known rotor equations (current model):

$$T_r \frac{d\psi_{dr}}{dt} = L_m i_{ds} - \psi_{dr} - \omega_r T_r \psi_{qr} \tag{8.91}$$

$$T_r \frac{d\psi_{qr}}{dt} = L_m i_{qs} - \psi_{qr} + \omega_r T_r \psi_{dr} \tag{8.92}$$

$$\frac{d\psi_{xr}}{dt} = -\frac{R_{xr}}{L_r} \cdot \psi_{xr} \tag{8.93}$$

$$\frac{d\psi_{yr}}{dt} = -\frac{R_{yr}}{L_{lr}} \cdot \psi_{yr} \tag{8.94}$$

The MRAS model is using the reference model of equations (87–90) and the adaptive model of equations (91–94) as two models for the rotor flux estimation. The angular difference between the two rotor fluxes is used as the speed tuning signal (error signal). The adaptation mechanism of MRAS is based on using a simple PI controller:

$$\hat{\omega}_r = K_p \xi + K_i \int \xi dt \tag{8.95}$$

where the input of the PI controller is

$$\xi = \psi_{ds} \hat{\psi}_{qs} - \psi_{qs} \hat{\psi}_{ds} \tag{8.96}$$

and  $K_p$  and  $K_i$  are arbitrary positive constants (parameters of the PI controller) and  $\xi$  is the error signal. The complete Simulink diagram of the MRAS block for the control of the five-phase induction motor is shown in Figures 8.23 and 8.24. The MRAS block takes currents and

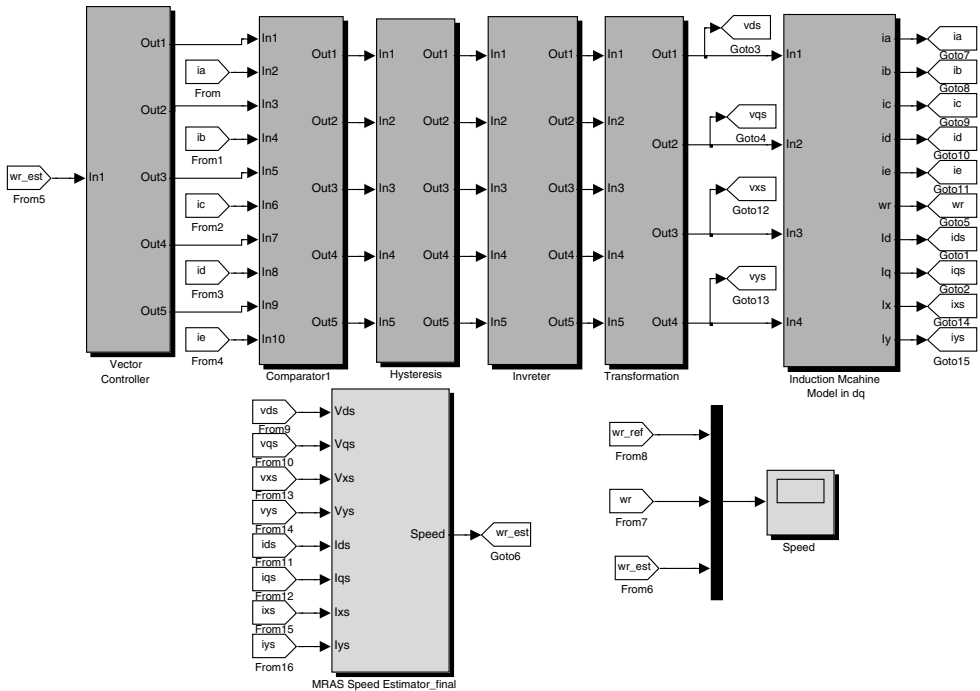


**Figure 8.23** Simulink block diagram of vector control of five-phase induction motor with MRAS estimator

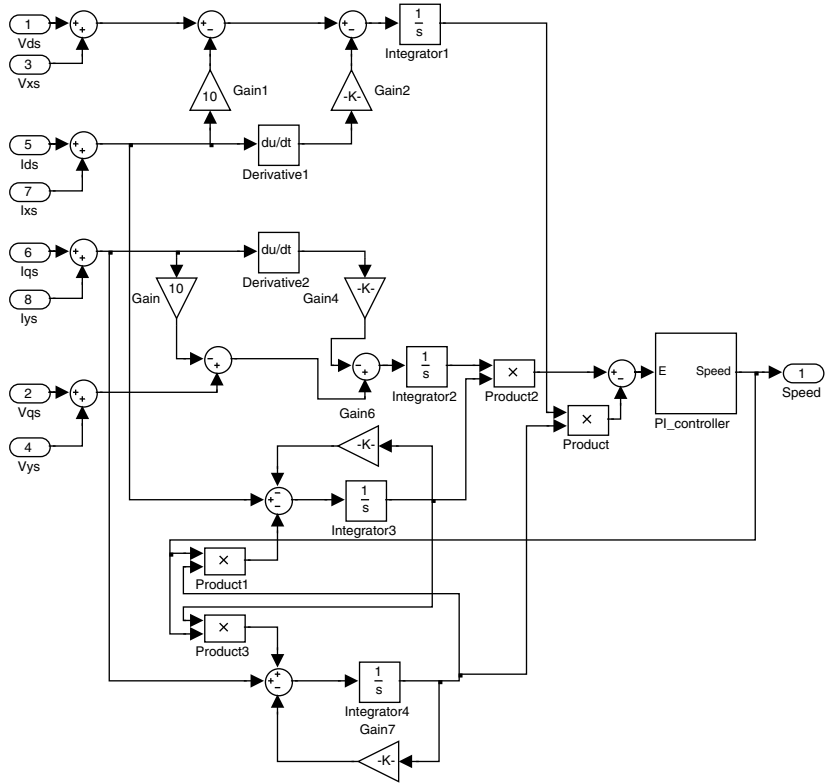


Figure 8.24 Simulink diagram of MRAS speed estimator for a five-phase machine.

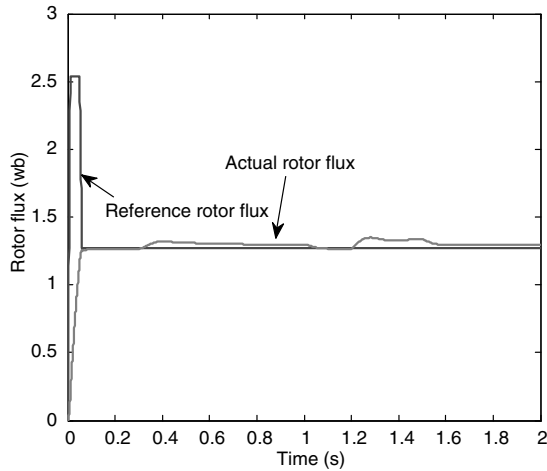
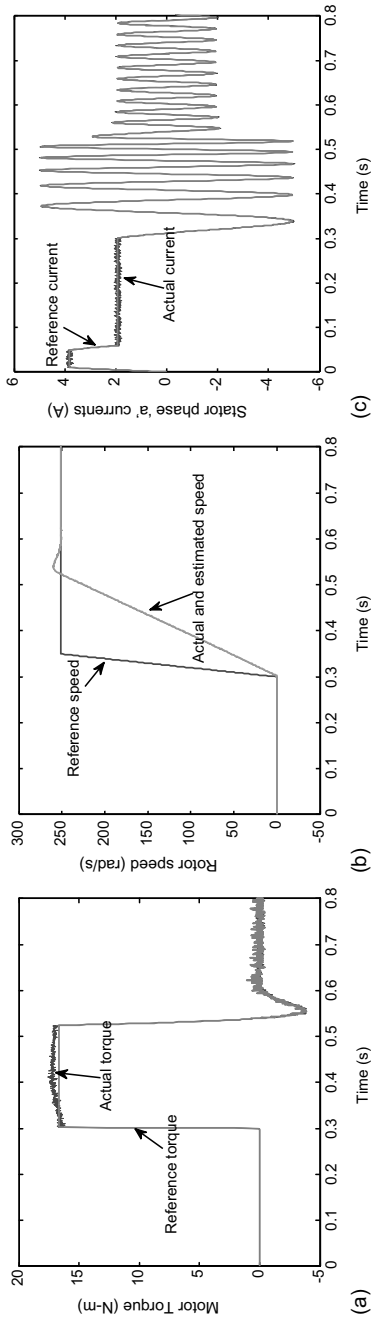
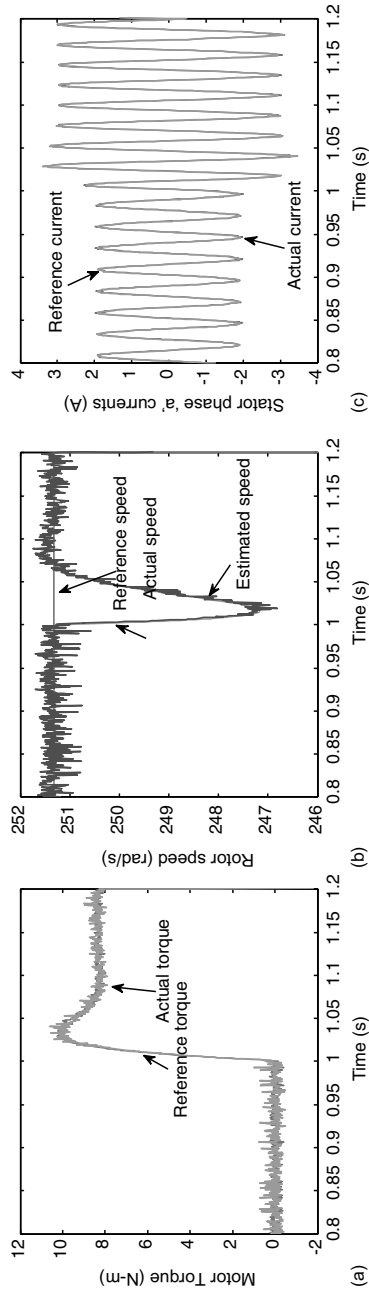


Figure 8.25 Actual and reference rotor flux of five-phase induction motor



**Figure 8.26** IRFOC of a five-phase IM: excitation and acceleration transient: (a) motor torque; (b) motor speed; and (c) phase current



**Figure 8.27** IRFOC of a five-phase IM: disturbance rejection behavior: (a) motor torque; (b) motor speed; and (c) phase current

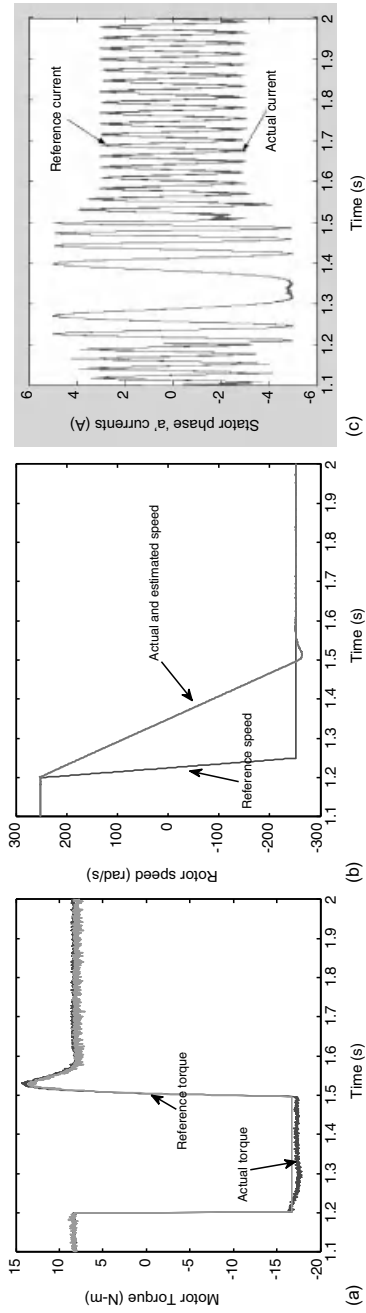


**Figure 8.28** IRFOC of a five-phase IM: reversing transient: (a) motor torque; (b) motor speed; and (c) phase current

voltages from motor terminals. The simulation block diagram shows a five-phase motor, a vector controller, and an MRAS block. The Simulink software file of vector control of the five-phase IM model is [*Five\_phase\_MRAS*]. The motor parameters are located in the file model properties within the initial function. Parameters should run automatically.

### 8.4.2 Simulation Results

The motor parameters of the simulated five-phase IM are

$$R_s = 10 \, \Omega, \quad R_r = 6.3 \, \Omega, \quad L_{ls} = L_{lr} = 0.04 \, \text{H}, \quad L_m = 0.42 \, \text{H}.$$

Inertia and the number of pole pairs are  $0.03 \, \text{kgm}^2$  and 2, respectively. The rated phase current, phase voltage, and per-phase torque are 2.1 A, 220 V, and 1.67 Nm, respectively. The rated (rms) rotor flux is 0.5683 Wb. The drive is operating in a speed control mode with feedback signal taken from the MRAS estimator.

Simulation results of different operating points are shown on Figures 8.25–8.28.

## References

- Holtz, J. (2006) Sensorless control of induction machines: With or without signal injection? *IEEE Trans. Ind. Elect.*, **53**(1), 7–30.
- Holtz, J. (2002) Sensorless control of induction motor drives. *Proc. IEEE*, **90**(8), 1359–1394.
- Holtz, J. and Quan, J. (2002) Sensorless vector control of induction motors at very low speed using a nonlinear inverter model and parameter identification. *IEEE Trans. Ind. Appl.*, **38**(4), 1087–1095.
- Lascu, C., Boldea, I., and Blaabjerg, F. (2005) Very-low speed variable-structure control of sensorless induction machine drives without signal injection. *IEEE Trans. Ind. Appl.*, **41**(2), 591–598.
- Kubota, H. (2003) Closure to discussion of regenerating-mode low-speed operation of sensorless induction motor drive with adaptive observer. *IEEE Trans. Ind. Appl.*, **39**(1).
- Depenbrock, M., Foerth, C., and Koch, S. (1999) Speed sensorless control of induction motors at very low stator frequencies. *8th Europ. Power Elect. Conf. (EPE)*, Lausanne.
- Schauder, C. (1992) Adaptive speed identification for vector control of induction motors without rotational transducers. *IEEE Trans. Ind. Appl.*, **28**, 1054–1061.
- Abu-Rub, H., Guzinski, J., Krzeminski, Z., and Toliyat, H. (2004) Advanced control of induction motor based on load angle estimation. *IEEE Trans. Ind. Elect.*, **51**(1), 5–14.
- Yan, Z., Jin, C., and Utkin, V. I. (2000) Sensorless sliding-mode control of induction motors. *IEEE Trans. Ind. Elect.*, **47**(6), 1286–1297.
- Ohyama, K., Asher, G. M., and Sumner, M. (2006) Comparative analysis of experimental performance and stability of sensorless induction motor drives. *IEEE Trans. Ind. Elect.*, **53**(1), 178–186.
- Armstrong, G. J. and Atkinson, D. J. (1997) A comparison of model reference adaptive system and extended Kalman filter estimators for sensorless vector drives. *Proc. Int. Conf. Power Elect. Appl. (EPE)*, Trondheim, Norway, pp. 1.424–1.429.
- Salvatore, N., Cascella, G. L., Stasi, S., and Cascella, D. (2007) Stator flux oriented sliding mode control of sensorless induction motor drives by Kalman filter. *33rd Ann. Conf. IEEE Ind. Elect. Soc. (IECON)*, pp. 956–961.



13. Kim, Y-R., Sul, S. K., and Park, M. H. (1994) Speed sensorless vector control of induction motor using extended Kalman filter. *IEEE Trans. Ind. Appl.*, **30**(5), 1225–1233.
14. Boldea, I. (2008) Control issues in adjustable-speed drives. *IEEE Ind. Elect. Mag.*, **September 8**, 32–50.
15. Hinkkanen, M. and Luomi, J. (2004) Stabilization of regenerating-mode operation in sensorless induction motor drives by full-order flux observer design. *IEEE Trans. Ind. Elect.*, **51**(6), 1318–1328.
16. Guzinski, J., Abu-Rub, H., and Toliyat, H. (2003) An advanced low-cost sensorless induction motor drive. *IEEE Trans. Ind. Appl.*, **39**(6), 1757–1764.
17. Abu-Rub, H., Guzinski, J., Krzeminski, K., and Toliyat, H. (2003) Speed observer system for advanced sensorless control of induction motor. *IEEE Trans. Ener. Conv.*, **18**(2), 219–224.
18. Briz, F., Degner, M. W., Diez, A., and Lorenz, R. D. (2001) Measuring, modeling, and decoupling of saturation-induced saliencies in carrier-signal injection-based sensorless AC drives. *IEEE Trans. Ind. Appl.*, **37**, 1356–1364.
19. Briz, F., Degner, M. W., Guerrero, J. M., and Diez, A. (2001) Improving the dynamic performance of carrier signal injection based sensorless AC drives. *Proc. 9th Eur. Conf. Power Elect. Appl. (EPE-2001)* Graz, 27–29 August, CD-ROM.
20. Abu-Rub, H. and Oikonomou, N. (2008) Sensorless observer system for induction motor control. *39th IEEE Power Elect. Spec. Conf. (PESC08)* Rhodes.
21. Abu-Rub, H. and Hashlamoun, W. (2001) A comprehensive analysis and comparative study of several sensorless control system of asynchronous motor. *ETEP J (Europ. Trans. Elect. Power)*, **11** (3), 203–210.
22. Abu-Rub, H. and Titi, J. (2005) Comparative Analysis of fuzzy and Pi sensorless control systems of induction motor using power measurement. *4th Int. Workshop CPE 2005 Compatibility in Power Electronics, Gdynia, Poland* (in English).
23. Hori, Y., Ta, C., and Uchida, T. (1998) MRAS-based speed sensorless control for induction motor drives using instantaneous reactive power. *IECON*, Nov./Dec. 1991, pp. 1417–1422.
24. Vas, P. (1998) *Sensorless Vector and Direct Torque Control*. Oxford, Oxford University Press.
25. Rajashekara, K., Kawamura, A., and Matsuse, K. (1996) *Sensorless Control of AC Motors*. IEEE Press, Piscataway, NJ.
26. Elbulck, M. E., Tong, L., and Husain, I. (2002) Neural network based model reference adaptive systems for high performance motor drives and motion controls. *IEEE Trans. Ind. Appl.* Vol. **38**, May/June.
27. Abu-Rub, H., Khan, M. R., Iqbal, A., and Ahmed, S. M. (2010) MRAS-based sensorless control of a five-phase induction motor drive with a predictive adaptive model. *Ind. Elect.(ISIE), 2010 IEEE Int. Symp. Ind. Elect.* pp. 3089–3094.
28. Khan, M. R., Iqbal, I., and Mukhtar, A. (2008) MRAS-based sensorless control of a vector controlled five-phase induction motor drive. *Elect. Power Syst. Res.*, **78**(8), 1311–1321.
29. Khan, M. R. and Iqbal, I. (2008) MRAS-based sensorless control of series-connected five-phase two-motor drive system. *Korian J. Elect. Eng. Tec.*, **3**(2), 224–234.
30. Luo, Y-C. and Lin, C-C. (2010) Fuzzy MRAS based speed estimation for sensorless stator field oriented controlled induction motor drive. *Int. Symp. Comp.Comm. Cont. Auto. (3CA)*, **2**, 152–155.
31. Li, Z., Cheng, S., and Cai, K. (2008) The simulation study of sensorless control for induction motor drives based on MRAS. *Asia Simul. Conf.: 7th Inter. Conf. Syst. Simul. Sci. Comp., ICSC 2008* pp. 235–239.
32. Rashed, M., Stronach, F., and Vas, P. (2003) A new stable MRAS-based speed and stator resistance estimators for sensorless vector control induction motor drive at low speeds. *Ind. Appl. Conf., 38th IAS Ann. Mtg.*, **2**, 1181–1188.
33. Sayouti, Y., Abbou, A., Akherraz, M., and Mahmoudi, H. (2009) MRAS-ANN based sensorless speed control for direct torque controlled induction motor drive. *Int. Conf. Power Eng., Ener. Elect. Drives. POWERENG '09*, pp. 623–628.

34. Ta, C.-M., Uchida, T., and Hori, Y. (2001) MRAS-based speed sensorless control for induction motor drives using instantaneous reactive power. *Ind. Elect. Soc., IECON '01. 27th Ann. Conf. IEEE*, **2**, 1417–1422.
35. Yushui, H. and Dan, L. (2008) Realization of sensorless vector control system based on MRAS with DSP. *Cont. Conf., CCC 2008*, pp. 691–694.
36. Gao, L., Guan, B., Zhou, Y., and Xu, L. (2010) Model reference adaptive system observer based sensorless control of doubly-fed induction machine. *Int. Conf. Elect. Mach. Syst. (ICEMS)*, pp. 931–936.
37. Xiao, J., Li, B., Gong, X., Sheng, Y., and Chai, J. (2010) Improved performance of motor drive using RBFNN-based hybrid reactive power MRAS speed estimator. *IEEE Inter. Conf. Info. Auto. (ICIA)*, pp. 588–593.
38. Kim, Y. S., Kim, S. K., and Kwon, Y. A. (2003) MRAS based sensorless control of Permanent magnet synchronous motor. *SICE Ann. Conf. Fukui*, 4–6 August, Fukui University, Japan, pp. 1632–1637.
39. Shahgholian, G., Rezaei, M. H., Etesami, A., and Yousefi, M. R. (2010) Simulation of speed sensor less control of PMSM based on DTC method with MRAS. *IPEC, Conf. Proc.*, pp. 40–45.
40. Xu, H. and Xie, J. (2009) A Vector-Control System Based on the Improved MRAS for PMSM. *Inter. Works. Intell. Syst. Appl., ISA 2009*, pp. 1–5.
41. Bingyi, Z., Xiangjun, C., Guanggui, S., and Guihong, F. (2005) A Position sensorless vector-control system based on MRAS for LOW SPEED AND HIGH TORQUE PMSM drive. *Proc. 8th Int.l Conf. Elect. Mach. Syst. ICEMS*, Vol. 2.
42. Zhao, G., Liu, J., and Feng, J. (2010) The research of speed sensorless control of PMSM based on MRAS and high frequency signal injection method. *Int. Conf. Comp. Mech., Cont. Elect. Eng. (CMCE)*, **4**, 175–178.
43. Xingming, Z., Xuhui, W., Feng, Z., Xinhua, G., and Peng, Z. (2010) Wide-speed-range sensorless control of Interior PMSM based on MRAS. *Int. Conf. Elect. Mach. Syst. (ICEMS)*, pp. 804–808.
44. Liu, Y., Wan, J., Li, G., Yuan, C., and Shen, H. (2009) MRAS speed identification for PMSM based on fuzzy PI control. *4th IEEE Conf. Ind. Elect. Appl., ICIEA*, pp. 1995–1998.
45. Yan, W., Lin, H., Li, H., and Lu, J. (2009) A MRAS based speed identification scheme for a PM synchronous motor drive using the sliding mode technique. *Int. Conf. Mech. Auto. ICMA*, pp. 3656–3661.
46. Zhou, F., Yang, J., and Li, B. (2008) a novel speed observer based on parameter-optimized MRAS for PMSMs. *IEEE Int. Conf. Network., Sens. Cont., ICNSC 2008*.
47. Yaojing, F. and Kai, Y. (2010) Research of sensorless control for permanent magnet synchronous motor systems. *Int. Conf. Elect. Mach. Syst. (ICEMS)*, pp. 1282–1286.
48. Kojabadi, H. M. and Ghribi, M. (2006) MRAS-based adaptive speed estimator in PMSM drives. *9th IEEE Int. Works. Adv. Mot. Cont.*, pp. 569–572.
49. Baohua, L., Jianhua, Y., and Weiguo, L. (2009) Study on speed sensorless SVM-DTC system of PMSM. *9th Int. Conf. Elect. Meas. Instr., ICEMI '09*, pp. 2914–2919.
50. Kang, J., Zeng, X., Wu, Y., and Hu, D. (2009) Study of position sensorless control of PMSM based on MRAS. *IEEE Int. Conf. Ind. Tech., ICIT 2009*, pp. 1–4.
51. Finch, J. W. and Giaouris, D. (2008) Controlled AC electrical drives. *IEEE Ind. Elect.*, **55**(2), 481–491.
52. Vas, P. (1998) *Sensorless Vector and Direct Torque Control*. Oxford, Oxford University Press.
53. Acarnley, P. P. and Watson, J. F. (2006) Review of position-sensorless operation of brushless permanent-magnet machines. *IEEE Trans. Ind. Elect.*, **53**(2), 352–362.
54. Tae-Hyung, K., Hyung-Woo, L., and Mehrdad, E. (2004) Advanced sensorless drive technique for multi-phase BLDC motors. *Proc. IECON 2004*, 2–6 November, Busan, South Korea, CD-ROM.

55. Hwang, T. S. and Seok, J-K. (2007) Observer-based ripple force compensation for linear hybrid stepping motor drives. *IEEE Trans. Ind. Elect.*, **54**(5), 2417–2424.
56. White, D. C. and Woodson, H. H. (1959) *Electromechanical Energy Conversion*. New York, John Wiley & Sons.
57. Nahid-Mobarakeh, B., Meibody-Tabar, F., and Sargos, F-M. (2007) Back emf estimation-based sensorless control of PMSM: Robustness with respect to measurement errors and inverter irregularities. *IEEE Trans. Ind. Appl.*, **43**(2), 485–494.
58. García, P., Briz, F., Raca, D., and Lorenz, R. D. (2007) Saliency-tracking-based sensorless control of AC machines using structured neural networks. *IEEE Trans. Ind. Appl.*, **43**(1), 77–86.
59. Elloumi, M., Ben-Brahim, L., and Al-Hamadi, M. (1998) Survey of speed sensorless controls for IM drives. *Proc. IEEE IECON'98*, **2**, 1018–1023.
60. Ben-Brahim, L., Tadakuma, S., and Akdag, A. (1999) Speed control of induction motor without rotational transducers. *IEEE Trans. Ind. Appl.*, **35**(4), 844–850.
61. Parsa, L. and Toliyat, H. (2004) Sensorless direct torque control of five-phase interior permanent magnet motor drives. *IEEE Ind. Appl. Conf., IEEE-IAS 2004, Ann. Mtg*, Oct 3–7.
62. Abu-Rub, H., Guziński, J., Rodriguez, J., Kennel, R., and Cortés P. (2010) Predictive current controller for sensorless induction motor drive. *Proc. IEEE-ICIT 2010 Int. Conf. Ind. Tech.*, 14–17 March, Viña del Mar, Chile.
63. Akagi, H., Kanazawa, Y., and Nabae, A. (1983) *Generalised Theory of the Instantaneous Reactive Power in Three-Phase Circuits*. IPEC, Tokyo.
64. Parasiliti, F., Petrella, R., and Tursini, M. (2002) *Speed Sensorless Control of an Interior PM Synchronous Motor*. IEEE.
65. Pajchrowski, T. and Zawirski, K. (2005) Robust speed control of servodrive based on ANN. *IEEE ISIE 20–23 June, Dubrovnik, Croatia*.
66. Foo, G. and Rahman, M. F. (2008) A novel speed sensorless direct torque and flux controlled interior permanent magnet synchronous motor drive. *39th IEEE Power Elect. Spec. Conf. (PESC 2008)*, 15–19 June, Rhodes.
67. Zawirski, K. (2005) *Control of Permanent Magnet Synchronous Motors* (in Polish), Poznan, Poland.
68. Krzemiński, Z. (1999) A new speed observer for control system of induction motor. *Proc. IEEE Int. Conf. Power Elect. Drive Syst., PESC '99, Hong Kong*, pp. 555–560.
69. Krzeminski, Z. (2008) Observer of induction motor speed based on exact disturbance model. *Int. Conf. EPE-PEMC' 2008, Poznan, Poland*.
70. Batran, A., Abu-Rub, H., and Guziński, J. (2005) Wide range sensorless control of induction motor using power measurement and speed observer. *11th IEEE Int. Conf. Meth. Models Auto. Robot, MMAR '05, Miedzyzdroje, Poland*.

# 9

## Selected Problems of Induction Motor Drives with Voltage Inverter and Inverter Output Filters

### 9.1 Drives and Filters – Overview

Nowadays drives with induction motors and voltage type inverters are commonly used as adjustable speed drives (ASD) in industrial systems [1].

The inverters are built with insulated gate bipolar transistors (IGBT), whose dynamic parameters are very high, i.e. the on- and off-switch times are extremely short. Fast switching of power devices causes high  $dv/dt$  at the rising and falling edges of the inverter output waveform.

High  $dv/dt$  in modern inverters is the source of numerous adverse effects in the drives systems [2,3]. The main negative effects are faster motor bearings degradation, over-voltages on motor terminals, failure or degradation of motor winding insulation due to partial discharges, increase of motor losses, and higher electromagnetic interference levels. Other negative effects are increased by the long cables used to connect the inverter and motor.

The prevention or limitation of the negative effects of  $dv/dt$  is possible if proper passive or active filters are installed in the drive. In particular, passive filters are preferable for industrial applications (Figure 9.1).

Passive filters used in induction motor drivers are called inverter output filters or motor filters. Depending on filter structures and their parameters, the following filters are specified [4,5]:

- differential mode filters;
- common mode (CM) filter; and
- $dv/dt$  filters.

With differential mode filters, the motor supply voltage is smoothed to almost a sinusoidal shape contrary to the inverter output voltage (filter's input), which is composed of a series of short rectangular pulses (Figure 9.2). The differential mode filters are also known as sinusoidal filters or LC filters.

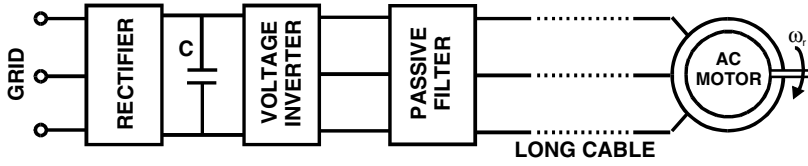


Figure 9.1 Induction motor drives with the inverter output filter

The CM filters are used mainly to limit the motor leakage currents, which flow through motor parasitic capacitances. The major part of leakage current flow is through the motor bearing to the motor case and to the ground.

The role of dv/dt filters is to eliminate the wave reflection effect in long cables, in order to avoid over-voltages on the motor terminal, as well as to prevent failure of the motor windings

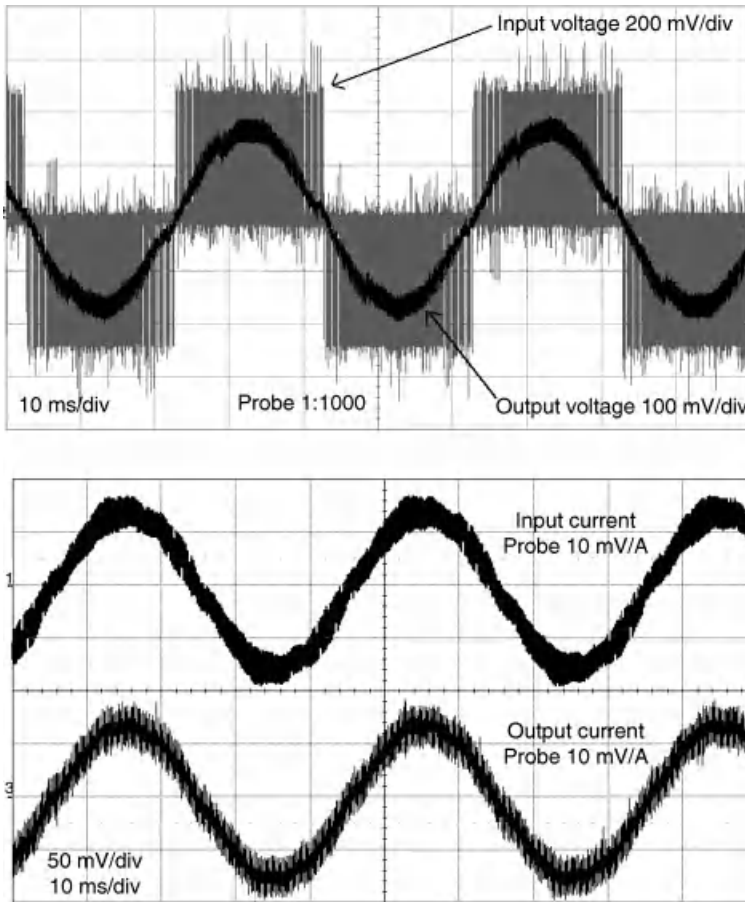


Figure 9.2 The results of differential mode filter operation

insulation. The wave reflections are due to incompatibility between the cable and motor wave impedances. In extreme conditions, the peak of the motor terminal over-voltages can reach twice the value of the inverter supply voltage.

This chapter presents the basic problems associated with electric drives and inverter output filters. The basic mathematical transformations, CM voltage descriptions, and filter structures are first presented. Next, the filter models and design procedures are shown. An essential part of this chapter is dedicated to modifications in the original estimation and control algorithms required in the use of differential mode filters in the drive system. Also, the diagnostic solutions for selected faults in the drive with filters are presented.

This chapter is supported by simulation and experimental validation. Simulation models are discussed for better understanding and analysis.

## 9.2 Three-phase to Two-phase Transformations

For a deeper analysis of electric drives with filters, knowledge of filter models is required.

The natural frame of co-ordinates for a three-phase system is a three-axis co-ordinate with a 120-degree shift, but for a better analysis of the system, the use of the orthogonal co-ordinates is more useful, as well as easier to understand. Therefore, for the next analysis, proper co-ordinate transformations are presented. Two kinds of transformations are used, one for constant vectors magnitudes and another for constant power of the three-phase and two-phase frames of reference.

The transformation matrix for the conversion from a three-phase ABC co-ordinate to a two-phase  $\alpha\beta 0$  co-ordinate for constant vector magnitude is described as

$$\mathbf{A}_w = \begin{bmatrix} \frac{1}{3} & \frac{1}{3} & \frac{1}{3} \\ \frac{2}{3} & -\frac{1}{3} & -\frac{1}{3} \\ 0 & \frac{1}{\sqrt{3}} & -\frac{1}{\sqrt{3}} \end{bmatrix} \quad (9.1)$$

and the transformation matrix for constant power of the system is

$$\mathbf{A}_p = \begin{bmatrix} \frac{1}{\sqrt{3}} & \frac{1}{\sqrt{3}} & \frac{1}{\sqrt{3}} \\ \frac{\sqrt{2}}{\sqrt{3}} & -\frac{1}{\sqrt{6}} & -\frac{1}{\sqrt{6}} \\ 0 & \frac{1}{\sqrt{2}} & -\frac{1}{\sqrt{2}} \end{bmatrix} \quad (9.2)$$

Using equations (9.1) or (9.2), each of the model variables  $x$  can be transformed from ABC to two-phase  $\alpha\beta 0$  co-ordinates according to

$$\begin{bmatrix} x_0 \\ x_\alpha \\ x_\beta \end{bmatrix} = \mathbf{A}_w \begin{bmatrix} x_A \\ x_B \\ x_C \end{bmatrix} \quad (9.3)$$

where the variables retain the same magnitude in each co-ordinate.

The next relation is used when the constant power of both systems is fulfilled:

$$\begin{bmatrix} x_0 \\ x_\alpha \\ x_\beta \end{bmatrix} = \mathbf{A}_p \begin{bmatrix} x_A \\ x_B \\ x_C \end{bmatrix} \quad (9.4)$$

The parameter transformations are required for system modeling, so the resistances matrix is

$$\mathbf{R}_{ABC}^w = \mathbf{R}_{ABC}^p = \begin{bmatrix} R & 0 & 0 \\ 0 & R & 0 \\ 0 & 0 & R \end{bmatrix} \quad (9.5)$$

The three-phase choke with symmetrical coils on the toroidal core is

$$\mathbf{M}_{ABC}^w = \mathbf{M}_{ABC}^p = \begin{bmatrix} 3M & 0 & 0 \\ 0 & 0 & 0 \\ 0 & 0 & 0 \end{bmatrix} \quad (9.6)$$

and for a three-phase choke with an E-shape, the core is

$$\mathbf{M}_{ABC}^w = \mathbf{M}_{ABC}^p = \begin{bmatrix} 0 & 0 & 0 \\ 0 & \frac{3}{2}M & 0 \\ 0 & 0 & \frac{3}{2}M \end{bmatrix} \quad (9.7)$$

In equation (9.6) it is evident that the toroidal three-phase symmetrical choke has parameters only for the CM, whereas in equation (9.7) the E-core choke has parameters only for the differential mode. Such a conclusion is essential for choosing the correct choke core selection in the filters design process.

### 9.3 Voltage and Current Common Mode Component

As mentioned at the beginning of this chapter, unwanted bearing currents appear in the drives with voltage inverters. This occurs because the voltage inverter with classical pulse width modulation (PWM) is a source of CM voltage, which forces the bearing current to flow.

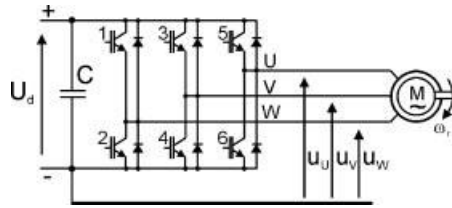


**Figure 9.3** Structure of the voltage inverter with output voltages notations

To clarify the CM voltage effect, the voltage inverter structure presented in Figure 9.3 is analyzed.

In voltage inverters, only one of eight transistor switching combinations is possible. Due to the voltage notation presented in Figure 9.3, the inverter output voltages for each of the eight states are presented in Table 9.1.

It is noted that the zero-component voltage changes according to changes in the transistors switching combination. The peak value of the  $u_0$  voltage is very high and equal to the inverter DC link voltage  $U_d$ . The  $u_0$  frequency is equal to the inverter PWM switching frequency. A typical  $u_0$  voltage waveform is presented in Figure 9.4.

### 9.3.1 MATLAB/Simulink Model of Induction Motor Drive with PWM Inverter and Common Mode Voltage

The MATLAB/Simulink model of induction motor drive *Symulator.mdl* is presented in Figure 9.5.

The *Symulator.mdl* model consists of a three-phase inverter with a space vector PWM algorithm (*PWM\_SFUN*), and induction motor model (*MOTOR\_SFUN*). Both blocks are Simulink S-functions from C code. The C code files are as follows:

- *declarations.h* – list of predefined values;
- *pwm.h* – declaration of global variables for PWM inverter model;

**Table 9.1** Voltage inverter output voltages for possible switching combination

	Binary notation for transistor switching combination							
	100	110	010	011	001	101	000	111
$u_u$	$U_d$	$U_d$	0	0	0	$U_d$	0	$U_d$
$u_v$	0	$U_d$	$U_d$	$U_d$	0	0	0	$U_d$
$u_w$	0	0	0	$U_d$	$U_d$	$U_d$	0	$U_d$
$u_0$	$\frac{U_d}{\sqrt{3}}$	$\frac{2U_d}{\sqrt{3}}$	$\frac{U_d}{\sqrt{3}}$	$\frac{2U_d}{\sqrt{3}}$	$\frac{U_d}{\sqrt{3}}$	$\frac{2U_d}{\sqrt{3}}$	0	$\sqrt{3}U_d$
$u_\alpha$	$\frac{\sqrt{2}U_d}{\sqrt{3}}$	$\frac{U_d}{\sqrt{6}}$	$-\frac{U_d}{\sqrt{6}}$	$-\frac{\sqrt{2}U_d}{\sqrt{3}}$	$-\frac{U_d}{\sqrt{6}}$	$\frac{U_d}{\sqrt{6}}$	0	0
$u_\beta$	0	$\frac{U_d}{\sqrt{2}}$	$\frac{U_d}{\sqrt{2}}$	0	$-\frac{U_d}{\sqrt{2}}$	$-\frac{U_d}{\sqrt{2}}$	0	0



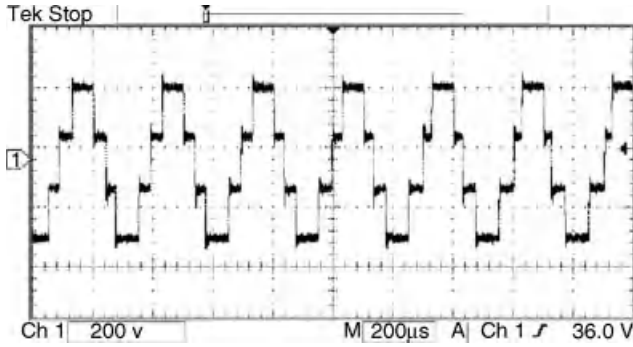


**Figure 9.4** The CM voltage waveform in a voltage inverter

- *pwm.c* – source file of PWM inverter model;
- *motor.h* – declaration of global variables for induction motor model;
- *motor.c* – source file of induction motor model.

The commanded values are:

- *Timp* – inverter switching period in milliseconds;
- *Td* – inverter dead time in milliseconds;
- *US* – module of the commanded inverter output voltage;
- *omegaU* – inverter output voltage pulsation;
- *ud* – inverter DC link supply voltage;
- *m0* – motor load torque.

All variables and parameters are in per unit (p.u.) system, where the fundamental base values are presented in Table 9.2.

The simulated drive is working according to the  $V/f = \text{const}$  principle. No ramp is added for stator voltage pulsation, so when the simulation starts the motor direct start-up is performed.

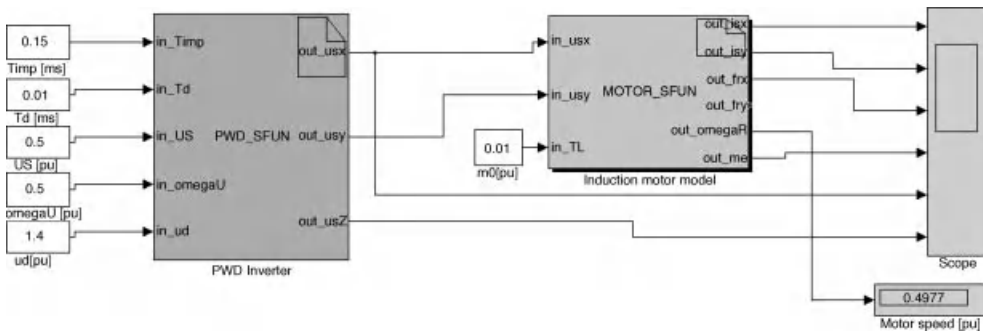


**Figure 9.5** MATLAB/Simulink model of induction motor drive with PWM inverter and common mode voltage (*Symulator.mdl*)

**Table 9.2** Base values for p.u. system used in the MATLAB/Simulink model

Definition	Description
$U_b = \sqrt{3}U_n$	base voltage
$I_b = \sqrt{3}I_n$	base current
$Z_b = U_b/I_b$	base impedance
$m_b = (U_b I_b p)/\omega_0$	base torque
$\Psi_b = U_b/\omega_0$	base flux
$\omega_b = \omega_0/p$	base mechanical speed
$L_b = \Psi_b/I_b$	base inductance
$J_b = m_b/(\omega_b \omega_0)$	base inertia
$\tau = \omega_0 t$	relative time

where  $\omega_0 = 2\pi f_N$  is nominal grid pulsation.

The model of 4 poles,  $P_N = 1.5$  kW,  $U_N = 380$  V induction motor is used. The motor parameters are given in the *pwm.h* file. Examples of simulation results for motor commanded frequency  $\omega_u = 0.5$  p.u. (i.e. 25 Hz) and at DC link voltage  $u_d = 1.4$  p.u. (i.e. 540 V) are given in Figures 9.6 and 9.7. In Figure 9.6 the process of the motor start-up is presented for the complete simulation time. In Figure 9.7, the inverter output voltage of  $\alpha$  and  $\beta$  components, as well as the

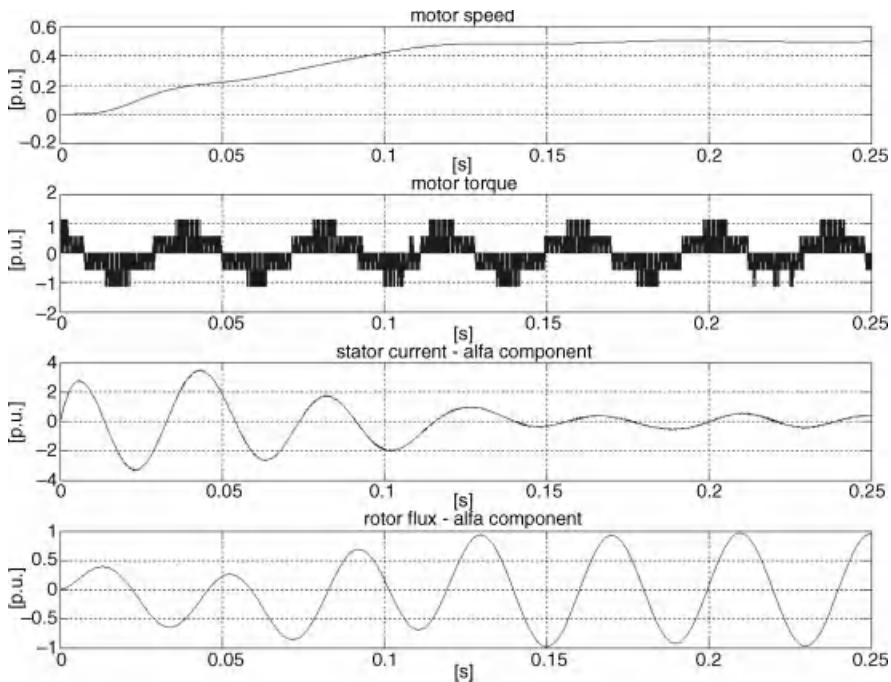


**Figure 9.6** Simulation results for motor start-up

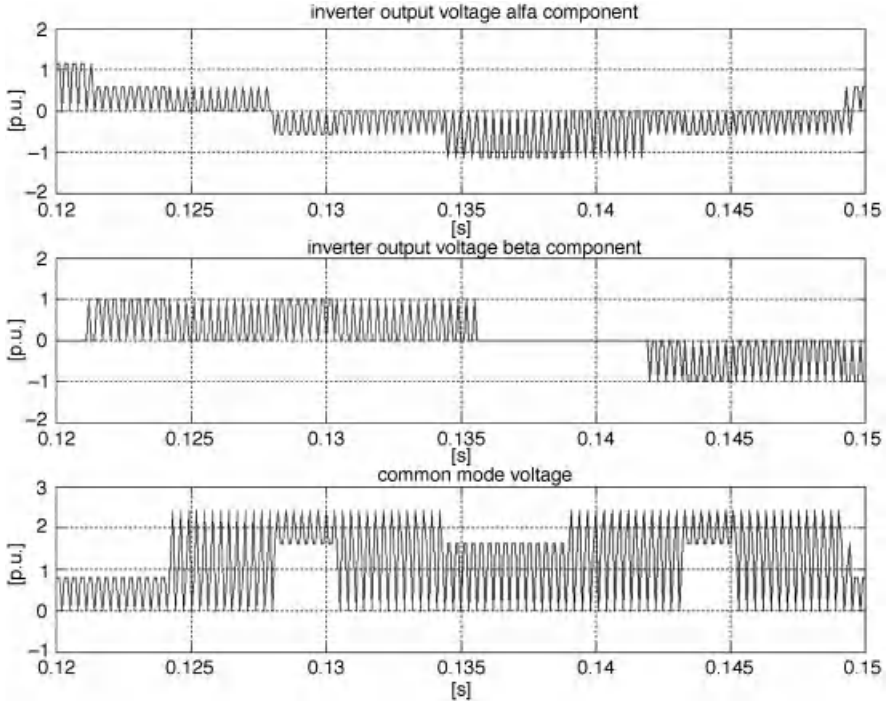


Figure 9.7 Common mode voltage in PWM inverter

CM voltage, are presented in wider zoom. The CM voltage is related to the negative terminal of the inverter DC link supply.

The complete MATLAB/Simulink model is available in the CD-ROM provided with this book.

### 9.4 Induction Motor Common Mode Circuit

The motor has some parasitic capacitances with small values, in the order of picofarads. The CM voltage on the stator windings creates a shaft voltage by capacitive coupling through the motor air gap. Therefore electrostatic discharges are generated through the bearing lubricating film. Such parasitic currents cause a reduction in the lifetime of the bearings. The motor's main parasitic capacitances are presented in Figure 9.8.

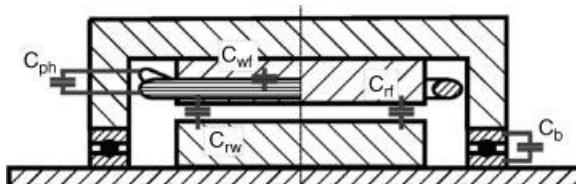


Figure 9.8 Parasitic capacitances in the induction motor

In Figure 9.8, the following motor parasitic capacitances are labeled as:

- $C_{wf}$  – parasitic capacitance between stator windings and stator frame;
- $C_{wr}$  – parasitic capacitance between stator winding and rotor winding;
- $C_{rf}$  – parasitic capacitance between the rotor and frame;
- $C_b$  – equivalent capacitance of motor bearings;
- $C_{ph}$  – parasitic capacitance between stator windings.

All the parasitic capacitances, except  $C_{ph}$ , are significant for the CM. So in the next explanation, the phase-to-phase capacitance  $C_{ph}$  is omitted.

The  $C_{wf}$  capacitance is dependent on the motor's mechanical size, according to empirical relation [6]:

$$C_{wf} = 0.00024 \cdot H^2 - 0.039 \cdot H + 2.2 \quad (9.8)$$

where  $C_{wf}$  is in [nF] and motor mechanical size  $H$  is in [mm].

The bearing capacitance is dependent on the bearing dimensions and mechanical properties. The value of  $C_b$  is of the order of picofarads and close to the  $C_{wr}$  value. In practice, it is assumed that  $C_b \approx C_{wr}$ . The motor parasitic capacitance between the stator windings and the rotor  $C_{wr}$  is dependent on motor size, winding type, and motor magnetic circuit. The  $C_{wr}$  calculation is complicated and requires a lot of data, which can be obtained only from the motor manufactures. The same goes for the  $C_{rf}$  calculations. More in-depth explanations can be found in [6].

In spite of the small values of the capacitances, the parasitic current can reach large values, because the switching frequency in modern inverters is high. Part of the parasitic current circulates inside the motor, while some flows to the motor case and to the ground. The current flow path to the ground is presented in Figure 9.9.

An equivalent circuit of the motor and feeder cable for CM current is presented in Figure 9.10.

In Figure 9.10, the motor CM circuit elements are:

- **Feeder cable parameters:**
  - $R_c$  – cable resistance;
  - $L_c$  – cable inductance;
  - $C_c$  – cable capacitance.

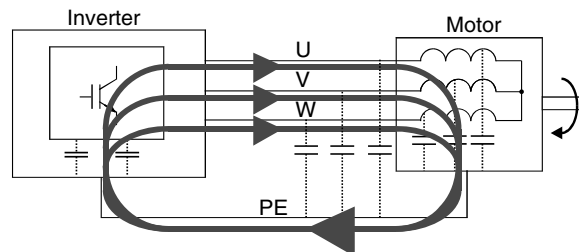


**Figure 9.9** Common mode current path flow in electric drives with voltage inverter

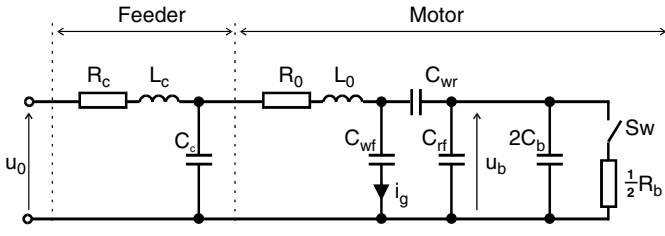


**Figure 9.10** An equivalent circuit of the motor and feeder cable for CM current [7].

• **Motor parameters:**

- R – stator winding copper resistance;
- L – stator winding inductance;
- R<sub>b</sub> – equivalent resistance of motor bearings;
- Sw – switch, when closed indicates the breakdown of the bearing lubricating film.

### 9.5 Bearing Current Types and Reduction Methods

The motor bearing currents are of several types. In Figure 9.11, four classes of bearing current are presented.

The capacitance bearing current has a small value close to 510 mA at temperature  $T_b \approx 25^\circ\text{C}$  and motor speed  $n \approx 100$  rpm. For higher temperatures and motor speeds, the current increases but will not exceed 200 mA. Contrary to other bearing current values, the current is negligible for bearing degradation analysis.

The machine discharging current appears when the bearing oil film breaks down. According to the literature, the value of that current peak is up to 3 A [6].

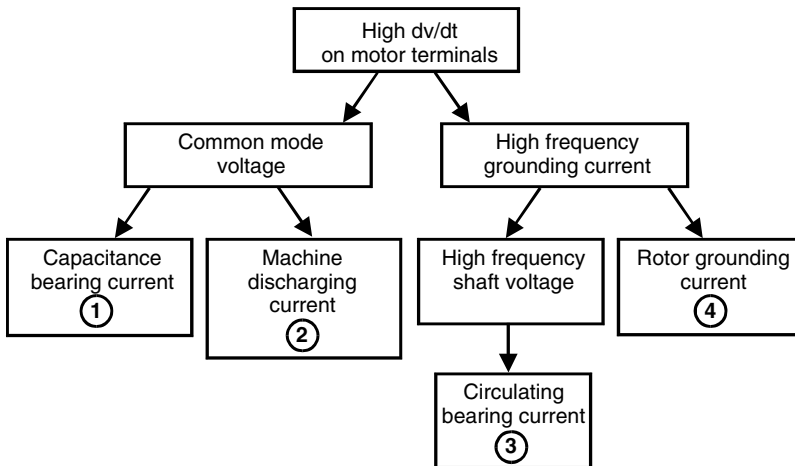


**Figure 9.11** Bearing current classes [6]

The bearing circulating current  $i_{bcir}$  is induced by a motor shaft voltage  $u_{sh}$ . The  $u_{sh}$  appears due to parasitic motor flux  $\Psi_{cir}$ . In [6], the practical condition for  $i_{bcir}$  calculation is given by

$$i_{bcir(max)} \leq 0.4 \cdot i_{g(max)} \quad (9.9)$$

where  $i_{g(max)}$  is the maximum value of the measured grounding current.

An in-depth explanation on the particular bearing currents calculation and measurements can also be found in [6].

The rotor grounding current can appear when a galvanic connection between the rotor and ground appears, i.e. caused by a load machine coupled with a motor shaft.

In [6], the types of bearing currents are correlated with motor mechanical size  $H$ , as follows:

- if  $H < 100$  mm, then machine discharging current,  $i_{bEDM}$ , is dominant;
- if  $100 \text{ mm} < H < 280$  mm, then both  $i_{bEDM}$  and circulating bearing currents  $i_{bcir}$  are dominant;
- if  $H > 280$  mm, then circulating bearing currents are dominant.

To prevent bearing current flow, the methods presented in Table 9.3 can be used.

**Table 9.3** Bearing current prevention methods [6]

**Reduction of electric discharge current  $i_{bEDM}$ :**

- ceramic bearings;
- CM passive filters;
- active compensation systems of CM voltage;
- decreasing of inverter switching frequency;
- motor shaft grounding by brushes use;
- conductive grease in the bearings.

**Reduction of circulating bearing current  $i_{bcir}$ :**

- CM choke;
- active compensation systems of CM voltage;
- decreasing of inverter switching frequency;
- one or two insulated bearings use;
- one or two ceramic bearings use;
- $dv/dt$  filter.

**Reduction of rotor grounding current  $i_{gr}$ :**

- CM choke;
- active compensation systems of CM voltage;
- decreasing of inverter switching frequency;
- one or two insulated bearings use;
- one or two ceramic bearings use;
- screened cable for motor supply.

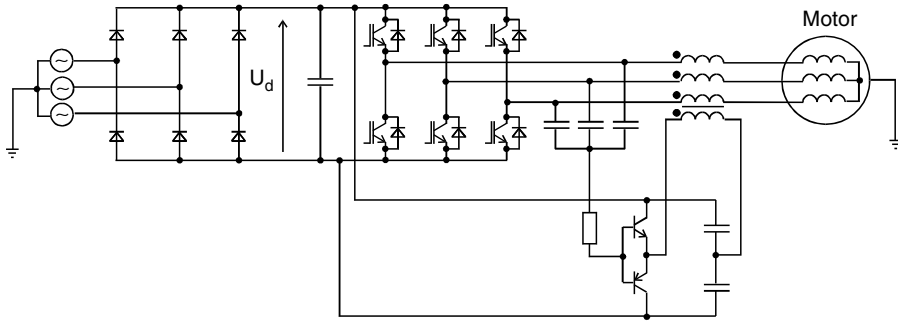


**Figure 9.12** System with active CM filter for voltage source inverter [40]

In addition to the use of passive filters for CM, current active methods are also used, such as series active filter (Figure 9.12), or by changing the PWM algorithm.

Active filters are unpopular in MV drives, because they operate at a high switching frequency, which is not recommended from a loss point of view. In this book, the CM active filters are not discussed and only the PWM algorithms modifications reducing the CM current will be described in this chapter.

### 9.5.1 Common Mode Choke

Among the numerous methods for bearing current reduction, the most popular is known from small electronics circuits is a three-phase CM choke (Figure 9.13).

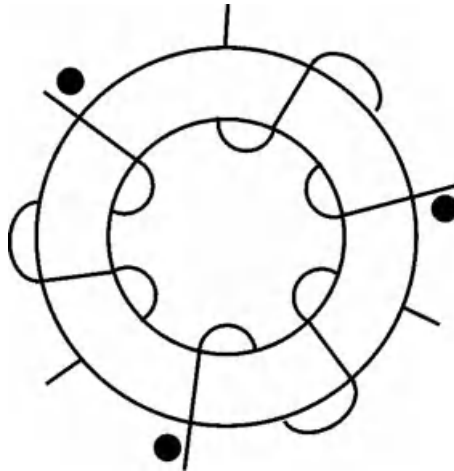


**Figure 9.13** Structure of the common mode choke for three-phase system

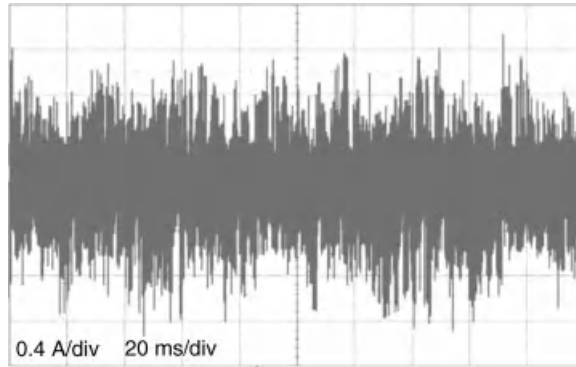


**Figure 9.14** Waveform of the current measured in the motor grounding wire in 1.5 kW industrial drive **without** CM choke use

A CM choke is built in the form of three symmetric coils wound on a toroidal shaped core. The choke has a negligible inductance in a differential mode for the orthogonal components  $\alpha\beta$ ; however, it has a significant inductance,  $L_{10}$ , for the path of the CM current:

$$L_{10} = 3M_1 \quad (9.10)$$

where  $M_1$  is the inductance of each CM mode choke.

Figures 9.14 and 9.15 present the results of using CM choke in the 1.5 kW induction motor industrial drive.

In both Figures 9.14 and 9.15, the current in the motor grounding wire is measured. Previously, the CM choke used had current peaks up to 1 A (Figure 9.14). When the CM choke of inductance  $M_1 = 14$  mH was installed, the current peaks were strongly limited (Figure 9.15).

To achieve maximum limiting of CM current, a maximum choke inductance is needed. A realization of the CM choke is based on using a maximum number of windings on the selected toroidal shaped core. It is important for a CM choke that all windings are identical, to ensure

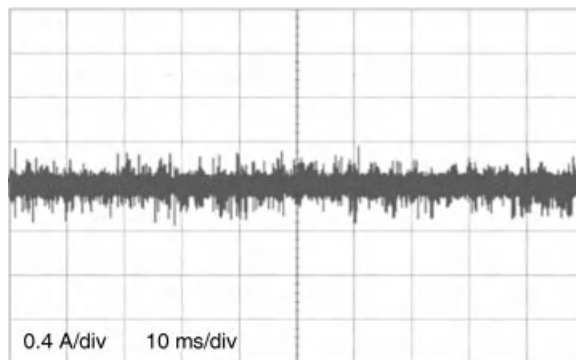


**Figure 9.15** Waveform of the current measured in the motor grounding wire in 1.5 kW industrial drive **with** CM choke use



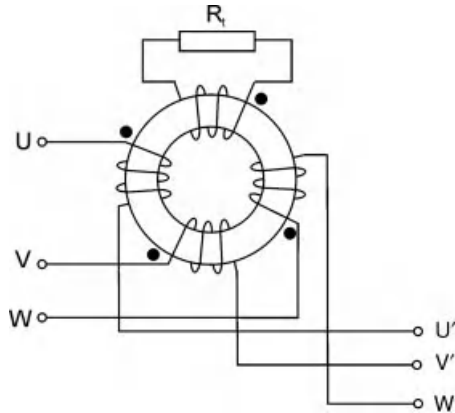


**Figure 9.16** Common mode transformer

low leakage inductances. For differential mode circuits only, the CM choke leakage inductance can appear.

For high power motors, large-sized toroids for CM chokes cannot be accessible, so CM current reduction can be achieved by a few CM chokes connected in series.

### 9.5.2 Common Mode Transformers

The value of the CM voltage may be reduced by using a CM transformer. The difference between the CM choke and the CM transformer is the additional winding shorted by the resistor (Figure 9.16).

In the CM transformer, an additional fourth winding is wound with the same number of turns as the choke phase windings. A CM transformer makes it possible to reduce the CM current in the motor by up to 25%, while using less core volume than when using a CM choke [8].

If a CM transformer is used, then the CM circuit consists of an additional inductance  $L_t$  and resistance  $R_t$ . The equivalent circuit of the CM transformer is shown in Figure 9.17.

An equivalent circuit of the CM transformer, inverter, feeder cable, and motor is given in Figure 9.18.

In Figures 9.17 and 9.18,  $R_t$  is operating as a dumping resistance for a resonant circuit. If the CM transformer leakage inductance is neglected, the CM current circuit is [9]

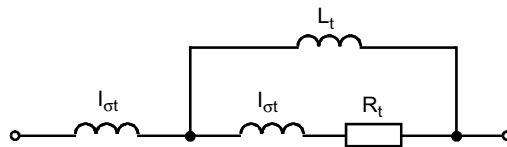


**Figure 9.17** Equivalent circuit of CM transformer ( $I_{\sigma t}$  – leakage inductance of the transformer)

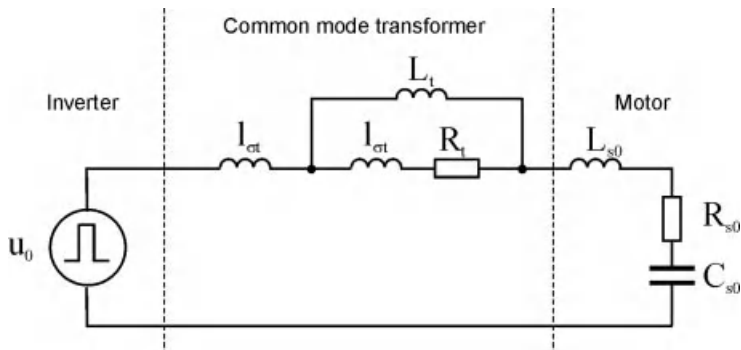


**Figure 9.18** Equivalent circuit of CM transformer, inverter, feeder cable, and motor

$$I_0(s) = \frac{sL_t C_{s0} + R_t U_d}{s^3 L_t L_{s0} C_{s0} + s^2 (L_t + L_{s0}) C_{s0} R_t + sL_t + R_t} \quad (9.11)$$

The analysis of equation (9.11) calculates the  $R_t$  value that limits both maximal and rms CM current values. According to [9], the proper condition for  $R_t$  selection is

$$2Z_{00} \leq R_t \leq \frac{1}{2}Z_{0\infty} \quad (9.12)$$

where  $Z_{00}$  and  $Z_{0\infty}$  are wave impedances of the circuit presented in Figure 9.18, if  $R_t = 0$  and  $R_t = \infty$ .

### 9.5.3 Common Mode Voltage Reduction by PWM Modifications

Typical methods for limiting the CM current, such as different configurations of CM chokes or active compensation of CM voltages, are mostly expensive solutions and require additional hardware.

However, limiting the CM current in the drive system is possible in a way that does not require inverter reconstruction. The CM current can be limited by only changing the PWM algorithm. Changing the PWM should be done in such a way that it eliminates or decreases the CM voltage generated by the inverter. Different methods based on PWM algorithm modifications are suggested in the literature [10].

The following are the PWM modifications required for CM reduction:

- elimination of zero voltage vectors;
- use of active vectors, which have the same value of zero sequence voltage  $u_0$ .

Such approaches come under the analysis shown in Table 9.4.

In Table 9.4, the active vectors are named as parity or non-parity vectors. Each of the parity and non-parity vectors has the same value of zero component  $u_0$ .

**Table 9.4** Zero sequence vectors of inverter output voltage

Vectors type	Arrangement of switches states of three-phase voltage inverter							
	Active				Zero			
Vectors notation	$U_{w4}$	$U_{w6}$	$U_{w2}$	$U_{w3}$	$U_{w1}$	$U_{w5}$	$U_{w0}$	$U_{w7}$
Vector binary notation	100	110	010	011	001	101	000	111
Vector decimal notation	4	6	2	3	1	5	0	7
Vectors number	1	2	3	4	5	6	0	7
$u_{N0}$	$\frac{1}{3}U_d$	$\frac{2}{3}U_d$	$\frac{1}{3}U_d$	$\frac{2}{3}U_d$	$\frac{1}{3}U_d$	$\frac{2}{3}U_d$	0	$U_d$
$u_0$ (Co-ordinate system $\alpha\beta$ )	$\frac{U_d}{\sqrt{3}}$	$\frac{2U_d}{\sqrt{3}}$	$\frac{U_d}{\sqrt{3}}$	$\frac{2U_d}{\sqrt{3}}$	$\frac{U_d}{\sqrt{3}}$	$\frac{2U_d}{\sqrt{3}}$	0	$\sqrt{3}U_d$
Notation <sup>(1)</sup>	NP	P	NP	P	NP	P	Z	Z

<sup>(1)</sup> Vector: NP –non-parity, P –parity, Z –zero.

For classical PWM methods, an example of a voltage  $u_{N0}$  waveform is presented in Figure 9.19.

The  $u_{N0}$  is the voltage between the mid-point of the star connected load and the negative potential of the inverter supply.

It is evident from Figure 9.19 that the highest changes of the voltage  $u_{N0}$  happen during zero vector changes. It is also obvious that an elimination of such vectors can significantly limit the CM current. If only active vectors that are equivalent to  $u_0$  are used, then the CM current will decrease. For example, in [11] a PWM algorithm without using zero vectors is presented. with the algorithm only, the output voltage is built with parity and non-parity active vectors.

The disadvantage of the PWM based only on parity or odd active vectors is that without over-modulation, the inverter output voltage is decreased. This is explained in Figure 9.20 for a three non-parity active vectors (3NPAV) algorithm.

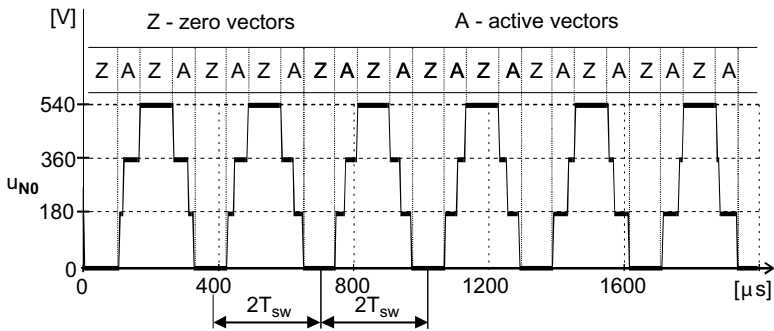


**Figure 9.19** Example of  $u_{N0}$  waveform with classical space vector PWM algorithm (the inverter DC input voltage is  $U_d = 540$  V)

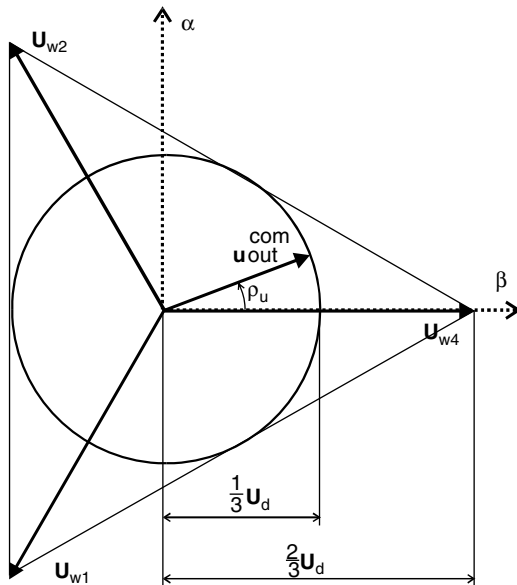


**Figure 9.20** The output voltage vector for 3NPVM modulation strategy

In Figure 9.21, the inverter output voltage vector  $\mathbf{u}_{\text{out}}^{\text{com}}$  is generated using three non-parity vectors  $\mathbf{U}_{w4}$ ,  $\mathbf{U}_{w2}$ ,  $\mathbf{U}_{w1}$ :

$$\mathbf{u}_{\text{out}}^{\text{com}} \cdot T_{\text{imp}} = \mathbf{U}_{w4}t_4 + \mathbf{U}_{w2}t_2 + \mathbf{U}_{w1}t_1 \quad (9.13)$$

The vectors switching times  $t_4$ ,  $t_2$  i  $t_1$  are [12]

$$t_4 = \frac{1}{3} \left( 1 + \frac{2U_{\text{out}}^{\text{com}}}{U_d} \left( \cos\left(\frac{\pi}{3} + \rho_u\right) + \sin\left(\frac{\pi}{6} + \rho_u\right) \right) \right) \quad (9.14)$$

$$t_2 = \frac{1}{3} \left( 1 - \frac{2U_{\text{out}}^{\text{com}}}{U_d} \cos\left(\frac{\pi}{3} + \rho_u\right) \right) \quad (9.15)$$

$$t_1 = \frac{1}{3} \left( 1 - \frac{2U_{\text{out}}^{\text{com}}}{U_d} \sin\left(\frac{\pi}{6} + \rho_u\right) \right) \quad (9.16)$$

$$T_{\text{imp}} = t_4 + t_2 + t_1 \quad (9.17)$$

where  $U_{\text{out}}^{\text{com}}$  and  $\rho_u$  are the length and position angle of the inverter output voltage vector  $\mathbf{u}_{\text{out}}^{\text{com}}$ , respectively.

By using non-parity active vectors, the CM voltage is

$$u_0 = \frac{U_d}{\sqrt{3}} \quad (9.18)$$

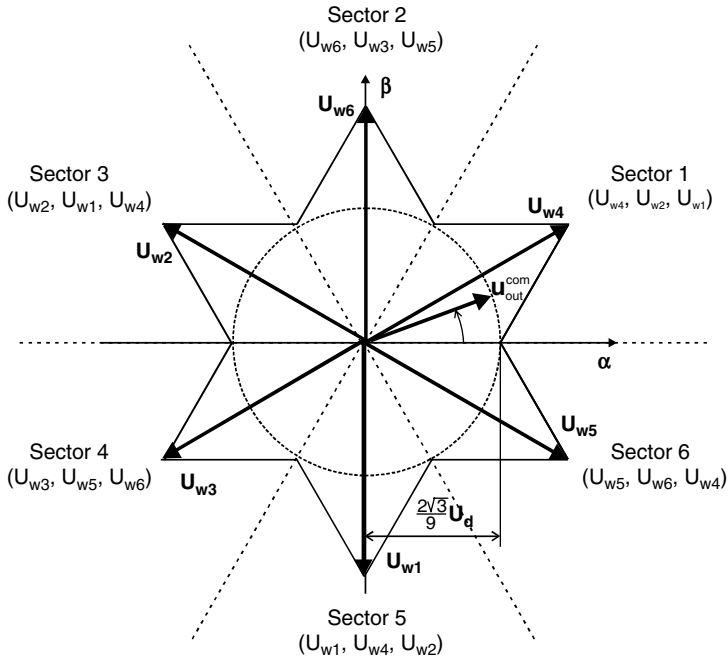


**Figure 9.21** Output voltage vector for 3AVM modulation strategy

It is obvious that the constant value of  $u_0$  does not allow for zero sequence current flow,  $i_0$ , through the internal machine’s capacitances. The disadvantage of the 3NPAV is that the maximum inverter output voltage is limited to  $U_d/3$ .

A higher use of the inverter output voltage with simultaneous CM current reduction is made possible by using the modulation method with only active vectors. The method is close to the classical PWM and was proposed in [12] where a 3AVM is presented. In the 3AVM method, the position of the voltage vector is divided into six sectors and displaced by 30 degrees from the original sectors in the classical space vector modulation SVPWM (Figure 9.21).

When the 3AVM algorithm is used, both the value and frequency of  $u_0$  are decreased, therefore the CM current is significantly limited. Simultaneously, the inverter output voltage amplitude equals  $2\sqrt{3}/9 \cdot U_d$ . It is 15.5% more in comparison with the 3NPAV and 3PAV.

Another modulation method that reduces the CM current is the active zero vector control method (AZVC) presented in [12,13]. In the AZVC algorithm, the zero voltage vectors are replaced by two opposite active vectors (AZVC-2) (Figure 9.22), or one active vector (AZVC-1) (Figure 9.23).

The algebraic relations for AZVC-1 and AZVC-2, for the situation presented in Figures 9.22 and 9.23, are

$$\mathbf{u}_{out}^{com} \cdot T_{imp} = \mathbf{U}_{w4}t_4 + \mathbf{U}_{w6}t_6 + \mathbf{U}_{w2}t_2 + \mathbf{U}_{w5}t_5 \quad \text{for AZVC-2} \quad (9.19)$$

$$\mathbf{u}_{out}^{com} \cdot T_{imp} = \mathbf{U}_{w4}t_4 + \mathbf{U}_{w6}t_6 + \mathbf{U}_{w3}t_3 + \mathbf{U}_{w4}t_4^* \quad \text{for AZVC-1} \quad (9.20)$$

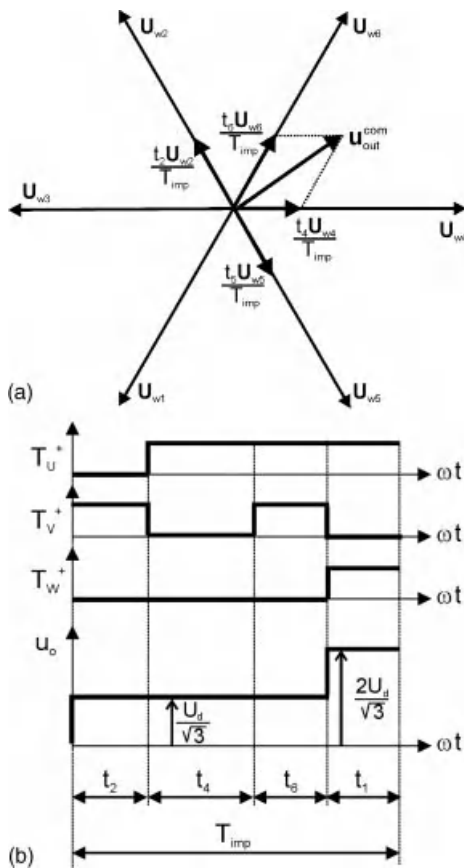


Figure 9.22 AZVC-2 modulation: (a) vectors; and (b) timings

$$t_4 = T_{imp} \cdot \frac{U_{out\alpha}^{com} \cdot U_{w6\beta} - U_{out\beta}^{com} \cdot U_{w6\alpha}}{U_d \cdot w_t} \tag{9.21}$$

$$t_6 = T_{imp} \cdot \frac{-U_{out\alpha}^{com} \cdot U_{w4\beta} + U_{out\beta}^{com} \cdot U_{w4\alpha}}{U_d \cdot w_t} \tag{9.22}$$

$$t_2 = t_5 = \frac{1}{2} (T_{imp} - t_4 - t_6) \quad \text{for AZVC-2} \tag{9.23}$$

$$t_3 = t_4^* = \frac{1}{2} (T_{imp} - t_4 - t_6) \quad \text{for AZVC-1} \tag{9.24}$$

where

$$w_t = U_{w4\alpha} U_{w6\beta} - U_{w4\beta} U_{w6\alpha} \tag{9.25}$$

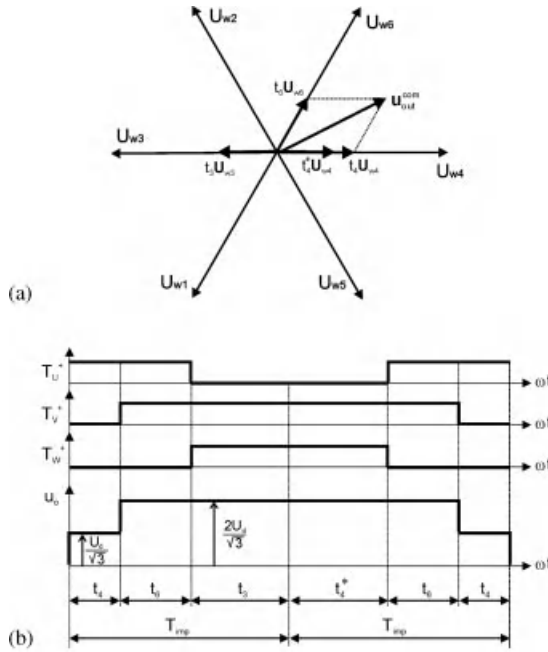


Figure 9.23 AZVC-1 modulation: (a) vectors; and (b) timings

In both AZVC methods, the same maximum inverter output voltage is obtained, and is the same as in the classical SWPWM algorithm.

The disadvantage of the modified PWM method is with the proper inverter output currents measurement. In classical SVPWM, current measurements are synchronized with the SVPWM operation and performed under zero voltage vector generation. Current values sampled in the middle of the zero vector’s duration are identical with the values of the inverter output current’s first harmonic component. When using PWM modulations without zero vectors, it is essential to use additional filtering elements for inverter output currents.

## 9.6 Inverter Output Filters

### 9.6.1 Selected Structures of Inverter Output Filters

The improvement of the AC motor operation in inverter fed drives is possible, if the shape of the stator voltage becomes as close as possible to the sinusoidal.

A motor fed by such waveforms shows higher efficiency as a result of decreasing miscellaneous losses in the machine. Motors fed by non-sinusoidal waveforms have higher eddy current losses. For high switching frequency, those losses are the dominating losses in the machine, compared to copper and hysteresis losses [14–16].

In inverter fed drives, the use of the voltage inverter output filters reduces the disturbance levels in the current and voltage waveforms.

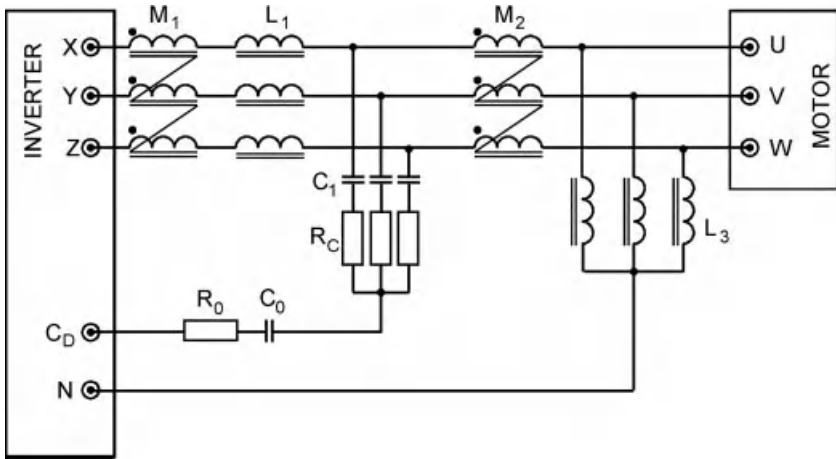


**Figure 9.24** Inverter output filter – Structure 1

Motor side filters may be categorized into three basic types:

1. sine filter – LC filter;
2. CM filter;
3.  $du/dt$  filter.

The three types of filters can be used separately or combined together in different combinations, for example, connecting a sine filter with a CM filter. In this chapter, different filters configurations are analyzed, as shown in Figures 9.24–9.30.

The filter shown in Figure 9.24 is a combination of a sinusoidal filter and a CM filter. Connection of such filters makes it possible to obtain sinusoidal voltage and current at the filter output, and also limits the CM current. In such situations, it is possible to use a long cable

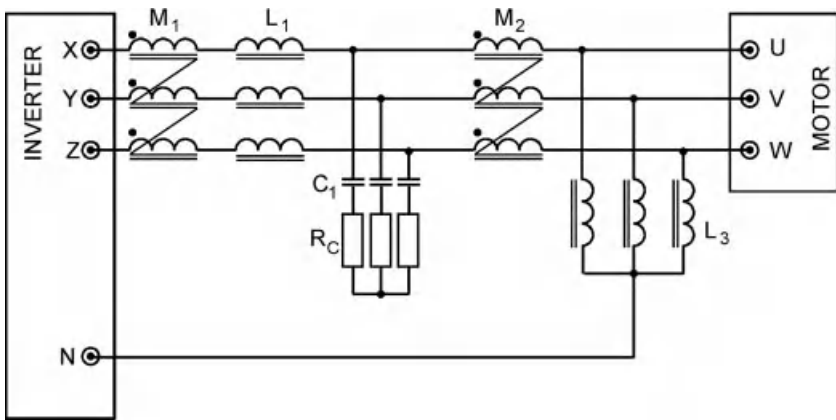


**Figure 9.25** Inverter output filter – Structure 2



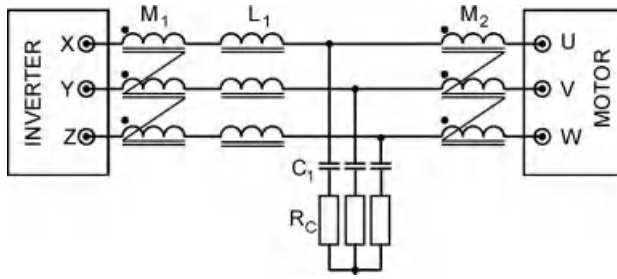


**Figure 9.26** Inverter output filter – Structure 3

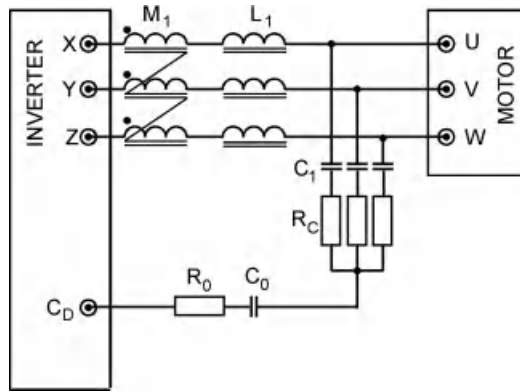


**Figure 9.27** Inverter output filter – Structure 4

between the filter and the motor. The length of the cable will be limited only by the allowed voltage drop in the cable.

Elements  $L_1$ ,  $C_1$ , and  $R_1$  represent the sinusoidal filter, while  $M_1$ ,  $M_2$ ,  $R_0$ , and  $C_0$  represent the CM filter. These filters create a closed circuit during inverter operation through the capacitor in the DC bus. The coupled choke,  $M_2$ , limits the CM current in the circuit external to the filter and inverter. Chokes  $L_1$  are single phase, while chokes  $M_1$  and  $M_2$  are three-phase coupled chokes made on the toroidal cores (Figure 9.31).

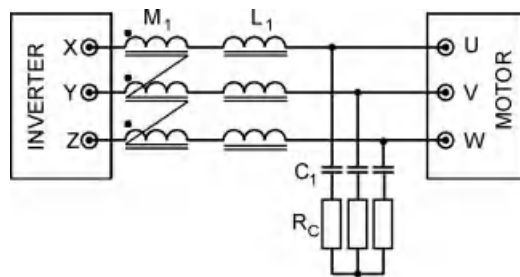


**Figure 9.28** Inverter output filter – Structure 5

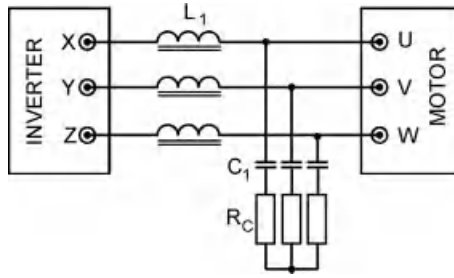


Figure 9.29 Inverter output filter – Structure 6

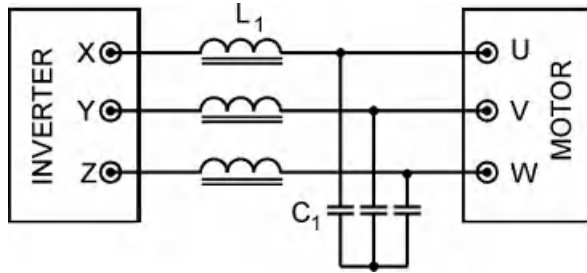
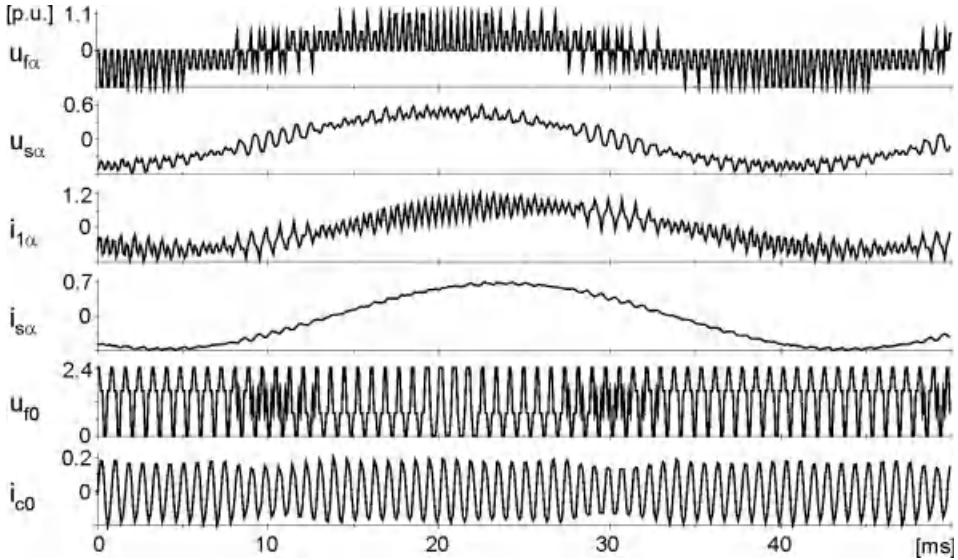


Figure 9.30 Inverter output filter – Structure 7

Resistances  $R_1$  and  $R_0$  are the damping elements protecting the system from oscillations. The chokes  $L_3$  are used to protect the system from an uncontrolled voltage increase on the filter capacitor. Such dangerous increases in the voltage may occur in the case of asymmetry in individual inverter output phases. Present in this case is the DC voltage component, which may



Figure 9.31 Three-phase common mode choke



**Figure 9.32** Voltage and current waveforms in inverter fed drives, with filter from Figure 9.24

provide an increment in the DC link voltage on the capacitors, which will operate as integrating elements.

The input and output terminals of the filter are labeled XYZ and UVW, respectively. Terminal  $C_D$  should remain connected to the DC link voltage. In most cases, it is accessible for the user to use the positive polarity of the DC bus battery, which corrects the external braking resistor. The star point of the chokes  $L_3$  is connected with a neutral conductor N.

Examples of the voltage and current waveforms in the inverter fed drive, with the filter from Figure 9.24, are shown in Figure 9.32.

In Figure 9.32, the smoothed motor current and voltage waveforms are clearly noted. The level of smoothing of the voltage and current depends on the filter parameters and motor load. For the proper selection of filter parameters, it is important to assume rated motor loading to ensure minimum THD in the voltage and current, and also to ensure minimum voltage drop in the filter.

In the filter from Figure 9.25, the branch containing the parameters  $R_0$  and  $C_0$  were dropped, which aided in increasing CM current in the motor compared with the solution from Figure 9.24. However, such a solution excludes the necessity of using a resistor  $R_0$  with relatively high power and therefore also large dimensions. With high transistor switching frequency, a large current flows through  $R_0$  and  $C_0$ . This forces the use of a high power resistor,  $R_0$  and the necessity of using a special capacitor,  $C_0$ .

In filter Structure 3, the choke  $L_3$  does not exist. The use of such chokes is limited to systems with high asymmetry and inaccuracies in generating an inverter output voltage, which may be caused by the large asymmetry in transistor control. The use of choke  $L_3$  is also essential for specialized systems [17]. By not using  $L_3$ , a dangerous rise of the DC link voltage is avoided when using vector or sinusoidal PWM methods. The use of choke  $L_3$  is beneficial for limiting CM current in the motor when connecting a star point of choke  $L_3$  with a protective conductor

PE. Unfortunately, such solutions exclude the possibility of using residual current devices for electric shock protection in frequency converters, because the connection used forces CM current to flow in the protective conductor PE [18].

The filter shown in Figure 9.27 is presented in [4,5]. This is a limited version of the filter from Figure 9.24, from which the chokes  $L_3$  and  $M_2$  were excluded. Eliminating the elements  $R_0$  and  $C_0$  provides the structure shown in Figure 9.28.

Figure 9.29 presents a filter from which the CM choke,  $M_2$ , was removed as, according to experimental verifications, in the external circuit for the filter and inverter there is negligible CM current. Such a structure is only a sinusoidal filter containing damping resistor  $R_1$ . A sinusoidal filter is practically the only filter that causes complications in the control of electric drives. The use of sinusoidal filter with the damping resistor  $R_1$  is essential only with the inaccurate generation of voltages and incomplete compensation of dead time or in systems without such compensation. In this case there exist small voltages with frequencies close to the filter resonance frequency, while the resistor  $R_1$  protects the system against damage. If the higher harmonics are very small, then it is possible to exclude the resistor  $R_1$  from the circuit and obtain a simpler and less expensive version of the sinusoidal filter, as shown in Figure 9.30.

## 9.6.2 Inverter Output Filters Design

Selection of inverter output filters is a complex task. This chapter presents a method for selecting parameters of the filter shown in Figure 9.24. This selection procedure is presented in [5,8,17].

The selection methods discussed in this chapter also fits the structures shown in Figures 9.25–9.30.

The combined filter structure from Figure 9.24 may complicate the selection of its parameters. Nevertheless, assuming that  $M_1 \gg L_1$  and  $C_0 \ll C_1$ , this allows separate selection of filter elements components  $\alpha\beta$  and for CM.

When selecting filter parameters, it is convenient to use a transformation from a three-phase system to a rectangular one, while maintaining the power of the system during transformation. For simplification, the leakage inductance of the coupled chokes  $M_1$  and  $M_2$ , as well as the circuit branch that contains the choke  $L_3$ , is neglected. Note that  $L_3$  is chosen based on the motor power.

The structure of the filter shown in Figure 9.24, for the orthogonal co-ordinate system  $\alpha\beta 0$ , is presented in Figure 9.33.

Resistances  $R_{L1}$ ,  $R_{M1}$ , and  $R_{M2}$  are copper resistances of the chokes  $L_1$ ,  $M_1$ , and  $M_2$ , respectively. Considerations on the selection of individual elements of the filter are presented in the following sections.

### 9.6.2.1 Selection of Differential Mode (Normal Mode) Filter Elements

The first selections are the elements of sinusoidal filter. The selection of the sinusoidal filter decides:

- assumed acceptable level of output voltage distortion;
- maximum allowed voltage drop in the filter;
- switching frequency of the power switches.

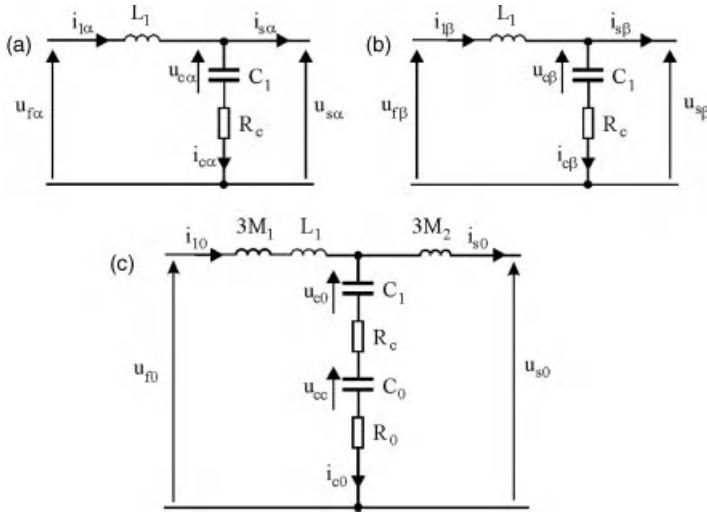


**Figure 9.33** Equivalent circuits of the filter for components: (a)  $\alpha$ ; (b)  $\beta$ ; and (c)  $0$

Selection of filter elements requires specific compromise between total harmonic distortion (THD) in the voltage waveform, weight, dimension, cost of the filter, and current parameters of the inverter. For the selection of sinusoidal filters from the filter for uninterruptable power supply (UPS), the THD is not a determining value for the parameters of the filter. In UPS systems, the THD does not exceed 5% under full load. In drive systems, a higher level of THD is allowed, even above 20%. This is because minimizing THD is the only reason of using a filter. The level of THD in the stator voltage has an effect mainly on the motor efficiency. Since one additional reason for using a filter in drive systems is to avoid voltage wave reflection on the motor terminals, a filter with a THD higher than 5% may probably fit the set tasks while being economically acceptable. It is important to note that the transistors' switching frequency has a significant effect on the value of filter inductances and capacitances. This switching frequency is much lower in drive systems than in UPS systems.

For further analysis on the selection of filter parameters, it is assumed that the pulse frequency is the inverse of the time per duration of two adjacent passive vectors ( $z$ ) and four active vectors ( $n$ ) in a cycle  $z1-n1-n2-z2-n2-n1$ . This corresponds to a notation of a sampling period for a sinusoidal PWM.

As a first element of the filter, it is selected as choke  $L_1$ . One of the methods for selecting a choke for the sinusoidal filter is identifying  $L_1$  on the basis of choke reactance  $X_1$ , which is obtained according to the assumed AC current component  $\Delta I_s$  for inverter switching frequency  $f_{imp}$  [5]. A three-phase voltage inverter with sinusoidal filter and squirrel cage induction motor can be represented as  $f_{imp}$ , as in an equivalent circuit shown in Figure 9.34.

The equivalent circuit, shown in Figure 9.34, results from the situation that during a sinusoidal PWM and space vector PWM, one of the DC link polarities is connected to one output phase, while the other polarity is connected to two parallel output phases. This is a correct assumption, assuming that the selection of the filter elements is done for the whole control range; this is a maximum inverter output voltage without over-modulation. Therefore,

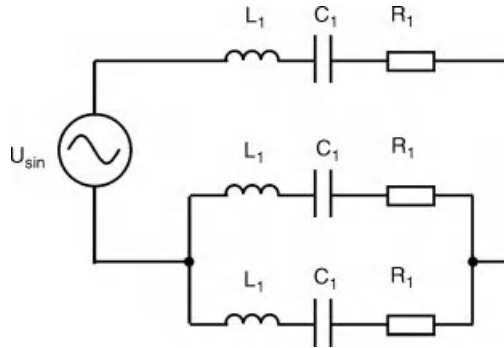


**Figure 9.34** Equivalent circuit of the inverter and sinusoidal filter

in such inverter controls, it is possible to neglect zero vectors. In this schematic, the stator copper resistance and the motor leakage inductance is neglected, because their values are too small compared with filter parameters with high pulse frequency. The schematic in Figure 9.34 is reduced, as shown in Figure 9.35.

In Figures 9.34 and 9.36, an inverter is replaced by a sinusoidal voltage source  $U_{\sin}$ . The rms value of this voltage  $U_{\sin}$  under full control, maximum voltage without over-modulation, is

$$U_{\sin} = \frac{U_d}{\sqrt{2}} \quad (9.26)$$

where  $U_d$  is the average value of the DC bus voltage.

The voltage  $U_d$ , in the case of feeding an inverter from a three-phase grid through a diode rectifier, is

$$U_d = \sqrt{2} U_n \frac{6}{\pi} \sin \frac{\pi}{6} \quad (9.27)$$

where  $U_n$  is the rms value of the line voltage on the rectifier terminals. Therefore:

$$U_{\sin} = U_n \frac{6}{\pi} \sin \frac{\pi}{6} \approx 0,95 U_n \quad (9.28)$$

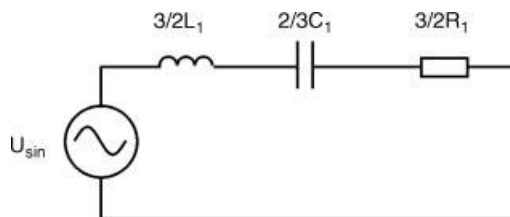


**Figure 9.35** Reduced equivalent circuit of the inverter and sinusoidal filter

In Figure 9.35, the element smoothing the current is mainly the choke  $L_1$ . The reactance of this choke is much greater than the reactance of the capacitor for a given switching frequency, therefore can be written as

$$2 \cdot \pi \cdot f_{\text{imp}} \cdot \frac{3L_1}{2} \cdot \Delta I_s = \frac{U_d}{\sqrt{2}} \quad (9.29)$$

where  $\Delta I_s$  means switching ripple inductor current. Ripple frequency is the equal transistor's switching frequency.

It is assumed that  $\Delta I_s$  should be lower than 20% of the rated current.

After conversion of equation (9.29) the relationship for an inductance of choke  $L_1$  is

$$L_1 = 2 \frac{U_d}{\sqrt{2} \cdot 2 \cdot \pi \cdot f_{\text{imp}} \cdot 3 \cdot \Delta I_s} \quad (9.30)$$

An inductance  $L_1$ , computed according to equation (9.5), is much higher than the leakage inductance of the motor [5].

Because of the dimension, weight, and cost, the filter inductance  $L_1$  should be as small as possible. Small  $L_1$  means small voltage drop on the filter and less losses in the drive.

Another method of identifying inductance  $L_1$  is by computing its value on the basis of assumed voltage drop in the filter  $\Delta U_1$  and on the known maximum value of the first voltage component  $U_{\text{out 1h}}$ . In drives systems, it is assumed that the voltage drop in the filter for the first component  $f_{\text{out 1h}}$  should be less than 5% of the motor rated voltage under full current loading  $I_n$  [8]. With such assumptions, an inductance is calculated as

$$L_1 = \frac{\Delta U_1}{2\pi f_{\text{out 1h}} I_n} \quad (9.31)$$

After identifying  $L_1$ , the next parameter to be selected is  $C_1$ , which is described from the relationship of the resonance frequency of the system:

$$f_{\text{res}} = \frac{1}{2\pi \sqrt{L_1 C_1}} \quad (9.32)$$

hence:

$$C_1 = \frac{1}{4\pi^2 f_{\text{res}}^2 L_1} \quad (9.33)$$

where  $f_{\text{res}}$  is the resonance frequency of the filter.

To assure good filtering capabilities of the filter, the resonance frequency should be lower than the switching frequency of the transistors  $f_{\text{imp}}$ . At the same time, to avoid the resonance

phenomenon, the capacitance  $C_1$  should be higher than the maximum frequency of the first harmonic of the inverter output voltage  $f_{wy\ 1h}$ . The safety range is [8]

$$10 \cdot f_{out\ 1h} < f_{res} < \frac{1}{2} \cdot f_{imp} \quad (9.34)$$

The upper range of  $C_1$  is described by the maximum value of the current flowing through this capacitor during rated operating conditions of the drive. The value of this current for the first harmonic cannot exceed 10% of the rated motor current.

The risk of resonance existence in the sinusoidal filter occurs during drive operation in the over-modulation region. In such a situation, the current flowing through the branch with  $C_1$  contains multiples of the fundamental harmonic, in addition to the fundamental harmonic.

A filter damping resistor should be selected in such a way that during the existence of the resonance, the current flowing in a capacitor should not exceed 20% of the rated inverter current. Hence, for computing  $C_1$ , it is necessary to know the voltage component with a frequency close to the filter resonance frequency. Relationships are given in [19]. In practice, because of the complicated analytical analysis, the harmonic component of resonance frequency is identified in simulation.

Another method of damping resistor selection is by choosing a value of  $R_1$  so that the total stray losses on the filter damping resistors are kept at the acceptable level of 0.1% of the converter power rating [5]. With a resistance  $R_1$  selected in such way, a filter quality factor is identified as

$$Q = \frac{Z_0}{R_1} \quad (9.35)$$

where  $Z_0$  is the natural frequency of the filter:

$$Z_0 = \sqrt{\frac{L_1}{C_1}} \quad (9.36)$$

To ensure sufficient attenuation, filters should have the same time minimum power losses and quality factor in the range 5–8 [5].

Knowing the parameters of the transverse branch of the sinusoidal filter  $C_1$ ,  $R_1$ , and assuming the sinusoidal shape of the filter output voltage, the power of the element  $R_1$  for the first harmonic of filter output current and voltage should be computed:

$$P_{R1\ 1har} = \frac{U_{s\ ph}^2}{R_1} \quad (9.37)$$

where  $U_{s\ p}$  is phase filter output voltage.

With power selection of resistors  $R_1$ , it is important to take into consideration that the filter output voltage contains a component with a frequency equal to the transistors switching frequency. With proper design of the filter, this component is small. However, because of its high frequency, the impedance of the transverse branch of  $C_1$  and  $R_1$  for this frequency is small.



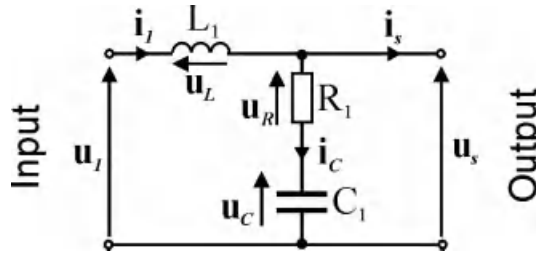


Figure 9.36 Equivalent circuit of the filter for  $\alpha$  component

This can cause a flow of essential current with high frequency in this branch. The power of  $R_1$  for the voltage component with a modulation frequency is

$$P_{R1 \text{ imp}} = \frac{U_{s \text{ imp}}^2}{R_1} \tag{9.38}$$

where  $U_{s \text{ imp}}$  is the filter output voltage component for PWM frequency.

The value of  $U_{s \text{ imp}}$  corresponds to the values that result from the assumed THD of the voltage in the design process.

For the chosen elements of the sinusoidal filter, it is possible to find its frequency characteristic based on the known filter transfer function presented as a two-port network in Figure 9.36.

Elements  $L_f$ ,  $C_f$ , and  $R_f$  correspond to the values  $3/2L_1$ ,  $2/3C_1$ , and  $3/2R_1$ , respectively, for the reduced filter scheme shown in Figure 9.24. Figure 9.37 presents a sinusoidal filter that has a two-port network consisting of two impedances,  $Z_1$  and  $Z_2$ .

Impedances  $Z_1$  and  $Z_2$  are described as

$$Z_1(j\omega) = j\omega L_f \tag{9.39}$$

$$Z_2(j\omega) = R_f + \frac{1}{j\omega C_f} \tag{9.40}$$

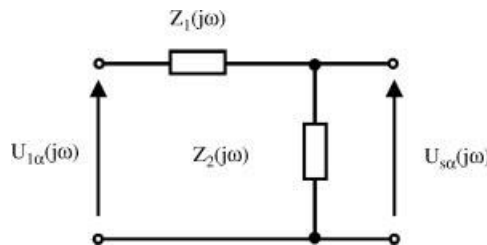


Figure 9.37 Equivalent circuit of the two-port network – sinusoidal filter for component  $\alpha$

or in the form of a transfer function:

$$Z_1(s) = sL_f \quad (9.41)$$

$$Z_2(s) = R_f + \frac{1}{sC_f} \quad (9.42)$$

The transfer function of the filter for voltages is described as

$$G_{fu}(s) = \frac{U_{s\alpha}}{U_{1\alpha}} = \frac{Z_{wy}(s)}{Z_{we}(s)} = \frac{Z_2(s)}{Z_1(s) + Z_2(s)} = \frac{R_f + \frac{1}{sC_f}}{sL_f + R_f + \frac{1}{sC_f}} \quad (9.43)$$

which is

$$G_{fu}(s) = \frac{U_{s\alpha}}{U_{1\alpha}} = \frac{sR_fC_f + 1}{s^2L_fC_f + sR_fC_f + 1} \quad (9.44)$$

The cut-off frequency of the filter is described according to

$$f_{3dB} = \frac{1}{2\pi\sqrt{L_fC_f}} \quad (9.45)$$

while the damping coefficient is

$$\xi = \frac{R_f}{2\sqrt{L_f/C_f}} = \frac{1}{2Q} \quad (9.46)$$

and Q is the filter quality factor of the filter:

$$Q = \frac{\sqrt{L_f/C_f}}{R_f} \quad (9.47)$$

Examples of phase and magnitude characteristics of the sinusoidal filter are shown in Figure 9.38.

Knowledge of filter parameters and characteristic of parameters is essential for the correct consideration of such filters in drive systems.

An operation of a filter, presented in Figure 9.24, is shown in Figures 9.39 and 9.40 for a rated load of a 5.5 kW squirrel cage induction motor.

With a fully loaded motor, voltage and current waveforms are significantly filtered with minimum voltage drop on the filter and minimum phase shifts of voltages and currents before and after the filter.

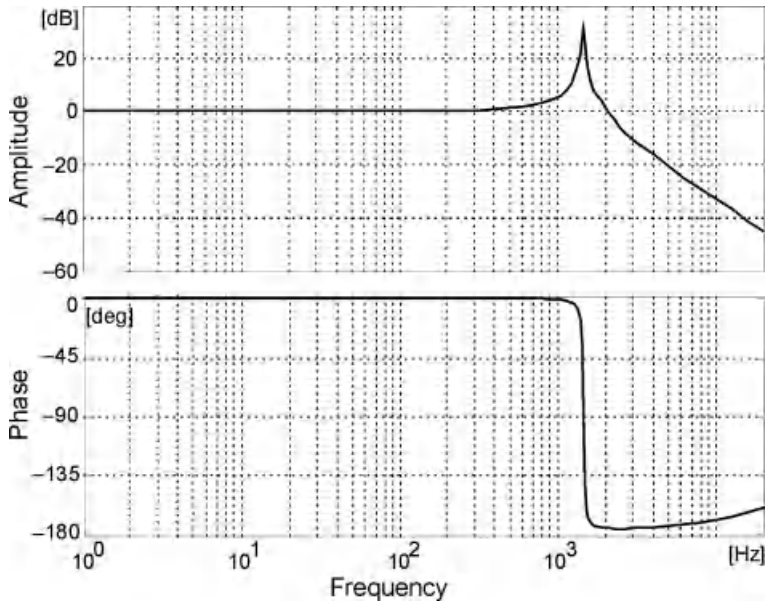


**Figure 9.38** Phase and magnitude plots of a sinusoidal filter (filter chosen for a 1.5kW motor;  $L_f = 4$  mH,  $C_f = 3$   $\mu$ F,  $R_f = 1$   $\Omega$ )

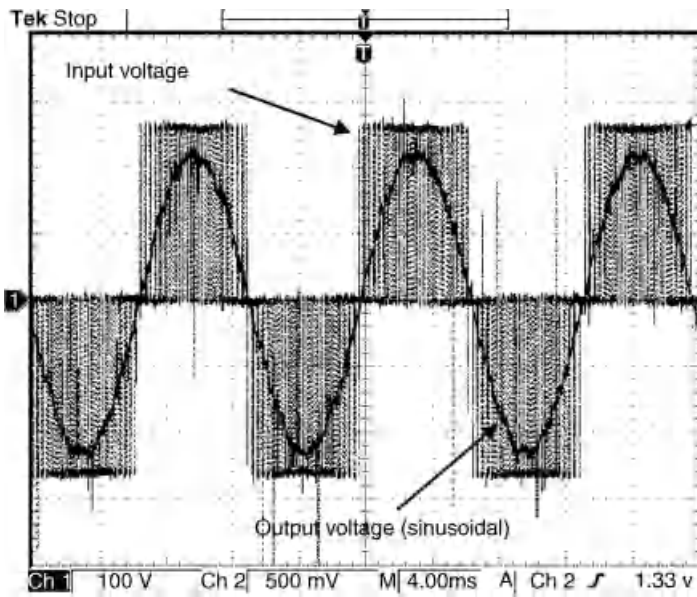


**Figure 9.39** Voltage waveforms on input and output of the sinusoidal filter for 40Hz inverter output voltage frequency

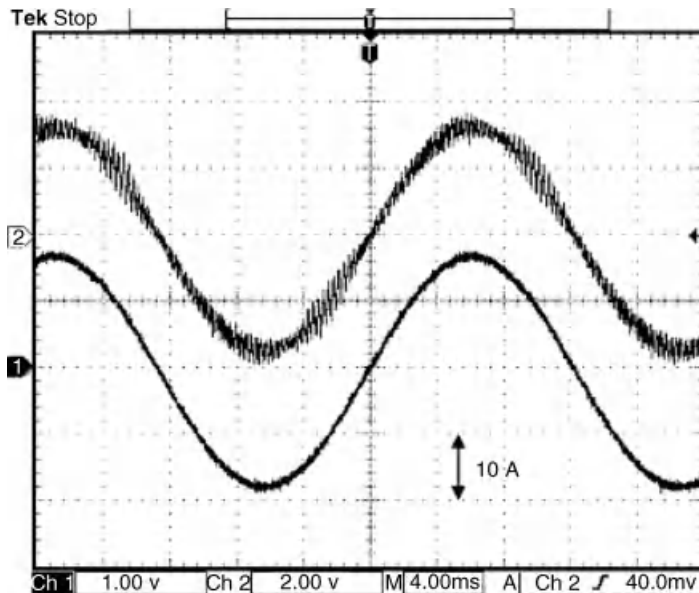


**Figure 9.40** Current waveforms before (Ch 1) and after (Ch 2) of the sinusoidal filter for 40 Hz inverter output voltage frequency

**9.6.2.2 Selection of Elements for Zero Sequence (Common Mode)**

Selection of the filter elements for CM starts from choosing CM chokes  $M_1$  and  $M_2$ . In the integrated filter structure shown in Figure 9.24, it is assumed that both chokes are identical. The inductances of CM chokes should be the same. During the selection of filter elements, it is assumed that  $M_1 \gg L_1$ . While selecting  $M_1$  and  $M_2$ , it is important to pay special attention to the possibility of their practical realization. Such possibilities result from the parameters of the used toroidal cores. In practical solutions, the measurement of CM voltage  $u_{cm}$  is used, which enables description of the flux in the choke core [5]:

$$\psi_{cm} = \frac{1}{N_{cm}} \int u_{cm} dt \tag{9.48}$$

where  $N_{cm}$  is the number of turns in one phase of the CM choke.

The magnetic field density in the choke is

$$B_{cm} = \frac{\psi_{cm}}{S_{cm}} = \frac{1}{S_{cm}N_{cm}} \int u_{cm} dt \tag{9.49}$$

where  $S_{cm}$  is the cross-sectional area of the CM choke.

The computed magnetic field density  $B_{cm}$  should be lower than  $B_{sat}$ , which is the saturated value of the magnetic field density in the core used for the design of the CM choke. Manufacturers of magnetic materials currently offer dedicated cores for CM chokes with  $B_{sat} = 1 \dots 1.2T$ .

The CM choke inductance with known dimensions is described as

$$L_{cm} = \frac{\mu S_{cm} N_{cm}^2}{l_{cm}} \quad (9.50)$$

where  $l_{cm}$  is an average path length of the magnetic field in the CM choke core.

Neglecting the small leakage inductance of the CM choke, it is possible to assume that  $M_1 = M_2 = L_{cm}$ .

For a constant product  $S_{cm} N_{cm}$ , the peak value of the CM current  $I_{cm \max}$  is proportional to the ratio  $l_{cm}/N_{cm}$ . Decreasing the dimensions of chokes by reducing the flux path length to  $l_{cm}$  and increasing the number of turns  $N_{cm}$  has the advantage of limiting the current peak value  $I_{cm \max}$ . At the same time, it should be noted that the planned number of turns can fit in the window of the selected core.

Searching for an optimal CM choke according to the described method is a complicated, iterative process requiring special measuring tools that allow for the identification of  $u_{cm}$  and  $I_{cm \max}$ . Therefore, to simplify the process of the filter design, manufacturers of magnetic materials frequently suggest specialized solutions of cores and complete CM chokes depending on motor power.

The capacitance  $C_0$  is determined using the known values of inductances  $M_1$  and  $M_2$ , and the resonance frequency  $f_{rez}$ :

$$C_0 = \frac{1}{4\pi^2 f_{rez}^2 L_{cm}} \quad (9.51)$$

while the resistance  $R_0$ :

$$R_0 = \frac{\sqrt{L_{cm}/C_{cm}}}{Q_0} \quad (9.52)$$

where  $Q_0$  is the assumed quality factor of the CM filter in the range 5–8.

The power of the resistor  $R_0$ :

$$P_{R0} = \frac{U_{cm}^2}{R_0} \quad (9.53)$$

where  $U_{cm}$  is rms value of the CM voltage, which is

$$U_{cm} \leq \frac{U_d}{\sqrt{2}} \quad (9.54)$$

In the case of filters, where it is essential to use chokes  $L_3$ , it is assumed that the current flowing through the choke  $L_1$  is close to the 10% rated motor current:

$$L_3 \approx \frac{1}{2\pi f_n} \frac{U_n}{0.1 \cdot I_n} \quad (9.55)$$

where  $U_n$ ,  $I_n$ , and  $f_n$  are voltage, current, and rated frequency of the inverter, respectively.

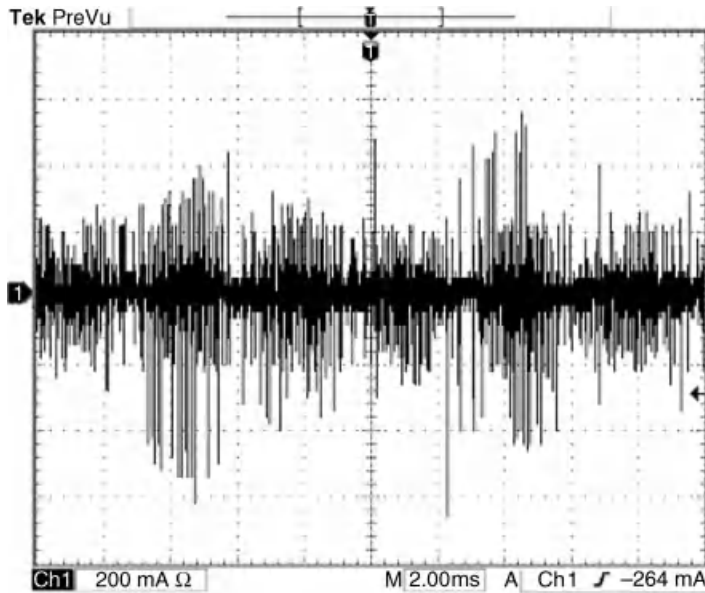


**Figure 9.41** Current waveform in a shielded conductor PE of a 5.5 kW motor fed by an inverter **without** output filter

Operation of the CM filter, shown in Figure 9.24, is presented in Figures 9.41 and 9.42.

In comparison with a drive without a filter, the CM current in a shielded conductor PE for a 5.5 kW motor (Figure 5.20) is limited after using a CM filter, as shown in Figure 5.21.

### 9.6.3 Motor Choke

Motor chokes are used in many inverter fed drives. They represent the simplest form of inverter output filters. In three-phase systems, motor chokes are three-phase or three single-phase bulks connected between motor and inverter terminals, as shown in Figure 9.43

The main task of the motor choke in AC drives is to limit the voltage rise ( $dv/dt$ ) on the motor terminals, which decreases the danger of damaging the insulation of the motor.

Motor chokes are also used for limiting short circuit currents before running the internal short circuit protection of the inverter.

While neglecting the copper resistance, a motor choke could be represented as a linear inductance, as shown in Figure 9.44.

According to Figure 5.23, a motor choke may be represented as

$$\frac{di_s}{d\tau} = \frac{1}{L_1} (\mathbf{u}_1 - \mathbf{u}_s) \tag{9.56}$$

where  $L_1$  is motor choke inductance.

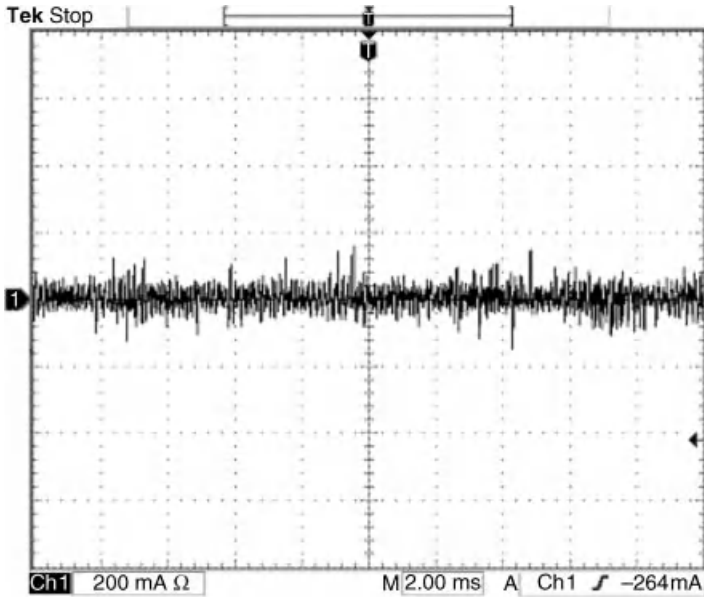


**Figure 9.42** Current waveform in a shielded conductor PE of a 5.5 kW motor fed by an inverter with output filter

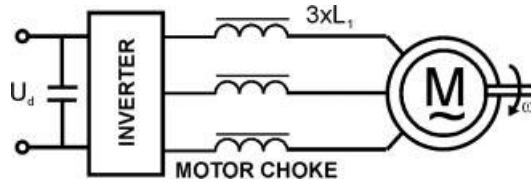


**Figure 9.43** Electric drive with induction motor, voltage inverter, and motor choke

The selection of motor choke  $L_1$  is performed by assuming that the voltage drop on the motor choke of the first component  $f_{out\ 1h}$  is lower than 5% of the rated motor voltage under loading the filter with rated current  $I_n$ :

$$L_1 = \frac{\Delta U_1}{2\pi f_{out\ 1h} I_n} \tag{9.57}$$

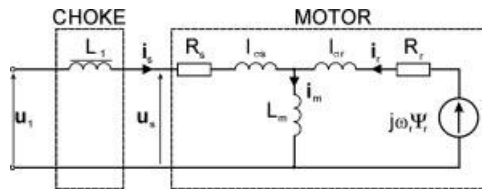


**Figure 9.44** Equivalent circuit of the motor choke and induction motor

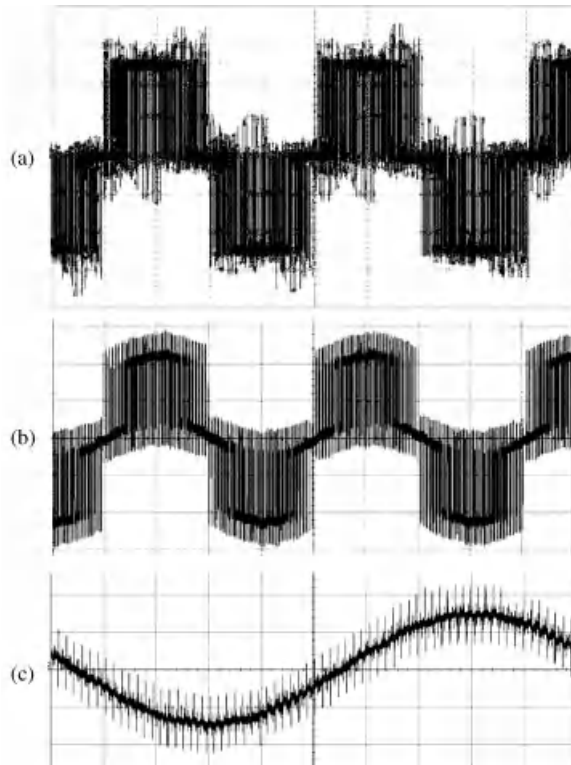


**Figure 9.45** Waveforms registered from experimental setup with induction motor and motor choke: (a) inverter output voltage; (b) voltage on motor terminals; (c) motor current (a, b – 200 V/div, 5 ms/div; c – 5 A/div, 2 ms/div, motor 1.5 kW 300 V, choke  $L_1 = 11$  mH, motor loaded with rated condition – registered waveforms are not synchronized)

Figure 9.45 shows examples of currents and voltages waveforms from an experimental setup with a squirrel cage induction motor and motor choke.

In the system with motor choke, the voltage feeding the motor has a pulse shape superimposed with an additional small component of the sinusoidal voltage.

The motor choke effect on  $du/dt$  is shown in Figure 9.46.

In the waveforms shown in Figure 9.46, it is possible to note the clear limit of motor voltage  $dv/dt$  after connecting a motor choke.

#### 9.6.4 MATLAB/Simulink Model of Induction Motor Drive with PWM Inverter and Differential Mode (Normal Mode) LC Filter

The MATLAB/Simulink model of induction motor drive with inverter and LC filter *sys\_LC\_filter.mdl* is presented in Figure 9.47.





**Figure 9.46** Waveforms: (a) inverter output voltage; (b) motor current for the drive with motor choke (scale  $10\ \mu\text{s}/\text{div}$ ,  $200\ \text{V}/\text{div}$  – waveforms are not synchronized)

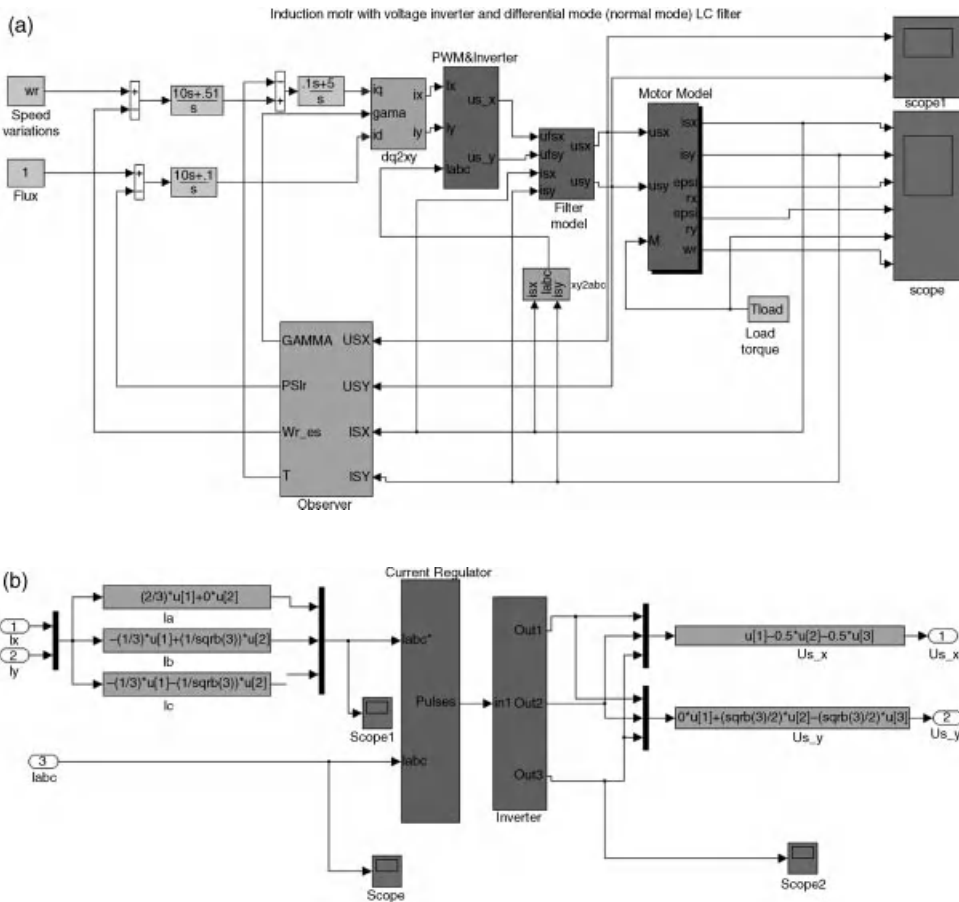


**Figure 9.47** MATLAB/Simulink model of induction motor drive with PWM inverter and LC filter - *sys\_LC\_filter.mdl*: (a) whole structure; (b) inverter and PWM sub-system; and (c) LC filter sub-system

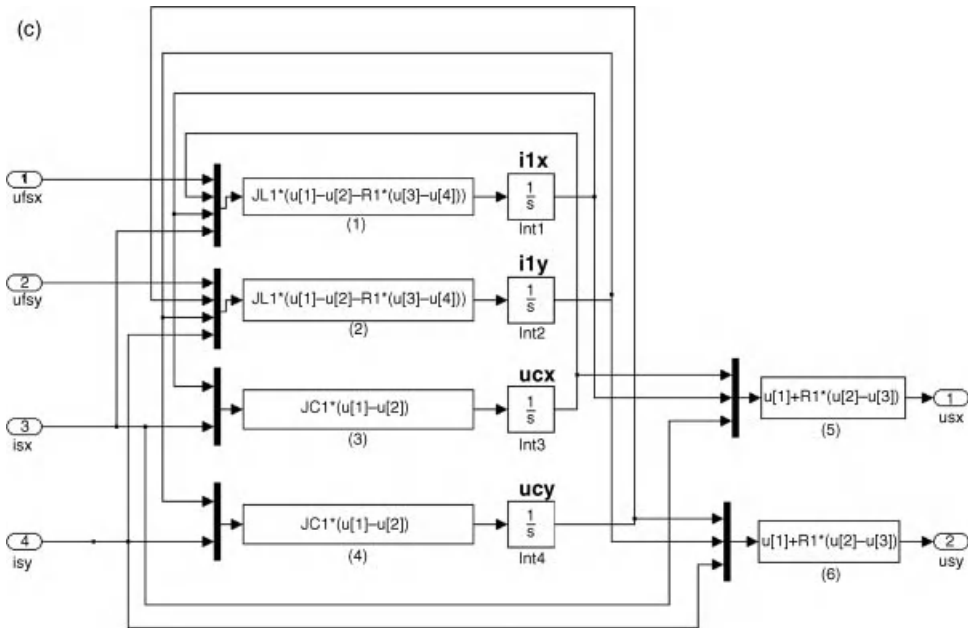


Figure 9.47 (Continued)

The simulated system is prepared as the single file *sys\_LC\_filter.mdl*. The model consists of the following blocks (sub-systems):

- Three-phase inverter with space vector PWM algorithm (*PWM&Inverter*);
- LC filter model (*Filter model*);
- induction motor model (*Motor model*);
- frame of references transformation (*dq2xy, xy2abc*);
- flux and speed observer (*Observer*);
- PI controllers, commanded signals and scopes.

The commanded values are speed and flux. The motor control algorithm is the classical FOC. Both control systems and the observer are the classical solutions, without any changes due to LC filter use. To assure the system works correctly, the dynamics of the drive is limited, because the aim of the simulation is to present the LC filter properties only.

The induction motor model is 4 poles,  $P_N = 1.5 \text{ kW}$ ,  $U_N = 300 \text{ V}$ . All the system parameters, including filter and motor parameters, are given in the preload function (*File → Model properties → Callbacks*).

In the simulation test, the constant motor flux is retained, whereas the commanded motor speed is changed. Due to the speed variations, the motor voltage supply frequency changes. The LC filter assures that motor voltages and currents are sinusoidal in shape. In Figures 9.48 and 9.49, the example of the motor voltages and currents are presented.

The complete MATLAB/Simulink model is available in the CD-ROM provided with this book.

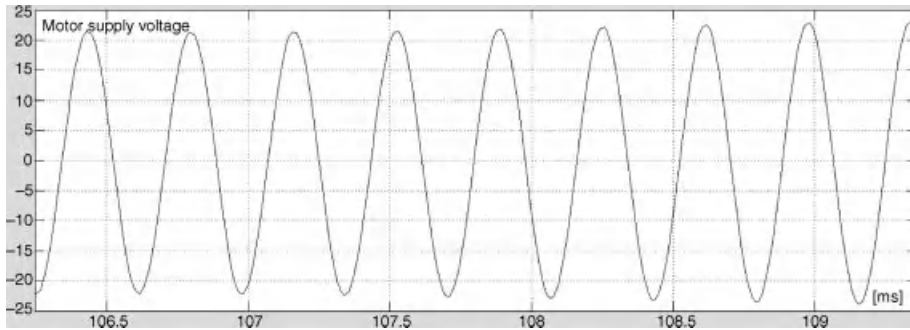


Figure 9.48 Motor supply voltage

## 9.7 Estimation Problems in the Drive with Filters

### 9.7.1 Introduction

For motor closed loop control purposes, the actual controlled state variables have to be known. In most control systems, the controlled variables are mechanical speed, magnetic flux, and motor torque. The speed is easy to measure; however, measuring other variables is not so simple. In spite of the easy speed measurement in modern drives, the requirements for speed sensor elimination exists. To solve these problems, numerous estimation methods are used and

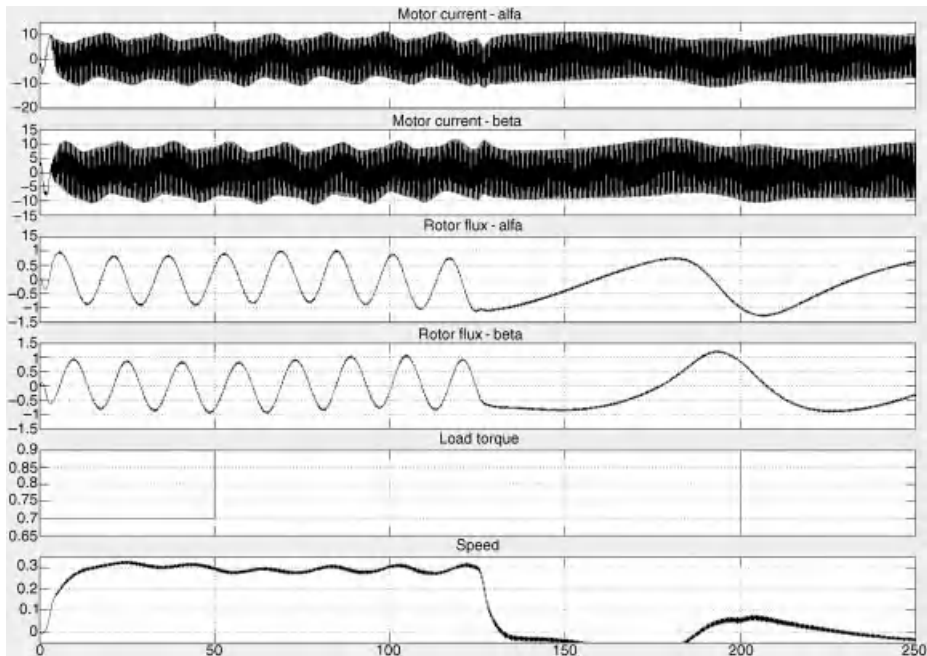
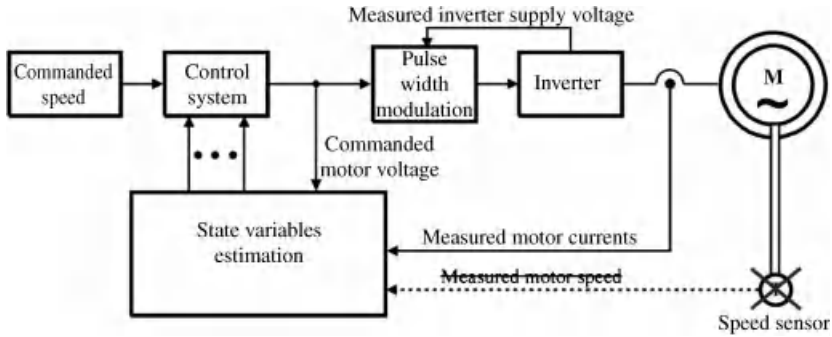


Figure 9.49 Simulation of the drive start-up and speed variations



**Figure 9.50** General structure of the sensorless AC drive

the variables are calculated on-line. Then the sensors are limited to only the current and voltage sensors installed inside the converter. To prevent noise, all sensors should be installed inside the converter box. A drive with such limited sensors is known as a sensorless drive. The general structure of the sensorless AC drive is presented in Figure 9.50.

In the literature, numerous sensorless solutions are proposed. A comprehensive review can be found in [20]. But most of the solutions presented are applicable for the drives without motor filter use.

In the case of motor filter use, the estimation process is more complicated. Some of the solutions propose the installation of voltage and current sensors outside the converter for direct motor current and voltage measurement [21,22]. Unfortunately, as was mentioned earlier, this is not an applicable solution. The more useful solution is to implement the filter model in the estimation algorithm, where the sensor structure will be the same as in drives without filter use. Then the general structure of the sensorless drive with the LC filter is as presented in Figure 9.51.

Only the differential model filter has influence on motor control and estimation algorithms.

Only a limited amount of literature presents estimation solutions for driver with filters, some of which are proposed in [23–25]. The most common estimation method is to add the filter model dependencies into some known observer structure and to change

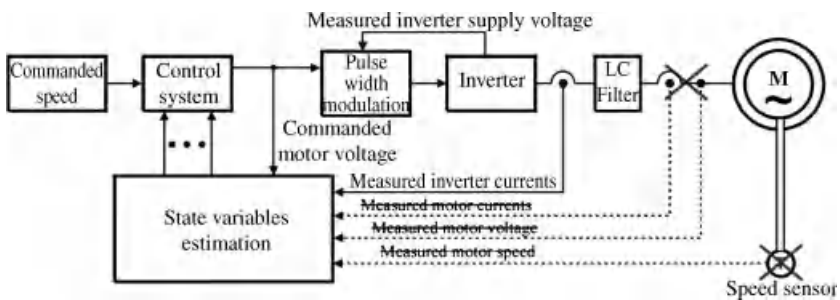


**Figure 9.51** General structure of the sensorless AC drive with motor LC filter use

the observer correction parts. Some of the possible solutions are presented in the following sections.

### 9.7.2 Speed Observer with Disturbances Model

The operation of modern complex asynchronous motor electric drives requires application of the calculating system, which computes on-line all the state variables used in control systems. Nowadays, frequent solutions in state variable calculations are to use a state observer. In this chapter, the state observer presented in [26] has been converted into a system with a sine filter.

The base observer structures for the drive, without the sine filter in  $\alpha\beta$  references, are

$$\frac{d\hat{i}_{s\alpha}}{d\tau} = -\frac{R_s L_r^2 + R_r L_m^2}{L_r w_\delta} \hat{i}_{s\alpha} + \frac{R_r L_m}{L_r w_\delta} \hat{\psi}_{r\alpha} + \frac{L_m}{w_\delta} \xi_\beta + \frac{L_r}{w_\delta} u_{s\alpha}^{\text{com}} + k_3 (i_{s\alpha} - \hat{i}_{s\alpha}) \quad (9.58)$$

$$\frac{d\hat{i}_{s\beta}}{d\tau} = -\frac{R_s L_r^2 + R_r L_m^2}{L_r w_\delta} \hat{i}_{s\beta} + \frac{R_r L_m}{L_r w_\delta} \hat{\psi}_{r\beta} + \frac{L_m}{w_\delta} \xi_\alpha + \frac{L_r}{w_\delta} u_{s\beta}^{\text{com}} + k_3 (i_{s\beta} - \hat{i}_{s\beta}) \quad (9.59)$$

$$\begin{aligned} \frac{d\hat{\psi}_{r\alpha}}{d\tau} = & -\frac{R_r}{L_r} \hat{\psi}_{r\alpha} - \xi_\beta + R_r \frac{L_m}{L_r} \hat{i}_{s\alpha} - k_2 S_b \hat{\psi}_{r\alpha} + S k_2 k_3 \hat{\psi}_{r\beta} (S_b - S_{bF}) \\ & + S k_5 ((S_x - S_{xF}) \hat{\psi}_{r\alpha} - (S_b - S_{bF}) \hat{\psi}_{r\beta}) \end{aligned} \quad (9.60)$$

$$\begin{aligned} \frac{d\hat{\psi}_{r\beta}}{d\tau} = & -\frac{R_r}{L_r} \hat{\psi}_{r\beta} + \xi_\alpha + R_r \frac{L_m}{L_r} \hat{i}_{s\beta} - k_2 S_b \hat{\psi}_{r\beta} - S k_2 k_3 \hat{\psi}_{r\alpha} (S_b - S_{bF}) \\ & + S k_5 (-(S_x - S_{xF}) \hat{\psi}_{r\beta} - (S_b - S_{bF}) \hat{\psi}_{r\alpha}) \end{aligned} \quad (9.61)$$

$$\frac{d\hat{\xi}_\alpha}{d\tau} = -\hat{\omega}_{\psi r} \hat{\xi}_\beta - k_1 (i_{s\beta} - \hat{i}_{s\beta}) \quad (9.62)$$

$$\frac{d\hat{\xi}_\beta}{d\tau} = \hat{\omega}_{\psi r} \hat{\xi}_\alpha + k_1 (i_{s\alpha} - \hat{i}_{s\alpha}) \quad (9.63)$$

$$\frac{dS_{bF}}{d\tau} = \frac{1}{T_{Sb}} (S_b - S_{bF}) \quad (9.64)$$

$$\frac{d\hat{\omega}_{rF}}{d\tau} = \frac{1}{T_{KT}} (\hat{\omega}_r - \hat{\omega}_{rF}) \quad (9.65)$$

$$\frac{dS_{xF}}{d\tau} = \frac{1}{T_{Sx}} (S_x - S_{xF}) \quad (9.66)$$

$$S = \begin{cases} 1 & \text{if } \hat{\omega}_{\psi r} > 0 \\ -1 & \text{if } \hat{\omega}_{\psi r} \leq 0 \end{cases} \quad (9.67)$$

$$S_x = \hat{\xi}_\alpha \hat{\psi}_{r\alpha} + \hat{\xi}_\beta \hat{\psi}_{r\beta} \quad (9.68)$$

$$S_b = \hat{\xi}_\alpha \hat{\psi}_{r\beta} - \hat{\xi}_\beta \hat{\psi}_{r\alpha} \quad (9.69)$$

$$\hat{\omega}_{\psi r} = \hat{\omega}_{rF} + R_r \frac{L_m}{L_r} \left( \frac{\hat{\psi}_{r\alpha} \hat{i}_{s\beta} + \hat{\psi}_{r\beta} \hat{i}_{s\alpha}}{\hat{\psi}_{r\alpha}^2 + \hat{\psi}_{r\beta}^2} \right) \quad (9.70)$$

$$\hat{\omega}_r = \frac{\hat{\xi}_\alpha \hat{\psi}_{r\alpha} + \hat{\xi}_\beta \hat{\psi}_{r\beta}}{\hat{\psi}_{r\alpha}^2 + \hat{\psi}_{r\beta}^2} \quad (9.71)$$

where  $\xi_\alpha, \xi_\beta$  are components of the motor electromotive forces;  $\omega_{\psi r}$  is the angular speed of the motor flux vector;  $k_1, k_2, k_3, k_4, k_5$  are the observer gains;  $S_x, S_{xF}, S_b, S_{bF}$  are additional variables used to stabilize the observer work;  $T_{Sb}, T_{KT},$  and  $T_{Sx}$  are the time constants of the filters; and  $S$  is the sign of the rotor flux speed.

The state observer equations (9.58) to (9.71) need to be modified to assure the proper function of the electric drive, as presented in [27].

For the system with the sine filter, the observer equations (9.58) to (9.71) are extended with LC filter model equations.

The circuit of the LC filter, presented in Figure 9.52, can be described as

$$\frac{du_{c\alpha}}{d\tau} = \frac{i_{c\alpha}}{C_1} \quad (9.72)$$

$$\frac{di_{1\alpha}}{d\tau} = \frac{u_{1\alpha} - R_1 i_{1\alpha} - R_c i_{c\alpha} - u_{c\alpha}}{(L_1 + L_{\sigma M1})} \quad (9.73)$$

$$i_{c\alpha} = i_{1\alpha} - i_{s\alpha} \quad (9.74)$$

$$u_{s\alpha} = R_c (i_{1\alpha} - i_{s\alpha}) + u_{c\alpha} \quad (9.75)$$

$$\frac{du_{c\beta}}{d\tau} = \frac{i_{c\beta}}{C_1} \quad (9.76)$$

$$\frac{di_{1\beta}}{d\tau} = \frac{u_{1\beta} - R_1 i_{1\beta} - R_c i_{c\beta} - u_{c\beta}}{(L_1 + L_{\sigma M1})} \quad (9.77)$$

$$i_{c\beta} = i_{1\beta} - i_{s\beta} \quad (9.78)$$

$$u_{s\beta} = R_c (i_{1\beta} - i_{s\beta}) + u_{c\beta} \quad (9.79)$$

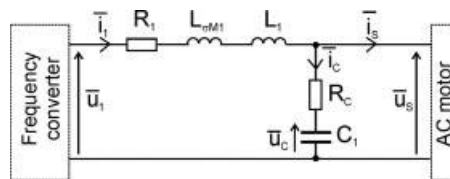


**Figure 9.52** Equivalent circuit of the differential inverter output LC filter

The correction parts in equations (9.58) and (9.59) are changed to the difference between measured and calculated inverter output current. Instead of the commanded motor voltages in equations (9.58) and (9.59), the commanded inverter output voltages are used in equations (9.51) and (9.52). In equations (9.2) and (9.6) of the LC filter model, the new correction terms are added.

Equations of the modified state observer for electric drives with inverter output filter are

$$\frac{d\hat{i}_{s\alpha}}{dt} = -\frac{R_s L_r^2 + R_r L_m^2}{L_r w_\delta} \hat{i}_{s\alpha} + \frac{R_r L_m}{L_r w_\delta} \hat{\psi}_{r\alpha} + \frac{L_m}{w_\delta} \xi_\beta + \frac{L_r}{w_\delta} \hat{u}_{s\alpha} + k_3 (i_{1\alpha} - \hat{i}_{1\alpha}) \quad (9.80)$$

$$\frac{d\hat{i}_{s\beta}}{dt} = -\frac{R_s L_r^2 + R_r L_m^2}{L_r w_\delta} \hat{i}_{s\beta} + \frac{R_r L_m}{L_r w_\delta} \hat{\psi}_{r\beta} - \frac{L_m}{w_\delta} \xi_\alpha + \frac{L_r}{w_\delta} \hat{u}_{s\beta} + k_3 (i_{1\beta} - \hat{i}_{1\beta}) \quad (9.81)$$

$$\begin{aligned} \frac{d\hat{\psi}_{r\alpha}}{dt} = & -\frac{R_r}{L_r} \hat{\psi}_{r\alpha} - \xi_\beta + R_r \frac{L_m}{L_r} \hat{i}_{s\alpha} - k_2 S_b \hat{\psi}_{r\alpha} - S k_2 k_3 \hat{\psi}_{r\beta} (S_b - S_{bF}) \\ & + S k_5 ((S_x - S_{xF}) \hat{\psi}_{r\alpha} - (S_b - S_{bF}) \hat{\psi}_{r\beta}) \end{aligned} \quad (9.82)$$

$$\begin{aligned} \frac{d\hat{\psi}_{r\beta}}{dt} = & -\frac{R_r}{L_r} \hat{\psi}_{r\beta} + \xi_\alpha + R_r \frac{L_m}{L_r} \hat{i}_{s\beta} - k_2 S_b \hat{\psi}_{r\beta} - S k_2 k_3 \hat{\psi}_{r\alpha} (S_b - S_{bF}) \\ & + S k_5 (-(S_x - S_{xF}) \hat{\psi}_{r\beta} - (S_b - S_{bF}) \hat{\psi}_{r\alpha}) \end{aligned} \quad (9.83)$$

$$\frac{d\hat{\xi}_\alpha}{d\tau} = -\hat{\omega}_{\psi r} \hat{\xi}_\beta - k_1 (i_{1\beta} - \hat{i}_{1\beta}) \quad (9.84)$$

$$\frac{d\hat{\xi}_\beta}{d\tau} = \hat{\omega}_{\psi r} \hat{\xi}_\alpha + k_1 (i_{1\alpha} - \hat{i}_{1\alpha}) \quad (9.85)$$

$$\frac{d\hat{u}_{c\alpha}}{d\tau} = \frac{i_{1\alpha} - \hat{i}_{s\alpha}}{C_1} \quad (9.86)$$

$$\frac{d\hat{u}_{c\beta}}{d\tau} = \frac{i_{1\beta} - \hat{i}_{s\beta}}{C_1} \quad (9.87)$$

$$\frac{d\hat{i}_{1\alpha}}{d\tau} = \frac{u_{1\alpha}^{\text{com}} - \hat{u}_{s\alpha}}{L_1} + k_A (i_{1\alpha} - \hat{i}_{1\alpha}) - k_B (i_{1\beta} - \hat{i}_{1\beta}) \quad (9.88)$$

$$\frac{d\hat{i}_{1\beta}}{d\tau} = \frac{u_{1\beta}^{\text{com}} - \hat{u}_{s\beta}}{L_1} + k_A (i_{1\beta} - \hat{i}_{1\beta}) + k_B (i_{1\alpha} - \hat{i}_{1\alpha}) \quad (9.89)$$

$$\hat{u}_{s\alpha} = \hat{u}_{c\alpha} + (i_{1\alpha} - \hat{i}_{s\alpha}) R_c \quad (9.90)$$

$$\hat{u}_{s\beta} = \hat{u}_{c\beta} + (i_{1\beta} - \hat{i}_{s\beta}) R_c \quad (9.91)$$

$$\frac{dS_{bF}}{d\tau} = \frac{1}{T_{Sb}} (S_b - S_{bF}) \quad (9.92)$$

$$\frac{d\hat{\omega}_{rF}}{d\tau} = \frac{1}{T_{KT}} (\hat{\omega}_r - \hat{\omega}_{rF}) \quad (9.93)$$

$$\frac{dS_{xF}}{d\tau} = \frac{1}{T_{Sx}} (S_x - S_{xF}) \quad (9.94)$$

$$S = \begin{cases} 1 & \text{if } \hat{\omega}_{\psi r} > 0 \\ -1 & \text{if } \hat{\omega}_{\psi r} \leq 0 \end{cases} \quad (9.95)$$

$$S_x = \hat{\xi}_\alpha \hat{\psi}_{r\alpha} + \hat{\xi}_\beta \hat{\psi}_{r\beta} \quad (9.96)$$

$$S_b = \hat{\xi}_\alpha \hat{\psi}_{r\beta} - \hat{\xi}_\beta \hat{\psi}_{r\alpha} \quad (9.97)$$

$$\hat{\omega}_{\psi r} = \hat{\omega}_{rF} + R_r \frac{L_m}{L_r} \left( \frac{\hat{\psi}_{r\alpha} \hat{i}_{s\beta} + \hat{\psi}_{r\beta} \hat{i}_{s\alpha}}{\hat{\psi}_{r\alpha}^2 + \hat{\psi}_{r\beta}^2} \right) \quad (9.98)$$

$$\hat{\omega}_r = \frac{\hat{\xi}_\alpha \hat{\psi}_{r\alpha} + \hat{\xi}_\beta \hat{\psi}_{r\beta}}{\hat{\psi}_{r\alpha}^2 + \hat{\psi}_{r\beta}^2} \quad (9.99)$$

where  $k_A$  and  $k_B$  are the additional observer gains.

The small resistance  $R_1$  and leakage inductance  $L_{\sigma M1}$  could be omitted in the modified observer procedure.

### 9.7.3 Simple Observer based on Motor Stator Models

Some estimations of algorithms are based on the motor stator circuit model. These methods are simple in implementation, but have an inseparable problem with voltage drift [28]. In the literature, some suggestions for motor stator based estimation improvements are proposed [29,30]. For example, in [30], the observer is based on the voltage model of the induction motor with combination of rotor and stator fluxes and stator current relationships:

$$\tau_s' \frac{d\hat{\psi}_{s\alpha}}{d\tau} + \hat{\psi}_{s\alpha} = k_r \hat{\psi}_r + \mathbf{u}_s \quad (9.100)$$

where  $\hat{\psi}_s = [\hat{\psi}_{s\alpha}, \hat{\psi}_{s\beta}]^T$  is stator flux vector;  $\hat{\psi}_r = [\hat{\psi}_{r\alpha}, \hat{\psi}_{r\beta}]^T$ ,  $\mathbf{u}_s = [u_{s\alpha}, u_{s\beta}]^T$ ;  $\tau_s' = \sigma L_s / R_s$  is time constant, and  $k_r = L_m / L_r$  is the rotor coupling factor.

To prevent problems of voltage drift and offset errors, instead of pure integrators, low pass filters (LPFs) are used. The limitation of the estimated stator flux is tuned to the stator flux nominal value. In addition, the extra compensation part is added, as presented in [30].

This section presents the observer system from [30], which is changed adequately to fit the drive with the LC filter requirements – the structure of the observer is extended, taking into account the model of the filter [30]. For the drive with the LC filter, the extra filter simulator relations are used. In the filter dynamics simulator block, the estimated values of the motor current and voltage are calculated as  $\hat{\mathbf{i}}_s$  and  $\hat{\mathbf{u}}_s$ . These estimated variables are calculated on the basis of the inverter commanded voltage  $\mathbf{u}_1^{\text{com}}$  and the measured inverter output current  $\mathbf{i}_1$ .



The simulator calculations are performed in an open loop, according to equations (9.18) to (9.23) filter model:

$$\frac{d\hat{\mathbf{u}}_s}{d\tau} = \frac{\mathbf{i}_1 - \hat{\mathbf{i}}_s}{C_1} \quad (9.101)$$

$$\frac{d\hat{\mathbf{i}}_1}{d\tau} = \frac{\mathbf{u}_1 - \hat{\mathbf{u}}_s}{L_1} \quad (9.102)$$

where  $\mathbf{i}_1 = [i_{1\alpha}, i_{1\beta}]^T$ ,  $\hat{\mathbf{i}}_1 = [\hat{i}_{1\alpha}, \hat{i}_{1\beta}]^T$ ,  $\hat{\mathbf{i}}_s = [\hat{i}_{s\alpha}, \hat{i}_{s\beta}]^T$ ,  $\mathbf{u}_1 = [u_{1\alpha}, u_{1\beta}]^T$ ,  $\hat{\mathbf{u}}_s = [\hat{u}_{s\alpha}, \hat{u}_{s\beta}]^T$

The other rotor flux and stator flux observer equations are computed as

$$\frac{d\hat{\psi}_{s\alpha}}{d\tau} = \frac{-\hat{\psi}_{s\alpha} + k_r \hat{\psi}_{r\alpha} + \hat{u}_{s\alpha}}{\tau'_s} - k_{ab} (\mathbf{i}_1 - \hat{\mathbf{i}}_1) \quad (9.103)$$

$$\hat{\psi}_r = \frac{\hat{\psi}_s - \sigma L_s \hat{\mathbf{i}}_s}{k_r} \quad (9.104)$$

where  $k_{AB} = \begin{bmatrix} k_A & -k_B \\ k_B & k_A \end{bmatrix}$  is the observer gains matrix.

The rotor flux magnitude and angle position are

$$|\hat{\psi}_r| = \sqrt{\hat{\psi}_{r\alpha}^2 + \hat{\psi}_{r\beta}^2} \quad (9.105)$$

$$\hat{\rho}_{\psi r} = \arctan \frac{\hat{\psi}_{r\beta}}{\hat{\psi}_{r\alpha}} \quad (9.106)$$

The estimated current  $\hat{\mathbf{i}}_s$ , appearing in equation (9.103), is

$$\hat{\mathbf{i}}_s = \frac{\hat{\psi}_s - k_r \hat{\psi}_r}{\sigma L_s} \quad (9.107)$$

The rotor flux pulsation is

$$\hat{\omega}_{\psi r} = \frac{d\hat{\rho}_{\psi r}}{d\tau} \quad (9.108)$$

The rotor slip is obtained from

$$\hat{\omega}_2 = \frac{\hat{\psi}_{r\alpha} \hat{i}_{s\beta} - \hat{\psi}_{r\beta} \hat{i}_{s\alpha}}{|\hat{\psi}_r|^2} \quad (9.109)$$

The rotor mechanical speed is the difference between the rotor flux pulsation and slip frequencies:

$$\hat{\omega}_r = \hat{\omega}_{\psi r} - \hat{\omega}_2 \quad (9.110)$$

The observer structure is presented in Figure 9.53.

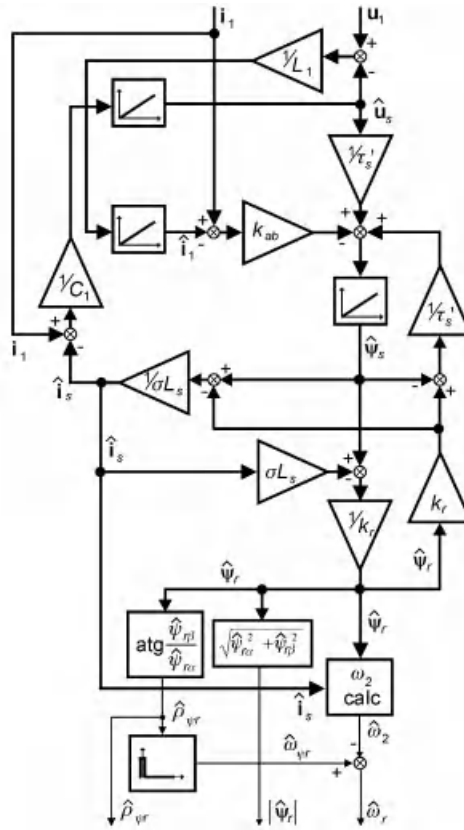


Figure 9.53 Close-loop observer structure

The presented closed-loop flux observer has high robustness of the ASD, with the observer based on the stator model, and the results can be found in [30]. The observer is not affected by stator resistance and other motor parameters mismatch. This significantly extends the stable operating region, even without precise parameter tuning.

## 9.8 Motor Control Problems in the Drive with Filters

### 9.8.1 Introduction

The differential mode motor filter has considerable influence on the control process. This is because each filter adds a voltage drop and a phase shift between the current and voltages on the filter input and output. For example, a typical LC filter for a 5.5 KW motor, under nominal load and frequency, gives ca. 5% and 5 degrees of voltage drop and phase shift, respectively. An example of real voltages on the filter input and output are presented in Figure 9.54.

As a result, most of the sophisticated sensorless drives cannot work properly when the filter is installed. It is also necessary to take into account the filter's components in the control process.

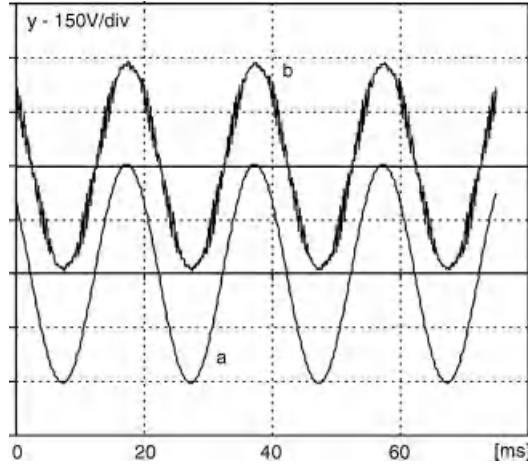


**Figure 9.54** Drive with LC filter – waveforms of: (a) commanded inverter output voltage; and (b) real motor supply voltage

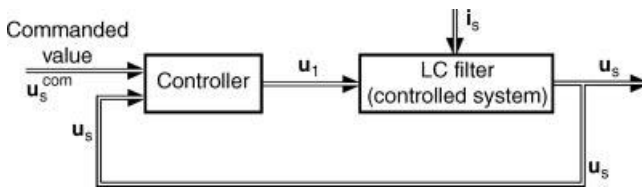


**Figure 9.55** Structure of the LC filter control system

The general concept is to extend the corresponding steering algorithm with its subordinated control system for some of the filter state variable controls.

A differential mode LC filter is a two-dimensional linear stationary controlled system. The controlled state variables are motor supply voltage  $u_s$  and inverter output current  $i_1$ , whereas the control quantity is an inverter output voltage  $u_1$ . Current  $i_1$  represents the filter’s internal variables.

The basic structure of the LC filter control system is presented in Figure 9.55.

In the control structure shown in Figure 9.55, the commanded signal is a motor supply voltage  $u_s^{com}$ . The commanded signal is compared with a real motor supply voltage  $u_s$  and the proper controller evaluates the desired inverter output voltage  $u_1$ , which should be directly set to the controlled system, LC filter. For the control process, the motor current  $i_s$  is a disturbance. The disturbance influence on the control process is possible, if it takes into account the control algorithm. The disturbance has to be compensated for, as presented in Figure 9.56.

In the control systems presented in Figures 9.55 and 9.56, the inverter output current  $i_1$  is not controlled, which is unadvisable because of the lack of inverter current protection. To control the inverter current and motor voltage, the multi-loop control system proposed in [22] can be used (Figure 9.57).

The control system presented in Figure 9.57 requires information on the actual  $i_1$  and  $u_s$  signals. Current  $i_1$  is easily measured, but  $u_s$  requires sensors outside the inverter, which is not

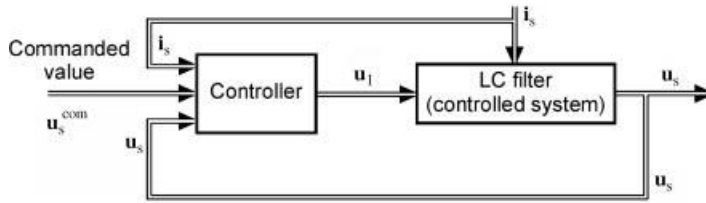


Figure 9.56 Structure of the LC filter control system

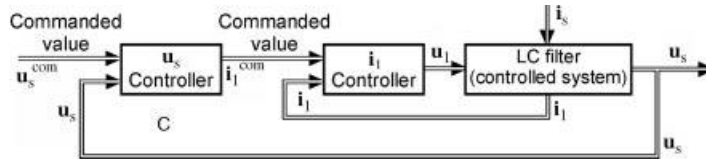


Figure 9.57 Structure of the multi-loop LC filter control system

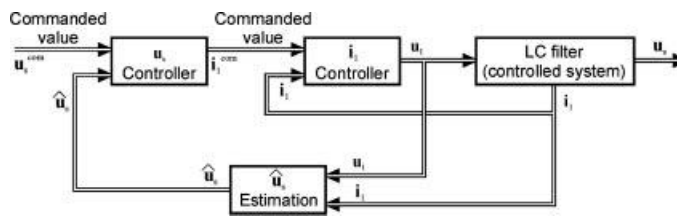


Figure 9.58 Structure of the multi-loop LC filter control system with motor voltage estimation

recommended. So instead of the  $u_s$  measurement, the estimation process for  $\hat{u}_s$  can be used. The corresponding system structure is presented in Figure 9.58.

The multi-loop control structure of the LC filter can be applied in numerous motor regulation algorithms. Some of them are presented in the following sections.

### 9.8.2 Field Oriented Control

Among the induction motor closed loop drives, the most popular is the field oriented control (FOC) system. The control principle is widely presented in the literature [31], as well as in previous chapters of this book. Here the FOC is used in the drive with an LC filter and only the necessary information is given.

The base FOC structure is presented in Figure 9.59 and the vectors relations in Figure 9.60.

In Figure 9.61, the operation of the classical FOC system for the driver without an LC filter is presented. The same operations are presented in Figure 9.62, but with the LC filter installed.

In both cases, the controller setting and control structure are kept the same. The influence of the observer is eliminated, because all control variables are assumed as measured on-line. When Figures 9.61 and 9.62 are compared, they shows that when an LC filter is installed, the

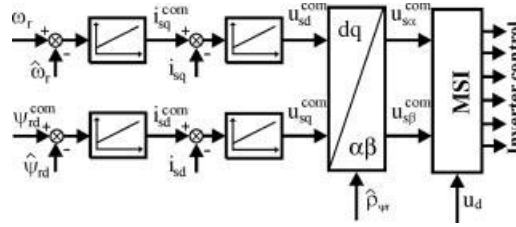


Figure 9.59 Classical field oriented control structure

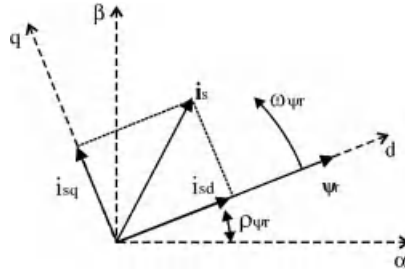


Figure 9.60 Relations between vectors in FOC system

system’s performance degenerates. It is especially visible in the motor torque waveforms, where high frequency oscillations appear as a result of the controlled object structure change.

This disadvantage can be compensated for if the FOC structure is modified with respect to the multi-loop filter control conception. The additional control variables of capacitor voltages  $u_{c\alpha}$ ,  $u_{c\beta}$  and inverter currents  $i_{1\alpha}$ ,  $i_{1\beta}$  are controlled by additional blocks.

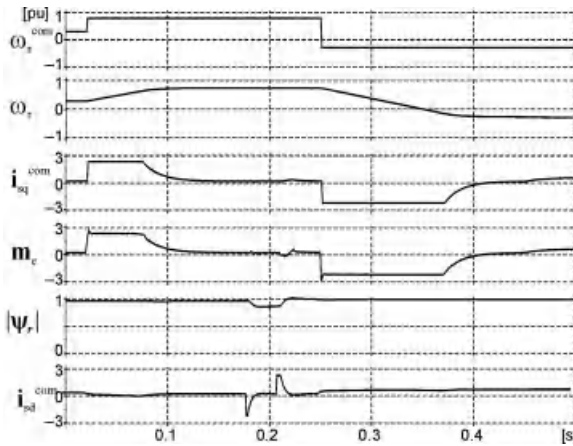
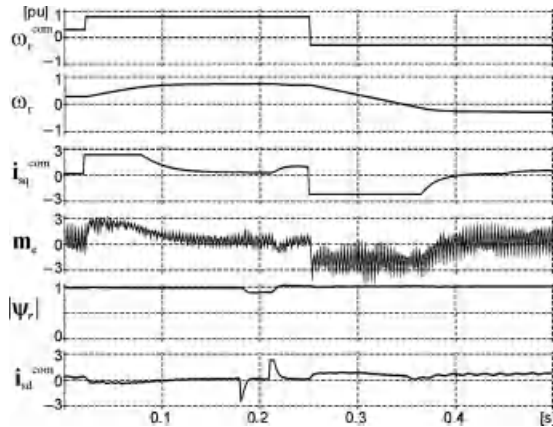


Figure 9.61 Operation of the classical FOC system in driver without LC filter – system without observers



**Figure 9.62** Operation of the classical FOC system in driver **with** LC filter – system without observers

Assuming that  $u_{s\alpha} \approx u_{c\alpha}$  and  $u_{s\beta} \approx u_{c\beta}$ , the LC filter model is described in the dq frame of references:

$$\frac{du_{sd}}{d\tau} = \frac{i_{cd}}{C_1} \quad (9.111)$$

$$\frac{di_{1d}}{d\tau} = \frac{u_{1d} - u_{sd}}{L_1} \quad (9.112)$$

$$\frac{du_{sq}}{d\tau} = \frac{i_{cq}}{C_1} \quad (9.113)$$

$$\frac{di_{1q}}{d\tau} = \frac{u_{1q} - u_{sq}}{L_1} \quad (9.114)$$

$$i_{cd} = i_{1d} - i_{sd} \quad (9.115)$$

$$i_{cq} = i_{1q} - i_{sq} \quad (9.116)$$

In the multi-loop, structured  $u_{sd}$ ,  $u_{sq}$ , and  $i_{1d}$ ,  $i_{1q}$  are controlled by correct PI elements.

In Figure 9.63, the modified FOC structure is presented.

The operation of the control system, presented in Figure 9.63, is show in Figure 9.64.

The modified FOC structure properties (Figure 9.61) are similar to those in classical FOC (Figure 9.58). The only notable difference is the lower dynamics of the drive with an LC filter, which is the result of the higher stator current time constant. However, the difference is insignificant.

The examples of the modified FOC operations in the speed sensorless mode are presented in Figures 9.65 to 9.67.

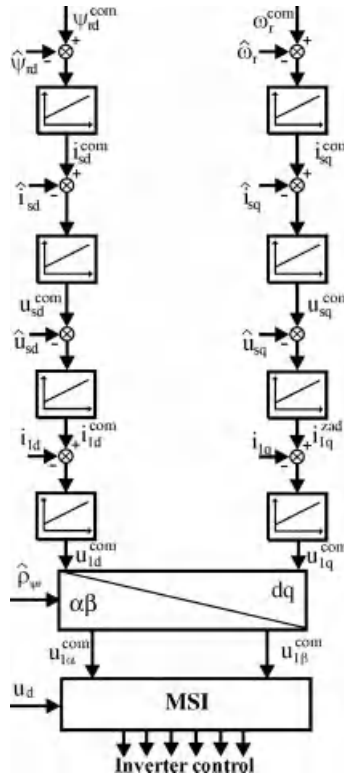


Figure 9.63 Field oriented control structure modified due to LC filter use

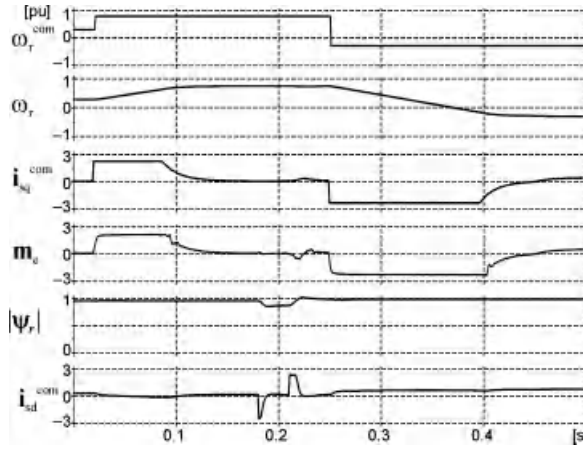
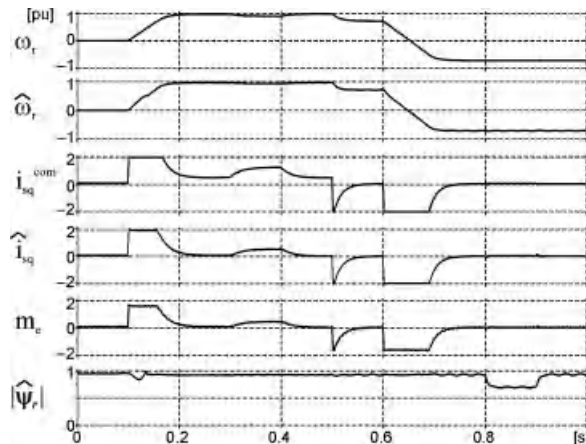


Figure 9.64 Operation of the modified FOC system for driver with LC filter – system without observers



**Figure 9.65** Operation of the modified FOC system for a drive with LC filter in sensorless mode – system with variables estimation

### 9.8.3 Non-Linear Field Oriented Control

The most popular industrial induction motor (IM) control is rotor field oriented control (RFOC) [31]. In classical RFOC, the coupling between flux and torque exists. Therefore, to improve the RFOC properties, a decoupling control is often used. The most popular decoupling system relies on adding electromotive rotation compensation components appearing in motor model equations (9.1) and (9.2):  $a_3\omega_r\psi_{ry}$  and  $-a_3\omega_r\psi_{rx}$  to the motor commanded voltages  $u_{sx}^{com}$ ,  $u_{sy}^{com}$ . Other solutions for decoupling of the motor also exist. One such method is proposed in [32], in order to control a motor electromagnetic torque  $t_e$  instead of the  $q$  current component (in [32] the controlled  $t_e$  variable is noted as  $x$ ):

$$t_e = i_{sq}\psi_{rd} \tag{9.117}$$

The motor torque  $t_e$  is accepted as an additional state variable. With such an assumption, the motor model equations (9.1) to (9.5) can be rewritten, using the rotating  $dq$  co-ordinates, as

$$\frac{di_{sd}}{d\tau} = a_1 i_{sd} + a_2 \psi_{rd} + t_e \frac{\omega_{\psi r}}{\psi_{rd}} + a_4 u_{sd} \tag{9.118}$$

$$\frac{dt_e}{d\tau} = \left( a_5 - \frac{R_s L_r}{w_\sigma} \right) t_e + a_6 t_e \frac{i_{sd}}{\psi_{rd}} - \omega_{\psi r} \psi_{rd} (i_{sd} + a_3 \psi_{rd}) + a_4 \psi_{rd} u_{sq} \tag{9.119}$$

$$\frac{d\psi_{rd}}{d\tau} = a_5 \psi_{rd} + a_6 i_{sd} \tag{9.120}$$

$$\frac{d\omega_r}{d\tau} = \frac{1}{J} \left( \frac{L_m}{L_r} t_e - t_L \right) \tag{9.121}$$





**Figure 9.66** Operation of the modified FOC system for a drive with LC filter in sensorless mode – system with variables estimation – experiment (C1 –  $\omega_r$ , C2 –  $\hat{\omega}_r$ , C3 –  $\hat{i}_{sq}^{com}$ , C4 –  $\hat{i}_{sq}$ , C5 –  $|\hat{\psi}_r|$ , C6 –  $|\hat{i}_s|$ )

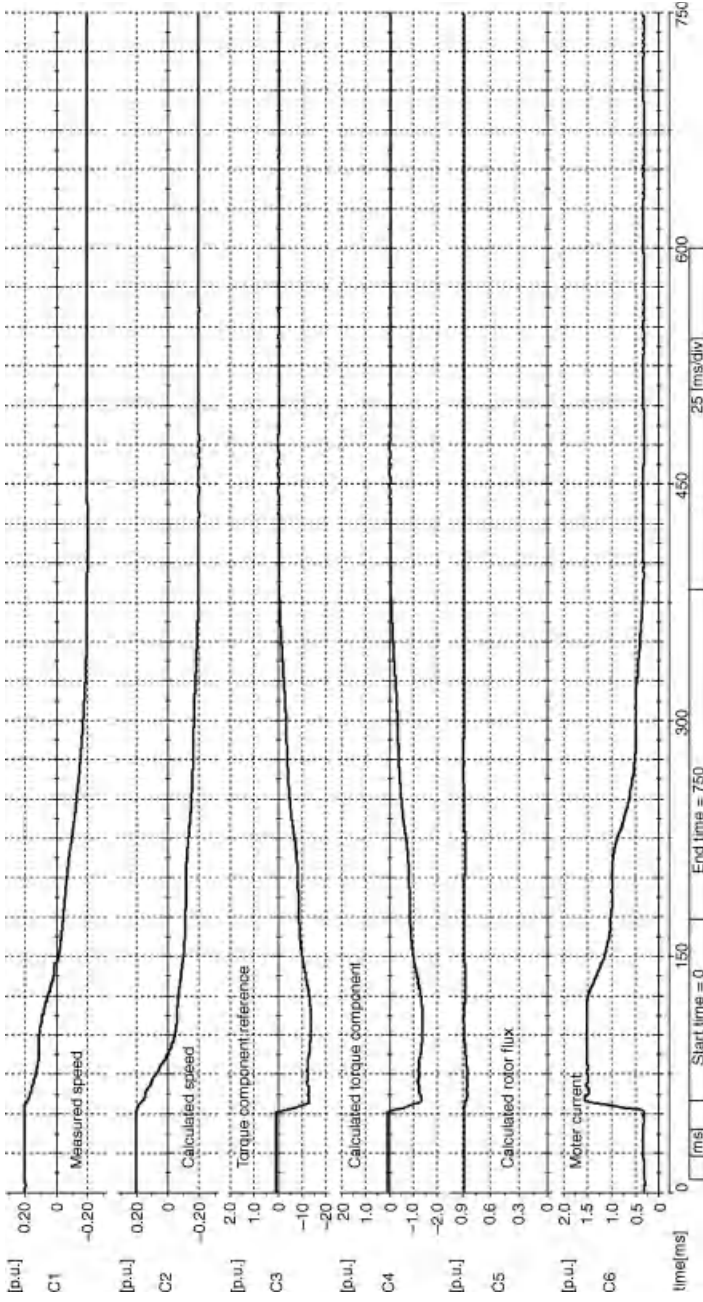


**Figure 9.67** Operation of the modified FOC system for a drive with LC filter in sensorless mode – system with variables estimation – experiment (C1 –  $\omega_r$ , C2 –  $\hat{\omega}_r$ , C3 –  $i_{sq}^{com}$ , C4 –  $\hat{i}_{sq}$ , C5 –  $|\hat{\psi}_r|$ , C6 –  $|\hat{i}_s|$ )

where  $\omega_{\psi r} = a_6 i_{sq} / \psi_{rd} + \omega_r$  and  $i_{sd}$ ,  $i_{sq}$ ,  $u_{sd}$ ,  $u_{sq}$ ,  $\psi_{rd}$  are motor stator current, voltages, and rotor flux in  $dq$  co-ordinates.

Equations (9.118) to (9.121) describe the model of the induction motor in  $dq$  co-ordinates, which is a non-linear and coupled system. If the following, control variables  $v_1$  and  $v_2$  are

$$v_1 = a_6 t_e \frac{i_{sd}}{\psi_{rd}} - \omega_{\psi r} \psi_{rd} (i_{sd} + a_3 \psi_{rd}) + a_4 \psi_{rd} u_{sq} \quad (9.122)$$

$$v_2 = \omega_{\psi r} \frac{t_e}{\psi_{rd}} + a_2 \psi_{rd} + a_4 u_{sd} \quad (9.123)$$

the motor model  $dq$  equations (9.7) to (9.10) are converted into two linear decoupled sub-systems:

$$\frac{di_{sd}}{d\tau} = a_1 i_{sd} + v_2 \quad (9.124)$$

$$\frac{d\psi_{rd}}{d\tau} = a_5 \psi_{rd} + a_6 i_{sd} \quad (9.125)$$

$$\frac{dt_e}{d\tau} = (a_5 - R_s a_4) t_e + v_1 \quad (9.126)$$

$$\frac{d\omega_r}{d\tau} = \frac{1}{J} \left( \frac{L_m}{L_r} t_e - t_L \right) \quad (9.127)$$

The base structure of the non-linear field oriented control method is presented in Figure 9.68.

In Figure 9.68, the angle  $\rho_{\psi r}$  represents the position of the rotor flux vector and  $u_d$  is the voltage in the inverter DC link. A block marked as  $dq/\alpha\beta$  represents the Park transformation from the rotating  $dq$  into the stationary  $\alpha\beta$  frame of references. The  $\alpha\beta$  co-ordinates are natural for PWM space vector algorithm.

### 9.8.3.1 Extended Control System

In order to assure control of the system with the LC filter, the motor control structure presented in previous section has been extended by using additional controllers.

The cascaded multi-loop PI controllers are used to control the motor supply voltages  $u_{sd}$ ,  $u_{sq}$  and inverter output currents  $i_{1d}$ ,  $i_{1q}$  [21,22]. In the filter control sub-system, the disturbance compensation on the stator voltage controllers is used.

In order to eliminate a phase shift in the PI units, the control of the filter state variables is done by the synchronous  $dq$  co-ordinates synchronized with the rotor flux vector – the same co-ordinates as used in the basic RFOC control system.

The disadvantage of multi-loop solutions is a necessity of the motor voltage and current knowledge. Unfortunately the real sensors are not practical in this solution, as noted in the introduction. The variables are calculated on-line in the complex observer structure.

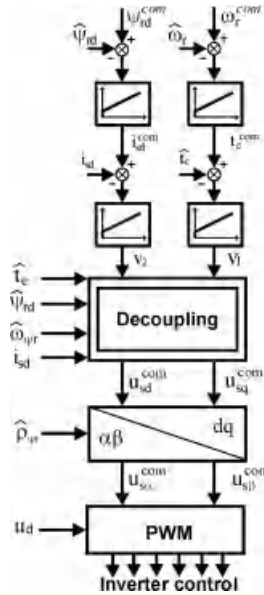


**Figure 9.68** Base control system for decoupled rotor field oriented method

In this section, instead of the full multi-loop structure, only the PI controllers for motor stator voltage are implemented. The whole structure of the extended control system of the drive with induction motor, inverter, and LC filter is presented in Figure 9.69.

In the extended control system presented in Figure 9.66, two additional PI controllers appear. The controllers directly control the motor stator voltage. The inverter output current is not controlled explicitly. This happens because the capacitor current is small, contrary to the motor current. The motor current controllers are present in the FOC structure, so that the inverter output current is controlled indirectly.

The commanded inverter voltage components,  $u_{ld}^{com}$  and  $u_{lq}^{com}$ , are transformed to the stationary  $\alpha\beta$  co-ordinates,  $u_{l\alpha}^{com}$  and  $u_{l\beta}^{com}$ , and are treated as the inputs of the PWM module.

### 9.8.4 Non-Linear Multiscalar Control

In this section, the non-linear multiscalar control system, designed to be operated with the LC filter, is presented. For the control, only one sensor is used to measure the inverter DC supply voltage and two sensors are used to measure the two inverter output currents. The control system is divided into two sub-systems, the superior motor control and the subordinate LC filter control. The control structure is part of the motor speed sensorless system presented in Figure 9.70.

#### 9.8.4.1 Motor Control Sub-system

In the motor control sub-system, the non-linear control using non-linear feedback is used. That control is based on the methods of the differential geometry and was first adapted to the electric

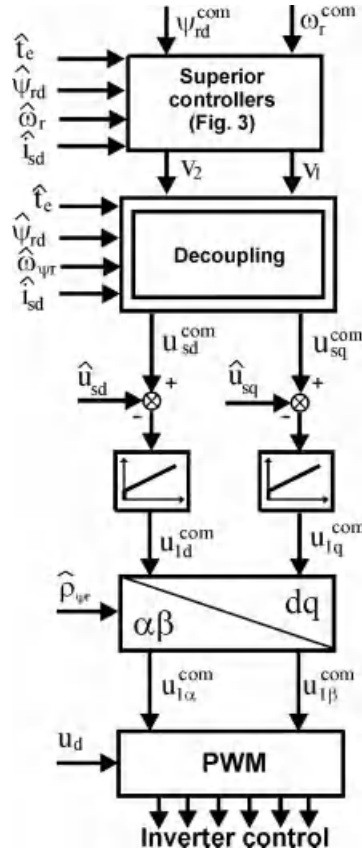


**Figure 9.69** Induction motor and LC filter non-linear field oriented control system structure

drive in [32] (MMB) and presented in other papers later, but only for the drive without LC filter. In MMB, the non-linear and decoupled object is converted into a linear one with use of the new state variables and the non-linear feedbacks. The four MMB state variables are

$$x_{11} = \omega_r \tag{9.128}$$

$$x_{12} = \psi_{r\alpha} i_{s\beta} - \psi_{r\beta} i_{s\alpha} \tag{9.129}$$

$$x_{21} = \psi_{r\alpha}^2 + \psi_{r\beta}^2 \tag{9.130}$$

$$x_{12} = \psi_{r\alpha} i_{s\alpha} + \psi_{r\beta} i_{s\beta} \tag{9.131}$$

where  $x_{11}$  is rotor angular speed;  $x_{12}$  is proportional to the motor torque;  $x_{21}$  is square of rotor flux;  $x_{22}$  is scalar product of the stator current and rotor flux vectors; and  $i_s$  and  $\psi_r$  are the magnitudes of the stator current and rotor flux, respectively.



With the multiscalar variables  $x_{12}x_{12}x_{12}x_{12}$  equations (9.128) to (9.131), the next model of the motor is

$$\frac{dx_{11}}{d\tau} = x_{12} \frac{L_m}{JL_r} - \frac{T_L}{J} \quad (9.132)$$

$$\frac{dx_{12}}{d\tau} = -\frac{1}{T_v} x_{12} - x_{11} \left( x_{22} + x_{21} \frac{L_m}{w_\sigma} \right) + u_1 \frac{L_r}{w_\sigma} \quad (9.133)$$

$$\frac{dx_{21}}{d\tau} = 2R_r \left( -\frac{1}{x_{21}} + x_{22} \frac{L_m}{L_r} \right) \quad (9.134)$$

$$\frac{dx_{22}}{d\tau} = -\frac{1}{T_v} x_{22} + x_{11} x_{12} + x_{21} R_r \frac{L_m}{L_r w_\sigma} + \frac{R_r L_m (x_{12}^2 + x_{22}^2)}{L_r x_{21}} + u_2 \frac{L_r}{w_\sigma} \quad (9.135)$$

where  $T_v = w_\sigma L_r / (R_r w_\sigma + R_s L_r^2 + R_r L_m^2)$ .

The compensation of non-linearities in equations (9.12) to (9.15) leads to the new driving functions  $m_1$  and  $m_2$ :

$$u_1 = \frac{w_\sigma}{L_r} \left[ x_{11} \left( x_{22} + x_{21} \frac{L_m}{w_\sigma} \right) + m_1 \right] \quad (9.136)$$

$$u_2 = \frac{w_\sigma}{L_r} \left( -x_{11} x_{12} - x_{21} \frac{R_r L_m}{L_r w_\sigma} - \frac{R_r L_m (x_{12}^2 + x_{22}^2)}{L_r x_{21}} + m_2 \right) \quad (9.137)$$

The components of the commanded motor stator voltage vector in the stationary frame are

$$u_{s\alpha}^{com} = \frac{\psi_{r\alpha} u_2 - \psi_{r\beta} u_1}{x_{21}} \quad (9.138)$$

$$u_{s\beta}^{com} = \frac{\psi_{r\beta} u_2 - \psi_{r\alpha} u_1}{x_{21}} \quad (9.139)$$

With equations (9.8) to (9.11) and (9.16) to (9.19), the asynchronous motor model is decoupled and converted into two separate linear sub-systems, mechanical equations (9.20) and (9.21), and electromagnetic equations (9.22) and (9.23):

$$\frac{dx_{11}}{d\tau} = x_{12} \frac{L_m}{JL_r} - \frac{T_L}{J} \quad (9.140)$$

$$\frac{dx_{12}}{d\tau} = -\frac{1}{T_v} x_{12} - m_1 \quad (9.141)$$

$$\frac{dx_{21}}{d\tau} = 2R_r \left( -\frac{1}{x_{21}} + x_{22} \frac{L_m}{L_r} \right) \quad (9.142)$$

$$\frac{dx_{22}}{d\tau} = -\frac{1}{T_v} x_{22} + m_2 \quad (9.143)$$

The fully decoupled sub-systems make it possible to use this method in the case of a changing flux vector and to obtain simple system structure, which is not easily achieved in the case of vector control methods. It is possible to use cascade structure of simple proportional-integral PI controllers in the decoupled, linear control sub-systems.

The motor stator current does not exist in the control system distinctly. So to limit the motor current to the maximum allowed  $I_{s \max}$ , the output of the  $x_{11}$  controller is variably limited according to the relation:

$$x_{12}^{\text{limit}} = \sqrt{I_{s \max}^2 x_{21} - x_{22}^2} \quad (9.144)$$

#### 9.8.4.2 LC Filter Control Sub-system

In the case of a drive without the LC filter, the MMB output variables  $u_{s\alpha}^{\text{com}}$  and  $u_{s\beta}^{\text{com}}$  are commanded for the PWM block. The PWM controls the inverter transistors to obtain the commanded voltage on the inverter output.

When the LC filter is used, the inverter output voltage changes the form of the motor supply voltage. So the error in the MMB control loop will appear. To solve this problem, the multi-loop controller loops, presented in previous section, is used.

The filter output sensors are not used because of the proper observer use. To omit the phase shift of PI controllers, the filter variables are operated in the rotating frame of references. The frame of reference is noted as the  $dq$  system, where the position of the  $d$ -axis is connected with the commanded inverter output vector  $\mathbf{u}_s$ .

## 9.9 Predictive Current Control in the Drive System with Output Filter

In this section, the predictive current controller (PCC) is presented in the IM speed sensorless system with a FOC method and load angle regulation, to show how the system is modified due to motor choke installation.

### 9.9.1 Control System

Among different control algorithms, the control of the load angle FOC exists [33]. The structure of the load angle control seems simpler than the FOC, because they do not need Park transformations. The load angle  $\delta$  is noted as the angle between the  $\psi_r$  and  $\mathbf{i}_s$  vectors. The



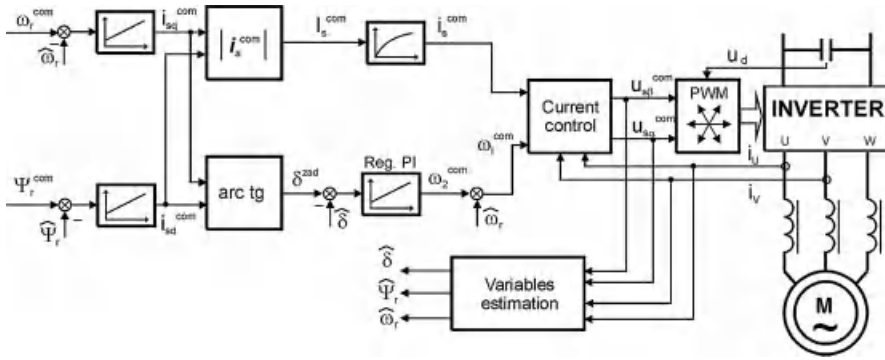


**Figure 9.71** Base structure of the FOC algorithm with load angle control ( $\hat{\cdot}$  denotes variables evaluated in estimation block)

control of the vector amplitudes and mutual position makes it possible to control the motor electromagnetic torque  $T_e$ :

$$T_e = k \cdot \text{Im}(\Psi_r^* \mathbf{i}_s) = k |\Psi_r| |\mathbf{i}_s| \sin \delta \tag{9.145}$$

where  $k$  is the constant of proportionality.

The FOC load angle control system base structure, based on equation (9.145), is presented in Figure 9.71.

In the control system shown in Figure 9.71, the measured variables are the inverter output currents and inverter DC link voltage. The motor currents and motor voltages are not measured. The load angle is controlled by commanding the motor slip frequency  $\omega_2$ . The sum of  $\omega_2$  and the motor speed  $\omega_r$  is noted as current commanded angular frequency  $\omega_i^{\text{com}}$ . The signal  $\omega_i^{\text{com}}$ , along with the commanded stator current magnitude  $i_s^{\text{com}}$ , are simultaneously controlled by the current controller algorithm. The current controller co-operates with the PWM procedure. The commanded values of  $I_s$  and  $\omega_i$  are set by speed and flux module controllers, with the output signals  $I_s^{\text{com}}$  and  $\delta^{\text{com}}$ :

$$I_s^{\text{com}} = \sqrt{(i_{sd}^{\text{com}})^2 + (i_{sq}^{\text{com}})^2} \tag{9.146}$$

$$\delta^{\text{com}} = \text{arc tg} \left( \frac{i_{sq}^{\text{com}}}{i_{sd}^{\text{com}}} \right) \tag{9.147}$$

The amplitudes of the  $\Psi_r$  and  $\mathbf{i}_s$  vectors are kept constant, while the motor torque is controlled by changing the angle  $\delta$ . Unfortunately, in transients, some coupling and interactions appear between the controlled variables, due to inherent non-linearities and couplings in the induction motor.

To prevent these negative features from appearing in the drive, the non-linear control principles [34] are implemented [32].

The non-linear control principle is implemented for the FOC system presented in Figure 9.71. The linearization and decoupling of the Figure 9.71 structure is based on the equations of the current controlled induction motor model described by the next dependencies:

$$\frac{di_s}{d\tau} = \frac{1}{T_i} (i_s - I_s^{\text{com}}) \quad (9.148)$$

$$\frac{d\delta}{d\tau} = -\frac{R_r L_m}{L_r} \frac{i_s}{\psi_r} + \omega_i - \omega_r \quad (9.149)$$

$$\frac{d\psi_r}{d\tau} = -\frac{R_r}{L_r} \psi_r + \frac{R_r L_m}{L_r} i_s \cos \delta \quad (9.150)$$

$$\frac{d\omega_r}{d\tau} = -\frac{1}{J_M} \left( \frac{L_m}{L_r} \psi_r i_s - t_L \right) \quad (9.151)$$

where  $i_s$  and  $u_s$  are stator current and voltage modules, respectively;  $\psi_r$  is rotor flux module;  $I_s^{\text{com}}$  is commanded stator current; and  $T_i$  is the time constant of the LPF related to the inertia of elements appearing in the current control loop.

Equation (9.148) exists only in the control system and is added to model the physical limitations of the stator current pulsation changes.

Based on the analysis of equations (9.149) and (9.150), the linearization and decoupling of the system are performed. To assure system stability, the relationship of  $\cos \delta$  in equation (9.150) should be positive, otherwise positive feedback can appear in the control loop. To insure  $\cos \delta > 0$ , the angle  $\delta$  is limited to the  $(-\pi/2 \dots \pi/2)$  range and then a new control variable  $\psi_r^*$  is introduced:

$$\psi_r^* = L_m i_s \cos \delta \quad (9.152)$$

From equation (9.152), the commanded stator current module is

$$i_s^{\text{com}} = \frac{\psi_r^*}{L_m \cos \delta} \quad (9.153)$$

The LPF equation (9.148) is replaced by the LPF dependency for the rotor flux magnitude:

$$\frac{d\psi_{ri}^*}{dt} = \frac{1}{T_\psi} (\psi_{ri}^* - \psi_r^*) \quad (9.154)$$

where  $\psi_{ri}^*$  is an output signal of the LPF and  $T_\psi$  is LPF inertia.

According to equation (9.154), equation (9.153) has the form:

$$i_s^{\text{com}} = \frac{\psi_{ri}^*}{L_m \cos \delta} \quad (9.155)$$

If the control signal equation (9.152) is substituted into equation (9.149), then the dynamic of the load angle is transformed into the form:

$$\frac{d\delta}{d\tau} = -\frac{R_r}{L_r} \frac{\psi_{ri}^*}{\psi_r \cos \delta} + \omega_i - \omega_r \quad (9.156)$$

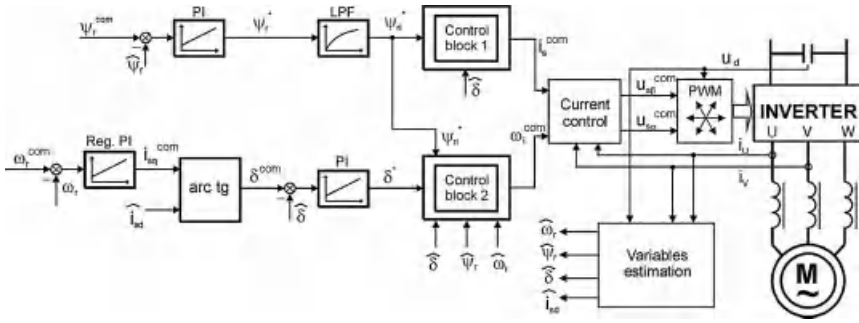


**Figure 9.72** Structure of the non-linear FOC with load angle control

which is still non-linear. To transform equation (9.156) into a linear form, the commanded motor current pulsation should be

$$\omega_i^{com} = \omega_r + \frac{R_r}{L_r} \frac{\psi_r^*}{\psi_r \cos \delta} + \frac{1}{T_\delta} (\delta^* - \delta) \tag{9.157}$$

where  $\delta^*$  and  $T_\delta$  are desired load angle and time constant of the load angle dynamic system, respectively.

Regarding equations (9.152) and (9.157), the next dynamic system for the load angle and rotor flux control is

$$\frac{d\delta}{d\tau} = \frac{1}{T_\delta} (\delta^* - \delta) \tag{9.158}$$

$$\frac{d\psi_r}{d\tau} = \frac{R_r}{L_r} (\psi_{r1}^* - \psi_r) \tag{9.159}$$

It is noted that the dynamic system equations (9.158) and (9.159) are linear and decoupled. The structure of the non-linear FOC with the load angle controller is presented in Figure 9.72.

In the system shown in Figure 9.72, the commanded value of the load angle is

$$\delta^{com} = \arctan \left( \frac{i_{sq}^{com}}{\hat{i}_{sd}} \right) \tag{9.160}$$

The commanded stator current amplitude is calculated in control block 1, based on equation (9.155), and the commanded stator current pulsation is calculated in control block 2, based on equation (9.157). Both blocks are indicated in Figure 9.72.

### 9.9.2 Predictive Current Controller

The integral part of the FOC system is the IM stator current controller. Many different methods for current control are presented in the literature. A comprehensive survey is presented in [35].

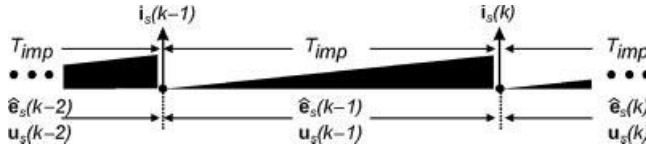


**Figure 9.73** Samples notation for switching period  $T_{imp}$

Good results of current control are reported in [36], where a variety of predictive control methods (PCM) were used.

The filters significantly affect the structure of the system, so some of the predictive controllers cannot work properly. The simplest version of the inverter output filter is a motor choke, which reduces the reflected waves in long cables connected to the motor, prevents over-voltages on motors and inverter transistors, and reduces the radio frequency interference level. However, in drives with motor chokes, the predictive controller's algorithm should also be modified.

In the control system presented in this section, the motor stator current is controlled. The controller uses actual values of the induction motor electromagnetic forces  $\mathbf{e}$  (emf) to obtain proper current regulation. Values of the emf are calculated in the observer system described in the next section.

The notation for the presented current controller is explained in Figure 9.73.

The basic assumption is that the PWM inverter is working in such a way that the inverter output voltage  $\mathbf{u}_s$  is equal to its commanded value  $\mathbf{u}_s^{\text{com}}$ :

$$\mathbf{u}_s \approx \mathbf{u}_s^{\text{com}} \quad (9.161)$$

The current controller principle is based on the dynamic equation that describes the model of the system. An equivalent model of the presented system contains three parts, inductance, resistance, and emf. Because a motor choke is installed in the ASD, it is acceptable to neglect an equivalent resistance of the load. With such an assumption, the system dynamic is

$$\frac{d\mathbf{i}_s}{d\tau} = \frac{1}{L_1 + L_\sigma} (\mathbf{u}_s^{\text{com}} - \mathbf{e}) \quad (9.162)$$

where  $\mathbf{u}_s^{\text{com}}$  is the inverter commanded voltage vector and  $T_{imp}$  is the inverter switching frequency period.

For small  $T_{imp}$ , equation (9.162) is approximated as

$$\frac{\mathbf{i}_s(k) - \mathbf{i}_s(k-1)}{T_{imp}} = \frac{1}{L_1 + L_\sigma} (\mathbf{u}_s^{\text{com}}(k-1) - \mathbf{e}(k-1)) \quad (9.163)$$

If  $(k-1) \dots (k)$  is the time period taken into account, the variables  $\mathbf{i}_s(k)$  and  $\mathbf{e}(k-1)$  are unknown and should be predicted on the basis of previous known examples.

In the presented system, emf is calculated on-line in the estimation block:

$$\hat{\mathbf{e}} = \omega_r \hat{\boldsymbol{\Psi}}_r \quad (9.164)$$

Motor emf equation (9.74) is calculated inside an observer structure presented in section 9.9.3.

The samples of  $\hat{\mathbf{e}}(k-2)$  and  $\hat{\mathbf{e}}(k-3)$ , calculated in the observer, are memorized and used to predict the value of  $\hat{\mathbf{e}}(k-1)$ :

$$\hat{\mathbf{e}}^{\text{pred}}(k-1) = \mathbf{C}_{\text{EMF}}\hat{\mathbf{e}}(k-2) \quad (9.165)$$

where

$$\mathbf{C}_{\text{EMF}} = \begin{bmatrix} \cos(\Delta\varphi_e) & \sin(\Delta\varphi_e) \\ -\sin(\Delta\varphi_e) & \cos(\Delta\varphi_e) \end{bmatrix} \quad (9.166)$$

and  $\Delta\varphi_e$  is  $\mathbf{e}$  vector angular position change:

$$\Delta\varphi_e = \arctan \frac{\hat{e}_\alpha(k-3)\hat{e}_\beta(k-2) - \hat{e}_\alpha(k-2)\hat{e}_\beta(k-3)}{\hat{e}_\alpha(k-2)\hat{e}_\alpha(k-3) + \hat{e}_\beta(k-2)\hat{e}_\beta(k-3)} \quad (9.167)$$

For the calculated  $\hat{\mathbf{e}}^{\text{pred}}$  value, the current sample at (k) is predicted as

$$\mathbf{i}_s^{\text{pred}}(k) = \mathbf{i}_s(k-1) + \frac{T_{\text{imp}}}{L_1 + L_\sigma} (\mathbf{u}_s^{\text{com}}(k-1) - \hat{\mathbf{e}}^{\text{pred}}(k-1)) \quad (9.168)$$

The current regulation errors at the instant (k-1) and (k) are calculated as

$$\Delta\mathbf{i}_s(k-1) = \mathbf{i}_s^{\text{com}}(k-1) - \mathbf{i}_s(k-1) \quad (9.169)$$

$$\Delta\mathbf{i}_s(k) = \mathbf{i}_s^{\text{com}}(k) - \mathbf{i}_s^{\text{pred}}(k) \quad (9.170)$$

In order to minimize the stator current regulation error at the (k+1) instant, the proper voltage vector  $\mathbf{u}_s^{\text{com}}(k)$  should be applied [30]:

$$\mathbf{u}_s^{\text{com}}(k) = \frac{L_1 + L_\sigma}{T_{\text{imp}}} (\mathbf{i}_s^{\text{com}}(k+1) - \mathbf{i}_s^{\text{pred}}(k) + \mathbf{D}_{\text{Is}}) + \hat{\mathbf{e}}^{\text{pred}}(k) \quad (9.171)$$

where  $\mathbf{D}_{\text{Is}}$  is the current controller correction feedback:

$$\mathbf{D}_{\text{Is}} = W_1\mathbf{C}_{\text{EMF}}\Delta\mathbf{i}_s(k) + W_2\mathbf{C}_{2\text{EMF}}\Delta\mathbf{i}_s(k-1) \quad (9.172)$$

and

$$\hat{\mathbf{e}}^{\text{pred}}(k) = \mathbf{C}_{2\text{EMF}}\hat{\mathbf{e}}(k-2) \quad (9.173)$$

$$\mathbf{C}_{2\text{EMF}} = \begin{bmatrix} \cos(2\Delta\varphi_e) & \sin(2\Delta\varphi_e) \\ -\sin(2\Delta\varphi_e) & \cos(2\Delta\varphi_e) \end{bmatrix} \quad (9.174)$$

and  $W_1$  and  $W_2$  are tuned parameters.

The PCC structure is presented in Figure 9.74.

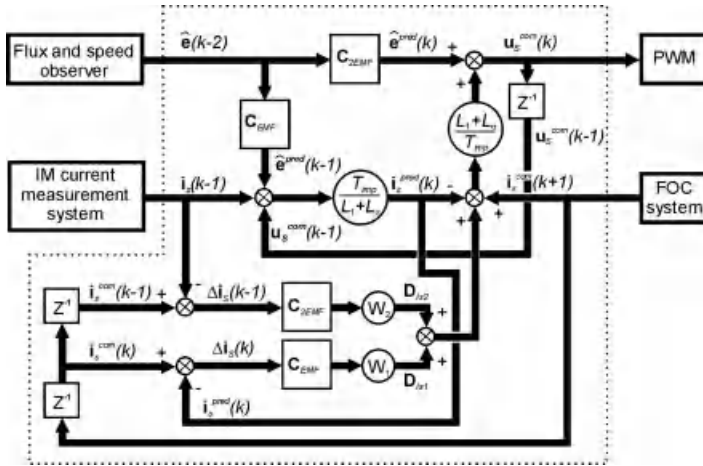


Figure 9.74 Predictive current controller structure for ASD with motor choke

An important parameter of the system is the inductance that appears in current controller relationships. Therefore, it is important to add the motor choke inductance  $L_1$  to the current controller equations.

### 9.9.3 EMF Estimation Technique

In the case of the ASD with motor choke, the disturbance observer is modified in a similar way to the solution presented in [37].

In this section, the disturbance observer [26] is presented, taking into account the presence of the motor choke. In the observer, the motor emf is treated as a disturbance with components in the  $\alpha\beta$  co-ordinates calculated using the exact disturbance model [38]:

$$\frac{d\xi}{dt} = \frac{R_r}{L_r} \xi + R_r \frac{L_m}{L_r} \omega_r i_s + j\omega_r \xi \tag{9.175}$$

where

$$\xi_\alpha = \psi_{r\alpha} \omega_r \tag{9.176}$$

$$\xi_\beta = \psi_{r\beta} \omega_r \tag{9.177}$$

$$\xi = [\xi_\alpha \quad \xi_\beta]^T \tag{9.178}$$

In the case of the ASD with motor choke, the disturbance observer is modified in a similar way to the solution presented in [37]. In the case of the ASD with motor choke, the  $L_1$  inductance is added to the motor model (Figure 9.75).

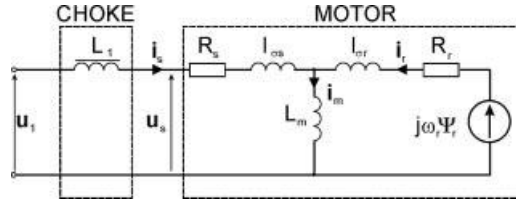


Figure 9.75 Induction motor drive with voltage inverter and motor choke

The equations of the observer for the ASD with motor choke are

$$\frac{d\hat{\mathbf{i}}_s}{d\tau} = -\frac{R_s L_r^2 + R_r L_m^2}{L_r w_{\sigma 1}} \hat{\mathbf{i}}_s + \frac{R_r L_m}{L_r w_{\sigma 1}} \hat{\boldsymbol{\psi}}_r - j \frac{L_m}{w_{\sigma 1}} \hat{\boldsymbol{\xi}} + \frac{L_r}{w_{\sigma 1}} \mathbf{u}_1^{com} + k_1 (\mathbf{i}_s - \hat{\mathbf{i}}_s) \tag{9.179}$$

$$\frac{d\hat{\boldsymbol{\psi}}_r}{d\tau} = \frac{R_r}{L_r} \hat{\boldsymbol{\psi}}_r + R_r \frac{L_m}{L_r} \hat{\mathbf{i}}_s + j \hat{\boldsymbol{\xi}} + \mathbf{e}_{\psi} \tag{9.180}$$

$$\frac{d\hat{\boldsymbol{\xi}}}{d\tau} = \frac{R_r}{L_r} \hat{\boldsymbol{\xi}} + R_r \frac{L_m}{L_r} \omega_r \hat{\mathbf{i}}_s + j \omega_r \hat{\boldsymbol{\xi}} + j k_4 (\mathbf{i}_s - \hat{\mathbf{i}}_s) \tag{9.181}$$

$$\frac{dS_{bF}}{d\tau} = k_{fo} (S_b - S_{bF}) \tag{9.182}$$

where  $\mathbf{e}_{\psi} = \left[ -k_2 S_b \hat{\psi}_{r\alpha} + k_3 \hat{\psi}_{r\beta} (S_b - S_{bF}) \quad -k_2 S_b \hat{\psi}_{r\beta} - k_3 \hat{\psi}_{r\alpha} (S_b - S_{bF}) \right]^T$ ;  $k_1$ ,  $k_2$ , and  $k_4$  are observer gains;  $S_b$  is the observer stabilizing component;  $S_{bF}$  is the  $S_b$  filtered value; and

$$w_{\sigma 1} = L_r (L_s + L_l) - L_m^2 \tag{9.183}$$

The rotor mechanical speed is estimated as

$$\hat{\omega}_r = \frac{\hat{\xi}_{\alpha} \hat{\psi}_{r\alpha} + \hat{\xi}_{\beta} \hat{\psi}_{r\beta}}{\Psi_r^2} \tag{9.184}$$

In equations (9.179) to (9.182), due to the assumption of the small step of the observer calculation, the derivative of estimated speed is neglected. For the PCC, the value of the motor emf  $\mathbf{e}$  is equal to  $\boldsymbol{\xi}$ , calculated in equation (9.181).

Figure 9.76 presents the operation of the drive only with PCC, without the FOC loop. The controller operates correctly with a current regulation error of less than 5%. At the 100 ms instant, the inductance of the motor choke  $L_1$  is set to zero. It is noticeable that if the choke parameters are not taken into account, the drive is not operating correctly.

Figure 9.77 presents the operation of the full control system without non-linear feedback. The structure of the system is based on the scheme presented in Figure 9.71. In steady state, the system correctly controls the commanded speed and flux, but in transients, the interaction

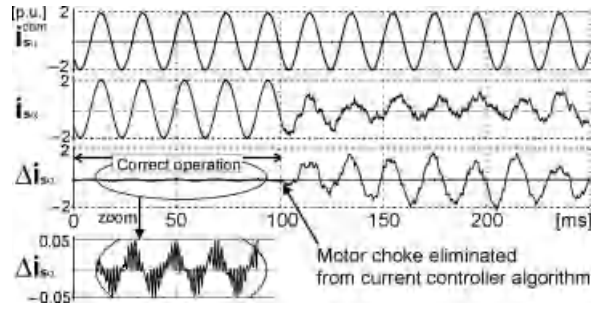


**Figure 9.76** Current controller operation – at instant 100 ms the motor choke  $L_1$  is eliminated from current controller equations

between both the regulation systems appears. In the case of the speed reverse, a huge flux error appears. In the real system, the drive operating without the decoupled control will not work in a stable manner. The stable work of this system is possible only when the dynamics of the system are limited. In the real system, the flux will be limited due to magnetic circuit saturation. This is not observed in the simulation, because a linear model of the motor is assumed.

In Figures 9.78–9.81, the operation in the speed sensorless non-linear FOC system with load angle controller is presented.

In Figure 9.78, the speed changes are commanded. In comparison with Figure 9.77, better properties are observed. The decrease of the motor speed at 0.1 s has no influence on the motor flux. The estimated load angle is the same as the commanded value. Only for speed reverse is the calculated flux decreased, whereas the real flux is kept constant. It is the result of passing the observer through an unstable point that typically appears in the low-speed regenerative mode. Such a phenomenon is typical for induction motor observers and is reported in [39]. Fortunately, the phenomenon has negligible influence on how the system works.

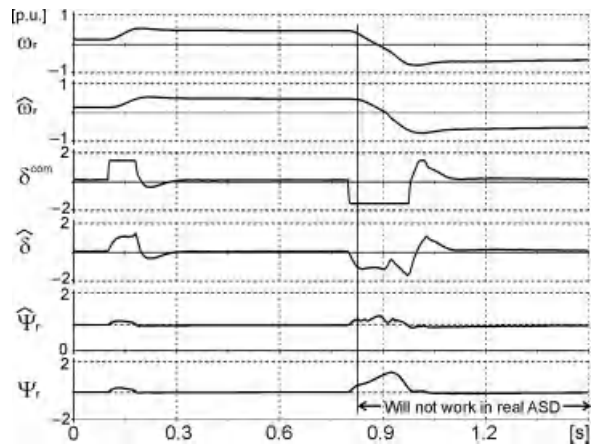


**Figure 9.77** The speed sensorless adjustable speed drive (ASD) in case of the speed variation in the control system without linearization feedback – the control structure is as presented in Figure 9.71



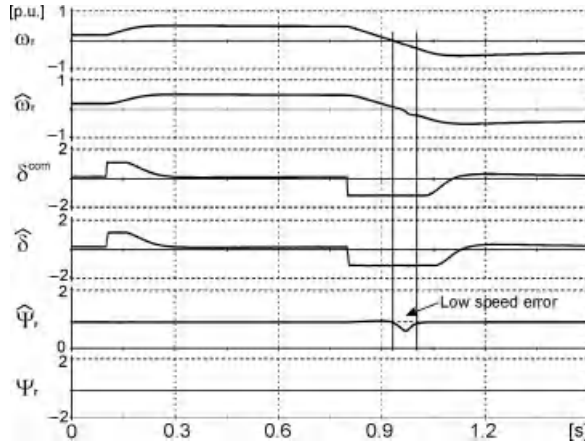


**Figure 9.78** The speed sensorless induction motor control in case of the speed variation in the control system **with linearization feedback** for speed variations – the control structure is as presented in Figure 9.72

In Figure 9.79, the operation of the ASD under flux and load torque variations is presented. The flux variations have no influence on the speed control loop, except at the moments where controller saturation occurs. Under the step change of the load torque at 1 s instant, a small speed drop appears until it is compensated for by the speed controller at 1.3 s instant.

In Figure 9.80, the ASD operation under speed variations, including low speed ranges, is presented. The system correctly keeps the commanded speed and flux. Interactions between torque and flux regulations result from the controller’s saturation, when passing the regenerative mode during speed reverse.

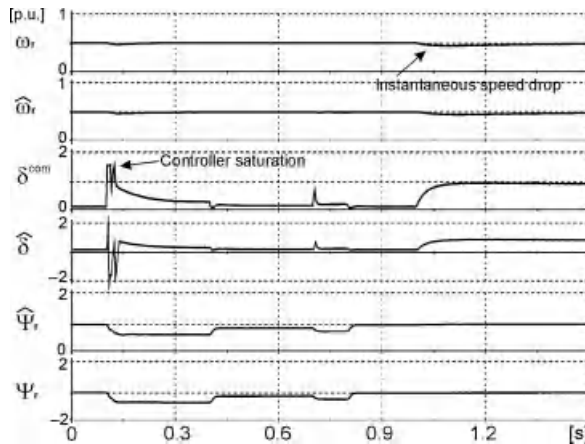


**Figure 9.79** Speed variation for the sensorless control system **with linearization feedback** with flux and load torque variations – control structure as in Figure 9.72

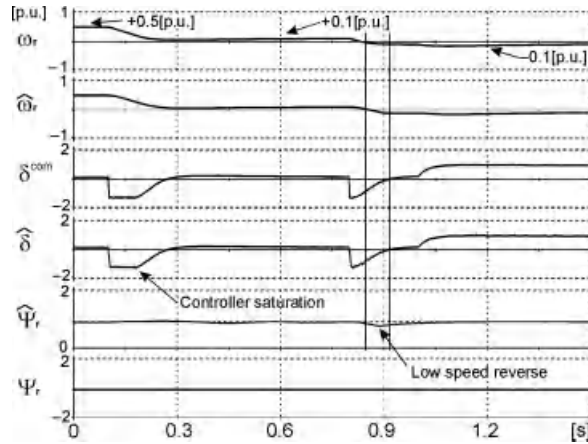


**Figure 9.80** Speed variation for the sensorless control system with linearization feedback and low speed variations – control structure from Figure 9.72

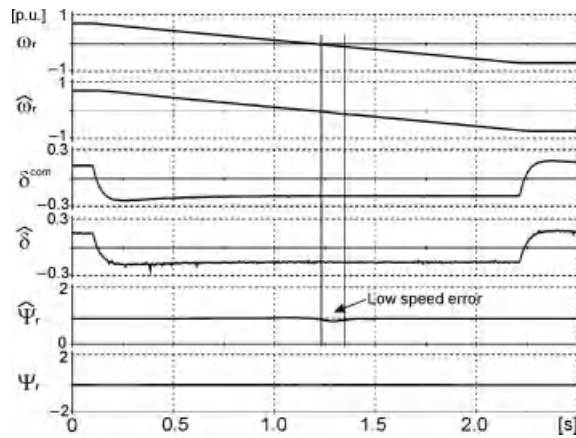


**Figure 9.81** Speed variation in the sensorless control system with linearization feedback for slow speed reverse – the control structure is presented in Figure 9.72

A slow reverse of the proposed ASD with feedback linearization is presented in Figure 9.81. In comparison with the previous fast speed reverse, the estimated flux, which appears during passing through the regenerative mode, is smaller.

### 9.10 Problems

#### Problem 9.1

Design the differential filter (normal mode filter) with L, C, and R dampings for the drive with a voltage inverter, and induction motor. The filter topology is presented in Figure 9.29. The three-phase induction motor data is  $P_n = 3 \text{ kW}$ ,  $U_n = 380 \text{ V}$  (Y connected), and  $I_n = 6.4 \text{ A}$ . The

inverter DC supply voltage is 540 V, transistor switching frequency is  $f_{\text{imp}} = 3.3 \text{ kHz}$ , and inverter output maximal frequency is  $f_{\text{out 1h}} = 100 \text{ Hz}$ . The desired system property is switching ripple current  $\Delta I_s = 20\%$ .

**Solution:** First the inductor is selected. The motor ripple current is

$$\Delta I_s = 0.1 \cdot I_n = 0.2 \cdot 6.4 = 1.28 \text{ A} \quad (9.185)$$

The  $L_1$  inductance is

$$L_1 > 2 \frac{U_d}{\sqrt{2} \cdot 2 \cdot \pi \cdot f_{\text{imp}} \cdot 3 \cdot \Delta I_s} = 2 \frac{540}{\sqrt{2} \cdot 2 \cdot \pi \cdot 3300 \cdot 3 \cdot 1.28} = 9.5 \text{ mH} \quad (9.186)$$

The voltage drop on  $L_1$  for the motor nominal frequency  $f_n$  and nominal load is

$$\Delta U_1 = I_n 2\pi f_n L_1 = 6.4 \cdot 2\pi \cdot 50 \cdot 0.0095 = 19 \text{ V} \quad (9.187)$$

The assumed  $L_1 = 9.5 \text{ mH}$  satisfies the limiting current ripple and permitted voltage drop.

The  $L_1$  nominal current is equal to the motor nominal  $I_{L1n} = I_n = 6.4 \text{ A}$ .

Next the  $C_1$  is selected. The  $C_1$  is related to the assumed resonant frequency  $f_{\text{res}}$ . The value of the  $f_{\text{out 1h}}$  should satisfy:

$$\begin{aligned} 10 \cdot f_{\text{out 1h}} < f_{\text{res}} < \frac{1}{2} \cdot f_{\text{imp}} \\ 10 \cdot 100 < f_{\text{res}} < \frac{1}{2} \cdot 3300 \\ 1000 < f_{\text{res}} < 1650 \end{aligned} \quad (9.188)$$

so the resonant frequency is selected:

$$f_{\text{res}} = 1333 \quad (9.189)$$

hence:

$$C_1 = \frac{1}{4\pi^2 f_{\text{res}}^2 L_1} = \frac{1}{4 \cdot \pi^2 \cdot 1333^2 \cdot 0.0095} = 1.5 \mu\text{F} \quad (9.190)$$

For the capacitor, the nominal voltage should be at least as much as the inverter supply voltage:

$$C_1 > U_d = 540 \text{ V} \quad (9.191)$$

Because the  $C_1$  current consists of a high frequency ripple  $f_{\text{imp}} = 3.3 \text{ kHz}$ , the proper capacitor type should be selected.

The values of  $L_1$  and  $C_1$  calculated in the above way satisfy that the filter output voltage THD factor is not greater than 5%.

For the selected  $L_1$  and  $C_1$ , the filter characteristic impedance is

$$Z_0 = \sqrt{\frac{L_1}{C_1}} = \sqrt{\frac{9.5e-3}{1.5e-6}} = 80 \Omega \quad (9.192)$$

if damping resistance  $R_1 = 10 \Omega$ , so the filter quality factor is

$$Q = \frac{Z_0}{R_1} = \frac{80}{10} = 8 \quad (9.193)$$

The calculated quality factor is in the acceptable range of  $Q = 5-8$ , which gives a good filter quality and satisfies the dumping properties.

The nominal voltage of  $R_1$  is the same as for  $C_1$ .

The total power of  $R_1$  is the sum of two parts, related to  $f_{\text{out 1har}}$  and  $f_{\text{imp}}$ . For both frequencies, the impedances of  $C_1$  and  $R_1$  connected in series are

$$Z_{R1 \text{ 1har}} \approx X_{C1 \text{ 1har}} = \frac{1}{2\pi f_{\text{out 1har}} C_1} = \frac{1}{2\pi \cdot 100 \cdot 1.5e-6} = 1062 \Omega \quad (9.194)$$

$$Z_{R1 \text{ imp}} \approx X_{C1 \text{ imp}} = \frac{1}{2\pi f_{\text{imp}} C_1} = \frac{1}{2\pi \cdot 3300 \cdot 1.5e-6} = 32 \Omega \quad (9.195)$$

It is noticeable that the most important  $R_1$  power part is related to the ripple current. So finally the power of  $R_1$  should be

$$P_{R1} > R_1 \left[ \left( \frac{U_n}{\sqrt{3} Z_{R1 \text{ 1har}}} \right)^2 + \left( \frac{U_{\text{THD}}}{Z_{R1 \text{ imp}}} \right)^2 \right] = 10 \left[ \left( \frac{380}{\sqrt{3} \cdot 1062} \right)^2 + \left( \frac{0.05 \cdot 540}{32} \right)^2 \right] = 7.5 \text{ W} \quad (9.196)$$

and  $P_{R1} = 10 \text{ W}$  was selected.

### Problem 9.2

Design the differential filter (normal mode filter) with L, C, and R dampings for the drive with voltage inverter and induction motor. The filter topology is presented in Figure 9.29. The three-phase induction motor data is  $P_n = 5.5 \text{ kW}$ ,  $U_n = 400 \text{ V}$  (Y connected), and  $I_n = 11 \text{ A}$ . The inverter DC supply voltage is  $540 \text{ V}$ , transistors switching frequency is  $f_{\text{imp}} = 5 \text{ kHz}$ , and inverter output maximal frequency is  $f_{\text{out 1h}} = 80 \text{ Hz}$ . The desired system properties are switching ripple current  $\Delta I_s = 20\%$ . When the filter is calculated, prepare the simulation in Simulink (Hint: use the *sys\_LC\_filter.mdl* example).

**Solution:** Because the design process is the same as in Problem 9.1, so some comments are omitted and mainly the calculations and results are presented.

The motor ripple current:

$$\Delta I_s = 0.2 \cdot I_n = 0.2 \cdot 11 = 2.2 \text{ A} \quad (9.197)$$

The  $L_1$  inductance is

$$L_1 > 2 \frac{U_d}{\sqrt{2} \cdot 2 \cdot \pi \cdot f_{\text{imp}} \cdot 3 \cdot \Delta I_s} = 2 \frac{540}{\sqrt{2} \cdot 2 \cdot \pi \cdot 5000 \cdot 3 \cdot 2.2} = 1.8 \text{ mH} \quad (9.198)$$

The voltage drop on  $L_1$  is

$$\Delta U_1 = I_n 2\pi f_n L_1 = 11 \cdot 2\pi \cdot 50 \cdot 0.0018 = 6.2 \text{ V} \quad (9.199)$$

The resonant frequency  $f_{\text{res}}$  should fulfill condition:

$$800 < f_{\text{res}} < 2500 \quad (9.200)$$

so  $f_{\text{res}}$  is selected:

$$f_{\text{res}} = 1650 \quad (9.201)$$

Capacitance  $C_1$  is

$$C_1 = \frac{1}{4\pi^2 f_{\text{res}}^2 L_1} = \frac{1}{4 \cdot \pi^2 \cdot 1650^2 \cdot 0.0018} = 5.2 \mu\text{F} \quad (9.202)$$

The filter characteristic impedance is

$$Z_0 = \sqrt{\frac{L_1}{C_1}} = \sqrt{\frac{1.8\text{e}-3}{5.2\text{e}-6}} = 18.6 \Omega \quad (9.203)$$

For the quality factor  $Q=5$ , the  $R_1$  is

$$R_1 = \frac{Z_0}{Q} = \frac{18.6}{5} = 3.7 \Omega \quad (9.204)$$

The impedances  $Z_{R1 \text{ 1har}}$  and  $Z_{R1 \text{ imp}}$  are

$$Z_{R1 \text{ 1har}} \approx X_{C1 \text{ 1har}} = \frac{1}{2\pi f_{\text{out 1har}} C_1} = \frac{1}{2\pi \cdot 80 \cdot 5.2\text{e}-6} = 382 \Omega \quad (9.205)$$

$$Z_{R1 \text{ imp}} \approx X_{C1 \text{ imp}} = \frac{1}{2\pi f_{\text{imp}} C_1} = \frac{1}{2\pi \cdot 5000 \cdot 5.2\text{e}-6} = 6 \Omega \quad (9.206)$$

The power of  $R_1$  should be no less than

$$P_{R1} > R_1 \left[ \left( \frac{U_n}{\sqrt{3} Z_{R1 \text{ lhar}}} \right)^2 + \left( \frac{U_{\text{THD}}}{Z_{R1 \text{ imp}}} \right)^2 \right] = 3.7 \left[ \left( \frac{400}{\sqrt{3} \cdot 382} \right)^2 + \left( \frac{0.05 \cdot 540}{6} \right)^2 \right] = 76 \text{ W} \quad (9.207)$$

Power  $P_{R1} = 100 \text{ W}$  is selected.

## 9.11 Questions

Q1. Why does the common mode voltage appears in PWM voltage inverters?

A1. The common mode voltage is inherent for PWM voltage inverters. It is the result of transistors switching sequence. It should be explained by the analysis of zero voltage components for each voltage vector, as presented in Table 9.2.

Q2. Explain the bearing current phenomena.

A2. The bearing current phenomena are explained in Section 9.4.

Q3. Why is the differential mode filter used?

A3. The main purpose of the differential mode filter use is to obtain the sinusoidal motor supply voltage. As the result of the supply voltage shape improvement, the motor has greater efficiency, is less noisy, and the disturbance level is decreased.

Q4. Which type of filter is correct for bearing current limitation?

A4. The common mode filter limits the common mode current and bearing currents.

Q5. Specify the method for motor protection in the drive with a voltage inverter.

A5. This is explained in Section 9.5 and Table 9.3.

Q6. Describe the design process of the differential mode filter.

A6. The design process is presented in Section 9.61.

Q7. Describe the design process of the common mode filter.

A7. The design process is presented in Section 9.61.

Q8. Sketch the structure of the common mode choke. Where should the CM choke be installed?

A8. The structure of the common mode choke is presented in Figure 9.13, with a description given in Section 9.5.1. The CM choke is installed on the output of the voltage inverter?

Q9. If the long cable connection is used to connect the inverter and motor, where should the LC filter be installed? Explain why.

A9. The LC filter should always be installed close to the motor. It is because the sinusoidal shaped voltage is in the whole cable, which connects the inverter/filter with the motor. When the voltage in cable is sinusoidal in shape, the risk of inducted noise is strongly limited in comparison with the rectangular high  $dv/dt$  shape.

## References

1. Bose, B. K. (2009) Power electronics and motor drives recent progress and perspective. *IEEE Trans. Ind. Elec.*, **56**(2), February.

2. Erdman, J., Kerkman, R., Schlegel, D., and Skibinski, G. (1995) Effect of PWM inverters on AC motor bearing currents and shaft voltages. *IEEE APEC Conf.* Dallas, TX.
3. Muetze, A. and Binder, A. (2003) High frequency stator ground currents of inverter-fed squirrel-cage induction motors up to 500 kW. *EPE Conf.* Toulouse.
4. Akagi, H. (2002) Prospects and expectations of power electronics in the 21st century. *Power Conv. Conf. PCC'2002.* Osaka.
5. Akagi, H., Hasegawa H., and Doumoto, T. (2004) Design and performance of a passive EMI filter for use with a voltage-source PWM inverter having sinusoidal output voltage and zero common-mode voltage. *IEEE Trans. Power Elect.*, **19**(4), July.
6. Muetze, A. and Binder, A. (2007) Practical rules for assessment of inverter-induced bearing currents in inverter-fed AC motors up to 500 kW. *IEEE Trans. Ind. Elect.*, **54**(3), June.
7. Binder, A. and Muetze, A. (2008) Scaling effects of inverter-induced bearing currents in AC machines. *IEEE Trans. Ind. Appl.*, **44**(3), May/June.
8. Xiyu, C., Bin, Y., and Tu, G. (2002) The engineering design and optimization of inverter output RLC filter in AC motor drive system. *IECON, USA.*
9. Ogasawara, S. and Akagi, H. (1996) Modeling and damping of high-frequency leakage currents in PWM inverter-fed AC motor drive systems. *IEEE Trans. Ind. Appl.*, **22**(5), September/October.
10. Zitzelsberger, J. and Hofmann, W. (2003) Reduction of bearing currents by using asymmetric, space-vector-based switching patterns. *EPE'03, Toulouse.*
11. Cacciato, M., Consoli, A., Scarcella, G., and Testa, A. (1999) Reduction of common-mode currents in PWM inverter motor drives. *IEEE Trans. Ind. Appl.*, **35**(2), March/April.
12. Hofmann, W. and Zitzelsberger, J. (2006) PWM-control methods for common mode voltage minimization: A survey. *Int. Symp. Power Elect., Elect. Dr., Auto. Mot., SPEEDAM 2006*, 23–26 May, Taormina, Italy.
13. Lai, Y. S. and Shyu, F.-S. (2004) Optimal common-mode voltage reduction PWM technique for inverter control with consideration of the dead-time effects, Part I: Basic development. *IEEE Trans. Ind. Appl.*, **40**(6), November/December.
14. Ruderman, A. and Welch, R. (2005) Electrical machine PWM loss evaluation basics. *Int. Conf. Ener. Effic. Mot. Dr. Syst. (EEMODS)*, vol. 1, September, Heidelberg, Germany.
15. Ruifangi, L., Mi, C. C., Gao, D. W. (2008) Modeling of iron losses of electrical machines and transformers fed by PWM inverters. *IEEE Trans. Magn.*, **44**(8), August.
16. Yamazaki, K. and Fukushima, N. (2009) Experimental validation of iron loss model for rotating machines based on direct eddy current analysis of electrical steel sheets. *Elect. Mach. Dr. Conf., IEMDC'09*, 3–6 May, Miami, FL.
17. Krzeminski, Z. and Guziński, J. (2005) Output filter for voltage source inverter supplying induction motor. *Int. Conf. Power Elect., Intell. Mot. Power Qual., PCIM'05.* 7–9 June, Nuremberg.
18. Czapp, S. (2008) *The Effect of Earth Fault Current Harmonics on Tripping of Residual Current Devices.* International School on Non-sinusoidal Currents and Compensation, Łagów, Poland.
19. Franzo, G., Mazzucchelli, M., Puglisi, L. and Sciutto G. (1985) Analysis of PWM techniques using uniform sampling in variable-speed electrical drives with large speed range. *IEEE Trans. Ind. Appl.*, **IA-21**(4).
20. Rajashekara, K., Kawamura, A., and Matsuse, K. (1996) Sensorless control of AC motor drives. *IEEE Ind. Elect. Soc.*, IEEE Press, USA.
21. Kawabata, T., Miyashita T., and Yamamoto, Y. (1991) Digital control of three phase PWM inverter with LC filter. *IEEE Trans. Power Elect.*, **6**(1), January.
22. Seliga, R. and Koczara, W. (2001) Multiloop feedback control strategy in sine-wave voltage inverter for an adjustable speed cage induction motor drive system. *Eur. Conf. Power Elect. Appl., EPE'2001.* 27–29 August, Graz, Austria.
23. Adamowicz, M. and Guziński, J. (2005) Control of sensorless electric drive with inverter output filter. *4th Int. Symp. Auto. Cont. AUTSYM 2005.* 22–23 September. Wismar, Germany.

24. Guzinski, J. and Abu-Rub, H. (2008) Speed sensorless control of induction motors with inverter output filter. *Int. Rev. Elect. Eng.*, **3**(2), 337–343.
25. Salomaki, J. and Luomi, J. (2006) Vector control of an induction motor fed by a PWM inverter with output LC filter. *EPE J.*, **16**(1), February.
26. Krzemiński, Z. (2000) Sensorless control of the induction motor based on new observer. *PCIM 2000*. Nürnberg, Germany.
27. Guzinski, J. (2008) Closed loop control of AC drive with LC filter. *13th Int. Power Elect. Mot. Conf. EPE-PEMC 2008*. 1–3 September, Poznań, Poland.
28. Holtz, J. (1995) The representation of AC machine dynamics by complex signal flow graph. *IEEE Trans. Ind. Elect.*, **42**(3), June.
29. Abu-Rub, H. and Oikonomou, N. (2008) Sensorless observer system for induction motor control. *39th IEEE Power Elect. Spec. Conf., PESCO'08*, 15–19 June, Rodos, Greece.
30. Abu-Rub, H., Guzinski, J., Rodriguez, J., Kennel, R., and Cortés, P. (2010) Predictive current controller for sensorless induction motor drive. *IEEE-ICIT 2010*, Vina del Mar, Valparaiso, Chile.
31. Vas, P. (1990) *Vector Control of AC Machines*. Oxford University Press, Oxford.
32. Krzemiński, Z. (1987) Non-linear control of induction motor. *Proc. 10th IFAC World Cong. Auto. Cont.*, vol. 3, Munich.
33. Bogalecka, E. (1992) Control system of an induction machine. *EDPE 1992*, High Tatras, Stara Lesna, Slovakia.
34. Isidori, A. (1995) *Non-linear Control Systems*, 3rd edn. Springer-Verlag, London.
35. Kaźmierkowski, M.P., and Malesani, L. (1998) Current control techniques for three-phase voltage-source PWM converters: A Survey. *IEEE Trans. Ind. Elect.*, **45**(5), 691–703.
36. Tsuji, M., Ohta, T., Izumi, K. and Yamada, E. A. (1997) Speed sensorless vector-controlled method for induction motors using  $q$ -axis flux. *IPEMC*. Hangzhou, China.
37. Guzinski, J. (2009) Sensorless AC drive control with LC filter. *13th Eur. Conf. Power Elect. App. EPE 2009*. 8–10 September. Barcelona.
38. Krzemiński, Z. (2008) Observer of induction motor speed based on exact disturbance model. *Proc. Int. Conf. EPE-PEMC 2008*, Poznan, Poland.
39. Kubota, H., Sato, I., Tamura, Y., Matsuse, K., Ohta, H., and Hori, Y. (2002) Regenerating-mode low-speed operation of sensorless induction motor drive with adaptive observer. *IEEE Trans. Ind. App.* **38**(4), July/August.
40. Sun Y., Esmaeli A., Sun L. (2006) A new method to mitigate the adverse effects of PWM inverter, 1st IEEE Conference on Industrial Electronic and Applications. *ICIEA'06*, 24–26, May, Singapore.



# Index

- AC machines models, 19
- Active power, 153
- Adjacent line-to-line voltage, 311, 317
- Artificial neural network, 5
- Arbitrary common reference frame *see* machine model, 298
  
- Back EMF, *see* Electromotive force
- Base values, 406
- Bearing
  - capacitance, 408–409
  - circulating current, 411
  - current, 404, 410
    - calculation, 410
    - classification, 410–20
    - reduction, 410–11
    - types, *see* Bearing current classification
  - discharging current, 410
- BLDC, 234–5
- Butterworth filter, 206–207, 223
  
- Cable parameters, 409
- Choke
  - 3 phase, 404
  - E shape, 404
  - toroidal, 404, 412–13, 422, 433
- Clarke transformation, *see* transformation Clarke
- Common mode
  - circuit, 408
  - component, 404, 415
  - filter, 402
    - inductance, 434
    - magnetic field density, 433
  - choke, 412–14, 423
    - design, 433
  - current, 409
    - path, 409
  - flux, 433
  - motor parameters, 410
  - reduction, 415
    - active zero voltage vector AZVC, AZVC-1, AZVC-2, 418–20
    - three active vectors 3AVM, 418
  - transformer 414–15
    - equivalent circuit, 415
  - voltage, 11, 60, 307, 309, 405–406, 408, 415–20
    - reduction, 415
    - waveform, 406
- Comparator
  - flux comparator, 183, 236, 240
  - torque comparator, 183, 236, 240–42
- Compensation, 202, 211, 213–17
- Computational, 233
- Control problems, 447–61
- Co-ordinate Transformation, *see* motor model, 297
- Cost function *see* Model Predictive Control, 355
- Current limit, 153
  
- Damper winding, 235
- DC motor, 19–24
  - separately excited, 20–22
    - analogy, 143–4
    - series excited, 22–4
- DC link, 305, 307, 310, 316, 321, 332
- Dead time, 307
  - dead band, 53
  - effect, 129
- Direct torque control, 6, 8
- Differential mode, *see* Sinusoidal filter
- Double fed induction generator
  - autonomous generation system 153
  - base values, 34
  - control system, 158–9

- Double fed induction generator (*Continued*)  
 grid connected system, 153–4  
 model, 32–5  
 vector control, 153–9
- DSC direct self control, 253
- DTC direct torque control, 173–6, 179, 182–5,  
 189, 191–7, 199–200, 202, 206, 209,  
 211–20, 227, 229–30, 233–4, 236–7,  
 243–4, 253–4
- Dumping resistance, 414
- dv/dt 401  
 effects, 401, 437  
 filters, 401, 411
- Dwell time, *see* Space vector PWM, 75
- Dynamic model, 179, 181, 199–200, 202,  
 209, 234
- Electric drive system, 2, 5, 10
- Electromotive force EMF, 23  
 estimation, 467
- Estimation, 172, 182–4, 206, 213, 233,  
 237, 239,
- Field oriented method 139, 145–6, 344, 347  
 direct, 148–9  
 with filter, 449–53  
 indirect, 148–9  
 stator oriented, 152
- Field weakening control, 152–3
- Five-phase, 293  
 five-phase drive system, 294  
 five-phase induction motor model, 295  
 five-phase inverter model, 307  
 five-phase supply, 327  
 five-phase VSI, 304, 307, 310, 326, 328
- Fourier Series, 48, 316
- Flux  
 adaptive observer, 150–51  
 air gap flux, 205–206, 234  
 estimation, 141–2, 149  
 rotor rotor flux, 173–6, 186, 233–4, 236, 253  
 stator stator flux, 172–9, 181–8, 191–4, 196,  
 198–9, 205–6, 208–9, 211, 213, 220, 222,  
 224, 228, 233, 236–7, 239–41, 243, 246,  
 249, 251–2
- Flux vector acceleration, 254
- Frequency modulation ratio, 49, 66
- Gate drive signal, 307–8
- High performance drive, 6, 9
- Hysteresis band, 172–4, 177–9, 182, 233, 240,  
 242, 252
- Impedance, 429–30, 473  
 base, 407  
 characteristic, 473–4  
 wave, 403, 415
- Impedance Source or Z-Source inverter, 117
- Induction motor, 172–4, 176, 179, 182–7, 191,  
 193–5, 199–203, 209–11, 214, 217–18,  
 220, 226, 229, 233  
 common mode model, 404–408  
 dq model, 144  
 five phase, 388–96  
 control, 388–96  
 parameters, 396  
 machine control, 139–53  
 per unit model, 30–32  
 scalar control, 139–40  
 sensorless control, 365–80  
 squirrel cage, 25, 139  
 stator resistance, 141  
 vector control, 143–9
- Inverter output filter, 420  
 control, 447–61  
 design, 425–33  
 estimation, 440–47  
 structures, 420–25
- Iron losses, 185, 202–203, 206, 209–20, 224,  
 226–32
- LC filter, *see* Sinusoidal filter, 4
- Leg/pole Voltage  
 five-phase, 307, 309–10  
 three-phase, 62
- Load angle control, 461–4
- Long cable connection, 401–402, 421, 465
- Look-up table, 179, 187, 189, 243
- Maximum torque production, 153
- Magnetizing inductance, 180–81, 218–20, 225
- Matlab, 182, 184–5, 191, 199, 202, 209, 218,  
 236, 243
- Medium voltage drive, 10
- Model reference adaptive system MRAS, *see*  
 Observer model reference adaptive system
- Modulation index definition, 49, 51
- Model predictive control, 352, 354
- Model transformation, *see* Five-phase, 297
- Motor torque, 297

- Multi-loop control, 448–9, 461
- Multi-phase, 293–4
- Multi-level inverters, 104, 326
  - cascaded H-bridge, 112
  - diode clamped, 106
  - flying capacitor, 109
- Multiscalar control with filter, 457–61
  
- Nonlinear field oriented method NFOC with filter, 6, 453–6
- Normal mode filter, *see* Sinusoidal filter
- Non-adjacent line-to-line voltage, 311, 316–17
  
- Observer, 9, 442–7
  - adaptive back stepping, 383–5
  - close loop, 366–75, 445–7
    - structure 1, 367–9
    - structure 2, 370–72
    - structure 3, 372–5
  - disturbance, *see* Observer speed
  - flux, *see* Observer close loop
  - Luenberger, 151
  - model reference adaptive system MRAS, 365, 375–8
    - five-phase induction motor, 388–9
    - observer 1 structure, 376–8
    - PMSM, 385–8
    - speed estimator, 389–96
  - simple, *see* Observer close loop
  - speed, 366, 442–5
- Over-modulation, 90
  - over-modulation I, 91
  - over-modulation II, 94
  
- Parasitic
  - capacitances, 402, 408
  - current, 408–409
- Passive filter, 401–402, 411–12
- Park transformation, 25, 29–30
- Per unit system, 14, 38–9, 406
- Permanent magnet synchronous motor, 160–68
  - back EMF observer, 380–82
  - control, 164–5, 382–3
    - scalar, 166–8
    - sensorless, 380–88
  - model, 35–6, 162
    - base values, 39
    - in  $\alpha\beta$  coordinates, 40–41
    - in dq coordinates, 36–8
    - in per unit, 38–40
    - properties, 161
    - vector control, 160–61
- Phase shifting network, 321
- Phase variable model, *see* Five-phase induction motor, 295
- Phase voltage or phase-to-neutral voltage, 62, 307, 309
- PI controller, *see* Proportional-integral PI controller
- Power calculation, 153, 158, 378, 380
- Power measurement, *see* Power calculation
- PMSM, 233–7, 239, 243–8, 250–52
- Predictive control, 233
- Predictive current control with filter, 461–71
- Proportional-integral PI controller, 142–3, 145, 158–9, 303, 346–7, 375, 386, 391, 439, 456, 457, 461
  - cascaded, 163
- Pulse width modulation PWM, 4, 326, 328
  - ANN based PWM, 96
  - carrier-based PWM, 64, 328, 332, 335
  - discontinuous PWM, 46, 77
  - fifth harmonic injection, 332–3, 337
  - offset addition, three-phase, 69, 71
    - five-phase, 336
  - space vector PWM three-phase, 72
    - five-phase, 294, 338, 342
  - sinusoidal PWM control, 294
  - synchronous and asynchronous, 51
  - third harmonic injection, 67
  - unipolar, bipolar, 55–6
  - modifications, 415–20
  
- Quality factor, 429, 431, 434, 473–4
- Quasi impedance source or qZSI inverter, 127
  
- Reactive power, 153
- Ripple
  - flux ripple, 191, 233
- Torque ripple, 191, 196, 200, 211, 233
- Ripple inductor current, 428, 472–4
- Rotor flux estimation, 149
  
- Saturation, 179, 184–5, 217–20, 224, 227–32
- Sensorless speed control, 5, 9, 365
- Sector, 172–3, 176–9, 183–5, 187–8, 236, 239–41
- Simulation, 181–2, 184–5, 191, 193–4, 199–202, 206, 209, 214, 217–18, 220, 229–30, 233, 236–8, 243

- Simulink, 182, 184–6, 189–91, 199, 202, 209, 218, 229, 236–7, 243
- Sinusoidal filter, 401, 421–2, 425–7, 429
  - characteristics, 430
  - circuit, 430
  - design, 429–30
  - elements, *see* Sinusoidal filter design
  - model, 437, 439
- Sinusoidal wave shape, 233
- Six-step mode, 60
- Space vector, 25
  - five-phase, 328
  - representations of AC machines, 143
  - three-phase, 72
- Space Vector Modulation, 233
- Speed control, 172–3, 182–5, 191, 193–7, 199, 202, 209, 211–12, 214, 216–8, 229–30, 243, 252
- SPMSM, 233–7, 239, 243–8, 250–52
- Stator current relationship, 157
- Steady state equivalent circuit, *see* Five-phase system, 300
- SVPWM, 233
- Switching combination 405
- Switching Frequency
  - changing switching frequency, 233
  - constant switching frequency, 233
- Switching table, 176, 178, 183, 185, 187, 236, 243
- Ten step operation, *see* Five-phase system, 294, 310
- Torque control, 171–6, 177–9, 181–2, 185, 193, 196, 199, 202, 206, 213–15, 218, 220, 227–9, 233, 236
- Transformation
  - Clarke, 26–9, 145
  - matrix constant
    - magnitude, 403
    - power, 404
  - Park, 29–30
  - variables, 147, 156–7, 164
- Trapezoidal wave shape, 234
- Uniform cylindrical surface, 234
- Variable speed drives, 235
- Voltage source inverter, *see* three-phase, 56
  - five-phase, 304, 307, 310, 326, 328
- Voltage space vector, 173–7, 182, 185, 187, 190, 233
- Wind generation systems, 154
- Zero sequence component, *see* Common mode, 331